UNIVERSITÉ DU LUXEMBOURG

PhD-FSTM-2022-047
The Faculty of Science, Technology and Medicine

DISSERTATION

Defence held on 17/05/2022 in Esch-sur-Alzette

to obtain the degree of

DOCTEUR DE L'UNIVERSITÉ DU LUXEMBOURG

EN BIOLOGIE

by

Yahaya Abubakar YABO
Born on 20 May 1987 in Yabo (Nigeria)

INTERROGATING INTRA-TUMORAL HETEROGENEITY AND TREATMENT RESISTANCE IN GLIOBLASTOMA PATIENT DERIVED XENOGRAFT MODELS USING SINGLE-CELL RNA SEQUENCING

Dissertation defence committee

Dr Anna Golebiewska, dissertation supervisor
Group leader, Luxembourg Institute of Health

Dr Tobias Weiss
University of Zurich

Dr Alexander Skupin, Chairman
Professor, Université du Luxembourg

Dr Andrei Zinovyev
Scientific Coordinator of Cancer Systems Biology, Institut Curie

Dr Simone P. Niclou, Vice Chairman
Director, Department of Cancer Research, Luxembourg Institute of Health
Professor, University of Bergen

Dissertation Supervisor

Dr. Anna Golebiewska

Dissertation Defense Committee

Prof. Dr. Alexander Skupin, Chairman

University of Luxembourg (Luxembourg)

Prof. Dr. Simone Niclou, Vice-chairman

University of Luxembourg (Luxembourg)

Dr. Anna Golebiewska, Dissertation supervisor and jury member

Luxembourg Institute of Health (Luxembourg)

Dr. Tobias Weiss, Jury member

University of Zurich (Switzerland)

Dr. Andrei Zinovyev, Jury member

Institut Curie (France)

The work presented in this thesis was conducted at the:

NORLUX Neuro-oncology Laboratory

Department of Oncology

Luxembourg Institute of Health

The work presented in this thesis was supported by:

GLIOTRAIN Horizon 2020 ITN

This project was funded by the European Union's Horizon 2020 research and innovation programme under the Marie Skłodowska-Curie Actions

Grant agreement No 766069

H2020-MSCA-ITN-2017
Grant Agreement number: 766069

Doctoral School in Systems and Molecular Biomedecine (DS_SMB)

University of Luxembourg

Fondation du Pélican de Mie et Pierre Hippert-Faber

Under the aegis of the Fondation de Luxembourg

Affidavit

I Yahaya Abubakar Yabo hereby confirm that the PhD Thesis entitled “Interrogating Intra-Tumoral Heterogeneity and Treatment Resistance in Glioblastoma Patient-Derived Xenograft Models Using Single-Cell RNA Sequencing” has been written independently and without any other sources than cited.

Luxembourg, the 7th April 2022

Dedication

To my parents Mallam Garba Yabo and Hajiya Halimatu Shehu Shagari

Acknowledgments

As the saying goes, whatever has a beginning must have an end, and so does my PhD journey. Although I enjoyed most of this journey, I must admit that the last months of this journey seem like an eternity. For this, I am immensely grateful to God Almighty for the health, strength, courage, and guidance He bestowed on me while undertaking this enormous and difficult journey. I always find solace in Him when overwhelmed, especially during the toughest moments.

Like every good thing, this PhD had the support of so many people, I would like to use this medium to acknowledge their support.

First, I would like to express my gratitude to Anna for the support and mentorship you have given me over the last 4 years. You were a great teacher, my advocate, and my promoter. You promoted me like your own brand and patiently guided me through this journey. I appreciate the trust and the freedom you gave me to pursue this work and for always pushing me beyond my imaginary boundaries. I learned so much under your supervision and have grown as a scientist under your mentorship. Even beyond science, I learned so much from you, especially your diplomatic skills in handling complex and tense situations. I am glad and thankful that we had a peaceful mentor-mentee relationship. You have been generous to me both with your time, advice, and even beyond. You never scolded me for pestering you with the “good” and the “bad” news about my work and sometimes the “not really bad” as you would say. As far as I could remember, we agree on almost everything except of course the choice of colors for the plots.

To Simone, thank you for giving me the rare and valuable opportunity to do my PhD in your lab. There is no better place for me to do my PhD than the NORLUX lab. I am grateful and proud of all the collaborative opportunities and the training I received. You are a role model we all admire for your scientific rigor, management strategy, and professionalism. Always remember that you have made the dream of a “little poor boy” become a reality.

This thesis would not have been possible without the funding from the EU-H2020 MSCA ITN project. Thank you Prof. Annette Byrne and all the GLIOTRAIN consortium members for this great initiative and the feedback during the annual meetings. Thanks to Alice for a great job managing the project and for providing all the support to the ESRs right from onboarding until the last day.

I would like to extend my special thanks to Dr. Alexander Skupin for agreeing to be part of my CET committee. Your support and feedback over the years have immensely helped in shaping this work to its current form. I am also very grateful to Dr. Tobias Weiss and Dr. Andrei Zinovyev for agreeing to be the external jury members.

While undertaking this project, I had the opportunity of working with many people beyond my group and institution. A big thanks to Alessandro and the NIG team members, especially Aurelie for the several meetings and your unrelenting support and feedback in the PDOX TME project. Thanks to Petr and Reka as well as Tony and Arnaud from the BIOMOD group at LIH, I appreciate and learned so much from the several meetings and discussions we had. Thanks to Kamil, Thais, and Dimitrios from the Integrative signaling group at LSCB. I wish to also thank Andreas Kremer and his team at ITTM for hosting me during my secondment. Thanks to the Pelican foundation sponsorship, I had the rare opportunity of working as a visiting researcher in the lab of Prof. Roel Verhaak at the Jackson Laboratory of genomic medicine, USA. Thank you Roel, for accepting me, and thanks to all the lab members especially the two Kevins (K^2) and Floris for exposing me to the world of big data genomics and the US academia.

Andres, Mohammed, Yolanda, Rédouane and Carina, how time flies? I have learned so much from you guys, from the administration to life in Lux, to your PhD experiences and the several happy moments we shared together. Hugo later joined us with so much humor, and Lara finally completed the circle in the office. You have all been amazing colleagues and I cherish every moment with you in that office. Thank you Lara and Hugo for the lengthy discussions we had about the exotic life in Africa, you always reminded me about home and my childhood, and I hope you will travel to Africa one day. To the new office mates, Kim, Andrea, Frida, Lucas, and Hanane, thank you for your company in the last few months. To Mohaned and other PhD students at DoCR, you have all been nice and friendly. I wish you all success in your projects.

To my other colleagues at NORLUX lab, it has been a great pleasure to work with you all. I appreciate your constant support and feedback. Special thanks to Anais, for implanting the PDOX models. Thanks to Virginie B. and the biopsy team, indeed you are the bedrock of my work and that of many others in the lab. Thank you Sabrina, Ann-Christin, Virginie N., and Monika for your kind feedback and guidance. Maggie, Anuja, Luca, and Mahsa thank you all for the words of encouragement and support, I appreciate your kindness and wish you success in your projects. Pilar, thank you for all the amazing stainings and the flow data, I wish you a lot of success in your project. Fred, you have been very nice and kind-

hearted to me, I appreciate your support. I would also like to appreciate the administrative support and guidance I received over the years from Malou, Magali, and Siu-Thin. You have been very helpful in this journey. To other colleagues in DoCR, especially Eric and Clement, thank you for the discussions during the departmental and CANBIO meetings and privately.

To all my teachers and mentors, especially Profs. A. A. Mohammed, A. A. Magaji, U. M. Chafe, B. R. Alkali, A. U. Junaidu, F.M Tambuwal, M. S. Abubakar, A. S. Yakubu, Edilbert Van Driessche, Drs. Aminu Shittu, Pieter Monsieurs, Faruku Bande, Abdussalam Isiaku, and many others too numerous to mention, you were my inspiration and you guided me towards this path, thank you so much for your guidance. To my friends, colleagues, and well-wishers in Nigeria, I appreciate all your cheers, words of encouragement, the exchanges on social media, and most importantly your prayers. Those kept me going and undaunted throughout this journey. I could not afford to disappoint you all.

A special thanks to my lovely wife Asma'u and my kids Ammar and Halimatu. You are my pillars and supporters. You endured several days of my absence, even during the toughest times of the century, the COVID-19 pandemic. I owe you so much time that I hope to pay back someday. I would like you to know that my absence was not because I don't care, but because that is my way of showing I do really care. To all my siblings and other family members, you painstakingly took care of all my needs in Nigeria while I am here, thank you all for the unconditional love and support.

It is sad and unfortunate that my parents did not live long to witness this day. I am sure my dad had imagined a day like this and my mom had been hopeful and prayerful that I would go this far in life. I am sure they would have been over the moon on a day like this, as they have always been whenever I return home at the end of every school year with prizes. You have both sacrificed so much to get me educated, I am sorry you cannot be here to see the fruit of your labor, may God Almighty grant you both paradise. I will end by paraphrasing the words of the 2003 Nobel laureate in Literature J. M. Coetzee ***"And for whom, anyway, do we do the things that lead to" a PhD "if not for our mothers?"***.

List of figures

List of abbreviations

A

aCGH	-	Array-Comparative Genomic Hybridization
ACOD1	-	Aconitate Decarboxylase 1
AC	-	Astrocytic
α-KG	-	Alpha-ketoglutarate
ALA	-	Aminolevulinic acid
APC	-	Antigen Presenting Cells
ATRX	-	Alpha Thalassemia/mental Retardation Syndrome X-linked

B

BAMs	-	Border-Associated Macrophages
BBB	-	Blood Brain Barrier
BER	-	Base Excision Repair
bFGF	-	Basic Fibroblast Growth Factor
BMDM	-	Bone Marrow-Derived Macrophages
BSA	-	Bovine Serum Albumin
BTIC	-	Brain-Tumor Initiating Cell

C

Ca2+	-	Ionized Calcium
CaCl2	-	Calcium Chloride
CAR	-	Chimeric antigen receptor
CBTRUS	-	Central Brain Tumor Registry of the United States
CDK	-	Cyclin Dependent Kinase
CDKN	-	Cyclin Dependent Kinase Inhibitor
cDNA	-	Complementary Deoxyribonucleic Acid
CHI31	-	Chitinase 3 Like 1
ChIP-seq	-	Chromatin immunoprecipitation sequencing
CHI3L1	-	Chitinase 3-like 1
CIC	-	Capicua
cIMPACT	-	Consortium to Inform Molecular and Practical Approaches to CNS Tumor Taxonomy
CL	-	Classical
CNA	-	Copy number alteration
CNER	-	National Ethics Committee for Research
CNS	-	Central Nervous System
CNV	-	Copy Number Variation
CO2	-	Carbon Dioxide
CRISPR	-	Clustered regularly interspaced short palindromic repeats
CSC	-	Cancer Stem Cell
CSF-1R	-	Colony-stimulating factor-1 receptor
CTLA	-	Cytotoxic T-lymphocyte–associated antigen
CTR	-	Control
Cx43	-	Connexin 43

D

dH2O	-	Distilled Water
DAPI	-	4′,6-Diamidin-2-phenylindol
DEG	-	Differentially expressed genes
DC	-	Dendritic Cells
DGE	-	Digital Gene Expression
DMEM	-	Dulbecco's Modified Eagle Medium
DMSO	-	Dimethyl Sulfoxide
DNA	-	Deoxyribonucleic Acid
DNMTs	-	DNA methyltransferases
DSB	-	Double-strand break

E

ECM	-	Extracellular Matrix
ecDNA	-	Extrachromosomal DNA
EDTA	-	Ethylenediaminetetraacetic Acid
EEG	-	Electroencephalography
eGFP	-	enhanced Green Fluorescent Protein
EGF	-	Epidermal Growth Factor
EGFR	-	Epidermal Growth Factor Receptor
EU	-	European Union
EV	-	Extracellular Vesicles

F

FACS	-	Fluorescence Activated Cell Sorting
FBS	-	Fetal Bovine Serum
FDA	-	Food and Drug Administration
FGFR	-	Fibroblast Growth Factor Receptor
FOV	-	Field of View
FSC	-	Forward Scatter
FUBP1	-	Far Upstream Element Binding Protein 1

G

Gap43	-	Growth-associated protein 43
GBM	-	Glioblastoma
G-CIMP	-	CpG island methylator phenotype
GEMMs	-	Genetically engineered mouse models
GFAP	-	Glial Fibrillary Acidic Protein
GL261	-	Glioma 261
GLOBACON	-	Global Cancer Data
GPM	-	Glycolytic/plurimetabolic
GSC	-	Glioma Stem Cells

H

HBSS	-	Hank's Balanced Salt Solution
H&E	-	Hematoxylin and Eosin
HIF	-	Hypoxia Inducible Factor
2-HG	-	2-hydroxyglutarate

HGG	-	High grade gliomas
H_2O	-	Water
HR	-	Homologous recombination
I		
IDH	-	Isocitrate Dehydrogenase
IFNγ	-	Interferon gamma
IL13RA2	-	Interleukin-13 receptor subunit alpha-2
ITH	-	Intratumoural heterogeneity
J		
JAK	-	Janus Kinase
L		
LIF	-	Leukemia Inhibitory Factor
M		
MAPK	-	Mitogen-activated protein kinase
MARCO	-	Macrophage receptor with collagenous structure
MDM	-	Monocyte-derived macrophage
MET	-	MET Proto-Oncogene, Receptor Tyrosine Kinase
MES	-	Mesenchymal
Mg	-	Microglia
Mg2+	-	Ionized Magnesium
MGMT	-	O^6-methylguanine-DNA methyltransferase
MHC	-	Major histocompatibility complex
MIR	-	Mortality-to-incidence ratio
MLH1	-	MutL Homolog 1
MMPs	-	Matrix metalloproteinases
MRI	-	Magnetic Resonance Images
mRNA	-	Messenger Ribonucleic Acid
MTC	-	Mitochondrial
N		
N2	-	Nitrogen
NES	-	Nestin
NEU	-	Neuronal
NF1	-	Neurofibromin 1
NG2	-	Neuron-glial antigen 2
NHEJ	-	Non-homologous end-joining
NK	-	Natural killer
NLGN3	-	Neuroligin-3
NOD/SCID	-	Non-Obese Diabetic/ Severe Combined Immunodeficiency
NOS	-	Not Otherwise Specified
NPC	-	Neural progenitor cells
NSC	-	Neural Stem Cell
NSG	-	NOD/SCID gamma

O

O_2	-	Oxygen
Olig2	-	Oligodendrocyte Transcription Factor 2
OPC	-	Oligodendrocyte progenitor cell
OPN	-	Osteopontin
OS	-	Overall survival

P

PBS	-	Phosphate Buffered Saline
PD-1	-	Programmed cell death protein 1
PDGFRα	-	Platelet Derived Growth Factor Receptor Alpha
PCR	-	Polymerase Chain Reaction
PCNA	-	Proliferating Cell Nuclear Antigen
PDOX	-	Patient Derived Orthotopic Xenograft
PDX	-	Patient Derived Xenograft
PI3K	-	Phosphatidylinositol-4,5-Bisphosphate 3-Kinase Catalytic Subunit Alpha
PFA	-	Paraformaldehyde
PN	-	Proneural
PPR	-	Proliferative/progenitor
PROM1	-	Prominin 1
PTEN	-	Phosphatase and Tensin Homolog
PTPRZ1	-	Protein tyrosine phosphatase receptor type Z1

R

RB1	-	RB Transcriptional Corepressor 1
RNA	-	Ribonucleic Acid
RNA-seq	-	RNA-Sequencing
RTK	-	Receptor Tyrosine Kinase

S

scATAC-seq	-	Single cell assay for transposase-accessible chromatin with high-throughput sequencing
scDNA-seq	-	Single Cell DNA Sequencing
scDNAme	-	Single-cell DNA methylation
scRNA-seq	-	Single Cell RNA Sequencing
SEPP1	-	Selenoprotein P
SEM	-	Standard Error of the Mean
SIP1	-	Sphingosine-1-Phosphate 1
SLC12A5	-	Solute Carrier Family 12 Member 5
snRNA-seq	-	Single nuclei RNA sequencing
SSB	-	Single-Strand Break
SSC	-	Side Scatter
SSEA-1	-	Stage-Specific Embryonic Antigen 1
STAT	-	Signal Transducer and Activator of Transcription
SPF	-	Specific-Pathogen-Free
SOX	-	Sex determining region Y-box

T

TAM	-	Tumor associated microglia/macrophages
TBS	-	Tris-Buffered Saline
TCA	-	Tricarboxylic acid
TCGA	-	The Cancer Genome Atlas
TCR	-	T-cell receptor
TERT	-	Telomerase reverse transcriptase
TF	-	Transcription factor
TGF-β	-	Growth factor-β
TIC	-	Tumor initiating cell
TIL	-	Tumor inlfiltrating lymphocytes
TME	-	Tumor microenvironment
TMZ	-	Temozolomide
TOP2A	-	DNA Topoisomerase II Alpha
TP53	-	Tumor Protein P53
tRNA	-	Transfer Ribonucleic Acid
tSNE	-	t-Distributed Stochastic Neighbor Embedding
Ttyh1	-	Tweety-homolog 1
TTFields	-	Tumor treating fields
TUBB3	-	Tubulin Beta 3 Class III

U

UMAP	-	Uniform Manifold Approximation and Projection
UMI	-	Unique Molecular Identifier
USA	-	United States of America

V

VEGF	-	Vascular Endothelial Growth Factor
VHL	-	van Hippel-Lindau
VIM	-	Vimentin

W

WES	-	Whole Exome Sequencing
WGS	-	Whole-genome sequencing
WHO	-	World Health Organization

Y

YAP/TAZ	-	Yes-associated protein/ tafazzin

Original publications

This thesis is based on the following listed original publications. Certain topics presented in Chapter 1 (Introduction) are further elaborated in the review publication presented in Chapter 3.

I. **Yabo, Y. A**., Niclou, S. P., & Golebiewska, A. (2021). Cancer cell heterogeneity and plasticity: A paradigm shift in glioblastoma. Neuro-oncology, noab269. https://doi.org/10.1093/neuonc/noab269

II. Oudin, A., Baus, V., Barthelemy, V., Fabian, C., Klein, E., Dieterle, M., Wantz, M., Hau, A. C., Dording, C., Bernard, A., Michelucci, A., **Yabo, Y. A.**, Kanli, G., Keunen, O., Bjerkvig, R., Niclou, S. P., & Golebiewska, A. (2021). Protocol for derivation of organoids and patient-derived orthotopic xenografts from glioma patient tumors. STAR protocols, 2(2), 100534. https://doi.org/10.1016/j.xpro.2021.100534

III. Golebiewska, A., Hau, A. C., Oudin, A., Stieber, D., **Yabo, Y. A.**, Baus, V., Barthelemy, V., Klein, E., Bougnaud, S., Keunen, O., Wantz, M., Michelucci, A., Neirinckx, V., Muller, A., Kaoma, T., Nazarov, P. V., Azuaje, F., De Falco, A., Flies, B., Richart, L., … Niclou, S. P. (2020). Patient-derived organoids and orthotopic xenografts of primary and recurrent gliomas represent relevant patient avatars for precision oncology. Acta neuropathologica, 140(6), 919–949. https://doi.org/10.1007/s00401-020-02226-7

IV. **Yabo, Y. A.**, Pires-Afonso, Y., Moreno-Sanchez, P. M., Oudin, A., Kaoma, T., Toth, R., Kyriakis, D., Grzyb, K., Poovathingal, S. K., Klink, B., Poli, A., Hertel, F., Mittelbronn, M., Nazarov, P. V., Skupin, A., Niclou, S. P., Michelucci, A., Golebiewska, A. (2022) Glioblastoma instructed microglia transit to heterogeneous phenotypic states with dendritic cell-like features in patient tumors and patient-derived orthotopic xenografts.

Other publications

The following publications also form a substantial amount of my PhD work but are out of the focus of this thesis. They are presented in the Annex section as listed below.

I. **Yabo, Y. A** , Oudin, A., Grzyb, K , Nazarov, P. V., Skupin, A., Niclou, S. P., Golebiewska A. Deciphering treatment-induced changes in tumor cells and TME in GBM PDOXs using scRNA-seq. Preliminary results.

II. Pires-Afonso, Y., Muller, A., Grzyb, K., Oudin, A., **Yabo, Y. A.**, Sousa, C., Scafidi, A., Poli, A., Cosma, A., Halder, R., Coowar, D., Golebiewska, A., Skupin, A., Niclou, S. P., Michelucci, A. (2021) Elucidating tumour-associated microglia/macrophage diversity along glioblastoma progression and under ACOD1 deficiency. Under revision in Molecular Oncology

Abstract

Despite available treatment options for glioblastoma (GBM), GBM has one of the poorest prognosis, resist treatment, and recur aggressively in the majority of cases. Intra-tumoral heterogeneity and phenotypic plasticity are major factors contributing to treatment resistance and underlie tumor escape in GBM. Several potential therapeutic agents showing promising therapeutic effects against GBMs at the preclinical level failed to translate into effective therapies for GBM patients. This is partly attributed to the inadequacy of preclinical models to fully recapitulate the complex biology of human GBMs. This project aimed to characterize the transcriptomic heterogeneity and understand the dynamic GBM ecosystem in patient-derived xenograft (PDOX) models at the single-cell level. To achieve this aim, I established cell purification and cryopreservation protocols that enable the generation of high-quality single-cell RNA seq data from PDOX models including longitudinal and treated PDOXs. Different computational strategies were used to interrogate the transcriptomic features as well as the interactions between GBM cells and the surrounding microenvironment. This work critically analyzed and discussed key components contributing to intra-tumoral heterogeneity and phenotypic plasticity within the GBM ecosystem and their potential contributions to treatment resistance. Here, we provide evidence that PDOX models retain histopathologic and transcriptomic features of parental human GBMs. PDOX models were further shown to recapitulate major tumor microenvironment (TME) components identified in human GBMs. Cells within the GBM ecosystem were shown to display GBM-specific transcriptomic features, indicating active TME crosstalk in PDOX models. Tumor-associated microglia/macrophages were shown to be heterogeneous and display the most prominent transcriptomic adaptations following crosstalk with GBM cells. The myeloid cells in PDOXs and human GBM displayed a microglia-derived TAMs signature. Notably, GBM-educated microglia display immunologic features of migration, phagocytosis, and antigen presentation that indicates the functional role of microglia in the GBM TME. Taking advantage of a cohort of longitudinal PDOXs and treated PDOX models, I demonstrated the utility of PDOX models in elucidating longitudinal changes in GBM. We show that temozolomide treatment leads to transcriptomic adaptation of not only the GBM tumor cells but also adjacent TME components. Overall, this work further highlights the importance and the clinical relevance of PDOX models for the testing of novel therapeutics including immunotherapies targeting certain tumor TME components in GBM.

Table of contents

Chapter 1

General Introduction

1.1 Cancer: a general overview

Cancer stands out as the number one leading cause of death in Luxembourg and most other European countries (Sung et al., 2021). In Luxembourg, four different cancer types account for 4 out of the 10 top diseases with the highest mortality rates across all ages in 2019. According to the World Health Organization (WHO), cancer is currently the number one leading cause of premature deaths in people below the age of 70 worldwide (Sung et al., 2021). About 19.3 million new cancer cases and 10 million cancer-related deaths are estimated to have occurred worldwide in 2020 according to the global cancer data (Sung et al., 2021). By the year 2040, the global cancer burden is estimated to rise to about 28.4 million cases. In Europe alone, over 4.2 million cancer cases were estimated to have occurred with about 2 million deaths in 2020. Luxembourg had an estimated 3,271 cancer cases with an estimated 1,121 deaths due to cancer in 2020 (Sung et al., 2021).

1.1.1 Tumors of the central nervous system

Tumors arising from the brain and the spinal cord are generally referred to as 'the central nervous system (CNS)' tumors (Lapointe et al., 2018). The incidence rate of the tumors arising from the CNS excluding cases of metastasis is highly variable from 0 cases to over 20 cases in people aged 0 to 100 years per 100,000 population globally (Patel et al., 2019). In 2020 an estimated 308,102 cases of central nervous system tumors occurred globally resulting in an estimated 251,329 deaths. This translates to a mortality-to-incidence ratio (MIR) of 80% (Sung et al., 2021). These estimates are comparable to the most recently compiled data on the global brain and nervous system tumors incidence and mortality (Patel et al., 2019). The global MIRs estimates also reflect the rates in Europe. Luxembourg, with an estimate of 39 new cases of brain and nervous system tumors resulting in an estimated 33 deaths in 2020, had a MIR similar to the global and European ratio (Sung et al., 2021).

Metastasis of cancer cells from their primary organ or tissue to the brain is a common complication of most cancers (Nayak et al., 2012). These tumors are seeded by metastasizing cancer cells that compromise and extravasate through the blood-brain barrier (BBB). Upon the successful crossing of the BBB barrier, the brain microenvironment is then conditioned by the metastatic cells to enhance their integration, survival, and growth in the brain (Srinivasan et al., 2021). Epidemiological evidence indicates an incidence rate of 7.3 cases per 100,000 cancer patients in the United States, with primary lung cancers accounting for 80% of these metastases. Melanoma and breast cancer account for 3.8% and 3.7% of all brain metastases respectively, while kidney and renal pelvis cancers

account for 3.0%. Other cancers such as that of the esophagus, colon, and rectum have also been reported to contribute to the brain metastasis burden although fewer cases have been reported (Singh et al., 2020). The increasing trend of metastatic brain tumors reported is likely influenced by improved treatment options and increased survival of patients with non-brain cancer types.

Primary brain tumors arise *de novo* without any evidence of a less malignant precursor lesion while secondary brain tumors arise from a lower grade brain tumor. While primary tumors mostly manifest in elderly patients, secondary tumors are mostly seen in young patients (Ohgaki and Kleihues, 2013). Malignant transformation of the different cell types within the CNS gives rise to a diverse range of primary brain tumors. These tumors are either malignant or non-malignant (benign) (Lapointe et al., 2018). Malignant primary brain tumors are aggressive, highly invasive, and fatal. They account for about 30% of all primary tumors arising from the CNS while the non-malignant tumors are less aggressive, mostly non-invasive, and less fatal. Non-malignant brain tumors account for the majority of the primary brain and CNS tumors (Miller et al., 2021; Ostrom et al., 2020) (**Figure 1**). Glioblastoma (GBM), a malignant brain tumor, and meningioma (non-malignant) are the most common types of primary brain tumors, with the GBMs accounting for about half (48.6%) of the malignant tumors and meningiomas accounting for over half of the non-malignant tumors (Miller et al., 2021; Tan et al., 2020). Malignant brain tumors are reported at a higher rate in the male population, while non-malignant tumors are more common in females (Miller et al., 2021; Patel et al., 2019). Whilst the overall survival (OS) of patients with malignant brain tumors varies according to tumor type and age, the prognosis of these tumors is worse. On the contrary, patients with non-malignant brain tumors have a better OS with a narrower margin of difference in OS between young and old patients (95% - 84%) (Miller et al., 2021). The average number of annual deaths due to primary malignant brain and CNS tumors is 4.42 deaths in 100,000 patients in the USA (Ostrom et al., 2020).

Globally brain and CNS tumors result in a substantial number of deaths and both the number of new cases and deaths have increased between 1990 and 2016 (Patel et al., 2019). Several factors have been attributed as risk factors for developing brain tumors. These include exposure to ionizing radiation in children, hereditary and environmental factors as well as receiving prior cranial radiation treatment (Miller et al., 2021). A systematic review recently linked brain tumor occurrence with exposure to pesticides used in farming (Gatto et al., 2021).

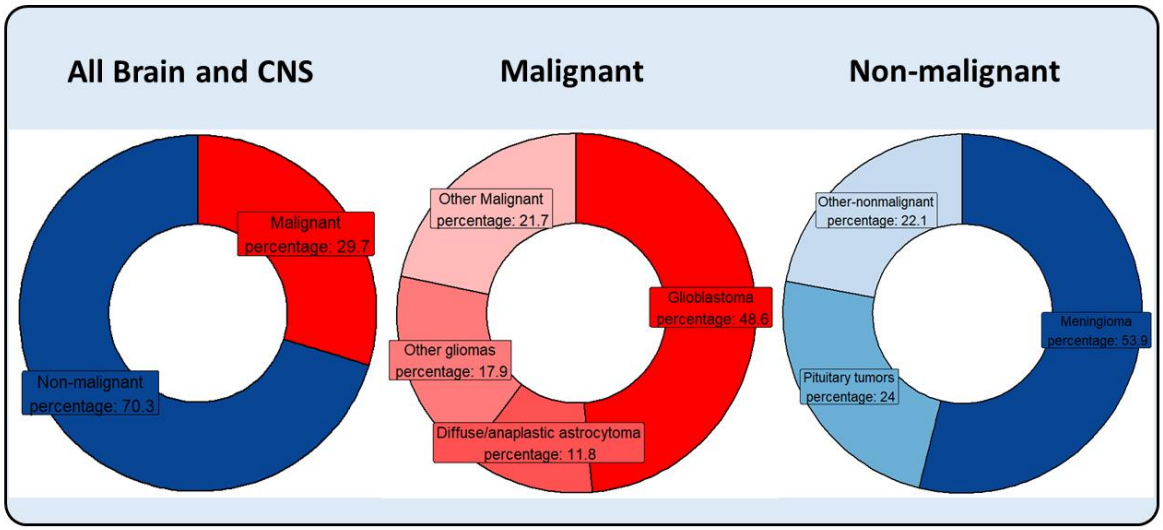

Figure 1. Distribution of different types of primary brain and CNS tumors diagnosed in the USA between 2013 to 2017. Brain and CNS tumors are mainly grouped into malignant and non-malignant types. Glioblastoma accounts for almost 50% of all malignant primary brain tumors (Data sourced from Miller et al., 2021).

1.1.2 Gliomas

Gliomas are malignant tumors generally thought to arise from the glial cells in the brain although, the definitive cell of origin of gliomas is still under intense discussion (Alcantara Llaguno and Parada, 2016). The recent WHO classification of CNS tumors has revised the previous broad categorization of diffuse gliomas into “adult-type diffuse gliomas” and “pediatric-type diffuse gliomas” to account for the differences in glioma subtypes observed in these populations (Louis et al., 2016, 2021). The pediatric-type diffuse low-grade gliomas consist of diffuse astrocytoma, angiocentric glioma, and polymorphous low-grade neuroepithelial tumor of the young as distinct tumor types within this sub-group. While the pediatric-type diffuse high-grade gliomas sub-group consists of diffuse midline glioma, diffuse hemispheric glioma, diffuse pediatric-type high-grade glioma, and Infant-type hemispheric glioma as tumor types. The tumor sub-types under the adult-type diffuse gliomas with their corresponding *Isocitrate dehydrogenase (IDH*) status, WHO grades, and associated molecular characteristics are depicted in **Figure 2** and will be discussed further in this thesis.

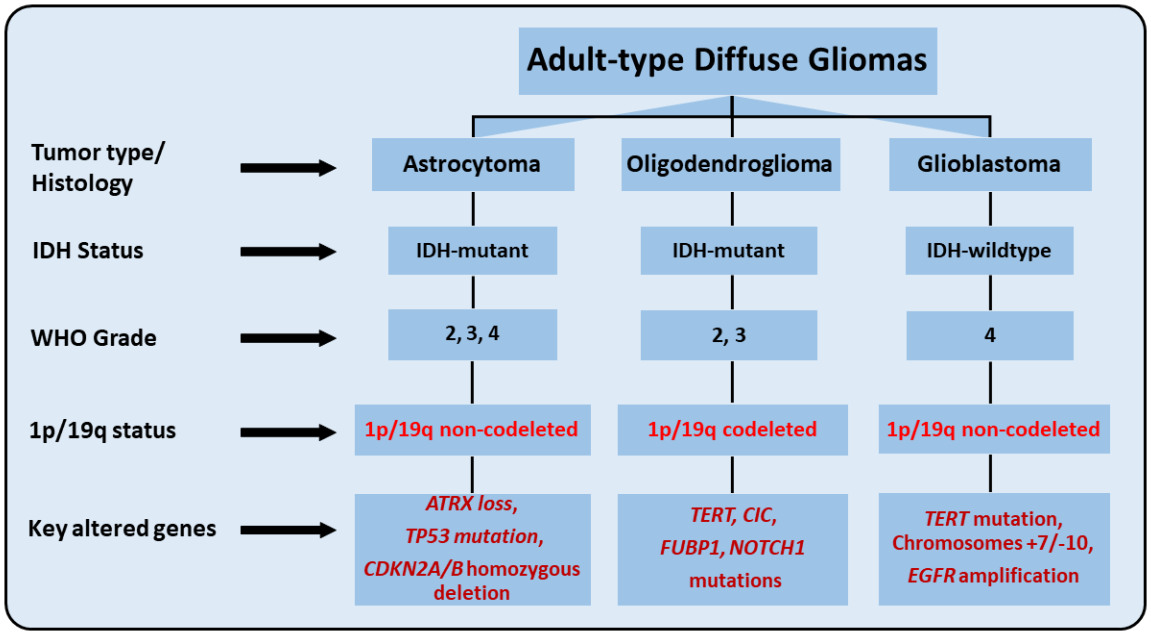

Figure 2. The 2021 WHO classification of adult diffuse gliomas. The WHO grade provides information on the clinical nature of the tumors, with grade 1 tumors being curable and fully excisable with good prognosis, while grade 4 tumors are incurable and cannot be fully excised. The 2021 WHO Classification of Tumors of the Central Nervous System integrates histopathologic, genetic, and molecular information to arrive at a more robust description of the cellular organization and histological appearance of CNS tumors (Louis et al., 2021). Glioblastomas (GBMs) are characterized as grade 4 IDH wildtype gliomas. IDH1/2 mutated (IDHmut) GBMs have been classified in 2021 as a separate grade IV entity within IDH-mutant astrocytomas based on their unique genetic and molecular alterations. Oligodendrogliomas are distinguished from astrocytomas based on the 1p/19q deletion status; Tumor protein 53 (TP53), Alpha thalassemia/mental retardation syndrome X-linked (ATRX), Cyclin-dependent kinase 4/6 (CDKN2A/B), Capicua (CIC), Far Upstream Element Binding Protein 1 (FUBP1), Telomerase reverse transcriptase (TERT), Epidermal growth factor receptor (EGFR). Adapted from Louis et al., 2021.

1.1.3 IDH mutant gliomas

Isocitrate dehydrogenase (IDH) is an important metabolic enzyme that catalyzes the oxidative decarboxylation reaction that converts isocitrate to α-ketoglutarate (α-KG), a TCA cycle intermediate under normal physiological conditions. Gliomas with mutations in the IDH genes are referred to as IDH mutant (IDHmut) gliomas. IDH1 and IDH2 are the 2 isoforms mainly altered in gliomas. A missense mutation in the *IDH* gene results in the replacement of arginine (R) with histidine (H) in positions 132 (R132H) and 172 (R172H) in IDH1 and IDH2 enzymes respectively (Han et al., 2020; Parsons et al., 2008; Yan et al., 2009). IDH mutation leads to the production and accumulation of the oncometabolite 2-hydroxyglutarate (2-HG) a competitive inhibitor of α-KG that fuels tumor growth and progression (Dang et al., 2009).

The previously known IDHmut GBMs are now regarded as high-grade astrocytomas and are considered distinct tumor types independent of IDHwt GBMs (Louis et al., 2021). IDH-mutant diffuse astrocytic tumors that were previously classified into 3 different tumor types in 2016 based on their histologic features as either diffuse astrocytoma, anaplastic astrocytoma, or IDHmut glioblastoma are now collectively referred to as Astrocytomas irrespective of their histological characteristics. However, the new astrocytomas are assigned 2, 3, or 4 WHO grades based on the clinical nature of the disease with WHO grade 4 astrocytomas being the most aggressive form. In addition to its histological and clinical features, the key molecular features of astrocytomas include *Tumor protein 53* (*TP53)* and *Alpha thalassemia/mental retardation syndrome X-linked* (*ATRX*) mutations as well as *Cyclin-dependent kinase 4/6 (CDKN2A/B)* loss (Louis et al., 2021). Oligodendrogliomas are generally classified based on their distinct histological features, IDH1/2 mutations, codeletions in chromosomes 1p/19q, a *Telomerase reverse transcriptase* (*TERT)* promoter mutation as well as mutations in *Capicua* (*CIC*) and *Far Upstream Element Binding Protein 1 (FUBP1)* genes. *NOTCH1* gene mutation is also a key molecular feature characterizing oligodendrogliomas (Louis et al., 2021). Oligodendrogliomas were also assigned 2 different WHO grades (2 or 3) depending on the clinical course of the tumors (**Figure 2)** (Louis et al., 2021).

1.1.4 Glioblastoma

Glioblastoma is an aggressive, invasive, and difficult to treat tumor (Aldape et al., 2018). It is the most commonly diagnosed malignant brain tumor in the USA (Ostrom et al., 2020). GBM is characterized as IDH wildtype (IDHwt) and assigned WHO grade 4 indicating its aggressive nature and dismal prognosis (Louis et al., 2021). The typical clinical presentation of GBM includes neurological symptoms such as headache, epilepsy, neurocognitive impairment, and other signs and symptoms resulting from intracranial pressure imposed by tumor growth. The detection of GBM following a magnetic resonance imaging (MRI) scan is considered the gold standard for the diagnosis of the tumor. Other diagnostic tools such as positron emission tomography (PET) scans and electroencephalography are useful for tumor detection and monitoring (Weller et al., 2021; Wen et al., 2020). The use of liquid biopsies to detect circulating cell-free tumor DNA in plasma and cerebrospinal fluid is emerging but has not been adopted as a standard diagnostic procedure (Weller et al., 2021). Histopathologically, GBM is characterized by microvascular proliferation and pseudopalisading necrosis which are considered the hallmarks of GBM. Other typical histologic features of GBM include nuclear atypia, cellular polymorphism, and a high mitotic

index (Oronsky et al., 2021; Wen et al., 2020). Pseudopalisades are characterized by tumor cells migrating from the nutrient-deprived tumor core and surrounding the necrotic foci. Pseudopalisading cells are hypoxic and have been shown to express hypoxia inducible factor-1 (HIF-1) and VEGF, which induce microvascular hyperplasia and neovascularisation that in turn promotes GBM proliferation (Rong et al., 2006).

The incidence rate of GBM increases with age, with the highest occurrence seen in people older than 75 years. Just like the other types of malignant brain tumors, males are more likely to develop GBM than females (Miller et al., 2021; Ostrom et al., 2020; Tan et al., 2020; Wang et al., 2021). With only an 8-month median survival rate, GBM has the worst prognosis among all primary malignant brain and CNS tumors (Ostrom et al., 2020). The incidence rate in males is approximately 6 cases per 100,000 people, while that of females is about 4 cases per 100,000 people in the United States. The age-adjusted incidence rate in GBM is 3.21 cases per 100,000 people (Ostrom et al., 2020; Tan et al., 2020). Most GBMs occur as primary tumors, while a smaller subset of GBMs occurs as secondary tumors emanating from lower-grade gliomas. These secondary tumors mostly occur in younger patients and are largely characterized as IDHmut Astrocytomas based on WHO 2021 classification (Ohgaki and Kleihues, 2013).

Although over the years several lines of aggressive treatments have been offered to patients with GBM, survival rates remain very low except in a few cases (Miller et al., 2021; Tan et al., 2020). While an appreciable increase from 23% to 36% was recorded in the five-year relative survival between 1975 to 1977 and 2009 to 2015 in all malignant brain tumors combined, in GBM there has been only a slight increase in the relative survival from 4% to 7% within the same years in reference. This is mainly due to the lack of development of new treatment strategies against GBM in the last several decades (Miller et al., 2021; Ostrom et al., 2020).

GBM has a diverse and heterogeneous pattern of occurrence that affects treatment response. The incidence and mortality differ based on age, gender, geographical spread, race, and ethnicity (Davis, 2016; Lapointe et al., 2018; Miller et al., 2021; Weller et al., 2015). GBM affects a significant number of people and the lack of advancement in its treatment results in the death of most patients. More research is needed to identify causal/risk factors associated with GBM and better disease models to enable the development and testing of new treatment options that will improve the quality of life and the OS of GBM patients (Miller et al., 2021).

1.1.5 Treatment strategies in glioblastoma

The current clinical management of GBM involves a multimodal approach and usually involves 3 stages in most patients, mainly pre-surgical, surgical, and post-surgical interventions (Tan et al., 2020). Corticosteroids, usually dexamethasone, are the common pre-surgical drugs administered in GBM patients (Lapointe et al., 2018; Wen et al., 2020). These drugs are administered to reduce intracranial pressure and accompanying symptoms such as headache resulting from the edema around the tumor (Wen et al., 2020). The subsequent interventions include a radical surgical approach with extensive tumor resection followed by chemotherapy with temozolomide (TMZ) and radiotherapy with ionizing radiation which collectively form the standard-of-care treatment in GBM (Davis, 2016; Stupp et al., 2005; Weller et al., 2021). Maximal surgical resection of T1-weighted MRI contrast-enhanced tumors was shown to have a clear benefit with an increased OS of patients when compared to patients whose tumors were not maximally resected (Molinaro et al., 2020). The use of a biochemical derivative 5-aminolevulinic acid (5-ALA) that labels tumor cells under fluorescent light to help in separating normal brain cells from tumor cells has improved the ability of surgeons to maximally resect tumor cells during fluorescence-guided surgery with minimal damage to the normal brain tissue (Díez Valle et al., 2011; Gandhi et al., 2019). As much as 98% resection of the contrast-enhancing tumor volume can be achieved using 5-ALA (Díez Valle et al., 2011). In addition to having a higher volume of tumor resection in patients that received 5-ALA before surgery, an additional 6-month progression-free survival was reported in patients that received 5-ALA compared to those who did not and had less volume of their tumor resected (Eatz et al., 2022; Stummer et al., 2006). However, due to the highly invasive nature of GBM, complete surgical resection is unachievable with some invading tumor cells located far away from the primary tumor site (Spiteri et al., 2019; Wen et al., 2020) and thus chemo and radiotherapy are needed to target invading tumor cells.

Ionizing radiation (IR) targeted at the tumor region during radiotherapy damages the DNA by breaking both strands of the DNA (double-strand breaks) leading to the death of cells that are unable to repair or ineffectively repair the damaged DNA (Erasimus et al., 2016). The alkylating effect of TMZ induces DNA damage, and in the absence of an effective DNA damage repair system such as the mismatch repair (MMR), programmed cell death is achieved in TMZ sensitive cells (Lee, 2016).

Radiotherapy alone or in combination with TMZ has been reported to improve the survival of GBM patients (Keime-Guibert et al., 2007; Stupp et al., 2005). Patients that received chemo and radiotherapy following surgery were reported to have a median OS of 14.6

months and a median survival benefit of 2.5 months when compared to patients that received radiotherapy only in addition to surgical resection. In addition, the standard-of-care treatment was found to provide GBM patients with a significantly increased 2-year survival rate and a better progression-free survival compared to other treatment strategies (Stupp et al., 2005). This treatment approach was also reported to increase the 5-year survival rate of GBM patients to up to 10% (Stupp et al., 2009). However, the reported benefits are dependent on the patient tumor's *O^6-methylguanine-DNA methyltransferase (MGMT)* promoter methylation status, which is known to be a predictive marker of TMZ efficacy (Hegi et al., 2005). MGMT promoter hypermethylation and subsequent MGMT gene silencing, inhibit cell-intrinsic DNA repair mechanisms thus conferring a treatment and survival advantage to TMZ therapy in this subset of patients (Hegi et al., 2005; Stupp et al., 2005). Still, despite concurrent and adjuvant chemo-radiotherapy, a subset of tumor cells escape therapy leading to relapse (Spiteri et al., 2019). In these residual cells, functional DNA repair mechanisms enable escape from TMZ and IR-induced DNA damage resulting in surviving clones with a high mutational burden in some glioma and GBM patient samples (Lee, 2016; Touat et al., 2020). GBM tumor recurs aggressively with a median OS of 6 – 11 months due to the invasive tumor cells that cannot be fully eliminated by standard-of-care treatment (Wen et al., 2020).

The development of therapeutic agents that target angiogenesis, which is an important hallmark of GBM, brought some hope in the quest to find a cure for GBM. Bevacizumab (Avastin) was approved for the treatment of recurrent GBM by the United States Food and Drug Administration (FDA) following encouraging phase II clinical trials (Kreisl et al., 2009). However, the use of bevacizumab alone in newly diagnosed GBM or in combination with other chemotherapeutic agents in recurrent GBM only confers a marginal increase in progression-free survival. Treatment with bevacizumab alone does not surpass the standard-of-care treatment in terms of overall survival (Gilbert et al., 2014; Niclou, 2018; Wick et al., 2017).

Tumor-treating fields (TTFields) emerged as a novel non-invasive and non-toxic treatment strategy in GBM. In this treatment modality, transducers delivering low-intensity alternating electric fields are attached to the scalp of the patient. The electric fields generated have a detrimental effect on tumor cells causing mitotic arrest, impairment of DNA repair process, activation of autophagy, and inhibition of cancer cell migration (Rominiyi et al., 2021). The clinical benefit of the TTFields was demonstrated in a clinical trial that led to its approval by the FDA (Cohen et al., 2005). Patients with primary GBM treated with adjuvant TMZ and TTFields had a significantly higher PFS and OS compared to patients that received only the

standard-of-care treatment. Interestingly, the addition of TTFields to the treatment regimen was not associated with significant adverse events in patients (Kesari et al., 2017; Rominiyi et al., 2021; Stupp et al., 2015, 2017). However, no improvements in the OS were detected in a clinical trial that compared patients receiving chemotherapy only with those receiving chemotherapy and TTFields in patients with recurrent GBMs (Stupp et al., 2012). Moreover, the high cost of TTFields and their cumbersome nature limit their clinical use (Fabian et al., 2019; Liu et al., 2021a).

In recent years, immunotherapy has emerged as a novel therapeutic option in the treatment of solid tumors (Rusch et al., 2018). The primary goal of immunotherapy is to stimulate an immune response toward tumor cells and include adoptive cell therapies such as chimeric antigen receptor T cell (CAR T cell), T cell receptor (TCR), and tumor-infiltrating lymphocyte (TIL) (Lapointe et al., 2018; Lynes et al., 2018). The tumor's immune-suppressed environment can also be reversed through the inhibition of immune checkpoint molecules such as anti-cytotoxic T lymphocyte-associated protein 4 (CTLA-4) and anti-programmed death-1 (PD-1). Tumor vaccination using patients' dendritic cells (DCs) or peptides (e.g. targeting *EGFR*) are also explored to enhance the immune memory of T cells and induce a more effective and sustained elimination of tumor cells (Lynes et al., 2018). Although there are ongoing preclinical and clinical studies on different cocktails of immune cells (Lapointe et al., 2018), these are yet to be translated into a cure for GBM patients mainly due to the heterogeneity and "cold" nature of these tumors with often few targetable mutations which facilitates immune escape (Sampson et al., 2020). The use of oncolytic viruses to treat GBM is also being explored. Recently, results from phase I clinical trials using recombinant oncolytic adenoviruses and a chimera of polio and rhinovirus used to attack GBM cells were reported with encouraging results allowing proceeding into phase II clinical trials (Desjardins et al., 2018; Fares et al., 2021).

Whilst there are several drug candidates are at various stages of development and clinical trials (Wen et al., 2020), GBM remains refractory to current treatment strategies due to the inevitable development of drug resistance. Ultimately, this has led to the stagnation of survival outcomes of GBM patients within the last 15 years.

1.2 Inter-tumoral heterogeneity and molecular subtypes in glioblastoma

Inter-tumoral heterogeneity at different levels is a significant barrier to the effective treatment of GBM. These differences are mostly due to the molecular peculiarities of tumors in each patient and may be translated into variable treatment responses even in patients presenting with histologically similar tumors. This underscores the importance of patient stratification using various molecular approaches in GBM diagnoses and personalized treatment.

1.2.1 Genetic landscape and subtypes in glioblastoma

Large-scale research efforts such as the cancer genome atlas (TCGA) and others have advanced our understanding of the molecular features of GBM (McLendon et al., 2008; Parsons et al., 2008; Weinstein et al., 2013). Using next-generation sequencing technology demonstrated extensive genomic alterations in GBM (Brennan et al., 2013). GBMs commonly carry *TERT* promoter mutation and copy number changes at chromosomes 7 and 10 (+7/-10). Genetic alterations such as amplification of *Epidermal growth factor receptor* (*EGFR)*, *Platelet-derived growth factor receptor α* (*PDGFRα),* and *Cyclin-dependent kinase 4/6* (*CDK4/6)*, as well as deletions or inactivating mutations in *TP53*, *Phosphatase and tensin homolog* (*PTEN)*, *Neurofibromin 1* (*NF1)* and loss of *Cyclin-dependent kinase inhibitor 2A/B* (*CDKN2A/B),* are key determinants of inter-patient variability (Brennan et al., 2013; Louis et al., 2021; Wen et al., 2020). These genomic alterations affect several signaling pathways with important implications for GBM tumor initiation and progression. 67.3% of all tumor types analyzed (largely within the category of adult diffuse gliomas in the latest WHO 2021 classification), had alterations in at least one Receptor tyrosine kinase (RTK) leading to Mitogen-activated protein kinase (MAPK) signaling pathway activation. Similarly, 85.3% of these tumors had a dysregulated *p53* pathway, while alterations affecting Rb function were detected in 78.9% of the tumors (Brennan et al., 2013; Molinaro et al., 2019). Genetic aberrations provide the basis for the inter-patient categorization of GBMs and classify GBMs into 3 major subgroups. One subgroup of GBMs is characterized by enhanced amplifications in *PDGFRα* and *CDK4.* Another by a higher frequency of *EGFR* amplifications with deep deletions of *CDKN2A/B*. The third subgroup of GBMs is characterized by *NF1* loss (Brennan et al., 2013; Verhaak et al., 2010; Wen et al., 2020). The identified genetic subgroups were later linked to the gene expression and DNA methylation profiles of GBM.

The genetic and cellular inter-patient difference affects treatment sensitivity and resistance in GBM. Skaga et al. demonstrated extensive inter-patient variability in the sensitivity to

several anti-cancer drugs response in patient-derived glioma cultures (Skaga et al., 2019). Inter-patient *MGMT* promoter methylation status is a predictive marker for TMZ treatment response and survival in GBM (Hegi et al., 2005). Patients' stratification based on *TERT* mutation and *MGMT* status have identified clinically relevant subgroups with variable treatment outcomes in GBM (Arita et al., 2016).

1.2.2 Gene expression-based subtypes

The molecular classification of GBM based on the bulk transcriptomic signatures of patient tumor samples revealed important inter-patient differences. Initial analysis by Phillips et al., using bulk gene expression signatures of high-grade gliomas (mostly fall classified as GBMs and high-grade astrocytomas in the latest WHO 2021 classification), identified 3 distinct molecular groups namely, proneural, mesenchymal, and proliferative subtypes. These molecular subtypes were linked to the disease prognosis (Phillips et al., 2006). Tumors with proneural signatures have significantly longer survival compared to those with a mesenchymal or proliferative signature. Moreover, these subtypes associated very well with glioma tumor grades. Samples histologically classified as WHO grade III were mostly proneural and grade IV tumors displayed signatures of 3 subtypes while mesenchymal and proliferative signatures were exclusive to grade IV tumors samples with necrosis (Phillips et al., 2006).

Subsequent work by the TCGA consortium (Verhaak et al., 2010), reclassified the molecular subgroups using bulk gene expression data of GBMs, considering both IDHwt and IDHmut tumors. This resulted in 4 new molecular subtypes namely, proneural, neural, classical, and mesenchymal. In addition, these new subtypes were linked to specific genetic alterations, with the proneural subtype associated with *PDGFRα* & *IDH1* alterations, while the classical and mesenchymal subtypes associated with *EGFR* and *NF1* alterations respectively. In addition, this subtype classification provided some insight into the variability in response to treatment among the different subtypes (Verhaak et al., 2010). A caveat of this classification however contamination of normal brain cells in bulk expression analysis. Further fine-tuning of the signatures with the advances in single-cell RNA sequencing (scRNA-seq) allowed the selection of tumor-intrinsic genes from single tumor cells and non-neoplastic populations in only IDHwt GBMs. This new approach revealed that the initial four subtypes were influenced by the signal from non-tumor cells particularly in the tumor microenvironment (TME) on the overall bulk transcriptomic profiles. This led to the refinement of the initial 4 subtypes into 3 tumor intrinsic subtypes, namely, proneural (PN), classical (CL), and mesenchymal (MES) (Wang et al., 2017).

Although these molecular subtypes based on the transcriptomic profiles of GBM have helped in GBM patients' stratification and prognosis, they have not yet translated into therapeutic benefits for patients.

1.2.3 Methylation-based subtypes

DNA methylation and other epigenetic-based mechanisms of regulating gene expression such as chromatin remodeling and histone modification play an important role in shaping the gene expression dynamics (Bommarito and Fry, 2018; Chaligne et al., 2021; Johnson et al., 2021; Jones and Baylin, 2007; Noushmehr et al., 2010; Wang and Wu, 2018). DNA methylation occurs when a methyl group ($-CH_3$) is added at position 5 of the cytosine ring in the CpG site of the DNA sequence by a group of enzymes known as DNA methyltransferases (DNMTs) (Moore et al., 2013). DNA methylation at the regulatory regions leads to alterations in gene expression without a permanent change to the nucleotide sequence of the cell, often translating into a corresponding change in the phenotype of the affected cell(s) (Wang and Wu, 2018). The general pattern of DNA methylation in cancer is the presence of a global genome hypomethylation with hypermethylation of CpG islands located at the promoter region of specific genes often involved in cell differentiation (Jones and Baylin, 2007). Hypermethylation at these CpG islands results in the silencing of gene expression of the gene whose promoter is affected (Bommarito and Fry, 2018; Wang and Wu, 2018).

Gene signatures defining GBM transcriptional subtypes are regulated at the epigenetic level and can be predicted from methylation patterns. DNA methylation profiles were used to effectively delineate the heterogeneity of GBMs and to stratify them based on their distinct methylation profiles into several subclasses that correlate with transcriptomic subtypes (Capper et al., 2018; Ceccarelli et al., 2016; Noushmehr et al., 2010). In the framework of the TCGA project, gliomas were initially classified based on DNA methylation alterations observed in the promoter regions known as the glioma CpG island methylator phenotype (G-CIMP). Two subgroups were identified in the adult diffused gliomas analyzed, namely, G-CIMP positive and G-CIMP negative tumors (Noushmehr et al., 2010). Comparison between the G-CIMP positive tumors with the glioma molecular subtypes (Verhaak et al., 2010) revealed that G-CIMP positive tumors mostly correspond to proneural GBMs and other lower-grade gliomas with IDH mutation, while the G-CIMP negative represent mostly classical and mesenchymal GBMs (Noushmehr et al., 2010).

The integration of several layers of “omics” data comprising DNA methylation, whole-genome sequencing (WGS), gene expression, and protein expression data further allowed the refinement of DNA methylation subclasses in both IDHwt and IDHmut GBM separately (Ceccarelli et al., 2016). Analyses of the DNA methylation profiles of GBM revealed inter-tumoral differences based on bulk DNA methylation profiles of these samples (Capper et al., 2018; Ceccarelli et al., 2016). This new DNA methylation classification grouped IDHmut GBM into LGm1, LGm2, LGm3 subtypes, and the IDHwt GBM also into 3 subtypes, namely LGm4, LGm5, LGm6 (Ceccarelli et al., 2016). As previously described, the LGm1-3 subclasses are mostly G-CIMP positive and display genome-wide hypermethylation, unlike the LGm4-6 subclasses that are mostly G-CIMP negative with a hypomethylated genome. Still, the IDHwt subclasses LGm4 and LGm5 are enriched for classical- and mesenchymal-like features respectively, while the third subclass LGm6 comprises GBM and pilocytic astrocytoma-like tumors (Ceccarelli et al., 2016).

Using a machine learning algorithm, Capper et al., developed a new DNA methylation-based classification of the CNS tumors termed the “Heidelberg” subtypes (Capper et al., 2018). In this new classification, IDHwt GBMs were classified into 8 subtypes namely: GBM RTK I, GBM RTK II, GBM RTK III, and GBM MES. These DNA methylation classes are broader and readily applicable for routine diagnosis (Capper et al., 2018). A comparison between the Capper et al. and the pan-glioma DNA methylation subtypes of IDHwt GBMs revealed an overlap between LGm4 and GBM RTK II as well as an overlap between LGm5 and GBM MES and GBM RTK I classes (Capper et al., 2018).

Although inter-tumoral heterogeneity has highlighted important insights into the molecular features of GBM at different levels and aided patients stratification, improvements in the resolution of molecular techniques that allows the characterization of individual cells and the analysis of multiple biopsies from the same tumors revealed extensive intra-tumoral heterogeneity in GBM (Gates et al., 2019; Patel et al., 2014; Sottoriva et al., 2013). This indicates that the potential effect of tumor sampling must be considered when defining inter-patient differences in GBM.

1.3 Intra-tumoral heterogeneity and plasticity in glioblastoma

Genomic instability in cancers as a result of somatic mutations and chromosomal aberrations as well as epigenomic instability leads to cellular and phenotypic variations often referred to as intra-tumoral heterogeneity (ITH) (Greaves, 2015). ITH favors tumor cell propagation and contributes to treatment resistance that ultimately shapes the clinical course of the disease (Iacobuzio-Donahue et al., 2020; Turajlic et al., 2019). GBM is characterized by complex cellular and molecular features (Puchalski et al., 2018). Based on its diversified cellular organization and histological appearance, GBMs have historically been considered among the most heterogeneous tumors and were referred to as 'multiforme'. GBMs encompass distinct histopathologic features such as diffuse infiltration, microvascular proliferation, and necrosis. Tumor cells reside in different TME niches, where they display distinct phenotypic features, including abnormal cell morphology and protein expression (**Figure 3A**). ITH in GBM has since been described at various molecular levels, including at genetic, transcriptomic, epigenetic, and functional levels (**Figure 3**). TME as an additional layer of ITH contributing to the complex molecular GBM landscape will be discussed in a separate section of this thesis.

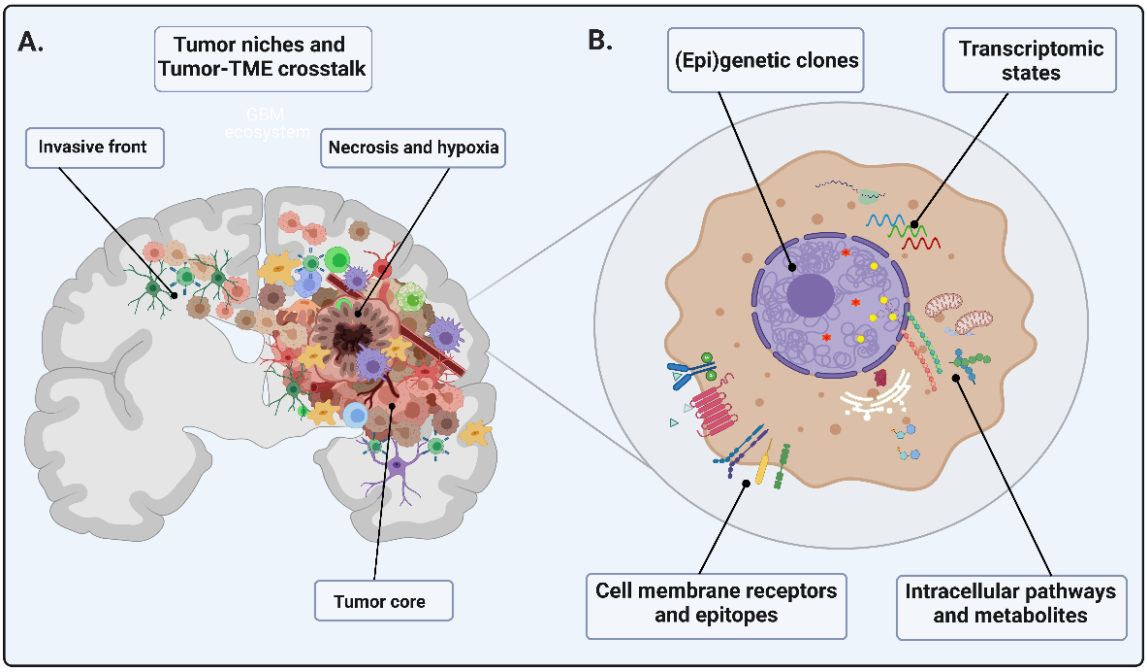

Figure 3. Factors contributing to intra-tumoral heterogeneity in GBM. A. The GBM cellular ecosystem comprises diverse tumor cells residing in different TME niches. Composition of tumor cells and crosstalk with TME vary across different niches B. GBM cells display heterogeneity at different molecular levels: genetic, epigenetic, transcriptomic, proteomic, and metabolomic. GBM cells may express diverse cell membrane epitopes and intracellular signaling pathways.

1.3.1 Intra-tumoral genetic heterogeneity

Genetic ITH is a well-established phenomenon in high-grade gliomas. The emergence and evolution of genetic heterogeneity is known as a hierarchical process that follows the general neo-Darwinian principles. Distinct genetic clones arise due to genomic instability and continuous clonal evolution, allowing for the diversification of the tumor genetic landscape (Turajlic et al., 2019). Genetic events occurring late in clonal evolution are often subclonal (Körber et al., 2019) e.g., the *EGFRvIII* structural variant is present only in a subpopulation of GBM cells (Francis et al., 2014). If present in the same tumor, *EGFR,* and *PDGFRα* gene amplification occur in different subclones, which may be differentially distributed across different tumor niches (Szerlip et al., 2012). Genetic heterogeneity is also well described for point mutations, including genes such as *EGFR* and *ATRX*. Aneuploidy is generally a late event in GBM evolution and >35% of GBMs contain clones with different ploidy levels and underlying changes in chromosomal content and structure (Stieber et al., 2014). Genetic analysis of several biopsies from the tumors of 11 patients revealed extensive ITH in GBM (Sottoriva et al., 2013). Genome-wide copy number analysis revealed the heterogeneous occurrence of key somatic alterations in GBM in different clones of the same tumor. Copy number amplifications of *PDGFRα* and *PTEN* deletion were variably observed in the different fragments of the same tumor. These findings were earlier demonstrated when Snuderl et al., observed variability in the amplification of RTK genes (*PDGFRα*, *EGFR*, *MET*) by different cells within the same tumor in GBM (Snuderl et al., 2011). Whole exome sequencing of GBMs also identified *PDGFRα* amplifications and or mutations coexisting with *EGFR* amplifications in the same tumors (Brennan et al., 2013), indicating that these events are not mutually exclusive and can be present in the same tumor but different locations.

Extrachromosomal DNA (ecDNA) carrying oncogenes also contributes to the development of ITH in GBM (Kim et al., 2020b; Turner et al., 2017). As ecDNA molecules do not contain centromeres, they are randomly distributed to daughter cells, resulting in an additional layer of genetic heterogeneity (Verhaak et al., 2019). Genetic heterogeneity based on ecDNA carrying *EGFRvIII* is also rapidly reconstituted from purified cells with or without *EGFRvIII* amplification, further demonstrating the ability of ecDNA to rapidly generate ITH (Decarvalho et al., 2018). EcDNA circular amplicons were recently shown to be prevalent in many cancer types with GBM showing the highest frequency of occurrence. Interestingly, ecDNAs were not detected in normal cells. This emphasizes the role of ecDNA in creating and maintaining ITH in cancer (Kim et al., 2020b).

1.3.2 Transcriptomic heterogeneity and plasticity

The advent of single cells sequencing technologies in recent years has advanced our understanding of the transcriptomic heterogeneity of cancer cells (Tirosh and Suvà, 2018). Bulk transcriptomic analysis of multiple biopsies from the same tumor provided the initial indication that GBMs are transcriptionally heterogeneous. Sottoriva et al. showed that 6 out of the 10 GBMs analyzed had fractions with different GBM subtypes (Sottoriva et al., 2013). As observed in the genetic analyses, this indicated each tumor had an admixture of multiple gene expression subtypes and the underlying tumor genetic ITH may dictate transcriptomic ITH.

The identification of the transcriptomic signatures of individual tumor cells using single-cell RNA-seq (scRNA-seq) technology provided more insight into the transcriptomic profiles of GBM cells. This approach further highlighted the remarkable intra-tumoral heterogeneity in GBM, where signatures of different GBM molecular subtypes (proneural, classical, mesenchymal) were found to be present within the same tumor (Patel et al., 2014). Individual tumor cells were found to possess signatures of different subtypes and thus defined as hybrids with intermediary phenotypes, suggesting state transitions between subtypes and, a departure from the initial understanding that each tumor has a single molecular subtype (Patel et al., 2014). Analysis of signatures linked to stemness, hypoxia, and quiescence did not reveal distinct cellular subpopulations (Patel et al., 2014). Transcriptomic heterogeneity relied rather on continuous gradients, confirming expression profiles detected regularly at the protein level by flow cytometry. Proliferating cells were defined in different phenotypic states and the main axis of variation ranged from a proneural to a mesenchymal state (Wang et al., 2019). On the contrary, the transcriptomic features of IDHmut gliomas required a different set of genes defining phenotypic states and suggested a more hierarchical organization. Both tumor types presented proliferating cells mostly in the stem-like states, whereas Astro-like and Oligo-like cells rarely contained cells in the cell cycle phase (Tirosh et al., 2016; Venteicher et al., 2017).

Further in-depth single-cell analysis of GBMs revealed the existence of 4 different cellular states with distinct gene expression profiles namely: astrocytic (AC)-like, neural progenitor cells (NPC)-like, oligodendrocytes progenitor cells (OPC)-like and mesenchymal (MES)-like (**Figure 4**) (Neftel et al., 2019). At least two of the GBM cellular states were present in each GBM and always contained a fraction of proliferating cells, arguing against a hierarchical organization in GBM. Numerous cells were also defined as intermediary or hybrid cell states indicating a transition between transcriptomic states.

Although the genetic background of each tumor did not entirely dictate the phenotypic states, it contributed to the transcriptomic ITH (Tirosh and Suvà, 2018). GBMs rarely contained equal proportions of cellular states (Bhaduri et al., 2020), and ratios were skewed by the inter-patient genetic associations, where the most abundant phenotypic state defined the overall molecular subtype. In general, the most abundant phenotypic state defined the bulk molecular subtype. For example, GBMs dominated by AC-like cells are generally of classical subtype and carry *EGFR* gene amplification; GBMs of predominantly MES-like cell state are of a mesenchymal subtype with *NF1* locus mutations. The proneural subtype characterizes GBMs consisting of predominantly OPC-like or NPC-like cell states, with *PDGFRα* and *CDK4* amplifications respectively (**Figure 4).**

scRNA-seq allows the correlation of transcriptomic profiles with defined copy number alterations. Each genetic clone in GBM and IDHmut gliomas present within the tumor was shown to recapitulate phenotypic heterogeneity and exist in different transcriptomic states (Filbin et al., 2018; Patel et al., 2014; Venteicher et al., 2017). Interrogation of mutations from scRNA-seq data is still tedious due to limited mRNA capture and readout sensitivity.

Since transcriptomic data only provides a snapshot of the gene expression in a cell at a particular point in time, and complete overlap of differentially expressed genes between 2 gene expression datasets from the same tissue is rarely achieved (Kim et al., 2012), pathway analysis allows the inference of other expressed genes and their corresponding targets and actions within a cell (Joshi-Tope et al., 2005). Using prior knowledge of gene-to-gene as well as protein-protein interactions, pathways with more meaningful biological information can be reconstructed from the gene expression data (Joshi-Tope et al., 2005). Garofano et al., leveraged information from biological pathways and developed a classification system that identifies tumor intrinsic biological processes in individual GBM cells as well as whole tumor samples using gene expression information obtained from scRNA-seq and bulk transcriptomics (Garofano et al., 2021). In this pathway-based classification, GBM cells were grouped into 4 main stable subtypes namely: glycolytic/plurimetabolic (GPM), mitochondrial (MTC), neuronal (NEU), and proliferative/progenitor (PPR) subtypes. Pathways enriched in the GPM subtype include hypoxia, immune and mesenchymal activities as well as glucose, amino acids, and fatty acids metabolism. In the MTC subtype, mitochondrial activities mainly the tricarboxylic acid (TCA) and OXPHOS pathways are enriched (Garofano et al., 2021). The NEU subtype represents cells enriched for neuronal activities and importantly the glioma-neuron synapse. The PPR subtype is enriched with stem-like progenitor biological pathways as well as cell cycle and DNA replication, damage, and repair pathways (Garofano et al., 2021).

Correlation analysis between these pathway-based GBM subtypes with transcriptomic-based cellular states showed a relationship between the NEU and PPR subtypes with NPC-like and OPC-like cell states mirroring their common involvement in neurodevelopmental processes. The GPM and MTC subtypes showed similarities with AC-like and MES-like cell states respectively (Garofano et al., 2021). Moreover, the GPM subtype mostly correlated with the MES subtypes of both Phillips et al., and Wang et al., while the NEU subtypes fitted well with the PN, and CL (Wang et al., 2017), as well as Prolif and PN subtypes (Phillips et al., 2006). With the advent of the pathway-based classification of GBM, it remains to be seen whether may influence a patient's prognosis and the choice of therapeutic interventions in the clinic.

As seen earlier in the gene expression and DNA methylation subtypes, single-cell analysis has revealed the presence of different phenotypic states representing the different pathway-based subtypes in a single GBM sample. Gene-expression, DNA methylation, and pathway-based GBM subtyping identified the transcriptomic MES subtype, the pathway-based GPM subtype and DNA methylation-based subtypes with mesenchymal features (LGm5) have been associated with poor survival compared to other subtypes with non-mesenchymal features (Ceccarelli et al., 2016; Garofano et al., 2021; Phillips et al., 2006; Wang et al., 2017).

Although the dissection of GBM heterogeneity, tumor classification, and patient stratification have significantly improved in recent years and significantly improved our understanding of GBM, it remains to be seen to what extent the different layers of ITH will impact the outcome of precision medicine approaches based on distinct (epi)genetic molecular profiles.

1.3.3 Epigenetic heterogeneity

Similar to genetic and transcriptomic levels, ITH has also been demonstrated at the epigenetic level. For instance, *MGMT* promoter methylation status, a predictor of the response to TMZ, can differ across cells of the same tumors (Meyer et al., 2015). Similarly, disparate DNA methylation is found in spatially separated GBM biopsies. Although most differences were in less conserved 'open sea' regions, 5/12 tumors displayed different DNA methylation subclasses in distinct tumor zones (Wenger et al., 2019).

Using concurrent mapping of chromatin accessibility and DNA methylation (MAPit-patch) at single-molecule resolution, Nabilsi et al., revealed ITH both at the DNA methylation and chromatin accessibility levels (Nabilsi et al., 2014). Chromatin accessibility controls

promoters of genes such as Prominin-1/CD133 (*PROM1)* and MutL Homolog 1 (*MLH1)*, which are not classically regulated by DNA methylation. Single cell-based assay for transposase-accessible chromatin using sequencing (scATAC-seq) profiles further exposed distinct active DNA regulatory regions in proneural and mesenchymal cells, and their partial overlap in intermediate states (Wang et al., 2019). Recent scATAC-seq revealed several chromatin accessibility modules in each GBM. While at least 2 chromatin accessibility modules were linked to the GBM MES-like state, both NCP- and OPC-like cells were found in the same module, whereas AC-like states show heterogeneous accessibility profiles across several modules (Guilhamon et al., 2021). This result indicates that chromatin accessibility profiles of cells within a similar state may differ, thus highlighting ITH at the single cells level both at the transcriptomic state and the chromatin accessibility profiles.

Recent data using combined gene expression, DNA methylation profiling, and genotyping of single cells revealed extensive ITH at the DNA methylation level in GBM (Chaligne et al., 2021; Johnson et al., 2021). Stochastic alterations in DNA methylation patterns observed are key drivers of intra-tumoral epigenetic heterogeneity in GBM. GBM exhibits higher DNA methylation disorder that facilitates adaptation and cellular heterogeneity, unlike the more hierarchically organized IDHmut tumors (Johnson et al., 2021). Lineage trees reconstructed from DNA methylation data annotated with cell states inferred from the scRNA-seq data confirmed the heritability of DNA methylation alterations and cell states in glioma (Chaligne et al., 2021). These data indicate the transferability and evolution of ITH across generations in GBM cells.

Single-cell multi-omics analysis also allowed the fine-tuning of bulk-based DNA methylation subtypes in gliomas (Chaligne et al., 2021). By combining scRNA-seq and scDNAme (single-cell DNA methylation), Chaligne et al., showed a correlation between cells classified as LGm4 with mostly AC-and MES-like GBM cell states while LGm5 correlated with NPC- and OPC-like GBM cell states. LGm6 was, however, found to correlate with non-malignant glial and immune cells. Overall, this recent data suggests that each tumor is composed of a mixture of cells enriched with different DNA methylation features, and that bulk subtypes not only suffer from contamination by non-malignant cells present in the analyzed tumors but also represent an over-representation of a particular subtype (Chaligne et al., 2021).

1.3.4 Cancer stem-like states, phenotypic heterogeneity and plasticity

Cancer stem cells (CSCs) have long been considered to be the source of ITH in many cancers. The initial CSC hypothesis, established over 20 years ago described the so-called CSCs, or tumor-initiating cells (TICs), to be exclusively responsible for tumor development and maintenance of ITH. CSCs are defined to be cells with the functional "ability to self-renew and generate differentiated progeny". In addition, these cells must possess the ability to generate tumors with heterogeneous cell types upon transplantation. CSCs progenies that are committed to a particular cell fate are referred to as differentiated cells. (Vescovi et al., 2006). Identification of CSCs in GBM has been based on the expression of cell membrane antigens, such as CD133, CD15/SSEA, CD44, or A2B5, or intracellular markers such as Sox2 and Nestin (Anido et al., 2010; Ogden et al., 2008; Singh et al., 2004; Son et al., 2009; Tchoghandjian et al., 2010). However, the presence and distribution of these CSCs in GBM patient tumors were shown to be heterogeneous between and within tumors. Extensive ITH in the number of cells expressing these putative CSCs markers has been shown in patient tumors. Interestingly, one study found that in the total of 6 GBMs analyzed, a variable proportion of CSCs was observed and these CSCs also significantly differed in the number and type of CSC markers they express (Galdieri et al., 2021). Dirkse et al. earlier reported ITH in the expression of an overlapping set of CSC markers in patient-derived orthotopic xenograft (PDOX) models and stem-like cultures (Dirkse et al., 2019).

Numerous studies showed that irrespective of CSC marker expression, GBM cells can self-renew, proliferate indefinitely and form tumors *in vivo* in experimental models. Cellular states appeared non-hierarchical, reversible, and occurred via stochastic state transitions of existing populations, evolving towards an equilibrium instructed by the microenvironment (Dirkse et al., 2019). The characterization of phenotypic heterogeneity in GBM was further enhanced by the ability to link transcriptomic states with cell membrane markers. As the transcriptomic states could be linked to the expression of cell membrane epitopes such as CD44 and CD24 (**Figure 4**), these phenotypic states were purified and functionally assessed. FACS-purified positive and negative fractions formed tumors *in vivo* and reconstituted transcriptomic heterogeneity. As tumor development time was not systematically assessed, it is currently unclear whether transcriptomic states differ in tumorigenic potential and if they reconstitute heterogeneity at the same speed (Neftel et al., 2019). These results led to a novel model explaining phenotypic intra-tumoral heterogeneity, which is based strongly on intrinsic tumor plasticity. Only a very limited differentiation axis is present in GBM, both CSCs and more differentiated GBM phenotypes represent different states that can flexibly interchange while subjected to various stimuli in

TME or upon treatment. The evolution of the CSC hypothesis towards the plasticity model has been widely discussed in our review manuscript, which is present in **Chapter 3**.

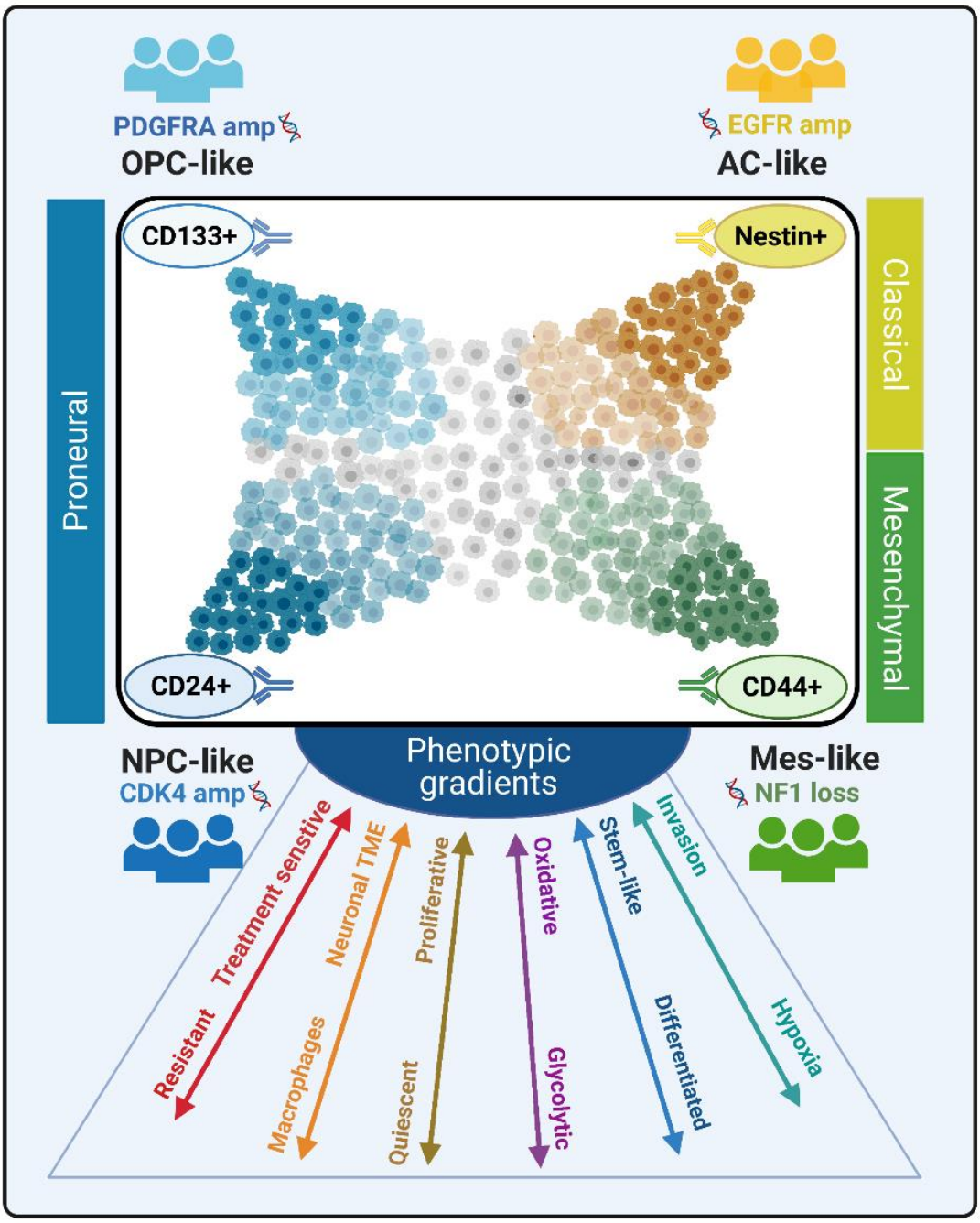

Figure 4. Transcriptomic heterogeneity in GBM. GBM cells exist in gradients of transcriptomic states, with multiple axes of variation. Most defined states lie on the proneural (OPC-like and NPC)-like states to mesenchymal (AC-like and MES-like states) axis. These states express various CSC-associated markers and display extensive phenotypic plasticity. The final equilibrium is dictated by the genetic background (e.g., *PDGFRα*, *EGFR* and *CDK4* amplification, *NF1* loss)) and TME cues. Further gradients can be defined on additional axes.

1.3.5 Glioblastoma tumor niches and functional heterogeneity

GBM, like other solid tumors, can be considered a complex aberrant organ. GBM cells exist in an ecosystem with different non-malignant cell types interacting with the tumor cells and forming tumor niches with specific characteristics. These tumor niches are defined by the phenotypic features of the cells within each niche as well their modulatory effects allowing tumor cells to adjust their metabolic needs, escape immune attacks and enhance invasion and tumor cell survival (Hambardzumyan and Bergers, 2015). Initial reports attributed GBM cells expressing stem cell markers to specific tumor niches (Flavahan et al., 2013; Hjelmeland et al., 2011; Jin et al., 2017), suggesting preselection of GSCs in niches such as hypoxic, perivascular, and invasive niches (Hambardzumyan and Bergers, 2015; Prager et al., 2019). However, recent data suggest that these cells represent rather reversible phenotypes best adapted to the subjected TME niches.

1.3.5.1 Tumor core and perivascular niche

Proliferating tumor cells in the tumor core trigger the development of new blood vessels by the secretion of proangiogenic growth factors like the Vascular endothelial growth factor (VEGF) to promote angiogenesis and to ensure the continuous supply of oxygen (O_2) and nutrients. Tumor cells residing close to newly formed or preexisting blood vessels have relatively good access to O_2 and nutrients. The so-called perivascular niche is also reported to be enriched in GBM cells with high expression of stem cell markers (Lathia et al., 2015; Quail and Joyce, 2017; Schiffer et al., 2019). Interestingly, the expression of stem cell markers such as Nestin, CD34, and CD133 were found to be heterogeneous within different microvascular regions in the perivascular niche (Chen et al., 2017a), thus highlighting the contribution of the perivascular niche in the development and maintenance of ITH in GBM. CD133 expressing CSCs have been shown to reside along the blood vessels and express high levels of VEGF. These growth factors inducing angiogenesis lead to the development of enlarged aberrant vessels that are leaky (**Figure 5**). The resulting aberrant blood vessels and the activity of invading tumor cells between these vessels and astrocytes that are firmly attached to the vessels via their end feet lead to the disruption of the tight junctions of the BBB (Hambardzumyan and Bergers, 2015; Schiffer et al., 2019). Disrupted BBB allows the infiltration of monocytes into the brain that modulates the TME into an immunosuppressive environment as well as triggering immune evasion by tumor cells (Prager et al., 2019; Quail and Joyce, 2017). Using intravital two-photon microscopy, several GBM cells within the perivascular niche lodging between the astrocytes and endothelial cells in the BBB were found to be stagnant for many days. When compared with other GBM cells in the brain

parenchyma, cells within the perivascular niche were found to be significantly less dividing, implying an activation of a quiescent state (Jung et al., 2021). GBM cells residing in the perivascular niche demonstrated stronger treatment resistance against both radiation and chemotherapy compared to other cells within the brain parenchyma in xenograft models. This resistance was due to the networks of interconnected cells via tumor microtubes as well as the activation of the NOTCH pathway (Jung et al., 2021). Quiescent CSC-marker expressing GBM cells have previously been shown to be TMZ resistant as well as spurring recurrence in GBM (Chen et al., 2012).

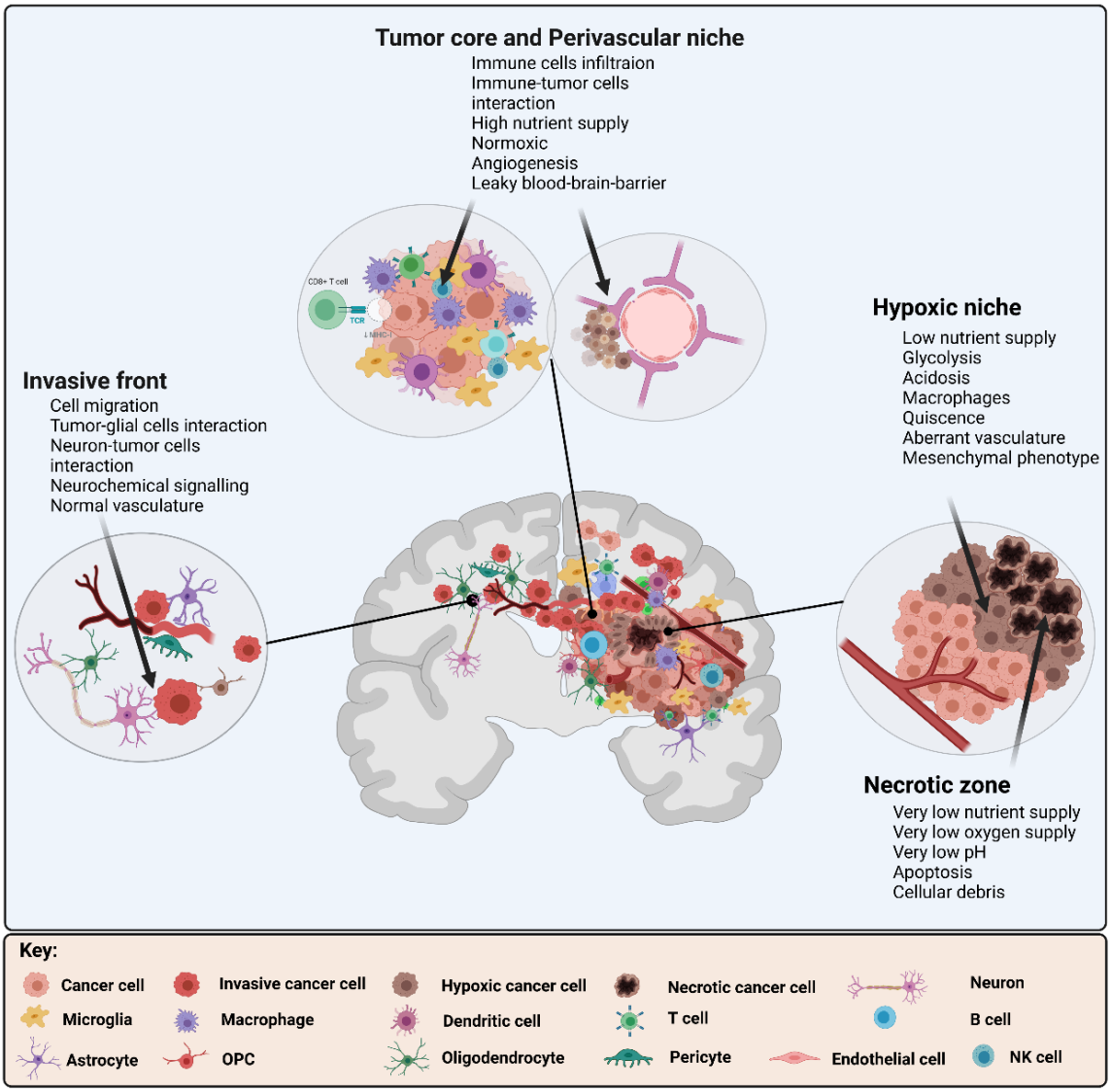

Figure 5. GBM tumor microenvironmental niches and associated cell types. Tumor cells interact with the different cell types within a particular tumor niche.

1.3.5.2 Hypoxic niche

By its distinctive histopathological feature, GBM is described with pseudopalisading necrosis resulting from blood supply obstruction and leading to the development of a hypoxic niche surrounding the necrotic zone (Rong et al., 2006) (**Figure 5**). The obstruction of blood supply to the tumor core results in the restriction of O_2 and nutrient supply to rapidly growing tumor cells leading to hypoxia, which is characterized by the upregulation of HIF1α expression, acidification, and aerobic glycolysis adopted by tumor cells to escape the consequences of low O_2 supply and produce the energy needed for protein and lipid synthesis. This milieu supports the maintenance of stem-like phenotype, ITH, immune evasion, and therapeutic resistance (Terry et al., 2020). Under hypoxic stress, GBM cells with stem-like properties express high levels of HIF-1, which promotes VEGF expression and angiogenesis (Agnihotri and Zadeh, 2016; Hambardzumyan and Bergers, 2015; Prager et al., 2019). Hypoxia and associated decreased *pH* and glucose levels also induce changes in the tumor cell phenotype (Flavahan et al., 2013; Hjelmeland et al., 2011). The resulting conditions imposed by hypoxia lead to quiescence and the activation of survival mechanisms such as autophagy and invasion (Abdul Rahim et al., 2017; Prager et al., 2019).

Hypoxia is a strong modulator of the GBM cells. Using scRNA-seq analysis, Patel et al., uncovered a varying degree of hypoxia among GBM cells (Patel et al., 2014). The MES cell state in GBM was linked to the strong expression of hypoxia genes such as *HILPDA*, indicating the impact of hypoxic conditions on the development of ITH in GBM (Neftel et al., 2019). Recently, a hypoxic environment was confirmed to be critical for the establishment of the MES GBM cell state. A strong positive correlation between MES and hypoxia signatures was observed in cells from patient tumors, xenograft models, and GBM tumor organoids (Hara et al., 2021; Johnson et al., 2021; Pine et al., 2020). Furthermore, the expression *CEBPB* and *STAT3*, key master regulators known to maintain the MES cell state were also associated with a hypoxic and necrotic TME (Behnan et al., 2019; Kim et al., 2021). Cooper et al., demonstrated hypoxia-induced expression of *CEBPB* in U87MG cell lines (Cooper et al., 2012).

Hypoxic niches consequently promote therapeutic resistance in tumor cells with a reduction in O_2 levels directly associated with reduced radiosensitivity. In normoxic conditions, ionizing radiation reacts with intracellular H_2O and O_2 to produce free radicals that cause severe DNA damage in targeted cells (Amberger-Murphy, 2009). In hypoxic conditions, this effect is difficult to achieve due to low O_2 levels, and induced DNA damage is easily repaired by tumor cells. Moreover, decreased cell proliferation leads to inhibited efficacy of classical

chemotherapeutics, including TMZ. Collectively, the acidic environment, limited O_2 and nutrient availability, as well as therapeutic agents act as selection pressures for tumor subpopulations capable of adapting and surviving in these harsh conditions. This ultimately promotes a shift towards adaptation to nutrient deprivation and treatment resistance.

1.3.5.3 Invasive front

A major feature of adult diffuse gliomas, especially GBM, is the ability of the tumor cells to invade from the tumor core into the brain parenchyma. Invading tumor cells can travel to the normal brain area along the blood vessels or via the white matter tracts and the subarachnoid space (Fabian et al., 2021). GBM cells invade either as single cells or collectively through brain parenchyma, along blood vessels and neuronal tracks. Barcoding technology showed that multiple cells clones within GBM invade the surrounding brain uniformly with similar invasive capacity (Lan et al., 2017). Invasive cells activate several mechanisms allowing them to digest the extracellular matrix and migrate with the least resistance into the brain parenchyma (Vollmann-Zwerenz et al., 2020). Several proteases, particularly matrix metalloproteinases (MMPs) MMP-2 and MMP-9 secreted by invading GBM cells have been shown to promote GBM cells invasion (Hatoum et al., 2019). Invasive GBM cells also remodel their cytoskeletal structure through the formation of invadopodia and lamellipodia to aid their motility during brain invasion (Fabian et al., 2021; Velásquez et al., 2019). Recently, Bhaduri et al., using scRNA-seq uncovered the role of outer radial glia-like GBM cells in the reactivation of normal developmental programs that influence the composition of cell types and invasive phenotype in GBM. *PTPRZ1* expression was shown to mediate mitotic somal translocation in radial glia-like cells thereby increasing their invasive capacity. Knockdown of *PTPRZ1* in these outer radial glia-like cells significantly reduced their invasive capacity in xenograft models (Bhaduri et al., 2020).

1.3.5.4 Tumor network

GBM tumor cells communicate with each other via numerous mechanisms, including direct cell-cell contacts, paracrine cytokine-based signaling, and exosomes (Monje, 2020). Recent studies revealed an extraordinary network, allowing GBM cells to interconnect directly via ultra-long tumor microtubes protruding from the cell membranes(Jung et al., 2017; Osswald et al., 2015; Weil et al., 2017). These networks are exclusive to IDHwt GBM and IDHmut high-grade astrocytomas but absent in 1p/19q co-deleted oligodendrogliomas (Osswald et al., 2015). Tumor microtubes form a functional syncytium allowing the transfer of small molecules such as Ca^{2+}, secondary messengers, and RNAs (Osswald et al., 2015) via connexin 43 (*Cx43*)- containing gap junctions. Tumor network development depends on growth-associated protein 43 (*Gap43*) (Osswald et al., 2015) and tweety-homolog 1 (*Ttyh1*),

(Jung et al., 2017), key drivers of normal neurite-like membrane protrusions and neurodevelopment. Unlike tunneling nanotubes, microtubes are thin, long, and more stable (Winkler and Wick, 2018) allowing for interconnections of invasive cells with the tumor core over long distances and calcium homeostasis. GBM cells show heterogeneous abilities to form microtubule-based connections: while GBM cells in the tumor core remain highly connected, those in the perivascular and invasive region remain less connected or do not produce any microtubes (Jung et al., 2021). GBM cells with 1-2 microtubes and high *Ttyh1* expression are invasive, whereas highly connected cells (>4 microtubes) are largely immobile (Jung et al., 2017). While knockdown of *Ttyh1* led to impaired invasion and subsequent brain colonization, *Ttyh1*-deficient cells remained highly connected, highlighting heterogeneous functionalities within the network. The self-repair function of the tumor network-enabled enhanced tumor cell survival and resistance to radiotherapy (Osswald et al., 2015) and chemotherapy (Weil et al., 2017), while the unconnected tumor cells showed higher sensitivity to treatment. This suggests an important role played by the tumor network in GBM plasticity and survival. Tumor networks have recently been shown to possess enhanced stem-like features (Xie et al., 2021). Interestingly, this functional network was recently shown to play an active role in phenotypic state transitions during tumor growth, invasion, and treatment escape (Jung et al., 2021). *NOTCH1* was shown to be the central mediator of resistance in perivascular GBM cells and its absence leads to slowed tumor growth and rapid formation of tumor networks that enhance resistance while limiting tumor invasion.

1.4 GBM tumor microenvironment

Different non-neoplastic cell types play important roles in supporting the survival of tumor cells. These cells forming the so-called TME are found intertwined with the core tumor cells and serve as a scaffold for the tumor cells to thrive. By their presence and interactions with the tumor cells (tumor-TME crosstalk), they can perturb the tumor cells within their vicinity and have the capacity to alter the inherent heterogeneity within the tumor cells or even trigger a new pattern of tumoral heterogeneity (Hanahan and Weinberg, 2011; Kreso and Dick, 2014; Pine et al., 2020). The use of scRNA-seq has allowed the delineation of the different cell types within the TME in GBM, thereby uncovering the abundance, heterogeneity, and transcriptomic features associated with these cells types (Bhaduri et al., 2020; Darmanis et al., 2017; Neftel et al., 2019; Wang et al., 2019; Yu et al., 2020). The GBM TME can be broadly classified into two main compartments: (1) the immune compartment represented by the myeloid cells (TAMs, dendritic cells (DCs), neutrophils, mast cells, and platelets) (De Leo et al., 2021; Pombo Antunes et al., 2021) and the lymphoid cells (T cells, B cells, and the natural killer (NK) cells) (Friebel et al., 2020; Pombo Antunes et al., 2021; Quail and Joyce, 2017); (2) The non-immune brain-derived cell types, consisting of cells such as astrocytes, oligodendrocytes, oligodendrocyte progenitor cells (OPCs), endothelial cells, pericytes, and ependymal cells (Bhaduri et al., 2020; Johnson et al., 2021; Wang et al., 2019). The myeloid component of the TME forms a major component of my thesis and thus, will be extensively discussed in the subsequent sections with a brief mention of other cellular components of the GBM TME.

1.4.1 The immune compartment

1.4.1.1 Tumor-associated microglia and macrophages

Microglia (Mg) and macrophages within and around the GBM tumor cells are referred to as the tumor-associated Mg and macrophages (TAMs) and collectively are the most numerous cell type in the TME making up to 40-50% of cells identified (Andersen et al., 2021; Buonfiglioli and Hambardzumyan, 2021; Hambardzumyan et al., 2015; Pires-Afonso et al., 2020; Quail and Joyce, 2017). TAMs represent the most abundant immune cell types within the TME and thus are exploited for targeted and immune therapy (De Leo et al., 2021).

Mg cells are the resident phagocytic cells in the brain and were shown to be present in the brain during early embryonic development, arising from the hematopoietic progenitors in the yolk sac (Andersen et al., 2021; Gomez Perdiguero et al., 2015). In GBM, Mg cells are recruited to GBM tumors, where they differentiate into TAMs. Such Mg-derived TAMs (Mg-TAMs) were initially reported to populate peritumoral regions (Chen et al., 2017b). However,

a recent detailed histopathologic analysis of patient tumors revealed a heterogeneous presence of Mg-TAMs in GBM. A substantial number of Mg-TAMs in the tumor core area almost equal their proportion in the peritumor area (Zeiner et al., 2019). In contrast, monocytes from the blood infiltrate the brain and differentiate into TAMs (Andersen et al., 2021; Bowman et al., 2016; Buonfiglioli and Hambardzumyan, 2021; Ginhoux et al., 2010). In GBM, monocyte-derived TAMs (Mo-TAMs, also referred to as bone marrow-derived macrophages (BMDM)) are located around the leaky blood vessels embedded in the tumor core (Chen et al., 2017b). Recently, a substantial pool of non-blood-derived monocytes with distinct gene expression profiles was discovered and shown to originate from the skull. They reside in the meningeal barrier and infiltrate the brain parenchyma during brain injury, neuroinflammation, and possibly brain tumors (Cugurra et al., 2021). It is not fully clear whether these non-blood derived myeloid cells (Cugurra et al., 2021) represent the so-called border-associated macrophages (BAMs) identified to reside in the meninges, choroid plexus, and brain parenchyma of both tumor-bearing (Ochocka et al., 2021) and non-tumor bearing mice, although they are also thought to partially originate from the bone marrow (Van Hove et al., 2019).

The abundance of TAMs and proportions of Mg-TAMs, Mo-TAMs, and BAMs within the TAMs vary with tumor type. In IDHwt GBM, Mo-TAMs were reported to be more abundant than Mg-TAMs, while the reverse is the case in IDHmut GBM. While the myeloid compartment accounts for about 75% of the TME cells in GBMs, lymphocytes only account for about 25% of the cells (Klemm et al., 2020). Recent studies using scRNA-seq indicate further that recurrent IDHwt GBM shows a higher proportion of Mo-TAMs than primary IDHwt GBMs (Abdelfattah et al., 2022; Pombo Antunes et al., 2021) arguing against previous reports that used deconvolution methods to estimate cell type abundance in bulk gene expression data (Wang et al., 2017). A higher percentage of Mo-TAMs compared to Mg-TAMs was also reported to be present in *p53* deficient tumor cells (Wang et al., 2017). TAMs have been reported to be enriched in GBMs with *NF1* mutations that are linked to the MES subtype and MES-like cell states (Hara et al., 2021; Neftel et al., 2019; Wang et al., 2017). This implies that tumor cell genetics dictate the abundance and type of myeloid cells within the TME (Akkari et al., 2020; Friebel et al., 2020).

TAMs heterogeneity

Mg can transit to several phenotypic states, allowing the enactment of different functions in the brain, both in normal and disease contexts (Masuda et al., 2019, 2020; Sousa et al., 2018). Single-cell protein and gene expression profiling allowed for the extensive characterization of Mg subpopulations in GBM based on their gene expression programs

(Friedrich et al., 2021; Klemm et al., 2020) and surface protein expression (Friebel et al., 2020; Van Hove et al., 2019; Sankowski et al., 2019), hence allowing the uncovering of Mg-TAMs heterogeneity in GBM beyond the traditional binary pro-inflammatory and anti-inflammatory (M1/M2) states (Hara et al., 2021; Müller et al., 2017; Ochocka et al., 2021; Pombo Antunes et al., 2021). Recently, Ochocka et al. identified eight Mg subpopulations (MG1 to M8) in the GBM GL261 mouse model. MG1 expresses homeostatic Mg genes *P2ry12 and Cst3* and MG2 expressing transcription factors *Jun* and *Fos* were found in both tumor-bearing and non-tumor bearing mice, while MG3 has *Bmp2k* and *Blhhe41* among top markers, MG4, MG5 expressing *Plp1* and *Mbp*, and MG6 cluster expressing *Cd63* and *Cd9* were specific to non-tumor bearing mice, and MG7 expressing *Cd74* and *H2.Ab1* and MG8 expressing *Top2a* and *Tubb5* clusters were found in only tumor-bearing mice. Different functions were attributed to the Mg clusters ranging from the homeostatic function of MG1 and the triggering of an anti-inflammatory response by the MG3 cluster. Cells in the MG2 cluster express mainly transcription factors signifying active transcriptional activity in the cells. While cells in MG5 express myelin-related genes, cells in MG6 cluster encode proteins linked to extracellular vesicles. MG7 cells upregulate MHCI and MHCII genes while MG8 cells represent proliferating Mg. No specific function was attributed to the MG4 cluster that was only present in female non-tumor-bearing mice (Ochocka et al., 2021). These studies using patient GBM samples, tumor, and non-tumor bearing mice have effectively revealed the extensive heterogeneity of Mg subpopulations resulting in differences in cellular states linked to their spatial location within the brain as well as their function (Cugurra et al., 2021; Ochocka et al., 2021). More recently, single cells analysis identified four distinct clusters (MC1, MC2, MC6, and MC7) expressing Mg genes among 9 subpopulations identified in myeloid cells from 18 gliomas biopsies, out of which 16 are IDHwt GBMs (Abdelfattah et al., 2022). MC1 cluster referred to as i-Mic express markers such as *CCL3*, *CCL4*, and *CD83* that are indicative of microglial activation while MC2 named h-Mic express *CST3*, a homeostatic Mg marker. MC6 named AP-Mic expresses dual Mg and macrophage markers such as *TGFBI*, *B2M*, *CD163* while MC7 named a-Mic expresses *SPRY1*, *PYRY13* in addition to activated Mg genes.

Mo-TAMs are also heterogeneous and possess the ability to alter their gene expression profile into an Mg-like state. Several subpopulations of Mo-TAMs were described with different transcriptional features and functions in recurrent GBM samples that are conserved in the GBM GL261 mouse model (Friedrich et al., 2021; Pombo Antunes et al., 2021). These gene expression programs include “transitory” Mo-TAMs that are actively differentiating into macrophages in GBM (Pombo Antunes et al., 2021). A subpopulation of Mo-TAMs express genes known to be core microglial genes such as *CX3CR1* and *BIN1* suggesting a transition

to an Mg-like phenotype. With this ability to switch their phenotype and function, these monocytes are considered to replace Mg in the event of Mg depletion in the brain and especially during GBM recurrence (Andersen et al., 2021; Pombo Antunes et al., 2021). Other subsets of Mo-TAMs are the phagocytic monocytes with a phagocytosis and lipid metabolism signature, the hypoxic monocytes expressing hypoxic and glycolytic genes, and the subsets upregulating *Selenoprotein P* (*SEPP1)* and genes responsible for anti-inflammatory activation. Lastly, a subset of these monocytes was shown to display an interferon-induced signature. Recent data also show at least two monocyte subpopulations in biopsies from glioma patients (Abdelfattah et al., 2022). These subpopulations were named s-Mac1 and s-Mac2. While s-Mac1 expresses key monocyte markers such as CD14 and polarized macrophage markers e.g. CD163, s-Mac2 expresses genes like *LYZ*, *CD163*, *S100A4*, and genes indicative of immune suppression such as *IL10* and *TGFB1*.

BAMs were also recently reported as a subset of myeloid cells and are widely distributed along the brain borders in both tumor and non-tumor-bearing mice brains. These unique subpopulations express distinct markers such as *Mrc1, Pf4, F13a1, and Dab2* and account for about 3.5% of all the immune cells isolated in GL261 models. They however share a more similar gene expression profile with Mo-TAMs than Mg-TAMs (Ochocka et al., 2021).

A GBM specific TAMs state was recently identified that expresses a different gene expression program than the TAMs feature seen in other gliomas and defines a subset of TAMs linked to the GBM MES cell state. The transcriptomic profile of these TAM subsets shows a program that is between Mg-TAMs and Mo-TAMs (Hara et al., 2021). Interestingly, another subpopulation of TAMs expressing macrophage receptor with collagenous structure (MARCO), a scavenger receptor, was exclusively found in GBM. IDHmut gliomas show a marked decrease in the expression of MARCO. These MARCO-expressing TAMs also correlated with a MES GBM state. Additionally, GBM patients with $MARCO^{+}$ TAMS show worse overall survival compared to $MARCO^{-}$ patients (Chen et al., 2021a).

GBM-TAMs crosstalk and plasticity

TAMs are not only heterogeneous but very plastic (Andersen et al., 2021; Klemm et al., 2020; Ye et al., 2021). This plasticity is influenced by the extensive molecular crosstalks with tumor cells and other neighboring cells, which adapt TAMs to effectively support tumor growth by altering their transcriptional profile and functional state (Klemm et al., 2020). Recent studies suggest that the expression of Leukemia Inhibitory Factor (LIF) (a cytokine) by tumor cells is associated with TAMs infiltration in GBMs (Pascual-García et al., 2019). LIF recruits EZH2 and triggers the repression of CXCL9 expression by TAMs, thereby

blocking the infiltration of cytotoxic $CD8^+$ T cells in tumor cells. Blocking LIF in tumors was shown to activate the chemo-attracting function of CXCL9, leading to $CD8^+$ T cells infiltration, attenuating anti-tumor immune response, tumor regression, and increased overall survival in LIF expressing GL261N-derived GBM model. LIF-CXCL9 interaction is only one of the many ways tumor cells escape immune attack by ensuring an immunodeficient TME. However, it is still not clear how non-LIF expressing GBMs modulate the immune response.

One of the well-described TAMs-GBM interactions is the CD47-SIRPα crosstalk. GBMs and other solid tumors upregulate CD47 the "don't eat me" signal that binds to SIRPα on myeloid cells with high affinity and inhibiting their phagocytic ability (Hu et al., 2020a; Willingham et al., 2012). Immunological inhibitors targeting CD47-SIRPα mainly anti-CD47 and in combination with TMZ have been developed and were reported to enhance innate immune antitumor response resulting in prolonged survival in mouse models of brain and other tumors (Gholamin et al., 2017; Li et al., 2018; von Roemeling et al., 2020; Willingham et al., 2012). Interestingly, a marked increase in the microglial phagocytic effect was observed following anti-CD47 treatment in xenograft models with corresponding survival benefits in mice that received treatment (Hutter et al., 2019). Recently, crosstalk between GBM cells and macrophages was demonstrated by Hara et al., where macrophages were found to secrete oncostatin M (OSM) which interacts with the OSM receptor or LIF receptor expressed by GBM cells. This crosstalk activates STAT3 leading to the subsequent transition of interacting GBM cells to a MES-like cell state (Hara et al., 2021). Tumor-associated macrophages were also shown to interact with GBM cells via SPP1 expressed by macrophages and CD44 receptors in GBM and promote a shift toward a MES-like phenotype. High expression of both SPP1 and CD44 correlated with poor survival in GBM patients (He et al., 2021). These results raise hope for the development of immune checkpoint therapies targeting specific GBM-immune interactions and the potential benefits of TAMs re-education as a strategy against GBM cells.

More evidence on tumor cell immune interactions is emerging. $CD8^+$ T cells were shown to prime microglia by expressing CCL4 and microglia, in turn, express CCL5 which supports tumor cell growth in low-grade glioma (Guo et al., 2020). CX3CR1 a chemokine and CCR2 expressed by Mg-TAMs have also been shown to play a critical role in supporting tumor growth and progression (Pan et al., 2018). However, the role of tumor cells in establishing the crosstalk with the T cells-educated microglia is yet to be elucidated.

1.4.1.2 Dendritic cells and the neutrophils

Other myeloid cell types are DCs and neutrophils. DCs are antigen-presenting cells with a critical function in modulating the tumor immune microenvironment (Andersen et al., 2021). DCs similarly to Mg, present tumor antigens to T cells, leading to their activation (Quail and Joyce, 2017; Wculek et al., 2020). The preselection of $CD45^{+}$ immune cells from human and mice GBM samples allowed the interrogation of DCs using scRNA-seq (Pombo Antunes et al., 2021). A heterogeneous population of DCs with diverse gene expression programs and functions including conserved subsets in human and mouse GBM were identified (Friebel et al., 2020; Pombo Antunes et al., 2021). Due to the different phenotypic features and functions of DCs such as a monocytes/macrophage-like gene expression program as well as their role in invasion and angiogenesis (Quail and Joyce, 2017), they are now being further interrogated for potential capacity to enhance immunotherapy and also the development of DC vaccines (De Leo et al., 2021; Quail and Joyce, 2017; Wculek et al., 2020). Neutrophils are the most abundant leukocytes in circulation and infiltrate the brain in GBM upon the disruption of the BBB (Fossati et al., 1999; De Leo et al., 2021). They are found to be more abundant in GBMs compared to other gliomas (Fossati et al., 1999). Gene expression studies, especially the scRNA-seq often miss neutrophils because of the low number of genes expressed by these cells type compared to other cell types within the TME, and thus applying the default and often recommended threshold for quality control results in the depletion of these cells at the bioinformatic level (Wauters et al., 2021). Neutrophils have been linked to play a pro-inflammatory and immune-suppressive function in brain tumors by their ability to change their phenotype via upregulation of ADORA2A, adenosine receptor, and MET respectively (Klemm et al., 2020). Importantly, neutrophils were shown to enhance necrosis in GBM through ferroptosis-induced cell death (Yee et al., 2020).

1.4.1.3 Lymphoid cells

The lymphoid part of the immune compartment within the TME is comprised of lymphocytes, mainly T and B cells and NK cells (Quail and Joyce, 2017). A variety of lymphocytes infiltrate brain tumors with variable abundance based on tumor type (Friebel et al., 2020; Friedrich et al., 2021), these lymphocytes are by far outnumbered by TAMs and other glial cell types (Andersen et al., 2021; Fu et al., 2020). Interpatient differences exist in T cells predilection in GBM. MES GBM subtypes show a higher T cell enrichment compared to classical and proneural subtypes (Hara et al., 2021). Interestingly, MES-like GBM cells are highly correlated with cytotoxic T cell markers *GZMB* and *PRF1* while displaying marginal correlation with T regulatory cells marker *FOXP3* and exhaustion markers *LAG3*, *PDCD1*,

TIGIT, which are linked to immunosuppression. This indicates variation in the functionality of different T cells subpopulations in GBM. Using scRNA-seq, Mathewson et al., recently revealed the heterogeneity in glioma infiltrating T cells. This analysis broadly identified 4 major T cells clusters namely, CD4 conventional T cells, CD8 T cells, CD4 regulatory T cells, and cycling T cells. Both CD4 conventional T cells, and CD8 T cells were found to have at least 6 gene expression programs representing different T cell functions. Additionally, a novel subpopulation of T cells with a cytotoxic program (NK-like T cells) expressing several NK cell receptors including CD161 which shields glioma cells from T cells attack was discovered (Mathewson et al., 2021).

Under normal conditions, tumor-infiltrating lymphocytes are primed upon interacting with the antigen presenting cells (APCs) and elicit an effector function (Quail and Joyce, 2017). However, in GBM and other cancers this function is impaired leading to immunosuppression (Grabowski et al., 2021; Thommen and Schumacher, 2018). In addition, GBM is a notoriously “cold” tumor with limited T cells infiltration and immune surveillance due to its low mutational burden (Frederico et al., 2021; Jackson et al., 2019; Vella and Bergers, 2018). Furthermore, GBM cells were shown to evade immune surveillance by orchestrating T cells paucity within the TME through the secretion of factors that are responsible for *Sphingosine*-1-phosphate 1 (*SIP1*) loss on the surface of circulating T cells in the brain and the subsequent accumulation of these T cells in the bone marrow (Chongsathidkiet et al., 2018).

Recently, a novel interaction between T cells and GBM cells was uncovered. Cytotoxic T cells were shown to express CD161, an NK cells receptor that interacts with CLEC2D on GBM cells to inhibit T cell anti-tumor function. Blocking this receptor with antibodies enhanced the T cell anti-tumor effect and induced tumor cells death *in vitro* and also enhanced the T cell anti-tumor effect in humanized mouse models (Mathewson et al., 2021). This novel crosstalk could be exploited and targeted to enhance immunotherapy in GBM.

While both B and NK cells were reported in GBM TME, the role of these cells in GBM is not fully understood. Initial studies identified B cells signals in only a subset (40 %) of human GBMs (Lee-Chang et al., 2019). scRNA-seq profiling identified B cells subpopulation representing matured and cycling B cells in human GBM samples (Bhaduri et al., 2020). However, other reports only identified a single cluster with only a few B cells compared to T lymphocytes (Abdelfattah et al., 2022; Friebel et al., 2020; Klemm et al., 2020) as reported in various syngeneic mouse models (Khalsa et al., 2020). Notably, an increase in the infiltration of lymphocytic cells including B and NK cells was reported in recurrent GBMs (Pombo Antunes et al., 2021). The function of B cells remains the least explored among the

lymphocytes in the TME of GBM. So far, they have been shown to act as APCs and interact with T cells to induce anti-tumor responses (Candolfi et al., 2011). NK cells are also present in the TME of GBMs (Abdelfattah et al., 2022; Friebel et al., 2020; Klemm et al., 2020; Pombo Antunes et al., 2021). However, they were mostly shown to be immature in GBM unlike in low-grade gliomas that appear to be highly cytotoxic (Friebel et al., 2020). These immature NK cells are non-functional and contribute to immune suppression in the TME (Fu et al., 2020). More studies are needed to fully characterize and understand the functionalities of B and NK cells in GBM to exploit these immune cell types for targeted or immune therapy.

1.4.2 The non-immune TME compartment

Neurons, astrocytes, oligodendrocytes, OPCs, and neural stems cells (Liddelow and Barres, 2015) have been reported in GBM patient samples with varying proportions (Bhaduri et al., 2020; Johnson et al., 2021; Neftel et al., 2019; Wang et al., 2019; Yu et al., 2020).

1.4.2.1 Neurons

Recent data highlighted the critical role of the interconnection between the brain tumor cells network and neurons during tumorigenesis. These crosstalks occur via physical contact, molecular and electrochemical signaling, forming neurogliomal synapses that allow gliomas including GBMs to hijack the neuronal network in the brain and receive electrochemical signals that promote tumor progression and invasion (Venkataramani et al., 2019; Venkatesh et al., 2019). Interestingly, blocking these electrochemical transmissions between neurons and glioma cells attenuated glioma growth while depolarization of glioma cells which enhances cellular communications amplified tumor growth. This highlights a feedback loop modulated by both neuronal activity and glioma cell response. The TME contributes to this neuro-glioma enhanced tumor growth by secreting growth factors such as neuroligin-3 (NLGN3), which are critical for tumor signaling and the formation of neurogliomal synapses (Venkatesh et al., 2015). These data emphasize the interaction between the reversible interaction between tumor cells and neurons, which are further enhanced by the TME to facilitate tumor growth and progression.

1.4.2.2 Astrocytes

Astrocytes are the most prevalent of the glial cell population in the brain and serve important functions in normal and GBM contexts (Andersen et al., 2021; Brandao et al., 2019). In a

healthy brain, astrocytes form part of the BBB structure and help in maintaining tight junctions in BBB. They also respond to CNS damage by undergoing phenotypic changes, becoming more reactive through a process known as astrogliosis, which enables the repair of damaged tissue (Brandao et al., 2019; Escartin et al., 2021). In brain tumors, reactive gliosis occurs during GBM progression (Quail and Joyce, 2017). However, this process instead supports tumor propagation and enhances GBM growth and aggressiveness (Henrik Heiland et al., 2019; Okolie et al., 2016; Wurm et al., 2019). Astrocytes have been extensively studied in the normal brain as well as in the context of neuroinflammation and were found to be heterogeneous with up to 5 different subpopulations in human and mouse brains (Batiuk et al., 2020; Bayraktar et al., 2020; Escartin et al., 2021; John Lin et al., 2017; Zhang et al., 2016b). In GBM, the existence of different astrocytic subpopulations with distinct transcriptional programs shaped by reactive states has been shown (Henrik Heiland et al., 2019). Reactive astrocytes were shown to have an enriched IFNγ response and activation of the JAK/STAT signaling pathway, known to enhance immunosuppression and tumor proliferation. However, less is known about the functions of the different astrocyte subpopulations and how they interact with GBM cells as well as other cells within the TME.

Six subpopulations of astrocytes (A, B, C, D, E, and Neg) were identified with distinct markers in normal mouse brains using FACS analysis, out of which subpopulations A-D were identified in primary GBM (John Lin et al., 2017). A comparison of the gene expression profiles of these astrocyte subpopulations within GBM subtypes showed a correlation between A, B, C, and D subsets with classical GBM while neural subtype correlated with A, B, and C subpopulations. The mesenchymal subtype associated with the B subpopulation while the proneural subtype did not correlate with any of the astrocyte subpopulations. Enrichment of genes associated with synaptogenesis and synapse function in subpopulations C and D alongside data from the monitoring seizure onset in glioma models suggest these subpopulations are linked to tumor-associated epilepsy in GBM (John Lin et al., 2017). Subpopulations B and D were found to be more enriched for cellular migration than C. These findings suggest heterogeneity in the abundance and function of diverse astrocytic subpopulations in GBM. Additionally, these diverse tumor-activated astrocytes serve pro-tumor functions at various stages of GBM progression.

Crosstalk between GBM cells and astrocytes has been shown to enhance the growth of GBM cells. Human astrocytes co-cultured with GBM cell lines and patient-derived GBM cells showed significantly increased growth compared to monocultured GBM cells. The communication between GBM cells and astrocytes was shown to occur via a paracrine mechanism involving the secretion of *Periostin* and *Serglycin* genes by GBM cells. This

suggests GBM cells which depend on the reactive state of astrocytes directly mediate astrocyte activation (Mega et al., 2020). GBM associated astrocyte signature derived from upregulated genes identified following astrocyte-GBM co-cultures compared to astrocytes cultured alone was applied to score the TCGA GBM cohort. A high astrocyte signature score correlated with poor prognosis and vice versa. Astrocyte-GBM co-cultures increased GBM proliferation while intracranial implantation of GBM cells together with reactive astrocytes in mouse models resulted in an increased tumor growth and a decreased survival in mice (Mega et al., 2020). Astrocytes were also shown to upregulate Chitinase 3-like 1 (*CHI3L1*) upon crosstalk with GBM cells via interleukin-13 receptor subunit alpha-2 (IL13RA2). This activates the MAPK signaling pathway and promotes a subtype switch towards a mesenchymal state in GBM (Wurm et al., 2019). A recent study suggests the involvement of reactive astrocytes in a tripartite crosstalk between GBM cells, astrocytes, and microglia leading to the reprogramming of myeloid cells towards an anti-inflammatory state. This, in turn, promotes an immunosuppressive TME in GBM. Therapeutic inhibition of JAK/STAT signaling in brain slice cultures reversed myeloid cell states from an anti-inflammatory to a pro-inflammatory state (Henrik Heiland et al., 2019). These initial findings reveal important insights on astrocyte-GBM crosstalk and enhancement of GBM progression. Further studies are needed to fully unravel the heterogeneity, functions, and the mechanisms of astrocyte activation in GBM.

1.4.2.3 OPCs and oligodendrocytes

OPCs are the precursors of oligodendrocytes. However, not all OPCs differentiate into oligodendrocytes with myelination function. A subset of OPCs exists as resident glial cells in the CNS (Laug et al., 2018). OPCs express neuron-glial antigen 2 (NG2) and are also referred to as “NG2 cells”. Functionally, OPCs are heterogeneous and a subset of these cells display plasticity, particularly at the early developmental stage (Bergles and Richardson, 2015; Dietmann et al., 2019). Upon the differentiation of OPCs to oligodendrocytes and during brain injury, adjacent OPCs rapidly migrate to the site of OPCs depletion or injury and proliferate to restore population density (Hughes et al., 2013). OPCs have also been shown to regulate neuroinflammation via the expression of LRP1 and promoting myelin repair (Fernández-Castañeda et al., 2020). In GBM patient tumors, distinct OPC and oligodendrocyte clusters have been reported following scRNA-seq analysis. Markers such as *PDGFRα*, *CSPG4,* and *VGF* identify *OPCs* populations while *OLIG1, OLIG2, MOG,* and *SOX2* expression classify oligodendrocytes (Bhaduri et al., 2020; Darmanis et al., 2017; Neftel et al., 2019; Yuan et al., 2018). OPCs have been investigated in the context of glioma initiation and are thought to represent one of the cells of origin of gliomas (Laug et al., 2018; Lee et al., 2018; Liu et al., 2011; Wang et al., 2020b).

A single-cell survey of tumor-host interactions revealed crosstalks between GBM cells and oligodendrocytes (Caruso et al., 2020). Although most of the ligand (tumor cells)-receptor (oligodendrocytes) pairs such as MDK-LRP2, JAM2-JAM3, CNTN2-NRCAM involved in these interactions were not expressed in all the patient samples, a significant number of GBMs and oligodendrocytes express them. These interactions relate to signaling pathways linked to cell growth, gliogenesis, and neurogenesis. The significance of these interactions remains underexplored.

1.4.2.4 Endothelial cells, pericytes, and ependymal cells

Although endothelial cells, pericytes, and ependymal cells have all been reported as cell types within the GBM TME with distinct gene expression signatures (Bhaduri et al., 2020; Johnson et al., 2021; Quail and Joyce, 2017; Wang et al., 2019), the heterogeneity of these cell types has not been extensively investigated in the GBM context. While endothelial cells have been shown to play an important role in angiogenesis in GBM (Bougnaud et al., 2016), both endothelial cells and pericytes are key components of the BBB structure helping to prevent leakiness by maintaining tight junctions (Quail and Joyce, 2017). Endothelial cells are also instructed by tumor cells and thus express differential transcriptomic features in comparison to their status in the normal brain. For example, angiogenic tumor cells influence endothelial cells formation of aberrant blood vessels via several mechanisms involving pathways such as VEGF and TGFβ pathways (Bougnaud et al., 2016). Endothelial cells have been shown to communicate with GBM cells through the secretion of SIP and the overexpression of its receptors (SIP1 and SIP3) by GBM cells (Abdel Hadi et al., 2018). This communication mechanism enhances proliferation and angiogenesis in GBM.

Collectively, the different cellular components of the TME alongside the crosstalk which occurs with GBM cells enable flexibility and adaptation to a dynamic tumor microenvironment within the context of a complex brain ecosystem. The complex molecular crosstalk between tumor and TME has potential implications for immunotherapy and targeted therapy. However, these interactions, particularly upon treatment, are still largely ambiguous and further studies are needed to unravel this important axis aiding tumor cells therapy escape.

1.5 Treatment resistance in glioblastoma

The main drivers of treatment resistance in GBM can be broadly divided into tumor intrinsic and non-tumor intrinsic factors. Tumor intrinsic factors include genetic and epigenetic mechanisms within the tumor cells, while the non-intrinsic factors are external factors from TME which enable adaptation to treatment pressure (Eyler et al., 2020; Lee, 2016). GBM cells escape treatment and develop resistance through the combination of several mechanisms. Below, I discuss DNA repair mechanisms and genetic clonal evolution as important factors in GBM resistance. I further introduce the role of stemness features, phenotypic tumor heterogeneity, and plasticity as additional key mechanisms leading to inevitable intrinsic resistance. These topics are further elaborated in our recent review, presented in **Chapter 3.**

1.5.1 DNA repair mechanism

The main mechanism of action of IR and TMZ used as the standard-of-care treatment in GBM is the induction of DNA damage in GBM cells (Chalmers et al., 2009). IR induces double-strand breaks (DSB), DNA base damage, and single-strand breaks (SSB). Intrinsic cellular mechanisms mainly homologous recombination (HR) and non-homologous end-joining (NHEJ) for DSB and SSB repair for SSB, as well as base excision repair (BER) for damaged bases, are deployed to repair these damaged lesions. TMZ as an alkylating agent inflicts DNA damage by adding a methyl group at N^7 and O^6 sites on guanine residues of DNA resulting in N^7-methylguanine and O^6-methylguanine respectively. An additional methyl group on the N^3 site on adenine residue results in N^3-methyladenine in the DNA of GBM cells. The alkylation of the guanine residue at O^6 is the most cytotoxic lesion. O^6-methyl group obstructs efficient pairing of guanine and cytosine and causes mismatched pairing with thymine on the newly synthesized DNA. These mismatches lead to ineffective repair cycles by the mismatch repair pathway and persistent single-strand DNA breaks. Inheritance of this mismatched cytotoxic DNA molecule in daughter cells is deleterious due to the absence of an efficient DNA repair process (Erasimus et al., 2016; Lee, 2016). The alkylation-induced lesions in the case of N^7-methylguanine and N^3-methyladenine can be repaired through the BER mechanism. O^6-methylguanine is however repaired by the MGMT enzyme. MGMT undergoes a 2-step suicidal transfer of the methyl group from the O^6 methylated site of the guanine to a cysteine residue in its catalytic pocket. This reaction leads to the degradation of the enzyme (Erasimus et al., 2016; Haar et al., 2012; Lee, 2016). The expression of *MGMT* is regulated by the methylation of its promoter. GBM cells with

methylated *MGMT* promoter lack the repair activity and are more sensitive to TMZ treatment. In the absence of this promoter methylation, the active MGMT enzyme renders TMZ treatment ineffective, therefore *MGMT* methylation status is an important predictive marker for the sensitivity of TMZ in GBM patients (Haar et al., 2012). Targeting DNA repair mechanisms thus emerges as a promising therapeutic approach against GBM (Erasimus et al., 2016; Sharma et al., 2021a).

1.5.2 Genetic heterogeneity and clonal evolution as mechanisms of resistance

Clonal evolution of tumor cells as a result of treatment pressure is implicated as a critical driver of treatment resistance and recurrence in different tumor types (McGranahan and Swanton, 2017). Several studies point towards some degree of genetic evolution in GBMs (Aldape et al., 2018; Barthel et al., 2019; Draaisma et al., 2020; Körber et al., 2019). However, only a handful of genetic and epigenetic changes were reported at recurrences such as rare cases of hypermutation, loss or emergence of certain mutations, and global DNA demethylation (Kim et al., 2015; Körber et al., 2019; Sottoriva et al., 2013; de Souza et al., 2018). Hypermutations resulting in high mutational diversity are seen as a contributing factor to treatment resistance (Kim et al., 2015). However, these events are rarely observed in GBMs but do occur in other glioma subtypes. This may suggest increased susceptibility to treatment resistance via this mechanism in other gliomas compared to GBM. Several studies have shown the existence of minor subclones present in primary tumors which are expanded during therapy. Subsequently, these subclones initiate tumor recurrence with altered clonal rearrangement facilitating evasion of pressure during the initial therapy (Kim et al., 2015; Spiteri et al., 2019). Following analysis of the clonal architecture of longitudinal GBM samples assessing the tumor core and periphery, Spiteri et al., showed that residual cells are often resistant to therapy, have altered clonal arrangements, and possess the ability to re-seed in the primary or distal location in the brain. Analysis of whole-genome sequencing (WGS) and whole-exome sequencing (WES) data revealed that chemoradiation-induced pressure can lead to clonal selection and rarely hypermutation both *in vitro* and *in vivo* (Barthel et al., 2019; Körber et al., 2019; Spiteri et al., 2019). This suggests a form of convergent evolution due to treatment-induced selective pressure in resistant cells (Fortunato et al., 2017; Kim et al., 2015) leading to a recurrent tumor of multiclonal origin. Emerging sub-clones in recurrent tumors can show additional driver mutations not seen in the primary tumors (Körber et al., 2019). Clonal evolution may be shaped by tumor genetics. For instance, Kim et al. showed that TP53 alterations in primary GBMs define the level of clonality seen at recurrence (Kim et al., 2015). At recurrence, TP53 mutated tumors harbor multiple new clones while TP53 non-mutated GBMs are monoclonal.

It is still not clear how the multiplicity of genetic alterations influences resistance in recurrent tumors. Although certain genetic modifications are observed at recurrence, these changes appear stochastic, rare, and patient-specific. Unlike other cancers, no common emerging mutations are observed and overall clonal architecture remains similar over time (Barthel et al., 2019).

1.5.3 Phenotypic tumor heterogeneity and plasticity as mechanisms of resistance

Recent data suggest a key role of phenotypic heterogeneity, stemness features, and intrinsic plasticity in resistance to treatment in GBM. Intra-tumoral phenotypic heterogeneity and cellular plasticity are well-established factors hampering the efficacy of current treatments (Aldape et al., 2019; Vasan et al., 2019). Pre-existing resistant populations i.e. resistant phenotypic states which allow tumor propagation upon treatment selection following classical neo-Darwinian selection principles. Moreover, phenotypic plasticity represents a powerful mechanism for overcoming selective pressures, not only during tumor development and adaptation to changing microenvironments but also following treatment.

Molecular GBM subtype switching has been reported between primary and recurrent tumors. Subtype switching upon recurrence was reported in some GBM patients where the transition from GBM PN to MES subtype was observed by Phillips et al., (Phillips et al., 2006), suggesting progression towards a more aggressive disease. Further interrogation of this hypothesis with more longitudinal GBM patient samples and refinement of tumor-intrinsic gene expression subtypes revealed subtype switching towards CL and PN subtypes as well as MES at recurrence (Wang et al., 2017). While MES tumors appeared most stable, shifts in PN and CL tumors were observed and had a propensity to switch towards PN and MES phenotypes at recurrence. Additionally, several studies subsequently reported transitions of PN GBM cells to MES upon treatment in different GBM models. Piao et al. reported a MES transition upon anti-VEGF therapy in GBM cultures developed from treated orthotopic xenograft models (Piao et al., 2013). Halliday et al., also reported radiation-induced PN to MES switch upon radiation in mouse models (Halliday et al., 2014). A gradient of radiation and multitherapy resistance in GBM cultures was linked to a PN to MES gradient (Segerman et al., 2016). We further discuss the importance of intratumoral phenotypic heterogeneity, stemness programs, preexistent resistant cells, and phenotypic plasticity upon resistance to standard-of-care as well as targeted therapies in our recent review, presented in **Chapter 3**.

1.5.4 The role of tumor microenvironment in therapy resistance

Cells within the TME employ different strategies in aiding GBM cells to evade treatment pressure and establish resistance. Analysis of longitudinal models revealed the re-composition of the TME of treated tumors, e.g. MES GBMs show an increased proportion of M2 macrophages/microglia over blood-derived monocytes, whereas hypermutated tumors contain more $CD8^+$ T cells (Wang et al., 2017). Radiotherapy was shown to alter the TME dynamics and induce plasticity of TAMs within the GBM TME. Akkari et al. identified radiotherapy-induced changes in the proportion and transcriptional features of TAMs in engineered glioma mice models upon irradiation (Akkari et al., 2020). While Mg-TAMs decreased over the course of radiation and at recurrence, Mo-TAMs gradually increased, thus distorting the baseline ratio of the different TAMs subpopulations where Mg-TAMs had the highest proportion in control mice and at the start of irradiation. Gene expression analysis revealed short-term transcriptional adaptation in TAMs after 5 days of irradiation with the up-regulation of 64 common genes (e.g *Mrc1*, *Lyve1 Cd163*, *Ccr1*, *Il10*, *Ccl8*, *Ccl24*) by the different TAMs subpopulations of tumor-bearing mice compared to control mice, termed the TAM-IR transcriptional signature. Mo-TAMs showed more transcriptional adaptation with 710 up-regulated genes compared to the 125 up-regulated genes in Mg-TAMs. Genes forming the TAM-IR signature were shown to be enriched in cell cycle, DNA damage response mechanism, and macrophage alternative activation. However, in the long-term at recurrence, both Mg- and Mo-TAMs adopted a more converged gene expression profile despite their ontogenies, with an almost similar number of up-regulated genes that are mostly common between the different subpopulations. These commonly upregulated genes are mainly enriched for transforming growth factor-β (TGF-β) and Notch signaling pathways. Interestingly, targeting TAMs using a colony-stimulating factor-1 receptor (CSF-1R) inhibitor in combination with radiotherapy resulted in improved survival in mice (Akkari et al., 2020). These results indicate that TAMs subpopulation alters their transcriptomic profiles to support tumor cells in escaping the deleterious effect of radiation during therapy. Therefore, targeting these TME subpopulations has the potential to enhance tumor cell elimination and prolong the survival of GBM patients.

It was previously demonstrated that changes induced by anti-angiogenic therapy (anti-VEGF bevacizumab therapy) in GBM PDOX induce a metabolomic switch in tumor cells, with a net result of increased glycolysis and tumor cell invasion into the brain (Fack et al., 2015). These results were later corroborated in phase III clinical trials (Gilbert et al., 2014). Tumor cells were also shown to adapt to TME changes by upregulating MES features. ZEB1 a master transcription factor (TF) induced by NF-κβ was found to regulate MES transition in response to anti-angiogenic therapy in GBM (Chandra et al., 2020). It appears that both

the MES phenotype and NF-κβ activated pathway are linked to immune cells infiltration and complement each other in enhancing tumor cells plasticity to rewire the TME in response to treatment pressure in GBM.

Overall, the dynamic reprogramming of TME alongside the plasticity of tumor cells is an impediment to cancer therapy that must be tackled to avoid treatment resistance (Gupta et al., 2019). How plasticity in tumor cells and TME combine forces and enable tumor cells to escape therapy remains to be fully understood. While stable changes occurring during treatment and tumor progression can be assessed by analyzing longitudinal patient tumors, analysis of plastic temporary changes requires the use of clinically-relevant laboratory models.

1.6 Preclinical glioblastoma models

The development of preclinical models that adequately recapitulate patient tumors remains one of the biggest barriers to curing brain tumors (Aldape et al., 2019). Different models for cancer research have been developed over the years to advance the understanding of tumor biology and facilitate preclinical testing of novel therapeutics (Akter et al., 2021). Ideal models of brain tumors should be molecularly and histologically similar to human gliomas. It should recapitulate the genetic, epigenetic, and transcriptomic profiles of the tumor cells and retain inter-tumoral as well as intra-tumoral heterogeneity. Ideally, intercellular interactions with TME cells should be preserved with comparable immunogenicity (Lenting et al., 2017; Szatmári et al., 2006). Despite the availability of several cellular and animal models of brain tumors, an ideal model is yet to be developed. The merits and demerits of each model have been widely enumerated (Akter et al., 2021; Gómez-Oliva et al., 2021; Haddad et al., 2021; Huszthy et al., 2012; Shahzad et al., 2021) thus allowing for the selection of the best model that fits the experiment of interest.

GBM models derived from the patient tumors as illustrated in **Figure 6A** are divided into 5 types. The oldest and the most widely used *in vitro* models are the adherent cell lines. In recent years, both stem-like 3D cultures and *ex vivo* grown organoids became popular in cancer research (Drost and Clevers, 2018). Organoids were increasingly shown to recapitulate patient tumors better than both adherent and stem-like cultures. Variable types of *in vivo* models otherwise known as animal models have been used for cancer studies for many years. These animal models are derived by either xenografting cancer cells of human origin in the brain (orthotopic models) or below the skin in the mice flank (subcutaneous models) (Ben-David et al., 2017; Byrne et al., 2017; Huszthy et al., 2012; Lenting et al., 2017).

Since naturally occurring brain tumors in mice are very rare, chemical induction of brain tumors in mice was the main source of tumor models of mouse origin (Lenting et al., 2017; Miyai et al., 2017; Seligman et al., 1939; Ward and Rice, 1982). Tumors from the mice were used to generate *in vitro* adherent cell lines that can be propagated indefinitely. These cell lines are implanted intracranially in immunocompetent mice to generate *in vivo* mice models (**Figure 6B**). Genetically engineered mouse models (GEMMs) have also been designed by targeting the major GBM oncogenes and are used in GBM research as immunocompetent models with intact TME.

In addition to the popular patient-derived and mouse-based animal models, other experimental animal models such as dogs, rats, fruit flies, worms, and zebrafish are also emerging in GBM (Herranz et al., 2016; Hicks et al., 2017; Shahzad et al., 2021; Ward and

Rice, 1982). The use of animal models has helped in overcoming some of the shortcomings of the *in vitro* models. They allow the study of tumor cells in a living system as well as cross-talk with the majority of the TME cells types, including vasculature. In some of these animal models like dogs, tumors grow naturally as in humans, thus allowing direct comparison without altering the immune system of the host animal (Herranz et al., 2016; Hicks et al., 2017).

The main focus of this thesis is on the GBM models used in the scope of my research project namely: I. Adherent cell lines, II. Stem-like cultures, III. Patient-derived organoids, IV. Patient-derived orthotopic xenografts V. Syngeneic mouse models.

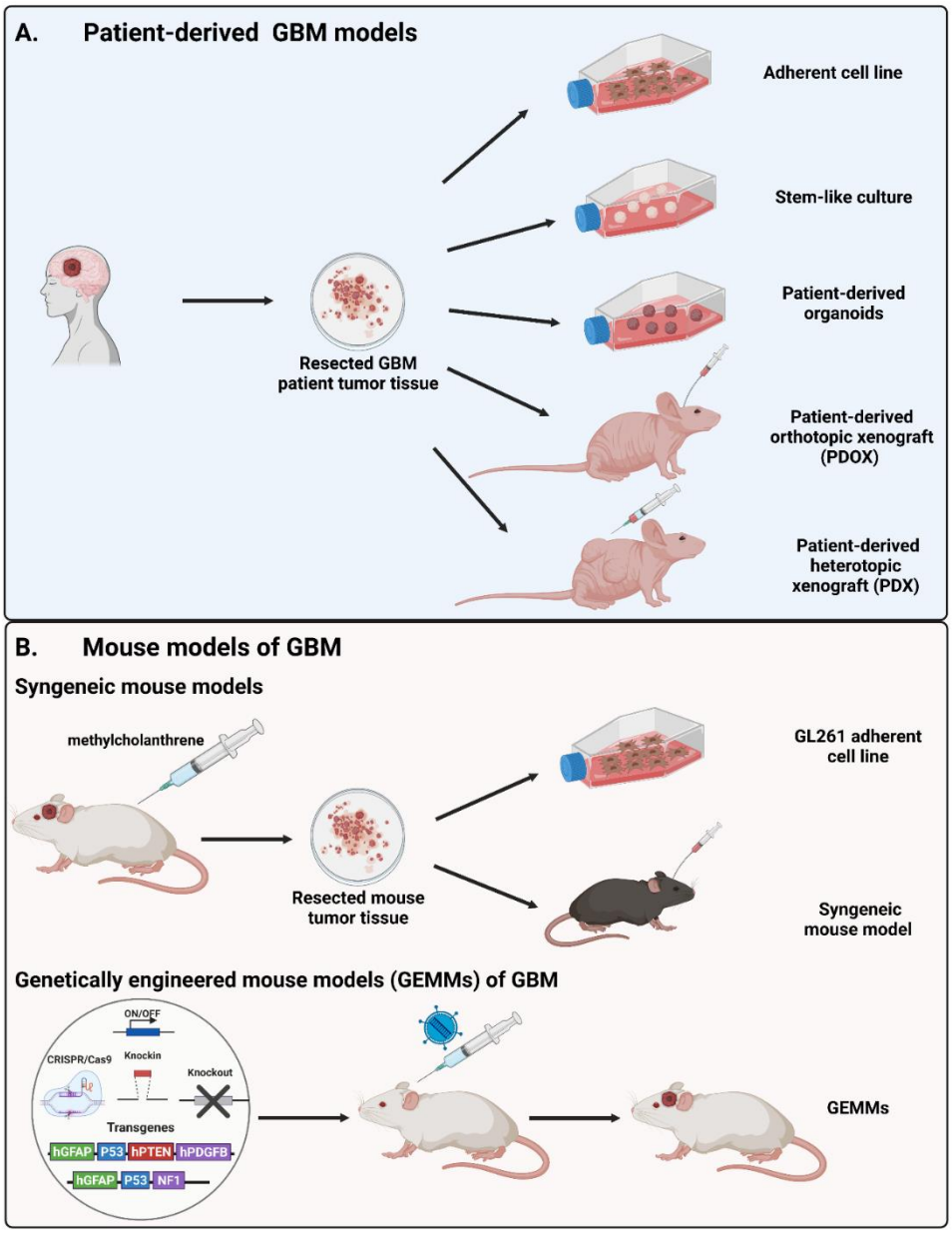

Figure 6. Schematic overview of preclinical animal models used in GBM research. (A) Workflow for the derivation of GBM models based on patient tumors; (B) Workflow for the derivation of GBM models of mouse origin: Chemically induced models and GEMMs.

1.6.1 Adherent cell lines

Human cancer-derived cell lines represent the most widely used models in cancer research (Ben-David et al., 2018). These cell lines are readily accessible at low cost, easy to work with, maintain and use for large-scale experiments. They are amenable to genetic manipulations. In addition, these cell lines have been extensively characterized with publicly available genomic and transcriptomic data (Ben-David et al., 2019). However, cancer cell lines usually evolve over time, resulting in genetic and transcriptomic changes that translate to functional differences between different batches of the same cell line (Ben-David et al., 2018; Nugoli et al., 2003). Analysis of 106 human MCF7 (breast cancer cell line) of similar origin obtained from different laboratories showed significant genetic and transcriptomic variations. Importantly, these different MCF7 clones responded differently to anti-cancer drugs (Ben-David et al., 2018). Such data was obtained in other cancer cell lines. Cross-contamination with other cell lines, the impact of culture conditions, and variable results obtained by different laboratories using similar cell lines further raised concerns about their use and questioned the translatability of results obtained from experiments applying these cell lines (Allen et al., 2016; Alston-Roberts et al., 2010; Ben-David et al., 2018; Capes-Davis et al., 2010; Chatterjee, 2007; Ledur et al., 2017). Importantly, the absence of BBB and other TME components in addition to the instability of the cell lines limits in vitro models in meeting the requirements needed for GBM models to recapitulate the patient tumor (Lenting et al., 2017).

Classical GBM cell lines were derived from patient samples many decades ago (PONTÉN and MACINTYRE, 2009). These cell lines e.g. U87 and U251 are commercially available and have been propagated over many passages under adherent conditions in serum-containing media. Since their derivation, many advancements have been made in the understanding of the molecular features of GBM cells using these cell lines (Gómez-Oliva et al., 2021). Despite their widespread use, long-term cultured cell lines have been heavily criticized (Allen et al., 2016; Lenting et al., 2017). Thanks to the sequencing of the U87 genome, extensive genomic alterations were uncovered, further raising more doubts on the fidelity of these cell lines to the parent patient sample (Clark et al., 2010). Surprisingly, when the original U87 was compared with other commercially available U87 cell lines, none of the commercially available U87 cells had a similar genotype to the parental U87 and only the mitochondrial DNA profile of the parental U87 matched that of the patient tumor from which it was derived (Allen et al., 2016). Although the origin of the commercially available U87 could not be identified, this cell line showed high transcriptomic similarity with other cell lines of CNS origin. This points to a possible mislabelling or cross-contamination of these commercially available cell lines at some point during several passages.

A thorough characterization of different batches of U251 cell lines revealed long-term culture-induced changes in highly passaged U251. Highly passaged cells varied from patient samples with additional amplifications and deletions in several chromosomes, while the low passaged U251 had similar genetic aberrations to the original tumor (Torsvik et al., 2014). These subclones also had variable cell size, growth patterns, and cell distribution in culture as well as cytoskeletal structure. *In vivo* tumorigenicity of highly passaged subclones increased in agreement with a corresponding increase in growth rate (Li et al., 2008; Torsvik et al., 2014). Furthermore, a comparison of gene expression profiles of U87 and U251 cell lines with GBM tumor samples revealed marked differences with the cell lines clustering differently from the primary GBM samples (Li et al., 2008). Although the majority of adherent GBM cell lines grow in the brain of immunodeficient rodents, developed tumors are generally circumscribed with very limited invasion of brain parenchyma. Together these important findings highlight the changes acquired by cell lines over time due to selection pressure imposed on the competing cells by culture conditions. Thus, these classical cell lines represent limited recapitulation of primary GBM tumors.

1.6.2 Stem-like cultures

Following the strong evidence against the validity of the classical GBM cell lines as a good model recapitulating primary tumors, non-adherent stem-like cell cultures grown as 3D spheres emerged as a promising alternative, especially for functional assays and drug screening (Baskaran et al., 2018; Galli et al., 2004; Gomez-Roman et al., 2016; Lee et al., 2006; Pollard et al., 2009). These cultures are generally referred to as glioma stem cell (GSC) or brain-tumor initiating cell (BTIC) cultures in the literature. 3D serum-free cultures recapitulate the major GBM genomic characteristics and share similar copy number alterations with their parental tumors. The inter-patient differences are generally preserved, and intra-tumoral heterogeneity is also partially recapitulated in 3D spheres (Dirkse et al., 2019). Still, preservation of certain gene amplifications, notably *EGFR*, appears particularly challenging (Liffers et al., 2015). As expected from the efficient *in vitro* propagation, these serum-free cultures also suffer from clonal selection and loss of heterogeneity over time resulting in genomic and transcriptomic changes (Baskaran et al., 2018; Shen et al., 2019). Moreover, they show a phenotypic bias towards the enrichment of stem-like features and high proliferation (Balvers et al., 2013). This indicates long-term cellular preselection and/or molecular alterations in these cultures at the transcriptomic level. Importantly, the majority of stem-like cultures develop tumors *in vivo*, which preserve invasive properties (Bougnaud et al., 2016). Additional investigations showed that although these 3D cultures may

resemble the GBM patient tumors genetically, they showed inconsistent histopathological features when xenotransplanted and drug response after long-term passage in serum-free medium become erratic (García-Romero et al., 2016).

Taken together, the limitations of *in vitro* cell lines as a result of genomic and phenotypic changes as well as an absence of a viable TME have slowed down progress in the development of novel anti-cancer therapeutics. This further highlights the need to develop alternative preclinical models for GBM research that recapitulate patient tumors both genetically and functionally.

1.6.3 Patient-derived organoids

Derivation of organoids started with the use of pluripotent stem cells to develop models that could recapitulate organs in the body. Since then, three-dimensional (3D) organoids cultured in serum-free conditions and organized with 3D structures have been developed to model the development of various human organs and diseases of different types (Clevers, 2016). Brain organoids, the so-called “mini-brains” were among the first 3D organoids developed recapitulating certain brain regions (Eiraku and Sasai, 2012; Lancaster et al., 2013).

One of the early reports on the establishment of organoids from GBM patient material was by Bjerkvig et al. in 1990 (Bjerkvig et al., 1990). Tissue from glioma patients was cultured short-term on agar overlay, resulting in a complex multicellular tumor-like tissue referred to as organotypic spheroids. Extensive microscopic analysis revealed similar morphology between the organotypic spheroids and the patient tissue they were derived from. Interestingly, these spheroids retain blood vessels and other components of TME.

A more recent protocol employs the use of GSCs to generate organoids. Characterization of these GSC-based 3D organoids in GBM showed that they indeed maintain the histological features when xenografted orthotopically displaying the ability to invade the surrounding brain tissue, thus recapitulating patient tumors more closely than in xenografted cell lines (Hubert et al., 2016). Interestingly, these organoids also show stable heterogeneous expression of SOX2, a prominent CSC marker as well as a hypoxic gradient with the inner core of the organoids being more hypoxic with less SOX2 expression than the outer surface. Hubert et al. also demonstrated the suitability of these organoids for functional analysis by exposing them to radiation. Notably, both radiosensitive and radioresistant cell populations were found in the organoids (Hubert et al., 2016).

Recently, an enhanced derivation protocol and extensive characterization of organoids generated from GBM patient samples based on mechanically cut tumor tissue propagated under serum-free conditions was reported (Jacob et al., 2020). In addition to maintaining tumor cell heterogeneity as in parental tumors, this analysis showed that organoids also maintained certain TME cell types during early time points and included their heterogeneous molecular features. scRNA-seq revealed patient-specific clustering of tumor cells from both parental tumors and matched organoids derivations from those tumors while non-neoplastic cells from both organoids and parent samples clustered in a non-patient specific manner (Jacob et al., 2020). Further analysis confirmed the presence of intra-tumoral heterogeneity in the tumor cells, with subclusters scoring high for the previously identified cell states in GBM, mainly AC-like and OPC-like. In addition, cells having oligodendrocytes-like and neuron-like signatures were also identified in both the organoids and their parental tumors. This indicates the transcriptomic similarity between tumor cells in the organoids and the parental patient tumors. Among the non-neoplastic cells, key microglia and macrophage genes such as *SPP1*, *ITGAM,* and *CD74* and cytokines (*TNF*, *IL1B*, *TGFB1*) showed similar expression between the parental tumors and their corresponding organoids. This indicates that the organoids retain some TME cells 2 weeks after derivation. This observation was further confirmed by the presence of $IBA1^+$ and $CD3^+$ cells in the organoids at 2 weeks, indicating the presence of microglia/macrophage and T cells, albeit at lower numbers compared to the parental tumors. Single analysis of organoids at later time points (8 and 24 weeks) confirmed the limited persistence of these TME cell types over time.

3D organoids derived from GBM patient samples have emerged as a more relevant *in vitro* preclinical model for GBM research. These 3D organoids offer further advantages over both the 2D cell lines and 3D cultures (Gómez-Oliva et al., 2021; Klein et al., 2020). They recapitulate the complex cell-cell interactions, inter and intra-tumoral heterogeneity, and some microenvironmental features (Ben-David et al., 2019; Gómez-Oliva et al., 2021; Hubert et al., 2016; Jacob et al., 2020; Klein et al., 2020). Given their short derivation time, organoids represent a huge shift in the development of cancer models as they are shown to be a good option for testing both targeted and immunotherapy responses in GBM and thus could be applied for personalized treatment strategies (Jacob et al., 2020). However, 3D organoids are also faced with some limitations mitigating their use at a large scale. These limitations include a lack of standardized culture conditions, high production and labor cost, immune-limited environment, absence of vascularisation, and the need to have a fresh and relatively large amount of viable patient tumor material that is generally difficult to acquire. These have resulted in a variable success rate in the derivation of these organoids (Ben-David et al., 2019; Gómez-Oliva et al., 2021; Klein et al., 2020). Therefore,

there is the need for further standardization and optimization of the 3D organoid derivation protocols as well as improvement of the organoids to retain viable and efficient TME as seen in the patient tumors.

1.6.4 Patient-derived heterotopic and orthotopic xenografts

Patient-derived animal models were designed to propagate the original patient tumor in a living system, closer to physiological conditions than *in vitro* culture, and represent the histologic and genetic characteristics of the original tumor better than the syngeneic model (Ben-David et al., 2019; Byrne et al., 2017). This is achieved by engrafting patient tumor tissue, patient tumor-derived organoids, or established cell lines into an immunodeficient mouse to avoid immune rejection (Haddad et al., 2021; Huszthy et al., 2012; William et al., 2017; Zeng et al., 2020). This process of engrafting tissue originating from a different species (human) to another (mouse or rat) is known as xenografting (Ben-David et al., 2019; Woo et al., 2021). When these tumors are implanted subcutaneously in an immune-deficient mouse they are simply referred to as patient-derived (heterotopic) xenografts (PDX) as illustrated in **Figure 6A** (Ben-David et al., 2019; Lenting et al., 2017). PDX models have been shown to recapitulate human GBM histopathologic and genetic features and have been generated from gliomas of different grades (Vaubel et al., 2020; William et al., 2017; Zeng et al., 2020). However, heterotopic PDX models are limited by the absence of cells forming the brain TME that are important for GBM cells growth and development and thus have failed to fully recapitulate the brain TME (Hidalgo et al., 2014; Lenting et al., 2017; William et al., 2017). A recent analysis of several PDX models of different tumor types, including GBM, reported the spontaneous development of novel copy number alterations (CNA) not seen in parental tumors (Ben-David et al., 2017). Although a subsequent large-scale study did not observe CNA differences between PDXs and parental tumors (Vaubel et al., 2020; Woo et al., 2021), the anecdotal alterations earlier reported may be imposed by the interactions between tumor cells and the heterotopic TME, especially in the case of brain tumors.

To overcome the limitations of the PDX model, GBM patient tissue fragments, organoids, tumor single cells, or spheres can be implanted in the brain of an immunodeficient mouse to allow the tumor cells to grow in the normal anatomical location in which brain tumors naturally occur. This novel approach is referred to as patient-derived orthotopic xenograft (PDOX) (Wang et al., 2009). PDOXs allow the propagation of patient GBMs in form of live biobank without imposing genomic alterations due to pressure from unnatural TME. In

addition to fully representing the histological and molecular characteristics of patient GBMs, the PDOXs have the unique advantage of having *in situ* structures of the brain such as an intact BBB, glial cells, and neurons that allow the recapitulation of the interactions between the tumor and cells within the TME. Furthermore, the metabolic components of the brain, specifically the cerebrospinal and interstitial fluids are present in PDOXs (Haddad et al., 2021; Huszthy et al., 2012; Lenting et al., 2017; Patrizii et al., 2018). Different mouse strains with varying levels of immunodeficiency are used as the recipients. These mouse strains range from the less immunodeficient nude mice lacking only T cells to the medium non-obese diabetic/severe combined immunodeficiency (NOD/SCID) mice, that lack both T and B cells, and the most immune-deficient NOD/SCID-Gamma null (NSG) mice lacking T, B, and NK cells (Gómez-Oliva et al., 2021).

Initial attempts to generate orthotopic xenograft models of brain tumors started with nude rats (Sakariassen et al., 2006; Wang et al., 2009). Patient brain tumor tissues from 29 gliomas including many GBMs were successfully xenografted into the brain of nude rats with a 96% success rate. The tumor take rate increased after several passages *in vivo*. In this approach, patient tumor tissue was minced into small fragments and briefly cultured in agar overlay until they formed organotypic spheroids (i.e. organoids). These organoids are then implanted into the brain of nude rats as soon as they are formed. Histopathologic analysis of tumors formed in the brain of the rats revealed that these tumors were highly invasive, however, necroses and microvascular proliferations key features in GBM were not observed in some tumors in the first generation tumors. Following 3-4 passages, tumors that are both invasive and highly vascularised with microvascular proliferation and pseudopallisading necroses typical of GBM emerged (Wang et al., 2009). Interestingly, after repeated passaging of these tumors in rats, they tend to adapt to the host immune system and engraft in immunocompetent rats without rejection (Huszthy et al., 2015). However, the long tumor generation time of about 4 – 5 months and the serial passaging required to fully recapitulate human GBMs are limitations in using rats to generate PDOXs (Wang et al., 2009). In addition, challenges associated with the handling of rats as a result of their size and aggressive behavior as well as high maintenance costs further limited PDOX generation in rats and accelerated the use of mouse-based PDOX models (Barth and Kaur, 2009).

PDOXs were also generated by implanting patient tumor fragments directly into the brain of immunocompromised mice (Joo et al., 2013). The generation of these PDOXs resulted in an 80-90% success rate and tumors in these PDOXs show morphologic and histopathologic similarity with patient tumors. Genomic and transcriptomic features of patient tumors were

retained in the PDOXs. However, attempts to implant tumor fragments directly in the brain of immunocompromised mice by others failed (Kim et al., 2016).

The development of PDOXs by introducing a brief *in vitro* culture step as demonstrated in the rats (Wang et al., 2009) resulted in more reproducible and stable models, with less latency and higher success rates (Bougnaud et al., 2016; Golebiewska et al., 2013; Keunen et al., 2011). Histopathologic evaluation of PDOXs generated by implanting organotypic spheroids in the brain of NOD/SCID mice showed the recapitulation of patient histological phenotypes reported in GBM patients. These phenotypes represent the different degrees of angiogenesis and invasiveness observed in human GBM, namely: invasive, intermediate, and angiogenic phenotypes. Tumors in these PDOXs also show different levels of necrosis. Genomic heterogeneity of parental GBM tissue was also retained in the PDOXs. Furthermore, different histological phenotypes, as well as inter and intratumoral genomic aberrations present in patient GBMs, were retained in PDOXs. (Bougnaud et al., 2016; Stieber et al., 2014). Importantly, the ploidy of GBM cells was retained over serial transplantations in PDOXs (Stieber et al., 2014). In addition, efficient functional interaction between human GBM cells and mouse endothelial cells was reported (Bougnaud et al., 2016), and morphological change toward normalization of the aberrant blood vessels following anti-human VEGF treatment (Abdul Rahim et al., 2017; Keunen et al., 2011). These PDOX also showed a remarkable recapitulation of metabolic adaptation to anti-angiogenic therapy observed in GBM patient tumors (Fack et al., 2015). Analyses of PDOX models from other laboratories were shown to retain the metabolic properties of invasive GBM cells in comparison to patient tumors from which the PDOXs were generated (Cudalbu et al., 2021). Recently, organoids implanted in the brain of nude mice also showed the typical histological features of patient GBMs with varying degrees of tumor cells infiltration into the contralateral and ipsilateral hemispheres (Jacob et al., 2020; Mansour et al., 2018). In addition to displaying angiogenic features, these xenografts maintained both *EGFR* amplification and *EGFRvIII* mutant expression present in parental tumors.

PDOX models have also been generated from CSCs cultured from fresh surgical biopsies and organoids developed from CSCs (Hubert et al., 2016; Irtenkauf et al., 2017). Analysis of CSC-based PDOXs also showed a recapitulation of GBMs both histologically and genetically. This preselection protocol did not provide any added advantage over PDOXs generated from GBM tissue fragments. Interestingly, tumor take rate widely varies between xenografted CSCs and CSCs-derived organoids, indicating poor reproducibility and preselection bias.

While PDOXs generated in NOD/SCID mice have an intact TME including the myeloid cells that are the major immune cell types in the brain as well as mostly intact innate immune system, they lack the lymphocytes that are an integral part of the adaptive immune response, thus limiting their applications in immune-related studies. Important insights on the crosstalk between lymphocytes and GBM cells as well as other TME cell types cannot be studied using these models. Thus, there is a need to generate PDOXs in mice models which better recapitulate adaptive immune cell presence such as the B lymphocytes that are present in the nude mice. Furthermore, these studies involved only a few PDOXs, therefore a more comprehensive, reproducible, and extensive molecular characterization of both the tumor cells and TME cell types in a larger cohort of PDOX is needed. Especially the characterization of the molecular features of tumor cells from PDOXs in line with the new GBM classification.

1.6.5 Syngeneic mouse models

Naturally occurring brain tumors in mice are very rare. As a result, most of the brain tumors of mice origin used in preclinical studies were chemically induced using carcinogens (Ward and Rice, 1982). Brain tumors in mice were initially derived by intracranial injection of methylcholanthrene resulting in the development of a densely compacted tumor mass described to be histologically similar to gliomas and termed Glioma 261 (GL261) (Seligman et al., 1939). The syngeneic (the implantation of tumor cells derived from the same species) GBM mouse model was derived by subcutaneous and intracranial injection of tumor fragments from GL261 into immunocompetent C57BL/6 mice, thus giving rise to the now popular GL261 model (Ausman et al., 1970). Currently, adherent cell lines established from GL261 tumors are now used for orthotopic implantation in C57BL/6 mice to establish the syngeneic GL261 model (**Figure 6B**) (Ausman et al., 1970; Lenting et al., 2017; Oh et al., 2014; Szatmári et al., 2006). The GL261 syngeneic model is among the most common and frequently used GBM animal models and has been used extensively to study the immunosuppressive GBM microenvironment, tumor-immune cells interactions, and novel immunotherapeutic approaches (Khalsa et al., 2020; Maes and Van Gool, 2011; Ochocka et al., 2021; Oh et al., 2014; Pombo Antunes et al., 2021; Szatmári et al., 2006). However, these models do not fully recapitulate gross and histopathologic features as well as the immunogenicity of human GBM. The GL261 was shown to be stable over many generations and remains histologically the same even after 100 transplantations (Ausman et al., 1970). Histopathologic analysis of tumors in the GL261 model showed some resemblance with human gliomas, albeit more hemorrhagic, circumscribed, and grossly demarcated from the

normal brain (Ausman et al., 1970; Seligman et al., 1939). GL261 model was also shown to harbor some genetic alterations reported in human GBM, mainly mutations in tumor suppressor gene *p53* and K-ras oncogene. While *p53* mutation is a frequent feature of GBM, K-ras mutation is uncommon in human GBM. Unlike the human GBM, the GL261 tumor is characterized with a hypermutator phenotype coupled with a high MHCI expression but low MHCII (Oh et al., 2014). Deeper characterization of GL26 tumor which is closely related to GL261 and GL261 demonstrated that tumors from these models are angiogenic and express vimentin with massive infiltration of inflammatory cells mainly Mo-TAMs and $CD3^+$ T cells, but significantly lower number of APCs when compared to human GBM samples (Candolfi et al., 2007; Khalsa et al., 2020; Szatmári et al., 2006). Other histologic features of GL26 tumors include nuclear atypia, pleomorphism, and hypercellularity. However, some important hallmarks of human GBM such as pseudopalisading necrosis and microvascular proliferation were absent in the GL26 model (Candolfi et al., 2007; Szatmári et al., 2006). These differences with human GBM may have resulted in the inability to translate promising results obtained in preclinical studies using GL261 models to human GBMs (Haddad et al., 2021; Johanns et al., 2016; Khalsa et al., 2020; Maes and Van Gool, 2011; Miyai et al., 2017).

Recently, a comparison of the immune phenotypes among different syngeneic mice models of brain tumors shows variable immunogenicity, indicating that the unique genetic background of each model influences their immune phenotypes (Khalsa et al., 2020). GL261 and 005 models were shown to be more immune active than the CT2A and Mut3 models. Overall comparison with human IDHwt GBM samples revealed that the 005 and the GL261 models more closely but not fully resemble the human GBM immune phenotype than other syngeneic models (Khalsa et al., 2020), indicating better recapitulation of the immune landscape of GBM by the GL261 model compared to other immunocompetent GBM models.

1.6.6 GEMMs

Generating GEMMs involves the genetic manipulation of the mouse genome to induce brain tumors *de novo*. However, GEMMs are very expensive, cumbersome, and very slow to generate, thus limiting their use in GBM research. Moreover, most of the GEMMs used in GBM research are limited in their ability to fully recapitulate intra-tumoral heterogeneity in GBM and only recapitulate some specific genetic alterations in GBM such as *NF1*, *TP53*, *PTEN*, *PDGFB,* and *EGFR*. GEMMs may therefore be more suitable for the investigation of specific genetic alterations and their response to particular targeted therapy (Haddad et al.,

2021; Hicks et al., 2021; Huszthy et al., 2012; Kersten et al., 2017; Lenting et al., 2017). Importantly, most of these GEMMs produce tumors that are histologically more similar to oligodendrogliomas and astrocytomas that were previously considered as IDHmut GBMs (Hambardzumyan et al., 2009; Tchougounova et al., 2007; Zhu et al., 2005)

Some of the common strategies used to generate GEMMs include, targeted knockin of human genes into a mouse gene locus (e.g human *PDGFRα* into mouse collagen1α1 gene locus) (Hede et al., 2009; Jun et al., 2018) and conditional or inducible knockouts resulting in somatic or germline replacement of mouse genes with human genes forming transgenic mice overexpressing such inserted human oncogenes (Hambardzumyan et al., 2011; Huse and Holland, 2009; Macleod and Jacks, 1999; Zhu et al., 2009, 2005). Engineered GBM-inducing genetic material is usually delivered using different viral-loaded systems (Hede et al., 2009). Recently, the CRISPR/Cas9 mediated gene editing system is used as a novel tool to enhance precision and efficiency of the genetic modifications in GBM models (**Figure 6B**) (Chow et al., 2017; Mao et al., 2016; Zuckermann et al., 2015).

Chapter 2

Scope and Aims

2.1 Scope and Aims of the Thesis

Phenotypic heterogeneity and cellular plasticity are major factors contributing to tumor progression and treatment failure in GBM. Inter and intratumoral heterogeneity have been described in GBM tumors. GBM tumors consist of cells with different cellular states and each cellular state possesses the ability to transit to another phenotypic state and reconstitute initial intratumoral heterogeneity. In addition, plasticity allows GBM cells to adapt to external pressures from the microenvironmental cues in the developing tumor. Non-neoplastic cells within the GBM TME, especially the tumor-associated microglia and macrophages also play an important role in shaping the tumor ecosystem towards an immune-suppressive environment. These cell types are currently under intensive investigation as a potential target for the development of novel therapeutics. How these TAMs functionally interact with GBM tumor cells remains to be fully understood.

Current treatment strategies against GBM have failed in curing patient disease and thus tumor recurrence is inevitable. Based on existing and emerging evidence on phenotypic heterogeneity and plasticity in GBM (Chaligne et al., 2021; Dirkse et al., 2019; Johnson et al., 2021; Neftel et al., 2019), we hypothesized that tumor cells undergo phenotypic adaptation toward treatment-resistant phenotypes. Therefore, to provide a cure for GBM there is a need to design therapeutics that target the dynamic cellular states in GBM rather than targeting specific cellular subpopulations. However, how plasticity enables GBM cells to escape treatment is currently less understood and more studies are needed to uncover the drivers of plasticity and treatment resistance in GBM.

GBM *in vivo* preclinical models are important tools for functional assessment of tumor biology and preclinical therapeutic studies. The development of novel therapies has been hampered by the lack of efficient preclinical models that fully recapitulate GBM patient tumors. This has resulted in the failure of several drug candidates at the clinical trials after passing the initial preclinical testing stage. Therefore, there is a need to develop and characterize preclinical models that will enhance the development of new therapeutic strategies by producing clinically relevant study outcomes. Furthermore, models with intact TME which recapitulate the crosstalk between tumor cells and TME are needed to understand and assess novel treatment strategies such as immunotherapies that aim to remodel the TME.

Orthotopic xenografts recapitulate the tumor ecosystem *in vivo* allowing the study of tumor cells in their natural milieu. Initial reports describing GBM PDOXs suggested faithful recapitulation of the genetic profiles and histopathological features of patient tumors.

Recapitulation of other molecular features, including epigenetic and transcriptomic profiles has not been reported systematically. The transcriptional state of tumor cells is a reflection of genetic background, epigenetic state as well as tumor cell interactions with the surrounding TME and as such, better represents tumor cell phenotypes. An additional less understood feature of GBM PDOXs is the composition of the TME created in the brain of immunodeficient mice. Although initial analyses of the vascular compartment suggested reciprocal cross-talk between human tumor cells and mouse TME, the clinical relevance of the overall TME remains questionable in the research community. Numerous studies showed that GBM PDOX models show clinically-relevant responses. By assessing transcriptomic changes at the single-cell level in tumor cells and adjacent TME directly upon treatment, we hope to reveal dynamic mechanisms regulating resistance to treatment in GBM.

Initial transcriptomics studies at the bulk level have so far focused mostly on the assessment of inter-tumoral differences in GBM (Wang et al., 2017). The development of single-cell transcriptomic techniques revolutionalized the field, as scRNA-seq allows the characterization of individual cells based on their transcriptomic features and has thus been instrumental in dissecting the heterogeneity in different tumors, including GBM (Neftel et al., 2019; Patel et al., 2014; Tirosh and Suvà, 2018). Although the composition of GBM tumors has been assessed by numerous recent studies, the changes occurring during treatment at the single-cell level have not yet been comprehensively evaluated. Currently, there is no existing scRNA-seq data comparing paired primary and recurrent GBM patient samples. Moreover, while the stable changes may be revealed by assessing directly patient tumors, the assessment of dynamic and reversible adaptation of tumor cells upon treatment will require clinically-relevant research models recapitulating the heterogeneous GBM ecosystem.

This thesis aims to uncover answers to the outlined problems with the following specific aims:

- To establish efficient protocols for cell purification and analysis pipelines for assessment of tumor composition in GBM PDOX models by single-cell transcriptomics.
- To characterize the transcriptomic heterogeneity of the GBM ecosystem in PDOX models at the single-cell level.
- To decipher treatment-induced changes in tumor cells and TME in GBM PDOXs at the single-cell level

Chapter 3

Cancer Cell Heterogeneity and Plasticity: A Paradigm Shift in Glioblastoma

Yabo YA, Niclou SP, Golebiewska A

Neuro Oncol . 2021 Dec 21;noab269

doi.org/10.1093/neuonc/noab269

3.1 The rationale of the study

In this manuscript, we comprehensively reviewed recent literature and highlighted historical progress made towards the understanding of heterogeneity and phenotypic plasticity in GBM. We critically examined the current models explaining the creation and maintenance of phenotypic heterogeneity in GBM. We focused particularly on the evolution of the CSC hypothesis towards the plasticity model. We presented an overview of factors at the center of phenotypic states equilibrium in GBM. We introduced and outlined key publications supporting tumor cell plasticity as an emerging hallmark in GBM which enables tumor cell adaptation to environmental and treatment pressure. We further highlighted the importance of clinically-relevant GBM models and single-cell techniques as state-of-the-art tools to better characterize adaptive treatment-resistant states in the future. We concluded by giving our perspective on how to identify master transcriptional regulators enabling tumor cell plasticity and the prospect of targeting these regulators as treatment opportunities in GBM patients.

Personal contributions

This review represents a very important output of this thesis, enabling a comprehensive review of the current literature on the GBM ecosystem. It further aided the refinement of research questions posed throughout this project assessing the recapitulation of the GBM ecosystem in PDOX models (**Chapters 4-6**) as well as my preliminary work focusing on the role of tumor heterogeneity and plasticity as resistance mechanisms in GBM (**Annex I**). I contributed to the conceptualization of the review and performed a literature search to identify relevant published works that present recent evidence highlighting tumor cells heterogeneity and plasticity in GBM. I summarised these publications in **Table 1**. I contributed to the writing of the initial draft of the manuscript. I also contributed to the design of all the **Figures (1, 2, and 3)** and further contributed to the revision of the manuscript.

3.1.1 Result

Neuro-Oncology

1

XX(XX), 1–14, 2021 | https://doi.org/10.1093/neuonc/noab269 | Advance Access date 21 December 2021

Cancer cell heterogeneity and plasticity: A paradigm shift in glioblastoma

Yahaya A. Yabo, Simone P. Niclou, and Anna Golebiewska

NORLUX Neuro-Oncology Laboratory, Department of Oncology, Luxembourg Institute of Health, Luxembourg, Luxembourg (Y.A.Y., S.P.N., A.G.); Faculty of Science, Technology and Medicine, University of Luxembourg, Esch-sur-Alzette, Luxembourg (Y.A.Y.); Department of Biomedicine, University of Bergen, Bergen, Norway (S.P.N.)

Corresponding Author: Anna Golebiewska, PhD, Department of Oncology, Luxembourg Institute of Health, 84, Val Fleuri, L-1526 Luxembourg, Luxembourg (anna.golebiewska@lih.lu).

Abstract

Phenotypic plasticity has emerged as a major contributor to intra-tumoral heterogeneity and treatment resistance in cancer. Increasing evidence shows that glioblastoma (GBM) cells display prominent intrinsic plasticity and reversibly adapt to dynamic microenvironmental conditions. Limited genetic evolution at recurrence further suggests that resistance mechanisms also largely operate at the phenotypic level. Here we review recent literature underpinning the role of GBM plasticity in creating gradients of heterogeneous cells including those that carry cancer stem cell (CSC) properties. A historical perspective from the hierarchical to the nonhierarchical concept of CSCs towards the recent appreciation of GBM plasticity is provided. Cellular states interact dynamically with each other and with the surrounding brain to shape a flexible tumor ecosystem, which enables swift adaptation to external pressure including treatment. We present the key components regulating intra-tumoral phenotypic heterogeneity and the equilibrium of phenotypic states, including genetic, epigenetic, and microenvironmental factors. We further discuss plasticity in the context of intrinsic tumor resistance, where a variable balance between preexisting resistant cells and adaptive persisters leads to reversible adaptation upon treatment. Innovative efforts targeting regulators of plasticity and mechanisms of state transitions towards treatment-resistant states are needed to restrict the adaptive capacities of GBM.

Keywords

glioblastoma | plasticity | treatment resistance | tumor heterogeneity | tumor microenvironment

Despite aggressive treatment available for glioblastoma (GBM) patients including surgical resection, radiation, and chemotherapy, tumor recurrence is unavoidable. According to the 2021 WHO classification of CNS tumors, GBMs are classified as *Isocitrate dehydrogenase* (*IDH*) wild-type (IDHwt) and represent the most aggressive form of diffuse gliomas.[1] Based on their diverse cellular organization and histological appearance, GBMs were historically considered among the most heterogeneous tumors and were referred to as "multiforme". GBMs commonly carry *TERT* promoter mutation and copy number changes at chromosomes 7 and 10 (+7/–10). Genetic alterations such as amplification of *EGFR*, *PDGFRA*, and *CDK4/6*, as well as deletions or inactivating mutations in *TP53*, *PTEN*, *NF1*, and *CDKN2A/B* are key determinants of inter-patient variability. GBMs corresponding to *IDH1/2* mutated (IDHmut) tumors are currently a separate grade IV entity within IDHmut astrocytomas.[1] Large-scale genetic and epigenetic profiling studies have uncovered molecular GBM subgroups characterized by distinct DNA methylation[2,3] and/or expression patterns,[4] highlighting the molecular heterogeneity of this disease. Although to date these subgroups have limited clinical relevance, it remains to be seen to what extent the different layers of inter-patient and intra-tumoral heterogeneity will inform future treatment decisions.

Accumulating evidence underscores the existence of extensive intra-tumoral phenotypic heterogeneity and plasticity in GBM (Table 1). Intrinsic plasticity adds another layer of tumor complexity, allowing flexible adaptation of tumor cells during tumor initiation, progression, and treatment escape. Here we

Table 1 A Summary of Recent Key Findings Showing Evidence of Tumor Cell Plasticity Shaping Phenotypic Heterogeneity in GBM

Highlights	Main Technology	Main Cellular Source	Reference
➢ GBM cells display variable expression of diverse programs related to oncogenesis ➢ GBM cells show a continuum of stemness signature	scRNA-seq	GBM patient material	Patel et al.[49]
➢ Developmental and transcriptomic signature genes are epigenetically primed for expression via bivalent domains at their promoters	ChIP-seq, RNA-seq	GBM patient material, GBM cell lines	Hall et al.[70]
➢ Phenotypic heterogeneity accelerates tumor growth ➢ Paracrine signaling from "differentiated" GBM cells supports CSC growth	FACS, functional assay	GBM stem-like cultures, GBM PDOXs	Wang et al.[93]
➢ GBM cells can transit between NG2 positive and negative states to establish phenotypic equilibrium ➢ Tumorigenic potential in vivo depends on the phenotypic equilibrium of implanted cells	FACS, functional assays, Microarray	GBM stem-like cultures	Al-Mayhani et al.[27]
➢ Phenotypic states in GBM are plastic and reversible ➢ Phenotypic heterogeneity arises from nonhierarchical, reversible stochastic state transitions ➢ Phenotypic equilibrium is dictated by TME ➢ Fast reconstitution of phenotypic heterogeneity provides growth advantage	FACS, functional assays, scRNA-seq	GBM PDOXs, GBM stem-like cultures	Dirkse et al.[29]
➢ Phenotypic heterogeneity is a result of nonhierarchical organization of proliferating phenotypic states ➢ Phenotypic states can undergo state transitions ➢ Equilibrium between cellular states is dictated by genetic background and TME cues	scRNA-seq, lineage barcoding, FACS, functional assays	GBM patient material	Neftel et al.[50]
➢ Proliferating GBM cells exist on the main axis of variation between mesenchymal and proneural states, representing tumor core and invasive cells respectively	scRNA-seq, snRNA-seq, scATAC-seq	GBM patient material	Wang et al.[52]
➢ GBM cells transition to a slow-cycling, persister-like state upon pressure from RTK inhibitors ➢ State transitions are reversible and depend on epigenetic remodeling ➢ Adaptive resistance can coexist with irreversible genetic evolution towards novel resistant clones	ChIP-seq, scRNA-seq, functional assays	GBM patient material, GBM stem-like cultures	Eyler et al.[141] Liau et al.[140]
➢ Developmental programs are reactivated in GBM ➢ Active stemness programs exist in different phenotypic states and are patient-specific ➢ Multiple GBM populations give rise to heterogeneous tumors with TME-specific composition ➢ PTPRZ1-positive GBM cells resembling outer radial glia promote invasion	scRNA-seq, FACS, functional assays	GBM patient material, GBM PDOXs	Bhaduri et al.[55]
➢ Transcriptomic gradient centered around proliferating glial progenitor-like cells based on fetal brain signatures ➢ Glial progenitor states are enriched in stem-like cultures and show strongest tumorigenicity	scRNA-seq, FACS	GBM patient material, GBM stem-like cultures, Normal fetal brain cells	Couturier et al.[28]
➢ Main axis of variation associated with neurodevelopmental programs ➢ The "naïve" CSC state, distinct from other phenotypic states, is maintained by YAP/TAZ	scRNA-seq, functional assays	GBM patient material, GBM stem-like cultures	Castellan et al.[51]
➢ GBM cells are distributed across neurodevelopmental and metabolic axes ➢ Metabolic states have divergent mitochondrial, glucose, glutamine, and lipid metabolism	scRNA-seq, bulk RNA-seq, Metabolic assays	GBM patient material, GBM stem-like cultures	Garofano et al.[53]
➢ GBM transcriptional states exist across the axis between neurodevelopmental and injury response programs ➢ Cultured stem-like cells display phenotypic heterogeneity similar to GBM tumors	scRNA-seq, snRNA-seq, Genome-wide CRISPR–Cas9 screens	GBM patient material, GBM stem-like cultures	Richards et al.[54]
➢ GBM cell-macrophage crosstalk induces GBM cell transition to mesenchymal-like cell state	scRNA-seq, FACS, MERFISH, functional assays	GBM patient material, Transgenic mouse model	Hara et al.[89]

Abbreviations: GBM, glioblastoma; scRNA-seq, single-cell RNA sequencing; snRNA-seq, single nuclei RNA sequencing; scATAC-seq, single-cell assay for transposase-accessible chromatin with high-throughput sequencing; FACS, fluorescence-activated cell sorting; PDOX, Patient-derived orthotopic xenograft; ChIP-seq, chromatin immunoprecipitation sequencing; RNA-seq, ribonucleic acid sequencing; TME, tumor microenvironment; RTK, receptor tyrosine kinase; CSC, cancer stem cell; NG2, neuron-glial antigen 2; PTPRZ1, protein tyrosine phosphatase receptor type Z1; YAP/TAZ, yes-associated protein/tafazzin; CRISPR, clustered regularly interspaced short palindromic repeats; MERFISH, multiplexed error-robust fluorescence in situ hybridization.

review the role of GBM plasticity in creating a heterogeneous and dynamic tumor ecosystem, where distinct GBM phenotypic states coexist, interacting with each other and with the evolving tumor microenvironment (TME). We consider how phenotypic heterogeneity and plasticity allow tumor cells to escape treatment and develop resistance mechanisms. Finally, we discuss the therapeutic potential of targeting molecular regulators determining GBM heterogeneity and plasticity.

Cancer Stem Cells and Intrinsic Developmental Plasticity – An Evolving Concept

Intra-tumoral heterogeneity in GBMs has been described at various molecular levels. Distinct genetic clones arise following Darwinian principles of hierarchical evolution where the selection of the fittest clones leads to a final genetic equilibrium.[5] Models explaining the creation and maintenance of phenotypic heterogeneity, defined as diversity in epigenetic, transcriptomic, proteomic, and metabolic profiles, are more complex. The initial cancer stem cell (CSC) hypothesis, established over 20 years ago posits that so-called CSCs or Tumor Initiating Cells (TICs) are solely responsible for tumor development and establishment of intra-tumoral phenotypic heterogeneity in a hierarchical manner. CSCs were postulated to display diverse stem cell properties and to be highly tumorigenic in experimental models *in vivo*. Identification of CSCs in GBMs was largely based on the expression of stemness-associated cell membrane antigens such as CD133, CD15/SSEA, CD44, or A2B5 or intracellular markers such as Sox2 and Nestin.[6–12] Recently, Glycerol-3-phosphate dehydrogenase 1 (GPD1) was proposed as a marker of dormant GBM CSCs with a distinct metabolic profile.[13] A hierarchical organization of GBM was also suggested based on cell clone tracing via genetic barcoding upon serial xenotransplantation[14] and lineage tracing in mouse models.[15] CSC phenotypes are maintained by a plethora of signaling pathways commonly active in healthy stem cells, such as WNT, Notch, TGFβ, and MET pathways.[16–18] In analogy to neural stem cells that terminally differentiate to neuronal and glial cells, GBM CSCs may give rise to more differentiated phenotypes with astrocytic or neuronal features (Figure 1).[6] A number of molecules regulating the switch between CSCs and non-CSCs have been described and include nitric oxide driving activation of Notch signaling and CSC phenotypes,[16] Bone morphogenetic protein 4 (Bmp4) driving astroglia-like differentiation and quiescence,[19,20] and retinoic acid driving the aberrant neuronal differentiation process.[21] These mechanisms are currently considered as potential therapeutic targets.

At the same time, a growing body of evidence emerged indicating that a unidirectional hierarchical CSC model is not entirely applicable to GBMs. Numerous studies showed that irrespective of CSC marker expression, cells were able to self-renew and proliferate indefinitely. Diverse GBM cells were tumorigenic in experimental models: consistently all

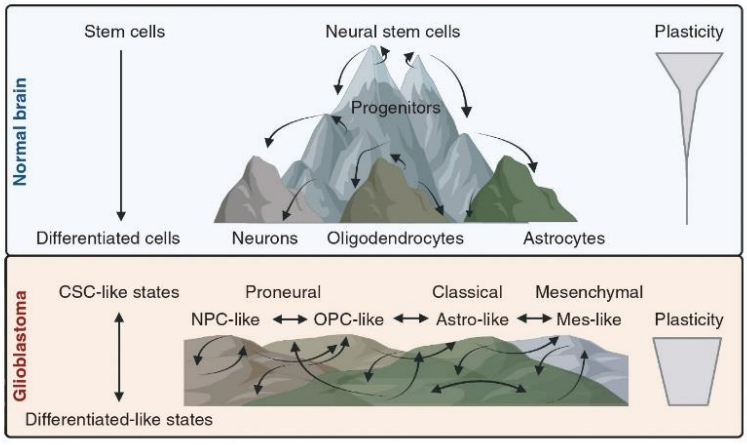

Fig. 1 Dynamic organization of phenotypic heterogeneity in GBM. The creation of phenotypic heterogeneity in GBM differs from the hierarchical differentiation process of normal stem cells. Neural stem cells create various committed progenitors and differentiated cells in a unidirectional hierarchical process. Reversibility of the differentiation process is very limited and can occur only between closely related progenitors and stem cell populations. In contrast, GBM constitutes dynamic and diverse tumor cell populations, where high plasticity is retained in all cells and differences between CSC-like and differentiated-like states are rather small. GBM cells exist in gradients of transcriptomic states, with multiple axes of variation. Interchanges have been documented between TCGA subtypes (Proneural, Classical, Mesenchymal), single-cell states (Neural progenitor cell (NPC)-like, Oligodendrocyte progenitor cell (OPC)-like, Astrocyte (Astro)-like and Mesenchymal (Mes)-like) as well as CSC-like and differentiated-like states. The phenotypic equilibrium at the population level is dictated by the genetic background, TME cues and treatment. Created with Biorender.com.

cell populations gave rise to tumors either with equal[11,22,23] or with different potency.[24–29] Similarly, both CSCs and non-CSCs were found to be multipotent and able to regain the initial heterogeneity,[22–24,26,29,30] incongruent with the concept of hierarchical organization. In line with this, we have shown that cellular states arise via stochastic state transitions of existing populations, evolving towards a heterogeneous equilibrium instructed by the TME.[29] Mathematical modeling confirmed the lack of a hierarchical process, yet different subpopulations may differ in the time required to establish the equilibrium. Interestingly, most plastic subpopulations (ie, fast in regenerating heterogeneity) displayed accelerated tumor growth *in vivo*.[29] A similar effect was seen with $NG2^+$ and $NG2^-$ subpopulations that displayed differential tumorigenicity *in vivo* following direct implantation, while this effect was lost after the recreation of initial heterogeneity *in vitro* prior to implantation.[27] Thus, although certain GBM subpopulations may exhibit differences in functional assays, CSCs do not appear to constitute a defined cellular entity, but rather a flexible cellular state cooperating with other states and adapting to TME cues. Importantly, unlike neural stem cell differentiation, differentiation of CSCs is not terminal, and "differentiated" GBM cells (ie, GBM cells expressing differentiation markers) can revert to CSC phenotypes (Figure 1).[19,21,29] Extensive tumor cell plasticity has also been uncovered in other malignancies, which lead to an evolving concept of the classical CSC hypothesis.[31–34] Plasticity is defined as the inherent ability to interconvert from one cellular state to another in a stochastic nonhierarchical manner.[35–37] Current data point to a very limited differentiation axis in GBMs where CSCs appear as a context-dependent phenotype (Figure 1). Both CSCs and more differentiated GBM phenotypes represent different states that can flexibly interchange while subjected to various stimuli in TME or upon treatment. While CSC-like states retain a full plasticity potential, differentiated-like phenotypes may show a more stringent potential, requiring longer times for phenotypic interchange.[37] It remains to be seen, whether the axis of bidirectional conversions between CSCs and more differentiated phenotypes can be therapeutically exploited. Whilst we refer the readers to recent seminal reviews in the CSC field,[37–42] we will focus here on novel findings highlighting GBM heterogeneity and plasticity at different molecular levels and in the context of the complex GBM ecosystem.

Transcriptomic Heterogeneity and Inferred Plasticity

Initial attempts to study cellular heterogeneity in GBMs, including CSCs, were based on a limited number of markers and isolation of cells for *in vitro* studies, which carry several limitations. Marker-based purification methods are not 100% efficient and do not take into account the underlying genetic heterogeneity. Many stemness markers are also expressed by nonneoplastic cells in the brain, further obscuring cell purification.[4,11,43,44] Isolated CSC and non-CSC populations were often cultured under different conditions[6] leading to a divergence of molecular profiles that reflect culture conditions rather than intrinsic cellular properties.[45] While only a limited number of markers was generally assessed at the functional level, a defining set of CSC markers could not be established for GBMs. Furthermore, it has been shown that self-renewal *in vitro* may not predict *in vivo* tumorigenic potential[29,46] and cells subjected to brain TME show distinct growth dependencies.[47] Meanwhile the assessment of intra-tumoral heterogeneity in patient samples was long hampered by capturing data from bulk populations and limited deconvolution algorithms. Bulk transcriptomic profiles of patient tumors allowed to identify inter-patient differences, which led to the initial TCGA subtyping (neural, proneural, classical, and mesenchymal) based on TME-dependent signatures.[48] More refined studies revealed that the neural subtype represents samples with limited tumor content, retaining the tumor-intrinsic signatures of proneural, classical, and mesenchymal.[4]

Application of single-cell and single nuclei RNA sequencing (scRNA-seq and snRNA-seq respectively) to capture transcriptomic signatures within GBM patients revolutionized our understanding of the underlying molecular heterogeneity. The initial study by Patel et al.[49] showed that GBMs are composed of cells of different TCGA subtypes with multiple cells of intermediary signatures, suggestive of state transitions between phenotypes. Signatures linked to stemness, hypoxia, and quiescence revealed continuous gradients of expression, rather than distinct cellular subpopulations. Using scRNA-seq and cell lineage tracing combined with functional assays, Neftel et al.[50] ultimately demonstrated cellular transitions based on four single-cell transcriptomic signatures dictating the primary axis of variation: Astrocyte (AC)-like, Neural progenitor cell (NPC)-like, Oligodendrocyte progenitor cell (OPC)-like and Mesenchymal (MES)-like (Figure 1). While NPC, OPC, and AC-like expression signatures resemble neurodevelopmental programs, MES-like cells do not mirror any normal brain cells. Multiple cellular states are present in each GBM and all contain proliferating cells, incompatible with a hierarchical organization. These transcriptomic states are partially correlated with expression of cell membrane epitopes. Again, such marker-defined fractions (positive and negative) are tumorigenic *in vivo* and reconstitute the transcriptomic heterogeneity of the parental tumor.[50] It remains to be determined if different states reconstitute heterogeneity and *in vivo* tumor growth at the same speed. Recent studies revealed additional gradients based on various cellular properties including proliferation, stemness and neurodevelopmental programs,[51] proneural-to-mesenchymal axis,[52] cellular specialization, metabolism,[53] TME and injury responses (Table 1).[54] The continuous gradients of transcriptomic heterogeneity across tumor cells are in line with protein expression profiles commonly detected, for example, by flow cytometry. Though the interdependence between different gradients appears evident, the exact inter-correlations remain to be determined. Of note, proliferating cells are consistently found in multiple phenotypic states and common CSC markers are broadly expressed and patient-specific, suggesting a variety of active stemness programs across different phenotypes.[55]

Single-cell transcriptomic states in IDHwt GBMs differ from those identified in lower-grade IDHmut

astrocytomas,[56] oligodendrogliomas,[57] and H3K27 mutant pediatric gliomas.[58] Analyses of IDHmut and H3K27 mutant gliomas require different gene signatures and suggest a more hierarchical organization. Here proliferating cells reside mostly in stem-like states, whereas Astro-like and Oligo-like cells rarely contain cycling cells. The limited availability of patient-derived preclinical models of IDHmut lower-grade gliomas hampers the functional validation of multipotency of these states. The proportion of cycling stem-like cells increases in the most aggressive high-grade IDHmut gliomas and is high in H3K27 mutant gliomas,[56,58] suggesting that stemness and plasticity correlate with tumor aggressiveness. A recent analysis revealed common pan-glioma signatures, which combine previously described entities into differentiated-like (IDHwt AC/MES-like states and IDHmut Astro/Oligo-like states), stem-like, and proliferating stem-like states (IDHwt NPC/OPC-like states and IDHmut stem-like states).[59]

The identification of cellular states and reversible plasticity between states raises the question of the underlying factors that drive these phenomena. Below we review tumor-intrinsic and TME-driven factors that contribute to the complex and dynamic organization of the GBM ecosystem (Figure 2).

Intrinsic Tumor Characteristics Defining Intra-tumoral Phenotypic Heterogeneity and Plasticity

Genetic Background

The underlying genetic background of the tumor directly contributes to plasticity and phenotypic heterogeneity. GBMs rarely contain equal proportions of single-cell transcriptomic states and the ratio is skewed by patient-specific genetic associations (eg, *PDGFRA*, *EGFR*, and *CDK4* amplification, *NF1* loss), where the most abundant phenotypic state defines the molecular subtype at the bulk level.[50] *PDGFRA* amplified tumors are generally enriched for OPC-like states, *CDK4* amplified tumors for NPC-like states, and *EGFR* amplified tumors for AC-like states, while GBMs with *NF1* loss contain higher proportions of MES-like states. The molecular mechanisms behind these differences are still unknown. Regardless of this genetic bias, scRNA-seq showed that genetic clones defined, for example, by different chromosomal aberrations present within the same tumor clearly recapitulate phenotypic heterogeneity and display multiple transcriptomic states.[49,50] At the functional level it was shown that genetic clones defined by different ploidy (ie, number of sets of chromosomes) display heterogeneous cell membrane marker expression and recreate phenotypic heterogeneity at the population level, suggesting that phenotypic heterogeneity provides a survival advantage to the tumor.[60] These heterogeneous profiles can adapt upon clonal selection, most likely in response to TME niches.[29] Genetic clones are also spatially distributed across different niches,[61] further impacting phenotypic heterogeneity in the spatial context. This implies that phenotypic heterogeneity and plasticity of GBM cells represent a general phenomenon also in the framework of underlying genetic heterogeneity.

In contrast to the hierarchical process of conventional genetic evolution, extrachromosomal DNA (ecDNA) carrying oncogenes shows a more plastic behavior. As ecDNA structures do not contain centromeres, they are randomly distributed to daughter cells, creating an additional level of heterogeneity.[62] Although the mechanisms regulating ecDNA maintenance are not fully understood, it was found that the generation of ecDNA can be flexibly regulated following therapeutic stress. *EGFRvIII*-containing ecDNAs are lost upon treatment with erlotinib and reemerge rapidly in surviving GBM cells.[63] Genetic heterogeneity based on ecDNA carrying *EGFRvIII* is also rapidly reconstituted from purified cells with or without *EGFRvIII* amplification, further demonstrating the plastic behavior of ecDNA emergence. Whether other sub-clonal ecDNA events such as *EGFR* or *PDGFRA* amplifications display similar plasticity remains to be seen. Gene amplifications carried on ecDNAs are often dynamic during glioma treatment,[64] and it is currently unclear if this is due to clonal selection, plasticity of ecDNA production, or both.

Permissive Epigenome

Epigenetic mechanisms such as DNA methylation, histone modification, and chromatin remodeling are essential in shaping dynamic gene expression. The phenotypic equilibrium in GBM is dictated in part by the cell of origin,[65] implicating a key role of the subjacent epigenome in shaping phenotypic heterogeneity. DNA methylation further magnifies the outcome of chromosomal aberrations, as amplified genomic regions (eg, chromosome 7) show low DNA methylation, whereas regions of copy number loss appear highly methylated.[66] Copy number alterations also associate with DNA methylation disorder, that is, discordant DNA methylation status comprising methylated and unmethylated CpGs in regulatory sequences, which mark epigenetically dynamic regions.[59] DNA methylation profiles enable the stratification of GBMs into several subclasses that largely correlate with transcriptomic subtypes.[2,3] Similar to transcriptomic states, disparate DNA methylation and chromatin accessibility profiles are found not only in spatially separated tumor zones but also at the single-cell level in different phenotypic states.[52,66–68] The recent analysis by Chaligne et al.[66] showed that IDHmut gliomas contain cells with LGm1-LGm3 DNA methylation subtypes, while IDHwt GBMs show gradients of LGm4-LGm5 subtypes. LGm4 cells represent AC-like and MES-like states and LGm5 cells are mostly NPC-like and OPC-like, highlighting a closer resemblance of these state pairs at the DNA methylation level.

Still, the epigenetic regulation of flexible GBM cellular states remains poorly understood. Globally, DNA of GBM cells is hypomethylated, creating open and active chromatic areas similar to pluripotent states. Analysis of phylogenetic trees based on DNA methylation revealed that most differences between phenotypic states arise from stochastic passenger changes, rather than encoded cell state differentiation events.[66] Promoter regions regulated by Polycomb repressive complex 2 (PRC2, responsible

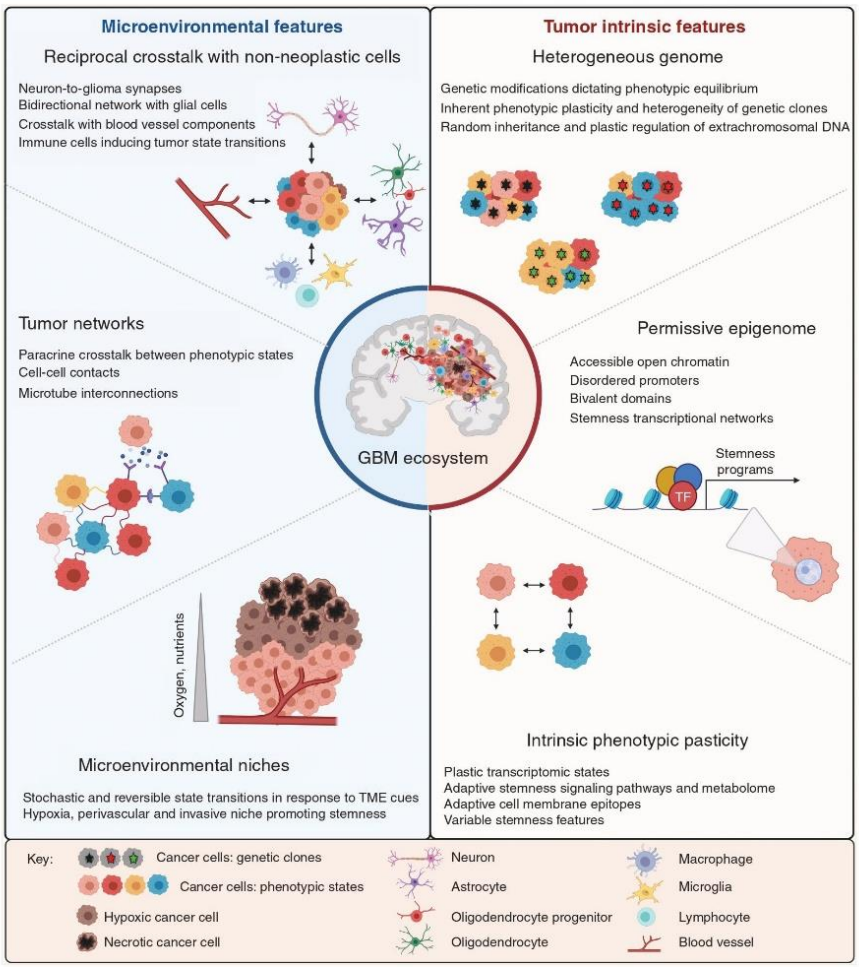

Fig. 2 Intrinsic and microenvironmental features of the GBM ecosystem defining plasticity and intra-tumoral heterogeneity. The GBM cellular ecosystem comprises of diverse tumor cells residing in different TME niches. Tumor cell plasticity and the equilibrium of phenotypic states at the population level is defined by multiple tumor-intrinsic features and extrinsic cues from the TME. Created with Biorender.com.

for depositing H3K27me3 repressive mark) linked to stemness pathways show strong hypomethylation and low DNA methylation disorder (HOX and Homeobox genes, lineage-specific transcription and growth factors).[59,66] Interestingly, NPC/OPC-like states show modestly higher DNA hypomethylation of PRC2 targets than AC/MES states, which correlates with enhanced chromatin accessibility and increased active histone marks such as H3K4me3 and H3K27ac.[66] On the other hand, regulatory elements of AC/MES-like signature genes are highly hypomethylated and accessible in these states, suggesting a combined role of DNA and histone methylation with DNA accessibility in state transitions. Intermediate states at the proneural–mesenchymal axis show heterogeneous profiles with partial overlap of proneural (NPC/OPC-like) and mesenchymal accessibility features, and appear largely associated with AC-like states.[52,69] Again, stemness-associated chromatin profiles were present across different phenotypic states and heterogeneous CSC-like states. The relative difference in DNA methylation levels between phenotypic states are minor and certain gene promoters (eg, *Prominin-1/CD133* (*PROM1*), *MutL Homolog 1* (*MLH1*)) show heterogeneous accessibility profiles without detectable DNA methylation. Promoters of many developmental and signature-specific genes were also identified as bivalent in GBM, defined by the presence of active H3K4me3 and repressive H3K27me3 histone marks combined with low DNA methylation levels.[70] Bivalent domains, initially described in pluripotent

stem cells, are indicative of plasticity as they allow for temporal suppression of transcription while protecting the genes from irreversible silencing by DNA methylation and keeping them "poised" for action.[71] Such domains were reported on PRC2 target gene promoters and were enriched in NPC/OPC-like states.[66] Although the simultaneous presence of active and repressive histone marks remains unproven at the single-cell level, current data suggest a "primed" status of nonexpressed signatures and epigenetically-encoded plasticity between transcriptomic states. On the other hand, higher DNA methylation levels and DNA methylation disorder are present at the promoters of genes associated with cell differentiation processes, leading to reduced gene expression. High DNA methylation disorder is also present at DNA elements regulated typically by transcription factors associated with extracellular stress stimuli such as hypoxia (eg, *HIF1A*), most probably facilitating plasticity during stress.[59] Continuous pressure via hypoxia or radiotherapy leads to accumulation of additional DNA methylation disorder, further enhancing GBM plasticity.

Stemness Transcriptional Network

GBMs highjack core transcriptional networks of reprogramming reminiscent of pluripotent stem cells. The pluripotency reprogramming transcription factors Sox2 and c-Myc are widely active in GBM cells; Oct3/4, Nanog, and Klf4 were also reported though at lower levels.[72] Genetic activation of pluripotency or of neural-specific transcription factors (Brn2, Sox2, Sall2, Olig2) induces tumorigenic CSC-like states in GBM via modulation of epigenetic regulators (eg, Rcor2/Lsd1 histone demethylase, DNA methyl transferase Dnmt1) and noncoding RNAs (eg, HOTAIR, MALAT-1).[73–76] Such reprogramming can be triggered by oncogenic pathways, such as HGF/cMET signaling,[77] or TME cues, such as hypoxia.[78] Of note, Sox2 expression appears rather ubiquitous in GBM cells, regulating distinct downstream gene networks in stem-like and differentiated-like cells.[79] A set of active enhancers and transcription factors were also found to be subtype-specific, where Sox10 repression led to chromatin remodeling and transition towards the mesenchymal state.[80] Other factors, such as Ascl1 can activate a switch towards more differentiated states.[81]

GBM Plasticity and the Tumor Microenvironment

Tumor Microenvironmental Niches

TME conditions have a strong impact on the phenotypic equilibrium of spatial and temporal heterogeneity in GBM. While initial reports suggested a preselection of CSCs in TME niches, such as hypoxia, perivascular area, or invasive zone, it has become clear that GBM cells undergo dynamic and reversible transitions in response to TME changes. Barcoding technology confirmed the lack of cellular selection during invasion into the surrounding brain, highlighting phenotypic adaptation as the main mode of action.[14] Invasive cells activate diverse molecular mechanisms, for example, reminiscent of radial glia or proneural features, allowing for digestion of extracellular matrix and migration.[55,82,83] TGF-β driven mesenchymal phenotypes were also reported to be highly invasive.[84] Similarly, hypoxia and associated *pH* and glucose levels are potent inducers of phenotypic adaptation[85,86] leading to quiescence, activation of survival mechanisms such as autophagy,[87] and mesenchymal features.[52,88,89] A phenotypic switch towards CSC-like states can be induced, for example, by HIF1α-driven activation of VEGFA and CD133 in severe hypoxia (<1% O_2),[90,91] by HIF2α-driven activation of a pluripotent transcriptional network in modest hypoxia (2–5% O_2),[78] or by endothelial cell-derived nitric oxide in the perivascular niche.[16] Hypoxia may decrease global DNA methylation by reducing the availability of methionine and induction of nicotinamide N-methyltransferase (NNMT), leading to a mesenchymal switch and increased tumorigenicity.[92] TME-driven gradients depend on variable chromatin regulators such as Polycomb repressive complexes: while proneural states are driven by EZH2 in vascular niches, hypoxic mesenchymal states depend on BMI1, depositing H3K27me3 or H2AK119Ub histone marks respectively.[88] Niche adaptation follows a stochastic state transition model, where GBM cells create patchworks encompassing the most favorable phenotypic states.[29] Interestingly, although TME drives distinct phenotypic states towards TME-specific equilibria, the transition speed may not be equal across all tumor cells.[29] Analysis at the single-cell epigenetic level is needed to understand why certain GBM cells can create TME-specific equilibria faster than others.

Molecular Crosstalk and Tumor Networks

Paracrine crosstalk between phenotypic states plays a key role in shaping the overall GBM ecosystem. Wang et al. showed that reciprocal crosstalk between tumor cells of different phenotypes creates supportive growth stimuli via BDNF-NTRK2-VGF paracrine signaling.[93] Cells with more differentiated phenotypes stimulate stem-like states, promoting tumor initiation and growth.[93,94] Such paracrine mechanisms could explain the increased tumor growth capacity of those GBM subpopulations, that are more efficient in recreating heterogeneity.[29] Paracrine crosstalk via soluble CD109 was reported between cells of the tumor core and invasive edge.[83] Apoptotic GBM cells in the necrotic zone release extracellular vesicles that transport components of spliceosomes to neighboring viable cells, which subsequently modulate RNA splicing and promote survival in the recipient cells.[95] Phenotypic crosstalk also exists between different genetic clones, for example, *EGFRvIII*-amplified cells release cytokines such as Il-6 and LIF, which directly activate gp130 and *EGFR* in surrounding *EGFRwt*-amplified cells, leading to sustained tumor growth.[96]

In addition to paracrine signaling, GBM cells communicate with each other via direct cell-cell contacts, via exosomes or microtubes. IDHwt GBM and IDHmut high-grade astrocytoma cells interconnect via ultra-long tumor microtubes protruding from the cell membrane, which enhances survival and resistance to radio- and

chemotherapy.[97,98] Recent data show that connected cells possess enhanced stem-like features[99] and compensate for the loss of cells in the perivascular niche following Notch1 inhibition.[100] It remains to be seen to what extent this functional network plays an active role in state transitions upon tumor expansion and treatment escape.

Crosstalk with TME Subpopulations

Direct interactions between tumor cells and nonneoplastic cells play a vital role in the maintenance of cellular plasticity in GBM. Recent data demonstrate a critical role for physical contacts between tumor cells and neurons, where crosstalk occurs via molecular and electrochemical signaling through a neuron-to-glioma cell synapse. Some glioma cells (10–30%) can thus hijack the neuronal network to receive electrochemical and paracrine signals promoting growth and invasion.[101,102] Membrane depolarization further enhances cellular communication, where depolarization-induced nonsynaptic calcium currents are amplified via gap junctions of the tumor network itself. Tumor cells are also impacted by the bidirectional crosstalk with nonneuronal cells, including glial cells, endothelial cells, pericytes, resident microglia and infiltrating immune cells. These interactions involve cell-cell contact and paracrine mechanisms, leading to phenotypic adaptation of both tumor and TME subpopulations in different tumor niches. This complex reciprocal interplay has been thoroughly reviewed elsewhere.[37,39,41,103,104]

The genetic and phenotypic status of tumor cells is important in the bidirectional crosstalk and in shaping the TME, although the "what comes first" question remains unresolved. For example, the immune component is influenced by the IDH status in gliomas and differs significantly from brain metastases.[105] IDHmut gliomas display an increased proportion of microglia-derived macrophages, whereas IDHwt GBMs show enhanced infiltration of monocyte-derived macrophages and lymphocytes. The TME varies across different transcriptional GBM subtypes: while mesenchymal tumors contain lower tumor content and a higher proportion of macrophages, neutrophils, and neuroglial cells, classical tumors have increased dendritic cell signatures.[4] Transitions towards mesenchymal/injury response-like GBM states may occur via inflammatory cytokines released by mesenchymal-specific macrophages[54,106,107] such as TNFα, CCL5, CCL12, and G-CSF, further underlining the reciprocal crosstalk between the TME and tumor cell phenotypic states. A recent study by Hara et al.[89] shows that Oncostatin M (OSM) released by macrophages induces GBM transitions towards the mesenchymal state through activation of OSMR/LIFR-GP130 receptors and STAT3 signaling in GBM cells.

The Role of Plasticity in Treatment Resistance and GBM Recurrence

GBM at Recurrence

GBMs relapse quickly independent of treatment, indicating strong intrinsic resistance mechanisms. DNA lesions induced by ionizing radiation and chemotherapy can be repaired by a plethora of DNA damage response mechanisms.[108] Standard-of-care temozolomide (TMZ) treatment confers a narrow survival advantage only to the subset of patients with a silenced *O-6-methylguanine-DNA methyltransferase* (*MGMT*) promoter.[109] Distinct genetic clones may confer variable responses to TMZ and other drugs.[110,111] Still, unlike other solid tumors, only limited genetic changes are detected upon recurrence, indicating a restricted role of genetic evolution in GBM resistance.[112–114] No common treatment-induced genetic trajectories were identified and loss or emergence of mutations is generally patient-specific.[114] Such genetic differences may arise from a different genetic make-up of cells remaining after surgery, rather than treatment-induced changes.[115] Likewise, hypermutation[116] and DNA methylation changes[61,117] are rare in IDHwt GBMs, indicating less pronounced (epi)genetic evolution compared to IDHmut gliomas. Of note, *MGMT* promoter methylation status can differ not only between patients but also within the same tumor, resulting in cells of varying sensitivity to TMZ.[110]

Accumulating evidence suggests the prevalence of resistance mechanisms linked to phenotypic adaptation of tumor cells and TME. At bulk level, GBMs may manifest transcriptomic subtype transitions upon recurrence, although the majority of tumors retain the same subtype.[4] It is plausible that transcriptional subtyping at the bulk level may not have the granularity to understand cellular resistance. Further deconvolution of transcriptomic signals revealed differences in TME composition upon treatment. While an overall tendency towards decreased blood-derived monocytes is observed, mesenchymal transitioning correlates with increased M2-like macrophages, whereas proneural transitions lack immune infiltration.[4] In contrast, recent single-cell data from unpaired patient tumors noted an increase in the proportion of monocyte-derived macrophages in recurrent tumors, while hypermutated GBMs had more CD8+ T cells.[118] Moreover, TME subpopulations were shown to adapt towards resistance-promoting phenotypes, for example, radiotherapy induced dynamic resistance-specific macrophages that can be reverted by Colony-stimulating factor-1 receptor (CSF-1R) inhibition.[119]

Tumor Plasticity as a Mechanism of Resistance

Plasticity allows for the creation of a plethora of cellular states with different sensitivity to the treatment.[120] Treatment-related phenotypic changes can generally be attributed to two scenarios: (1) increased proliferation and selection of preexisting resistant cellular states over time or (2) adaptation of tumor cells towards resistant phenotypes (Figure 3). Such plastic tumor cells, so-called drug-tolerant persisters, can survive therapeutic pressure by adapting towards treatment-resistant states with a faster response than Darwinian selection.[120] Although quiescence was proposed as a main feature of adaptation, proliferating persisters have also been reported.[121] Preexisting resistance may involve different genetic clones, different cellular states or both. While the selected treatment-resistant genetic clones and/or preexisting resistant phenotypic states retain their genotype and phenotype over time,

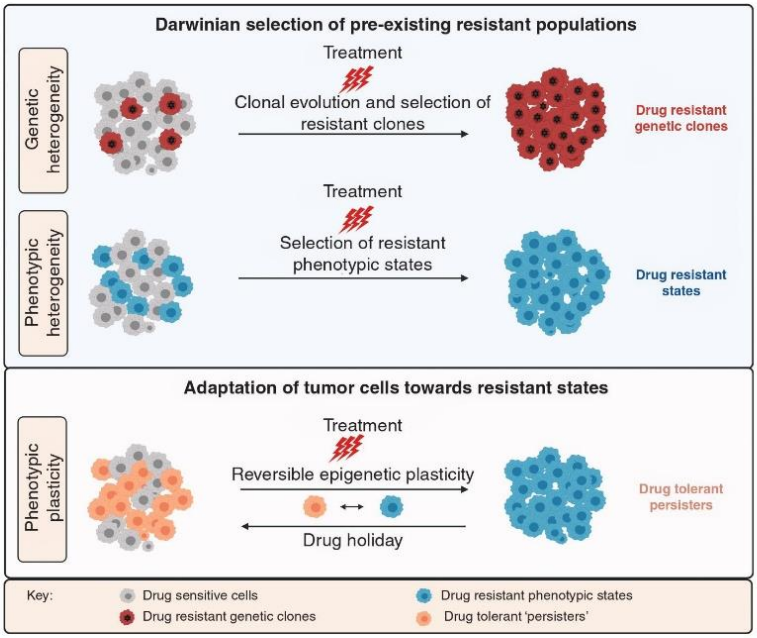

Fig. 3 Tumor heterogeneity and plasticity as resistance mechanisms. Tumors contain cells with varying sensitivity to treatment. Treatment leads to the eradication of drug-sensitive cells. Resistance can be driven by Darwinian selection of preexisting resistant cells with advantageous genetic or phenotypic tumor characteristics. Highly resistant genetic clones may also be acquired upon treatment (ie, clonal evolution and selection). Adaptive resistance is driven by drug-tolerant persisters that survive treatment and adapt towards resistant phenotypic states. Persisters can revert to their initial phenotypic states and recreate phenotypic heterogeneity when released from the treatment (ie, drug holiday). Drug resistance may thus be a result of reversible epigenetic plasticity combined with irreversible clonal expansion. Created with Biorender.com.

drug persisters can revert back to the initial states upon a drug holiday period. Recent reports from breast cancer,[122] lung cancer,[121,123] and melanoma[124] point to multifactorial resistance, indicating that heterogeneous subpopulations can undergo diverse state transitions and activate concurrent genetic and nongenetic resistance mechanisms upon treatment. By following so-called Lamarckian adaptation, that is, inheritance of acquired characteristics, cells surviving drug treatment first undergo plastic and reversible changes at the phenotypic level, some of which may become permanent over time.

To what extent GBM cells with different sensitivity to treatment are reflected by various phenotypic states remains to be determined. The initial CSC studies describe preexisting GBM CSCs to be highly resistant to radio- and chemotherapy through, for example, enhanced activation of DNA repair mechanisms (eg, via MGMT, Chk1, and Chk2), and inhibitors of apoptosis (eg, FLIP, BCL-2, and BCL-XL).[9,15,125] Mouse models show that GBM cells can also escape chemotherapy via ABCG2-driven drug efflux,[126] which is however not reflected in human GBM.[44,127,128] On the other hand, a preexisting proneural-to-mesenchymal gradient was shown to correlate with resistance to radiation and multi-drug treatment, without a direct link to CSC-like phenotypes.[129] Other studies also do not find convincing evidence for CSC selection and describe resistance in non-CSCs.[130–132] This controversy may in part be explained by diverse definitions of CSCs (eg, quiescent vs proliferative) and variable proliferative properties of the studied populations across patient tumors and preclinical models. Tumors containing quiescent CSC-like cells may show increased stemness upon treatment due to their lower susceptibility to radio- and chemotherapy, whereas tumors driven by proliferative CSC-like cells may not show such selection.[19] The recent insight into GBM plasticity proposes additional scenarios. While some GBM cells may preexist in highly treatment-resistant states, persister cells can activate various adaptive mechanisms upon treatment, such as quiescence,[13] induction of regulatory loops of mRNAs, small and long noncoding RNAs,[133] and transition to stem-like states.[25,130,134] Stemness pathways can then act as protectors against treatment, for example, Notch signaling attenuates resistance to radiotherapy via upregulation of PI3K/Akt and Bcl-2 survival pathways.[135] Ionizing radiation activates a switch from $CD133^+$ to $CD109^+$ stem-like phenotypes in invasive cells, concomitant with CCAAT/enhancer binding protein β (C/EBPβ)-mediated transition from proneural to YAP/TAZ-dependent mesenchymal signatures.[51,136] Similar plasticity has been described in the

context of anti-angiogenic treatment, where tumor cells adapt to TME changes by upregulating glycolysis, invasion, and mesenchymal features via ZEB1-regulated mechanisms.[137,138]

Cellular plasticity is also involved in the resistance to targeted drugs. Receptor tyrosine kinase inhibitors, a major class of targeted therapeutics, generally lead to plastic escape mechanisms via activation of alternative signaling pathways.[139] Dasatinib, a PDGFRA inhibitor, was shown to activate reversible GBM transitions towards quiescent Notch and KDM6-dependent persister states via remodeling of H3K27 modifications from H3K27me3 to H3K27ac and activation of neurodevelopmental programs.[140] These states can also preexist in treatment-naïve GBM and are high at baseline in certain stem-like cultures, suggesting a variable balance between preexisting and adaptive resistance in different tumors. Moreover, scRNA-seq combined with lineage tracing showed that this adaptive resistance coexists with irreversible genetic evolution towards novel resistant clones.[141] Adaptive resistance was also observed via single-cell phosphoproteomic analysis upon mTOR inhibition, where GBM cells shift from mTORC1/C2 to ERK and Src signaling.[142] Further studies are needed to reveal the molecular mechanisms and epigenetic regulators underlying treatment-induced GBM plasticity in the context of standard-of-care and targeted therapies. We speculate that GBMs may differ with regards to the ratio of preexisting resistant cells versus adaptive persisters. Based on the vast plasticity described in GBM, resistance most likely originates in large part from adaptive changes of drug-tolerant persister states. Moreover, the signatures of resistance are likely to be treatment-specific rather than universal.

Perspectives

The concept of CSCs at the apex of a hierarchical organization in GBM brought major hopes for straightforward therapies that could eradicate the entire tumor by specifically targeting CSCs at their roots. Over the years numerous promising targets have been proposed including cell membrane markers and stemness signaling pathways.[38,40] The evidence of powerful intrinsic cellular plasticity dampens these expectations as at the therapeutic level, tumor plasticity represents a conceptual departure from the classical CSC hypothesis. Indeed, so far none of the identified targets passed the preclinical efficacy. For example, $CD133^+$ CSCs with anti-CD133 antibodies or CD133-specific CAR-T cells did not result in complete elimination of GBM in preclinical models, only temporary effects are observed and tumors regrow as soon as the treatment is halted.[143] Similarly, cell differentiation protocols are largely unsuccessful in eliminating proliferating GBM cells. Thus, GBM eradication will require targeting the dynamic states rather than single entities. To achieve this, further studies are needed to reveal the drivers of plasticity and treatment escape. The molecular signatures of preexisting treatment-resistant and plastic persister GBM cells in the context of standard-of-care and targeted therapies remain largely unknown. Future studies should address which of the phenotypic changes are fast and reversible, and which are retained in tumors long after treatment. The assessment of the ratio between preexisting treatment-resistant and persister cells may allow patient stratification according to different treatments. Initiatives such as the GLASS consortium[112] will reveal long-term changes in longitudinal patient samples prior and after treatment. While scRNA-seq is still limited to fresh samples, adaptation of the technology to single nuclei extracted from frozen or fixed tissue samples opens new opportunities. Tumor multisampling, spatial-omics and emerging technologies permitting simultaneous assessment of genetic, epigenetic, and transcriptomic information will foster an integrative analysis of dynamic states in a spatio-temporal context.

On the other hand, identifying short-term reversible drug-induced adaptations will require experimental models. These changes may be masked in recurrent patient samples because of the drug holiday phenomenon and/or long-term evolution of the tumor post-treatment. Combining drug exposures directly with single-cell multi-omics[144] and functional analyses in clinically-relevant models will accelerate the functional characterization of preexisting and adaptive resistant states. In this context, patient-derived organoids[145–147] and orthotopic xenografts (PDOXs),[43,45,148,149] which recapitulate tumor heterogeneity and TME niches, should be preferred over *in vitro* cell lines. Barcoding lineage tracing strategies[50,121] will allow the tracking of single cells in a spatio-temporal manner. This may overcome the limitation of (sc)RNA-seq that captures gene expression at a specific snapshot in time and does not reveal the relationship between treatment-naive cells and their resistant progeny. Inclusion of (sc)RNA-seq analysis of tumor dynamics as part of clinical trials may be key to investigating resistance mechanisms towards targeted treatment and discriminate responders from nonresponders.

The pressing question remains on how to design therapies against a dynamic target. Gene regulatory networks, master regulators, and epigenetic modifiers dictating tumor plasticity may represent more powerful targets than signature molecules of resistant subpopulations per se.[88,150] Noncoding regulators, such as miRNAs or long noncoding RNAs are additional emerging therapeutic targets.[76] Reversible feedback loops in signaling pathways and selective translation of mRNAs marked by N6-methyladenosine (m^6A) modification are emerging examples of other molecular layers of plastic regulation of state transitions. Interestingly, Shen et al. showed that mRNAs selected for translation in melanoma persister cells largely comprise chromatin regulators and stress-response kinases.[151] Blocking cellular state transitions in melanoma[124] and other cancers[152,153] effectively decreased heterogeneity and delayed the onset of resistance. Targeting of Retinoid X receptor-γ (RXRG), a master regulator responsible for the reversible shift towards treatment-resistant melanoma, successfully inhibited transitions towards drug-resistant states.[124] Regulators of mesenchymal states, such as NF-kB, STAT3, YAP/TAZ, or C/EBPβ might represent therapeutic targets for GBM resisting standard-of-care therapy. On the other hand, mesenchymal states were recently linked to a higher abundance of cytotoxic T cells,[89] creating novel opportunities for immunotherapies. Lastly, the synergistic effects of genetic evolution and nongenetic state transitions upon treatment will have to be considered,[35] as new genetic modifications may influence the capacity of state transitions and the

population equilibrium of phenotypic states. Relying solely on hierarchical Darwinian selection (genetic or nongenetic) or tumor plasticity may not be sufficient.[154] Models developed by evolutionary ecology, which simultaneously take into account selective and adaptive factors, may bring novel understanding of the dynamic processes in tumors.[155] Novel modalities such as the use of nonlethal doses to control state transitions and retain sufficiently less aggressive drug-sensitive/permissive states in the tumor ecosystem merits experimental validation. In conclusion, major research efforts are needed to unravel the molecular mechanisms and regulators of GBM plasticity and generate effective drugs against a moving target.

Funding

This work was supported by the European Union's Horizon 2020 research and innovation programme under the Marie Skłodowska-Curie 'GLIOTRAIN' ITN initiative [agreement No 766069].

Conflict of interest statement. Authors declare no conflict of interest.

References

1. Louis DN, Perry A, Wesseling P, et al. The 2021 WHO classification of tumors of the central nervous system: a summary. *Neuro Oncol.* 2021; 23(8):1231–1251.
2. Capper D, Jones DTW, Sill M, et al. DNA methylation-based classification of central nervous system tumours. *Nature.* 2018; 555(7697):469–474.
3. Ceccarelli M, Barthel FP, Malta TM, et al.; TCGA Research Network. Molecular profiling reveals biologically discrete subsets and pathways of progression in diffuse glioma. *Cell.* 2016; 164(3):550–563.
4. Wang Q, Hu B, Hu X, et al. Tumor evolution of glioma-intrinsic gene expression subtypes associates with immunological changes in the microenvironment. *Cancer Cell.* 2017; 32(1):42–56.e6.
5. Turajlic S, Sottoriva A, Graham T, Swanton C. Resolving genetic heterogeneity in cancer. *Nat Rev Genet.* 2019; 20(7):404–416.
6. Lathia JD, Mack SC, Mulkearns-Hubert EE, Valentim CL, Rich JN. Cancer stem cells in glioblastoma. *Genes Dev.* 2015; 29(12):1203–1217.
7. Singh SK, Hawkins C, Clarke ID, et al. Identification of human brain tumour initiating cells. *Nature.* 2004; 432(7015):396–401.
8. Galli R, Binda E, Orfanelli U, et al. Isolation and characterization of tumorigenic, stem-like neural precursors from human glioblastoma. *Cancer Res.* 2004; 64(19):7011–7021.
9. Bao S, Wu Q, McLendon RE, et al. Glioma stem cells promote radioresistance by preferential activation of the DNA damage response. *Nature.* 2006; 444(7120):756–760.
10. Son MJ, Woolard K, Nam DH, Lee J, Fine HA. SSEA-1 is an enrichment marker for tumor-initiating cells in human glioblastoma. *Cell Stem Cell.* 2009; 4(5):440–452.
11. Ogden AT, Waziri AE, Lochhead RA, et al. Identification of A2B5+CD133-tumor-initiating cells in adult human gliomas. *Neurosurgery.* 2008; 62(2):505–514; discussion 514.
12. Anido J, Sáez-Borderías A, Gonzàlez-Juncà A, et al. TGF-β receptor inhibitors target the CD44(high)/Id1(high) glioma-initiating cell population in human glioblastoma. *Cancer Cell.* 2010; 18(6):655–668.
13. Rusu P, Shao C, Neuerburg A, et al. GPD1 specifically marks dormant glioma stem cells with a distinct metabolic profile. *Cell Stem Cell.* 2019; 25(2):241–257.e8.
14. Lan X, Jörg DJ, Cavalli FMG, et al. Fate mapping of human glioblastoma reveals an invariant stem cell hierarchy. *Nature.* 2017; 549(7671):227–232.
15. Chen J, Li Y, Yu TS, et al. A restricted cell population propagates glioblastoma growth after chemotherapy. *Nature.* 2012; 488(7412):522–526.
16. Charles N, Ozawa T, Squatrito M, et al. Perivascular nitric oxide activates notch signaling and promotes stem-like character in PDGF-induced glioma cells. *Cell Stem Cell.* 2010; 6(2):141–152.
17. Joo KM, Jin J, Kim E, et al. MET signaling regulates glioblastoma stem cells. *Cancer Res.* 2012; 72(15):3828–3838.
18. Peñuelas S, Anido J, Prieto-Sánchez RM, et al. TGF-beta increases glioma-initiating cell self-renewal through the induction of LIF in human glioblastoma. *Cancer Cell.* 2009; 15(4):315–327.
19. Sachdeva R, Wu M, Johnson K, et al. BMP signaling mediates glioma stem cell quiescence and confers treatment resistance in glioblastoma. *Sci Rep.* 2019; 9(1):14569.
20. Piccirillo SG, Reynolds BA, Zanetti N, et al. Bone morphogenetic proteins inhibit the tumorigenic potential of human brain tumour-initiating cells. *Nature.* 2006; 444(7120):761–765.
21. Campos B, Centner FS, Bermejo JL, et al. Aberrant expression of retinoic acid signaling molecules influences patient survival in astrocytic gliomas. *Am J Pathol.* 2011; 178(5):1953–1964.
22. Kenney-Herbert E, Al-Mayhani T, Piccirillo SG, et al. CD15 expression does not identify a phenotypically or genetically distinct glioblastoma population. *Stem Cells Transl Med.* 2015; 4(7):822–831.
23. Wang J, Sakariassen PØ, Tsinkalovsky O, et al. CD133 negative glioma cells form tumors in nude rats and give rise to CD133 positive cells. *Int J Cancer.* 2008; 122(4):761–768.
24. Chen R, Nishimura MC, Bumbaca SM, et al. A hierarchy of self-renewing tumor-initiating cell types in glioblastoma. *Cancer Cell.* 2010; 17(4):362–375.
25. Auffinger B, Tobias AL, Han Y, et al. Conversion of differentiated cancer cells into cancer stem-like cells in a glioblastoma model after primary chemotherapy. *Cell Death Differ.* 2014; 21(7):1119–1131.
26. Brescia P, Ortensi B, Fornasari L, Levi D, Broggi G, Pelicci G. CD133 is essential for glioblastoma stem cell maintenance. *Stem Cells.* 2013; 31(5):857–869.
27. Al-Mayhani TF, Heywood RM, Vemireddy V, Lathia JD, Piccirillo SGM, Watts C. A non-hierarchical organization of tumorigenic NG2 cells in glioblastoma promoted by EGFR. *Neuro Oncol.* 2019; 21(6):719–729.
28. Couturier CP, Ayyadhury S, Le PU, et al. Single-cell RNA-seq reveals that glioblastoma recapitulates a normal neurodevelopmental hierarchy. *Nat Commun.* 2020; 11(1):3406.
29. Dirkse A, Golebiewska A, Buder T, et al. Stem cell-associated heterogeneity in Glioblastoma results from intrinsic tumor plasticity shaped by the microenvironment. *Nat Commun.* 2019; 10(1):1787.
30. Brown DV, Filiz G, Daniel PM, et al. Expression of CD133 and CD44 in glioblastoma stem cells correlates with cell proliferation, phenotype stability and intra-tumor heterogeneity. *PLoS One.* 2017; 12(2):e0172791.
31. Meacham CE, Morrison SJ. Tumour heterogeneity and cancer cell plasticity. *Nature.* 2013; 501(7467):328–337.

32. Bjerkvig R, Johansson M, Miletic H, Niclou SP. Cancer stem cells and angiogenesis. *Semin Cancer Biol.* 2009; 19(5):279–284.
33. Li Y, Laterra J. Cancer stem cells: distinct entities or dynamically regulated phenotypes? *Cancer Res.* 2012; 72(3):576–580.
34. Nguyen LV, Vanner R, Dirks P, Eaves CJ. Cancer stem cells: an evolving concept. *Nat Rev Cancer.* 2012; 12(2):133–143.
35. Huang S. Reconciling non-genetic plasticity with somatic evolution in cancer. *Trends Cancer.* 2021; 7(4):309–322.
36. Gupta PB, Pastushenko I, Skibinski A, Blanpain C, Kuperwasser C. Phenotypic plasticity: driver of cancer initiation, progression, and therapy resistance. *Cell Stem Cell.* 2019; 24(1):65–78.
37. Prager BC, Bhargava S, Mahadev V, Hubert CG, Rich JN. Glioblastoma stem cells: driving resilience through Chaos. *Trends Cancer.* 2020; 6(3):223–235.
38. Saygin C, Matei D, Majeti R, Reizes O, Lathia JD. Targeting cancer stemness in the clinic: from hype to hope. *Cell Stem Cell.* 2019; 24(1):25–40.
39. Bayik D, Lathia JD. Cancer stem cell-immune cell crosstalk in tumour progression. *Nat Rev Cancer.* 2021; 21(8):526–536.
40. Ramos EK, Hoffmann AD, Gerson SL, Liu H. New opportunities and challenges to defeat cancer stem cells. *Trends Cancer.* 2017; 3(11):780–796.
41. Mitchell K, Troike K, Silver DJ, Lathia JD. The evolution of the cancer stem cell state in glioblastoma: emerging insights into the next generation of functional interactions. *Neuro Oncol.* 2021; 23(2):199–213.
42. Wainwright EN, Scaffidi P. Epigenetics and cancer stem cells: unleashing, hijacking, and restricting cellular plasticity. *Trends Cancer.* 2017; 3(5):372–386.
43. Golebiewska A, Hau AC, Oudin A, et al. Patient-derived organoids and orthotopic xenografts of primary and recurrent gliomas represent relevant patient avatars for precision oncology. *Acta Neuropathol.* 2020; 140(6):919–949.
44. Golebiewska A, Bougnaud S, Stieber D, et al. Side population in human glioblastoma is non-tumorigenic and characterizes brain endothelial cells. *Brain.* 2013; 136(Pt 5):1462–1475.
45. Pine AR, Cirigliano SM, Nicholson JG, et al. Tumor microenvironment is critical for the maintenance of cellular states found in primary glioblastomas. *Cancer Discov.* 2020; 10(7):964–979.
46. Barrett LE, Granot Z, Coker C, et al. Self-renewal does not predict tumor growth potential in mouse models of high-grade glioma. *Cancer Cell.* 2012; 21(1):11–24.
47. Miller TE, Liau BB, Wallace LC, et al. Transcription elongation factors represent in vivo cancer dependencies in glioblastoma. *Nature.* 2017; 547(7663):355–359.
48. Verhaak RG, Hoadley KA, Purdom E, et al.; Cancer Genome Atlas Research Network. Integrated genomic analysis identifies clinically relevant subtypes of glioblastoma characterized by abnormalities in PDGFRA, IDH1, EGFR, and NF1. *Cancer Cell.* 2010; 17(1):98–110.
49. Patel AP, Tirosh I, Trombetta JJ, et al. Single-cell RNA-seq highlights intratumoral heterogeneity in primary glioblastoma. *Science.* 2014; 344(6190):1396–1401.
50. Neftel C, Laffy J, Filbin MG, et al. An integrative model of cellular states, plasticity, and genetics for glioblastoma. *Cell.* 2019; 178(4):835–849. e21.
51. Castellan M, Guarnieri A, Fujimura A, et al. Single-cell analyses reveal YAP/TAZ as regulators of stemness and cell plasticity in glioblastoma. *Nat Cancer.* 2021; 2(2):174–188.
52. Wang L, Babikir H, Müller S, et al. The phenotypes of proliferating glioblastoma cells reside on a single axis of variation. *Cancer Discov.* 2019; 9(12):1708–1719.
53. Garofano L, Migliozzi S, Oh YT, et al. Pathway-based classification of glioblastoma uncovers a mitochondrial subtype with therapeutic vulnerabilities. *Nat Cancer.* 2021; 2(2):141–156.
54. Richards LM, Whitley OKNN, MacLeod G, et al. Gradient of developmental and injury response transcriptional states defines functional vulnerabilities underpinning glioblastoma heterogeneity. *Nat Cancer.* 2021; 2(2):157–173.
55. Bhaduri A, Di Lullo E, Jung D, et al. Outer radial glia-like cancer stem cells contribute to heterogeneity of glioblastoma. *Cell Stem Cell.* 2020; 26(1):48–63.e6.
56. Venteicher AS, Tirosh I, Hebert C, et al. Decoupling genetics, lineages, and microenvironment in IDH-mutant gliomas by single-cell RNA-seq. *Science.* 2017; 355(6332):eaai8478.
57. Tirosh I, Venteicher AS, Hebert C, et al. Single-cell RNA-seq supports a developmental hierarchy in human oligodendroglioma. *Nature.* 2016; 539(7628):309–313.
58. Filbin MG, Tirosh I, Hovestadt V, et al. Developmental and oncogenic programs in H3K27M gliomas dissected by single-cell RNA-seq. *Science.* 2018; 360(6386):331–335.
59. Johnson KC, Anderson KJ, Courtois ET, et al. Single-cell multimodal glioma analyses identify epigenetic regulators of cellular plasticity and environmental stress response. *Nat Genet.* 2021; 53(10):1456–1468.
60. Stieber D, Golebiewska A, Evers L, et al. Glioblastomas are composed of genetically divergent clones with distinct tumourigenic potential and variable stem cell-associated phenotypes. *Acta Neuropathol.* 2014; 127(2):203–219.
61. Sottoriva A, Spiteri I, Piccirillo SG, et al. Intratumor heterogeneity in human glioblastoma reflects cancer evolutionary dynamics. *Proc Natl Acad Sci U S A.* 2013; 110(10):4009–4014.
62. Verhaak RGW, Bafna V, Mischel PS. Extrachromosomal oncogene amplification in tumour pathogenesis and evolution. *Nat Rev Cancer.* 2019; 19(5):283–288.
63. Nathanson DA, Gini B, Mottahedeh J, et al. Targeted therapy resistance mediated by dynamic regulation of extrachromosomal mutant EGFR DNA. *Science.* 2014; 343(6166):72–76.
64. deCarvalho AC, Kim H, Poisson LM, et al. Discordant inheritance of chromosomal and extrachromosomal DNA elements contributes to dynamic disease evolution in glioblastoma. *Nat Genet.* 2018; 50(5):708–717.
65. Wang Z, Sun D, Chen YJ, et al. Cell lineage-based stratification for glioblastoma. *Cancer Cell.* 2020; 38(3):366–379.e8.
66. Chaligne R, Gaiti F, Silverbush D, et al. Epigenetic encoding, heritability and plasticity of glioma transcriptional cell states. *Nat Genet.* 2021; 53(10):1469–1479.
67. Wenger A, Ferreyra Vega S, Kling T, Bontell TO, Jakola AS, Carén H. Intratumor DNA methylation heterogeneity in glioblastoma: implications for DNA methylation-based classification. *Neuro Oncol.* 2019; 21(5):616–627.
68. Nabilsi NH, Deleyrolle LP, Darst RP, Riva A, Reynolds BA, Kladde MP. Multiplex mapping of chromatin accessibility and DNA methylation within targeted single molecules identifies epigenetic heterogeneity in neural stem cells and glioblastoma. *Genome Res.* 2014; 24(2):329–339.
69. Guilhamon P, Chesnelong C, Kushida MM, et al. Single-cell chromatin accessibility profiling of glioblastoma identifies an invasive cancer stem cell population associated with lower survival. *Elife.* 2021; 10:e64090.
70. Hall AW, Battenhouse AM, Shivram H, et al. Bivalent chromatin domains in glioblastoma reveal a subtype-specific signature of glioma stem cells. *Cancer Res.* 2018; 78(10):2463–2474.
71. Golebiewska A, Atkinson SP, Lako M, Armstrong L. Epigenetic landscaping during hESC differentiation to neural cells. *Stem Cells.* 2009; 27(6):1298–1308.
72. Rheinbay E, Suvà ML, Gillespie SM, et al. An aberrant transcription factor network essential for Wnt signaling and stem cell maintenance in glioblastoma. *Cell Rep.* 2013; 3(5):1567–1579.

73. Suvà ML, Rheinbay E, Gillespie SM, et al. Reconstructing and reprogramming the tumor-propagating potential of glioblastoma stem-like cells. *Cell*. 2014; 157(3):580–594.
74. Lopez-Bertoni H, Lal B, Li A, et al. DNMT-dependent suppression of microRNA regulates the induction of GBM tumor-propagating phenotype by Oct4 and Sox2. *Oncogene*. 2015; 34(30):3994–4004.
75. Acanda De La Rocha AM, López-Bertoni H, Guruceaga E, et al. Analysis of SOX2-regulated transcriptome in glioma stem cells. *PLoS One*. 2016; 11(9):e0163155.
76. Schwerdtfeger M, Desiderio V, Kobold S, Regad T, Zappavigna S, Caraglia M. Long non-coding RNAs in cancer stem cells. *Transl Oncol*. 2021; 14(8):101134.
77. Li Y, Li A, Glas M, et al. c-Met signaling induces a reprogramming network and supports the glioblastoma stem-like phenotype. *Proc Natl Acad Sci U S A*. 2011; 108(24):9951–9956.
78. Heddleston JM, Li Z, McLendon RE, Hjelmeland AB, Rich JN. The hypoxic microenvironment maintains glioblastoma stem cells and promotes reprogramming towards a cancer stem cell phenotype. *Cell Cycle*. 2009; 8(20):3274–3284.
79. Berezovsky AD, Poisson LM, Cherba D, et al. Sox2 promotes malignancy in glioblastoma by regulating plasticity and astrocytic differentiation. *Neoplasia*. 2014; 16(3):193–206, 206.e19.
80. Wu Y, Fletcher M, Gu Z, et al. Glioblastoma epigenome profiling identifies SOX10 as a master regulator of molecular tumour subtype. *Nat Commun*. 2020; 11(1):6434.
81. Park NI, Guilhamon P, Desai K, et al. ASCL1 reorganizes chromatin to direct neuronal fate and suppress tumorigenicity of glioblastoma stem cells. *Cell Stem Cell*. 2017; 21(3):411.
82. Darmanis S, Sloan SA, Croote D, et al. Single-cell RNA-Seq analysis of infiltrating neoplastic cells at the migrating front of human glioblastoma. *Cell Rep*. 2017; 21(5):1399–1410.
83. Bastola S, Pavlyukov MS, Yamashita D, et al. Glioma-initiating cells at tumor edge gain signals from tumor core cells to promote their malignancy. *Nat Commun*. 2020; 11(1):4660.
84. Joseph JV, Conroy S, Tomar T, et al. TGF-β is an inducer of ZEB1-dependent mesenchymal transdifferentiation in glioblastoma that is associated with tumor invasion. *Cell Death Dis*. 2014; 5:e1443.
85. Flavahan WA, Wu Q, Hitomi M, et al. Brain tumor initiating cells adapt to restricted nutrition through preferential glucose uptake. *Nat Neurosci*. 2013; 16(10):1373–1382.
86. Hjelmeland AB, Wu Q, Heddleston JM, et al. Acidic stress promotes a glioma stem cell phenotype. *Cell Death Differ*. 2011; 18(5):829–840.
87. Abdul Rahim SA, Dirkse A, Oudin A, et al. Regulation of hypoxia-induced autophagy in glioblastoma involves ATG9A. *Br J Cancer*. 2017; 117(6):813–825.
88. Jin X, Kim LJY, Wu Q, et al. Targeting glioma stem cells through combined BMI1 and EZH2 inhibition. *Nat Med*. 2017; 23(11):1352–1361.
89. Hara T, Chanoch-Myers R, Mathewson ND, et al. Interactions between cancer cells and immune cells drive transitions to mesenchymal-like states in glioblastoma. *Cancer Cell*. 2021; 39(6):779–792.e11.
90. Griguer CE, Oliva CR, Gobin E, et al. CD133 is a marker of bioenergetic stress in human glioma. *PLoS One*. 2008; 3(11):e3655.
91. Bar EE, Lin A, Mahairaki V, Matsui W, Eberhart CG. Hypoxia increases the expression of stem-cell markers and promotes clonogenicity in glioblastoma neurospheres. *Am J Pathol*. 2010; 177(3):1491–1502.
92. Jung J, Kim LJ, Wang X, et al. Nicotinamide metabolism regulates glioblastoma stem cell maintenance. *JCI Insight*. 2017; 2(10):e90019.
93. Wang X, Prager BC, Wu Q, et al. Reciprocal signaling between glioblastoma stem cells and differentiated tumor cells promotes malignant progression. *Cell Stem Cell*. 2018; 22(4):514–528.e5.
94. Yan K, Wu Q, Yan DH, et al. Glioma cancer stem cells secrete Gremlin1 to promote their maintenance within the tumor hierarchy. *Genes Dev*. 2014; 28(10):1085–1100.
95. Pavlyukov MS, Yu H, Bastola S, et al. Apoptotic cell-derived extracellular vesicles promote malignancy of glioblastoma via intercellular transfer of splicing factors. *Cancer Cell*. 2018; 34(1):119–135.e10.
96. Inda MM, Bonavia R, Mukasa A, et al. Tumor heterogeneity is an active process maintained by a mutant EGFR-induced cytokine circuit in glioblastoma. *Genes Dev*. 2010; 24(16):1731–1745.
97. Osswald M, Jung E, Sahm F, et al. Brain tumour cells interconnect to a functional and resistant network. *Nature*. 2015; 528(7580):93–98.
98. Weil S, Osswald M, Solecki G, et al. Tumor microtubes convey resistance to surgical lesions and chemotherapy in gliomas. *Neuro Oncol*. 2017; 19(10):1316–1326.
99. Xie R, Kessler T, Grosch J, et al. Tumor cell network integration in glioma represents a stemness feature. *Neuro Oncol*. 2021; 23(5):757–769.
100. Jung E, Osswald M, Ratliff M, et al. Tumor cell plasticity, heterogeneity, and resistance in crucial microenvironmental niches in glioma. *Nat Commun*. 2021;12(1):1014.
101. Venkatesh HS, Morishita W, Geraghty AC, et al. Electrical and synaptic integration of glioma into neural circuits. *Nature*. 2019; 573(7775):539–545.
102. Venkataramani V, Tanev DI, Strahle C, et al. Glutamatergic synaptic input to glioma cells drives brain tumour progression. *Nature*. 2019; 573(7775):532–538.
103. Quail DF, Joyce JA. The microenvironmental landscape of brain tumors. *Cancer Cell*. 2017; 31(3):326–341.
104. Pires-Afonso Y, Niclou SP, Michelucci A. Revealing and harnessing tumour-associated microglia/macrophage heterogeneity in glioblastoma. *Int J Mol Sci*. 2020; 21(3):689.
105. Klemm F, Maas RR, Bowman RL, et al. Interrogation of the microenvironmental landscape in brain tumors reveals disease-specific alterations of immune cells. *Cell*. 2020; 181(7):1643–1660.e17.
106. Bhat KPL, Balasubramaniyan V, Vaillant B, et al. Mesenchymal differentiation mediated by NF-κB promotes radiation resistance in glioblastoma. *Cancer Cell*. 2013; 24(3):331–346.
107. Sa JK, Chang N, Lee HW, et al. Transcriptional regulatory networks of tumor-associated macrophages that drive malignancy in mesenchymal glioblastoma. *Genome Biol*. 2020; 21(1):216.
108. Erasimus H, Gobin M, Niclou S, Van Dyck E. DNA repair mechanisms and their clinical impact in glioblastoma. *Mutat Res Rev Mutat Res*. 2016; 769:19–35.
109. Weller M, van den Bent M, Preusser M, et al. EANO guidelines on the diagnosis and treatment of diffuse gliomas of adulthood. *Nat Rev Clin Oncol*. 2021; 18(3):170–186.
110. Meyer M, Reimand J, Lan X, et al. Single cell-derived clonal analysis of human glioblastoma links functional and genomic heterogeneity. *Proc Natl Acad Sci U S A*. 2015; 112(3):851–856.
111. Reinartz R, Wang S, Kebir S, et al. Functional subclone profiling for prediction of treatment-induced intratumor population shifts and discovery of rational drug combinations in human glioblastoma. *Clin Cancer Res*. 2017; 23(2):562–574.
112. Aldape K, Amin SB, Ashley DM, et al. Glioma through the looking GLASS: molecular evolution of diffuse gliomas and the Glioma Longitudinal Analysis Consortium. *Neuro Oncol*. 2018; 20(7):873–884.
113. Barthel FP, Johnson KC, Varn FS, et al.; GLASS Consortium. Longitudinal molecular trajectories of diffuse glioma in adults. *Nature*. 2019; 576(7785):112–120.
114. Körber V, Yang J, Barah P, et al. Evolutionary trajectories of IDHWT glioblastomas reveal a common path of early tumorigenesis instigated years ahead of initial diagnosis. *Cancer Cell*. 2019; 35(4):692–704.e12.

115. Spiteri I, Caravagna G, Cresswell GD, et al. Evolutionary dynamics of residual disease in human glioblastoma. *Ann Oncol.* 2019; 30(3):456–463.
116. Kim J, Lee IH, Cho HJ, et al. Spatiotemporal evolution of the primary glioblastoma genome. *Cancer Cell.* 2015; 28(3):318–328.
117. de Souza CF, Sabedot TS, Malta TM, et al. A distinct DNA methylation shift in a subset of glioma CpG island methylator phenotypes during tumor recurrence. *Cell Rep.* 2018; 23(2):637–651.
118. Pombo Antunes AR, Scheyltjens I, Lodi F, et al. Single-cell profiling of myeloid cells in glioblastoma across species and disease stage reveals macrophage competition and specialization. *Nat Neurosci.* 2021; 24(4):595–610.
119. Akkari L, Bowman RL, Tessier J, et al. Dynamic changes in glioma macrophage populations after radiotherapy reveal CSF-1R inhibition as a strategy to overcome resistance. *Sci Transl Med.* 2020; 12(552):eaaw7843.
120. Shen S, Vagner S, Robert C. Persistent cancer cells: the deadly survivors. *Cell.* 2020; 183(4):860–874.
121. Oren Y, Tsabar M, Cuoco MS, et al. Cycling cancer persister cells arise from lineages with distinct programs. *Nature.* 2021; 596(7873):576–582.
122. Risom T, Langer EM, Chapman MP, et al. Differentiation-state plasticity is a targetable resistance mechanism in basal-like breast cancer. *Nat Commun.* 2018; 9(1):3815.
123. Stewart CA, Gay CM, Xi Y, et al. Single-cell analyses reveal increased intratumoral heterogeneity after the onset of therapy resistance in small-cell lung cancer. *Nat Cancer.* 2020; 1:423–436.
124. Rambow F, Rogiers A, Marin-Bejar O, et al. Toward minimal residual disease-directed therapy in melanoma. *Cell.* 2018; 174(4):843–855.e19.
125. Liu G, Yuan X, Zeng Z, et al. Analysis of gene expression and chemoresistance of CD133+ cancer stem cells in glioblastoma. *Mol Cancer.* 2006; 5:67.
126. Bleau AM, Hambardzumyan D, Ozawa T, et al. PTEN/PI3K/Akt pathway regulates the side population phenotype and ABCG2 activity in glioma tumor stem-like cells. *Cell Stem Cell.* 2009; 4(3):226–235.
127. Broadley KW, Hunn MK, Farrand KJ, et al. Side population is not necessary or sufficient for a cancer stem cell phenotype in glioblastoma multiforme. *Stem Cells.* 2011; 29(3):452–461.
128. Golebiewska A, Brons NH, Bjerkvig R, Niclou SP. Critical appraisal of the side population assay in stem cell and cancer stem cell research. *Cell Stem Cell.* 2011; 8(2):136–147.
129. Segerman A, Niklasson M, Haglund C, et al. Clonal variation in drug and radiation response among glioma-initiating cells is linked to proneural-mesenchymal transition. *Cell Rep.* 2016; 17(11):2994–3009.
130. Fouse SD, Nakamura JL, James CD, Chang S, Costello JF. Response of primary glioblastoma cells to therapy is patient specific and independent of cancer stem cell phenotype. *Neuro Oncol.* 2014; 16(3):361–371.
131. Beier D, Schulz JB, Beier CP. Chemoresistance of glioblastoma cancer stem cells–much more complex than expected. *Mol Cancer.* 2011; 10:128.
132. Berg TJ, Marques C, Pantazopoulou V, et al. The irradiated brain microenvironment supports glioma stemness and survival via astrocyte-derived transglutaminase 2. *Cancer Res.* 2021; 81(8):2101–2115.
133. Fritah S, Muller A, Jiang W, et al. Temozolomide-induced RNA interactome uncovers novel lncRNA regulatory loops in glioblastoma. *Cancers.* 2020; 12(9):2583.
134. Dahan P, Martinez Gala J, Delmas C, et al. Ionizing radiations sustain glioblastoma cell dedifferentiation to a stem-like phenotype through survivin: possible involvement in radioresistance. *Cell Death Dis.* 2014; 5:e1543.
135. Wang J, Wakeman TP, Lathia JD, et al. Notch promotes radioresistance of glioma stem cells. *Stem Cells.* 2010; 28(1):17–28.
136. Minata M, Audia A, Shi J, et al. Phenotypic plasticity of invasive edge glioma stem-like cells in response to ionizing radiation. *Cell Rep.* 2019; 26(7):1893–1905.e7.
137. Fack F, Espedal H, Keunen O, et al. Bevacizumab treatment induces metabolic adaptation toward anaerobic metabolism in glioblastomas. *Acta Neuropathol.* 2015; 129(1):115–131.
138. Chandra A, Jahangiri A, Chen W, et al. Clonal ZEB1-driven mesenchymal transition promotes targetable oncologic antiangiogenic therapy resistance. *Cancer Res.* 2020; 80(7):1498–1511.
139. Saraon P, Pathmanathan S, Snider J, Lyakisheva A, Wong V, Stagljar I. Receptor tyrosine kinases and cancer: oncogenic mechanisms and therapeutic approaches. *Oncogene.* 2021; 40(24):4079–4093.
140. Liau BB, Sievers C, Donohue LK, et al. Adaptive chromatin remodeling drives glioblastoma stem cell plasticity and drug tolerance. *Cell Stem Cell.* 2017; 20(2):233–246.e7.
141. Eyler CE, Matsunaga H, Hovestadt V, Vantine SJ, van Galen P, Bernstein BE. Single-cell lineage analysis reveals genetic and epigenetic interplay in glioblastoma drug resistance. *Genome Biol.* 2020; 21(1):174.
142. Wei W, Shin YS, Xue M, et al. Single-cell phosphoproteomics resolves adaptive signaling dynamics and informs targeted combination therapy in glioblastoma. *Cancer Cell.* 2016; 29(4):563–573.
143. Vora P, Venugopal C, Salim SK, et al. The rational development of CD133-targeting immunotherapies for glioblastoma. *Cell Stem Cell.* 2020; 26(6):832–844.e6.
144. Ye C, Ho DJ, Neri M, et al. DRUG-seq for miniaturized high-throughput transcriptome profiling in drug discovery. *Nat Commun.* 2018; 9(1):4307.
145. Jacob F, Salinas RD, Zhang DY, et al. A patient-derived glioblastoma organoid model and biobank recapitulates inter- and intra-tumoral heterogeneity. *Cell.* 2020; 180(1):188–204.e22.
146. Klein E, Hau AC, Oudin A, Golebiewska A, Niclou SP. Glioblastoma organoids: pre-clinical applications and challenges in the context of immunotherapy. *Front Oncol.* 2020; 10:604121.
147. Oudin A, Baus V, Barthelemy V, et al. Protocol for derivation of organoids and patient-derived orthotopic xenografts from glioma patient tumors. *STAR Protoc.* 2021; 2(2):100534.
148. Woo XY, Giordano J, Srivastava A, et al.; PDXNET Consortium; EurOPDX Consortium. Conservation of copy number profiles during engraftment and passaging of patient-derived cancer xenografts. *Nat Genet.* 2021; 53(1):86–99.
149. Vaubel RA, Tian S, Remonde D, et al. Genomic and phenotypic characterization of a broad panel of patient-derived xenografts reflects the diversity of glioblastoma. *Clin Cancer Res.* 2020; 26(5):1094–1104.
150. Aibar S, González-Blas CB, Moerman T, et al. SCENIC: single-cell regulatory network inference and clustering. *Nat Methods.* 2017; 14(11):1083–1086.
151. Shen S, Faouzi S, Bastide A, et al. An epitranscriptomic mechanism underlies selective mRNA translation remodelling in melanoma persister cells. *Nat Commun.* 2019; 10(1):5713.
152. Chaffer CL, Marjanovic ND, Lee T, et al. Poised chromatin at the ZEB1 promoter enables breast cancer cell plasticity and enhances tumorigenicity. *Cell.* 2013; 154(1):61–74.
153. Serresi M, Kertalli S, Li L, et al. Functional antagonism of chromatin modulators regulates epithelial-mesenchymal transition. *Sci Adv.* 2021; 7(9):eabd7974.
154. Marusyk A, Janiszewska M, Polyak K. Intratumor heterogeneity: the rosetta stone of therapy resistance. *Cancer Cell.* 2020; 37(4):471–484.
155. West J, You L, Zhang J, et al. Towards multidrug adaptive therapy. *Cancer Res.* 2020; 80(7):1578–1589.

Chapter 4

Protocol for Derivation of Organoids and Patient-Derived Orthotopic Xenografts from Glioma Patient Tumors

Oudin A, Baus V, Barthelemy V, Fabian C, Klein E, Dieterle M, Wantz M, Hau AC, Dording C, Bernard A, Michelucci A, **Yabo YA,** Kanli G, Keunen O, Bjerkvig R, Niclou SP, & Golebiewska A.

STAR protocols, 2021;2(2), 100534
doi.org/10.1016/j.xpro.2021.100534

4.1 The rationale of the study

This protocol paper provides a step-by-step guide for the derivation of organoids and glioma PDOX models established in the NORLUX Neuro-Oncology laboratory from glioma patient tumor samples. Following STAR Protocols guidelines, this manuscript presents key technical steps including critical points, time frames, and common troubleshooting needed for the derivation of organoids and PDOX models from tumor tissue obtained from glioma patients. This paper is an important resource to the community that will guide researchers to independently establish glioma organoids and PDOXs. It also guides on monitoring of tumor growth in PDOX models and the use of organoids and PDOXs for functional assays and preclinical drug testing.

Personal contributions

This work represents an important part of my PhD thesis as my project relied on the efficient derivation of PDOX models and subsequent characterization of human tumor compartment and mouse TME. I was actively involved in the optimization of the existing protocol for PDOX tissue processing described in the manuscript. Specifically, I optimized the purification of single cells suspension for single-cell transcriptomics and functional assays. To obtain pure cell suspension I combined two protocols based on magnetic cell sorting:

- myelin removal to separate single cells after enzymatic dissociation.
- mouse cell depletion to separate human tumor cells from the mouse TME.

The analysis of cell viability after the separation regularly showed >80% viable cells, thus further purification was not required. I further optimized the protocol for cell cryopreservation that allowed for the multiplexing of samples for scRNA-seq. I actively participated in the writing and editing of the manuscript and in designing **Figure 4** in the paper that illustrates the PDOX tissue processing steps. This protocol allowed me to perform successful sc-RNAseq experiments for assessing the transcriptomic diversity of tumor cells and the TME compartment in PDOX models (**Chapters 5-6, Annex I**).

4.1.1 Result

STAR Protocols

CellPress
OPEN ACCESS

Protocol

Protocol for derivation of organoids and patient-derived orthotopic xenografts from glioma patient tumors

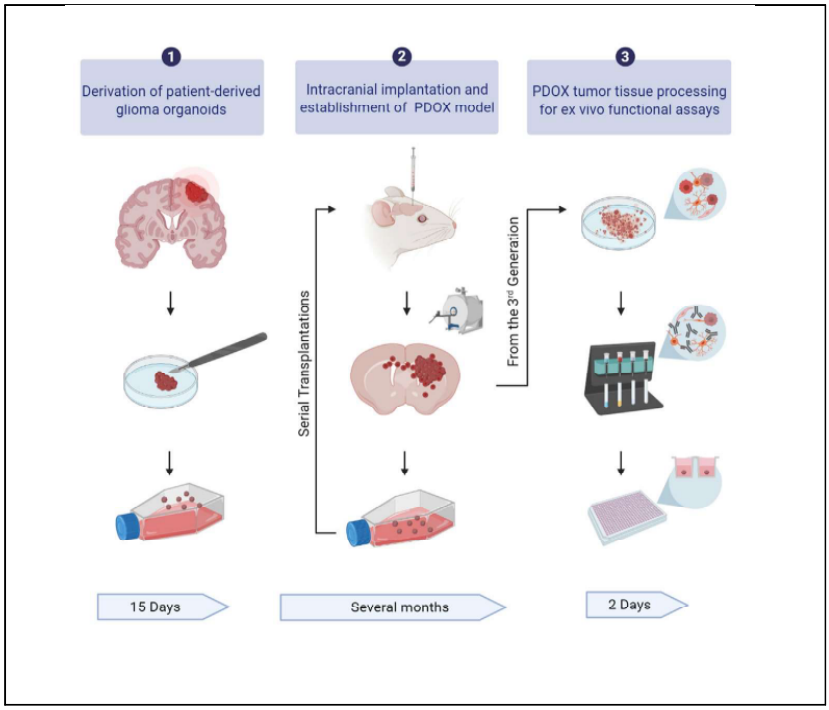

Tumor organoids and patient-derived orthotopic xenografts (PDOXs) are some of the most valuable pre-clinical tools in cancer research. In this protocol, we describe efficient derivation of organoids and PDOX models from glioma patient tumors. We provide detailed steps for organoid culture, intracranial implantation, and detection of tumors in the brain. We further present technical adjustments for standardized functional assays and drug testing.

Anaïs Oudin, Virginie Baus, Vanessa Barthelemy, ..., Rolf Bjerkvig, Simone P. Niclou, Anna Golebiewska

anais.oudin@lih.lu (A.O.)
anna.golebiewska@lih.lu (A.G.)

Highlights

Organoids can be generated from diverse glioma patient tumors

High-grade glioma organoids give rise to patient-derived orthotopic xenografts

Serial transplantation in vivo allows for consistent expansion of human tumor cells

The adapted protocol for reconstitution of uniform organoids for functional assays

Oudin et al., STAR Protocols 2, 100534
June 18, 2021 © 2021 The Author(s).
https://doi.org/10.1016/j.xpro.2021.100534

CellPress
OPEN ACCESS

Protocol

Protocol for derivation of organoids and patient-derived orthotopic xenografts from glioma patient tumors

Anaïs Oudin,[1,7,*] Virginie Baus,[1] Vanessa Barthelemy,[1] Carina Fabian,[1,2] Eliane Klein,[1] Monika Dieterle,[1] May Wantz,[1] Ann-Christin Hau,[1] Claire Dording,[1] Amandine Bernard,[1,3] Alessandro Michelucci,[1,3] Yahaya A. Yabo,[1,4] Georgia Kanli,[1,5,6] Olivier Keunen,[1,5,6] Rolf Bjerkvig,[1,2] Simone P. Niclou,[1,2] and Anna Golebiewska[1,8,*]

[1]NORLUX Neuro-Oncology Laboratory, Department of Oncology, Luxembourg Institute of Health, 1526 Luxembourg, Luxembourg

[2]Department of Biomedicine, University of Bergen, 5019 Bergen, Norway

[3]Neuro-Immunology Group, Department of Oncology, Luxembourg Institute of Health, 1526 Luxembourg, Luxembourg

[4]Faculty of Science, Technology and Medicine, University of Luxembourg, 4367 Belvaux, Luxembourg

[5]Quantitative Biology Unit, Luxembourg Institute of Health, 1445 Strassen, Luxembourg

[6]Translational Radiomics, Department of Oncology, Luxembourg Institute of Health, 1526 Luxembourg, Luxembourg

[7]Technical contact

[8]Lead contact

*Correspondence: anais.oudin@lih.lu (A.O.), anna.golebiewska@lih.lu (A.G.)
https://doi.org/10.1016/j.xpro.2021.100534

SUMMARY

Tumor organoids and patient-derived orthotopic xenografts (PDOXs) are some of the most valuable pre-clinical tools in cancer research. In this protocol, we describe efficient derivation of organoids and PDOX models from glioma patient tumors. We provide detailed steps for organoid culture, intracranial implantation, and detection of tumors in the brain. We further present technical adjustments for standardized functional assays and drug testing.

For complete details on the use and execution of this protocol, please refer to Golebiewska et al. (2020).

BEFORE YOU BEGIN

This protocol requires viable tumor tissue material obtained during surgery of glioma patients. Ethical approvals are required prior the collection and patients must give informed consent. Glioma patient tumors used in this protocol were collected at the National Department of Neurosurgery at the Centre Hospitalier de Luxembourg (CHL) after informed consent of the patients, and with the approval from the local research ethics committee (National Committee for Ethics in Research (CNER), Luxembourg; protocol REC-LRNO-20110708). All mouse experiments must be approved by the internal animal welfare structures and the national authorities responsible for animal experiments. Animal experiments described in this protocol were approved following the European Directive 2010/63/EU, under the references: LRNO-2014-01, LUPA2019/93 and LRNO-2016-01. Established PDOX models generated in this study are available at PDX Finder portal (www.pdxfinder.org).

Agar flasks for organoid culture

Timing: 1 h

1. Preheat 150 mL DMEM medium w/o supplements to 42°C.

CellPress OPEN ACCESS

STAR Protocols
Protocol

2. Weigh 1.8 g of Noble Agar and transfer to a sterile glass bottle.
3. Add 60 mL of sterile water and boil in microwave to dissolve, the agar should appear transparent.
4. Cool down to 42°C in the water bath. It is not necessary to autoclave the agar as boiling in the microwave sterilizes the solution. We advise to use a dedicated microwave within the tissue culture facility.
5. Work under the biological safety cabinet II (BSC II). Mix gently with preheated 150 mL of DMEM medium (w/o supplements) to achieve a final Agar concentration 0.85% (w/v).
6. Transfer liquid agar in a sterile culture flask with vent/close cap (15–16 mL per T75, 5–6 mL per T25) and leave to solidify under the BSC II w/o the cap.
7. Store flasks at 4°C with closed caps.

⚠ CRITICAL: Agar solidifies rapidly at temperatures below 42°C, thus it is important to apply DMEM pre-warmed at 42°C. Store agar Flask at 4°C for up to one month.

KEY RESOURCES TABLE

REAGENT or RESOURCE	SOURCE	IDENTIFIER
Chemicals, buffers, and reagents		
BD Difco™ Dehydrated Culture Media: Noble Agar	Fisher Scientific	11798223
Bone wax surgical specialties 2.5 g	Surgical Specialties Corporation	901
Bovine Serum Albumin	Sigma-Aldrich	A9418
BRAUNOL 7.5/100 G 1 FL HDPE 1000	Braun	3864154
Bupivacaine hydrochloride (Marcain 0.25%)	Aspen	N/A
DMEM High Glucose without L-Glutamine	Westburg	12-614F
DMSO, Dimethyl sulfoxide	Sigma	D4540-100ML
Fetal Bovine Serum, qualified, heat inactivated, Brazil	Gibco	10500064
Gadoterate, Dotarem, 0.5 mmol/mL	Guerbet	N/A
Hanks' Balanced Salt solution (HBSS) w/o Ca2+/Mg2+	Sigma	HBSS-H6648
Isoflurane	CP Pharma	G228L19A
Ketamine (Nimatek), 100 mg/mL	Dechra	N/A
Mouse Cell Depletion Kit	Miltenyi Biotec	130-104-694
Myeline Removal Beads II	Miltenyi Biotec	130-096-433
NaCl 0.9% (20 × 10 mL)	BRAUN	235 0748
Neural Tissue Dissociation Kit	Miltenyi Biotec	130-092-628
Non-essential amino acids 10 mM 1000× stock	Westburg	LO BE13-114E
Ocry-gel Ogen Honden/Katten Tube 10 g	TVM	48026T613/3
Penicillin-Streptomycin (Pen-Strep)	Westburg	DE17-602E
Sodium pyruvate solution 100mM	Sigma-Aldrich	S8636-100mL
Buprenorphine (Vetergesic Multidose) 0.3 mg/mL	Ecuphar	N/A
UltraGlutamine I (Alanyl-L-Glutamine) 200 mM (1000×)	Westburg	LO BE17-605E/U1
Xylasine (Rompun) 2%	Bayer	N/A
Experimental models: organisms/strains		
Mouse: NOD.Cg-Prkdc^{scid} Il2rg^{tm1Wjl}/SzJ (NSG)	Charles River	N/A
Software and algorithms		
ImageJ		N/A
PC-SAM	SA Instruments Inc.	N/A
Preclinical Scan	MR Solutions	N/A
Others		
10 mL Serological pipettes	Greiner	607180
15 mL CELLSTAR® Polypropylene Tube	Greiner	188271
25 mL Serological pipettes	Greiner	760180
50 mL CELLSTAR® Polypropylene tubes	Greiner	227261

(Continued on next page)

STAR Protocols
Protocol

CellPress
OPEN ACCESS

Continued

REAGENT or RESOURCE	SOURCE	IDENTIFIER
50 mL Serological pipettes	Greiner	768180
5 mL Serological pipettes	Greiner	606180
Aspiration pipettes	Carl Roth	NA41.2
Barrier OP Towel (50 cm × 50cm)	Barrier	706400
Bone Micro Probe	FST	10030-13
Burrs for Micro Drill	FST	19008-07
Cell culture Flask, 50 mL, 25 cm^2, PS, Red standard screw cap, Clear, CELLSTAR® TC, Sterile	Greiner	690160
Cell culture Flask, 250 mL, 75 cm^2, PS, Red standard screw cap, Clear, CELLSTAR® TC, Sterile	Greiner	658170
Cell culture Flask, 50 mL, 25 cm^2, PS, Red filter screw cap, Clear, CELLSTAR® TC, Sterile	Greiner	690175
Cell culture Flask, 50 mL, 75 cm^2, PS, Red filter screw cap, Clear, CELLSTAR® TC, Sterile	Greiner	658175
CellTrics™ 50 µm Sterile	Sysmex	04-004-2327
Disposable pasteur pipette, with cotton plug	VWR	612-1799
Dissecting Chisel	FST	10095-12
Ethilon polyamide 6 (3.0) 19 mm 75 cm 3/8C	Ethicon	EH7665
Extra Fine Bonn Scissors	FST	14085-08
Fine Scissors - Sharp	FST	14060-09
Graefe Forceps	FST	11051-10
Halsey Micro Needle Holder	FST	12500-12
High glass petri dish, 2 mm high, 100 mm diameter	VWR	391-2840
High Speed Rotary Micromotor Kit	Foredom	K.1070
LS column	Miltenyi Biotec	130-042-401
MediHeat warming cabinet (Customized)	PECOSERVICE	N/A
Mouse Ear Bar for SR Series	NARISHIGE	EB-3B
Mouse Homeothermic Blanket with YS451 Rectal Probe	Harvard Apparatus	HB101SM451
MRI 3 Tesla	MR Solutions	N/A
NovaFlex	World Precision Instruments	F0-150
PrimeSurface 384 well	FUJIFILM Wako Chemicals Europe GmbH	628-01449
QuadroMACS™ Separator	Miltenyi Biotec	130-091-051
Scalpel Handle - #3	FST	10003-12
Semken Forceps	FST	11009-13
Stereotaxic instrument	NARISHIGE	SR-5R
Stereotaxic microinjector	NARISHIGE	ISM-3
Stereotaxic micromanipulator	NARISHIGE	SM-15
Sterile Scalpel Cutfix®, 24	Carl Roth	X006.1
STERIPLAN Petri dish 100 mm	Fisher Scientific	11750844
Surgical blades carbon steel	Swann-Morton	203
Surgical patties	Codman	80-1402
Syringe 5 µL, Model 75 RN SYR, Small Removable NDL, 32 ga, 2 in	Hamilton	7105KH
Temperature control unit	Harvard Apparatus	HB101
Thermo Scientific™ Nalgene™ System 100™ Cryogenic Vials 1.5 mL	Thermo Fisher Scientific	5000-1020

CellPress OPEN ACCESS

STAR Protocols
Protocol

MATERIALS AND EQUIPMENT

Organoid medium		
Reagent	Final concentration	Amount
DMEM 4.5 g/L glucose w/o L-Glu		420 mL
Fetal Bovine Serum	10% (v/v)	50 mL
Pen-Strep	100 U/mL	5 mL
UltraGlutamine I	2 mM	5 mL
NEAA	100 μM	20 mL
Total	n/a	500 mL
Store at 4°C for two months maximum.		

Freezing medium		
Reagent	Final concentration	Amount
DMEM 4.5 g/L glucose w/o L-Glu	70% (v/v)	70 mL
Fetal Bovine Serum	20% (v/v)	20 mL
DMSO	10% (v/v)	10 mL
Total	n/a	100 mL
Aliquot and store at −20°C for six months maximum.		

MACS buffer		
Reagent	Final concentration	Amount
HBSS or PBS w/o Ca^{2+}/Mg^{2+}		95 mL
10% (w/v) BSA in HBSS	1. (v/v)	5 mL
Total	n/a	100 mL
Prepare fresh for each experiment. Store at 4°C until use.		

STEP-BY-STEP METHOD DETAILS

Derivation of organoids from glioma patient tumors

Timing: 15 days

This part describes the detailed step-by-step derivation of tumor organoids from viable tumor tissue obtained during patient surgery. This includes the processing of the tumor tissue after reception from the hospital, organoid culture and biobanking. The processes described below must be performed under Biosafety level 2 (BSL2) and sterile conditions.

Note: Prior to tissue manipulation, pre-warm organoid medium to 37°C in the water bath. Prepare sterile BSC II with required material and transfer agar flasks to BSC II prior tumor tissue collection.

Tumor tissue processing

Timing: 1 h

1. The resected viable tumor tissue (from male and female) remaining after neuropathology sample is collected is placed in 10 mL ice-cold DMEM in the operating theater and stored at 4°C in the

STAR Protocols
Protocol

CellPress
OPEN ACCESS

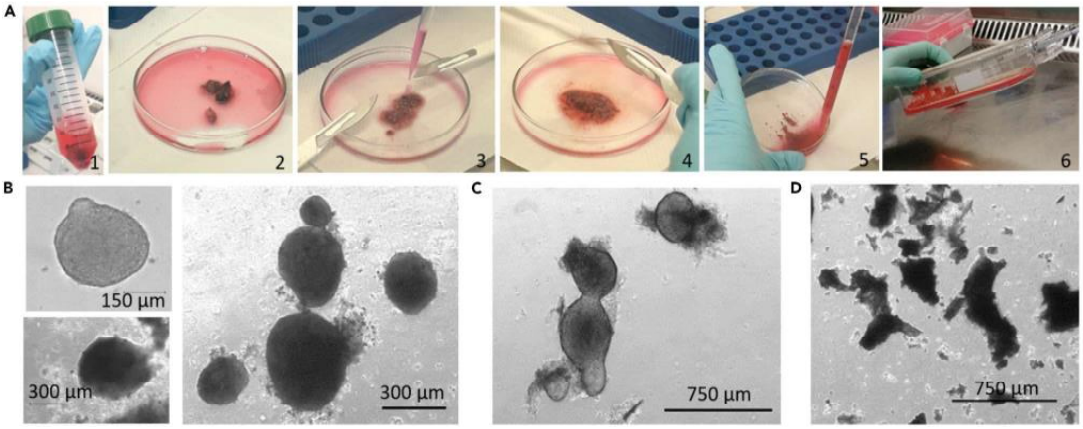

Figure 1. Derivation of organoids from tumor tissue

(A) Tumor tissue processing: (1) Tumor reception in DMEM, (2) Tissue transfer to a glass petri dish before cutting, (3–4) Mechanical mincing with scalpels, (5–6) Transfer of tissue fragments to culture flasks coated with agar.

(B) Examples of good quality organoids derived from brain tumor tissue.

(C) Examples of fused organoids after prolonged culture.

(D) Brain tumor tissue fragments that did not form organoids.

hospital until collection. Short time between surgery and collection is advised (Figure 1A). We regularly collect the tumor tissue within 30 min after end of the surgery.

2. Transfer tumor tissue to a glass petri dish under BSC II sterile conditions. Remove excess medium.

Note: We find most comfortable to cut tissue in glass petri dishes of 100 mm in diameter with 2 mm high glass borders. Cutting in plastic petri dishes leads to production of small plastic pieces floating in the culture. If 5-Aminolevulinic Acid (5-ALA) is used during surgery, we recommend working in the dark to limit a potential fluorescence-associated toxicity.

3. Add 0.5 - 1 mL of fresh organoid medium to ensure sufficient moisture of the tissue during processing.
4. If desired cut small tissue fragments and snap freeze for downstream molecular analysis.
5. Mince tumor tissue for approximately 10 - 20 min at 20°C–22°C with sterile scalpels until obtaining small tumor fragments invisible by eye (approximately 0.5 mm × 0.5 mm). Add more medium if needed. See troubleshooting 1 for problems during mincing.

Note: Visible bone fragments, fixed tissue or blood clots should be removed prior mincing. Certain tumor types can be difficult to cut and longer time may be required for larger samples.

6. Transfer tissue fragments into a 50 mL falcon tube. Rinse the petri dish with organoid medium to collect all fragments.
7. Allow tissue fragments to sediment at 20°C–22°C for approximately 5 min at the bottom of the falcon tube. Do not centrifuge!
8. Aspirate the medium and resuspend tissue fragments in fresh organoid medium. Transfer cultures to agar flasks. Volume needs to be adjusted to reach high culture density. On average 1–2 T75 flasks are sufficient (15–20 mL per flask). More than one flask may be needed for larger tumors. For smaller tumor tissue use one T25 flask (4–5 mL per flask).
9. Incubate the culture flasks in a standard cell culture incubator at 37°C with 5% CO_2 and 21% O_2. Keep the vent/close cap open or replace with a filter cap.

CellPress OPEN ACCESS

STAR Protocols
Protocol

10. Discard remaining material according to internal rules for the BSL2 waste.
11. After 1 - 2 days, verify cultures under the microscope for contamination and tissue fragments size. If tissue fragments appear too large see troubleshooting 2.
12. A high amount of blood in the tissue may also cause a change in pH. Proceed with medium change after 1 day in culture if pH change is observed. We do not recommend performing red blood cell lysis as we have noticed that glioma cells are particularly sensitive to the classical erythrocyte lysis buffers based on ammonium chloride.

Organoid culture

Timing: 7–14 days

13. Organoid cultures should be monitored on a regular basis. Change medium after 5 - 7 days of culture. If cultures appear too dense (e.g., change in pH indicated by yellow Phenol red) or high number of debris is observed proceed with medium change earlier.
14. Gently collect the tissue fragments and organoids in a 50 mL falcon tube.
15. Sediment organoids for approximately 5 min. Do not centrifuge.
16. Aspirate medium and resuspend organoids in an appropriate volume of pre-warmed organoid medium. Transfer cultures to fresh agar flasks. Culture for 10–14 days before freezing.

Note: If well-structured organoids are already formed after one week of culture (Figure 1B), freeze cultures following protocol described below. If organoids start to fuse, proceed with freezing (Figure 1C). Fused organoids can be re-minced with scalpels prior cryopreservation.

⚠ CRITICAL: Quality and quantity of organoids rely on size and quality of tumor tissue obtained. This step allows preselecting tissue with high tumor content, organoid derivation is limited from necrotic areas and normal brain with low tumor content. See troubleshooting 3 for organoid cultures with high amount of debris.

Organoid biobanking

Timing: 1 h

Organoids should be used directly for implantation or frozen after maximum 10 - 14 days in culture. Organoids will start to fuse after prolonged culture.

Freezing protocol

17. Gently collect the organoids in a 50 mL falcon tube. In case of cultures containing high amount of debris and dead tissue pieces (Figure 1D), collect good quality organoids under a binocular microscope. If possible, place the binocular under the BSCII and collect manually the healthy organoids.
18. Sediment organoids at the bottom of the falcon tube for approximately 5 min. Do not centrifuge.
19. Aspirate medium and resuspend organoids in an appropriate volume of ice-cold freezing medium.
20. Transfer 1 mL of organoids into cryogenic vials. Aim to freeze 35–40 organoids per 1 mL freezing medium in one cryogenic vial.
21. Place cryogenic vials in a Mr. Frosty freezing container (or equivalent) and transfer to −80°C for 12 - 24 h.
22. After 12–24 h, transfer cryogenic vials to a liquid nitrogen tank for long-term storage.

Note: The organoids derived from patient material correspond to the generation 0 (G0). Organoids obtained at later stages upon serial transplantation of PDOXs must be denoted with appropriate generation number (generation of organoids = generation of PDOX they were derived from).

Defrosting protocol

23. To defrost organoids for implantation or functional assays, thaw cryogenic vials with organoids rapidly at 37°C.
24. Gently transfer the defrosted solution with organoids to 15 mL tube. Add slowly drops of pre-warmed organoid medium up to 3 mL (1 mL per minute).
25. Shake gently up and down and incubate 5 min.
26. Add organoid medium up to 10 mL.
27. Sediment organoids for approximately 5 min, aspirate the medium containing DMSO.
28. Resuspend organoids in fresh organoid medium, transfer to agar flask and culture at 37°C in the incubator for 24 h to 72 h before surgery/experiment. For IDH mutated models showing compromised survival of organoids during cryopreservation see Troubleshooting 4.

Note: Organoid culture can be obtained from brain tumors of different types and grades, including gliomas, meningiomas and brain metastases. We have successfully obtained high quality organoids from 79% of GBMs and 68% of grade II-III gliomas. The growth of organoids depends on patient tumor and is generally limited after 7 days in culture. Viable organoids with a diameter between 400 μm and 1000 μm are selected for intracerebral implantation in mice. Our cultures can be adapted to the serum-free media supplemented with the growth factors (Christensen et al., 2010). However, we have not compared systematically organoids cultured in the two different media and we have not used organoids cultured in serum-free conditions for the implantation. For more discussion on organoid media composition see (Klein et al., 2020).

Establishment of patient-derived orthotopic xenografts (PDOXs)

Timing: up to 16 months

This part describes implantation of tumor organoids and mouse monitoring during development of PDOX models.

Cerebral implantation of organoids

Timing: 3 h

Intracortical implantation of organoids in immunodeficient mice is performed to induce tumor growth *in vivo* and to establish PDOX models. Animals must be housed in individually ventilated cages in a Specific Pathogen Free (SPF) facility, under controlled environment (temperature 22 ± 2°C, humidity between 45% and 65% and 12 h light / 12 h dark cycle) with free access to autoclaved and acidified water and irradiated food *ad libitum*.

Preparation of glioma organoids for implantation

29. Collect viable organoids of 400 - 1000 μm under binocular microscope or equivalent.

⚠ CRITICAL: This step requires gentle handling to avoid mechanical breaking of organoids.

30. Gently transfer selected organoids to a 50 mL falcon tube using 2 mL to 10 mL pipette.

31. Sediment organoids at the bottom of the falcon tube for approximately 5 min.
32. Aspirate the medium and wash organoids in 10 mL of DMEM w/o supplements. Repeat 2 times.
33. Resuspend organoids in 15 mL of DMEM and incubate on ice until surgery.

Optional: Cryopreserved organoids can be used for implantation. Defrost organoids as described above and culture in organoid medium for 24 - 72 h before surgery.

Intracortical implantation

Note: We routinely use NSG mice (NOD.Cg-Prkdc^{scid} Il2rg^{tm1Wjl}/SzJ, males and females, between 8 and 16 weeks) for PDOXs development due to their strong immunodeficiency and long survival. In initial experiments, we used NOD SCID mice (NOD.CB17-Prkdc^{scid}/NCrCrl, male and female) or eGFP^{+} NOD SCID (Niclou et al., 2008). However, the NOD SCID strain have high incidence of thymic lymphoma, which limits mice survival and experimental time frame. Nude mice can also be used for implantation of organoids obtained from well-established PDOX models for large-scale experiments. In general, we do not observe tumor growth differences between these strains.

34. Inject buprenorphine subcutaneously (volume of injection 10 mL/kg, dose 0.1 mg/kg) to NSG mice to ensure analgesia for 4 - 6 h time period.
35. Pre-warm the recovery chamber and the cover to 37°C.
36. Prepare the sterile field with all surgical instruments and reagents needed (Figure 2A).
37. Anesthetize the mouse with an intra-peritoneal injection (volume of injection 10 mL/kg) of a mixture of Ketamine (dose 100 mg/kg) and Xylazine (dose 10 mg/kg).

Note: If available, gaseous anesthesia by isoflurane decreases probability of mouse death due to adverse respiratory effect of Ketamine and Xylazine.

38. Shave and disinfect the skin using a sterile surgical pad and 70% ethanol.
39. Protect eyes of the mouse with a drop of Ocry-gel.
40. Place the head in a stereotaxic frame (Figure 2B).
41. Inject subcutaneously a local anesthetic (Bupivacaine (0.25% Marcain with Adrenalin), volume of injection 2 mL/kg; dose 5 mg/kg) on top of the skull.
42. Disinfect the Hamilton syringe with several flushing of Ethanol followed by 0.9% NaCl.
43. Fill the Hamilton syringe with organoids. Transfer organoids to the petri dish and manually aspirate 6 organoids in maximum volume of 2 µl. For problems during aspiration procedure, see Troubleshooting 5.
44. Fix the syringe in the syringe holder of the stereotactic frame.
45. Perform a short incision (~ 0.7 cm) and open the skin in order to expose the bregma, the sagittal and coronal sutures (Figure 2C).
46. Keep the needle at an angle of 90° to the skull and place it directly on the bregma to set the 0 position for the X and Y axis on the frame's ruler (Figure 2C).
47. Place the needle on the surface of the brain to set the 0 position for Z axis.
48. Using the stereotaxic ruler, move the needle to the X (2 mm right) and Y (1 mm front) coordinates to locate the drill site (Figure 2D). See Troubleshooting 6 for possible injection to the lateral ventricle.
49. Drill a small hole of 0.7 mm diameter.
50. Using the micro-scalpel, remove the remaining piece of bone and perform cross incision of the dura mater.
51. Place the needle on the surface of the brain to set the 0 position for Z axis on the frame's ruler and slowly lower the needle 0.5 mm deeper than the Z depth (2 mm).
52. Wait for 2 min, slightly retract (0.5 mm) the needle and inject slowly the organoids (1 min for 1 µl) (Figure 2E).

STAR Protocols
Protocol

CellPress
OPEN ACCESS

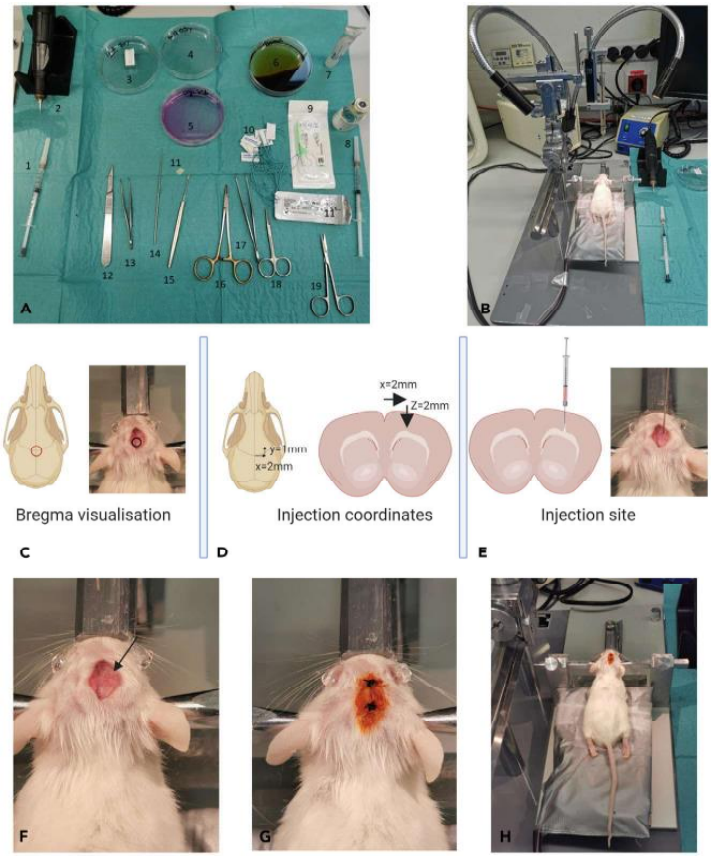

Figure 2. Intracranial operation procedure

(A) Sterile field with all materials. 1: Syringe with anesthetic mix, 2: Drill, 3: Ethanol 70%, 4: NaCl 0.9%, 5: Organoids on glass petri dish, 6: Braunol, 7: Ocry-gel, 8: Syringe of local anesthesia, 9: Ethilon polyamide 6 (3.0), 10: Surgical patties, 11: Bone wax, 12: Scalpel, 13: Graefe forceps, 14: Bone micro probe, 15: Bonn scissors, 16: Needle holder, 17: Semken forceps, 18: Extra Fine Bonn Scissors, 19: Fine scissors.

(B) Mouse placed on a warming cover, head fixed in the stereotaxic frame.

(C) Bregma visualization: Junction between sagittal suture and coronal suture (red circle), Bregma corresponds to the zero position.

(D) Drill site. Coordinates are applied from the Bregma position, 2 mm to the right side (X) and 1 mm to the front (Y).

(E) Insertion of the needle after meninges puncture with the bone micro probe. Insert first at 2.5 mm depth, then retracted to 2 mm depth.

(F) After injection, needle is removed and the hole is closed with bone wax (arrow).

(G and H) Skin is closed and disinfected, end of surgery. Illustration created with Biorender.com.

53. Keep the needle in place for 2 min and slowly withdraw the needle.
54. Wash the skull with 0.9% NaCl, verify if all organoids were implanted. For incomplete injection of organoids see Troubleshooting 7. Close the hole with the bone wax (Figure 2F) and close the skin with separated knots (Ethilon 3-0) (Figures 2G and 2H).
55. Place animal in a recovery chamber until it recovers from anesthesia.
56. Carefully monitor the scar for at least 5 - 7 days until loss of knots.

CellPress OPEN ACCESS

STAR Protocols
Protocol

Animal supervision and verification of tumor growth in vivo

Timing: up to 16 months

Development of glioma tumors in immunodeficient mice is expected to take between several weeks to several months after implantation. The growth depends on the neuropathological features of tumors (proliferation index, level of angiogenesis and invasion) (Bougnaud et al., 2016; Golebiewska et al., 2020). Animals are supervised daily for common behavioral patterns and specific symptoms indicating tumor growth. Magnetic resonance imaging (MRI) is applied to detect and quantify tumor growth.

MRI

Timing: 15–30 min

57. Anesthetize the mouse with 2.5% isoflurane / oxygen mix in the induction chamber.
58. Transfer the mouse to a pre-warmed Minerve bed adapted for mouse head imaging. The bed allows for constant body temperature at 37°C, and breath monitoring using a motion sensor pillow placed under the abdomen. Anesthesia is maintained through a nose mask with 2.5% isoflurane / oxygen mix.
59. Place the Minerve bed in the mouse head coil and insert the imaging cell (half pipe that contains the animal bed and the coil) in the magnet tunnel so that the head of the animal reaches the isocenter of the magnet.
60. Check the breathing rate before the start of the acquisition (PC-SAM software). Breathing rate must be between 50 and 100 per min. The anesthesia mix is adjusted during the scan session to maintain breathing in this range.
61. Acquire a multislices brain scout (Preclinical software MR solutions). This short scan allows verifying that the head of the animal is correctly positioned in the isocenter using 3 different plans (sagittal, coronal and transverse) and serves to correctly position slices packages for the next imaging protocols.

Note: Multi-slices brain scout (Gradient echo - GRE) is defined by an echo time (TE)/repetition time (TR) = 8/190 ms, 30 × 30 mm field of view, 9 slices, 1 mm slice thickness, and 256 × 192 matrix (spatial resolution = 0.1171 × 0.1563 mm), number of averages = 1, receiver bandwidth (BW) = 40 kHz, duration: 36 seconds.

⚠ CRITICAL: The parameters of the sequences described in this section are adapted for the 3T MRI system with a 3T horizontal bore 3017 magnet from MR Solutions, equipped with head and body quadrature coils for mouse and rats imaging. Parameters need to be adapted to the magnet with a different field strength.

62. Perform tuning and matching of the coil and magnetic field shimming to ensure high quality of the scans.
63. Select the Axial Fast Spin Echo T2-weighted MRI sequence (FSE T2w Scan).
64. Properly position the slices packages of the scan. Anatomical landmarks can be used to reproducibly position slices and facilitate comparisons in time series. The top of the frame should be aligned with the top of the brain in the coronal plan. The frame is then rotated in the Axial plane to correct for animal head side tilting by aligning symmetrical landmarks visible in the scout images parallel to the slices. In the sagittal plane, the left side of the frame must be aligned with the olfactory bulb and the cerebellum. The first 3 slices are placed to cover the olfactory bulbs.
65. Start the acquisition of the FSE T2w scan.

Note: Axial FSE-T2w scan is defined by echo time (TE)/repetition time (TR) = 68/3000 ms, 25 × 25 mm field of view, 15 Slices, 1 mm slice thickness, and 256 × 248 matrix (spatial resolution = 0.0977 × 0.1008 mm), echo train length = 8, number of averages = 4, receiver bandwidth (BW) = 20 kHz, duration: 6 min 12 seconds.

66. If Tumor contrast enhancement is desired, T1w scan with contrast is applied. Copy the slice position of the pervious FSE T2w scan, select the Axial Fast Spin Echo T1-weighted MRI sequence (FSE T1w scan) and paste the slices position.
67. Start the acquisition.
68. After the first acquisition, take out the imaging cell from the MRI. Avoid displacing the bed or the coil to keep the animal in the exactly the same position.
69. Inject subcutaneously 100 µl of Dotarem (Gadoterate 0.5 mmol/mL), put back the imaging cell in the machine and wait for 5 min.
70. Start the acquisition of the FSE T1w scan.

Note: Axial FSE-T1w scan is defined by echo time (TE)/repetition time (TR) = 17/1400 ms, 25 × 25mm field of view, 15 Slices, 1 mm slice thickness, and 256 × 256 matrix (spatial resolution = 100 × 100 µm), echo train length = 4, number of averages = 4, receiver bandwidth (BW) = 20 kHz, duration: 5 min 42 seconds.

71. Remove the imaging cell from the machine after the acquisition, then remove the mouse from the bed, place directly in the cage and supervise until awoken.

Note: Frequency of the MRI scans should be adapted according to the PDOX model. MRI can be performed once a week for PDOX with fast tumor growth. For PDOXs with slow tumor growth MRI once every 2 months is sufficient. For new PDOX models, MRI scan is advised upon first neurological symptoms.

⚠ CRITICAL: Highly invasive tumors are not detectable by MRI, close and strict supervision of each mouse is mandatory to recognize first neurological symptoms and avoid pain.

Tumor quantification based on MRI images (Figure 3).

72. Open MRI-obtained DICOM files in the ImageJ software.
73. Adjust the brightness of the images.
74. Delineate the tumor to define the area of the tumor on each slice.
75. Tumor volume in mm^3 is defined by the sum of the tumor area on each slice (slice thickness is 1 mm).

Note: Similarly to patient tumors, the invasive part of PDOX tumors is undetectable by MRI, thus immunohistochemistry is essential to confirm the size and the histopathological phenotype of the tumor. See (Bougnaud *et al.*, 2016) for detailed analysis of histopathological phenotypes.

Mouse supervision and PDOX tumor tissue processing

76. Verify the mouse every day and fill in the score sheet. The score sheet (Table 1) should contain observation regarding common behavior of each mouse and specific symptoms linked to brain tumor. Scoring criteria:
    Score 0 = no symptoms, normal behavior
    Score 1 = mild symptoms, start & body weight loss $\leq$ 5%,
    Score 2 = established symptoms & body weight loss >5% and <15%,
    Score 3 = severe symptoms, body weight $\geq$ 15% and tumor size bigger than 100 mm^3.

CellPress OPEN ACCESS

STAR Protocols
Protocol

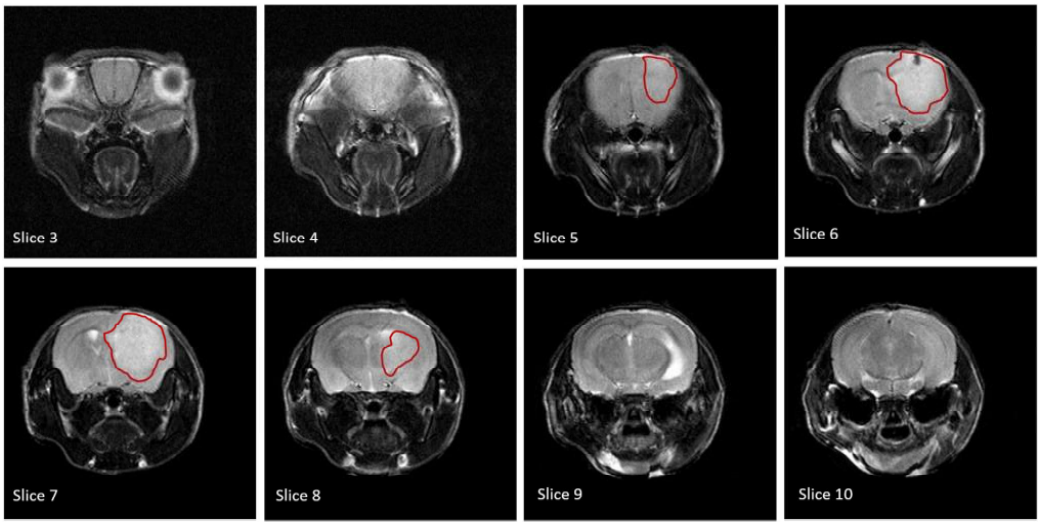

Figure 3. MRI Imaging of GBM tumor in PDOX brain

MRI slices of mouse head from the anterior part to the posterior part. Tumor visible as brighter area is delineated on each slice (red line). The area of each slice (mm^2) is summed to obtain the tumor volume in mm^3.

77. The mouse is euthanized when three symptoms reach a score of 2 or one symptom reaches a score of 3.
78. Euthanize the mouse by cervical dislocation.
79. Gently extract the brain.
80. Fresh mouse brain can be used to obtain organoids with the same protocol as described for patient tumor tissue. Remove the midbrain. Mechanically mince brain hemispheres with scalpels.

Note: If desired, two hemispheres can be processed separately to measure efficiency of organoid derivation from the tumor core (right hemisphere) and invasive zone (left hemisphere). For well-established PDOX models with known histopathological phenotype, select only part of the hemisphere(s) where tumor cells are expected.

81. Generated PDOX-derived organoids (G1) can be implanted directly for derivation of Generation 2 PDOXs or cryopreserved using the protocols described above.

Note: Serial transplantation involves subsequent intracranial implantations and derivation of organoids from PDOXs. We consider generation 3 (G3) PDOXs as stable models, which can be used for preclinical application. We have observed that genetically heterogeneous tumors may undergo clonal selection in the first two passages *in vivo* (Stieber et al., 2014). Although PDOXs at generation 1 can directly be used for experiments (see e.g., (Golebiewska et al., 2013)), this compromises significantly the number of organoids available for further implantation and maintenance of the PDOX models long term.

⚠ CRITICAL: 6 mice are commonly used per implantation series. This allows for detailed characterization of the PDOX model and biobanking of sufficient organoids for further use. Use of several mice per implantation series increases the success rate of the first generation, particularly in case of slowly growing tumors, as mice can be lost due to

Table 1. Score Sheet for establishment of PDOX models

	Common behavior					Symptoms link to brain tumor						Others		
Mouse number	Appearance of hair	Grooming	Nest building	Eating	Socialization	Abnormal movement or immobility	Inflammation at the injection site	CNS symptoms (seizure, vestibular disorder)	Kyphosis	Head shape	Weight loss	Swollen abdomen	Comment	Decision

0 = No symptoms , normal behavior, no body weight loss ; 1 (starting) = Starting symptoms and body weight loss ≤5% ; 2 (established) = Established symptoms, abnormal behavior and body weight loss between 5 and 15% ; 3 (strong)= Strong symptoms , body weight loss ≥15% and tumor size (if quantifiable ≥100% mm^3). Perform euthanasia if: 3 criteria = 2 or 1 criteria = 3

CellPress OPEN ACCESS

STAR Protocols
Protocol

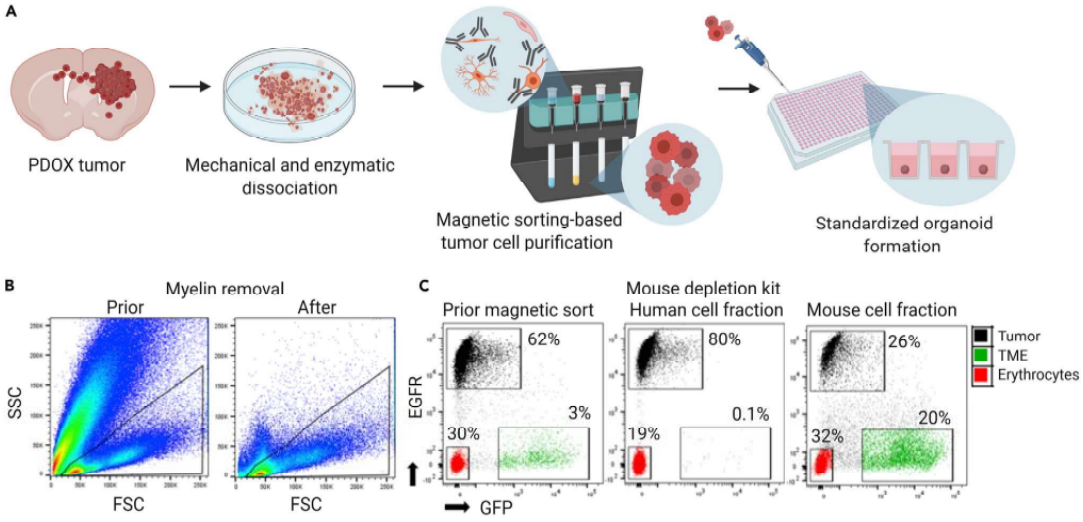

Figure 4. Tumor tissue processing for *ex vivo* functional assays

(A) Experimental workflow for purification of human tumor cells from PDOX-derived tumor tissue. Illustration created with Biorender.com.

(B) Flow cytometry-based analysis of PDOX-derived single cell suspension prior and after myelin removal. Magnetic sorting allows for efficient removal of myelin (recognized as FSC^{low}/SSC^{high} events), but not small cell debris ($FSS^{low}SSC^{low}$).

(C) Flow cytometry-based analysis of single cell suspension prior and after depletion of mouse TME cells. Analysis was performed on PDOX P8 implanted in $eGFP^{+}$ NOD/SCID mice (Golebiewska et al., 2013). Tumor cells are recognized as $EGFR^{+}GFP^{-}$ (black events). Mouse TME cells are $EGFR^{-}GFP^{+}$ (green events). Erythrocytes appear as $EGFR^{-}GFP^{-}$ (red events). Human cell fraction contains mouse erythrocytes. Mouse cell fraction is significantly contaminated by the tumor cells, due to non-specific capture at LS columns. Percentages of single viable cells are displayed for each fraction.

independent health problem and/or aging. In certain PDOX models, delay in tumor growth was observed if organoids were cultured for more than 15 days or due to sensitivity upon freezing-thawing process. Histological verification of tumor features is advised at each PDOX generation.

PDOX tissue processing and derivation of standardized organoids for *ex vivo* functional assays and drug testing

Timing: 3–5 h

Mechanical dissociation of PDOX tumor tissue and subsequent organoid culture limits the usage of the PDOX models for functional assays and preclinical drug testing requiring single cells and/or standardized organoids. In this part, we describe a protocol allowing for dissociation of brain tissue into single cells followed by purification of human tumor cells and xenograft-based murine cells constituting tumor microenvironment (TME) (Figure 4A). Isolated cells can be applied for varying functional assays and reconstitution of standardized organoids.

Enzymatic dissociation of PDOX-derived tumor tissue

Timing: 1 h

To dissociate glioma PDOX-derived tumors, enzymatic digestion based on papain and DNAse I is recommended. Here we describe the protocol based on the Neural Tissue Dissociation Kit (Miltenyi), however, other equivalent protocols are also available.

82. Preheat a water bath to 37°C.
83. Prepare enzyme mix 1 (EM1) by adding components specified in the Neural Tissue Dissociation Kit product leaflet and pre-warm to 37°C to ensure optimal enzymatic activity.
84. Remove olfactory bulbs (myelin-rich) and midbrain. Collect part of the brain hemisphere(s) containing tumor cells.
85. Moist tissue with ice-cold HBSS w/o Ca^{2+}/Mg^{2+}.
86. Cut tumor tissue with scalpels for several min and transfer tissue fragments into a 50 mL falcon tube, wash by adding ice-cold HBSS up to 20 mL.
87. Centrifuge at 300 *g* for 3 min at 4°C and discard the supernatant.
88. Resuspend tissue pellet in EM1 and incubate for 15 min at 37°C in water bath, mix tube gently every 5 min.
89. Prepare enzyme mix 2 (EM2) by adding components specified in the product leaflet, add EM2 to the tissue.
90. Dissociate tissue mechanically using a glass pipette with cotton plug. Pipet up and down 10 times, avoid air bubbles.
91. Incubate for 10 min at 37°C. Mix tube gently every 5 min during the incubation period.
92. Repeat mechanical dissociation with a glass pipette.

Optional: If tissue fragments are still visible, incubate another 10 min at 37°C.

93. Add 10 mL HBSS to the dissociated tissue and filter cells through a 50 μm sterile filter. Collect single cell suspension into a 15 mL falcon tube.
94. Centrifuge single cell suspension at 300 *g* for 3 min at 4°C.

Note: Single cells can be incubated on ice for a short period before next steps.

⚠ CRITICAL: For experiments requiring subsequent cell culture perform tissue dissociation under sterile conditions. For experiments requiring molecular analysis of isolated cells, except for tissue dissociation at 37°C, perform remaining steps at 4°C.

Optional: Myelin removal

Timing: 1 h

Amount of myelin depends on the tissue collected and histopathological features of each PDOX model. E.g., dissociation of angiogenic tumors leads to low amount of myelin fibers, invasive tumors may still show relatively high amount of myelin fibers after tissue dissociation. Removal of myelin prior to depletion of mouse cells is only needed if the experiment requires isolation of mouse TME cells. Myelin can be removed with magnetic sorting using MACS® Myelin Removal Beads II.

95. Resuspend tissue pellet in 1800 μl ice-cold MACS buffer per PDOX tumor. Add 200 μl of Myelin Removal Beads II.

Note: Indicated volumes are sufficient for up to 500 mg tissue.

96. Mix gently, do not vortex. Incubate for 15 min in the refrigerator (4°C, do not incubate on ice).
97. Wash cells by adding 13 mL ice-cold MACS buffer and centrifuge at 300 *g* for 10 min. Aspirate supernatant completely.
98. Add 3 mL of MACS buffer per 200 μl of Myelin Removal Beads II.
99. Use 3 LS columns per PDOX tumor. Place 50 μm sterile filter on top of each column (if not filtered before). Place LS columns in the magnetic field of a suitable MACS® magnetic cell separator.
100. Prepare LS columns by rinsing with 3 × 1 mL ice-cold MACS buffer per column. Collect buffer in 15 mL falcon tubes. . Discard tubes and collected buffer.

101. Place new 15 mL collection flacon tubes under the columns on ice.
102. Transfer 1 mL of single cell suspension through each filter and LS column. Collect flow-through fraction containing single cells.
103. Wash columns with 3 × 1 mL of ice-cold MACS buffer, collect to the same falcon tubes.
104. Pool collected cells from 3 falcon tubes. Adjust volume to 20 mL with ice-cold MACS buffer. Count the cells.

Note: Myelin fibers will be retained in the LS columns. The flow-through fraction should contain pure single cell suspension. Small debris will still be visible (Figure 4B).

Purification of human tumor cells

Timing: 1 h

Human tumor cells can be purified by depleting mouse cells constituting TME with magnetic sorting using Miltenyi's Mouse Cell Depletion kit.

105. Continue with single cell suspension obtained directly after tissue dissociation (collection of tumor cells only) or after myelin removal (for experiments requiring collection of mouse cells).
106. Determine total cell number or tumor cell number with a hemocytometer. Centrifuge at 300 *g* for 5 min at 4°C.
107. Aspirate buffer and resuspend cell pellet: 80 µl ice-cold MACS buffer per 2 × 10^6 tumor cells or 10^7 total cells including red blood cells.

Note: Visual discrimination between human tumor and mouse TME cells during counting is not always possible. Tumor cells often present similar size as certain mouse cells within TME.

108. Add 20 µl cell depletion cocktail per cell suspension in 80 µl ice-cold MACS buffer. Incubate for 15 min at 4°C in the fridge (do not incubate on ice).

Note: Cell number obtained from one mouse brain vary across PDOX models. 3 - 5 × 10^6 tumor cells per brain can be expected from small or highly invasive tumors, whereas larger and highly proliferative tumors contain > 30 × 10^6 tumor cells. Volume of the cell depletion cocktail and the number of LS columns needs to be adjusted accordingly.

109. Use one LS column per cell suspension in 80 µl ice-cold MACS buffer. If filtering was not performed before, place a 50 µm filter on top of each column. Place LS columns in the magnetic field of a suitable MACS® magnetic cell separator.
110. Prepare LS column(s) by rinsing with 3 × 1 mL MACS buffer per column. Collect buffer in 15 mL falcon tubes. Place new 15 mL collection flacon tubes under the columns on ice.
111. Adjust volume to 500 µl using ice-cold MACS buffer for up to 2 × 10^6 tumor cells or up to 10^7 total cells. Apply cell suspension to the LS column(s). Collect flow through fraction containing human tumor cells.
112. Wash LS column(s) with 5 × 1 mL of ice-cold MACS buffer and collect flow through fraction. This fraction represents human tumor cells.
113. If desired, collect mouse cells from the LS columns by washing the column with 3 mL ice-cold MACS buffer. Remove the column from the magnetic cell separator and push buffer with the plunger.

Note: Purification is not 100% efficient. Human fraction is contaminated with mouse erythrocytes, which lost mouse-specific membrane epitopes during tissue dissociation. Mouse cell fraction still contains human cells captured physically in the column (Figure 4C). If higher purification is required for functional assays, replace magnetic sorting with fluorescent-activated cell sorting (Bougnaud *et al.*, 2016; Golebiewska *et al.*, 2013).

STAR Protocols
Protocol

CellPress
OPEN ACCESS

⚠ CRITICAL: If the mouse is sacrificed too early due to other health problems, the number of tumor cells obtained from the brain of not fully developed PDOX can be limited.

114. If applicable, pool human tumor and mouse cell fractions from separate LS columns, respectively. Count cells with hemocytometer.
115. Centrifuge cell suspension at 300 *g* for 3 min at 4°C. Resuspend cell pellet in the buffer or medium adequate for the downstream application.
116. Single tumor and mouse cells can also be cryopreserved. Follow the protocol described for organoids.

⚠ CRITICAL: To ensure specific antibody binding, this procedure should be performed at 4°C. It is key to apply ice-cold MACS buffer to LS columns and collect cells on ice.

Formation of standardized organoids

Timing: 2 days

Standardized tumor organoids can be reformed from isolated single tumor cells. This allows also for co-cultures of tumor cells with subpopulations of TME cells in a standardized ratio (Bougnaud et al., 2016).

117. To reform standardized organoids use either freshly isolated or cryopreserved single tumor cells from above described workflow.
118. After defrosting, incubate tumor cells in 50 mL falcon tube in organoid medium for 20–30 min. Count cells to determine number of viable cells.

Note: Single tumor cells show variable viability after cryopreservation depending on the PDOX model. Dead cell staining should be used for cell counting (e.g., Trypan Blue). Adapted freezing media may be need to increase viability of single cells after cryopreservation.

119. Seed 1000 cells per well in 25 µl organoid medium in a 384-well u-shaped, low adherence plate. If using 96-well plates, adapt volume to 50 µl.

Note: Cell number can be adapted to the experimental needs. 1000 cells will allow for creation of small organoids of size between 100 - 300 µl (depending on the size of the tumor cells), applicable for preclinical drug testing protocols. Larger organoids, of size equivalent to organoids obtained by mechanical dissociation, can be grown from 10 - 50 * 10^4 cells.

120. Fill unused wells with 90 µl HBSS (or equivalent) according to the plate layout.

⚠ CRITICAL: Avoid seeding of cells in outer wells and edge well regions due to potential edge effect phenomenon on organoids during longer experimental protocols.

121. Centrifuge 384-well plates to pellet cells softly at maximum 300 *g* for 3–5 min at 4°C. If cells do not assemble at the bottom of the plate, repeat centrifugation.
122. Place plates on a 3D shaker in a standard incubator and shake at high speed (approximately 30 – 40 rpm) for 48 h to allow for organoid formation.
123. Proceed to the experimental protocol. Add 25 µl of organoid medium containing desired compound(s) to reach total volume of 50 µl.

CellPress OPEN ACCESS

STAR Protocols
Protocol

EXPECTED OUTCOMES

This protocol allows for efficient establishment of clinically relevant glioma models, which can be further applied for functional studies and preclinical drug testing. Derivation of organoids from glioma patient tumors has high success rate (Golebiewska et al., 2020). Contrary to cell lines, organoids can be derived also from less aggressive lower grade gliomas (Fack et al., 2017). The growth of organoids is limited *in vitro*. PDOX models allow for further propagation of organoids *in vivo* and multiplication of the patient material. We have shown that our organoids and PDOX models derived thereof recapitulate very well the histological, genetic, epigenetic and transcriptomic features of patient tumors (Golebiewska et al., 2020). Similarly to patient tumors, glioma cells create transcriptomic gradients of cells in different cell cycle phases, hypoxia and phenotypic states (Golebiewska et al., 2020). GBM organoids reaching a diameter of 300–1000 μm recapitulate hypoxic and phenotypic heterogeneity, and retain blood vessels and other TME cells to a certain extent (Bougnaud et al., 2016; Christensen et al., 2010). Despite replacement of human TME by the mouse counterparts, PDOX models recapitulate well histopathological features of patient GBMs such as invasion and angiogenesis in the mouse brain (Bougnaud et al., 2016). Organoids and PDOXs can be applied directly for a variety of functional assays including preclinical drug testing (Abdul Rahim et al., 2017; Golebiewska et al., 2020; Johansson et al., 2013; Keunen et al., 2011; Sanzey et al., 2015), biomarker discovery (Demeure et al., 2016), assessment of tumor heterogeneity (Bougnaud et al., 2016; Dirkse et al., 2019; Golebiewska et al., 2013; Stieber et al., 2014), or metabolism (Fack et al., 2015; Fack et al., 2017). Although immune component is compromised *in vivo* and *ex vivo*, PDOXs and organoids can be further developed towards immunocompetent conditions (Klein et al., 2020).

LIMITATIONS

Quality and quantity of patient tumor tissue represent the main limitation of the protocol. Close collaboration with the neurosurgeons and/or pathologists responsible for tumor removal and storage are key for high quality tissue. Poor organoid quality is the main reason for failure of *in vivo* growth of glioblastoma tumors. IDH1 mutated gliomas suffer from low yields of organoids, which are fragile during cryopreservation. Implantation of fresh organoids or tissue fragments increases tumor take.

TROUBLESHOOTING

Problem 1

Certain tumors are difficult to cut with scalpels. If too much medium is added to the tissue, mincing becomes difficult as tissue pieces float in the liquid.

Potential solution

Sediment tissue in the falcon tube for approximately 5 min. Remove excess medium. Transfer back to glass petri dish and proceed with mincing. Do not use plastic pipette, as larger fragments will be blocked inside. Use scalpels or sterile spoons to move tissue pellet. For difficult to cut tissue, additional mincing may be needed after 1–2 days in culture.

Problem 2

Tissue fragments are too large after 1 - 2 days in culture.

Potential solution

Sediment tissue in the falcon tube for approximately 5 min. Remove excess medium. Transfer back to glass petri dish and proceed with mincing. Do not use plastic pipette, as larger fragments will be blocked inside. Use scalpels or sterile spoons to move tissue pellet.

Problem 3

Limited amount of organoids and high amount of dead tissue fragments and debris.

STAR Protocols
Protocol

CellPress
OPEN ACCESS

Potential solution

The common reason for limited organoid growth is the original tissue quality. Derivation of organoids from necrotic tissue and brain regions with limited number of viable tumor cells is compromised. Discuss optimal tissue collection with the neurosurgeons. For cultures with high amount of debris, proceed with manual collection of good quality organoids with use of a binocular microscope.

Problem 4

Compromised survival of IDH1 mutated glioma organoids during cryopreservation.

Potential solution

Organoids obtained from IDH1 mutated gliomas are in general more fragile and very sensitive to cryopreservation. Implantation of cryopreserved organoids often lead to delayed growth *in vivo* and high variability in mice survival. Serial transplantation of fresh organoids allows for more reliable PDOX derivation. If organoid integrity is compromised, small fresh tissue fragments can be used for intracranial implantation directly after mechanical cutting. For implantation, aspirate 2 μl of mix of tissue fragments. Tissue fragments can also be cryopreserved following the protocol described for organoids.

Problem 5

Difficult to aspirate larger organoids in the Hamilton syringe.

Potential solution

Cut larger organoids mechanically shortly before surgery. Optionally, aspirate larger organoids separately and pipette back to the medium. Organoids will adapt the shape and second aspiration in smaller medium volume (2 μl) will be easier.

Problem 6

If the meninges are not properly punctured, the flat needle cannot enter straight in the soft brain tissue, potentially leading to the injection to the lateral ventricle. This could impact tumor growth and lead to more invasive tumor growth. Ventricular injection can be suspected if visible liquid (cerebrospinal fluid) is detected after needle removal at the injection site or by MRI.

Potential solution

Puncture dura mater and other meninges in straight direction under the injection hole. In case of quantitative *in vivo* study, mice injected in the lateral ventricle need to be excluded from the study.

Problem 7

Incomplete implantation of 6 organoids. Unimplanted organoid(s) is/are visible on the syringe plunger after implantation.

Potential solution

Implantation of < 6 organoids per brain should not impact directly tumor growth and derivation of the PDOX model. In case of quantitative study, animal should be excluded or tumor growth should be validated by MRI.

RESOURCE AVAILABILITY

Lead contact

Further information and requests for resources and reagents should be directed to and will be fulfilled by the lead contact, Anna Golebiewska (anna.golebiewska@lih.lu).

CellPress OPEN ACCESS

STAR Protocols
Protocol

Material availability

To facilitate the access to established glioma PDOX models, detailed information is available via PDXFinder (https://www.pdxfinder.org) and the EurOPDX Consortium (https://www.europdx.eu). Well-established models are available from the corresponding author.

Data and code availability

No exclusive data or code was used or generated for this method.

ACKNOWLEDGMENTS

We are grateful to the Neurosurgery Department of the Centre Hospitalier de Luxembourg, Laboratoire National de Santé, and Clinical and Epidemiological Investigation Center (CIEC) of the LIH for support in tumor collection. We acknowledge the financial support by the Luxembourg Institute of Health, Télévie-FNRS (grants GBModImm n°7.8513.18 and TETHER n°7.4615.18), the Luxembourg National Research Fund (FNR; CANBIO DTU PRIDE15/10675146), and the GLIOTRAIN ITN funded by the European Union's Horizon 2020 research and innovation programme under the Marie Skłodowska-Curie grant agreement no. 766069.

AUTHOR CONTRIBUTIONS

V. Barthelemy, E.K., M.D., M.W., C.F., C.D., A.B., R.B., S.P.N., and A.G. optimized patient tumor processing and organoid biobanking. A.O., V. Baus, and S.P.N. optimized *in vivo* experiments. E.K., A.-C.H, A.B., A.M., Y.A.Y., and A.G. optimized tissue processing and organoid derivation for functional assays. A.O., G.K., and O.K. optimized MRI protocol. R.B. and S.P.N. provided initial protocols. A.M., O.K., R.B., S.P.N., and A.G. supervised the work and obtained funding. A.O. and A.G. prepared the first manuscript draft. All authors reviewed and edited the manuscript.

DECLARATION OF INTERESTS

The authors declare no competing interests.

REFERENCES

Abdul Rahim, S.A., Dirkse, A., Oudin, A., Schuster, A., Bohler, J., Barthelemy, V., Muller, A., Vallar, L., Janji, B., Golebiewska, A., et al. (2017). Regulation of hypoxia-induced autophagy in glioblastoma involves ATG9A. Br. J. Cancer *117*, 813–825. https://doi.org/10.1038/bjc.2017.263.

Bougnaud, S., Golebiewska, A., Oudin, A., Keunen, O., Harter, P.N., Mäder, L., Azuaje, F., Fritah, S., Stieber, D., Kaoma, T., et al. (2016). Molecular crosstalk between tumour and brain parenchyma instructs histopathological features in glioblastoma. Oncotarget *7*, 31955–31971. https://doi.org/10.18632/oncotarget.7454.

Christensen, K., Aaberg-Jessen, C., Andersen, C., Goplen, D., Bjerkvig, R., and Kristensen, B.W. (2010). Immunohistochemical expression of stem cell, endothelial cell, and chemosensitivity markers in primary glioma spheroids cultured in serum-containing and serum-free medium. Neurosurgery *66*, 933–947. https://doi.org/10.1227/01.NEU.0000368393.45935.46.

Demeure, K., Fack, F., Duriez, E., Tiemann, K., Bernard, A., Golebiewska, A., Bougnaud, S., Bjerkvig, R., Domon, B., and Niclou, S.P. (2016). Targeted proteomics to assess the response to anti-angiogenic treatment in human glioblastoma (GBM). Mol. Cell. Proteomics *15*, 481–492. https://doi.org/10.1074/mcp.M115.052423.

Dirkse, A., Golebiewska, A., Buder, T., Nazarov, P.V., Muller, A., Poovathingal, S., Brons, N.H.C., Leite, S., Sauvageot, N., Sarkisjan, D., et al. (2019). Stem cell-associated heterogeneity in Glioblastoma results from intrinsic tumor plasticity shaped by the microenvironment. Nat. Commun. *10*, 1787. https://doi.org/10.1038/s41467-019-09853-z.

Fack, F., Espedal, H., Keunen, O., Golebiewska, A., Obad, N., Harter, P.N., Mittelbronn, M., Bahr, O., Weyerbrock, A., Stuhr, L., et al. (2015). Bevacizumab treatment induces metabolic adaptation toward anaerobic metabolism in glioblastomas. Acta Neuropathol. *129*, 115–131. https://doi.org/10.1007/s00401-014-1352-5.

Fack, F., Tardito, S., Hochart, G., Oudin, A., Zheng, L., Fritah, S., Golebiewska, A., Nazarov, P.V., Bernard, A., Hau, A.C., et al. (2017). Altered metabolic landscape in IDH-mutant gliomas affects phospholipid, energy, and oxidative stress pathways. EMBO Mol. Med. *9*, 1681–1695. https://doi.org/10.15252/emmm.201707729.

Golebiewska, A., Bougnaud, S., Stieber, D., Brons, N.H., Vallar, L., Hertel, F., Klink, B., Schrock, E., Bjerkvig, R., and Niclou, S.P. (2013). Side population in human glioblastoma is non-tumorigenic and characterizes brain endothelial cells. Brain *136*, 1462–1475. https://doi.org/10.1093/brain/awt025.

Golebiewska, A., Hau, A.C., Oudin, A., Stieber, D., Yabo, Y.A., Baus, V., Barthelemy, V., Klein, E., Bougnaud, S., Keunen, O., et al. (2020). Patient-derived organoids and orthotopic xenografts of primary and recurrent gliomas represent relevant patient avatars for precision oncology. Acta Neuropathol. *140*, 919–949. https://doi.org/10.1007/s00401-020-02226-7.

Johansson, M., Oudin, A., Tiemann, K., Bernard, A., Golebiewska, A., Keunen, O., Fack, F., Stieber, D., Wang, B., Hedman, H., and Niclou, S.P. (2013). The soluble form of the tumor suppressor Lrig1 potently inhibits in vivo glioma growth irrespective of EGF receptor status. Neuro Oncol. *15*, 1200–1211. https://doi.org/10.1093/neuonc/not054.

Keunen, O., Johansson, M., Oudin, A., Sanzey, M., Rahim, S.A., Fack, F., Thorsen, F., Taxt, T., Bartos, M., Jirik, R., et al. (2011). Anti-VEGF treatment reduces blood supply and increases tumor cell invasion in glioblastoma. Proc. Natl. Acad. Sci. U S A *108*, 3749–3754. https://doi.org/10.1073/pnas.1014480108.

Klein, E., Hau, A.C., Oudin, A., Golebiewska, A., and Niclou, S.P. (2020). Glioblastoma organoids: pre-clinical applications and challenges in the context of immunotherapy. Front. Oncol. *10*, 604121. https://doi.org/10.3389/fonc.2020.604121.

Niclou, S.P., Danzeisen, C., Eikesdal, H.P., Wiig, H., Brons, N.H., Poli, A.M., Svendsen, A., Torsvik, A., Enger, P., Terzis, J.A., and Bjerkvig, R. (2008). A novel eGFP-expressing immunodeficient mouse model to study tumor-host interactions. FASEB J. *22*, 3120–3128. https://doi.org/10.1096/fj.08-109611.

STAR Protocols
Protocol

CellPress
OPEN ACCESS

Sanzey, M., Abdul Rahim, S.A., Oudin, A., Dirkse, A., Kaoma, T., Vallar, L., Herold-Mende, C., Bjerkvig, R., Golebiewska, A., and Niclou, S.P. (2015). Comprehensive analysis of glycolytic enzymes as therapeutic targets in the treatment of glioblastoma. PLoS One *10*, e0123544. https://doi.org/10.1371/journal.pone.0123544.

Stieber, D., Golebiewska, A., Evers, L., Lenkiewicz, E., Brons, N.H., Nicot, N., Oudin, A., Bougnaud, S., Hertel, F., Bjerkvig, R., et al. (2014). Glioblastomas are composed of genetically divergent clones with distinct tumourigenic potential and variable stem cell-associated phenotypes. Acta Neuropathol. *127*, 203–219. https://doi.org/10.1007/s00401-013-1196-4.

Chapter 5

Patient-Derived Organoids and Orthotopic Xenografts of Primary and Recurrent Gliomas Represent Relevant Patient Avatars for Precision Oncology

Golebiewska A, Hau AC, Oudin A, Stieber D, **Yabo YA**, Baus V, Barthelemy V, Klein E, Bougnaud S, Keunen O, Wantz M, Michelucci A, Neirinckx V, Muller A, Kaoma T, Nazarov PV, Azuaje F, De Falco A, Flies B, Richart L, Poovathingal S, Arns T, Grzyb K, Mock A, Herold-Mende C, Steino A, Brown D, May P, Miletic H, Malta TM, Noushmehr H, Kwon YJ, Jahn W, Klink B, Tanner G, Stead LF, Mittelbronn M, Skupin A, Hertel F, Bjerkvig R, Niclou SP.

Acta Neuropathol. 2020;140(6):919-949.

doi: 10.1007/s00401-020-02226-7

5.1 The rationale of the study

This manuscript presents a detailed characterization of the cohort of glioma PDOX models established in the NORLUX Neuro-Oncology laboratory using different histopathological and molecular techniques. This work demonstrates that PDOX models recapitulate parental patient tumors at the histopathologic, genetic, epigenetic, and transcriptomic levels. It also confirmed the clinical relevance of glioma organoids and PDOXs for the testing of novel drugs and their suitability for personalized treatment studies. This work provides an important resource to the community that can be used in precision oncology and preclinical trials. Results from this paper provided the scientific basis for the subsequent work presented in this thesis.

Personal contributions

I contributed to the immunohistochemical characterization of brain tumors in PDOX models. In particular, I performed the microscopic evaluation of the tumor vasculature based on CD31 antibody staining against mouse endothelial cells. I performed immunostainings followed by detailed quantification of the average size of blood vessels and tumor area covered by the vasculature. This evaluation allowed for a more efficient characterization of the range of invasive and angiogenic features in PDOX models. Certain PDOXs show strong angiogenic features with localized tumor cells and aberrant blood vessels, whereas others display a more invasive and dispersed cellular distribution with blood vessels similar to the normal brain. This data is presented in **Figure 1c** of the paper.

I further contributed to the characterization of PDOXs models at the transcriptomic level. I analyzed the gene expression profiles of patient tumors and matched PDOX models, as well as GBM cell lines and their corresponding xenografts generated using microarrays technology. Unsupervised hierarchical clusters and principal components of this data revealed close transcriptomic similarity between PDOXs and their corresponding patient tumors, while GBM cell lines and their corresponding xenografts showed greater variations to the patient tumors. Differential expression and pathways analysis revealed an upregulation of tumor intrinsic genes and a downregulation of TME specific genes when PDOXs were compared with patient samples, indicating the replacement of human TME with mouse TME. These results are displayed in **Figure 5a-c.**

I further generated scRNA-seq data of an additional PDOX model and analyzed the newly generated and the existing data from three representative PDOX models to interrogate intratumoral heterogeneity of human tumor cells and mouse-derived TME in PDOXs. This analysis revealed that human tumor cells recapitulate inter and intra-tumoral heterogeneity and cellular states distribution in PDOXs as reported in the GBM patient tumors (Neftel et

al., 2019; Patel et al., 2014: Wang et al., 2017). This analysis is presented in **Figures 5f and 5g** in the paper**.** In addition, my analysis on the comparison of mouse-derived TME in a PDOX model to a normal brain (**Supplementary figure 5d (**401_2020_2226_MOESM1_ESM.pdf (springer.com)**)**) revealed a close resemblance to the TME of patient tumors. This analysis was a foundation for the detailed analysis of the transcriptomic diversity of mouse-derived TME in GBM PDOX models (**Chapter 6**). It also provided scientific evidence that informed the selection of longitudinal PDOXs and the aim of the project presented in Annex 1. Finally, I was actively involved in the critical appraisal of the generated results and contributed to the writing, designing of figures, proofreading and revision of the manuscript.

5.1.1 Result

Acta Neuropathologica
https://doi.org/10.1007/s00401-020-02226-7

ORIGINAL PAPER

Patient-derived organoids and orthotopic xenografts of primary and recurrent gliomas represent relevant patient avatars for precision oncology

Anna Golebiewska[1] · Ann-Christin Hau[1] · Anaïs Oudin[1] · Daniel Stieber[1,2] · Yahaya A. Yabo[1,3] · Virginie Baus[1] · Vanessa Barthelemy[1] · Eliane Klein[1] · Sébastien Bougnaud[1] · Olivier Keunen[1,4] · May Wantz[1] · Alessandro Michelucci[1,5,6] · Virginie Neirinckx[1] · Arnaud Muller[4] · Tony Kaoma[4] · Petr V. Nazarov[4] · Francisco Azuaje[4] · Alfonso De Falco[2,3,7] · Ben Flies[2] · Lorraine Richart[3,7,8,9] · Suresh Poovathingal[6] · Thais Arns[6] · Kamil Grzyb[6] · Andreas Mock[10,11,12,13] · Christel Herold-Mende[10] · Anne Steino[14,15] · Dennis Brown[14,15] · Patrick May[6] · Hrvoje Miletic[16,17] · Tathiane M. Malta[18] · Houtan Noushmehr[18] · Yong-Jun Kwon[9] · Winnie Jahn[19,20] · Barbara Klink[2,9,19,20,21] · Georgette Tanner[22] · Lucy F. Stead[22] · Michel Mittelbronn[6,7,8,9] · Alexander Skupin[6] · Frank Hertel[6,23] · Rolf Bjerkvig[1,16] · Simone P. Niclou[1,16]

Received: 30 July 2020 / Revised: 11 September 2020 / Accepted: 12 September 2020

Abstract
Patient-based cancer models are essential tools for studying tumor biology and for the assessment of drug responses in a translational context. We report the establishment a large cohort of unique organoids and patient-derived orthotopic xenografts (PDOX) of various glioma subtypes, including gliomas with mutations in *IDH1*, and paired longitudinal PDOX from primary and recurrent tumors of the same patient. We show that glioma PDOXs enable long-term propagation of patient tumors and represent clinically relevant patient avatars that retain histopathological, genetic, epigenetic, and transcriptomic features of parental tumors. We find no evidence of mouse-specific clonal evolution in glioma PDOXs. Our cohort captures individual molecular genotypes for precision medicine including mutations in *IDH1*, *ATRX*, *TP53*, *MDM2/4*, amplification of *EGFR*, *PDGFRA*, *MET*, *CDK4/6*, *MDM2/4*, and deletion of *CDKN2A/B*, *PTCH*, and *PTEN*. Matched longitudinal PDOX recapitulate the limited genetic evolution of gliomas observed in patients following treatment. At the histological level, we observe increased vascularization in the rat host as compared to mice. PDOX-derived standardized glioma organoids are amenable to high-throughput drug screens that can be validated in mice. We show clinically relevant responses to temozolomide (TMZ) and to targeted treatments, such as EGFR and CDK4/6 inhibitors in (epi)genetically defined subgroups, according to *MGMT* promoter and *EGFR/CDK* status, respectively. Dianhydrogalactitol (VAL-083), a promising bifunctional alkylating agent in the current clinical trial, displayed high therapeutic efficacy, and was able to overcome TMZ resistance in glioblastoma. Our work underscores the clinical relevance of glioma organoids and PDOX models for translational research and personalized treatment studies and represents a unique publicly available resource for precision oncology.

Keywords Glioma · Glioblastoma · Glioma recurrence · Patient-derived orthotopic xenograft · Organoid · Preclinical models · Precision medicine · IDH1 · MGMT · VAL-083

Introduction

Candidate therapeutics for personalized treatment in rare tumors are difficult to test in clinical trials because of inter-tumor differences and the limited number of patients representing specific genetic profiles. Adult diffuse gliomas are a particularly heterogeneous group of rare brain tumors, with grade IV glioblastoma (GBM) being the most malignant subtype [67]. Despite surgery, radiotherapy and chemotherapy,

Anna Golebiewska, Ann-Christin Hau, Anaïs Oudin equal contribution.

Electronic supplementary material The online version of this article (https://doi.org/10.1007/s00401-020-02226-7) contains supplementary material, which is available to authorized users.

✉ Simone P. Niclou
simone.niclou@lih.lu

Extended author information available on the last page of the article

Published online: 03 October 2020

the median survival of GBM patients is 14 months, and the recurrence is inevitable. GBM, characterized as *Isocitrate dehydrogenase* wild type (IDHwt), encompasses tumors with varying genetic backgrounds that affect distinct signaling networks [11, 14]. They can be classified into molecular subtypes with differing expression signatures [107, 112], display variable DNA ploidy [92] and have different DNA methylation status of the *O-6-methylguanine-DNA methyltransferase* (*MGMT*) gene promoter. The latter has been shown to predict the response to temozolomide (TMZ) [48], the standard-of-care chemotherapeutic agent approved for GBM [94]. A separate group of adult diffuse gliomas characterized by activating *IDH1* (IDH1mut) or *IDH2* (IDH2mut) mutations comprise *1p/19q* intact astrocytomas and *1p/19q* co-deleted oligodendrogliomas, with varying grades (II-IV) and survival rates [89], further displaying, e.g., *PDGFRA* and *CDK4* amplification, *CDKN2A/B* deletion, *ATRX*, *TP53,* or *TERT* promoter mutations [60, 83, 116], as well as a glioma CpG Island Methylator Phenotype (G-CIMP) [33, 79]. Several studies point towards an evolution of diffuse gliomas upon treatment and recurrence, where IDH1/2mut astrocytomas show most and IDHwt GBMs least changes in relapsed tumors [5, 29, 38, 57]. Still, most identified changes appear idiosyncratic and it remains unclear to what extent the current standard treatment leads to molecular changes that could affect drug responses for precision medicine. So far, all targeted treatment attempts in gliomas, e.g., targeting EGFR [41], have failed in clinical trials and effective treatment strategies are urgently needed.

A major reason for the numerous failures of clinical trials is the large gap between preclinical models and the treatment situation in patients where the existing preclinical models inaccurately represent human disease. Robust brain tumor models, able to reliably predict the sensitivity of novel personalized treatments in a molecularly defined group of patients, represent an unmet need [2]. For many years, the glioma research community relied on a handful of long-term adherent GBM cell lines that undergo significant genetic drift. In vivo such cell lines do not recapitulate certain histopathological features of patient tumors and display inadequate treatment outcomes [32, 34, 103]. Some of these shortcomings can be avoided by growing cells in defined serum-free conditions as 3D tumor spheres, adapted from neural stem/progenitor cultures (generally referred to as glioma stem cell (GSC) or brain-tumor initiating cell (BTIC) cultures) [18, 62]. However, these are generally limited to classical GBM [4] and still suffer from a loss of clonal heterogeneity and molecular adaptations to culture conditions [6, 88], in particular loss of focal amplifications related to high growth factor supply in the medium [66]. Patient-derived GBM organoids derived in serum-free conditions appear as a robust in vitro alternative, with a very good preservation of a heterogeneous tissue structure [49, 51]. However, their use is restricted by the limited availability of starting material (large amount of en bloc tissue required [51]), which is hardly compatible with modern neurosurgical practice of ultrasonic aspiration, and continuous passaging in vitro may lead to selection of proliferative GBM tumor cells. For several cancer types patient-derived xenografts (PDXs) established subcutaneously in immunodeficient animals brought a noteworthy advance, as they allow for propagation of primary patient tumors in less selective conditions and retain interactions with nonmalignant cells [16]. PDXs were shown to be more accurate in predicting treatment responses than common cell lines [46]. Several international initiatives, such as the EurOPDX and PDXNet consortia, now develop and standardize PDXs for preclinical studies [42, 72]. However, a recent evaluation of GBM PDXs highlighted drawbacks in retaining chromosomal copy number alterations (CNAs) [7], and it remains to be seen whether they represent a sustainable model for testing precision medicine regimens. As subcutaneous PDXs do not recapitulate the natural tumor microenvironment (TME), patient-derived orthotopic xenografts (PDOX) implanted directly in the brain may be more adequate for modeling gliomas in their natural milieu, preserving the physical and physiological constraints of the blood–brain barrier and the cerebrospinal fluid. To test this, it is important to assess whether PDOXs can recapitulate patient-specific genetic and epigenetic features, transcriptomic programs and intratumoral heterogeneity prior and after treatment, making them amenable as patient avatars for preclinical precision medicine.

We have previously reported that short-term culture of mechanically dissociated GBM tissue fragments allows for derivation of self-organizing 3D organoids, previously referred to as organotypic spheroids, which preserve tissue structure, intercellular connections, and TME components [10, 26]. Intracranial implantation of such GBM organoids in the brain of immunodeficient rodents allowed for conservation of tumor DNA ploidy and major histopathological features, such as angiogenesis and invasiveness [12, 86, 92, 97, 111]. Such GBM PDOXs recapitulate clinical responses towards antiangiogenic agents [1, 53]. Here, we provide systematic evidence that organoid-based glioma PDOXs are reproducible and clinically relevant models for functional precision medicine. By combining tumor organoids of various glioma subtypes with *in vivo* expansion in the brain microenvironment, we present a cohort of 40 PDOX generated from primary and paired recurrent gliomas with mixed genetic backgrounds including, among others, *IDH1* mutation and distinct *EGFR* variants. We show that these PDOXs preserve key histopathological structures of malignant gliomas (grade III/IV), recapitulate tumor-intrinsic genetic and molecular features at the individual patient level and retain intratumoral transcriptomic programs and stem-cell-associated heterogeneity. This also applies to our

unique selection of matched PDOX from paired recurrent glioma samples. We further show that glioma organoids and PDOXs represent adequate patient avatars for precision oncology, also in a high-throughput manner. Drug testing in 3D organoids allows for screening in vitro at reasonable cost with clinically-relevant responses, which can be further validated in vivo. Lastly, we highlight the promising therapeutic potential of dianhydrogalactitol (VAL-083), a bifunctional alkylating agent, for treatment of GBM. In summary, our PDOX live biobank represents an important resource for accelerating the development of novel treatment strategies for glioma patients.

Materials and methods

Clinical samples, organoid, and PDOX derivation

Glioma samples were collected at the Centre Hospitalier of Luxembourg (CHL; Neurosurgical Department) from patients having given informed consent, and with approval from the local research ethics committee (National Committee for Ethics in Research (CNER) Luxembourg). For patient information see Supplementary Table 1, online resource. Small pieces of tissue were flash frozen for further molecular analysis. If enough tumor material was obtained, 3D organoids from patient samples were prepared as previously described [12]. Briefly, mechanically minced fresh human glioma tissue pieces, without enzymatic digestion, were seeded on agar coated flasks (0.85%) and allowed to self-organize and form organoids (previously called organotypic spheroids) for up to 2 weeks at 37°C under 5% CO_2 and atmospheric oxygen in DMEM medium, 10% FBS, 2 mM L-Glutamine, 0.4 mM NEAA, and 100 U/ml Pen–Strep (all from Lonza). Organoids (generation 0) with a diameter of 300-1000 µm were then implanted in the brain of immunodeficient mice (NOD/Scid or NSG; 6 organoids per mice) using a Hamilton syringe (Hamilton, Reno, NV, USA). Animals (generation 1) were maintained under SPF conditions and sacrificed at the appearance of neurological (locomotor problems, uncontrolled movements) or behavioral abnormalities (prostration, hyperactivity) and weight loss. Optionally tumor volume was monitored by MRI. Organoids (generation 1) were further prepared from minced xenografted brains in the same way as for patient tissue and serially implanted for several generations. No mechanical and enzymatic digestion was performed prior implantation. A PDOX model was considered to be established at generation 3, when tumor phenotype and animal survival appeared stable. For specific purposes, experiments were performed in nude mice and/or eGFP expressing NOD/Scid mice [78]. Samples P8, P13 and P3 were obtained from Haukeland University Hospital (Bergen, Norway) following approval of the local ethics committee (approval number 2009/117). For these samples, organoids were initially implanted into the brain of nude rats (rnu; 10 organoids per rat: P3, P8, P13 models). Kaplan–Meier survival curves were produced in GraphPad with Wilcoxon signed-rank statistical test. The handling of animals and the surgical procedures were performed in accordance with the regulations of the European Directive on animal experimentation (2010/63/EU) and the Norwegian Animal Act, i.e., the experimental protocols were approved by the local ethics committee (Animal Welfare Structure of the Luxembourg Institute of Health; protocols LRNO-2014-01, LUPA2019/93, and LRNO-2016-01) and by the Luxembourg Ministries of Agriculture and of Health. PDOX models are available from the corresponding author or via EuroPDX consortium (https://www.europdx.eu/) and PDXFinder (https://www.pdxfinder.org/).

Magnetic resonance imaging

During image acquisition mice were kept under anesthesia with 2.5% of isoflurane, with constant monitoring of breathing and temperature. For routine follow up, mice were placed in the MRI (3T MR Solutions) and a Fast Spin Echo T2-weighted MRI sequence was applied, with field of view of 25 mm, matrix size of 256 × 256, TE of 68 ms, TR of 3000 ms, and slice thickness of 1 mm. To visualize the contrast enhancement, T1-weighted sequences without and with contrast injection were used. Fast-Spin Echo T1-weighted MRI was defined with the following parameters: field of view of 25 mm, matrix size of 256× 252, TE of 11 ms, TR of 1000 ms and slide thickness of 1 mm. Contrast agent (Gadodiamide, Omniscan, GE-Healthcare) at 0.5 mmol/kg was injected intravenously 1min prior to the scan. MRI data were analyzed by ImageJ.

Cell lines and cell line-derived xenografts

Glioma stem-like cell (GSC) cultures (P3NS, P13NS, T16NS, T158NS, T226NS, T384NS, T394NS, T407NS) were derived from PDOXs by papain-based enzymatic digestion of PDOX tissue and cultured as 3D spheres in serum-free medium based on Neurobasal® base medium (Life Technologies) supplemented with 1× B27 (Life Technologies) 2 mM L-glutamine, 30 U/ml Pen–Strep, 1 U/ml Heparin (Sigma), 20 ng/ml bFGF (Miltenyi, 130-093-841) and 20 ng/ml EGF (Provitro, 1325950500). GSC NCH601, NCH421k, and NCH644 lines [18] were cultured as non-adherent spheres in DMEM-F12 medium (Lonza) containing 1× BIT100 (Provitro), 2 mM L-Glutamine, 30 U/ml Pen–Strep, 1 U/ml Heparin (Sigma), 20 ng/ml bFGF (Miltenyi, 130-093-841), and 20 ng/ml EGF (Provitro, 1325950500). U87 and U251 cells (obtained from ATCC, HTB-14) were cultured as adherent monolayers in DMEM

containing 10% FBS, 2 mM L-Glutamine and 100 U/ml Pen–Strep (all from Lonza). Cell lines were regularly tested for mycoplasma contamination. Cell lines were authenticated by DNA profiling using an SNP-based multiplex approach and as compared to the other continuous cell lines in the DSMZ database. SNP profiles were unique. For in vivo experiments tumor cells (50,000–100,000 per mouse) were slowly injected through a Hamilton syringe (Hamilton, Reno, NV, USA) into the right frontal cortex. The animals were sacrificed upon weight loss, appearance of severe neurological (locomotor problems, uncontrolled movements) or behavioral abnormalities (prostration, hyperactivity).

Immunohistochemistry and neuropathological analysis

Coronal sections from paraffin-embedded brains were stained with hematoxylin (Dako) and 1% eosin (H&E) (Sigma). For immunostaining, sections were pretreated for 5min with Proteinase K (Dako) followed by 30 min incubation at 95 °C in retrieval solution (Dako). The Dako Envision+System-HRP was used following the manufacturer's instructions. Primary and secondary antibodies were incubated for 1 h. Signal was developed with 3,3′-diaminobenzidine chromogen in 5–20 min. Additional IHC preparations were performed using a Discovery XT automated staining module (Ventana) and standard protocols (list of antibodies in Supplementary Table 2, online resource). The existence of necrosis and the degree of invasion was assessed on the basis of H&E and human-specific Nestin staining. Proliferation index was determined as % Ki67-positive cells per whole cell population. An index of 37% was used to split Ki67 low and high models. IHC of mouse endothelial cells (CD31) was performed on isopentane flash-frozen tissues and cryostat sections (10 µm) were fixed with acetone and chloroform. Nonspecific binding was blocked with 2% FBS in TBS and antibodies were incubated for 1 h at RT. Pictures were acquired with a Leica DMI 6000B microscope. Vessel quantification was done using ImageJ software. Average vessel area (μm^2) was used as a proxy for vessel abnormality. Vessel area high and low models were analyzed after median split dichotomization into two groups. Kaplan–Meier survival analyses, including Log-rank and Wilcoxon testing were performed in GraphPad Prism 8. Other analyses were performed with two-tailed Student's *t* test.

Flow cytometry

Tumor and PDOX tissue was dissociated with MACS Neural Tissue Dissociation Kit (P) (Miltenyi) following manufacturers' instructions. For phenotyping flow experiments were performed as described [47]. Single cell suspensions were resuspended in DMEM, containing 2% FBS, 10 mM HEPES pH 7.4, and DNase I (10 µg/ml; Sigma) at 1×10^6 cells/ml followed by 90 min incubation with Hoechst 33342 (5 µg/ml, Bisbenzimide, Ho342; Sigma) at 37 °C. After washing, cells were resuspended in ice-cold HBSS 2% FBS, 10 mM HEPES pH 7.4 buffer (100 µl/test). Prior to flow cytometric analysis, cells were incubated with the IR-LIVE/DEAD® Fixable Dead Cell Stains (Invitrogen; 1 µg/ml) and appropriate preconjugated antibodies for 30 min at 4 °C in the dark (Supplementary Table 2, online resource). The data acquisition was performed on a FACS Aria™ SORP cytometer (BD Biosciences) fitted with a 632 nm (30 mW) red laser, a 355 (60 mW) UV laser, a 405 nm (50 mW) violet laser and a 488 nm (100 mW) blue laser was used. The data analyses were done with DIVA software (BD Bioscience). For cell sorting, single cell suspensions were stained with the TO-PRO®-3 shortly before sort. eGFP-negative tumor cells and eGFP-positive mouse non-neoplastic cells were sorted to cold flow cytometry buffer, centrifuged, and resuspended in organoid culture medium. Organoids free of non-neoplastic cells were obtained from sorted eGFP-negative tumor cells by plating 20,000 cells per well of 24-well plates precoated with agar. For mixed organoids 20,000 sorted tumor cells were premixed with 2000 sorted eGFP-positive non-neoplastic mouse cells (10%). Alternative, FACS-sorted GFP-negative tumor cells were washed in cold HBSS buffer and processed directly to RNA extraction.

Ploidy assessment

Nuclei were isolated from liquid nitrogen flash frozen PDOX tumors [92]. Samples were minced in DAPI buffer [10 µg/ml DAPI in 146 mM NaCl, 10 mM Tris–HCl (pH 7.5), 0.2% IPEGAL]. Nuclei were disaggregated subsequently with 20G and 25G needles and filtered through a 50 µm and a 30 µm mesh. Tumor nuclei were stained with the human-specific anti-Lamin A/C-PE antibody (Supplementary Table 2, online resource). Optionally, PDOX-derived single cell tumor cells and cell lines were stained with IR-LIVE/DEAD® Fixable Dead Cell Stains (Invitrogen; 1 µg/ml) and fixed with cold 80% ethanol. PBMCs were added to each sample as internal diploid control. Flow analysis was carried out with Aria™SORP or Canto™ flow cytometers (BD Biosystems). DNA content was analyzed with the FlowJo software.

Extraction and quality control of genomic DNA

DNA from flash frozen primary patient tissue, PDOX tumor tissue, PDOX-derived organoids, and GSC cultures was extracted using the AllPrep DNA/RNA Mini Kit® (Qiagen) following manufacturer's instructions for "Simultaneous purification of genomic DNA and total RNA from animal tissues". DNA was eluted in 50 µl of Nuclease-free water,

and concentrations were measured using a NanoDrop 1000 (Thermo Fisher Scientific). Integrity of gDNA was analyzed with a 1% E-Gel™ EX Agarose Gel (Thermo Fisher Scientific). To obtain DNA from formalin-fixed, paraffin-embedded (FFPE) samples, the tissue block was punched to obtain a tissue core of 2 mm containing at least 70% tumor tissue. After a deparaffinization step (Deparaffinization solution, Qiagen), DNA extraction was performed using QiAamp DNA FFPE tissue kit (Qiagen) according to the manufacturer's instruction. DNA concentrations were measured on the Qubit 4.0 fluorometer (Thermo Fisher Scientific), using the Qubit dsDNA BR Assay kit (Thermo Fisher Scientific).

Array comparative genomic hybridization (array-CGH)

Array-CGHs were performed as previously described [92] with the following changes. DNA was fragmented (200–500 bp) using enzymatic digestion with RSA1 and Alu1 (Agilent Technologies) and labeled with the BioPrime array-CGH Genomic labeling Kit (Life Technologies) and Cy3 and Cy5 dyes (GE Healthcare) following standard protocols for Agilent array-CGH (CGH enzymatic protocol v6.2; Ref # G4410-90010). Female or Male gDNA pool (Promega) was used as a reference. All labelling reactions were assessed using a Nanodrop 1000 (Thermo Fisher Scientific) before mixing and hybridized to either a 1 × 1 M, 2 × 400 K, 4 × 180 K or 8 × 60 K SurePrint G3 human CGH microarray (Agilent Technologies) according to manufacturer's instructions (CGH enzymatic protocol v6.2; Ref # G4410-90010). Microarray slides were scanned using an Agilent 2565C DNA scanner and images were analyzed with Agilent Feature Extraction version 12.5, using default settings. The data were assessed with a series of quality control metrics and analyzed using an aberration detection (ADM2) implemented in the CytoGenomics software versions 4.2 and 5.0.2.5 (Agilent Technologies). Aberrations were called using the ADM2 algorithm with a threshold setting of 6 and an aberration filter with a minimal number of probes = 3 and a minimal AvgAbsLogRatio = 0.25. For correlation analysis, each sample was initially processed with *Agilent CytoGenomics 4.2* in order to obtain the characterization of genomics regions (BED files) described as one of the following events: "amplification", "gain", "loss" or "deletion. Next, from each file, only regions > 50 kb were extracted in order to construct a reference mapping file using a combination of '*intersectBed*' and '*multiIntersectBed*' functions from the BEDtools suite. Finally, BED files were mapped on that common reference with their corresponding type of event. As a consequence the resulting matrix represents features detectable by any of the four array types. Chromosomes X and Y were removed. Hierarchical clustering showed no bias arising from the array type used. Pearson correlation was applied to assess relationships between genetic profiles of each sample. Next, we estimated the effects of the experimental factors on DNA copy number variation data. As these data were represented by integer values between − 2 and 2, we were unable to fit a global linear model. Instead, we used a chi-squared contingency table test implemented in the 'stat' package of R. Independently for each factor and for each DNA site we tested, whether a distribution of copy numbers is different for different factor levels of the corresponding factor. Mean − log10(p value) and mean chi-squared statistics were reported for graphical presentation.

Targeted DNA sequencing

500 ng of extracted gDNA were diluted in 130 µl low TE buffer (Qiagen) and sheared via sonication on a Bioruptor® UCD-200 (Diagenode) to an average fragment size of 150–300 bp. DNA fragment size was determined using the DNA 1000 Kit on the Bioanalyzer 2100 (Agilent Technologies). A custom-made Agilent SureSelect^{XT} Target Enrichment Library (Cat No. G9612B) was used for Illumina Paired-End Multiplexed Sequencing on a MiSeq® instrument (Illumina). The panel design 1 for the Target Enrichment Library was fully adapted from [85] (181 genes and 3 promoters). Further design changes were made using SureDesign—Agilent eArray (Agilent Technologies) to produce the panel design 2, containing additional regions (234 genes and 3 promoters). A total of 59 samples were sequenced 22 samples with the panel 1 and 37 samples with the panel 2. Library preparation was performed according to manufacturers' instruction. The Illumina MiSeq® Reagent Kit v3 (Cat No. MS-102-3003) was selected applying the Illumina reagent selection algorithm (https://emea.support.illumina.com/downloads/sequencing_coverage_calculator.html).

Variant calling was done as follows: Raw sequencing reads (fastq) were quality trimmed using the tool fastp (v. 0.20.0)[23]. Trimmed reads were aligned to an in silico fused reference genome (ICRG) containing the human genome GRCh37.75 (ENSEMBL) and the mouse genome mm10 using BWA mem (v. 0.7.17) [17]. Reads that mapped to human chromosomes were extracted from the bam file using SAMtools (v.1.9) and realigned to the human reference genome only [65]. Duplicates were annotated and removed using MarkDuplicates under GATK (v.4.0.5.1). Bam statistics were assessed using SAMtools and compared between the initial mapping to the ICRG, the realignment to the human genome and after removing duplicates. Single nucleotide variants (SNVs) and smaller insertions and/or deletions (indels) were called in the CLC Genomics Workbench (v.12.0.3) using deduplicated mappings. Variants were only called in regions with a minimum coverage of 10 reads and a minimal allele frequency of 5%. All variants that were likely to be polymorphisms and occurred in more

than 1% of the gnomAD (v.2.0.2) data base were filtered out. SNVs were annotated with COSMIC (v.89), ClinVar, and dbSNP (v.150) [61]. The primary focus in SNV calling was to determine coding changes (missense and inframe mutations), truncating (stop and frameshift mutations) and splice site mutations. Owing to poor coverage of *TERT* promoter, this region was excluded from the global analysis. All filtered variants were manually checked to exclude artefacts and variants were further classified according to the American College of Medical Genetics and Genomics (ACMG) [50]. Only pathogenic, likely pathogenic or variants of uncertain significance (VUS) were reported. For comparing the %-overlap of variants between patient tissues and PDOX, the following thresholds were applied: minimum coverage 10, minimum count 2, minimum frequency 5 %. Reads were mapped with a linear and an affine gap cost mapping and variants were merged after calling from both mappings.

Structural variants (SVs) and copy number alterations (CNAs) were analyzed using Manta (v. 1.6.0) and CNVkit (v.0.9.6) [24, 98]. For these analyzes alignment files with marked duplicates were used. SVs were annotated with SnpEff (v. 4.3.1t) [27] and filtered for variants with at least 5 supporting paired and/or split reads. CNAs were called in two separate groups, as two versions of the sequencing panels were used and the target region is important for CNA calling via CNVkit. For panel 1 no reference samples were sequenced and CNA calling was performed against a flat reference. CNAs of all samples that were sequenced with the panel 2 were normalized against a reference created from normal samples including the commercial available male (Cat No. G1471) or female (Cat No. G1521) references from Promega (Madison, Wisconsin, US) and DNA from blood of two patients. Segmentation was performed using circular binary segmentation according to default settings. Gene metrics were determined for all variants with a minimum log2 deviation of 0.4. Workflow automation was performed using the workflow manager snakemake (v.5.6.0) under conda (v.4.7.12) [58]. Additional data handling was performed applying R (v.3.6) in the environment of RStudio (v.1.1.456). All CNAs and the SVs in EGFR were visualized, manually checked, and compared to available data from array-CGH and array-based DNA methylation analysis.

Subclonal deconvolution via PyClone was performed in parallel with the above data in an independent manner. PyClone input requires variants and copy number. To acquire these data, reads were aligned to hg38, processed with Picard's MarkDuplicates {http://broadinstitute.github.io/picard/}, and GATK indel realignment and base recalibration performed [105]. Variants were called using mpileup (Samtools v.1.9) [65] and Varscan 2's (v.2.4.4) pileup2snp and mpileup2indel commands [65] with default settings but a p value of 1.00. Only positions in targeted regions were kept. Variants in dbSNP were filtered out. Absolute copy numbers were estimated using array-CGH. Log2 ratios were segmented using DNAcopy (v1.52.0) [87]. A custom script estimated purities and absolute copy numbers based on the assumption that chr7 likely had a clonal single copy gain, resulting in inference of one copy loss of chr10 and one copy gains of chr19 and chr20 (common events in GBM) in all analysed samples (T192, T233, T251, T158, T347, and T470), validating this approach. PyClone (v.0.13.1) [84] was run under default settings, with the addition of '–prior total_copy_number' to indicate the use of total copy numbers. Purities were taken from the array-CGH estimates for biopsies, and was set to 1.00 for PDOX samples.

Digital PCR

Digital PCR was used to detect and quantify IDH1 R132H in genomic DNA using QuantStudio 3D Digital PCR System and IDH1 Digital PCR Mutation Detection Assays from Thermo Fisher (Assay ID # Hs000000036_rm for c.395G>A (p. R132H)) according to the manufacturer's instructions. The reaction volume was 14.5 µl containing 7.5 µl QuantStudio 3D Digital PCR Master Mix v2 (Thermo Fisher Scientific, cat#: A26359), 0.73 µl of assay and sample DNA. Each assay contained forward and reverse primers, and 2 specific dye-labeled probes. The first one with a Vic reporter dye linked to the 5′end and an MGB linked to the 3′end to detect the WT allele. The second one with a FAM reporter dye at the 5′end and an MGB at the 3′end to detect the mutant allele. The thermal cycling conditions were 96 °C for 10 min; 39 cycles of 60 °C for 2 min and 98 °C for 30 s; final extension at 60 °C for 2 min. Two replicates of each sample were run and DNA input amount was 20 ng per chip. Human Genomic DNA Male (Promega, cat # G1471) and IDH1 R132H Reference Standard (Horizon, cat # HD677) were used as wild type reference DNA and positive reference respectively. Data analysis was done with the QuantStudio 3D Analysis Suite Cloud Software version 3.1.5; chips with < 15,000 partitions above the default quality threshold were omitted.

Array-based DNA methylation Analysis

Methylation arrays with Infinium® MethylationEPIC were processed by the Helmholtz Zentrum Muenchen (Research Unit of Molecular Epidemiology/Institute of Epidemiology, German Research Center for Environmental Health, Neuherberg, Germany) [59] or by the Laboratoire National de Santé in Luxembourg. Bisulfite conversion of 250–500 ng of gDNA was done using the EZ DNA Methylation Kit (Zymo Research) according to manufacturer's procedure, with the alternative incubation conditions recommended when using the Illumina Infinium® Methylation Assay. After bisulfite treatment, Infinium HD FFPE Restore kit (Illumina)

protocol was performed on 8 µl of DNA from FFPE samples. Genome-wide DNA methylation was assessed using the HumanMethylationEPIC BeadChip (Cat No. WG-317-1001), following the Illumina Infinium® HD Methylation protocol. This consisted of a whole genome amplification step using 4 µl and 8 µl (for fresh-frozen and FFPE samples, respectively) of each bisulfite converted sample, followed by enzymatic fragmentation, and hybridization of the samples to BeadChips (Illumina). After a step of single-nucleotide extension, the BeadChips were fluorescently stained and scanned with Illumina HiScan SQ scanner or iScan System. Additional Illumina HumanMethylation450 BeadChips were processed according to manufacturer's instruction at the German Cancer Research Center (DFKZ) Genomics and Proteomics Core Facility. Raw Intensity Data files (.idat) were exported from the BeadArray. Pearson correlation was applied to assess relationships between epigenetic profiles of each sample. The R package '*RnBeads*' was used to generate individual 450 k and EPIC RnBeadSets [74] that were normalized using the '*BMIQ*' method [100]. Both platforms were combined using the '*rnb.combine.arrays*' function in order to extract only common sites present in both objects with corresponding DNA methylation level. The DNA methylation level for each locus was measured as a beta-value score; that can range from zero to one with scores of zero indicating completely unmethylated DNA and scores of one indicating complete methylated DNA. Hierarchical clustering showed no bias arising from the array type used. Pearson correlation and Principal component analysis (PCA) were applied to assess relationships between epigenetic profiles of each sample.

As several of the considered factors were strongly correlated, we estimated their importance by consequent fitting unavailable ANOVA models, independently for each CpG site and factor. Mean *F* statistics over all variable CpG cites was then used to illustrate the importance of the factors. To detect differentially methylated regions (DMRs) or CpGs (DMCs), IDAT files were subjected to background correction, global dye-bias normalization, calculation of DNA methylation level, and detection *p* values using '*methylumi.noob*' within the '*RnBeads*' package. Differential methylation analysis was conducted on genomic site and region level according to sample groups (Patient vs. PDOX or IDHwt vs. IDH1mut) using '*limma*' and fitted using an empirical Bayes approach on *M* values [90]. In general, array probes were divided into 4 different genomic regions, giving info on functional genomic distribution: (1) tiling regions with a window size of 5kb distributed over the whole genome, (2) genes and (3) promoters annotated with Ensembl gene definitions from the biomaRt package. Promoters were defined as the region spanning 1500 bases upstream and 500 bases downstream of the TSS of the corresponding gene. (4) CpG islands tracked from UCSC genome browser. Furthermore, probes were divided into those within CpG islands (CGI), in CGI shores, shelves, or open seas (with or without overlapping gene bodies). In the comparison between 'Patient' and 'PDOX', the following criteria were selected: adj. p value < 0.01, absolute difference in mean methylation β value > 0.2. Beta value distribution plots for probe categories ('Open Sea', 'Shelf', 'Shore' or 'Island') were extracted from the integrated 'Exploratory Module' from '*RnBeads*'. Global beta value density plots for longitudinal samples were generated using the '*minfi*' package in R, after Noob background correction and global dye-bias normalization. The analysis of CpG methylation signatures was performed as described previously [33], where DNA methylation profiles were compared to a large cohort of the patient glioma tumors. DNA methylation-based glioma classification was performed by referencing data to the dataset of over 2800 neuropathological tumors at https://www.molecularneuropathology.org/mnp as described previously [20] .

Genome-wide gene expression analysis

Total RNA was extracted using the QIAGEN® RNeasy Mini Kit according to the manufacturer's protocol. GeneChip® Human Gene 1.0ST Arrays were used to determine the expression profiles. Total RNAs were processed using the Ambion WT expression kit (Life Techniologies) and the Affymetrix WT Terminal & Labeling kit before being hybridized on Affymetrix arrays according to the manufacturer's instructions (protocol P/N 702808 Rev.6). Upon hybridization, microarrays were washed, stained, and scanned according to manufacturer's standard procedures. Affymetrix CEL files containing hybridization raw signal intensities were processed to gene expression signals using the RMA (robust multichip average) algorithm implemented in the *oligo* package (version 1.44.0). *hugene10st-transcriptcluster.db* package version 8.7.0 was then used to map Affymetrix ID to entrez gene ID. R statistical environment was used for hierarchical clustering, principal component analysis and for empirical Bayesian statistics (LIMMA [90], R/Bioconductor). List of differentially expressed genes (DEG) were obtained with the eBayes/LIMMA. FDR was calculated with the Benjamini and Hochberg approach [8]. Thresholds were set up for FDR < 0.01 and absolute fold change (abs(FC)) ≥ 2. The Metascape® database [118] was used for data mining.

The similarity between our patient biopsies, PDOXs and cell lines with GBM tumors from The Cancer Genome Atlas (TCGA) cohort (538 GBM samples) was investigated using gene expression data [19]. Our cohort's data were ranked based on their interquartile ranges to select the top-5000 (most variable) probes across samples. We focused on probes with mapped gene symbols, for genes with multiple probes their expression values were (mean) merged with

Babelomics 5 [3]. Filtering resulted in 4069 unique gene symbols. TCGA data were downloaded from The Broad Institute GDAC Firehose (http://gdac.broadinstitute.org), and the preprocessed gene expression data (RSEM values) were analyzed. Gene symbols from our cohort were matched to the TCGA data, and 2420 unique symbols were unambiguously found in both datasets. Using the expression data for these genes, we measured (Spearman) correlation coefficients between our cohort samples and TCGA tumors. The resulting correlations with the TCGA tumors were ranked and graphically visualized in terms of individual samples and sample groups. Analyses were implemented with the R statistical language, packages corrplot, and ggplot2 (https://www.r-project.org).

Consensus independent component analysis (ICA), a data-driven dimensionality reduction method that performs a matrix decomposition, was applied to assess signals arising from nonmalignant cells. ICA with k components represents log2-transformed gene expression matrix X as a matrix product of matrices S (signals) and M (weights). The first shows contribution of genes in k statistically independent signals. Biological meaning of these signals was detected by functional annotation of the most contributing genes. In order to improve reproducibility of ICA decomposition, which can be affected by the selection of initial estimations, we applied consensus ICA approach [76]. ICA was run multiple times and the resulted matrices S and M were mapped and averaged between the runs. The analysis of the cell lines and TCGA reference dataset was performed as described in [76].

Single cell RNA-Seq using Drop-Seq

For scRNA-seq experiments PDOXs derived in nude mice were used. To obtain a pure population of single viable cells and to distinguish human tumor cells from mouse TME subpopulations PDOXs were dissociated and FACS-sorted (P3, P8, P13) or MACS-purified (T16, P13). For FACS we have separated hCD90 positive tumor cells from hCD90 negative mouse TME subpopulations [36]. MACS-based purification was performed with *Myelin Removal* Beads II followed by Mouse Cell Depletion kit (Miltenyi Biotec) according to manufacturer's protocols. Prior to cell loading on the Drop-seq chips, the viability of cells was verified and concentration was adjusted to ~ 150 cells/µl as optimal concentration to achieve single cell encapsulation within each droplet of ~ 1 nl. All samples analyzed had a cell viability > 95%.

Microfluidics devices were fabricated using a previously published design [70]. Soft lithography was performed using SU-8 2050 photoresist (MicroChem) on 4" silicon substrate to obtain a feature aspect depth of 100 µm. After overnight silanization (using Chlorotrimethylsilane, Sigma), the wafer masks were used for microfluidics fabrication. Drop-seq chips were fabricated using silicon based polymerization chemistry. Briefly, Polydimethylsiloxane (PDMS) base and crosslinker (Dow Corning), were mixed at a 10:1 ratio, mixed and degassed before pouring onto the Drop-seq master template. PDMS was cured on the master template, at 80 °C for 2 h. After incubation and cooling, PDMS slabs were cut and the inlet/outlet ports were punched with 1.25 mm biopsy punchers (World Precision Instruments). The PDMS monolith was plasma-bonded to a clean microscopic glass slide using a Harrick plasma cleaner. Immediately after pairing the plasma-treated surfaces of the PDMS monolith and the glass slide, flow channels of the Drop-seq chip were subjected to a hydrophobicity treatment using 1H,1H,2H,2H-Perfluorodecyltrichlorosilane (in 2% v/v in FC-40 oil; Alfa Aeser/Sigma). After 5 min of treatment, excessive silane was blown through the inlet/outlet ports. Chips were further incubated at 80 °C for 15 min.

Experiments followed the original Drop-seq protocol [70] with minor changes. Synthesized barcoded beads (Chemgenes corp., USA) were co-encapsulated with cells inside the droplets containing lysis reagents using an optimal bead concentration of 200 beads μl^{-1} in Drop-seq Lysis buffer medium. Cellular mRNA was captured on the beads via barcoded oligo (dT) handles synthesized on the surface. For cell encapsulation, 2 ml of cell and bead suspensions were loaded into 3 ml syringes (BD), respectively. To keep beads in homogenous suspension a microstirrer was used (VP scientific). The QX 200 carrier oil (Bio-rad) used as continuous phase in the droplet generation was loaded into a 20 ml syringe (BD). For droplet generation, 3.6 ml per h and 13 ml per h were used in KD scientific Legato syringe pumps for the dispersed and continuous phase flows, respectively. After stabilization of droplet formation, the droplet suspension was collected into a 50 ml Falcon tube. Collection of the emulsion was carried out until 1 µl of the single cell suspension was dispensed. Droplet consistency and stability were evaluated by bright-field microscopy using INCYTO C-Chip Disposable Hemacytometer (Fisher Scientific). Bead occupancy within droplets was carefully monitored to avoid multiple bead occupancy. The subsequent steps of droplet breakage, bead harvesting, reverse transcription, and exonuclease treatment were carried out in accordance to [70]. RT buffer contained 1× Maxima RT buffer, 4 % Ficoll PM-400 (Sigma), 1 µM dNTPs (ThermoScientific), 1 U/ml Rnase Inhibitor (Lucigen), 2.5 µM Template Switch Oligo, and 10 U/ml Maxima H-RT (ThermoScientific). Post Exo-I treatment, the bead counts were estimated using INCYTO C-Chip Disposable Hemacytometer, and 10,000 beads were aliquoted in 0.2 ml Eppendorf PCR tubes. PCR mix was dispensed in a volume of 50 µl using 1× Hifi HotStart Readymix (Kapa Biosystems) and 0.8 mM Template-Switch-PCR primer. The thermocycling program for the PCR amplification was modified for the final PCR cycles by 95 °C (3 min), four cycles of 98 °C (20 s),

65 °C (45 s), 72 °C (3 min), 10 cycles of 98 °C (20 s), 67 °C (20 s), 72 °C (3 min) and followed by a final extension step of 72 °C for 5 min. Post PCR amplification, libraries were purified with 0.6× Agencourt AMPure XP beads (Beckman Coulter), in accordance with the manufacturer's protocol. Finally, the purified libraries were eluted in 20 µl RNAse/DNAse-free molecular grade water. Quality and concentration of the sequencing libraries were assessed using BioAnalyzer High Sensitivity Chip (Agilent Technologies).

The 3′end enriched cDNA libraries were prepared by tagmentation reaction of 600 pg cDNA library using the standard Nextera XT tagmentation kit (Illumina). Reactions were performed according to the manufacturer's instructions, samples were barcoded using the N7xx index series and 400 nM custom P5 hybrid primer: (AATGATACGGCG ACCACCGAGATCTACACGCCTGTCCGCGGAAGCAGT GGTATCAACGCAGAG T*A*C). The PCR amplification cycling program used was: 95 °C 30 s; fourteen cycles of: 95 °C (10 s), 55 °C (30 s), 72 °C (30 s) followed by a final extension step of 72 °C (5 min). Libraries were purified twice to reduce primers and short-DNA fragments with 0.6× and 1× Agencourt AMPure XP beads (Beckman Coulter), respectively, in accordance with the manufacturer's protocol. Finally, purified libraries were eluted in 15 µl molecular grade water. Quality and quantity of the tagmented cDNA library was evaluated using BioAnalyzer High Sensitivity DNA Chip. The average size of the tagmented libraries prior to sequencing was between 400 and 700 bps. Purified Drop-seq cDNA libraries were sequenced using Illumina NextSeq 500 with the recommended sequencing protocol except for 6pM of custom primer (GCCTGTCCGCGGAAGCAGTGG TATCAACGCAGAGTAC) applied for priming of read 1. Paired end sequencing was performed with the read 1 of 20 bases (covering the random cell barcode 1–12 bases and the rest 13–20 bases of random unique molecular identifier (UMI) and for read 2 the 50 bases of the genes.

Bioinformatic processing followed the DropSeq protocol [70] using the DropSeq tool version 1.16. In brief, FASTQ files were assembled from the raw BCL files using Illumina's bcl2fastq converter and ran through the FASTQC codes [Babraham bioinformatics; https://www.bioinformatics.babraham.ac.uk/projects/fastqc/] to check library qualities by the assessment parameters (a) quality per base sequence, (b) per base N content, (c) per base sequence content and d) over-represented sequences. Libraries with significant deviation were re-sequenced. FASTQ files were subsequently merged and converted to binaries using PICARD's fastqtosam algorithm. The resulting digital gene expression matrix (DGE) was first cut based on knee plot analysis and subsequently filtered by the Seurat version 3 and Monocle version 2 packages (http://cole-trapnell-lab.github.io/monocle-release/) in R (version 3.6.0) based on ribosomal and mitochondrial genes as well as on low transcript content. The following threshold filters were used: only cells that expressed at least 200 genes and presented $1x10^6$ total mRNAs, and only genes which were expressed in at least 5 cells were considered for further analysis. To normalize for transcript capturing between the beads, the averaged normalized expression levels (log2(TPM+1)) were calculated. After filtering and normalization, our dataset included 3138 cells (per sample cell counts: P3 = 543 cells, P8 = 502 cells, P13 = 1295, T16 = 798 cells). To examine relative expression levels, we centered the data by subtracting the average expression of each gene from all cells. Digital gene expression matrix of the TME subpopulations of PDOX P8 and normal mouse brain was filtered and normalized as described above. After filtering and normalization, the dataset included 892 cells (per sample cell counts: P8 = 453 cells, Control = 439 cells). Dimensionality reduction and gene expression markers identification and visualization were done using UMAP implemented in the Seurat package version 3 [15, 93].

The cell cycle and hypoxia meta-signatures were determined based on the respective Molecular Signatures Database (MsigDB [95]) and only correlated genes ($R > 0.3$) were considered. The relative expression of common signature genes between all samples was depicted in the expression heatmaps. For each cell cycle and hypoxia signature, a specific meta-module was defined, taking into account all genes that were common among the samples, and the average relative expression for each specific meta-module was calculated. These meta-modules were used to score the cells by the average relative expression of all genes in the meta-module, and cells were sorted according to these scores. The global score for each sample was calculated as the average of all cell cycle and hypoxia meta-modules expression. Meta-modules were also defined for the G1/S and G2/M phases of the cell cycle, which enabled cells to be classified as cycling (mean relative expression ≥ 0.1 and qval < 0.05) and noncycling (mean relative expression < 0.1 and qval > 0.05). For each cell, the mean relative expression of unique tumor subtype genes was calculated and used to create a score for each respective subtype. The minimum and maximum score values were determined and only cell scores above the threshold (qval > 0.001) were used to generate the tumor subtype heatmaps. Single cell signature scores for cellular phenotypic states and meta-modules (MES, AC, NPC, and OPC-like) were implemented as described by Neftel et al. [77]. TCGA subtypes of single cells were assessed based on signatures described in Wang et al. [112]. Owing to the limitations of Drop-seq data, the signature scores for TCGA subtypes were determined according to scripts from Neftel et al. [77].

Western blot

Protein extraction was performed using minimal amounts of RIPA buffer (Thermo Fisher Scientific, Cat No. 89901) containing 1x protease inhibitor (Merck, cOmplete® protease inhibitor cocktail) and on ice incubation for 15min followed by brief sonication and a centrifugation step (13.000 ×*g*, 5 min, 4 °C) to remove cellular debris. iProtein extracts were resolved in NuPage™ 4–12% BisTris Protein Gels (Cat No. NP0321BOX, Thermo Fisher Scientific, MA, US), and blotted onto an Invitrolon™ PVDF (Thermo Fisher Scientific, Cat No. LC2005) or a Nitrocellulose membrane (Lifetech, Cat No. IB23001) according to standard protocols. After incubation with 5% nonfat milk in TBST (10 mM Tris, pH 8.0, 150 mM NaCl, 0.5% Tween 20) for 60 min, the membrane was rinsed with TBST and incubated with primary antibodies (Supplementary Table 2, online resource). Membranes were washed three times for 10 min and incubated with horseradish peroxidase (HRP)-coupled secondary antibodies (Jackson ImmunoResearch) for 1h at RT. Blots were washed with TBST three times, once with TBS, developed with a chemiluminescent substrate (ThermoFisher) and imaged with the ImageQuant 350 scanning system (cooled-CCD camera, GE Healthcare).

Ex vivo compound screening in 384-well plate format

PDOX tumors were dissociated with the MACS Neural Dissociation kit (Miltenyi Biotec) according to manufacturer's instructions. Mouse cells were removed with Mouse Cell Depletion kit (Miltenyi Biotec). Tumor cells were seeded 1000 cells/well in organoid medium in 384-well plates (PrimeSurface®, S-Bio) and cultured for 72 h to allow organoid formation. Organoids were treated with the following compounds: Erlotinib (EGFR, SelleckChem), Gefitinib (EGFR, SelleckChem), AZD3759 (EGFR, SelleckChem), AG-490 (JAK2, EGFR, SelleckChem), Daphnetin (EGFR, PKA/C, SelleckChem), Palbociclib (CDK4/6, SelleckChem), Abemaciclib (CDK4/6, SelleckChem), TMZ (Sigma) and 1,2:5,6-Dianhydrogalactitol (VAL-083, Delmar) in a fourfold and seven-point serial dilution series ranging from 1 µM to 1 mM (VAL-083, TMZ) or 12 nM to 48 µM (remaining inhibitors). After 3 (TMZ, VAL-083) or 6 (remaining inhibitors) days of incubation at 37 °C in a 5% CO_2 humidified incubator for respective inhibitors, cell viability and cytotoxicity were measured with CellTiter-Glo®2.0 and CellTox™-Green assays (Promega) respectively according to the manufacturer's instructions with a ClarioStar plate reader (BMG Labtech). The relative cell viability for each dose was obtained by normalization with untreated control (VAL-083) or dimethyl sulfoxide (DMSO, Sigma, remaining compounds) per each plate or condition. Dose response curves (DRCs) were fitted using GraphPad Prism 8: best-fit lines and the resulting IC_{50} values were calculated using log[inhibitor] versus normalized response—variable slope (four parameters). The area under the curve (AUC) for each DRC was calculated using GraphPad Prism 8. The experiments were performed with one (VAL-083, TMZ) or two (EGFR and CDK4/6 inhibitors) biological replicates, each comprising three technical replicates per PDOX model per each drug concentration. Statistical differences between genetically defined PDOXs groups were performed with unpaired 2-tailed *t* test. For LIVE/DEAD double labeling, organoids were incubated with 2 mM Calcein-AM and 4 mM Ethidium homodimer-1 (LIVE/DEAD assay kit, Molecular Probes) for up to 6 h. Imaging of viable (green) and dead (red) cells was done using LSM510 or LSM880 Confocal Laser microscopes (Zeiss).

Cell printing and high-throughput drug screening procedure

PDOX T434 tumors were dissociated with the MACS Neural Dissociation kit (Miltenyi Biotec) according to manufacturer's instructions. Mouse cells were removed with Mouse Cell Depletion kit (Miltenyi Biotec). Tumor cells were mixed with 1% alginate (ratio of 1:1) and printed on 384-pillar array (1000 cells with 250 nl) by ASFA Spotter ST (Medical & Bio Device, Suwon-si, South Korea). The pillars were washed by carefully combining the cell-pillar plates with 384-well plates containing 40 µl of cell culture medium (DMEM (Biowest), 10% FBS, 1% Pen–Strep, 4x NEAA (Lonza), 1% Ultraglutamine (Lonza)) in each well, and incubation for 30 min at 37 °C. The pillar plates were then combined with 384-well assay plates containing cell culture medium and incubated for 3 days at 37 °C and 5% CO_2 atmosphere. The pillar plates were then transferred to compound plates where the cells immobilized in alginate were exposed for 7 days to 41 FDA-approved drugs, in a fourfold and seven-point serial dilution series from 7.3 nM to 30 µM in duplicates. Bortezomib was used as an internal control. To determine end-point cell viability, the cells were stained using Calcein AM live cell staining and the images were acquired using High Content imaging instrument (CV8000, (Yokogawa, Tokyo, Japan). Cell viability was calculated based on Calcein AM fluorescence. The relative cell viability for each dose was obtained by normalization with dimethyl sulfoxide (DMSO) per each plate. The experiment was performed in two replicates on different 384 well plates. Dose Response Curves (DRC) were fitted using GraphPad Prism 8 (GraphPad). The AUC for each DRC was calculated using GraphPad Prism 8.

In vivo tumor treatment

T16 GBM organoids were orthotopically implanted into the right frontal lobe of Swiss nude mice. Animals were monitored daily and the following criteria were evaluated: (1) loss of > 10% of body weight, (2) exhibition of strong neurological signs (3) increased kyphosis or (4) swollen belly. Tumor growth was monitored by MRI (T1- and T2-weighted MRI protocol; 3T MRI system, MR Solutions). 35 days post-implantation most mice had visible tumors and were randomized into 4 treatment groups (7 mice per treatment group, 6 mice per control group): Control, Bevacizumab (Avastin) treatment, VAL-083 treatment and combined Bevacizumab + VAL-083 treatment. Drug concentrations and treatment schedule were as follows: Bevacizumab – 20 mg/kg, 1× week, VAL-083 – 3.5 mg/kg, 3× week. Control animals received saline (NaCl 0.9%) 4× week. Compounds and saline were delivered by intraperitoneal injections. Bevacizumab and VAL-083 injections were performed on different days. 49 days after implantation MRI T2 was applied to monitor tumor progression. T1 with contrast agent was applied to several mice to evaluate the response of tumor to Bevacizumab. 56 days after implantation one mouse in control group showed neurological symptoms and was euthanized directly after MRI. T2 and T1 + contrast MRI was applied to all mice. Remaining mice were euthanized the following day before mice developed symptoms and brains extracted. Tumor volume (mm^3) was measured in ImageJ as the sum of area obtained by tumor delineation in each slice and multiplying by slice thickness (1mm). Growth rate (GR) was calculated using the TV measurement as $GR = 100 \times \log(TVf/TV0)/(tf-t0)$, where TVf and TV0 are the tumor volumes at the late (day 56) and early (day 35 or day 49) time points, respectively, and tf−t0 is the difference in days between the time points. Tumor volumes are expressed in mm^3 and GR in % per day [80]. Statistical difference was assessed with ANOVA with Turkey's multiple comparison test.

Statistical tests

Different statistical approaches have been applied based on the data type and measurements across the manuscript. Statistical tests are described in each paragraph above corresponding to the associated experimental procedures. If not specified above, significant differences were calculated with the Student's *t* test.

Data availability

Our PDOX models are freely available to the scientific community. To facilitate the access to established models, we provide detailed information for the best characterized models via PDXFinder (https://www.pdxfinder.org/) [30]. New models will be regularly added to the resource with molecular and histopathological characterization. Our collection is also part of the EuroPDX consortium (https://www.europdx.eu/). Models are available from the corresponding author on reasonable request. The sharing procedure will depend on the expertise of the requesting laboratory. Groups experienced in organoid culture and intracranial implantation will be provided with the organoids. For less experienced groups we provide additional training or perform collaborative experiments in house. For small scale experiments we provide ready-to-use material, e.g., tissue sections, cryopreserved organoids, or single cells.'

Molecular data are available in the Gene Expression Omnibus repository (https://www.ncbi.nlm.nih.gov/geo/) under accession numbers as follows: (1) array-CGH: GSE137959; (2) DNA methylation: GSE137845; (30 gene expression: GSE134470; (4) scRNA-seq:GSE128195. Targeted DNA sequencing is available in the Sequence Read Archive (https://www.ncbi.nlm.nih.gov/sra) under accession number PRJNA627814.

Results

Glioma organoids and PDOXs can be generated across diverse clinical high-grade glioma specimens

Fresh tumor samples of 241 glioma patients (189 GBM, 52 grades II-III gliomas) were collected at surgery, including from multifocal samples and longitudinal samples of patients undergoing sequential operations (Fig. 1a, b, Supplementary Table 1, online resource). Organoids of 300–1000 µm were obtained by mechanical dissociation of tissue, without enzymatic digestion, followed by self-aggregation in short-term culture (up to 14 days). These cultures represent self-organizing structures, which preserve a heterogeneous 3D tumor tissue organization, including cell–cell interactions, non-neoplastic cells of the tumor microenvironment (TME) and extracellular matrix components. The initial culture step allows to shed necrotic cells and to standardize the organoids for intracranial implantations. Sufficient material was available for cultures from 72% (136 GBM, 37 grades II–III gliomas, total 173) of collected patient samples, of which 79% GBMs (107/136) and 68% (25/37) of grades II–III gliomas presented high quality organoids. Common reasons for lack of healthy organoids were necrotic tissue, tissue damage during surgical procedure or insufficient material. In general, organoids self-assembled into 3D structures within 3–5 days. The proliferation and growth of organoids was generally limited, but variable and patient specific. We used patient-derived organoids for downstream applications within 10–14 days of short-term

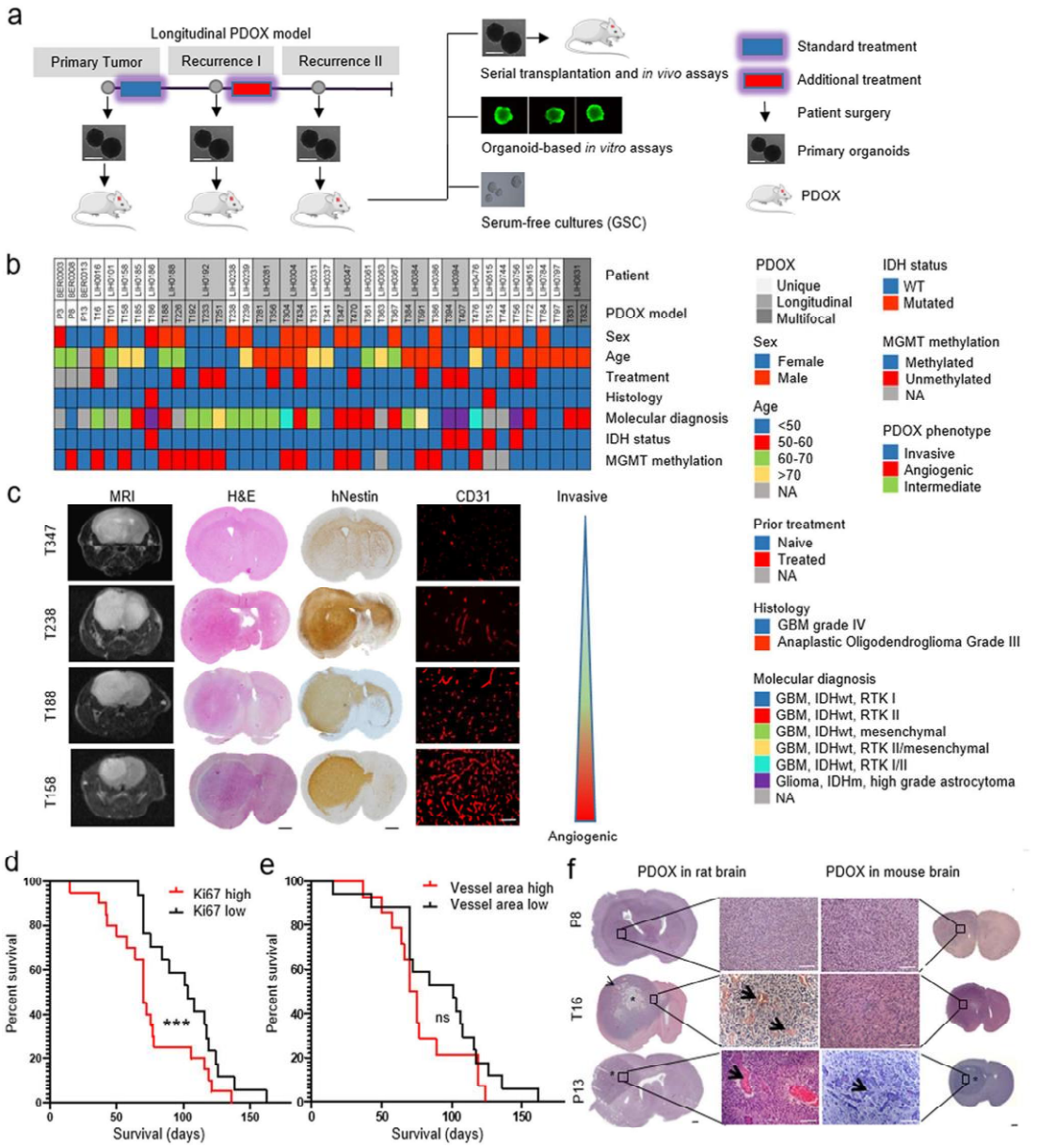

culture. Occasionally we mechanically recut larger organoids to ensure good quality and avoid necrosis. Although organoids can remain viable in culture over longer periods, they often fuse to re-aggregate into larger structures. We have not attempted further expansion and passaging in order to limit in vitro selection processes. Organoids were either frozen in DMSO-containing medium for later recovery or directly implanted into the rodent brain. No enzymatic or mechanical dissociation of organoids was applied prior implantation or cryopreservation.

To date, out of the 173 generated glioma organoids, we have performed 49 implantations into the mouse brain (41 GBM and 8 grade III gliomas). Organoids were implanted in immunodeficient mice (NOD/Scid, NSG) and tumors developed within 4–57 weeks depending on the parental tumor (Generation 1). The developed tumors were further

◂**Fig. 1** Clinical and histological characterization of the glioma PDOX cohort. **a** Schematic of derivation of PDOXs from primary and recurrent patient gliomas. Treatment refers to patients. PDOXs enable tumor expansion via serial transplantation, organoid-based in vitro assays including drug screening, genetic manipulations, and derivation of long-term in vitro sphere cultures. **b** Clinical patient information of corresponding 40 PDOXs (from 32 patients). PDOXs derived from longitudinal or multifocal samples of the same patients are highlighted. See Supplementary Table 1, online resource for more information. **c** MRI, Hematoxylin/Eosin, human-specific Nestin, and mouse-specific CD31 stainings were performed to assess histopathological characteristics of PDOXs. Representative PDOX models displaying a range of invasive and angiogenic features are shown. Scale bars represent 1mm (black) and 100µm (white). **d** Kaplan–Meier survival curves of PDOXs divided in high and low Ki67 positive cells (mean Ki67 positive cells per model - split by median), $^{***}p_{value} < 0.001$ (Wilcoxon signed-rank test). Mean survival of each model ≥ generation 3 was plotted in each group. **e** Kaplan–Meier survival curves of PDOXs divided by vessel area (Average vessel area in µm—split by median value), ns = not significant (Wilcoxon signed-rank test). Mean survival of each model ≥ generation 3 was plotted in each group. **f** Histopathological comparison of the same PDOXs derived in mice or rats. Angiogenic features are amplified in the rat brain (arrows, abnormal vessel morphology; stars, pseudopalisading necrosis; black bar, 1 mm; white bar, 100 µm). Examples are shown for pronounced invasive histopathology (P8), intermediate (T16) and increased angiogenic (P13) growth. Scale bars represent 1 mm. See more examples in Supplementary Fig. 1d, online resource

resected from the mouse brain and organoids (Generation 1) were obtained by applying the same protocol as for patient tumor tissue. IDHwt GBM organoids survived well a freezing–defrosting procedure, while IDH1mut (*R132H)* gliomas were more fragile, often requiring implantation of freshly prepared organoids or small unprocessed tissue fragments. Generally, mice showed a longer latency period at first passage (Supplementary Fig. 1a, online resource) and the most PDOXs reached a stable tumor development time per patient tumor at Generation 2–4. Successful engraftment and PDOX propagation via serial transplantation (> 3 passages) were obtained for 86% of GBMs (35/41, 6 failed due to poor organoid quality), 25% of grade III gliomas (2/8, no association with organoid quality). Grade II gliomas were not systematically implanted because of minimal prior success. Rare activating IDH2mut (*R172K)* gliomas are not yet present in the cohort. Three additional GBMs (PDOXs P3, P8, and P13) were initially derived in nude rats [111] and were further serially transplanted in mice. To date, we have generated a cohort of 40 glioma PDOX models from 32 patients, displaying different clinical characteristics and molecular backgrounds (Fig. 1b, Supplementary Table 1, online resource). Our PDOX cohort contains tumors from primary untreated gliomas as well as recurrent tumors after treatment. We obtained paired longitudinal samples, before and after treatment, from 7 patients and were able to generate 15 corresponding PDOXs. One patient (LIH0831) with a multifocal GBM led to 2 PDOX models derived from tumor tissue collected from two distinct locations. Out of 25 PDOX models cultured in serum free medium in vitro, 8 glioma stem cell-like (GSC) lines could be propagated long term, including 2 cell lines carrying the IDH mutation (Supplementary Table 1, online resource).

Glioma PDOXs display a range of invasive and angiogenic glioma features

PDOXs derived in immunodeficient mice preserved the major histopathological features of patient tumors and displayed a gradient of invasiveness and vascular pathology depending on the tumor of origin (Fig. 1c). Angiogenic tumors tended to grow in a more circumscribed manner and showed contrast enhancement on MRI, indicative of blood brain barrier disruption. In line with our previous report [12], mouse survival was a result of a combination of histopathological features (vascular proliferation, necrosis, and invasion) and proliferation index, where high proliferation correlated significantly with poor prognosis (Fig. 1d, e, Supplementary Table 1, online resource). Models derived from relapsed GBMs showed similar survival and proliferation index as compared to treatment-naïve tumors (Supplementary Fig. 1b, c, online resource). Based on the previous experiments with GBM PDOXs generated in rats [111], we were surprised to find that only a few PDOX models in mice displayed extensive abnormalities in blood vessels. Therefore, we compared identical patient GBMs implanted in either mouse or rat brain. While invasive tumors were similar in mice and in rats, vessel abnormalities were exacerbated in rats in the PDOXs showing only moderate defects in the mouse brain (Fig. 1f, Supplementary Fig. 1d, online resource), including pseudopalisading necrosis, dilated vessels, and endothelial cell proliferation. This indicates that the capacity of human GBM to induce angiogenesis is higher in rats as compared to mice, likely due to differences in size and cross-species interactions. These interspecies differences were also observed in xenografts derived from serum-free GSC lines (Supplementary Fig. 1d, online resource).

Tumor development was independent of non-neoplastic cells present in organoids

Non-neoplastic cells of the TME constituted between 3 and 25% of all cells in tumor cores in different PDOX models (Supplementary Fig. 1e, online resource) and these proportions remained stable over serial transplantations. To assess whether the nontumor compartment present within organoids influenced tumor formation upon implantation in vivo, we derived TME-free organoids from FACS-purified tumor cells grown in eGFP-expressing mice and compared them with TME-containing organoids (Supplementary Fig. 1f–g, online resource). Both conditions allowed for reformation

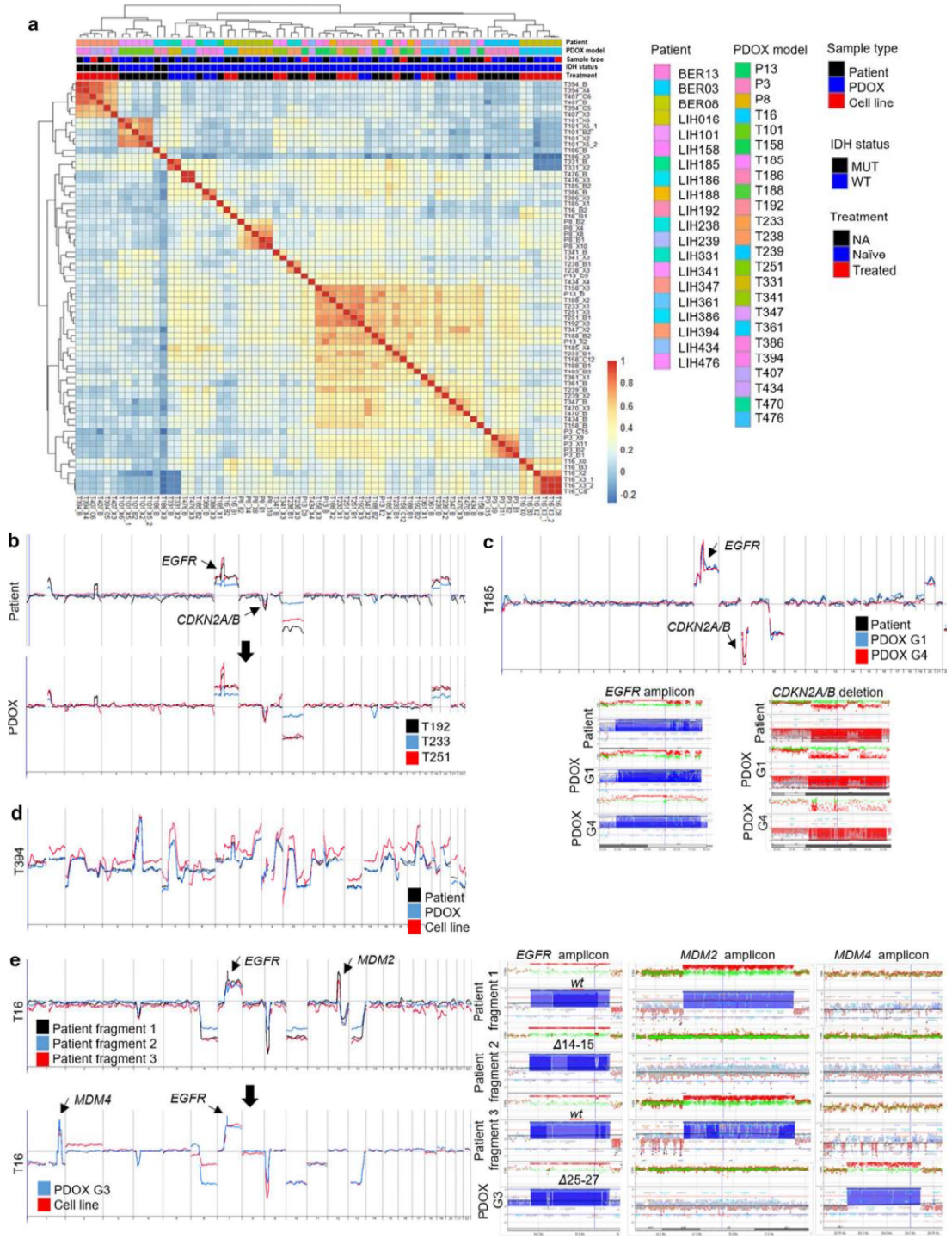
a
Patient
PDOX model
Sample type
IDH status
Treatment
BER13
BER03
BER08
LIH016
LIH101
LIH158
LIH185
LIH186
LIH188
LIH192
LIH238
LIH239
LIH331
LIH341
LIH347
LIH361
LIH386
LIH394
LIH434
LIH476
P13
P3
P8
T16
T101
T158
T185
T186
T188
T192
T233
T238
T239
T251
T331
T341
T347
T361
T386
T394
T407
T434
T470
T476
Patient
PDOX
Cell line
MUT
WT
NA
Naïve
Treated
1
0.8
0.6
0.4
0.2
0
-0.2
b
Patient
EGFR
CDKN2A/B
PDOX
T192
T233
T251
c
T185
EGFR
CDKN2A/B
Patient
PDOX G1
PDOX G4
EGFR amplicon
CDKN2A/B deletion
d
T394
Patient
PDOX
Cell line
e
T16
EGFR
MDM2
Patient fragment 1
Patient fragment 2
Patient fragment 3
MDM4
EGFR
PDOX G3
Cell line
EGFR amplicon
MDM2 amplicon
MDM4 amplicon
wt
Δ14-15
wt
Δ25-27

◂**Fig. 2** Recapitulation of copy number aberrations in PDOXs. **a** Pearson correlation between patient tumors, PDOXs, and cell lines derived based on array-CGH genetic profiles (B, patient; X, PDOX; C, cell line; adjacent numbers correspond to passage in vivo or in vitro respectively). For statistics see Supplementary Fig. 2b, online resource. **b** Array-CGH profiles of longitudinal samples (T192-T233-T251) of patient LIH0192 showing retention of genetic aberrations upon recurrence after treatment (radio + chemotherapy). The same profiles were recapitulated in PDOXs. **c** Example of an array-CGH profile of a GBM patient and corresponding PDOX model (T185 generation 1 and 4). No major changes were detected upon serial xenotransplantation. Identical chromosomal breakpoints are shown for *EGFR* amplicon and *CDKN2A/B* homozygous deletion. See more examples in Supplementary Fig. 2 and Supplementary Table 3, online resource. **d** Example of an IDH1mut glioma patient and corresponding PDOX and cell line showing high genome complexity. Patient was treated with radiotherapy before surgery. **e** Array-CGH profiles of 3 pieces of the same tumor (T16) from patient LIH0016 revealing intratumoral genetic heterogeneity (left panels). T16 PDOX and cell line were derived from additional *MDM4/EGFRΔ25-27*-amplified clone. Right panels show the different amplicons in patient tumor fragments and PDOX

of 3D organoid structures from sorted cells. Comparison of tumors derived from these two types of organoids showed no significant difference in survival over serial transplantations (Supplementary Fig. 1g, online resource). The resulting tumors appeared histologically similar, with the expected level of invasion and the presence of an abnormal vasculature. This shows that tumors quickly adapt to the new microenvironment and recreate their niche in the brain by recruiting host-derived TME at each passage.

Copy number alterations (CNAs) are well preserved in glioma PDOXs

Glial tumors display considerable genetic heterogeneity, with both inter- and intratumoral differences [91]. At the DNA ploidy level, we have previously shown that GBMs present as either mono- or polygenomic tumors where aneuploidy represents a late event in GBM evolution [92]. We found that the PDOXs retain the patient tumor ploidy states and that both pseudodiploid and aneuploid clones could be propagated by serial implantation (Supplementary Table 1, online resource). This is in contrast to long term cultures, where GSC lines of pseudodiploid tumors undergo additional aneuploidization at early passages (Supplementary Fig. 2a, online resource). By array-CGH, we show that at scale CNAs of the parental tumors were maintained with high fidelity in organoids and PDOXs both at low and high generations (Fig. 2a, Supplementary Fig. 2b, c, Supplementary Table 3, online resource). PDOXs clustered next to or in close proximity to their parental tumors. This was also true for longitudinal gliomas, where similar genomic profiles were seen in recurrent tumors after treatment (Fig. 2b, Supplementary Fig. 2d, online resource). Genomic aberrations were also assessed and confirmed by DNA Infinium Methylation EPIC arrays (Supplementary Table 3, online resource). Most GBM patients harbored classical genetic hallmarks, such as chromosome 7 gain, chromosome 10 loss and *CDKN2A/B* deletion, which were all retained in PDOXs. This is in contrast to subcutaneous PDXs, where classical GBM CNAs where reported to be lost [7]. Moreover, focal amplicons (*e.g., EGFR, MDM2, MDM4, PDGFRA, MET, CDK4/6*) with the exact same breakpoints were maintained in PDOXs over generations (Fig. 2c, Supplementary Fig. 2c, online resource). IDH1mut gliomas, of which PDOXs could be established, displayed a remarkable genomic complexity (Fig. 2d, Supplementary Tables 1, 3, online resource).

Rare genetic discrepancies reflect intratumor heterogeneity and tumor-specific evolution

It has been suggested that tumors may undergo mouse-specific tumor evolution in subcutaneous PDXs [7]. Here, in our orthotopic xenografts, we only detected minor differences between PDOXs and patients, which could largely be explained by clonal heterogeneity of the parental tumor, particularly at the level of focal amplifications known to be subclonal [45]. E.g., patient tumor T16 displayed intratumor genetic heterogeneity, where differences in gene amplicons for *EGFR* and *MDM2* were detected in different tissue fragments dissected from the tumor core (Fig. 2e). Yet another fragment carrying *MDM4* and *EGFR* amplification with *Δ25−27* structural variant generated the initial 3D organoids and was further propagated in vivo over subsequent passages. This was similar for PDOXs T341, P8 and T158 (Supplementary Fig. 2e, g, Supplementary Table 3, online resource). These changes are most likely caused by tissue sampling bias and selection of specific subclones upon engraftment. Occasionally, we observed acquisition of additional glioma-specific CNAs in later generations (e.g., +Chr16 and −Chr 6 in PDOX T101 G6, Supplementary Fig. 2c, online resource; -1p21.1-p31.2 in PDOX P13, Supplementary Fig. 2i, online resource) in line with continuous tumor evolution over time. Of note, these rare events occurred in individual tumors and always represented known genetic aberrations in gliomas. We did not detect common genetic modifications across the cohort which could be linked to tumor growth in the mouse microenvironment, as has been suggested for subcutaneous PDX [7]. Loss or acquisition of new aberrations was much more common in cultured GSC lines (Fig. 2e, Supplementary Fig. 2g–i, Supplementary Table 3, online resource), including loss of *EGFR* gene amplification and protein expression (Supplementary Fig. 2j, online resource), as noted previously [66].

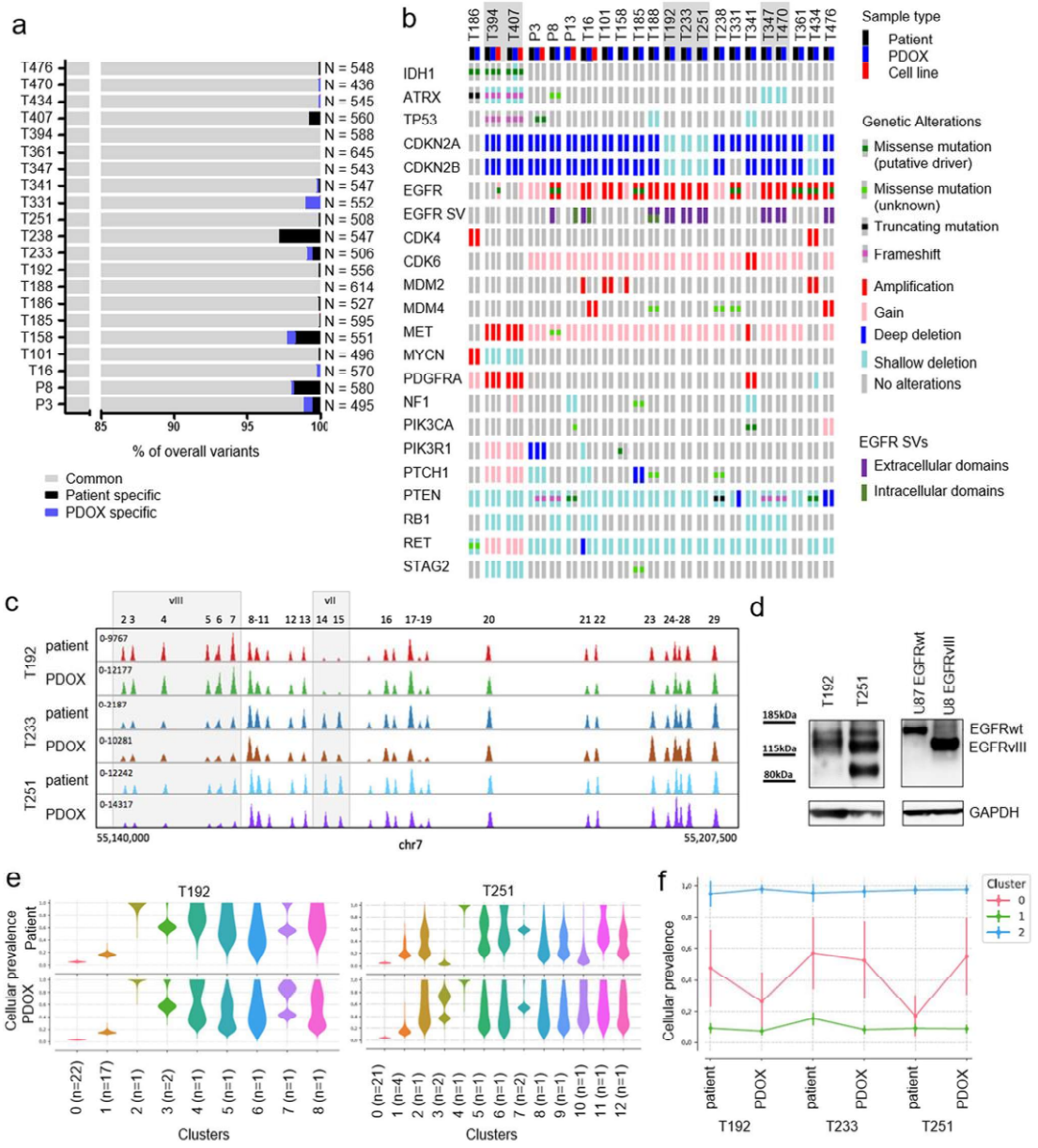

PDOXs recapitulate glioma driver mutations and genetic heterogeneity

To further assess the mutational content and clonal architecture of patient tissues and matching organoids and PDOXs, we applied targeted DNA sequencing to identify rare variants in disease associated genes using an extended glioma-specific diagnostic panel (up to 234 genes) [85]. Overall the PDOX models showed excellent recapitulation of the genetic variants identified in the patient tumors (Fig. 3a, b). The rare differences were mainly due to variants detected in patient tumors, but not in PDOXs tissues. These 'lost' variants were situated within chromosome regions deleted in the tumor and often had an allele frequency < 50 % (Supplementary Table 4, online resource), suggesting that these were germline variants with allelic loss in the tumor and

◂**Fig. 3** Recapitulation of DNA mutations and structural variants in PDOXs. **a** Recapitulation of overall variants determined by targeted sequencing. PDOXs were compared to respective patient tumors. The number of total variants detected for each patient tumor and PDOXs is displayed. **b** Summary of glioma specific somatic alterations including copy-number changes and mutations in patients and their derivative preclinical models. Samples highlighted in gray represent longitudinal PDOXs. **c** Example of longitudinal GBM samples (T192-T233-T251) of patient LIH0192 showing altered clonal distribution of *EGFR* structural variant *vII* to *vIII* upon relapse, which is recapitulated in the respective PDOXs. Distinct *EGFR* genomic regions deleted in respective variants are depicted. **d** Western blot against EGFR (cocktail antibody recognizing wild-type (wt) and structural variants) confirms protein expression of EGFRwt as well as the respective structural variants *EGFRvII* (in T192) and *vIII* (in T251) with decreased molecular weight. U87 cells overexpressing EGFRwt and EGFR*vIII* are shown for size reference. **e** Cellular prevalence estimates from PyClone representing clonal populations detected in longitudinal patient tumors and respective PDOXs. Examples shown for T192 and T251. Each cluster of mutations was computationally inferred to reflect a subclone. Number of genetic variants contributing to each clone is depicted. **f** Cellular prevalence estimates from PyClone representing clonal subpopulations detected in longitudinal patient LIH0192 and its respective PDOXs. Each line represents a cluster of mutations computationally inferred to reflect a subclone. Only genetic variants detected in all samples were considered for analysis

likely originate from normal human tissue (TME) present in the patients tumor, but not in the PDOX models. Only a handful of genetic variants private to PDOXs were detected and nearly all were located in noncoding regions (Fig. 3a, Supplementary Table 4, online resource). In comparison, PDOX-derived cell lines showed acquisition of further new variants in cultures (Supplementary Fig. 3a, online resource).

Targeted sequencing confirmed identified copy-number alterations and further revealed specific mutations characteristic for gliomas (Fig. 3b, Supplementary Table 5, online resource). Assessed IDH1mut gliomas (PDOX and parental tumor) carried mutations in *ATRX* and *TP53* genes, in line with the molecular diagnosis of astrocytomas obtained by CpG methylation profiling [20] (Fig. 1b). Digital PCR confirmed the presence of wild-type and *R132H* mutated *IDH1* alleles in PDOXs, although variations in ratio were observed probably due to TME signal in patient tumors and tumor aneuploidy (Supplementary Fig. 3b, online resource). In line with previous reports [68, 88], in vitro GSC cultures drastically reduced *IDH1* wild-type allele frequency in T394NS, i.e., cells had lost wild-type *IDH1* by passage 10, whereas T407NS retained still 20% of the wild-type *IDH1* allele at passage 13. This was combined with an acquisition of several new variants (Supplementary Fig. 3a, online resource). IDHwt GBM PDOXs retained common glioma mutations, including *EGFR, MDM4, PTEN*, *PIK3CA,* and *PTCH1* (Fig. 3b). One PDOX (P13) carried an *IDH2* missense mutation *(W244R)* of unknown significance, which has been described in the normal population (rs780131378) and is probably a rare private germline variant. It was not associated with increased 2HG production (Supplementary Table 5, online resource), and thus the tumor was considered as IDHwt. The *EGFR* gene status was remarkably well preserved in the PDOXs. *EGFR* point mutations were detected in the extracellular domain (*A289T, G598V, F254I, R108K*), and co-occurred with *EGFR* amplification. *EGFR* structural variants were present in the extracellular and/or intracellular domains, such as *Δ2-7 (EGFRvIII), Δ2-15, Δ6-7, Δ14-15 (EGFRvII),* and *Δ25-27* (Supplementary Table 5, online resource). Notably, in agreement with a previous report [9], PDOX P8 displaying *EGFR A289T* was one of the most invasive and proliferative GBM.

In general, our matched longitudinal models retained similar coding variants upon recurrence (Fig. 3b). Interestingly, LIH0192 patient tumor underwent heterogeneous complex structural rearrangements leading to a shift from *EGFRvII to EGFRvIII* upon relapse. These changes led to different EGFR protein expression and were retained in the respective PDOXs (Fig. 3c, d). LIH0347 patient-derived longitudinal PDOXs retained *EGFRΔ*2-15, which also showed immunoreactivity to EGFRvIII antibodies (Supplementary Fig. 3c, online resource).

We further used PyClone to follow the clonal dynamics upon engraftment of patient tissues and were able to demonstrate that PDOXs retain genetic heterogeneity at the subclonal level (Fig. 3e, Supplementary Fig. 3d, online resource). Subclonal fractions were also retained in longitudinal models of patients LIH0192 and LIH0347, although certain fluctuations in cellular prevalence were observed (Fig. 3f, Supplementary Fig. 3e, online resource). Interestingly, we also observed evolutionary dynamics in *EGFR* amplicons (Supplementary Fig. 3f, online resource), arising most probably from evolutionary trajectories of extrachromosomal double minutes [35]. In summary, glioma PDOXs largely recapitulate genetic aberrations and genetic heterogeneity of the parental tumors. Rare newly acquired genetic features in PDOXs recapitulate glioma mutations known in patients, suggesting that growth of human tumors in the rodent brain can serve as a proxy for ongoing genetic evolution in the brain microenvironment. This is in contrast to in vitro passaging of glioma cells which regularly leads to additional genetic aberrations which are not glioma specific.

Tumor intrinsic epigenetic profiles are preserved in PDOXs

Cancer-specific DNA methylation patterns are important drivers of gene expression and have been recognized as a preferred prognostic biomarker used for brain tumor subtyping [20, 22, 79]. Correlation analysis and principal component analysis (PCA) based on EPIC and 450K Illumina DNA methylation arrays showed an overall good

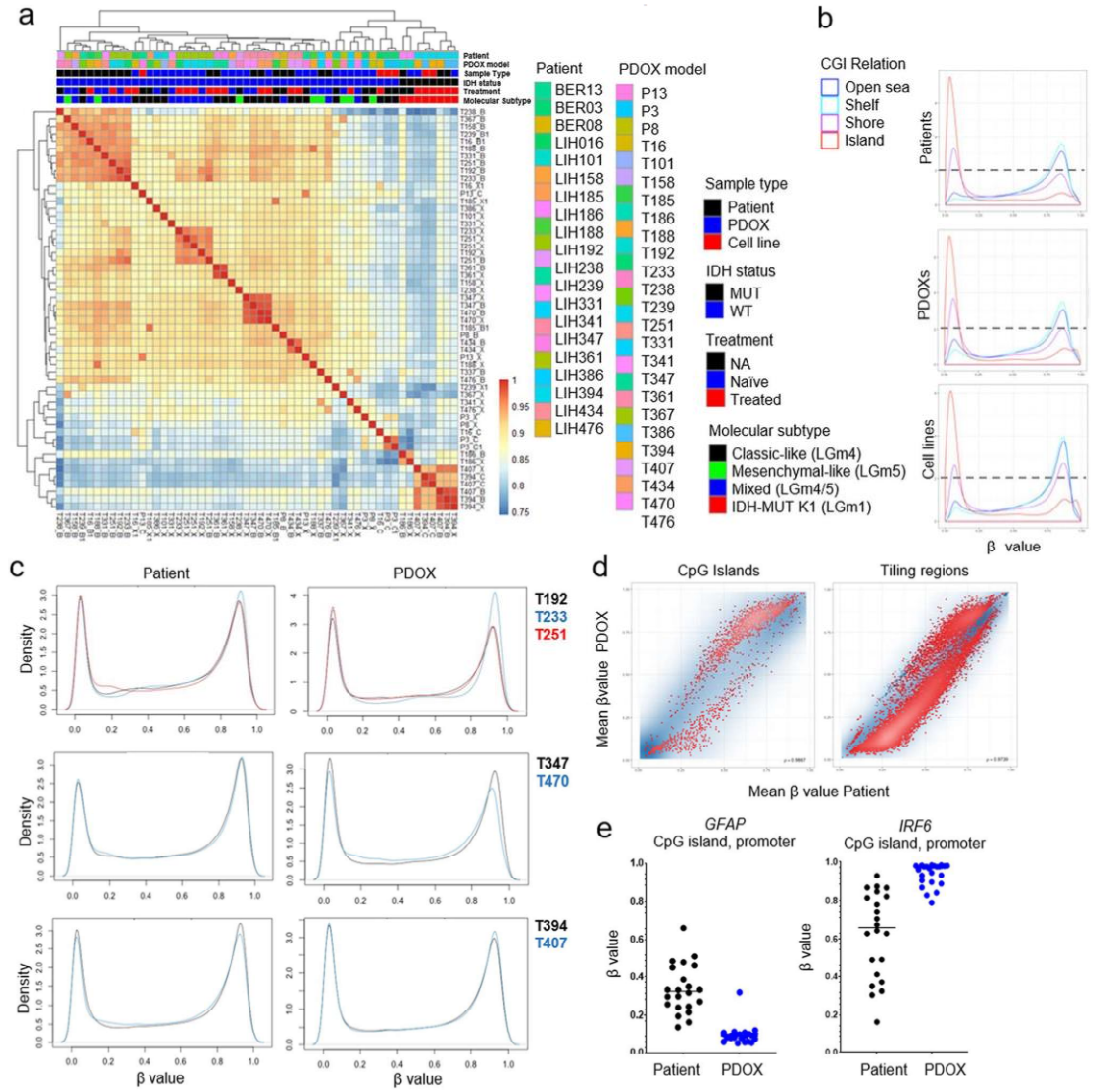

Fig. 4 DNA methylation profiling. **a** Pearson correlation of DNA methylation profiles between glioma patient samples, PDOXs and cell lines derived thereof based on 450 k and EPIC arrays (B, patient; X, PDOX; C, cell line, overlapping regions between arrays only). For statistics see Supplementary Fig. 4a, online resource. **b** Global beta-value distributions are very similar between patient samples and PDOXs. Cell lines displayed an increased DNA methylation at open sea, shelf, and shore regions. **c** Beta-value distributions are very similar upon tumor recurrence and are recapitulated in corresponding PDOXs. Examples are shown for longitudinal samples of patients LIH0192, LIH0347, and LIH0394, the latter being IDH1mut. **d** Mean beta-value distribution in patients and PDOXs show increased methylation in a subset of CpG islands and decreased methylation of tiling regions in PDOXs. CpG sites with FDR < 0.05 are displayed in red, remaining probes are shown in blue. **e** Examples of hypo- and hypermethylated CpG islands in PDOXs. *GFAP* is widely expressed in GBM, whereas *IRF6* is involved in innate immune response. Differentially methylated sites are changing from hemi-methylated in patient tumors to either unmethylated (*GFAP*) or methylated (*IRF6*) status in PDOXs

correlation between patient tumors and PDOXs (Fig. 4a, Supplementary Fig. 4a, online resource), where samples clustered based on IDH status. Although sample type also contributed to the source of variation in the cohort, the IDH status was the main source of variation (Supplementary Fig. 4b, online resource). IDH1mut gliomas displayed

divergent DNA methylation of specific CpG islands compared to IDHwt gliomas (Supplementary Fig. 4c, online resource). Yet, G-CIMP-low subtype dominated our IDH-1mut patient tumors and PDOXs (Supplementary Table 6, online resource), presumably in line with their increased aggressiveness [33]. The beta-value distributions were very similar between PDOXs and parental tumors, whereas GSC lines displayed increased DNA methylation at open sea, shelf, and shore genomic regions (Fig. 4b). This was supported by PCA analysis showing a lower similarity of GSC lines to patient tumors in comparison to PDOXs (Supplementary Fig. 4a, online resource). This was true for IDH1wt and mutated cell lines (Supplementary Fig. 4a, d, online resource). Importantly, the *MGMT* promoter DNA methylation status was preserved between PDOX and parental tumor in all but two PDOXs (Supplementary Table 6, online resource). Global DNA methylation profiles based on beta-value distributions were also well preserved in longitudinal glioma samples between each other and with their respective PDOXs. Overall, most tumors retained the same DNA methylation profile upon recurrence (Fig. 4c), including *MGMT* promoter methylation status (Supplementary Table 6, online resource), although differences at individual CpG sites are possible.

Statistical analysis of paired methylation profiles revealed only minor changes between patient tumors and respective PDOXs (Limma, FDR < 0.01). Only 35 individual CpG sites showed differences in mean methylation beta values above 0.4, corresponding to an essential switch in DNA methylation status, but none were gene annotated CpGs. A partial change of DNA methylation levels (beta value difference 0.2–0.4) was observed at CpG sites of 226 CpG islands, 89 promoters, 74 gene bodies and 943 tiling regions. Most sites that were demethylated in PDOX corresponded to tiling regions that changed from hemi- to unmethylated (894/943, Fig. 4d), pointing towards global hypomethylation characteristic for high-grade glioma [22]. This was also true for certain gene promoters specific to GBM cells (e.g., *GFAP*, Fig. 4e). An increase towards fully methylated CpG sites was observed typically at CpG islands (196/226, Fig. 4d), including promoters of genes expressed classically by the TME (e.g., *IRF6* for immune cells, Fig. 4e), reflecting the impact of non-neoplastic cells on methylation profiling [56]. Accordingly, the molecular classification based on previously defined DNA methylation classes [20, 22, 33] was well retained in PDOXs (Fig. 4a, Supplementary Table 6, online resource). Class switches between patient and PDOX occurred from mesenchymal-like to classic-like tumors (LGm5 to LGm4, mesenchymal to RTK II class, Supplementary Table 6, online resource), in line with the influence of the TME on DNA methylation profiles as has also been shown for gene expression signatures [112]. GSC cell lines displayed more divergent DNA methylation profiles with increased DNA methylation levels (Fig. 4a, b) and were not clearly classified (Supplementary Table 6, online resource). Although we did not detect a link between treatment history of patient tumors and molecular subtypes, more data will be required in the future to perform meaningful statistical analyses.

Gene expression analysis reveals close resemblance between patient tumors and PDOXs

To determine to what extent gene expression profiles of parental tumors are retained in glioma PDOXs, we performed genome-wide transcript analysis using human-specific microarrays (Fig. 5a). In parallel, we analyzed cell cultures and corresponding intracranial xenografts from GSC (NCH421k, NCH644) and adherent cell lines (U87, U251). Unsupervised hierarchical cluster and PCA analyses revealed close resemblance of PDOXs to corresponding patient tumors, although higher similarity of samples of the same type was observed (Fig. 5a, Supplementary Fig. 5a, online resource). Cell lines and their xenografts were more dissimilar and clustered according to their origin, in line with a higher cellular selection and adaptation in long term in vitro cultures. Transcriptomic profiles of PDOXs also displayed strongest similarity to GBMs from the TCGA cohort [19] (Supplementary Fig. 5b, online resource). Analysis of transcriptomic subtypes revealed differences when using the original molecular signatures proposed by Verhaak et al. [107]. However, with the recent tumor-intrinsic classification aimed at reducing the influence of TME [112], the subtyping remained constant (Supplementary Table 7, online resource), suggesting that transcriptomic differences between patient tumors and PDOXs arise from TME-associated gene expression. Cell lines retained transcriptomic subtypes were retained upon in vivo growth. Analysis of differentially expressed genes between PDOXs and parental tumors (2-way ANOVA, FDR<0.01, absFC≥2) revealed an increase in tumor intrinsic signals such as cell cycle and DNA repair (Fig. 5b), which was most prominent in highly proliferative PDOXs (P3, P8, P13, Fig. 5c). Genes downregulated in PDOXs were associated with TME processes, i.e., immune response, angiogenesis and macrophage activation (Fig. 5b, c). Specific markers of human TME components such as endothelial cells (*VWF, KDR*), microglia/macrophages (*ITGAX, AIF1, CD68*), pericytes/vascular smooth muscle cells (*PDGFRB, ACTA2*) and hematopoietic cells (*CTLA4, CD4, PTPRC*) were depleted in PDOXs (Fig. 5c). This included also *ABCB1* and *ABCG2,* which we have previously shown to be restricted to brain endothelial cells in human GBM [47]. The general depletion of human TME transcriptome upon xenografting was confirmed by independent component analysis (Fig. 5d) and flow cytometry (Fig. 5e). Interpatient differences were retained in PDOXs,

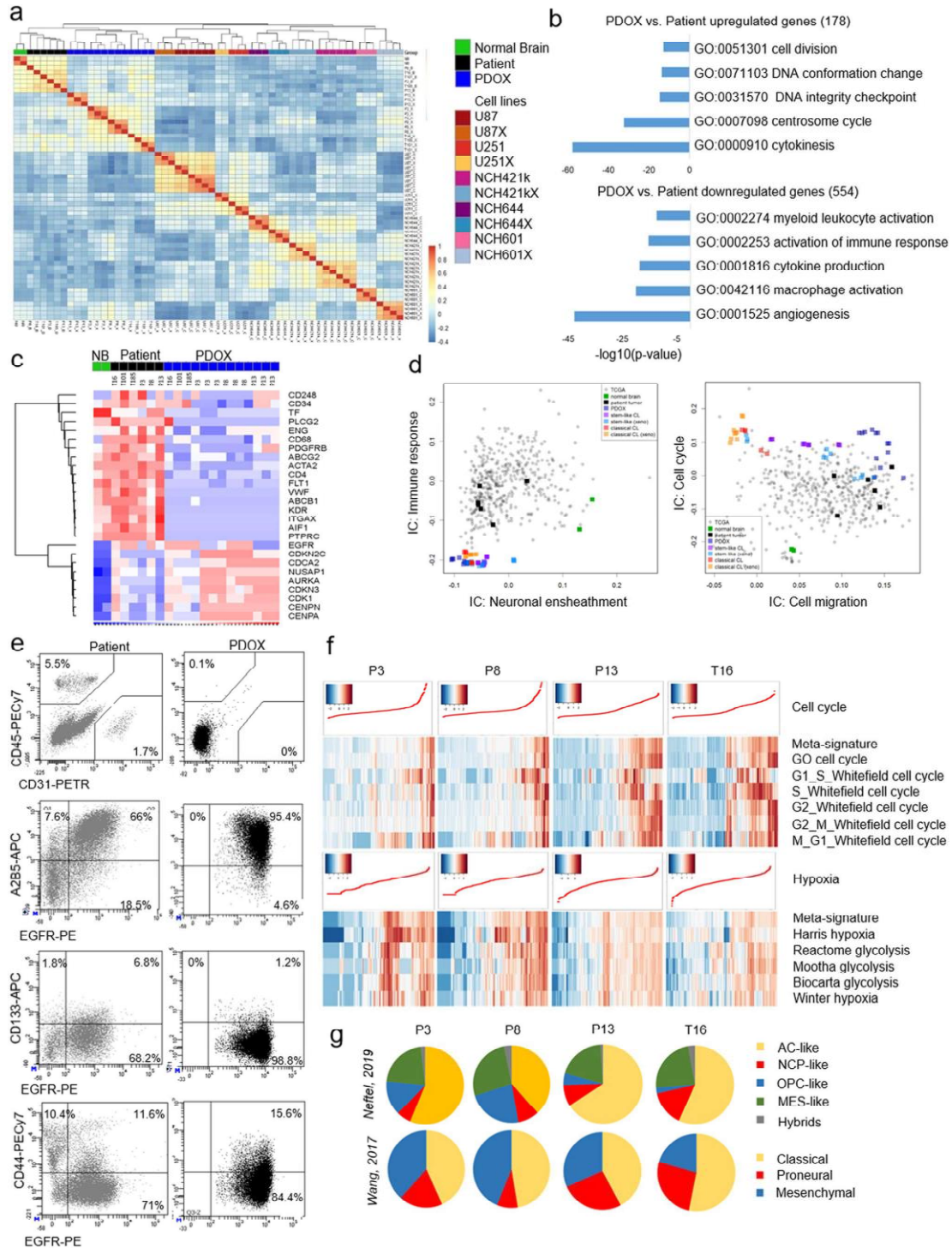
a
Normal Brain
Patient
PDOX
Cell lines
U87
U87X
U251
U251X
NCH421k
NCH421kX
NCH644
NCH644X
NCH601
NCH601X
b
PDOX vs. Patient upregulated genes (178)
GO:0051301 cell division
GO:0071103 DNA conformation change
GO:0031570 DNA integrity checkpoint
GO:0007098 centrosome cycle
GO:0000910 cytokinesis
PDOX vs. Patient downregulated genes (554)
GO:0002274 myeloid leukocyte activation
GO:0002253 activation of immune response
GO:0001816 cytokine production
GO:0042116 macrophage activation
GO:0001525 angiogenesis
-log10(p-value)
c
NB
Patient
PDOX
CD248
CD34
TF
PLCG2
ENG
CD68
PDGFRB
ABCG2
ACTA2
CD4
FLT1
VWF
ABCB1
KDR
ITGAX
AIF1
PTPRC
EGFR
CDKN2C
CDCA2
NUSAP1
AURKA
CDKN3
CDK1
CENPN
CENPA
d
IC: Immune response
IC: Neuronal ensheathment
IC: Cell cycle
IC: Cell migration
e
Patient
PDOX
CD45-PECy7
CD31-PETR
5.5%
1.7%
0.1%
0%
A2B5-APC
EGFR-PE
7.6%
66%
18.5%
0%
95.4%
4.6%
CD133-APC
EGFR-PE
1.8%
6.8%
68.2%
0%
1.2%
98.8%
CD44-PECy7
EGFR-PE
10.4%
11.6%
71%
15.6%
84.4%
f
P3
P8
P13
T16
Cell cycle
Meta-signature
GO cell cycle
G1_S_Whitefield cell cycle
S_Whitefield cell cycle
G2_Whitefield cell cycle
G2_M_Whitefield cell cycle
M_G1_Whitefield cell cycle
Hypoxia
Meta-signature
Harris hypoxia
Reactome glycolysis
Mootha glycolysis
Biocarta glycolysis
Winter hypoxia
g
P3
P8
P13
T16
Neftel, 2019
AC-like
NCP-like
OPC-like
MES-like
Hybrids
Wang, 2017
Classical
Proneural
Mesenchymal

◂**Fig. 5** Transcriptomic profiles and intratumoral heterogeneity. **a** Pearson's correlation indicating similarity of genome-wide gene expression profiles between normal human brain, glioma patient samples, PDOXs, GSC lines (NCH421k, NCH644) and classical glioma lines (U87, U251) grown in vitro or as xenograft ('X'). Human specific arrays were applied for transcriptome analysis. **b** Summary of main GO terms characterizing genes differentially present in PDOXs (FRD ≤ 0.01, ab(FC) ≥ 2, Limma). **c** Heatmap representing gene expression levels for a selection of classical TME and cell cycle markers in normal brain (NB), patients and respective PDOXs. **d** Independent component analysis showing depleted transcriptomic signals associated with immune response and neuronal ensheathment in PDOXs and cell lines. Cell cycle independent component (IC) was the highest in PDOXs and cell lines, cell migration-associated IC was the highest in patients and PDOXs. **e** Flow cytometric analysis to detect human cell subpopulations in patient samples and respective PDOXs. Examples are shown for PDOX T331 expressing EGFR in tumor cells. **f** Single cell signatures showing the presence of human tumor cells in distinct phases of cell cycle and hypoxic gradient in PDOXs. **g** Assessment of GBM cellular states [77] and TCGA GBM subtypes [112] at single cell level in PDOX tumor cells

e.g., *EGFR* expression was maintained at similar levels as in patients (Fig. 5c). We did not detect an upregulation of specific molecular pathways linked to stemness (i.e., cancer stem-like profiles), confirming the lack of a particular selection for tumor subpopulations. Indeed, the heterogeneous expression of stem cell markers in GBM, as previously reported [36], was retained in the respective PDOXs (Fig. 5e) and remained largely stable over serial transplantations (Supplementary Fig. 5c, online resource). Transcriptomic analysis at the single cell level revealed similar proportions of cycling cells and the presence of a hypoxic gradient in PDOX (Fig. 5f) as shown for GBM patients [81]. PDOXs also recapitulated intratumoral heterogeneity and phenotypic cellular states previously described in GBM patients [77, 112] (Fig. 5g). Mouse-derived TME, which replaced human TME, showed similar cellular subpopulations as detected in patient tumors including microglia/macrophages, oligodendrocyte progenitor cells (OPCs) and astrocytes comparable to human GBM TME [31] (Supplementary Fig. 5d, online resource). In conclusion, our data show that glioma PDOXs recapitulate well tumor-intrinsic transcriptomic profiles. Differences in gene expression signatures at the bulk level can be explained by the replacement of the human TME by mouse cells undergoing GBM-specific adaptation.

Preclinical drug testing in PDOX-derived standardized 3D glioma organoids provides clinically relevant outcomes

The PDOX cohort described above constitutes a living biobank maintained by serial transplantation of organoids obtained through mechanical cutting of tumor tissue. This allows to expand the patient tumor in its natural brain microenvironment, generating sufficient material for large scale preclinical drug testing. To this aim, we standardized the derivation of uniform GBM organoids amenable for reproducible drug screening. Organoids were generated from 1000 MACS-purified single tumor cells obtained from PDOXs, which were able to self-organize into 3D organoids within 72h in nonadherent conditions (Fig. 6a). This allowed for sensitive evaluation of cell viability and toxicity in a 384-well plate format (Supplementary Fig. 6a, online resource), similar to protocols described for other types of cancer organoids [44]. To assess whether PDOX-derived organoids recapitulate known mechanisms of drug sensitivity and achieve clinically relevant responses, we subjected a cohort of 18 GBM PDOXs to temozolomide (TMZ), the standard DNA-alkylating agent in clinical practice. Cell responses were calculated as the Area Under the Curve (AUC). In accordance with clinical data, GBM organoids showed only a partial response to TMZ (AUC 200-600, Fig. 6a, b, Supplementary Fig. 6b, online resource). Importantly, tumors with a methylated *MGMT* promoter appeared less resistant in comparison to *MGMT* promoter-unmethylated GBMs (Fig. 6c, Supplementary Fig. 6b, online resource). No differential response was observed between treatment-naïve organoids and organoids derived from patients previously exposed to chemoradiotherapy (Supplementary Fig. 6c, online resource).

Dianhydrogalactitol (VAL-083) exhibits strong efficacy against GBM independent of (epi)genetic background and treatment history

We further tested dianhydrogalactitol (VAL-083), a bifunctional compound able to alkylate N^7-guanine and form interstrand crosslinks and DNA double strand breaks [117]. VAL-083 is known to penetrate the blood–brain barrier and to accumulate in the cerebrospinal fluid and brain parenchyma [39]; it is currently tested in clinical trials for recurrent GBM (NCT02717962) as well as for treatment-naïve *MGMT* promoter unmethylated GBM patients (NCT03050736). In our cohort, VAL-083 was significantly more effective than TMZ (Fig. 6a, b) and the response was not dependent on *MGMT* promoter methylation status (Fig. 6c). The response was similar in treatment-naïve and relapsed organoids (Supplementary Fig. 6c, online resource), suggesting that VAL-083 is able to overcome TMZ resistance. In view of the strong efficacy of VAL-083 in the ex vivo assay we evaluated its ability to decrease tumor growth in vivo. Due to the structural similarity with glucose, we hypothesized that uptake of VAL-083 could be further enhanced under hypoxia; we therefore also applied a combination treatment with the antiangiogenic agent Bevacizumab previously shown to induce hypoxia in GBM [1, 53]. As expected, Bevacizumab treatment

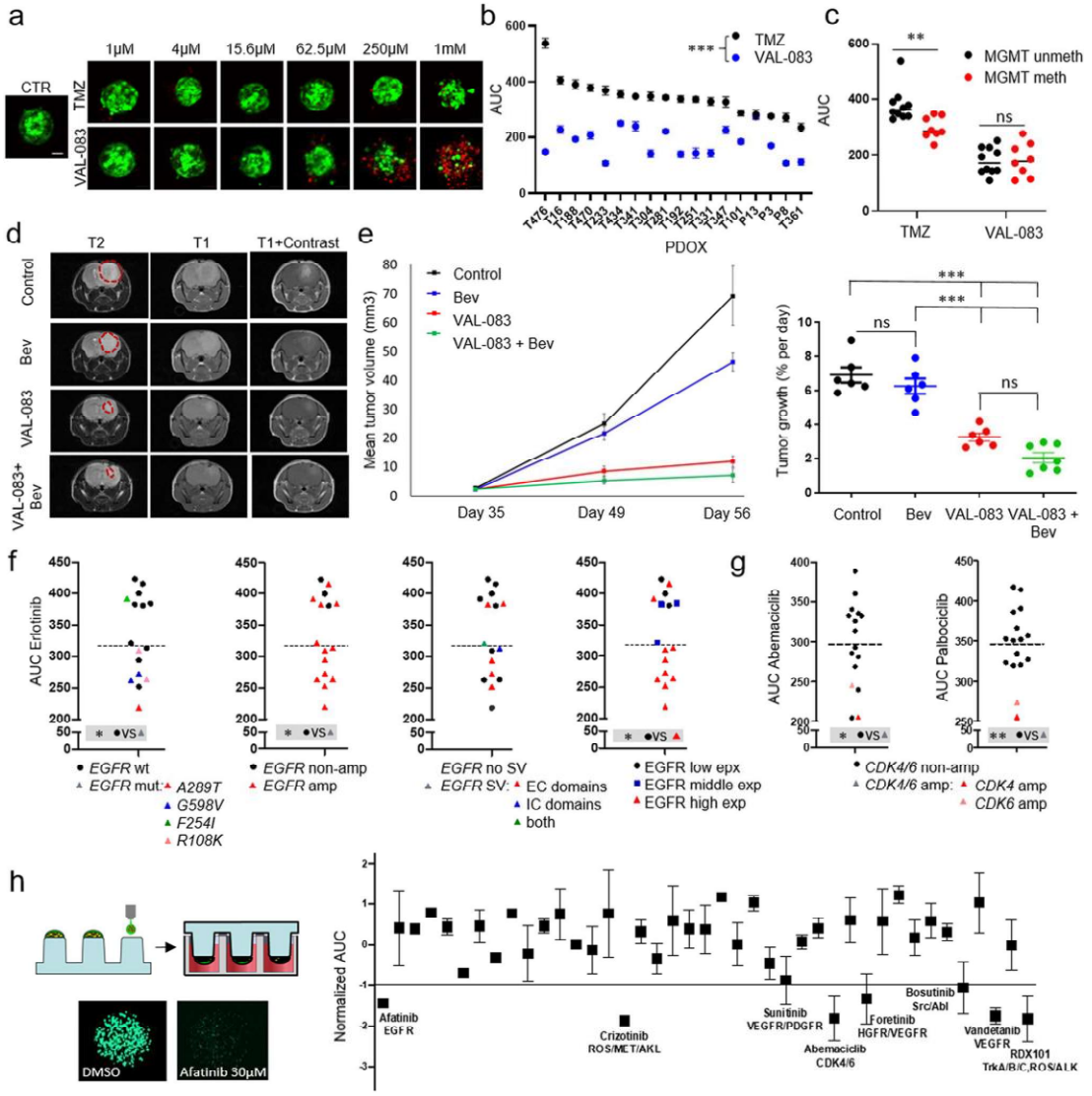

did not halt tumor progression despite decreased contrast enhancement on MRI (Fig. 6d) and blood vessel normalization (Supplementary Fig. 6d, online resource). VAL-083 monotherapy led to a dramatic reduction in tumor growth (Fig. 6e), an effect which was only mildly accentuated by combined treatment. Histological assessment of tumor-containing brains confirmed the strong reduction in tumor volume upon VAL-083 treatment (Supplementary Fig. 6e, online resource). This was paralleled by an increase in DNA damage in tumor cells, determined by H2AX phosphorylation (H2AX-P) (Supplementary Fig. 6f, online resource). Limited H2AX-P was also seen in normal brain cells close to the meninges and the subventricular zone, but to a much lower extent than in tumor cells. In summary, we show that VAL-083 has a consistently favorable drug profile against GBM; thus, representing a promising candidate for GBM treatment either alone or in combination with antiangiogenic compounds.

◂**Fig. 6** Drug response assessment in glioma organoids and PDOXs. **a** Drug response was evaluated in PDOX-derived organoids with standardized size (green, viable; red, dead cells). Representative images are shown for TMZ and VAL-083 treatment of T434-derived organoids. Scale bar = 50 µm. **b** Quantification of AUC upon exposure to TMZ and VAL-083. Mean AUC ± SEM is shown for each model. Experiment was performed once with three technical replicates per PDOX per drug concentration. VAL-083 is generally more effective in PDOX-derived organoids in comparison to TMZ (***$p_{value} < 0.001$, unpaired *t* test). **c** Mean AUC upon exposure to TMZ and VAL-083 in *MGMT* promoter methylated and unmethylated tumors. Tumors with methylated *MGMT* promoter show enhanced response to TMZ, while response to VAL-083 is independent of the *MGMT* promoter status (**$p_{value} < 0.01$, unpaired *t* test). **d** PDOX T16 treated *in vivo* with VAL-083, Bevacizumab or a combination. Tumor progression was assessed by T1-weighted and T2-weighted MRI images ($n = 6$–7 mice per group) prior treatment (day 35) and post treatment (day 49 and 56 equivalent of 14 and 21 days since beginning of treatment respectively). **e** Assessment of tumor progression over time reveals significant reduction of tumor growth upon VAL-083 treatment. Tumor growth rate between treatment groups was calculated during the entire study (day 35 vs. day 56, $n = 6$–7, ***$p_{value} < 0.001$, **$p_{value} < 0.01$, ANOVA with Tukey's Multiple Comparison Test). **f** Quantification of AUC upon exposure to EGFR inhibitor Erlotinib showing higher sensitivity in *EGFR* mutated tumors (vs EGFR wild type) and in EGFR amplified tumors (vs EGFR nonamplified). This is also recapitulated at the level of EGFR protein expression. No significant effect is seen for tumors with or without EGFR variants. (*$p_{value} < 0.05$, unpaired *t* test); wt, wild type; mut, mutated; Amp, amplified; SV, structural variant; EC, extracellular domains; IC, intracellular domains; exp, expression. **g** Quantification of AUC upon exposure to CDK4/6 inhibitors Palbociclib and Abemaciclib shows higher sensitivity of *CDK4* and *CDK6* amplified tumors (vs nonamplified tumors). (*$p_{value} < 0.05$, **$p_{value} < 0.01$, unpaired *t* test). For **f–g** experiments were performed twice with 3 technical replicates each. See Supplementary Table 8 for mean AUC ± SEM. **h** High-throughput screening with 42 FDA-approved drug library in PDOX T434. Drug response data are displayed as normalized AUC +/−SEM, ($n = 2$), '−1' value is indicated as a threshold for strongest hits

PDOX-derived organoids are amenable to high-throughput drug screening for precision medicine

To evaluate the potential for personalized treatment regimens of our models, we functionally assessed the response against a set of EGFR/ErbB small-molecule tyrosine kinase inhibitors (Erlotinib, Gefitinib, AZD3759, AG490, and Daphtenin) and CDK4/6 inhibitors (Abemaciclib, Palbociclib) with varying specificity in 16 PDOX-derived organoids with variable genetic makeup of these pathways. The inability to preserve gene amplification and *EGFR* structural variants in most cell culture models including GSCs [66], did so far not allow for accurate personalized preclinical studies. Our testing group included GBM with different status of *CDK4, CDK6,* and *EGFR* amplification, *EGFR* genetic variants and point mutations (Fig. 3b, Supplementary Table 5, online resource). The responses against EGFR inhibitors were highly variable across patient organoids (Fig. 6f, Supplementary Fig. 6g, online resource). In contrast to kinase domain mutations found in lung cancer, glioma-specific extracellular domain mutants are known to respond poorly to EGFR inhibitors [64]. Still, we found that GBMs carrying *EGFR* mutations, except for *EGFR F254I* (PDOX T434), were more sensitive to Erlotinib and AZD3759, but not to the other EGFR inhibitors, Gefitinib, AG490 and Daphtenin (Fig. 6f and Supplementary Fig. 6g, online resource). This is in accordance with the fact that *EGFR R108K*, *G598V,* and *A289T* are missense mutations leading to a gain-of-function, shown previously to sensitize tumors to Erlotinib [63]. The role of *EGFR F254I* is currently unclear. *EGFR* amplification and corresponding high protein expression also had an impact on the sensitivity to Erlotinib and AZD3759, where nonamplified tumors with low protein expression were most resistant. EGFR structural variants did not sensitize tumors in our cohort to any of the five compounds. Similarly, tumors carrying *CDK4* (PDOX T434) and *CDK6* (PDOX T341) amplification were most sensitive to CDK4/6 inhibitors Palbociclib and Abemaciclib (Fig. 6g).

Finally, we performed a proof-of-concept study on PDOX-derived organoids for high-throughput drug screening using the cell printing technology based on the ASFA Spotter ST [37]. PDOX T434 derived GBM cells were dispensed onto pillars (1000 cells per pillar), embedded into alginate drops and allowed to reform 3D organoids (Fig. 6h). A library of 42 FDA-approved drugs was then applied for 7 days and response was assessed via a High Content imaging system (CV 8000) recognizing viable cells. To select the strongest hits, we applied normalized AUCs (Z score, − 1 threshold) [64]. The screen showed similar responses as the 384-well plate protocol (Supplementary Fig. 6h, online resource), and confirmed sensitivity of T434 tumor cells to Abemaciclib and resistance to Erlotinib and Gefitinib. Interestingly, it revealed sensitivity to several other inhibitors, including Afatinib,—a second-generation EGFR inhibitor. In summary, we show that PDOX-derived GBM organoids display clinically relevant drug responses and can be applied for personalized drug screening in a high-throughput manner.

Discussion

Although major discoveries can be performed directly on patient tumors, biological material is restricted, generally limiting such studies to descriptive analyses and low-throughput preclinical assays. Here we present a living tumor biobank that encompasses the clinical diversity of high-grade diffuse gliomas. Over 160 organoids and 40 PDOX models were established from treatment-naïve glioma patients and patients that underwent standard-of-care, of which 15 represent paired longitudinal models. Glioma organoids grown in PDOX, combines the generation of a

powerful in vivo model for precision oncology with the expansion of patient tumor material in an appropriate TME setting not possible in vitro. Our PDOX cohort contains tumors of varying genetic and molecular background, and represents a unique tool for drug screening, functional studies and *in vivo* drug efficacy studies. We show that glioma PDOXs recapitulate (1) glioma tissue architecture, including features of angiogenesis and invasion, (2) genetic variants and CNAs, including rare gene amplifications (3) epigenetic and transcriptomic tumor intrinsic signatures, (4) intratumoral genetic, transcriptomic, and stem-cell-associated heterogeneity, (5) clinically relevant drug responses. Our models and associated molecular data are openly shared and available at the PDXFinder portal (https://www.pdxfinder.org/) and via the EurOPDX consortium (https://www.europdx.eu/). They represent a robust tool for reliable expansion of patient tumor material while maintaining close identity with the parental tumors, allowing for high-throughput drug testing and precision medicine.

Most available glioma PDX models are established and maintained through subcutaneous implantation of tumor fragments [21, 106], where the long term impact of a non-brain TME is unclear. Orthotopic GBM xenografts usually rely on single cell dissociation followed by in vitro cultures as GSCs (BTICs) prior to xenotransplantation [21, 35, 49, 52, 108], where cultures are often maintained for unspecified time and passage number. To minimize the loss of tissue architecture and clonal heterogeneity, we use organoids from mechanically minced glioma tissue, only briefly maintained in culture without any in vitro passaging. In order to maintain the heterogeneous nature of the primary tumor within self-organizing organoids, we did not try to achieve indefinite growth of organoids in vitro [49, 51], instead we orthotopic xenografting for tissue expansion and maintenance. We find that most GBMs and lower grade gliomas give rise to short-term organoids. Successful PDOX establishment enriches for high-grade tumors, including IDHwt GBMs and IDH1mut gliomas grades III and IV. This is in concordance with the general selection of aggressive tumors upon PDX generation in different tumor types, including pediatric brain tumors [13]. So far, only a handful of IDH1mut glioma models have been described, which all suffer from poor reproducibility, a long development time and/or changes in *IDH1* status [55, 69, 75, 99, 106, 109]. Successful IDH1mut models in our cohort were defined molecularly as high-grade astrocytomas with abundant chromosomal aberrations, *CDKN2A/B* loss, *ATRX,* and *TP53* mutations and G-CIMP-low signature. These molecular features correspond to the most aggressive IDH1mut gliomas [5, 33, 109]. Importantly, our models retain *R132H IDH1* heterozygosity and efficient production of 2HG [43]. In vitro cultures derived from these tumors either died or led to depletion of the wild-type *IDH1* allele, in line with previous reports [68, 104], suggesting that IDH1mut gliomas require components of the brain microenvironment to maintain their growth. Importantly, our fully annotated cohort displays a wide variety of genetic features not recapitulated in other models (e.g., *EGFR* and *PDGFRA* amplification), thus reflecting the wide interpatient heterogeneity of high-grade gliomas. Our PDOX biobank also contains 15 unique paired models derived from the same patients at initial diagnosis and upon disease relapse.

The recapitulation of histopathological features of gliomas has been challenging with classical serum-grown cell lines, as they largely lose the characteristic invasive potential of diffuse gliomas upon xenotransplantation [28, 71]. Infiltrative growth is maintained in all our PDOXs, although the extent of typical glioma features, including invasion, angiogenesis, and proliferation rate can greatly vary across models, likely reflecting interpatient heterogeneity. We find that prominent angiogenic features along with pseudopalisading necrosis are rare in mice compared to rats, which may arise from differences in brain size and/or in molecular interaction between species. This suggests that for studies addressing aspects of angiogenesis, hypoxia, and blood–brain barrier, rat PDOX models may be more appropriate. Others have also reported gradients of invasive and angiogenic features across GBM xenografts, with limited endothelial proliferation and necrosis in mouse brains [106, 109], while large subcutaneous tumors display extensive angiogenesis [106].

We have previously shown that GBM organoids and corresponding PDOXs faithfully retain tumor cell ploidy [92]. Here we demonstrate that glioma organoids and PDOXs accurately maintain distinct genetic backgrounds of parental tumors, including gene amplifications of *EGFR, PDGFRA, MET, MDM2/4,* and *CDK4/6*, which are difficult to derive and preserve in vitro [66, 88]. PDOXs also recapitulate complex *EGFR* variants and mutations present concomitantly with *EGFR* amplification. At scale, we found that individual genomic profiles are highly conserved in PDOXs. We did not detect major divergences in CNAs as reported for subcutaneous GBM PDXs [7]. The difference in results may be related to the subcutaneous transplantation, which may lead to a different tumor evolution than in the brain. Alternatively, it may be due to differences in data analysis, since array-CGH based CNA determination, employed by us, is known to be more accurate than CNAs inferred from gene expression profiles [115]. We further observed extensive preservation of genetic intratumoral heterogeneity, although some fluctuations in subclonal architecture were detected. Interestingly, we report a case of *EGFR* variant selection, observed both upon tumor relapse in patients as well as upon xenografting. This may be linked to high levels of *EGFR* amplification and the presence of extrachromosomal double minute structures, which are known to show evolutionary dynamics [35].

In rare cases PDOX models showed engraftment or expansion of specific genetic clones, with distinct gene

amplifications or mutations, differing from the originating tumor. Genomic events that were private to the PDOX correspond to classical glioma aberrations, known to be heterogeneous late events in GBM [54, 96], supporting the notion that the PDOX-dominating clones were a result of original intratumor heterogeneity revealed by sampling and natural glioma evolution over time. In contrast to a previous analysis of subcutaneous PDX [7], we did not detect any recurrent genetic changes across the cohort suggesting that the interaction of human tumor cells with mouse TME does not influence genetic features of the tumor per se. Minor changes in clonal trajectories have also been observed in certain PDX from GBMs [106], brain metastases [101] and other cancers [40, 46]. In this respect, PDOX models can be considered as a proxy for dynamic clonal evolution, which is difficult to measure in patients. We also did not observe major changes in paired longitudinal glioma samples neither in the parental patient tumor nor in the corresponding PDOX, in accordance with limited treatment-induced clonal evolution in diffuse gliomas [5]. We report a case of clonal evolution from *EGFRvII to EGFRvIII,* which was recapitulated in the corresponding PDOXs. Although *EGFRvIII* may be lost upon recurrence, cases with acquisition of this variant were also reported [38, 110]. Interestingly, longitudinal models also retained state-specific intratumoral heterogeneity and genetic subclones, highlighting the notion that these unique matched PDOXs provide an ideal platform to study specific molecular events in initial and recurrent disease side by side. We further show that propagation of GBM cells grown as GSCs *in vitro* leads to a faster genetic drift, including ploidy changes, and acquisition of new CNAs and genetic variants.

At scale tumor-intrinsic epigenetic and transcriptomic profiles of individual tumors were well recapitulated in PDOX. Our PDOX cohort represents diverse molecular subtypes and retains intratumoral heterogeneity and plasticity, in particular, we show that GBM PDOX display cellular state transitions recently described in patient samples [77]. No major molecular changes or selection of cellular subpopulations were detected, except for those related to the replacement of human TME by mouse counterparts. These changes are expected in bulk tissue analyses where methylation and transcriptome profiles are biased by TME-derived signals [56, 112]. In line with the previous reports [6, 88] in vitro cell lines showed increased global DNA methylation levels and more profound changes in transcriptomic profiles.

Limitations of PDOX models include possible interspecies differences at the molecular level and the lack of a complete immune system in immunocompromised animals. While the adaptive immune system is largely absent in these mice, they retain a largely functional innate immune system, including microglia, the brain resident immune effector cells, and peripheral myeloid cells. GBM are largely lymphocyte depleted tumors[102], while microglia and macrophages constitute the major immune component [82]. Here we show that classical glioma TME components such as microglia/macrophages, astrocytes, and OPCs are present in xenografted tumors, indicating that tumor cell interactions with the TME remain active in PDOX. Of note, we observe a similar transcriptomic shift in tumor-associated microglia/macrophages as described in GBM patients [31, 113]. It remains to be determined to what extent these models will be amenable to immunotherapeutic studies targeting tumor-associated microglia/macrophages. Although challenging, adaptation of glioma PDOXs to a humanized background might be possible and/or studies in an immunocompetent context could be performed with PDOX-derived organoids co-cultured with autologous immune cells.

Other drawbacks of patient-derived (orthotopic) xenografts, include high costs, complex logistics and an inherent low-throughput nature. Large-scale in vivo screens are possible; however, they are laborious and require specific statistical settings [46]. Expansion of human gliomas in PDOX and initial drug screens performed on PDOX-derived organoids appears as a good compromise between retention of glioma hallmarks and a cost-effective drug testing pipeline. In contrast to patient-derived short-term cultures and organoids [51, 64], it allows for tumor expansion and in vivo validation. We have developed our protocols to reconstitute 3D organoids of equal size, which allow for reproducible drug testing. Downscaling of cell number per organoid facilitated drug delivery, viability detection, and upscaling to high-throughput screens. These protocols can also be adapted to reintroduce TME components [12] and immune cells. We show that PDOX-derived organoids show clinically relevant responses: (1) organoids with *MGMT* promoter methylation showed higher sensitivity to TMZ, (2) *CDK4/6* amplified organoids responded better to CDK4/6 inhibitors, (3) organoids carrying *EGFR R108K*, *G598V,* and *A289T* gain-of-function mutations were most sensitive to Erlotinib and AZD3759, whereas EGFR low tumors were most resistant. Although EGFRvIII [73] and deletions in the C-terminal domain (Δ25-27/28) were shown to sensitize GBM cells to Erlotinib [25], none of the EGFR structural variants present in our testing group systematically sensitized tumors to any of the EGFR inhibitors. Of note, the tested organoids displayed *PTEN* loss, a known resistance factor leading to dissociation of EGFR inhibition from downstream PI3K pathway inhibition [73]. Remarkably, VAL-083 showed a significantly better response than TMZ against GBMs of different genetic backgrounds and irrespective of *MGMT* status. VAL-083 was able to overcome TMZ resistance in recurrent GBM and its efficacy was confirmed in vivo, with no toxicity observed, lending optimism to ongoing clinical trials.

Overall, our glioma PDOX cohort provides a powerful platform for understanding tumor biology and preclinical treatment interventions at the individual patient level. So

far, the co-clinical use of glioma PDOXs as patient avatars for treatment prediction remains challenging as in most cases the time to establish PDOXs in sufficient quantity required for preclinical drug testing (generation 2-3) takes longer than the survival of most high-grade glioma patients. Instead, PDOXs can play a key role as a preclinical platform in 'mouse clinical trials' [114] for personalized medicine regimens. Organoid cultures are further an excellent tool for high-throughput drug intervention studies at lower cost and can be used directly either established from the patient tumor tissue or from PDOXs. Longitudinal models further constitute a robust tool for the analysis of tumor evolution and resistance mechanisms following targeted or untargeted treatments. By sharing the models and molecular data, we aim to facilitate large collaborative future preclinical trials.

Acknowledgements We are grateful to the Clinical and Epidemiological Investigation Center (CIEC) of the LIH for support in tumor collection, and to Jean-Jacques Gerardy and Nathalie Nicot for technical assistance. We thank the Helmholtz Zentrum München (Research Unit of Molecular Epidemiology/Institute of Epidemiology, German Research Center for Environmental Health, Neuherberg, Germany) for processing the EPIC DNA methylation arrays. We acknowledge the financial support by the Luxembourg Institute of Health, Télévie-FNRS (Grants TETHER n°7.4632.17 and n°7.4615.18), Fondation Cancer Luxembourg (Pan-RTK Targeting), the Luxembourg National Research Fund (FNR; CORE Junior C17/BM/11664971/DEMICS, AFR/14206478 TregBar, INTER/DFG/17/11583046 MechEPI) and the GLIOTRAIN ITN funded by the European Union's Horizon 2020 research and innovation programme under the Marie Skłodowska-Curie grant agreement No 766069 (The material presented and views expressed here are the responsibility of the author(s) only. The EU Commission takes no responsibility for any use made of the information set out). MM would like to thank the Luxembourg National Research Fund (FNR) for the support (FNR PEARL P16/BM/11192868 grant).

Author contribution Conceptualization: AG, A-CH, AO, RB, SPN; methodology: AG, A-CH, AO, DS, AlS, SPN; investigation: AG, A-CH, AO, DS, YAY, ViB, VaB, EK, SB, OK, AlM, ADF, LR, SP, AlM, MM, formal analysis: AG, A-CH, AO, DS, YAY, VN, MW, ArM, TK, PVN, FA, ADF, BF, SP, TA, ArM, PM, HM, TMM, HN, Y-JK, WJ, BK, GT, LFS, resources: AlM, CH-M, AnS, DB, HM, AlS, FH, RB, SPN, supervision: AG, CH-M, BK, LFS, MM, AlS, RB, SPN, writing—original draft: AG, A-CH, SPN, writing—review & editing: all authors.

Compliance with ethical standards

Conflict of interest D Brown is CSO at Delmar Pharmaceuticals, A. Steino was preclinical study manager at Delmar Pharmaceuticals. A Golebiewska and S.P. Niclou received a research grant from Delmar Pharmaceuticals. No potential conflict of interest was disclosed by other authors.

References

1. Abdul Rahim SA, Dirkse A, Oudin A, Schuster A, Bohler J, Barthelemy V et al (2017) Regulation of hypoxia-induced autophagy in glioblastoma involves ATG9A. Br J Cancer 117:813–825. https://doi.org/10.1038/bjc.2017.263
2. Aldape K, Brindle KM, Chesler L, Chopra R, Gajjar A, Gilbert MR et al (2019) Challenges to curing primary brain tumours. Nat Rev Clin Oncol 16:509–520. https://doi.org/10.1038/s41571-019-0177-5
3. Alonso R, Salavert F, Garcia-Garcia F, Carbonell-Caballero J, Bleda M, Garcia-Alonso L et al (2015) Babelomics 5.0: functional interpretation for new generations of genomic data. Nucleic Acids Res 43:W117–121. https://doi.org/10.1093/nar/gkv384
4. Balvers RK, Kleijn A, Kloezeman JJ, French PJ, Kremer A, van den Bent MJ et al (2013) Serum-free culture success of glial tumors is related to specific molecular profiles and expression of extracellular matrix-associated gene modules. Neuro Oncol 15:1684–1695. https://doi.org/10.1093/neuonc/not116
5. Barthel FP, Johnson KC, Varn FS, Moskalik AD, Tanner G, Kocakavuk E et al (2019) Longitudinal molecular trajectories of diffuse glioma in adults. Nature. https://doi.org/10.1038/s41586-019-1775-1
6. Baskaran S, Mayrhofer M, Kultima HG, Bergstrom T, Elfineh L, Cavelier L et al (2018) Primary glioblastoma cells for precision medicine: a quantitative portrait of genomic (in)stability during the first 30 passages. Neuro Oncol 20:1080–1091. https://doi.org/10.1093/neuonc/noy024
7. Ben-David U, Ha G, Tseng YY, Greenwald NF, Oh C, Shih J et al (2017) Patient-derived xenografts undergo mouse-specific tumor evolution. Nat Genet 49:1567–1575. https://doi.org/10.1038/ng.3967
8. Benjamini Y, Hochberg Y (1995) Controlling the false discovery rate: a practical and powerful approach to multiple testing. J R Stat Soc Ser B (Methodol) 57:289–300
9. Binder ZA, Thorne AH, Bakas S, Wileyto EP, Bilello M, Akbari H et al (2018) Epidermal growth factor receptor extracellular domain mutations in glioblastoma present opportunities for clinical imaging and therapeutic development. Cancer Cell 34(163–177):e167. https://doi.org/10.1016/j.ccell.2018.06.006
10. Bjerkvig R, Tonnesen A, Laerum OD, Backlund EO (1990) Multicellular tumor spheroids from human gliomas maintained in organ culture. J Neurosurg 72:463–475. https://doi.org/10.3171/jns.1990.72.3.0463
11. Bonavia R, Inda MM, Cavenee WK, Furnari FB (2011) Heterogeneity maintenance in glioblastoma: a social network. Cancer Res 71:4055–4060. https://doi.org/10.1158/0008-5472.CAN-11-0153
12. Bougnaud S, Golebiewska A, Oudin A, Keunen O, Harter PN, Mader L et al (2016) Molecular crosstalk between tumour and brain parenchyma instructs histopathological features in glioblastoma. Oncotarget 7:31955–31971. https://doi.org/10.18632/oncotarget.7454
13. Brabetz S, Leary SES, Grobner SN, Nakamoto MW, Seker-Cin H, Girard EJ et al (2018) A biobank of patient-derived

pediatric brain tumor models. Nat Med 24:1752–1761. https://doi.org/10.1038/s41591-018-0207-3
14. Brennan CW, Verhaak RG, McKenna A, Campos B, Noushmehr H, Salama SR et al (2013) The somatic genomic landscape of glioblastoma. Cell 155:462–477. https://doi.org/10.1016/j.cell.2013.09.034
15. Butler A, Hoffman P, Smibert P, Papalexi E, Satija R (2018) Integrating single-cell transcriptomic data across different conditions, technologies, and species. Nat Biotechnol 36:411–420. https://doi.org/10.1038/nbt.4096
16. Byrne AT, Alferez DG, Amant F, Annibali D, Arribas J, Biankin AV et al (2017) Interrogating open issues in cancer precision medicine with patient-derived xenografts. Nat Rev Cancer 17:254–268. https://doi.org/10.1038/nrc.2016.140
17. Callari M, Batra AS, Batra RN, Sammut SJ, Greenwood W, Clifford H et al (2018) Computational approach to discriminate human and mouse sequences in patient-derived tumour xenografts. BMC Genomics 19:19. https://doi.org/10.1186/s12864-017-4414-y
18. Campos B, Wan F, Farhadi M, Ernst A, Zeppernick F, Tagscherer KE et al (2010) Differentiation therapy exerts antitumor effects on stem-like glioma cells. Clin Cancer Res 16:2715–2728
19. Cancer Genome Atlas Research N, Weinstein JN, Collisson EA, Mills GB, Shaw KR, Ozenberger BA et al (2013) The Cancer Genome Atlas Pan-Cancer analysis project. Nat Genet 45:1113–1120. https://doi.org/10.1038/ng.2764
20. Capper D, Jones DTW, Sill M, Hovestadt V, Schrimpf D, Sturm D et al (2018) DNA methylation-based classification of central nervous system tumours. Nature 555:469–474. https://doi.org/10.1038/nature26000
21. Carlson BL, Pokorny JL, Schroeder MA, Sarkaria JN (2011) Establishment, maintenance and in vitro and in vivo applications of primary human glioblastoma multiforme (GBM) xenograft models for translational biology studies and drug discovery. Curr Protoc Pharmacol Chapter 14:14–16. https://doi.org/10.1002/0471141755.ph1416s52
22. Ceccarelli M, Barthel FP, Malta TM, Sabedot TS, Salama SR, Murray BA et al (2016) Molecular profiling reveals biologically discrete subsets and pathways of progression in diffuse glioma. Cell 164:550–563. https://doi.org/10.1016/j.cell.2015.12.028
23. Chen S, Zhou Y, Chen Y, Gu J (2018) fastp: an ultra-fast all-in-one FASTQ preprocessor. Bioinformatics 34:i884–i890. https://doi.org/10.1093/bioinformatics/bty560
24. Chen X, Schulz-Trieglaff O, Shaw R, Barnes B, Schlesinger F, Kallberg M et al (2016) Manta: rapid detection of structural variants and indels for germline and cancer sequencing applications. Bioinformatics 32:1220–1222. https://doi.org/10.1093/bioinformatics/btv710
25. Cho J, Pastorino S, Zeng Q, Xu X, Johnson W, Vandenberg S et al (2011) Glioblastoma-derived epidermal growth factor receptor carboxyl-terminal deletion mutants are transforming and are sensitive to EGFR-directed therapies. Cancer Res 71:7587–7596. https://doi.org/10.1158/0008-5472.CAN-11-0821
26. Christensen K, Aaberg-Jessen C, Andersen C, Goplen D, Bjerkvig R, Kristensen BW (2010) Immunohistochemical expression of stem cell, endothelial cell, and chemosensitivity markers in primary glioma spheroids cultured in serum-containing and serum-free medium. Neurosurgery 66:933–947. https://doi.org/10.1227/01.NEU.0000368393.45935.46
27. Cingolani P, Platts A, le Wang L, Coon M, Nguyen T, Wang L et al (2012) A program for annotating and predicting the effects of single nucleotide polymorphisms, SnpEff: SNPs in the genome of Drosophila melanogaster strain w1118; iso-2; iso-3. Fly (Austin) 6:80–92. https://doi.org/10.4161/fly.19695
28. Claes A, Schuuring J, Boots-Sprenger S, Hendriks-Cornelissen S, Dekkers M, van der Kogel AJ et al (2008) Phenotypic and genotypic characterization of orthotopic human glioma models and its relevance for the study of anti-glioma therapy. Brain Pathol 18:423–433. https://doi.org/10.1111/j.1750-3639.2008.00141.x
29. Consortium G (2018) Glioma through the looking GLASS: molecular evolution of diffuse gliomas and the Glioma Longitudinal Analysis Consortium. Neuro Oncol 20:873–884. https://doi.org/10.1093/neuonc/noy020
30. Conte N, Mason JC, Halmagyi C, Neuhauser S, Mosaku A, Yordanova G et al (2019) PDX Finder: a portal for patient-derived tumor xenograft model discovery. Nucleic Acids Res 47:D1073–D1079. https://doi.org/10.1093/nar/gky984
31. Darmanis S, Sloan SA, Croote D, Mignardi M, Chernikova S, Samghababi P et al (2017) Single-Cell RNA-seq analysis of infiltrating neoplastic cells at the migrating front of human glioblastoma. Cell reports 21:1399–1410. https://doi.org/10.1016/j.celrep.2017.10.030
32. de Groot JF, Fuller G, Kumar AJ, Piao Y, Eterovic K, Ji Y et al (2010) Tumor invasion after treatment of glioblastoma with bevacizumab: radiographic and pathologic correlation in humans and mice. Neuro Oncol 12:233–242. https://doi.org/10.1093/neuonc/nop027
33. de Souza CF, Sabedot TS, Malta TM, Stetson L, Morozova O, Sokolov A et al (2018) A distinct DNA methylation shift in a subset of glioma CpG island methylator phenotypes during tumor recurrence. Cell reports 23:637–651. https://doi.org/10.1016/j.celrep.2018.03.107
34. De Witt Hamer PC, Van Tilborg AA, Eijk PP, Sminia P, Troost D, Van Noorden CJ et al (2008) The genomic profile of human malignant glioma is altered early in primary cell culture and preserved in spheroids. Oncogene 27:2091–2096
35. deCarvalho AC, Kim H, Poisson LM, Winn ME, Mueller C, Cherba D, Koeman J, Seth S et al (2018) Discordant inheritance of chromosomal and extrachromosomal DNA elements contributes to dynamic disease evolution in glioblastoma. Nat Genet 50:708–717. https://doi.org/10.1038/s41588-018-0105-0
36. Dirkse A, Golebiewska A, Buder T, Nazarov PV, Muller A, Poovathingal S et al (2019) Stem cell-associated heterogeneity in Glioblastoma results from intrinsic tumor plasticity shaped by the microenvironment. Nature Commun 10:1787. https://doi.org/10.1038/s41467-019-09853-z
37. Doh I, Kwon YJ, Ku B, Lee DW (2019) Drug efficacy comparison of 3D forming and preforming sphere models with a micropillar and microwell chip platform. SLAS Disc Adv Life Sci R & D 24:476–483. https://doi.org/10.1177/2472555218821292
38. Draaisma K, Chatzipli A, Taphoorn M, Kerkhof M, Weyerbrock A, Sanson M et al (2019) Molecular Evolution of IDH wild-type glioblastomas treated with standard of care affects survival and design of precision medicine trials: a report from the EORTC 1542 study. J Clin Oncol. https://doi.org/10.1200/JCO.19.00367
39. Eckhardt S, Csetenyi J, Horvath IP, Kerpel-Fronius S, Szamel I, Institoris L et al (1977) Uptake of labeled dianhydrogalactitol into human gliomas and nervous tissue. Cancer Treat Rep 61:841–847
40. Eirew P, Steif A, Khattra J, Ha G, Yap D, Farahani H et al (2015) Dynamics of genomic clones in breast cancer patient xenografts at single-cell resolution. Nature 518:422–426. https://doi.org/10.1038/nature13952
41. Eskilsson E, Rosland GV, Solecki G, Wang Q, Harter PN, Graziani G et al (2018) EGFR heterogeneity and implications for therapeutic intervention in glioblastoma. Neuro Oncol 20:743–752. https://doi.org/10.1093/neuonc/nox191
42. Evrard YA, Srivastava A, Randjelovic J, Consortium NP, Doroshow JH, Dean DA et al (2020) Systematic establishment of robustness and standards in patient-derived

xenograft experiments and analysis. Cancer Res. https://doi.org/10.1158/0008-5472.CAN-19-3101
43. Fack F, Tardito S, Hochart G, Oudin A, Zheng L, Fritah S et al (2017) Altered metabolic landscape in IDH-mutant gliomas affects phospholipid, energy, and oxidative stress pathways. EMBO Mol Med 9:1681–1695. https://doi.org/10.15252/emmm.201707729
44. Francies HE, Barthorpe A, McLaren-Douglas A, Barendt WJ, Garnett MJ (2019) Drug sensitivity assays of human cancer organoid cultures. Methods Mol Biol 1576:339–351. https://doi.org/10.1007/7651_2016_10
45. Francis JM, Zhang CZ, Maire CL, Jung J, Manzo VE, Adalsteinsson VA et al (2014) EGFR variant heterogeneity in glioblastoma resolved through single-nucleus sequencing. Cancer Discov 4:956–971. https://doi.org/10.1158/2159-8290.CD-13-0879
46. Gao H, Korn JM, Ferretti S, Monahan JE, Wang Y, Singh M et al (2015) High-throughput screening using patient-derived tumor xenografts to predict clinical trial drug response. Nature Med 21:1318–1325. https://doi.org/10.1038/nm.3954
47. Golebiewska A, Bougnaud S, Stieber D, Brons NH, Vallar L, Hertel F et al (2013) Side population in human glioblastoma is non-tumorigenic and characterizes brain endothelial cells. Brain J Neurol 136:1462–1475. https://doi.org/10.1093/brain/awt025
48. Hegi ME, Diserens AC, Gorlia T, Hamou MF, de Tribolet N, Weller M et al (2005) MGMT gene silencing and benefit from temozolomide in glioblastoma. N Engl J Med 352:997–1003. https://doi.org/10.1056/NEJMoa043331
49. Hubert CG, Rivera M, Spangler LC, Wu Q, Mack SC, Prager BC et al (2016) A three-dimensional organoid culture system derived from human glioblastomas recapitulates the hypoxic gradients and cancer stem cell heterogeneity of tumors found in vivo. Cancer Res 76:2465–2477. https://doi.org/10.1158/0008-5472.CAN-15-2402
50. Hulten A, Kerstell J, Larsson J, Olsson R, Svanborg A (1968) A method of calculating the nursing work load. Lakartidningen 65:1683–1686
51. Jacob F, Salinas RD, Zhang DY, Nguyen PTT, Schnoll JG, Wong SZH et al (2020) A Patient-Derived Glioblastoma Organoid Model And Biobank Recapitulates Inter- And Intra-Tumoral Heterogeneity. Cell 180(188–204):e122. https://doi.org/10.1016/j.cell.2019.11.036
52. Joo KM, Kim J, Jin J, Kim M, Seol HJ, Muradov J et al (2013) Patient-specific orthotopic glioblastoma xenograft models recapitulate the histopathology and biology of human glioblastomas in situ. Cell reports 3:260–273. https://doi.org/10.1016/j.celrep.2012.12.013
53. Keunen O, Johansson M, Oudin A, Sanzey M, Abdul Rahim SA, Fack F et al (2011) Anti-VEGF treatment reduces blood supply and increases tumor cell invasion in glioblastoma. Proc Natl Acad Sci USA. https://doi.org/10.1073/pnas.1014480108
54. Kim H, Zheng S, Amini SS, Virk SM, Mikkelsen T, Brat DJ et al (2015) Whole-genome and multisector exome sequencing of primary and post-treatment glioblastoma reveals patterns of tumor evolution. Genome Res 25:316–327. https://doi.org/10.1101/gr.180612.114
55. Klink B, Miletic H, Stieber D, Huszthy PC, Valenzuela JA, Balss J et al (2013) A novel, diffusely infiltrative xenograft model of human anaplastic oligodendroglioma with mutations in FUBP1, CIC, and IDH1. PLoS One 8:e59773. https://doi.org/10.1371/journal.pone.0059773
56. Klughammer J, Kiesel B, Roetzer T, Fortelny N, Nemc A, Nenning KH et al (2018) The DNA methylation landscape of glioblastoma disease progression shows extensive heterogeneity in time and space. Nat Med 24:1611–1624. https://doi.org/10.1038/s41591-018-0156-x
57. Korber V, Yang J, Barah P, Wu Y, Stichel D, Gu Z et al (2019) Evolutionary trajectories of IDH(WT) glioblastomas reveal a common path of early tumorigenesis instigated years ahead of initial diagnosis. Cancer Cell 35(692–704):e612. https://doi.org/10.1016/j.ccell.2019.02.007
58. Koster J, Rahmann S (2018) Snakemake-a scalable bioinformatics workflow engine. Bioinformatics 34:3600. https://doi.org/10.1093/bioinformatics/bty350
59. Kriebel J, Herder C, Rathmann W, Wahl S, Kunze S, Molnos S et al (2016) Association between DNA Methylation in whole blood and measures of glucose metabolism: KORA F4 study. Plos One 11:e0152314. https://doi.org/10.1371/journal.pone.0152314
60. Kristensen BW, Priesterbach-Ackley LP, Petersen JK, Wesseling P (2019) Molecular pathology of tumors of the central nervous system. Ann Oncol. https://doi.org/10.1093/annonc/mdz164
61. Landrum MJ, Lee JM, Benson M, Brown GR, Chao C, Chitipiralla S et al (2018) ClinVar: improving access to variant interpretations and supporting evidence. Nucleic Acids Res 46:D1062–D1067. https://doi.org/10.1093/nar/gkx1153
62. Lee J, Kotliarova S, Kotliarov Y, Li A, Su Q, Donin NM et al (2006) Tumor stem cells derived from glioblastomas cultured in bFGF and EGF more closely mirror the phenotype and genotype of primary tumors than do serum-cultured cell lines. Cancer Cell 9:391–403. https://doi.org/10.1016/j.ccr.2006.03.030
63. Lee JC, Vivanco I, Beroukhim R, Huang JH, Feng WL, DeBiasi RM et al (2006) Epidermal growth factor receptor activation in glioblastoma through novel missense mutations in the extracellular domain. PLoS Med 3:e485. https://doi.org/10.1371/journal.pmed.0030485
64. Lee JK, Liu Z, Sa JK, Shin S, Wang J, Bordyuh M et al (2018) Pharmacogenomic landscape of patient-derived tumor cells informs precision oncology therapy. Nat Genet 50:1399–1411. https://doi.org/10.1038/s41588-018-0209-6
65. Li H, Handsaker B, Wysoker A, Fennell T, Ruan J, Homer N et al (2009) The Sequence alignment/map format and SAMtools. Bioinformatics 25:2078–2079. https://doi.org/10.1093/bioinformatics/btp352
66. Liffers K, Lamszus K, Schulte A (2015) EGFR amplification and glioblastoma stem-like cells. Stem Cells Int 2015:427518. https://doi.org/10.1155/2015/427518
67. Louis DN, Perry A, Reifenberger G, von Deimling A, Figarella-Branger D, Cavenee WK et al (2016) The 2016 world health organization classification of tumors of the central nervous system: a summary. Acta Neuropathol 131:803–820. https://doi.org/10.1007/s00401-016-1545-1
68. Luchman HA, Chesnelong C, Cairncross JG, Weiss S (2013) Spontaneous loss of heterozygosity leading to homozygous R132H in a patient-derived IDH1 mutant cell line. Neuro Oncol 15:979–980. https://doi.org/10.1093/neuonc/not064
69. Luchman HA, Stechishin OD, Dang NH, Blough MD, Chesnelong C, Kelly JJ et al (2012) An in vivo patient-derived model of endogenous IDH1-mutant glioma. Neuro Oncol 14:184–191. https://doi.org/10.1093/neuonc/nor207
70. Macosko EZ, Basu A, Satija R, Nemesh J, Shekhar K, Goldman M et al (2015) Highly parallel genome-wide expression profiling of individual cells using nanoliter droplets. Cell 161:1202–1214. https://doi.org/10.1016/j.cell.2015.05.002
71. Mahesparan R, Read TA, Lund-Johansen M, Skaftnesmo KO, Bjerkvig R, Engebraaten O (2003) Expression of extracellular matrix components in a highly infiltrative in vivo glioma model. Acta Neuropathol 105:49–57. https://doi.org/10.1007/s00401-002-0610-0
72. Meehan TF, Conte N, Goldstein T, Inghirami G, Murakami MA, Brabetz S et al (2017) PDX-MI: minimal information for

patient-derived tumor xenograft models. Cancer Res 77:e62–e66. https://doi.org/10.1158/0008-5472.CAN-17-0582
73. Mellinghoff IK, Wang MY, Vivanco I, Haas-Kogan DA, Zhu S, Dia EQ et al (2005) Molecular determinants of the response of glioblastomas to EGFR kinase inhibitors. N Engl J Med 353:2012–2024. https://doi.org/10.1056/NEJMoa051918
74. Muller F, Scherer M, Assenov Y, Lutsik P, Walter J, Lengauer T et al (2019) RnBeads 2.0: comprehensive analysis of DNA methylation data. Genome biology 20:55. https://doi.org/10.1186/s13059-019-1664-9
75. Navis AC, Niclou SP, Fack F, Stieber D, van Lith S, Verrijp K et al (2013) Increased mitochondrial activity in a novel IDH1-R132H mutant human oligodendroglioma xenograft model: in situ detection of 2-HG and alpha-KG. Acta Neuropathol Commun 1:18. https://doi.org/10.1186/2051-5960-1-18
76. Nazarov PV, Wienecke-Baldacchino AK, Zinovyev A, Czerwinska U, Muller A, Nashan D et al (2019) Deconvolution of transcriptomes and miRNomes by independent component analysis provides insights into biological processes and clinical outcomes of melanoma patients. BMC Med Genomics 12:132. https://doi.org/10.1186/s12920-019-0578-4
77. Neftel C, Laffy J, Filbin MG, Hara T, Shore ME, Rahme GJ et al (2019) An integrative model of cellular states, plasticity, and genetics for glioblastoma. Cell 178(835–849):e821. https://doi.org/10.1016/j.cell.2019.06.024
78. Niclou SP, Danzeisen C, Eikesdal HP, Wiig H, Brons NH, Poli AM et al (2008) A novel eGFP-expressing immunodeficient mouse model to study tumor-host interactions. Faseb J 22:3120–3128. https://doi.org/10.1096/fj.08-109611
79. Noushmehr H, Weisenberger DJ, Diefes K, Phillips HS, Pujara K, Berman BP et al (2010) Identification of a CpG island methylator phenotype that defines a distinct subgroup of glioma. Cancer Cell 17:510–522. https://doi.org/10.1016/j.ccr.2010.03.017
80. Obad N, Espedal H, Jirik R, Sakariassen PO, Brekke Rygh C, Lund-Johansen M et al (2018) Lack of functional normalisation of tumour vessels following anti-angiogenic therapy in glioblastoma. J Cerebral Blood Flow Metabol 38:1741–1753. https://doi.org/10.1177/0271678X17714656
81. Patel AP, Tirosh I, Trombetta JJ, Shalek AK, Gillespie SM, Wakimoto H et al (2014) Single-cell RNA-seq highlights intratumoral heterogeneity in primary glioblastoma. Science 344:1396–1401. https://doi.org/10.1126/science.1254257
82. Pires-Afonso Y, Niclou SP, Michelucci A (2020) Revealing and harnessing tumour-associated microglia/macrophage heterogeneity in glioblastoma. Int J Mol Sci. https://doi.org/10.3390/ijms21030689
83. Reis GF, Pekmezci M, Hansen HM, Rice T, Marshall RE, Molinaro AM et al (2015) CDKN2A loss is associated with shortened overall survival in lower-grade (World Health Organization Grades II-III) astrocytomas. J Neuropathol Exp Neurol 74:442–452. https://doi.org/10.1097/NEN.0000000000000188
84. Roth A, Khattra J, Yap D, Wan A, Laks E, Biele J et al (2014) PyClone: statistical inference of clonal population structure in cancer. Nat Methods 11:396–398. https://doi.org/10.1038/nmeth.2883
85. Sahm F, Schrimpf D, Jones DT, Meyer J, Kratz A, Reuss D et al (2016) Next-generation sequencing in routine brain tumor diagnostics enables an integrated diagnosis and identifies actionable targets. Acta Neuropathol 131:903–910. https://doi.org/10.1007/s00401-015-1519-8
86. Sakariassen PO, Prestegarden L, Wang J, Skaftnesmo KO, Mahesparan R, Molthoff C et al (2006) Angiogenesis-independent tumor growth mediated by stem-like cancer cells. Proc Natl Acad Sci USA 103:16466–16471. https://doi.org/10.1073/pnas.0607668103
87. Seshan VE, A O (2019) DNAcopy: DNA copy number data analysis. R package version 1600
88. Shen Y, Grisdale CJ, Islam SA, Bose P, Lever J, Zhao EY et al (2019) Comprehensive genomic profiling of glioblastoma tumors, BTICs, and xenografts reveals stability and adaptation to growth environments. Proc Natl Acad Sci USA 116:19098–19108. https://doi.org/10.1073/pnas.1813495116
89. Shirahata M, Ono T, Stichel D, Schrimpf D, Reuss DE, Sahm F et al (2018) Novel, improved grading system(s) for IDH-mutant astrocytic gliomas. Acta Neuropathol 136:153–166. https://doi.org/10.1007/s00401-018-1849-4
90. Smyth G (2005) Limma: linear models for microarray data. In: Springer (ed) Bioinformatics and Computational Biology Solutions using R and Bioconductor. New York, pp 397–420
91. Sottoriva A, Spiteri I, Piccirillo SG, Touloumis A, Collins VP, Marioni JC et al (2013) Intratumor heterogeneity in human glioblastoma reflects cancer evolutionary dynamics. Proc Natl Acad Sci USA 110:4009–4014. https://doi.org/10.1073/pnas.1219747110
92. Stieber D, Golebiewska A, Evers L, Lenkiewicz E, Brons NH, Nicot N et al (2014) Glioblastomas are composed of genetically divergent clones with distinct tumourigenic potential and variable stem cell-associated phenotypes. Acta Neuropathol 127:203–219. https://doi.org/10.1007/s00401-013-1196-4
93. Stuart T, Butler A, Hoffman P, Hafemeister C, Papalexi E, Mauck WM 3rd et al (2019) Comprehensive integration of single-cell data. Cell 177(1888–1902):e1821. https://doi.org/10.1016/j.cell.2019.05.031
94. Stupp R, Mason WP, van den Bent MJ, Weller M, Fisher B, Taphoorn MJ et al (2005) Radiotherapy plus concomitant and adjuvant temozolomide for glioblastoma. N Engl J Med 352:987–996. https://doi.org/10.1056/NEJMoa043330
95. Subramanian A, Tamayo P, Mootha VK, Mukherjee S, Ebert BL, Gillette MA et al (2005) Gene set enrichment analysis: a knowledge-based approach for interpreting genome-wide expression profiles. Proc Natl Acad Sci USA 102:15545–15550. https://doi.org/10.1073/pnas.0506580102
96. Szerlip NJ, Pedraza A, Chakravarty D, Azim M, McGuire J, Fang Y et al (2012) Intratumoral heterogeneity of receptor tyrosine kinases EGFR and PDGFRA amplification in glioblastoma defines subpopulations with distinct growth factor response. Proc Natl Acad Sci USA 109:3041–3046. https://doi.org/10.1073/pnas.1114033109
97. Talasila KM, Soentgerath A, Euskirchen P, Rosland GV, Wang J, Huszthy PC et al (2013) EGFR wild-type amplification and activation promote invasion and development of glioblastoma independent of angiogenesis. Acta Neuropathol 125:683–698. https://doi.org/10.1007/s00401-013-1101-1
98. Talevich E, Shain AH, Botton T, Bastian BC (2016) CNVkit: Genome-Wide Copy Number Detection and Visualization from Targeted DNA Sequencing. PLoS Comput Biol 12:e1004873. https://doi.org/10.1371/journal.pcbi.1004873
99. Tateishi K, Nakamura T, Juratli TA, Williams EA, Matsushita Y, Miyake S et al (2019) PI3K/AKT/mTOR pathway alterations promote malignant progression and xenograft formation in oligodendroglial tumors. Clin Cancer Res 25:4375–4387. https://doi.org/10.1158/1078-0432.CCR-18-4144
100. Teschendorff AE, Marabita F, Lechner M, Bartlett T, Tegner J, Gomez-Cabrero D et al (2013) A beta-mixture quantile normalization method for correcting probe design bias in Illumina Infinium 450 k DNA methylation data. Bioinformatics 29:189–196. https://doi.org/10.1093/bioinformatics/bts680
101. Tew BY, Legendre C, Schroeder MA, Triche T, Gooden GC, Huang Y et al (2019) Patient-derived xenografts of central nervous system metastasis reveal expansion of aggressive minor clones. Neuro Oncol. https://doi.org/10.1093/neuonc/noz137

102. Thorsson V, Gibbs DL, Brown SD, Wolf D, Bortone DS, Ou Yang TH et al (2018) The immune landscape of cancer. Immunity 48:812–830 e814. https://doi.org/10.1016/j.immuni.2018.03.023
103. Torsvik A, Stieber D, Enger PO, Golebiewska A, Molven A, Svendsen A et al (2014) U-251 revisited: genetic drift and phenotypic consequences of long-term cultures of glioblastoma cells. Cancer Med 3:812–824. https://doi.org/10.1002/cam4.219
104. Unruh D, Mirkov S, Wray B, Drumm M, Lamano J, Li YD et al (2019) Methylation-dependent tissue factor suppression contributes to the reduced malignancy of IDH1-mutant gliomas. Clin Cancer Res 25:747–759. https://doi.org/10.1158/1078-0432.CCR-18-1222
105. Van der Auwera GA, Carneiro MO, Hartl C, Poplin R, Del Angel G, Levy-Moonshine A et al (2013) From FastQ data to high confidence variant calls: the Genome Analysis Toolkit best practices pipeline. Curr Protocols Bioinformatics 43:111011–111033. https://doi.org/10.1002/0471250953.bi1110s43
106. Vaubel RA, Tian S, Remonde D, Schroeder MA, Mladek AC, Kitange GJ et al (2020) Genomic and phenotypic characterization of a broad panel of patient-derived xenografts reflects the diversity of glioblastoma. Clin Cancer Res 26:1094–1104. https://doi.org/10.1158/1078-0432.CCR-19-0909
107. Verhaak RG, Hoadley KA, Purdom E, Wang V, Qi Y, Wilkerson MD et al (2010) Integrated genomic analysis identifies clinically relevant subtypes of glioblastoma characterized by abnormalities in PDGFRA, IDH1, EGFR, and NF1. Cancer CELL 17:98–110. https://doi.org/10.1016/j.ccr.2009.12.020
108. Wakimoto H, Mohapatra G, Kanai R, Curry WT Jr, Yip S, Nitta M et al (2012) Maintenance of primary tumor phenotype and genotype in glioblastoma stem cells. Neuro Oncol 14:132–144. https://doi.org/10.1093/neuonc/nor195
109. Wakimoto H, Tanaka S, Curry WT, Loebel F, Zhao D, Tateishi K et al (2014) Targetable signaling pathway mutations are associated with malignant phenotype in IDH-mutant gliomas. Clin Cancer Res 20:2898–2909. https://doi.org/10.1158/1078-0432.CCR-13-3052
110. Wang J, Cazzato E, Ladewig E, Frattini V, Rosenbloom DI, Zairis S et al (2016) Clonal evolution of glioblastoma under therapy. Nat Genet 48:768–776. https://doi.org/10.1038/ng.3590
111. Wang J, Miletic H, Sakariassen PO, Huszthy PC, Jacobsen H, Brekka N et al (2009) A reproducible brain tumour model established from human glioblastoma biopsies. BMC Cancer 9:465. https://doi.org/10.1186/1471-2407-9-465
112. Wang Q, Hu B, Hu X, Kim H, Squatrito M, Scarpace L et al (2017) Tumor evolution of glioma-intrinsic gene expression subtypes associates with immunological changes in the microenvironment. Cancer Cell 32(42–56):e46. https://doi.org/10.1016/j.ccell.2017.06.003
113. Weng Q, Wang J, Wang J, He D, Cheng Z, Zhang F et al (2019) Single-cell transcriptomics uncovers glial progenitor diversity and cell fate determinants during development and gliomagenesis. Cell Stem Cell 24(707–723):e708. https://doi.org/10.1016/j.stem.2019.03.006
114. Williams JA (2018) Using PDX for preclinical cancer drug discovery: the evolving field. J Clin Med. https://doi.org/10.3390/jcm7030041
115. Woo XY, Giordano J, Srivastava A, Zhao Z-M, Lloyd MW, de Bruijn R et al (2019) Conservation of copy number profiles during engraftment and passaging of patient-derived cancer xenografts. bioRxiv:861393. https://doi.org/10.1101/861393
116. Yang RR, Shi ZF, Zhang ZY, Chan AK, Aibaidula A, Wang WW et al (2019) IDH-mutant lower-grade (WHO Grades II/III) astrocytomas can be stratified for risk by CDKN2A, CDK4 and PDGFRA copy number alterations. Brain Pathol. https://doi.org/10.1111/bpa.12801
117. Zhai B, Steino A, Bacha J, Brown D, Daugaard M (2018) Dianhydrogalactitol induces replication-dependent DNA damage in tumor cells preferentially resolved by homologous recombination. Cell Death Dis 9:1016. https://doi.org/10.1038/s41419-018-1069-9
118. Zhou Y, Zhou B, Pache L, Chang M, Khodabakhshi AH, Tanaseichuk O et al (2019) Metascape provides a biologist-oriented resource for the analysis of systems-level datasets. Nature Commun 10:1523. https://doi.org/10.1038/s41467-019-09234-6

Affiliations

Anna Golebiewska[1] · Ann-Christin Hau[1] · Anaïs Oudin[1] · Daniel Stieber[1,2] · Yahaya A. Yabo[1,3] · Virginie Baus[1] · Vanessa Barthelemy[1] · Eliane Klein[1] · Sébastien Bougnaud[1] · Olivier Keunen[1,4] · May Wantz[1] · Alessandro Michelucci[1,5,6] · Virginie Neirinckx[1] · Arnaud Muller[4] · Tony Kaoma[4] · Petr V. Nazarov[4] · Francisco Azuaje[4] · Alfonso De Falco[2,3,7] · Ben Flies[2] · Lorraine Richart[3,7,8,9] · Suresh Poovathingal[6] · Thais Arns[6] · Kamil Grzyb[6] · Andreas Mock[10,11,12,13] · Christel Herold-Mende[10] · Anne Steino[14,15] · Dennis Brown[14,15] · Patrick May[6] · Hrvoje Miletic[16,17] · Tathiane M. Malta[18] · Houtan Noushmehr[18] · Yong-Jun Kwon[9] · Winnie Jahn[19,20] · Barbara Klink[2,9,19,20,21] · Georgette Tanner[22] · Lucy F. Stead[22] · Michel Mittelbronn[6,7,8,9] · Alexander Skupin[6] · Frank Hertel[6,23] · Rolf Bjerkvig[1,16] · Simone P. Niclou[1,16]

1 NORLUX Neuro-Oncology Laboratory, Department of Oncology, Luxembourg Institute of Health, 84, Val Fleuri, 1526 Luxembourg, Luxembourg

2 National Center of Genetics, Laboratoire National de Santé, 3555 Dudelange, Luxembourg

3 Faculty of Science, Technology and Medicine, University of Luxembourg, 4367 Belvaux, Luxembourg

4 Quantitative Biology Unit, Luxembourg Institute of Health, 1445 Strassen, Luxembourg

5 Neuro-Immunology Group, Department of Oncology, Luxembourg Institute of Health, 1526 Luxembourg, Luxembourg

6 Luxembourg Centre for Systems Biomedicine, University of Luxembourg, 4367 Belvaux, Luxembourg

[7] Luxembourg Center of Neuropathology, Luxembourg, Luxembourg

[8] National Center of Pathology, Laboratoire National de Santé, 3555 Dudelange, Luxembourg

[9] Department of Oncology, Luxembourg Institute of Health, 1526 Luxembourg, Luxembourg

[10] Division of Experimental Neurosurgery, Department of Neurosurgery, University of Heidelberg, 69120 Heidelberg, Germany

[11] Department of Medical Oncology, National Center for Tumor Diseases (NCT) Heidelberg, Heidelberg University Hospital, 69120 Heidelberg, Germany

[12] German Cancer Research Center (DKFZ) Heidelberg, 69120 Heidelberg, Germany

[13] German Cancer Consortium (DKTK), 69120 Heidelberg, Germany

[14] DelMar Pharmaceuticals, Inc., Vancouver, BC, Canada

[15] DelMar Pharmaceuticals, Inc., Menlo Park, CA, USA

[16] Department of Biomedicine, University of Bergen, 5019 Bergen, Norway

[17] Department of Pathology, Haukeland University Hospital, Bergen, Norway

[18] Department of Neurosurgery, Henry Ford Health System, Detroit, MI 48202, USA

[19] German Cancer Consortium (DKTK), 01307 Dresden, Germany

[20] Core Unit for Molecular Tumor Diagnostics (CMTD), National Center for Tumor Diseases (NCT), 01307 Dresden, Germany

[21] Institute for Clinical Genetics, Faculty of Medicine Carl Gustav Carus, Technische Universität Dresden, Fetscherstraße 74, 01307 Dresden, Germany

[22] Leeds Institute of Medical Research at St James's, St James's University Hospital, Leeds, UK

[23] Department of Neurosurgery, Centre Hospitalier Luxembourg, 1210 Luxembourg, Luxembourg

Chapter 6

Glioblastoma instructed microglia transit to heterogeneous phenotypic states with dendritic cell-like features in patient tumors and patient-derived orthotopic xenografts

Yabo YA, Pires-Afonso Y, Moreno-Sanchez PM, Oudin A, Kaoma T, Toth R, Kyriakis D, Grzyb K, Poovathingal SK, Klink B, Poli A, Hertel F, Mittelbronn M, Nazarov PV, Skupin A, Niclou SP, Michelucci A, Golebiewska A.

6.1 The rationale of the study

In this article, we present the single-cell landscape of the TME in GBM PDOXs and syngeneic mouse models. We extensively characterized the myeloid compartment of the TME in both GBM mouse models and human GBM tumors using scRNA-seq, flow cytometry, and immunohistochemistry techniques to decipher their underlying heterogeneity. In this work, we demonstrate that PDOX models recapitulate the TME present in patient tumors and present evidence of reciprocal crosstalk between GBM cells and TME. We further revealed the myeloid cell heterogeneity in GBM and identified key signatures of GBM-specific cell types within the myeloid compartment, and their functional and clinical significance. This work further confirmed the clinical relevance of GBM PDOXs for the testing of novel therapeutics including immunotherapeutics designed to target the myeloid compartment.

Personal contributions

This manuscript represents a major work of my PhD project. I contributed actively to the experimental design and the execution of the project. I generated scRNA-seq data of mouse-derived TME in nine representative PDOX models using the Drop-seq technique. These data were integrated with the in-house generated scRNA-seq of the TME from the syngeneic GL261 model (see my contribution to GL261 data analysis in **Annex 2**). I have performed scRNA-seq data preprocessing, integration, and in-depth analysis by applying a plethora of algorithms. I have confirmed the presence of all key subpopulations of GBM tumors in PDOXs and their transition toward GBM-specific states (**Figures 1 & 2**). To further strengthen my analysis, I identified and extensively re-analyzed publicly available scRNA-seq from the GL261 mouse model and human GBM patient tumors. This enabled us to further assess the heterogeneity of the different myeloid cell types in our datasets as shown in **Figures 3A, B, E, F, and G** of the manuscript. I identified different subpopulations and key genes as well as transcription factors defining the different myeloid cell types and phenotypic states, this data is shown in **Figures 4A, B, C, D, F, and G**. I further took advantage of the scRNA-seq data to infer functional properties of myeloid cells, with the focus on microglia migration, sensome, phagocytosis, and antigen presentation capacity presented in **Figures 5A and C and I**. I demonstrated the utility of our PDOX model through scRNA-seq analysis of data from TMZ treated PDOX model shown in **Figures 6D, E, F, I, and J**. I was fully involved in the project design, interpretation, and critical appraisal of results obtained, generation of **Figures 1-6** as well as in writing and proofreading of the manuscript. I further contributed to the generation of results presented in **Supplementary Figures S1-S6** and the data in **Tables 1-6.**

6.1.1 Result

Glioblastoma instructed microglia transit to heterogeneous phenotypic states with dendritic cell-like features in patient tumors and patient-derived orthotopic xenografts

Yahaya A. Yabo[1,2], Yolanda Pires-Afonso[2,3], Pilar M. Moreno-Sanchez[1,2], Anaïs Oudin[1], Tony Kaoma[4], Reka Toth[4], Dimitrios Kyriakis[5], Kamil Grzyb[5], Suresh K. Poovathingal[5,6], Barbara Klink[7,8,9,10], Aurelie Poli[3], Frank Hertel[5,11], Michel Mittelbronn[2,5,8,12,13,14], Petr V. Nazarov[4], Alexander Skupin[5,15,16], Simone P. Niclou[1,17], Alessandro Michelucci[1,5,#,*], Anna Golebiewska[1,#,*]

[1]NORLUX Neuro-Oncology Laboratory, Department of Cancer Research, Luxembourg Institute of Health, L-1526 Luxembourg, Luxembourg; [2]Faculty of Science, Technology and Medicine (FSTM), University of Luxembourg, L-4367 Belvaux, Luxembourg; [3]Neuro-Immunology Group, Department of Cancer Research, Luxembourg Institute of Health, L-1526 Luxembourg, Luxembourg; [4]Multiomics Data Science, Department of Cancer Research, Luxembourg Institute of Health, L-1445 Strassen, Luxembourg; [5]Luxembourg Centre for Systems Biomedicine, University of Luxembourg, L-4362 Esch-sur-Alzette, Luxembourg; [6]Single Cell Analytics & Microfluidics Core, Vlaams Instituut voor Biotechnologie-KU Leuven, 3000 Leuven, Belgium; [7]National Center of Genetics, Laboratoire National de Santé, L-3555 Dudelange, Luxembourg; [8]Department of Cancer Research, Luxembourg Institute of Health, L-1526 Luxembourg, Luxembourg; [9]German Cancer Consortium (DKTK), 01307 Dresden, Germany; Core Unit for Molecular Tumor Diagnostics (CMTD), National Center for Tumor Diseases (NCT), 01307 Dresden, Germany; German Cancer Research Center (DKFZ), 69120 Heidelberg, Germany; [10]Institute for Clinical Genetics, Faculty of Medicine Carl Gustav Carus, Technische Universität Dresden, 01307 Dresden, Germany; [11]Department of Neurosurgery, Centre Hospitalier Luxembourg, 1210 Luxembourg, Luxembourg; [12]Luxembourg Center of Neuropathology (LCNP), Luxembourg; [13]National Center of Pathology (NCP), Laboratoire National de Santé, L-3555 Dudelange, Luxembourg; [14]Department of Life Sciences and Medicine (DLSM), University of Luxembourg, L-4362 Esch-sur-Alzette, Luxembourg; [15]Department of Physics and Material Science, University Luxembourg, L-4367 Belvaux, Luxembourg; [16]Department of Neuroscience, University of California San Diego, La Jolla, CA 92093, USA; [17]Department of Biomedicine, University of Bergen, 5019 Bergen, Norway

# Equal contribution, *corresponding author

Running title: Glioblastoma instructed microglia

Corresponding authors:

Anna Golebiewska, PhD; Alessandro Michelucci, PhD

Luxembourg Institute of Health (LIH)

Department of Cancer Research

NORLUX Neuro-Oncology Laboratory

84, Val Fleuri, L- 1526 Luxembourg

Tel + 352-26970-244

Fax + 352-26970-390

E-mail anna.golebiewska@lih.lu; alessandro.michelucci@lih.lu

Funding

We acknowledge the financial support by the Luxembourg Institute of Health, the Luxembourg Centre for Systems Biomedicine (MIGLISYS), the GLIOTRAIN ITN funded by the European Union's Horizon 2020 research and innovation programme under the Marie Skłodowska-Curie grant agreement No 766069, the Luxembourg National Research Fund (FNR; PRIDE15/10675146/CANBIO, PRIDE19/14254520/i2TRON, INTER/DFG/17/11583046 MechEPI, PRIDE17/12244779/PARK-QC, FNR PEARL P16/BM/11192868), the Fondation du Pélican de Mie et Pierre Hippert-Faber Under the Aegis of Fondation de Luxembourg, and the National Biomedical Computation Resource (NBCR, NIH P41 GM103426 grant from the National Institutes of Health).

Conflict of Interest

The authors declare no competing interests.

Authorship

Conceptualization: YAY, SPN, AlM, AG; Methodology: YAY, SKP, AS, SPN, AlM, AG; Investigation: YAY, YPA, PM, AO, KG, SKP, BK, AP, MM, AlM, AG; Formal analysis: YAY, YPA, PM, TK, RT, PVN, DK, SKP, AlM, AG; Resources: FH, SPN, AlM, AG; Supervision: RK, PVN, AS, SPN, AlM, AG; Writing - Original Draft: YAY, AlM, AG; Writing - Review & Editing: all authors

ABSTRACT

Background: A major contributing factor to Glioblastoma (GBM) development and progression is its ability to evade the immune system by creating an immune-suppressive tumor microenvironment (TME). GBM-associated myeloid cells, including resident microglia, macrophages and other peripheral immune cells are generally geared towards tumor-supportive roles. It is however unclear whether such recruited myeloid cells are phenotypically and functionally identical. Here, we aim to understand the heterogeneity of the TME in GBM, using an unbiased, marker-free approach to systematically characterize cell type identities at the molecular and functional levels.

Methods: We applied single-cell RNA-sequencing, multicolor flow cytometry, immunohistochemical analyses and functional assays to examine the heterogeneous TME instructed by GBM cells. Multiple GBM patient-derived orthotopic xenografts (PDOXs) representing different tumor phenotypes were analyzed and compared to the mouse GL261 glioma model and patient tumors.

Results: We show that PDOX models recapitulate major components of the TME found in human GBM. Human GBM cells reciprocally interact with host cells to create a GBM-specific TME. During tumor progression the most prominent transcriptomic adaptations were found in tumor-associated macrophages (TAMs), which were largely of microglial origin. We reveal inter-patient and intra-tumoral heterogeneity of TAMs and identify key signatures of distinct phenotypic states within the microglia-derived TAMs across distinct GBM landscapes. GBM-educated microglia adapt expression of genes involved in immunosuppression, migration, phagocytosis and antigen presentation, which was confirmed at the functional level. We find novel phenotypic states and gene signatures with astrocytic and endothelial-like features and confirmed them in GBM patient tumor tissue. Finally we show that temozolomide treatment in vivo leads to transcriptomic plasticity not only of the GBM tumor cells but also of adjacent TME components.

Conclusion: Our data provide insight into the phenotypic adaptation of the heterogeneous TME instructed by GBM. We confirm a crucial role of microglia in the immunosuppressive TME and show that PDOXs allow to monitor the plastic GBM ecosystem and its phenotypic adaptations upon treatment. This work further supports the clinical relevance of PDOX avatars for testing novel therapeutics including modalities designed to target the myeloid compartment.

KEYWORDS

Glioblastoma, Tumor microenvironment, Myeloid cells, microglia, Patient-derived xenografts, Single-cell RNA-sequencing

KEY POINTS

- GBM-educated tumor microenvironment is faithfully recapitulated and modulated in PDOX models.
- Microglia represent the major myeloid cell population in the tumor microenvironment.
- GBM-educated microglia display reactive dendritic cell-like gene expression programs.

IMPORTANCE OF THE STUDY

This manuscript addresses tumor-immune interactions in brain cancer, focusing on the molecular changes of the myeloid compartment. We find that myeloid cells, the most abundant immune cell population in brain tumors, undergo the most prominent transcriptional adaptation in the tumor microenvironment. Resident microglia represent the major myeloid cell population in the tumor core, while peripheral-derived myeloid cells only appear to infiltrate the brain at sites of blood brain barrier disruption. We identify reactive dendritic cell-like gene expression programs in GBM-educated microglia, suggesting the capacity for antigen-presenting and anti-tumor activities. These findings have prospective impact for the design of future immunotherapy approaches, e.g. by enhancing anti-tumorigenic dendritic cell-like features on microglia. PDOX models recapitulate faithfully the major components of GBM-educated tumor microenvironment and allow assessment of phenotypic changes in the GBM ecosystem upon treatment.

INTRODUCTION

Cancer heterogeneity and progression are subject to complex interactions between neoplastic cells and their microenvironment, including the immune system. Glioblastomas (GBMs) form a very dynamic ecosystem, where heterogeneous tumor cells reciprocally interact with various components of the tumor microenvironment (TME) (Yabo et al., 2021). The brain TME includes endothelial cells, pericytes, reactive astrocytes, neurons, oligodendrocytes and immune cells. Although GBMs are known as 'cold tumors' with very little lymphocyte infiltration (Thorsson et al., 2018), the GBM TME contains up to 40% of tumor-associated macrophages (TAMs), creating a supportive environment that facilitates tumor proliferation, survival and migration (Charles et al., 2011; Quail and Joyce, 2017). TAMs constitute either resident parenchymal microglia (Mg), peripheral monocyte (Mo)-derived cells or perivascular macrophages referred to also as border-associated macrophages (BAMs) (Ricard et al., 2016). They are recruited by GBMs and in turn release growth factors and cytokines that affect the tumor. Recent studies have shown that TAMs display specific immune properties that are different from classical pro-inflammatory activated (immune-permissive) M1 or alternatively activated (immune-suppressive) M2 reactive profiles (Szulzewsky et al., 2015; Zeiner et al., 2018). Notably, it has been proposed that TAMs acquire different expression programs depending on GBM subtype and upon GBM recurrence (Wang et al., 2017). However, the effective mediators that determine the fate of TAMs and their interaction with tumor cells have not been fully elucidated. Also, it is not known whether TAMs acquire different functional phenotypes depending on specific tumor niches or along tumor development and progression (Hambardzumyan et al., 2016). Despite extensive characterizations of TME components in GBM, more information about the cross-talk between described subpopulations constituting TME at the functional level is needed.

The majority of functional studies on immune TME components of GBM are performed in mouse models due to their immunocompetent status. However, syngeneic and genetically engineered mouse models suffer from the limited resemblance to human disease. Reliable patient-derived brain tumor models are needed for functional studies and preclinical testing of novel treatments targeting the TME in molecularly defined groups of patients. GBM patient-derived organoids preserve certain TME components during initial days only and ex-vivo co-culture protocols are still immature (Klein et al., 2020). Patient-derived xenografts allow for propagation of primary patient tumors in less selective conditions than in vitro cultures (Woo et al., 2021). As subcutaneous xenografts do not recapitulate the natural TME, patient-derived orthotopic xenografts (PDOX) implanted in the brain may be more adequate for modeling gliomas. Although showing an excellent recapitulation of GBM

tumor features, PDOXs inevitably suffer from the immunocompromised environment and replacement of the human TME with mouse counterparts (Golebiewska et al., 2020). It is therefore important to assess to what extent PDOXs can recapitulate major TME features observed in GBM patient tumors.

We have previously reported that PDOX models recapitulate the genetic, epigenetic and transcriptomic features of human tumors. We have also shown that mouse cells interact with human GBM cells in the brain. In particular, endothelial cells forming blood vessels adapt their morphology and molecular features in analogy to the aberrant vasculature observed in patients (Bougnaud et al., 2016). We have further shown that mouse endothelial cells respond to anti-angiogenic treatment, as observed in GBM patients, leading to normalized blood vessels and treatment escape mechanisms towards more invasive tumors (Fack et al., 2015). Here, we further inferred the heterogeneity of the TME compartment across genetically and phenotypically diverse GBM landscapes recapitulated in PDOXs by single-cell transcriptomics. Focusing on TAMs, the most reactive cell population, we sought to distinguish resident versus peripheral macrophages across GBM landscapes and identify distinct molecular programs characteristic of both pro- and anti-tumor activities. Finally, we assess transcriptomic adaptation of TME components upon temozolomide (TMZ) treatment.

MATERIALS AND METHODS

Clinical GBM samples and patient-derived orthotopic xenografts (PDOXs)

Glioblastoma samples were originally received from the Centre Hospitalier in Luxembourg (Neurosurgical Department) or the Haukeland University Hospital (Bergen, Norway) from patients who had given their informed consent. All studies were conducted according to the Declaration of Helsinki, and with approval from the local ethics committees (National Committee for Ethics in Research (CNER) Luxembourg and local ethics committee Haukeland University Hospital in Bergen). PDOX derivation was previously described (Bougnaud et al., 2016; Golebiewska et al., 2020). All tumors samples used in this study were from patients with grade IV GBM (**Table S1**). For this study tumor organoids (diameter 300-400µm) were implanted (6 per brain) into the right frontal cortex of nude mice (athymic nude mice, Charles River Laboratories, France) following previously described protocol (Oudin et al., 2021). Animals were sacrificed at the appearance of neurological symptoms and/or weight loss >10%. The handling of animals and the surgical procedures were performed in accordance with the regulations of the European Directive on animal experimentation (2010/63/EU). The experimental protocols were approved by the local

ethics committee (Animal Welfare Structure of the Luxembourg Institute of Health; protocol LRNO-2014-01, LUPA2019/93 and LRNO-2016-01) and by the Luxembourg Ministries of Agriculture and of Health.

GL261 syngeneic model

Mouse glioma 261 (GL261) cells were maintained at 37ºC with 5% CO_2 in Dulbecco's Modified Eagle's Medium (DMEM (Gibco/Life Technologies) supplemented with 10% Fetal Bovine Serum (FBS; Gibco/Life Technologies) and pen-strep (100 U/ml; Gibco/Life 424 Technologies). Cells were tested for mycoplasma (MycoAlert PLUS Mycoplasma Detection Kit, Westburg, 426 The Netherlands) before mice implantation. GL261 cells were implanted intracranially (500 cells per brain) and mice were monitored as described before (Pires-Afonso et al., 2021). Tumors at three different stages were collected for scRNA-seq: early (5-10 mm^3), intermediate (20-25 mm^3) and late (30-35 mm^3) stage of tumor progression.

Temozolomide (TMZ) treatment

P3 GBM organoids were orthotopically implanted into the right frontal lobe of nude mice. Animals were monitored and evaluated daily for the loss of >10% of body weight, exhibition of strong neurological signs, increased lordosis or swollen belly. Tumor growth was monitored by MRI (T1- and T2-weighted MRI protocol; 3T MRI system, MR Solutions). T2 MRI was applied to all mice at three time points: 31, 37 and 41 days after implantation. 31 days post-implantation most mice had visible tumors and were randomized into 2 treatment groups: Control PDOXs were administered with NaCl 0.9% + 10% DMSO, while treatment group received 40mg/kg TMZ in NaCl 0.9% + 10% DMSO. Treatment was administered by orall gavage 5x per week with in total 8 doses for each PDOXs, where the last treatment dose was given shortly before the end point and tumor resection. Tumor volume (mm^3) was measured in ImageJ as the sum of area obtained by tumor delineation in each slice multiplied by the slice thickness (1mm). Growth rate (GR) was calculated using the TV measurement as GR = 100 × log (TVf/TV0)/(tf−t0), where TVf and TV0 are the tumor volumes at the late (day 41) and early (day 31) time points, respectively, and tf−t0 is the difference in days between the time points. Tumor volumes are expressed in mm^3 and GR in % per day. Statistical difference was assessed with two-tailed Student's t-test.

Single cell isolation for single-cell RNA-sequencing

All animals were perfused with ice-cold PBS to wash out brain tissue from circulating blood cells. GL261 tumors, PDOXs and normal brains were dissociated with the MACS Neural

Dissociation kit (Miltenyi Biotec) according to manufacturer's instructions. GL261-derived cells were purified with the Myelin Removal Beads kit (Myelin Removal Beads II, MACS Miltenyi Biotec) accordingly to the manufacturer's instruction as described before (Pires-Afonso et al., 2021). To separate human GBM tumor cells from mouse, TME subpopulations PDOX-derived cells were FACS-sorted (P8, nude control brain) or MACS-purified (remaining PDOXs). For FACS, we separated hCD90 positive tumor cells from hCD90 negative mouse TME subpopulations (Dirkse et al., 2019). MACS-based purification was performed with Myelin Removal Beads II followed by Mouse Cell Depletion kit (Miltenyi Biotec) according to manufacturer's protocols (Oudin et al., 2021). Except for tissue dissociation steps, tissue and single cell suspensions were handled on ice.

Single-cell RNA-sequencing and analysis

Mouse-derived TME was processed via Drop-seq. Human tumor cells were processed via Drop-seq (P3, P8, P13, T101, T16) or 10XGenomics (T192, T233, T347, T470). Drop-seq and data preprocessing were performed as previously described (Golebiewska et al., 2020; Pires-Afonso et al., 2021). For the 10XGenomics, purified single tumor cells were diluted to 10^6 cells/ ml with RNAse free DPBS + 0.05 % FBS. Diluted cells were filtered using a 50µm filter. The viability of cells was verified using Beckman coulter automatic cell counter and C-Chip – Disposable Haemocytometer (NanoEntek) viability analyzer. Cell concentration was adjusted to target the encapsulation of 3000 cells according to 10XGenomics cell preparation guidelines. Chromium Next GEM Chip with single-cell suspension was loaded to the Chromium Controller (10XGenomics) for generation of encapsulated cells and GEMs. scRNA-seq libraries were prepared using the Chromium Next GEM Single Cell 3' GEM, Library & Gel Bead Kit v3.1 and a Chromium i7 Multiplex kit according to the manufacturer's protocol. Libraries were purified using SPRIselect magnetic beads and analysed using Agilent 2100 Bioanalyzer. Seqencing was performed using NextSeq 500/550 High Output Kit v2.5 (75 Cycles).

scRNA-seq analysis was performed in R (v4.1.1) with the Seurat package (v4.0.5) (Hao et al., 2021). For 10XGenomics data, barcode processing and UMI filtering were performed using the Cell Ranger 4.0.0. Average saturation of the sequencing was 30-40% as calculated by Cell Ranger. Human and mouse cells were separated by mapping the scRNA-seq reads to both reference genomes human g38 and mouse mm10. The distributions of UMI counts and features expressed in each cell for each reference genome allowed for a clear separation of human and mouse cells. Only clusters with the highest number of genes mapping to the mouse genome were retained for further analysis. For each sample, QC thresholds were empirically applied per sample to exclude low quality cells based on the

number of counts and features in the digital gene expression (DGE) matrix before being merged together to preserve unique reads from each samples. Only genes expressed in at least 5 cells, cells expressing at least 200 features and cells with 30% or less mitochondrial reads were selected for further analysis. The merged counts were normalized using Seurat based 'LogNormalize' method that normalizes expression in each cell by the total expression with a scaling factor of 10,000 and subsequently log-transformed for downstream analysis. Batch correction was done by Harmony (v0.1.0) that group cells in similar embeddings base on cell types rather than datasets (Korsunsky et al., 2019). Clustering was done on harmony corrected data using default parameters of the Seurat package (v4.0.5). Dimensionality reduction was done using the Uniform Manifold Approximation and Projection (UMAP) of the Seurat package (v4.0.5). Differential expression analysis was done using Wilcoxon rank sum test, false discovery rate (FDR) was calculated using the Benjamini-Hochberg (BH) method. Cell clusters were identified based on expression of known marker genes and differentially expressed genes (DEGs) were determined by the 'FindAllMarkers' function of the Seurat package. The myeloid cells cluster was extracted from the dataset using the Seurat 'subset' function. Gene ontology analysis was performed by the gene functional classification tool METASCAPE (https://metascape.org/). Single cell trajectory inference analysis was done with the R package Monocle v2 and v3 using default parameters (Qiu et al., 2017). Z-score of genes was calculated by subtracting the mean of expression from the raw expression of each gene and normalization by the corresponding standard deviation. Gene expression was displayed as heatmap of z-scores. Single-cell gene set signature scores were calculated using the Seurat 'AddModuleScore' implemented in Seurat as described in (Tirosh et al., 2016). Identification of master transcriptional regulators was done using normalized counts from the annotated Mg cells. Gene regulatory network inference, identification of regulons, motif enrichment TFs prediction as well as the quantification of the activity of identified regulons in each cell were done according the standard SCENIC workflow (Aibar et al., 2017).

Reference Based Mapping

Myeloid cells were identified and extracted from publicly available GL261 scRNA-seq datasets by their over expression of key myeloid cell markers (Ochocka et al., 2021; Pires-Afonso et al., 2021; Pombo Antunes et al., 2021) where the Ochocka et al., 2021 dataset was used as the reference. Other datasets were projected onto the reference UMAP structure. The reference principal component analysis (PCA) space was computed using 2000 most variable genes, and the first 30 PCs were used to calculate the UMAP model. Next, we determined the common features of the reference and each of the query datasets

by Seurat's 'FindTransferAnchors' function with reduction method 'pcaproject' and parameter 'dims = 1:50'. Finally, we called 'MapQuery()' to transfer cell type labels and project the query data onto the UMAP structure of the reference.

Analysis of human GBM scRNA-seq data

Analysis of TME in human GBM was performed in publicly available Darmanis et al., dataset (Darmanis et al., 2017) via http://www.gbmseq.org. Downloaded human GBM scRNA-seq 10XGenomics datasets were obtained as preprocessed gene expression matrices (DEMs) from four recent publicly available datasets (Friedrich et al., 2021; Johnson et al., 2021; Pombo Antunes et al., 2021; Wang et al., 2019) that profiled a total of 36 IDHwt GBM patient tumors including newly diagnosed (n = 27) and recurrent (n = 9) GBMs. We started by analyzing each dataset separately to identify and extract myeloid cells. Selected cells were then integrated, harmonized for batch correction and analyzed for myeloid subpopulation identification and characterization. Newly diagnosed and recurrent GBM from Pombo-Antunes et al. datasets were considered separately. Myeloid cells were identified and extracted as follows: (1) For Friedrich's dataset, cells were identified according to author's annotation; (2) For Wang's, Johnson's and Pombo-Antunes's datasets, we used an approach that combines overexpression (OE) and clustering analysis. Each dataset was analyzed separately. First, genes with zero count in all cells were filtered out and 'NormalizeData' function was applied to log-normalize each cell with a scale factor of 10,000. UMAP was used to visualize the cells and clusters on 2 dimensions. Cluster identity was determined according to over-representation of a cell-type within the cluster as called by OE analysis. Myeloid cells were extracted for further analysis. Overall, 51,302 myeloid cells were extracted from the five datasets and united into one Seurat object. Genes with zero count in all cells were removed, and cells were log-normalized with a scale of 10,000. Harmony (0.1.0) package was used to remove variation due to batch effects. All PCs were used and theta was set to 1. Harmony embeddings were used for clustering analysis. Mouse gene lists were converted to human homologs automatically in R using capital letter (*toupper*) or the 'getLDS' function in biomaRt package (Durinck et al., 2009). All results were stored in a Cerebro object to enable data visualization and exploration (Hillje et al., 2020).

Immunohistochemistry and immunofluorescence analyses

The regular histological analysis of PDOX models (H&E, human Nestin/Vimentin, mouse CD31) has been performed as described previously (Bougnaud et al., 2016; Golebiewska

et al., 2020). Antibodies are listed in **Table S2.** Iba1 staining was performed on coronal 8 µm sections from paraffin-embedded brains. Sections were pre-treated for 5min with Proteinase K (Dako) followed by 30 min incubation at 95°C in retrieval solution (Dako). The Dako Envision+System-HRP was used following the manufacturer's instructions. Primary and secondary antibodies were incubated for 1h. Signal was developed with 3,3′-diaminobenzidine chromogen in 5–20 min (Envision+ System/HRP Kit; K4007, Agilent/Dako). $Iba1^+$ cells were quantified based on ImageJ plugin as described in (Abdul Rahim et al., 2017). For immunofluorescence, brains were perfused and post-fixed with 4% paraformaldehyde (PFA)/sucrose for 48 hours. Coronal sections of 12 µm tickness were prepared adopting the standard protocol with minor modifications (Buttini et al., 1999). Briefly, sections were washed (PBS with 0.1% Triton X-100), permeabilised (PBS with 1.5% Triton X-100), blocked (PBS with 5% BSA) and incubated with the primary antibodies. Secondary antibodies against the appropriate species were incubated for 2h at room temperature. Cell nuclei were counterstained with Hoechst (1 mg/ml; Sigma). Sections were mounted on glass slides cover slipped using FluoromountTM Aqueous Mounting Medium (Sigma). Images were obtained using a Nikon Ni-E or Zeiss LSM880 confocal microscopy. Z-stacks were done with 0.5µm steps in Z direction, with a XY resolution of 1.024 x 1.024 pixels.

Multicolor cell membrane phenotyping and flow cytometry settings

All animals were perfused with ice-cold PBS. PDOX brains were dissected into separate zones when specified: tumor core, invasive zone (corpus callosum and top left hemisphere, P3 only) and distant zone (left hemisphere, bottom hemisphere, P3 &P13). P8 PDOX was not dissected, due to its very invasive nature. PDOX tumors and control mouse brains were dissociated with MACS Neural Tissue Dissociation Kit (P) (Miltenyi) following the manufacturers' instructions. Single cells were resuspended in ice-cold HBSS, 2% FBS, 10mM HEPES buffer (100 µl/test) flow buffer. Fc receptors were blocked with CD16/CD32 antibody for 30 min at 4°C. Cells were incubated with the appropriate pre-conjugated antibodies for 30 min at 4°C in the dark (**Table S2**). Non-viable cells were stained with Hoechst (0.1µg/ml, Bisbenzimide, 33342; Sigma) or LIVE/DEAD™ Fixable Near-IR Dead Cell Stain Kit. Data acquisition was performed at 4°C on a FACS Aria™ SORP cytometer (BD Biosciences) fitted with a 632 nm (30 mW) red laser, a 355 (60 mW) UV laser, a 405 nm (50 mW) violet laser and a 488 nm (100 mW). Data were analyzed with FlowJo software (version 10.8.1).

Gene expression analysis by qPCR

Myelin was removed prior FACS-sorting with the Myelin removal beads II (Miltenyi) and CD11b$^+$ cells were FACS-sorted directly to Trizol® LS (Life Technologies) according to the manufacturer's protocol (n=2-3; from at least 3 animals each). RNA extraction and RT-PCR were conducted as previously described (Sousa et al., 2018). The sequences of the primers designed with the Primer-BLAST tool are as follows: *Spp1 F: CTGGCTGAATTCTGAGGGACT, R: TTCTGTGGCGCAAGGAGATT; P2ry12 F: GTGCAAGGGGTGGCATCTA , R: TGGAACTTGCAGACTGGCAT; Tmem119 F: TGCAATGTCGCTGTCACTCT, R: AGTTTGTGTTTCCACGGGGT Grp34 F: GGAAAGCTTCAACTCAGTTCCTG, R: TCCATGAGAGGAGCAAAGCC, Rpl27 F: ACATTGACGATGGCACCTC, R: GCTTGGCGATCTTCTTCTTG*

CD11b$^+$ myeloid cells isolation and functional assays

Mice were deeply anaesthetized with a mixture of ketamine (100 mg/kg) and xylazine (10 mg/kg) and transcardially perfused with ice-cold PBS. Brains were rapidly removed and the tissue was processed as previously described. Myeloid cells were enriched by magnetic separation using CD11b$^+$ beads (MACS Miltenyi Biotec). Briefly, 1 × 10^7 cells were resuspended in 90 µl of PBS supplemented with 0.5% BSA (Sigma-Aldrich) and 2 mM EDTA (MACS buffer) and incubated with 10 µl of CD11b beads (MACS Miltenyi Biotec). The cell suspension was incubated at 4°C for 20 min, washed and pelleted in 500 µl of MACS buffer at a density of 1 × 10^8 cells. The cell suspension was applied into the LS columns (MACS Miltenyi Biotec) and the CD11b$^+$ fraction was eluted. Ex vivo CD11b$^+$ migratory abilities were assessed using 8 µm pore size Boyden chambers (ThinCert cell culture inserts, Greiner), fitting into 24-well plate. 100,000 cells were seeded in the upper part of the Boyden chambers in DMEM-F12 medium. Upon 48 hours, cells were fixed in 4% PFA for 15 minutes and washed briefly 2 times in PBS. Cells were stained with DAPI for 15 minutes and washed 2 times in PBS before imaging. Migratory cells were quantified by counting the number of cells on the lower side of the membrane under light microscope with a 20x magnifying objective (5 representative fields per membrane). Experiments were conducted in 3 biological replicates (each with 2 technical replicates). The data was normalized according to the respective proliferation index and is represented as percentage of cells that migrated relative to the initial number of cells. Ex vivo phagocytic abilities were measured using the pHrodo Red E.coli bioparticles (Essen Bioscience, MI USA), according to the manufacturer's instructions. Briefly, 100,000 CD11b$^+$ freshly isolated cells were plated into the 96 well-plates in 100 µl and left for 2h to adhere. pHrodo Red E.coli bioparticles were added at 10 µg/ml and the plates were transferred into the Incucyte ZOOM (Essen

Bioscience, MI USA) platform. Four images per well from at least three technical replicates were taken every hour for a duration of 48 h using a 10x objective. Images were analyzed using the IncuCyte Basic Software. Red channel acquisition time was 800 ms and corresponding red channel background noise was subtracted with the Top-Hat method of background non-uniformity correction with a radius of 20 µm. Red fluorescence signal was quantified applying a mask and the parameter red object area was extracted for data analysis and visualization.

Statistical analyses

Statistical analysis details for each analysis are reported in the figure legends. In box plots, the box limits indicate the 25th and 75th percentiles and center lines show the medians; whiskers represent the minimal and maximal observed values. All data points are represented by dots.

Data Availability

PDOX models are available via PDXFinder (https://www.pdxfinder.org/) and are also part of the collection provided by the EuroPDX consortium (https://www.europ dx.eu/). The scRNA-seq data from the PDOX models have been deposited in the Gene Expression Omnibus repository (https://www.ncbi.nlm.nih.gov/geo/) with the accession number GSE128195 (human tumor cells). The scRNA-seq data of GL261 models are available in the GEO with accession number GSE158016 (Pires-Afonso et al., 2021).

RESULTS

Single-cell RNA-sequencing identifies recapitulation of major TME components in GBM PDOX models

To assess TME composition, we performed scRNA-seq on mouse-derived cells of PDOX models derived from treatment-naïve and recurrent GBMs using the Drop-seq technology (Macosko et al., 2015) (**Fig 1A**). PDOXs represented genetically and phenotypically diverse IDHwt GBMs (**Table S1, Fig S1A**) (Golebiewska et al., 2020). PDOXs were derived in nude mice, due to their least immunocompromised background and mouse-derived cells of the TME was purified by MACS or FACS technology (Oudin et al., 2021). All tumors were micro-dissected, following the histopathological features of each model, to ensure minimal contamination of healthy brain cells. In total we obtained 15,366 cells from nine PDOXs. The data were combined with TME of the GL261 syngeneic orthotopic GBM model derived

in C57BL6/N (BL6/N) wild-type immunocompetent mice ((Pires-Afonso et al., 2021), 3 time points collected, 2,492 number of cells in total). Normal brain controls were included for both mouse strains (1,692 cells for nude brain, 1,972 cells for BL/6J brain, **Fig 1A**). Unsupervised clustering and uniform manifold approximation and projection (UMAP) analysis based on 21,522 cells and 24,067 genes in total revealed nine major cellular clusters present in all samples analyzed (**Fig 1B-C**). Cell clusters were identified based on the expression of cell type-specific markers, and included well-known components of normal brain and GBM TME such as astrocytes, endothelial and ependymal cells, pericytes, oligodendrocytes and oligodendrocyte progenitor cells (OPCs) **(Fig 1D**). All the major cellular subpopulations were present in PDOXs, GL261 and normal brain controls **(Fig S1B**). As expected, myeloid cells constituted the major immune component in PDOXs and GL261 tumors (**Fig 1E**). T lymphocytes were largely depleted in PDOXs and few cells represented B cells, still functional in the nude mice (**Fig S1C-D**). As previously described (Ochocka et al., 2021; Pires-Afonso et al., 2021; Pombo Antunes et al., 2021), the majority of infiltrated lymphocytes in the GL261 TME were NK and T cells (**Fig S1D**). PDOXs also presented lower proportions of oligodendrocytes compared to GL261 tumors. In accordance to our previous report (Bougnaud et al., 2016), PDOXs with stronger angiogenic features (P13, T16, P3) had higher proportion of endothelial cells than more invasive PDOXs (**Fig 1E**) where no correlation between histopathological features and abundance of myeloid cells was observed. To some extent, the TME composition was patient specific, e.g., longitudinal models (LIH0347: T347/T470, LIH0192: T192/T233) showed similar cellular proportions, where PDOXs derived from LIH0192 patient showed a high percentage of myeloid cells, whereas PDOXs of LIH0347 patient were particularly abundant in astrocytes. This suggests a potential influence of the genetic background of tumor cells on TME composition, as has been suggested in human GBMs (Hara et al., 2021). Still, PDOXs with high myeloid content did not show increased abundance of mesenchymal-like GBM tumor cells (**Fig S1E**). We did not observe major differences between PDOXs derived from treatment-naïve and recurrent GBMs. A larger cohort will be needed to further interrogate the correlation between TME composition and GBM molecular features.

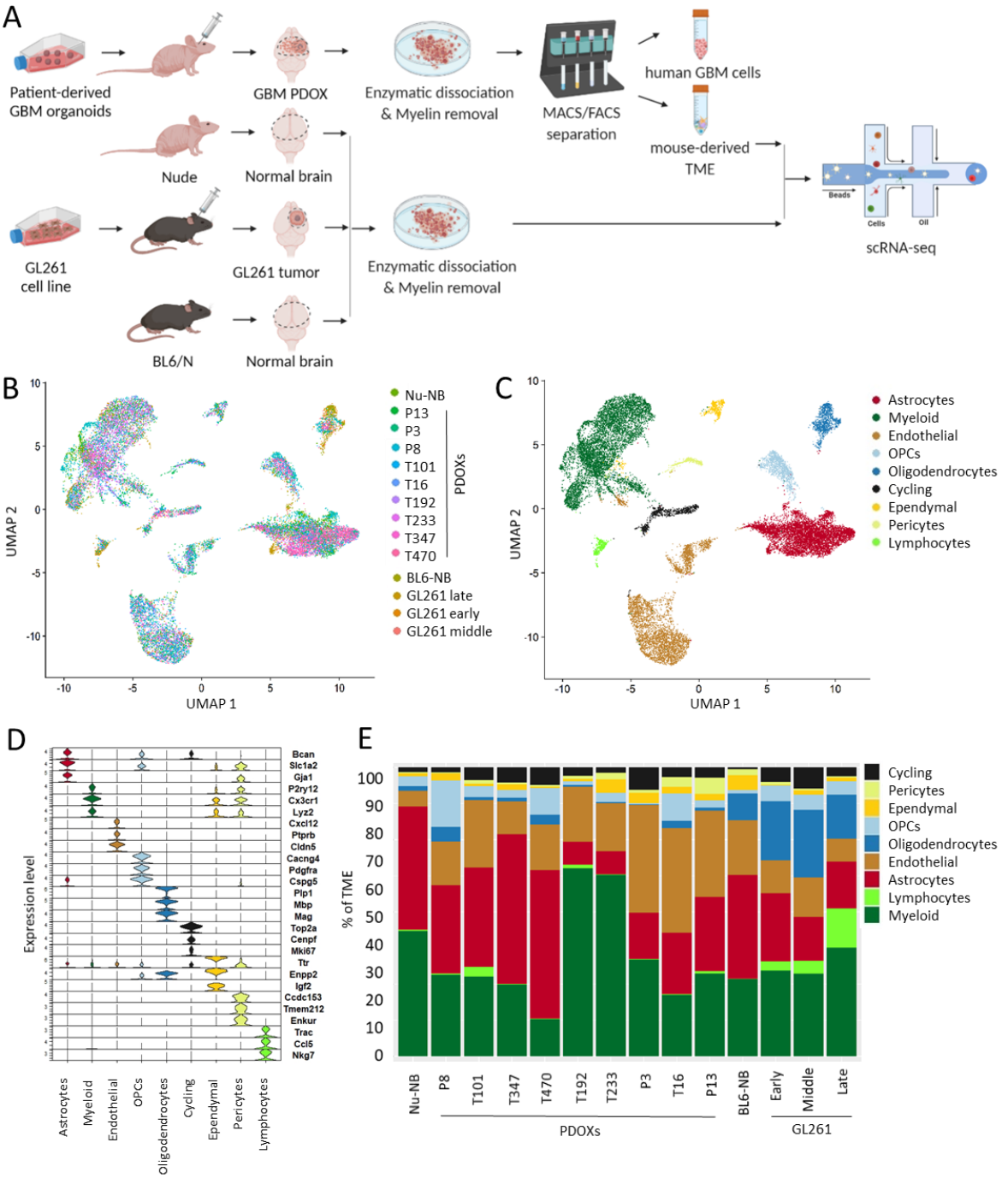

Figure 1. scRNA-seq analysis of TME components in GBM PDOX models in vivo. (A) Schematic illustration of the experimental workflow showing tumor implantation, processing and scRNA-seq for GBM PDOXs, GL261 syngeneic model and respective normal brain controls. See PDOX characteristics in **Fig. S1** and **Table S1 (B)** UMAP projection of harmony-corrected scRNA-seq data showing the overall gene expression relationship between TME cell types detected. Cells are color-coded based on the biological group: nude mouse normal brain (Nu-NB), PDOXs (9 models), Black 6 mouse normal brain (BL6-NB), GL261 tumor (3 collection time points: early, middle late). **(C)** Nine distinct cell types were identified based on their transcriptomic features. Cell types are color-coded; OPCs: oligodendrocyte progenitor cells. **(D)** Expression of marker genes specific to distinct cell types identified. Three top markers of each population are displayed (Wilcoxon Rank Sum Test). **(E)** Proportions of TME cell types across different tumors and normal brains.

TME subpopulations in PDOXs show transcriptional adaptation towards GBM-specific phenotypic states

To interrogate the influence of human GBM cells on the phenotypes of mouse-derived TME in PDOXs, we compared TME subpopulations in PDOXs to the equivalent cells in the normal nude brain. Pronounced transcriptomic differences were detected in all populations of the TME (**Fig 2A**), and were in general stronger than the changes observed in GL261 tumors versus normal brain. This indicates a functional crosstalk between human GBM tumor cells and mouse-derived TME. The transcriptomic adaptation was most pronounced in myeloid, endothelial cells, astrocytes, and OPCs (**Table S3**). Myeloid cells reactivated transcriptomic programs linked to cell migration, inflammation and cytokine production, pointing towards a GBM specific phenotype (**Fig 2B**). Indeed, key "homeostatic" Mg genes including *P2ry12*, *Tmem119* and *Gpr34* (Butovsky et al., 2014; Hickman et al., 2013) were downregulated (**Fig 2C, Fig S2A-B**). This is reminiscent of the decrease of homeostatic genes in reactive Mg, known to occur in GBM TME, but also under inflammatory and neurodegenerative conditions (Bennett et al., 2016; Chiu et al., 2013; Deczkowska et al., 2018; Sousa et al., 2018). At the same time, myeloid cells activated *Spp1* (Osteopontin), *Fn1*, *Cst7* and *Ch25h*, further indicating efficient transition towards GBM-specific tumor associated macrophages (TAMs). Myeloid activation was present in all PDOX models and GL261. This was confirmed by qPCR of FACS-sorted $CD11b^{+}$ cells (**Fig. S2C**) and is in accordance with data from syngeneic GBM models (Szulzewsky et al., 2015).

Other cell subpopulations within the PDOX TME also activated biological processes linked to phenotypic states in GBM, such as OPCs activated programs of tissue inflammation and regeneration (e.g., *Pdgfra, Cspg4, Cspg5, Cacng4* **Fig 2D-E, Fig S2C**), whereas astrocytes adapted metabolic processes and cellular shape, suggesting ongoing reactive gliosis (e.g., upregulated *Gfap*, *Vim*, downregulated *Slc1a2* and *Slc1a3,* **Fig 2F, Fig S2D**). In concordance with our previous study (Bougnaud et al., 2016), endothelial cells displayed an activated and proliferative phenotype associated with angiogenesis (**Table S3, Fig S2D**). These profiles were confirmed to be present in equivalent TME subpopulations of human GBM tumors (**Fig 2G, Fig S2E-F**).

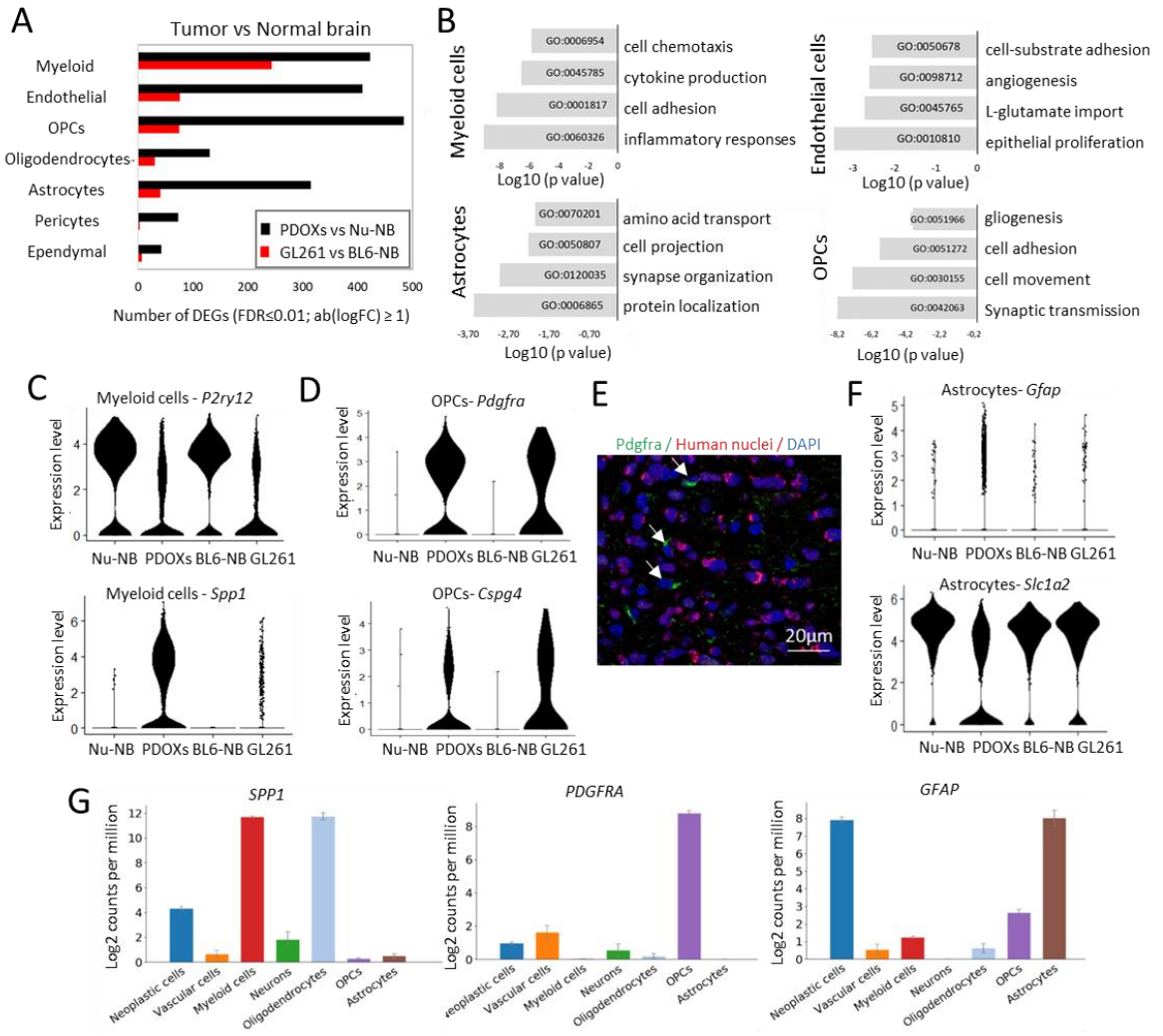

Figure 2. Transcriptomic adaptation of GBM-educated TME subpopulations. (A) Bar graph showing the number of differentially expressed genes (DEGs) between TME of PDOX and GL261 tumors and corresponding normal brains (Nu-NB: nude mouse normal brain, BL6-NB: BL6 normal brain) in identified cell types (FDR ≤0.01, $|\log_2 FC| \geq 1$, the Wilcoxon rank sum test with Benjamini-Hochberg correction); OPCs: oligodendrocyte progenitor cells. **(B)** Summary of top four gene ontology terms characterizing DEGs in PDOX versus Nu-NB. **(C)** Gene expression levels of homeostatic (*P2ry12*) and activated (*Spp1*) myeloid cell marker in myeloid cells of four biological groups: Nu-NB, PDOXs (9 models combined), BL-NB, GL261 tumor (3 time points combined). **(D)** Gene expression levels of OPC markers upregulated in GBM tumors. **(E)** Immunofluorescence staining showing Pdgfrα$^+$ cells in the tumor core of P8 PDOX. Arrows point Pdgfrα$^+$ mouse cells, negative for human nuclei staining. **(F)** Gene expression levels of markers associated with reactive astrocytes upregulated in GBM tumors. **(G)** Expression levels of *SPP1*, *PDGFRA* and *GFAP* in distinct cell types detected in human GBM tumors. Expression levels in single cells are displayed as mean ± SEM.

GBM-educated myeloid cells in PDOXs and human GBM are largely of microglial origin

Due to pronounced adaptation within the TME in GBM PDOXs, we further examined the ontogeny and heterogeneity of the myeloid compartment. To address the differences between PDOXs and GL261, we combined our dataset with previously published scRNA-

seq data of TME in GL261 tumors (Ochocka et al., 2021; Pombo Antunes et al., 2021) (**Fig 3A, Fig S3A-B**). After removing batch effects, we selected the myeloid cell population and reclustered. Referencing PDOXs myeloid cells to the Ochocka et al., dataset showed a high abundance of Mg-derived TAMs (Mg-TAMs, >95%) and a low proportion of Mo-derived TAMs (Mo-TAMs) and BAMs. P13 PDOX with pronounced angiogenic features showed a higher proportion of Mo-TAMs and BAMs, although Mo-TAMs were also present in invasive T101 PDOX. In contrast, GL261 tumors contained significantly more Mo-TAMs (**Fig 3A-B, Fig S3A-C**). Of note, the analysis revealed major differences between published datasets in the GL261 model: Ochocka et al. and Pires-Afonso et al. datasets contained Mo-TAMs in the range of 26-32%, whereas the Pombo Antunes et al. dataset revealed >78% Mo-TAMs. These differences were consistent with cell isolation strategies where the first studies isolated myeloid cells at early stages of tumor development from a larger part of the tumor-containing hemisphere, whereas Pombo Antunes et al., isolated cells at late stage only from the tumor core. This highlights the sensitivity of detecting distinct phenotypic states of TME subpopulations based on spatial location in the tumor and adjacent brain.

Flow cytometry analysis confirmed high proportions of Mg-TAMs ($CD45^+CD11b^+Ly6G^-Ly6C^-CD206^-$) in PDOX TME compared to normal brain (**Fig 3C, Fig S3D-E**). While BAM ($CD45^+CD11b^+Ly6G^-Ly6C^-CD206^+$) proportions remained similar, we confirmed higher proportions of Mo-TAMs ($CD45^+CD11b^+Ly6G^-Ly6C^+CD206^-$) in the tumor core of P13 PDOXs. It was accompanied by increased levels of neutrophils ($CD45^+CD11b^+Ly6G^+Ly6C^{middle}CD206^-$) and lymphocytes ($CD45^+CD11b^-$) suggesting that peripheral monocytic infiltration is limited to the angiogenic/necrotic tumor regions (**Fig S3F)** where the blood brain barrier is disrupted. Abundance of Mg was further confirmed by $Iba1^+$ staining in PDOXs (**Fig 3D**). While normal brain of nude mouse showed resting ramified Mg, GBM tumors in PDOXs displayed Mg-TAMs with different morphologies. The tumor core was in general occupied by Mg showing amoeboid or hyper-ramified morphology. Tumors displaying less invasive growth showed a gradient of Mg phenotypes at the invasive front, from ramified towards hyper-ramified and finally amoeboid Mg. Myeloid cells with mainly macrophagocytic morphology were especially present in areas of pseudopalisading necrosis (P13 PDOX). Invasive tumors showed more uniform, diffuse infiltration and activation of myeloid cells towards amoeboid states at the border with normal brain structures. This was in contrast to the much sharper delineated GL261 model, showing a strong concentration of Mg-TAMs at the tumor border (**Fig 3D**).

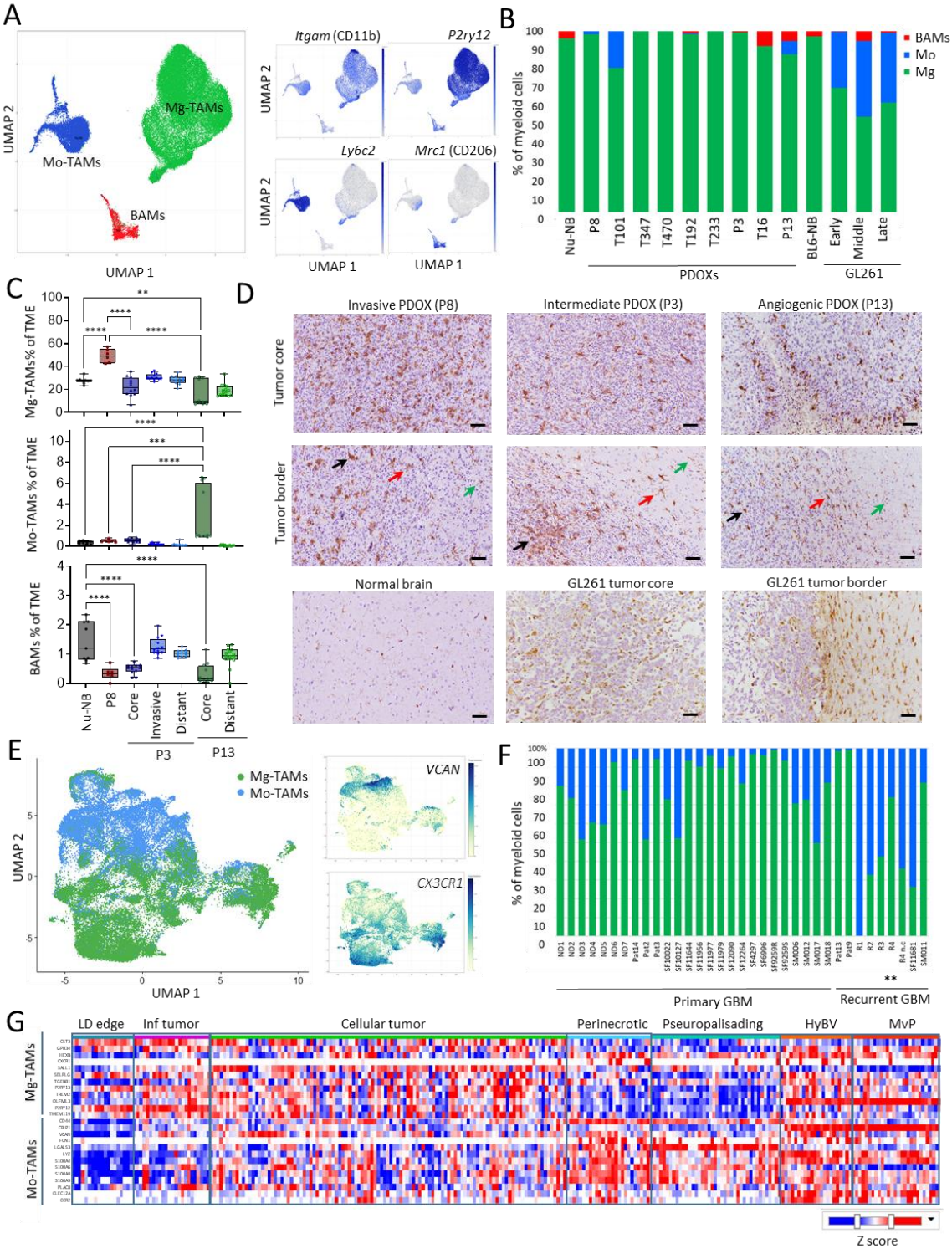

Figure 3. Heterogeneity and ontogeny of GBM-educated myeloid cells. (A) UMAP projection of reference-based mapping of myeloid cells in TME of GBM PDOXs and GL261 tumors (Ochocka et al., 2021; Pires-Afonso et al., 2021; Pombo Antunes et al., 2021). Three myeloid cells types were identified: Microglia-derived tumor associated macrophages (Mg-TAMs), blood monocyte-derived TAMs (Mo-TAMs) and border associated macrophages (BAMs). Inserts show expression of marker genes: pan-myeloid: *Itgam* (CD11b), Mg: *P2ry12*, monocytes: *Ly6c2*, BAMs: *Mrc1* (CD206). The color gradient represents expression levels. **(B)** Graph displaying proportions of myeloid cell subpopulations in nude mouse normal brain (Nu-NB), PDOXs (9 models), Black 6 mouse normal brain (BL6-NB), GL261 tumor (3 collection time points: early, middle late). **(C)** Box plots show flow cytometry quantification of $CD45^+CD11b^+Ly6G^-Ly6C^-CD206^-$ Mg-TAMs, $CD45^+CD11b^+Ly6G^-Ly6C^+CD206^-$ Mo-TAMs and $CD45^+CD11b^+Ly6G^-Ly6C^-CD206^+$ BAMs in Nu-NB and PDOX TME

across different tumor phenotypes and brain regions (n=6-15 from at least three different mouse brains each, one-way ANOVA, ***p<0.001, **p<0.01, *p<0.05). See gating strategy in **Fig S3D. (D)** Examples of Iba1 staining in PDOXs representing invasive (P8), intermediate (P3) and angiogenic (P13) tumor growth, normal nude brain and GL261 tumor. Tumor core and tumor border zones are highlighted. Arrows indicate examples of ramified (green), hyper-ramified (red) and amoeboid (black) Mg. Scale bar: 50 µm. **(E)** UMAP projection of myeloid cells in GBM patient tumors. Cells are color coded for Mg-TAMs and Mo-TAMs ontogeny based on established gene signatures. Inserts show expression levels of marker genes: Mg *CXCR1*, monocytes *VCAN*. The color gradient represents expression levels. **(F)** Proportions of Mg-TAMs and Mo-TAMs in individual GBM patient tumors. Recurrent GBMs show higher proportions of Mo-TAMs (**p<0.01, two-tailed Student's t-test). **(G)** Heatmap showing bulk RNA-seq profiles of laser-micro dissected regions of GBM patient tumors for Mg-TAMs and Mo-TAMs marker genes. Data extracted from the Ivy Glioblastoma Atlas Project (LD edge: leading edge; Inf tumor: infiltrative tumor; HyBV: hyperplastic blood vessels in cellular tumor; MvP: microvascular proliferation).

To further interrogate the clinical relevance of these models, we investigated the composition of myeloid cells in patient tumors based on available scRNA-seq datasets (Friedrich et al., 2021; Johnson et al., 2021; Pombo Antunes et al., 2021; Wang et al., 2019). Due to the lack of normal Mg and Mo cell references, we applied robust gene signatures for Mg (*HEXB, P2RY12, P2RY13, TMEM119, GPR34, CXCR1, TGFBR1, CST3, OLFML3, SALL1, SELPLG, TREM2*) and blood-derived Mo cells (*CCR2, PLAC8, CLEC12A, FCN1, VCAN, LYZ, LGALS3, CRIP1, S100A4/A6/A8/A9, CD44*) to assign TAM ontogeny (**Fig 3E, Fig S3G)**. Mg-TAMs constituted the majority of myeloid cells in treatment-naïve primary GBMs (**Fig 3F)**. As reported previously, recurrent GBMs showed generally increased proportions of Mo-TAMs, albeit with high interpatient differences, confirming inter-patient differences and potential sampling bias as observed in preclinical models. BAM signatures were rather weak and no clear separate cluster was identified (**Fig S3G)**. Signature expression profiles in different GBM tumor zones (Ivy Glioblastoma Atlas Project, (Bowman et al., 2016)) confirmed low abundance of Mo-TAMs in leading edge and infiltrative tumor (**Fig. 3G**). While cellular tumor core showed signature of both cellular ontogenies, perinecrotic and pseudopalisading zones showed higher expression of Mo-TAM markers, consistent with our findings in preclinical models. Of note, CD206 (*MRC1*), a historical M2-TAM marker, is highly activated by Mo-TAMs in GL261 tumors (**Fig S3H**), but not in PDOXs and patient tumors. These data confirm the high relevance of Mg in constituting TME in human, which is adequately recapitulated in PDOXs, but not in the GL261 mouse model.

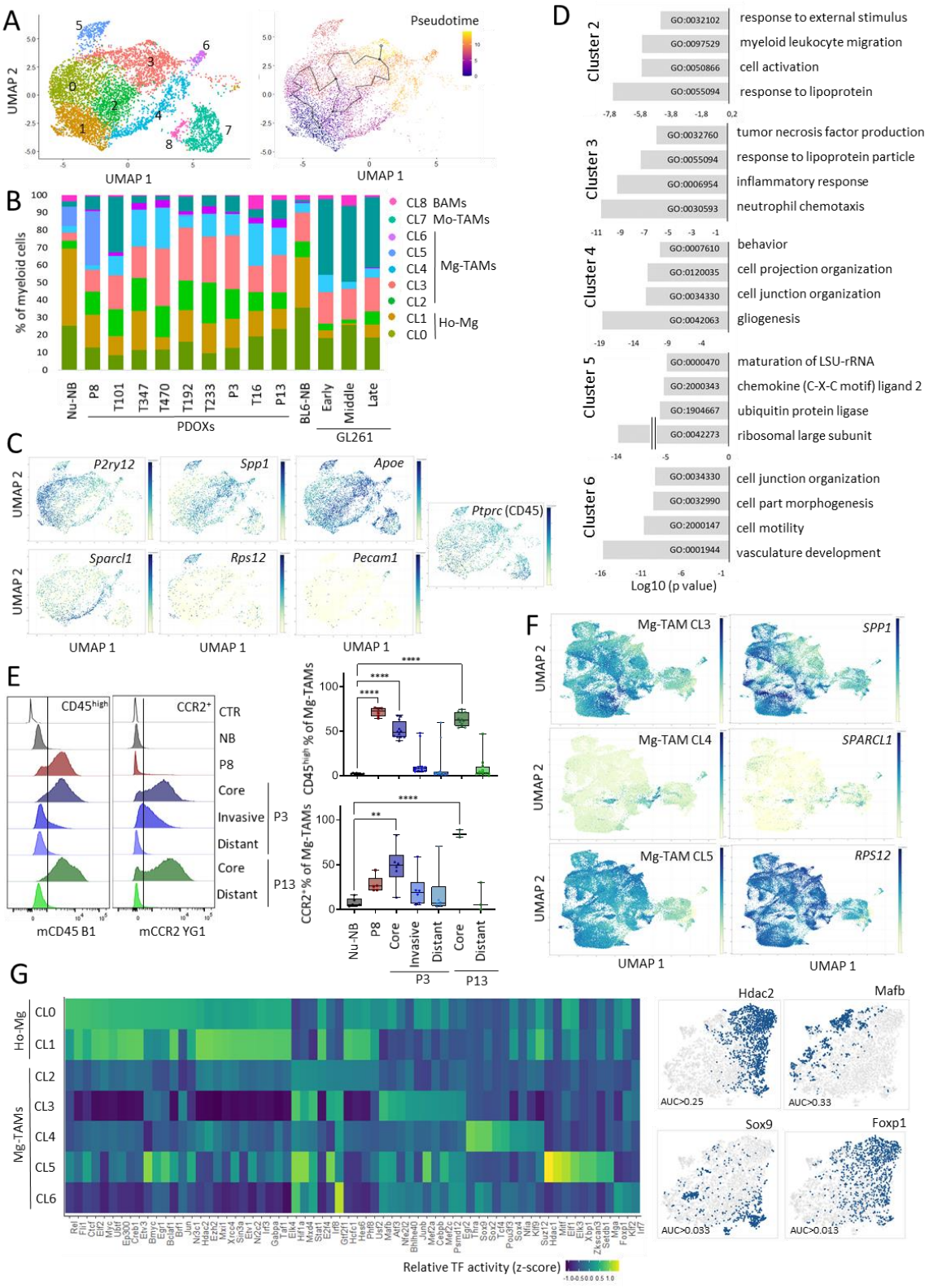

Figure 4. GBM-driven activation of homeostatic Mg towards heterogeneous Mg-TAMs. (A) Left: UMAP projection of unsupervised clustering of myeloid cells revealing nine distinct phenotypic states. Clusters 0-6 represent Mg-TAMs, Cluster 7 Mo-TAMs, Cluster 8 BAMs. Right: Monocle-based trajectory analysis of Mg-TAM clusters showing a trajectory from naïve to activated Mg. Both graphs display cells isolated form PDOXs, GL261 and normal brain controls. **(B)** Graph displaying proportions of cells assigned to nine clusters of myeloid cells in nude mouse normal brain (Nu-NB), PDOXs (9 models), Black 6 mouse normal brain (BL6-NB), GL261 tumor (3 collection time points: early, middle late). Clusters 0-1: homeostatic Mg (Ho-Mg), Clusters 2-6: Mg-TAMs, Cluster 7: Mo-

TAMs, Cluster 8: BAMs. **(C)** UMAP projections displaying expression levels of representative genes characteristic for Mg-TAM clusters. The color gradient represents expression levels. **(D)** Summary of top four gene ontology terms characterizing highly expressed genes (FDR ≤0.01, logFC ≥ 0.5, the Wilcoxon rank sum test with Benjamini-Hochberg correction) in respective Mg-TAM clusters. **(E)** Left panels: representative flow cytometry graphs of $CD45^{+}CD11b^{+}Ly6G^{-}Ly6C^{-}CD206^{-}$ Mg-TAMs showing increased levels of CD45 and CCR2 in tumor core of three PDOX models. Right panels: quantification of $CD45^{high}$ and $CCR2^{+}$ cells in Mg-TAMs across different tumor phenotypes and brain regions. (n=3-6 from at least three different mouse brains each, one-way ANOVA, ***p<0.001, **p<0.01, *p<0.05). **(F)** UMAP projection of human GBM myeloid cells displaying expression levels of signatures of Mg-TAM phenotypic states identified in PDOX TME. Examples of a key marker gene is shown per Mg-TAM signature. The color gradient represents expression levels. **(G)** Left: Heatmap displaying relative transcription factor (TF) activity of regulons identified by SCENIC in Ho-Mg and Mg-TAM phenotypic states. Right: tSNE projections based on binary regulon activity matrix. Examples of distinct TF activities are displayed in the binary format based on AUC threshold.

Microglia-derived TAMs display heterogeneous transcriptional programs

We next further took advantage of our unique dataset to interrogate phenotypic heterogeneity of Mg cells in normal brain and tumors of different histopathological features. Reference free analysis of our in-house data confirmed high abundance of Mg-TAMs in PDOXs (**Fig 4A-B**). Mg stratified into seven phenotypic clusters (CL0-6, **Fig 4A-B**), which partially overlapped with states identified by Ochocka et al. (Ochocka et al., 2021) (**Fig S4A-B)**, whereas CL7 and 8 expressed transcriptional profiles of Mo-TAMs and BAMs, respectively (**Table S4**)**.** Homeostatic Mg (Ho-Mg), highly enriched in normal brain, stratified into two clusters (CL0&1), where CL1 showed lower levels of homeostatic genes (e.g. *P2ry12, Tmem119, Gpr34,* **Fig 4C, Fig S4C**). Importantly, this was not the result of Mg activation via enzymatic digestion since the markers of enzymatically-activated Mg (e.g., *Erg1*, *Fos* (van den Brink et al., 2017)) were expressed rather by Ho-Mg in CL0 and overlapping with the MG2 state reported by Ochocka et al. (Ochocka et al., 2021) (**Fig S4D).** Five phenotypic states were further observed to be enriched in Mg-TAMs (CL2-6) **(Fig 4A-D, Table S4**). Trajectory analysis revealed a transition from Ho-Mg towards classical immunosuppressed anti-inflammatory Mg-TAMs (CL3: high for e.g. *Spp1, Cst7, Cxcl13*) via a transitory state (CL2 e.g. *Apoe*) (**Fig 4A, Fig S4E-F**). As expected, these Mg-TAMs showed highest *Ptprc* (CD45) expression (**Fig 4C**). Mg transition towards $CD45^{high}$ and $CCR2^{+}$ states in the tumor core was further confirmed by flow cytometry (**Fig 4E**). While Mg in distant brain areas (P3, P13 PDOXs) resembled normal brain characteristics, the invasive niche (P3 PDOX) showed partial activation of Mg towards Mg-TAMs. Of note, $CD45^{high}$ Mo-TAMs further increased CCR2 levels in the tumor core (**Fig S4G**). *Ccr2* transcripts were however not well captured by Drop-seq (**Fig S4C**). Additional branching included specific Mg-TAMs with astrocytic features (CL4, e.g. *Sparcl1, Gfap*), high transcriptional activity (CL5, e.g. *Rps12*) and high expression of endothelial cell markers (CL6, e.g., *Pecam1, Cldn5*). Interestingly, CL6 cells were enriched for expression of receptors known to play a

role in reciprocal crosstalk with tumor cells (e.g., *Flt1, Kdr*). Contamination from other TME subpopulations can be excluded as these cells display high expression of myeloid cell markers, including *Itgam* (CD11b, **Fig S4C**). Proliferating myeloid cells were detected, although they did not form a specific cluster (e.g., *Mki67*, *Cd34* **Fig S4C**). All PDOXs showed pronounced transitions towards heterogeneous Mg-TAM states, although with variable proportions. Precisely, P8 PDOXs showed a higher proportion of CL5 transcriptionally active Mg-TAMs in PDOX P8 (**Fig 4B**). Angiogenic T16 and P13 PDOXs contained prominent CL5/MG8 Mg-TAMs, whereas invasive T101 PDOX contained MG7 Mo-TAMs (**Fig S4B**). This suggests that human GBM tumor cells may activate Mg towards Mg-TAM states in a patient dependent manner. Despite the differences in proportions, the transcriptomic profiles of Mg-TAMs, Mo-TAMs and BAMs were generally similar between PDOXs and GL261 tumors, except for several key activation genes, e.g. higher levels of *Spp1*, *Apoe, Cxcl13* and lower *H2.Eb1* in PDOXs (**Fig S4H**).

Signatures obtained in mouse cells were further interrogated in myeloid cells of human GBM. Cell cycle analysis revealed presence of proliferating myeloid cells of both Mg and Mo origin (**Fig S5A**). Similarly to PDOXs, Mg expressing Ho-Mg signatures were present at lower levels (**Fig S5B**). As expected the strongest correlation was obtained for signatures of Mg-TAMs identified for CL2, 3 and 5 (**Fig 4F, Fig S5B**). Interestingly, we identified phenotypic states corresponding to astrocytic-like (CL5) and endothelial-like (CL6) TAMs. This confirms the transcriptomic heterogeneity of Mg-TAMs in GBM patient tumors and the presence of similar transcriptomic states as in PDOX models.

We next performed SCENIC analysis (Aibar et al., 2017) to reveal regulators of Mg phenotypic states (**Fig 4G**). A high number of regulons was identified for Ho-Mg states including Hdac2 and Ezh2. While Mg-TAM transitory state (CL2) did not show a particular enrichment of transcription factor activity, other Mg-TAMs displayed unique regulons. Inflammatory Mg-TAMs (CL3) appeared regulated by Hif1a, Stat1, Nfe2l2 and Mafb, suggesting a role of hypoxia in Mg state transitions. Astrocytic-like Mg-TAMs (CL4) showed high activity for Thra, Sox9 and Sox2 factors, known to regulate astrocytic states. Transcriptionally active Mg-TAMs (CL5) scored high for Hdac1, Mitf and Elf1 activity and endothelial-like Mg-TAMs (CL6) showed enrichment for Foxp1. These data further highlights the factual differences between phenotypic states of Mg and supports an impact of TME niches in shaping Mg heterogeneity in GBM.

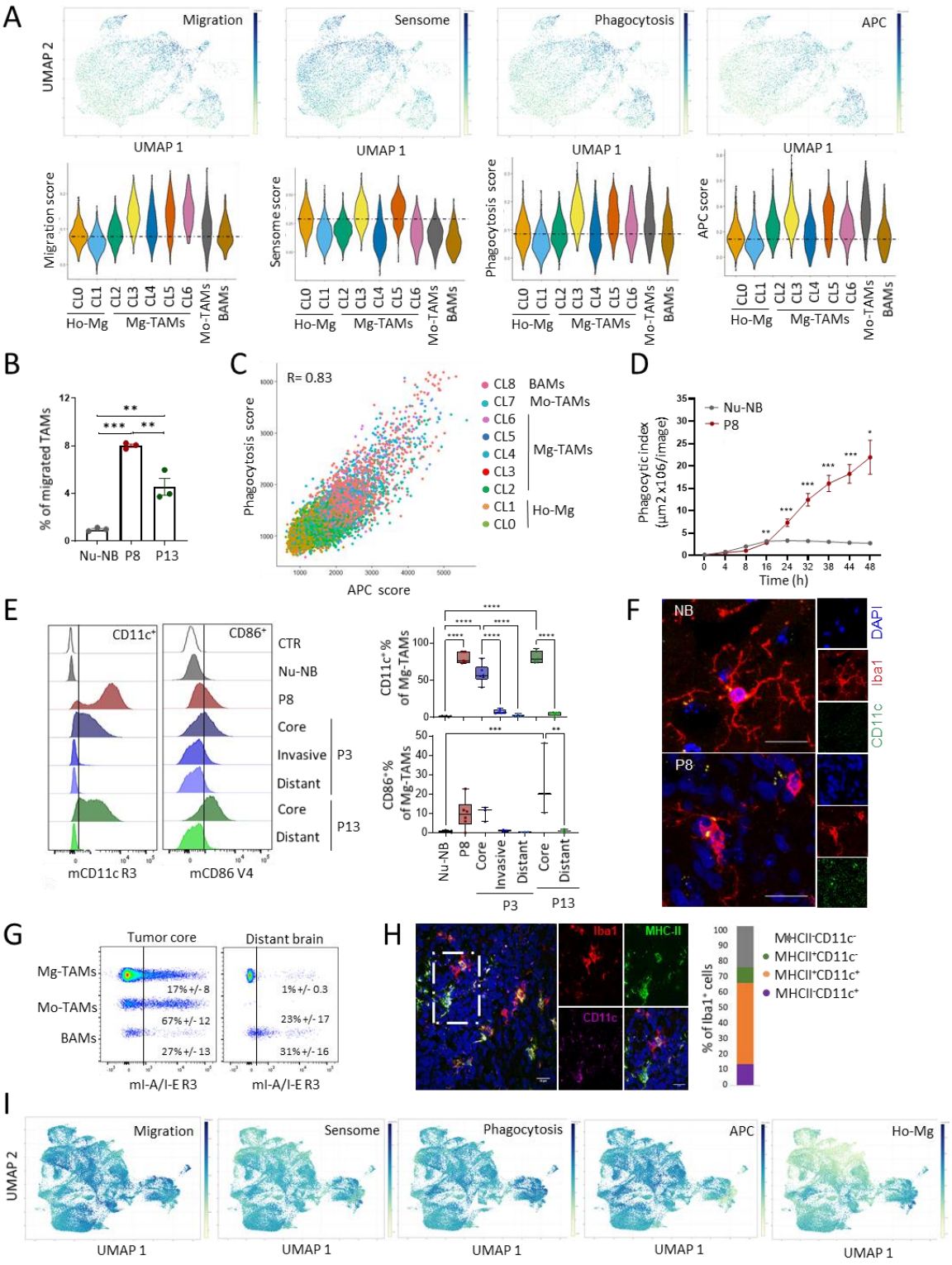

Figure 5. Functional properties of GBM-educated microglia. (A) Top: UMAP projections displaying expression levels of gene signature associated with migration, sensome, phagocytosis and antigen presentation cells (APC) (**Table S5**). Bottom: Signature score is depicted per myeloid cluster: CL0-1 homeostatic Mg (Ho-Mg), CL2-6: Mg-TAMs, CL7: Mo-TAMs, CL8: BAMs. **(B)** Ex vivo assessment of migratory capacity in CD11b$^+$ cells isolated from Nu-NB and PDOXs (P8, P13) **(**mean ± SEM, ** $p < 0.01$, *** $p < 0.001$, one-way ANOVA). **(C)** Correlation analysis between phagocytosis and APC signatures in myeloid cells. Cell clusters are color cored. **(D)** Phagocytic uptake of pHrodo E.coli bioparticles ex vivo in CD11b+ myeloid cells isolated from Nu-NB and PDOX P8 (n=4, mean +/- SEM, two-way ANOVA followed by Tukey's multiple comparisons, ***p<0.001, **p<0.01,

*p<0.05). **(E)** Left: representative flow cytometry graphs of $CD45^+CD11b^+Ly6G^-Ly6C^-CD206^-$ Mg-TAMs showing levels of CD11c and CD86 in nude mouse normal brain (Nu-NB) and three PDOX models. Unstained control is shown for each population (CTR). Right: quantification of $CD11c^+$ and $CD86^+$ cells in Mo-TAMs and BAMs across different tumor phenotypes and brain regions (n=3-6 from at least three different mouse brains each, one-way ANOVA, ***p<0.001, **p<0.01, *p<0.05). **(F)** Representative immunofluorescence pictures depicting CD11c staining of Iba1 cells in P8 PDOX tumor core. Scale bar = 20µm. **(G)** Representative flow cytometry graphs showing activation of MHC-II (I-A/I-E epitope) in Mg-TAMs and Mo-TAMs in tumor core versus distant brain. Examples shown for P13 PDOX. **(H)** Representative immunofluorescence pictures depicting MHC-II and CD11c co-expression of Iba1 cells in P8 PDOX tumor core. Scale bar = 20µm. **(I)** UMAP projection of human GBM myeloid cells displaying expression levels of functional signatures. The color gradient represents expression levels.

Mg-TAMs display immunologically active states with increased capacity for chemotaxis, sensome, phagocytosis and antigen presentation

We next interrogated functional properties of Mg-TAM subpopulations. GO analysis of genes activated in myeloid cells in PDOXs uncovered enrichment of terms associated with cell chemotaxis, cell adhesion and migration, and tumor-associated extracellular matrix proteins (**Fig 2A**). These were enriched globally in Mg-TAMs (CL2-6, **Fig 4B**). A migration score based on genes associated with monocyte, glial and neutrophil cell migration (e.g. *Fn1, Cxcl13, Ccl3*, *Postn,* **Table S5**) inferred a gradual increase in the migratory capacity during transition from Ho-Mg towards different phenotypic states of Mg-TAMs and in Mo-TAMs (**Fig 5A, Fig S6A**). Increased migration was functionally confirmed in $CD11b^+$ cells freshly isolated from PDOXs (P8, P13) compared to normal brain (**Fig 5B**). Mg sensome genes (**Table S5**) showed a higher score in certain clusters of Mg-TAMs compared to Ho-TAMs (**Fig 5A**). This was driven by genes such as *Cd74*, *Cd52* and *Clec7a*, and not homeostatic Mg (Ho-Mg) genes, which were highest in Ho-Mg (**Fig S6A-B**). Mg-TAMs also showed increased expression of genes related to phagocytosis (e.g. *Trem2, Tyrobp)* and antigen presentation (*Itgax***,** *Igf1, CD86* **Fig. 5A, Fig S6A**). These three signatures correlated to each other (**Fig 5C**) and were strongest in immunosuppressive Mg-TAMs (CL3) and in Mo-TAMs, but not BAMs. Indeed, $CD11b^+$ cells isolated from P8 PDOX displayed increased phagocytosis (**Fig 5D**). We also confirmed prominent CD11c and CD86 activation in Mg-TAMs, mainly in the tumor core of three PDOXs (**Fig 5E, Fig S6C**). Increased expression of CD11c was also detected by immunofluorescence in amoeboid $Iba1^+$ cells in the tumor core but not in ramified Mg in normal brain (**Fig. 5F**). CD11c and CD86 were also activated in Mo-TAMs and BAMs, consistent with gene expression profiles (**Fig S6C)**. We further confirmed activation of MHC-II expression (*H2-Eb1, H2-Ab1* and corresponding epitope I-A/I-E, **Fig 5G-H, Fig S6A**) in subpopulation of Mg-TAMs and Mo-TAMs in comparison to normal brain. Overall, this suggests that a subpopulation of Mg-TAMs is able to phagocyte and present antigens by displaying dendritic-cell programs under tumorigenic conditions. At the same time, Mg-TAMs and Mo-TAMs showed expression of check point inhibitors such as *Cd274* (PDL-1), *Havcr2* (TIM-3) and *Pdcd1* (PD-1, **Fig S6A**),

known to inhibit phagocytic capacity of macrophages. Interestingly, astrocytic-like (CL4) and endothelial-like (CL6) Mg-TAMs showed lower levels for phagocytosis and APC signatures than classical Mg-TAMs (CL3, CL5). The functionality and localization of these subpopulations needs further investigation. Of note, we did not detect increased expression of genes typically associated with macrophage immune suppression, namely M2 (e.g. *Arg1*; *Retnla*) or M0 (e.g. *Tgfb1*; *Il10*) marker genes in Mg-TAMs (**Fig S6A**). We validated our gene signatures in human GBM myeloid cells, confirming high activation of migratory and dendritic cell-like signatures in subpopulations of Mg-TAMs and Mo-TAMs in patient tumors (**Fig 5I**).

Temozolomide treatment leads to transcriptomic adaptation of GBM cells and adjacent tumor microenvironment.

Next we aimed to assess the adaptation of tumor cells and TME upon treatment (**Fig 6A**). We applied TMZ to P3 PDOXs representing *MGMT* promoter-methylated GBM. Tumor growth was validated by MRI and mice were treated 5 times a week in a period of 10 days with in total 8 received doses. Tumors were resected shortly after the last dose of TMZ. Prolonged TMZ treatment led to decreased tumor growth (**Fig 6B-C**). scRNA-seq assessment of isolated tumor cells revealed transcriptomic changes linked to survival mechanisms such as regulation of p53-associated signal transduction, apoptosis, cell death and cellular component organization (FDR≤0.01; $|\log_2 FC| \geq 0.5$, **Fig 6D-F**), suggesting activation of resistance mechanisms in surviving tumor cells. Assessment of GBM cellular subtypes revealed an increased proportion of mesenchymal-like states, in line with observations in GBM patients (Wang et al., 2017). The scRNA-seq analysis of TME revealed changes in the proportions of cell populations (**Fig 6G**). Interestingly, we observed an increased ratio of myeloid cells upon TMZ and a decrease of endothelial cells and astrocytes. Indeed, TMZ-treated tumors contained more Iba^+ myeloid cells in the tumor core (**Fig 6H**). The analysis of DEGs between TMZ treated and control tumors revealed pronounced transcriptomic changes of myeloid and endothelial cells, but not astrocytes (**Table S6**). Myeloid cells activated genes associated with inflammatory responses such as migration, chemotaxis, and gliogenesis (**Fig 6I**, e.g., *Cxcl13, Cx3Cr1, Csf1r*). Adaptation was visible at the level of regulation of translation, endocytosis (e.g. *Apoe, Lrp1*), cholesterol homeostasis (e.g. *Abca1, Abcg2*) and actin cytoskeleton (e.g. *Fscn1, Coro1a*). This correlated with decreased levels of TAM markers such as *Igfbp7, Ptn* and *Gng5,* involved in promoting tumor growth. Subsequently the heterogeneity of the myeloid compartment shifted to a higher ratio of Ho-Mg (CL0) and transitory Mg-TAMs (CL2, **Fig 6J**). At the same time, endothelial cells deregulated genes associated with cell development and death,

extracellular space, regulation of chemokine and cytokine production and acetylcholine receptor activity (e.g. up: *Ly6a/c1/e, H2.D1, Timp3, Cxcl12; down: Ctsd, Ctss*) as well as regulation of actin cytoskeleton and protein localization (**Fig S6D**). Taken together, these data show that TMZ not only induces transcriptomic adaptations in the tumor compartment and highlights the capacity of PDOXs to model overall plasticity of the GBM ecosystem upon treatment.

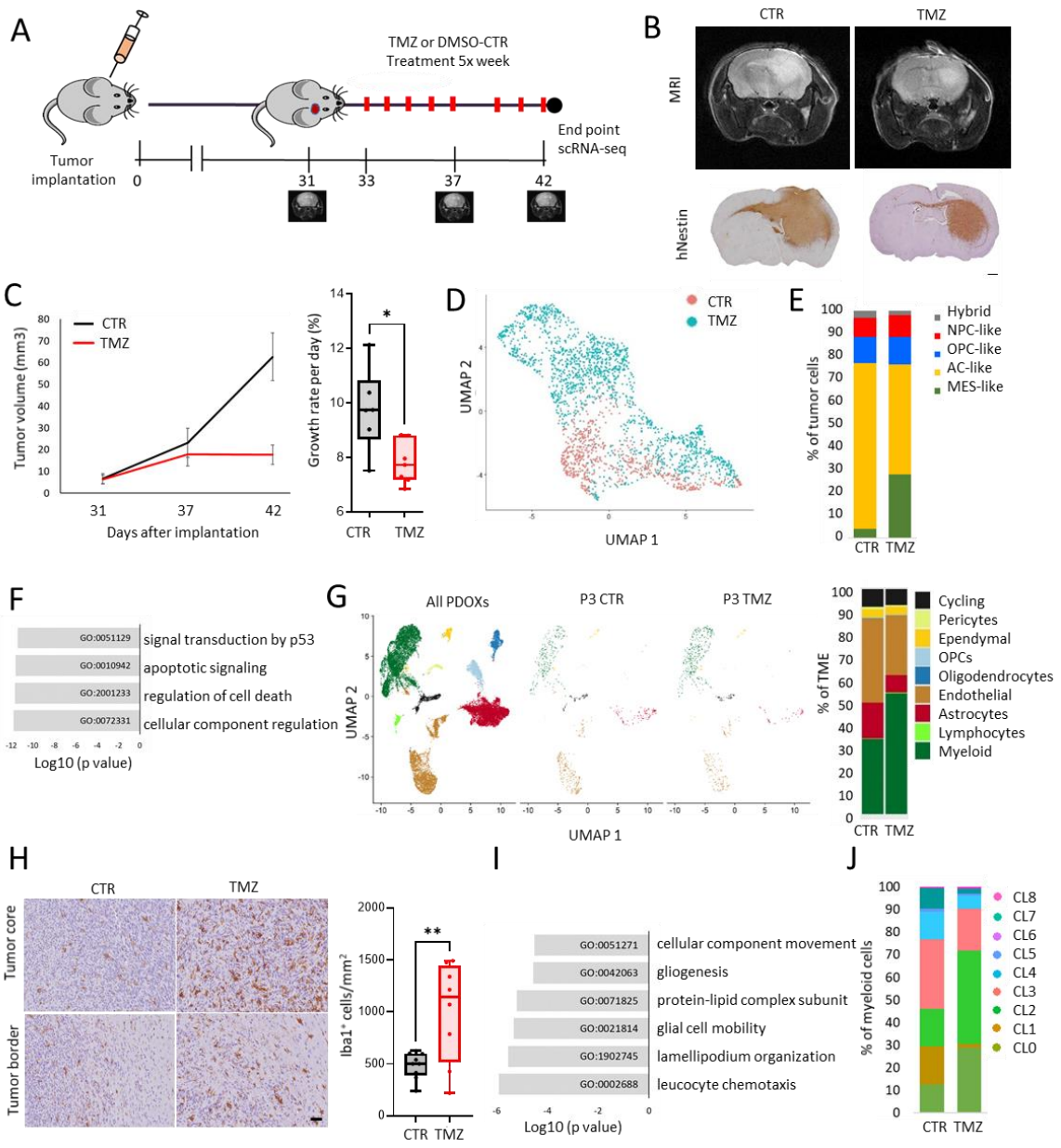

Figure 6. Transcriptomic adaptation of GBM tumor cells and TME upon TMZ treatment. (A) Schematic illustration of the TMZ treatment regimen in vivo. Day 0 = tumor implantation, day 31 = MRI validation of tumor growth, day 33= treatment start, day 36= intermediary MRI, day 42 = end point; **(B)** Representative MRI images and human-specific Nestin staining showing tumor growth in control P3 PDOXs (CTR) and TMZ-treated mice (TMZ). Scale bar = 100µm. **(C)** MRI-based assessment of tumor progression over time. Tumor growth rate was calculated during the entire study (day 42 vs day 31, n = 6-7, *p<0.05, two-tailed Student's t-test). **(D)** UMAP projection of harmony-corrected scRNA-seq data showing the overall gene expression relationship between TMZ treated and CTR GBM tumor cells; **(E)** Assessment of GBM cellular states (Neftel et al., 2019) at

single cell level in TMZ-treated and CTR GBM cells. **(F)** Summary of top four gene ontology terms characterizing DEGs in TMZ-treated versus CTR GBM cells (FDR ≤0.01, |logFC| ≥ 0.5 the Wilcoxon rank sum test with Benjamini-Hochberg correction); **(G)** Split UMAP projection of TME cells highlighting TME subpopulations detected in CTR and TMZ-treated P3 PDOX. TME cell types are color coded. Right: proportions of cell types in TME are displayed for CTR and TMZ-treated P3 PDOX; **(H)** Examples of Iba1 staining and quantification in CTR and TMZ-treated P3 PDOXs. Tumor cores are highlighted. Scale bar: 50 µm. (**p<0.01, two-tailed Student's t-test) **(I)** Summary of top six gene ontology terms characterizing DEGs in TMZ-treated versus CTR myeloid cells in TME (FDR ≤0.01, |logFC| ≥ 0.5 the Wilcoxon rank sum test with Benjamini-Hochberg correction); **(J)** Graph displaying proportions of cells assigned to nine clusters of myeloid cells in CTR and TMZ-treated P3 PDOX; Clusters 0-1: homeostatic Mg (Ho-Mg), Clusters 2-6: Mg-TAMs, Cluster 7: Mo-TAMs, Cluster 8: BAMs.

DISCUSSION

Various cellular components within the microenvironment of brain tumors are critical for the establishment of an immunosuppressive environment that facilitates tumor growth, progression, and treatment resistance. Using unbiased scRNA-seq analysis, we surveyed the TME of nine GBM PDOXs and compared it with the TME from the GL261 mouse glioma model and human GBM tumors. We show that GBM PDOX recapitulate major TME subpopulations present in human GBM and display extensive inter-and intra-tumoral TME heterogeneity. We reveal the presence of diverse cell types in the TME of PDOXs similar to those reported in human GBM (Darmanis et al., 2017; Johnson et al., 2021; Wang et al., 2017). We provide evidence that human tumor cells instruct the TME subpopulations in PDOX models towards a GBM associated phenotypic states. Myeloid cells, which represent the largest population of cells within the TME are largely of microglial origin in PDOX and human GBM. They exhibit a diverse cellular and molecular plasticity towards GBM-associated phenotypes reflecting both inter- and intra-patient heterogeneity.

Despite their distinct developmental origin and intrinsic transcriptional networks poised before the onset of tumor development, myeloid cells, such as resident parenchymal Mg, perivascular macrophages or peripheral monocyte-derived cells, are known to share signatures of tumor education, but also possess distinct transcriptional profiles and activation states (Bowman et al., 2016). In contrast to GL261, we find that tumor-educated myeloid cells in GBM PDOXs mainly display Mg expression programs. Different myeloid subpopulations were identified with close resemblance to previously identified clusters (Ochocka et al., 2021). Increased Mo-TAMs were observed mostly in necrotic and hypoxic areas with leaky blood brain barrier. Mg-TAM subpopulations ranged from homeostatic to activated (anti-inflammatory) states. Intriguingly, we identified additional clusters within Mg-TAMs expressing endothelial and astrocytic markers in addition to typical Mg markers. Activated myeloid cells have been reported to express angiogenic markers such as VEGF in line with the pro-angiogenic function of TAMs (Glass and Synowitz, 2014).

In contrast to previous work indicating a higher Mo-TAMs subpopulation in human GBMs (Wang et al., 2017), we found that resident Mg-TAMs represent an important fraction of myeloid cell population in both PDOXs and primary GBMs characterized at the single-cell level. We detect a higher proportion of Mo-TAMs in subgroup of recurrent human GBMs, supporting previous reports (Pombo Antunes et al., 2021). Of note we show that TAMs activation occurs in PDOXs generated in nude mice, which lack T cells, suggesting that the myeloid-T cell crosstalk may not be required for TAM activation. Since nude mice still possess B and NK cells as their main lymphocytic subpopulations, it remains to be seen whether the loss of T cells is compensated by other available lymphocytes.

We further show that activated Mg-TAMs display immunologic features and possess phagocytic and antigen-presentation capacity. Expression of phagocytic and APC genes were markedly increased in activated Mg-TAM subsets compared to homeostatic Mg-TAMs. Our data is in line with previous reports showing the phagocytic activity in GBM-associated Mg (Hutter et al., 2019; Saavedra-Lopez et al., 2020). Although not much is known about the functional implications of phagocytic Mg in GBM, emerging data suggests both a pro-tumor and anti-tumor effect. For instance, phagocytic Mg were shown to populate necrotic tumor zones and aid in the clearance of debris to enhance GBM cell invasion (Saavedra-Lopez et al., 2020). In addition, TAMs in the pseudopalisading region show different phenotypes of both pro- and anti-inflammatory states depending on their spatial location: TAMs in the hypercellular area are anti-inflammatory, while TAMs in the necrotic foci show a $MHCII^{+}$ pro-inflammatory phenotype. This suggests that microenvironmental changes based on spatial location of TAMs may result in a phenotypic switch from pro- to anti-inflammatory state. On the other hand, an anti-tumor role was associated with the enhanced phagocytic ability of TAMs following CD47 blockade (Gholamin et al., 2017; Hutter et al., 2019; Li et al., 2018), an effect that was more pronounced in combination with TMZ (von Roemeling et al., 2020). These results suggest that the phagocytic capacity of Mg-TAMs appears to be pervasive and may require fine tuning in the context of therapeutic reprogramming. Finally, we demonstrate the utility of our PDOX models in understanding GBM cell and TME adaptation upon treatment. Notably, we identified tumor cell and TME remodeling following treatment. GBM cells showed a marked transcriptomic alteration in cell state proportions as was previously shown following microenvironmental pressure such as hypoxia (Johnson et al., 2021) or targeted treatment (Eyler et al., 2020; Liau et al., 2017). Interestingly, tumor cell adaptation towards a MES-like cell state also correlated with an increase in myeloid cells infiltration. This corroborates recent findings linking myeloid cells with a switch towards a mesenchymal phenotype in GBM upon treatment (Hara et al., 2021). Further studies with a larger cohort of treated PDOXs will be needed to fully understand GBM cells and TME adaptation following treatment.

In summary, we uncovered diverse cellular and molecular specificities of the GBM-associated myeloid compartment. We found that resident Mg represent the main myeloid cell population in GBM, while peripheral-derived myeloid cells mostly appear to infiltrate the brain at sites of blood brain barrier disruption. Notably, we detected reactive dendritic cell-like gene expression programs in a subset of GBM-educated Mg. Further functional characterization is needed to harness their anti-tumor potential, for instance by addressing their capacity to recruit lymphocytes and their phagocytic ability against tumor cells. Our findings highlight the resemblance of the TME of patient-derived preclinical models with that of human GBM, especially the TAMs subpopulations, indicating the relevance of such models for preclinical research. Research efforts aimed at deciphering TAM heterogeneity associated with functional specificities may contribute to the development of novel immune therapeutic approaches in GBM patients. It remains to be seen if development of PDOX in mice with humanized immune system will restore missing TME components (Klein et al., 2020).

ACKNOWLEDGEMENTS

We are grateful to the Neurosurgery Department of the Centre Hospitalier Luxembourg and Clinical and Epidemiological Investigation Center of the LIH for support in tumor collection. We thank Virginie Baus and Jean-Jacques Gerardy for technical assistance. We acknowledge the excellent support from LIH's core facilities (animal facility, MRI, national cytometry platform) and LSCB sequencing platform.

REFERENCES

Abdul Rahim, S.A., Dirkse, A., Oudin, A., Schuster, A., Bohler, J., Barthelemy, V., Muller, A., Vallar, L., Janji, B., Golebiewska, A.*, et al.* (2017). Regulation of hypoxia-induced autophagy in glioblastoma involves ATG9A. Br J Cancer *117*, 813-825.

Aibar, S., Gonzalez-Blas, C.B., Moerman, T., Huynh-Thu, V.A., Imrichova, H., Hulselmans, G., Rambow, F., Marine, J.C., Geurts, P., Aerts, J.*, et al.* (2017). SCENIC: single-cell regulatory network inference and clustering. Nat Methods *14*, 1083-1086.

Bennett, M.L., Bennett, F.C., Liddelow, S.A., Ajami, B., Zamanian, J.L., Fernhoff, N.B., Mulinyawe, S.B., Bohlen, C.J., Adil, A., Tucker, A.*, et al.* (2016). New tools for studying microglia in the mouse and human CNS. Proc Natl Acad Sci U S A *113*, E1738-1746.

Bougnaud, S., Golebiewska, A., Oudin, A., Keunen, O., Harter, P.N., Mader, L., Azuaje, F., Fritah, S., Stieber, D., Kaoma, T.*, et al.* (2016). Molecular crosstalk between tumour and brain parenchyma instructs histopathological features in glioblastoma. Oncotarget *7*, 31955-31971.

Bowman, R.L., Klemm, F., Akkari, L., Pyonteck, S.M., Sevenich, L., Quail, D.F., Dhara, S., Simpson, K., Gardner, E.E., Iacobuzio-Donahue, C.A.*, et al.* (2016). Macrophage Ontogeny Underlies Differences in Tumor-Specific Education in Brain Malignancies. Cell Rep *17*, 2445-2459.

Butovsky, O., Jedrychowski, M.P., Moore, C.S., Cialic, R., Lanser, A.J., Gabriely, G., Koeglsperger, T., Dake, B., Wu, P.M., Doykan, C.E.*, et al.* (2014). Identification of a unique TGF-beta-dependent molecular and functional signature in microglia. Nat Neurosci *17*, 131-143.

Buttini, M., Orth, M., Bellosta, S., Akeefe, H., Pitas, R.E., Wyss-Coray, T., Mucke, L., and Mahley, R.W. (1999). Expression of human apolipoprotein E3 or E4 in the brains of Apoe-/- mice: isoform-specific effects on neurodegeneration. J Neurosci *19*, 4867-4880.
Charles, N.A., Holland, E.C., Gilbertson, R., Glass, R., and Kettenmann, H. (2011). The brain tumor microenvironment. Glia *59*, 1169-1180.
Chiu, I.M., Morimoto, E.T., Goodarzi, H., Liao, J.T., O'Keeffe, S., Phatnani, H.P., Muratet, M., Carroll, M.C., Levy, S., Tavazoie, S.*, et al.* (2013). A neurodegeneration-specific gene-expression signature of acutely isolated microglia from an amyotrophic lateral sclerosis mouse model. Cell Rep *4*, 385-401.
Darmanis, S., Sloan, S.A., Croote, D., Mignardi, M., Chernikova, S., Samghababi, P., Zhang, Y., Neff, N., Kowarsky, M., Caneda, C.*, et al.* (2017). Single-Cell RNA-Seq Analysis of Infiltrating Neoplastic Cells at the Migrating Front of Human Glioblastoma. Cell Rep *21*, 1399-1410.
Deczkowska, A., Keren-Shaul, H., Weiner, A., Colonna, M., Schwartz, M., and Amit, I. (2018). Disease-Associated Microglia: A Universal Immune Sensor of Neurodegeneration. Cell *173*, 1073-1081.
Dirkse, A., Golebiewska, A., Buder, T., Nazarov, P.V., Muller, A., Poovathingal, S., Brons, N.H.C., Leite, S., Sauvageot, N., Sarkisjan, D.*, et al.* (2019). Stem cell-associated heterogeneity in Glioblastoma results from intrinsic tumor plasticity shaped by the microenvironment. Nat Commun *10*, 1787.
Eyler, C.E., Matsunaga, H., Hovestadt, V., Vantine, S.J., van Galen, P., and Bernstein, B.E. (2020). Single-cell lineage analysis reveals genetic and epigenetic interplay in glioblastoma drug resistance. Genome Biol *21*, 174.
Fack, F., Espedal, H., Keunen, O., Golebiewska, A., Obad, N., Harter, P.N., Mittelbronn, M., Bahr, O., Weyerbrock, A., Stuhr, L.*, et al.* (2015). Bevacizumab treatment induces metabolic adaptation toward anaerobic metabolism in glioblastomas. Acta Neuropathol *129*, 115-131.
Friedrich, M., Sankowski, R., Bunse, L., Kilian, M., Green, E., Ramallo Guevara, C., Pusch, S., Poschet, G., Sanghvi, K., Hahn, M.*, et al.* (2021). Tryptophan metabolism drives dynamic immunosuppressive myeloid states in IDH-mutant gliomas. Nat Cancer *2*, 723-740.
Gholamin, S., Mitra, S.S., Feroze, A.H., Liu, J., Kahn, S.A., Zhang, M., Esparza, R., Richard, C., Ramaswamy, V., Remke, M.*, et al.* (2017). Disrupting the CD47-SIRPalpha anti-phagocytic axis by a humanized anti-CD47 antibody is an efficacious treatment for malignant pediatric brain tumors. Sci Transl Med *9*.
Glass, R., and Synowitz, M. (2014). CNS macrophages and peripheral myeloid cells in brain tumours. Acta Neuropathol *128*, 347-362.
Golebiewska, A., Hau, A.C., Oudin, A., Stieber, D., Yabo, Y.A., Baus, V., Barthelemy, V., Klein, E., Bougnaud, S., Keunen, O.*, et al.* (2020). Patient-derived organoids and orthotopic xenografts of primary and recurrent gliomas represent relevant patient avatars for precision oncology. Acta Neuropathol *140*, 919-949.
Hambardzumyan, D., Gutmann, D.H., and Kettenmann, H. (2016). The role of microglia and macrophages in glioma maintenance and progression. Nat Neurosci *19*, 20-27.
Hao, Y., Hao, S., Andersen-Nissen, E., Mauck, W.M., 3rd, Zheng, S., Butler, A., Lee, M.J., Wilk, A.J., Darby, C., Zager, M.*, et al.* (2021). Integrated analysis of multimodal single-cell data. Cell *184*, 3573-3587 e3529.
Hara, T., Chanoch-Myers, R., Mathewson, N.D., Myskiw, C., Atta, L., Bussema, L., Eichhorn, S.W., Greenwald, A.C., Kinker, G.S., Rodman, C.*, et al.* (2021). Interactions between cancer cells and immune cells drive transitions to mesenchymal-like states in glioblastoma. Cancer Cell *39*, 779-792 e711.
Hickman, S.E., Kingery, N.D., Ohsumi, T.K., Borowsky, M.L., Wang, L.C., Means, T.K., and El Khoury, J. (2013). The microglial sensome revealed by direct RNA sequencing. Nat Neurosci *16*, 1896-1905.
Hillje, R., Pelicci, P.G., and Luzi, L. (2020). Cerebro: interactive visualization of scRNA-seq data. Bioinformatics *36*, 2311-2313.

Hutter, G., Theruvath, J., Graef, C.M., Zhang, M., Schoen, M.K., Manz, E.M., Bennett, M.L., Olson, A., Azad, T.D., Sinha, R.*, et al.* (2019). Microglia are effector cells of CD47-SIRPalpha antiphagocytic axis disruption against glioblastoma. Proc Natl Acad Sci U S A *116*, 997-1006.
Johnson, K.C., Anderson, K.J., Courtois, E.T., Gujar, A.D., Barthel, F.P., Varn, F.S., Luo, D., Seignon, M., Yi, E., Kim, H.*, et al.* (2021). Single-cell multimodal glioma analyses identify epigenetic regulators of cellular plasticity and environmental stress response. Nat Genet *53*, 1456-1468.
Klein, E., Hau, A.C., Oudin, A., Golebiewska, A., and Niclou, S.P. (2020). Glioblastoma Organoids: Pre-Clinical Applications and Challenges in the Context of Immunotherapy. Front Oncol *10*, 604121.
Korsunsky, I., Millard, N., Fan, J., Slowikowski, K., Zhang, F., Wei, K., Baglaenko, Y., Brenner, M., Loh, P.R., and Raychaudhuri, S. (2019). Fast, sensitive and accurate integration of single-cell data with Harmony. Nat Methods *16*, 1289-1296.
Li, F., Lv, B., Liu, Y., Hua, T., Han, J., Sun, C., Xu, L., Zhang, Z., Feng, Z., Cai, Y.*, et al.* (2018). Blocking the CD47-SIRPalpha axis by delivery of anti-CD47 antibody induces antitumor effects in glioma and glioma stem cells. Oncoimmunology *7*, e1391973.
Liau, B.B., Sievers, C., Donohue, L.K., Gillespie, S.M., Flavahan, W.A., Miller, T.E., Venteicher, A.S., Hebert, C.H., Carey, C.D., Rodig, S.J.*, et al.* (2017). Adaptive Chromatin Remodeling Drives Glioblastoma Stem Cell Plasticity and Drug Tolerance. Cell Stem Cell *20*, 233-246 e237.
Macosko, E.Z., Basu, A., Satija, R., Nemesh, J., Shekhar, K., Goldman, M., Tirosh, I., Bialas, A.R., Kamitaki, N., Martersteck, E.M.*, et al.* (2015). Highly Parallel Genome-wide Expression Profiling of Individual Cells Using Nanoliter Droplets. Cell *161*, 1202-1214.
Ochocka, N., Segit, P., Walentynowicz, K.A., Wojnicki, K., Cyranowski, S., Swatler, J., Mieczkowski, J., and Kaminska, B. (2021). Single-cell RNA sequencing reveals functional heterogeneity of glioma-associated brain macrophages. Nat Commun *12*, 1151.
Oudin, A., Baus, V., Barthelemy, V., Fabian, C., Klein, E., Dieterle, M., Wantz, M., Hau, A.C., Dording, C., Bernard, A.*, et al.* (2021). Protocol for derivation of organoids and patient-derived orthotopic xenografts from glioma patient tumors. STAR Protoc *2*, 100534.
Pires-Afonso, Y., Muller, A., Grzyb, K., Oudin, A., Yabo, Y., Sousa, C., Scafidi, A., Poli, A., Cosma, A., Halder, R.*, et al.* (2021). Elucidating tumour-associated microglia/macrophage diversity along Glioblastoma progression and under ACOD1 deficiency in revision.
Pombo Antunes, A.R., Scheyltjens, I., Lodi, F., Messiaen, J., Antoranz, A., Duerinck, J., Kancheva, D., Martens, L., De Vlaminck, K., Van Hove, H.*, et al.* (2021). Single-cell profiling of myeloid cells in glioblastoma across species and disease stage reveals macrophage competition and specialization. Nat Neurosci *24*, 595-610.
Qiu, X., Mao, Q., Tang, Y., Wang, L., Chawla, R., Pliner, H.A., and Trapnell, C. (2017). Reversed graph embedding resolves complex single-cell trajectories. Nat Methods *14*, 979-982.
Quail, D.F., and Joyce, J.A. (2017). The Microenvironmental Landscape of Brain Tumors. Cancer Cell *31*, 326-341.
Ricard, C., Tchoghandjian, A., Luche, H., Grenot, P., Figarella-Branger, D., Rougon, G., Malissen, M., and Debarbieux, F. (2016). Phenotypic dynamics of microglial and monocyte-derived cells in glioblastoma-bearing mice. Sci Rep *6*, 26381.
Saavedra-Lopez, E., Roig-Martinez, M., Cribaro, G.P., Casanova, P.V., Gallego, J.M., Perez-Valles, A., and Barcia, C. (2020). Phagocytic glioblastoma-associated microglia and macrophages populate invading pseudopalisades. Brain Commun *2*, fcz043.
Sousa, C., Golebiewska, A., Poovathingal, S.K., Kaoma, T., Pires-Afonso, Y., Martina, S., Coowar, D., Azuaje, F., Skupin, A., Balling, R.*, et al.* (2018). Single-cell transcriptomics reveals distinct inflammation-induced microglia signatures. EMBO Rep.
Szulzewsky, F., Pelz, A., Feng, X., Synowitz, M., Markovic, D., Langmann, T., Holtman, I.R., Wang, X., Eggen, B.J., Boddeke, H.W.*, et al.* (2015). Glioma-associated microglia/macrophages display an expression profile different from M1 and M2 polarization and highly express Gpnmb and Spp1. PLoS One *10*, e0116644.

Thorsson, V., Gibbs, D.L., Brown, S.D., Wolf, D., Bortone, D.S., Ou Yang, T.H., Porta-Pardo, E., Gao, G.F., Plaisier, C.L., Eddy, J.A*., et al.* (2018). The Immune Landscape of Cancer. Immunity *48*, 812-830 e814.

Tirosh, I., Venteicher, A.S., Hebert, C., Escalante, L.E., Patel, A.P., Yizhak, K., Fisher, J.M., Rodman, C., Mount, C., Filbin, M.G*., et al.* (2016). Single-cell RNA-seq supports a developmental hierarchy in human oligodendroglioma. Nature *539*, 309-313.

van den Brink, S.C., Sage, F., Vertesy, A., Spanjaard, B., Peterson-Maduro, J., Baron, C.S., Robin, C., and van Oudenaarden, A. (2017). Single-cell sequencing reveals dissociation-induced gene expression in tissue subpopulations. Nat Methods *14*, 935-936.

von Roemeling, C.A., Wang, Y., Qie, Y., Yuan, H., Zhao, H., Liu, X., Yang, Z., Yang, M., Deng, W., Bruno, K.A*., et al.* (2020). Therapeutic modulation of phagocytosis in glioblastoma can activate both innate and adaptive antitumour immunity. Nat Commun *11*, 1508.

Wang, L., Babikir, H., Muller, S., Yagnik, G., Shamardani, K., Catalan, F., Kohanbash, G., Alvarado, B., Di Lullo, E., Kriegstein, A*., et al.* (2019). The Phenotypes of Proliferating Glioblastoma Cells Reside on a Single Axis of Variation. Cancer Discov *9*, 1708-1719.

Wang, Q., Hu, B., Hu, X., Kim, H., Squatrito, M., Scarpace, L., deCarvalho, A.C., Lyu, S., Li, P., Li, Y*., et al.* (2017). Tumor Evolution of Glioma-Intrinsic Gene Expression Subtypes Associates with Immunological Changes in the Microenvironment. Cancer Cell *32*, 42-56 e46.

Woo, X.Y., Giordano, J., Srivastava, A., Zhao, Z.M., Lloyd, M.W., de Bruijn, R., Suh, Y.S., Patidar, R., Chen, L., Scherer, S*., et al.* (2021). Conservation of copy number profiles during engraftment and passaging of patient-derived cancer xenografts. Nat Genet *53*, 86-99.

Yabo, Y.A., Niclou, S.P., and Golebiewska, A. (2021). Cancer cell heterogeneity and plasticity: A paradigm shift in glioblastoma. Neuro Oncol.

Zeiner, P.S., Preusse, C., Golebiewska, A., Zinke, J., Iriondo, A., Muller, A., Kaoma, T., Filipski, K., Muller-Eschner, M., Bernatz, S*., et al.* (2018). Distribution and prognostic impact of microglia/macrophage subpopulations in gliomas. Brain Pathol.

SUPPLEMENTARY FIGURES

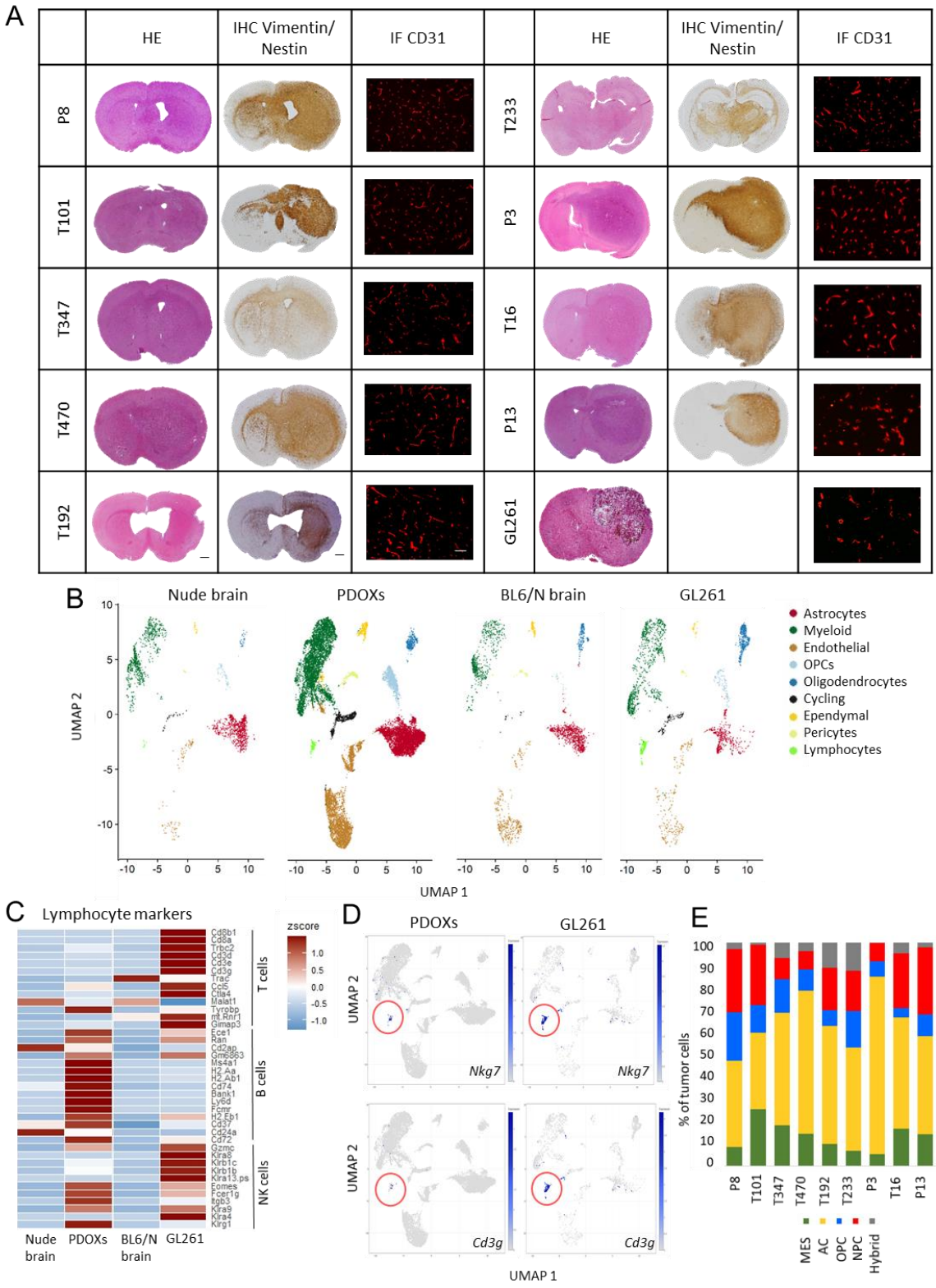

Fig. S1. Characterization of TME diversity in PDOX and GL261 GBM models. (A) Hematoxylin and Eosin (H&E), human-specific Vimentin/Nestin and mouse-specific CD31 staining of PDOX cohort and GL261 models. Human-specific Vimentin/Nestin staining highlights varying levels of invasion in PDOX models, while mouse-specific CD31 staining shows aberrant blood vessels in the GBM models. Scale bars represent 1mm (black) and 100µm (white). **(B)** Split UMAP projection showing representation of TME components in four sample groups. TME cell types are color coded **(C)** Analysis of lymphocyte cell cluster. Heatmap shows z-score of average expression of marker

genes for T, B and NK cells in lymphocytes detected in each sample group. **(D)** UMAP projection showing high expression of the NK marker *Nkg7* and T cell marker *Cd3g* in the lymphocytic cells in GL261 model). The color gradient represents expression levels. **(E)** Human tumor cells of PDOX models were assigned to four GBM transcriptomic states (Neftel et al., 2019): mesenchymal-like (MES), astrocytic-like (AC), oligodendrocyte progenitor cell-like (OPC) and neural stem cell–like (NPC). Hybrid states were grouped together.

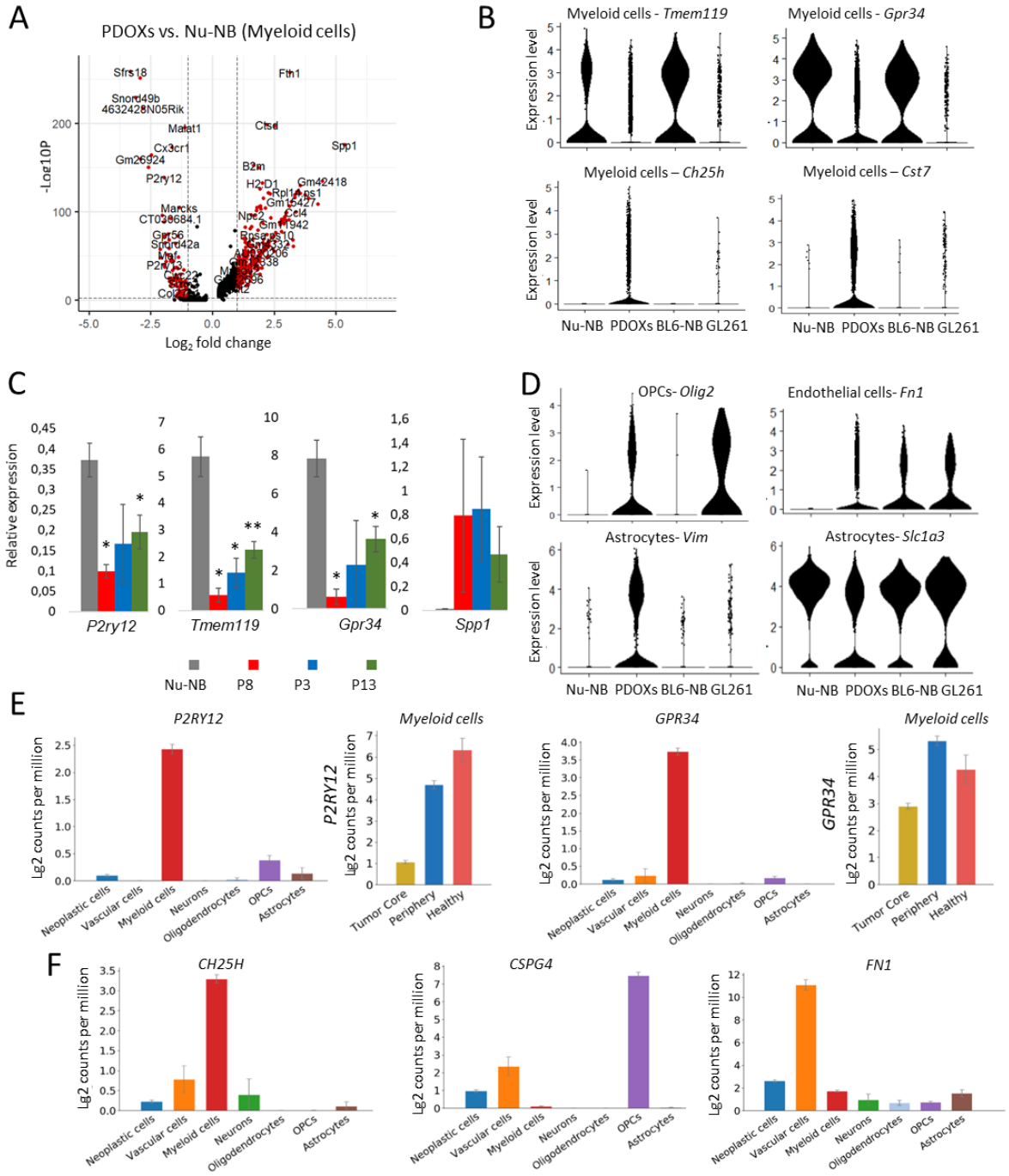

Fig. S2. Tumor-specific activation of TME cell types. (A) Volcano plot showing differentially expressed genes between TME of PDOXs vs nude mouse normal brain (Nu-NB) in myeloid cells. Threshold of FDR ≤0.01, $|\log_2 FC| \geq 1$ was applied in scRNA-seq analysis (the Wilcoxon rank sum test with Benjamini-Hochberg correction). **(B)** Gene expression levels of homeostatic myeloid markers

(*Tmem119, Gpr34*) and activated myeloid markers (*Cst7, Ch25h*) in myeloid cells of four biological groups: Nu-NB, PDOXs (9 models combined), BL6-NB, GL261 tumor (3 time points combined). **(C)** Decreased expression of homeostatic myeloid markers (*P2ry12*, *Tmem119, Gpr34*) and increased levels of activated myeloid marker (*Spp1*) were validated by Q-PCR in $CD11b^{+}$ myeloid cells isolated as bulk from TME of representative PDOX models (P3, P8, P13) and nude normal brain (Nu-NB); graphs show bulk mean relative expression levels ± SEM (n=2-5, $^{**}p<0.01$ $^{*}p<0.05$, two-tailed Student's t-test). *Rpl27* was used as a housekeeping gene. **(D)** Gene expression levels of representative markers differentially expressed between TME of PDOXs versus Nu-NB are shown for OPCs, astrocytes and endothelial cells. **(E)** Expression levels of homeostatic myeloid markers *P2RY12* and *GPR34* in distinct cell types detected in human GBM tumors (left graphs) and in myeloid cells isolated in different regions of GBM patient tumors (right graphs). The two markers are unique to myeloid cells and show decreased levels in GBM tumor core compared to normal brain regions. Expression levels in single cells are displayed as mean ± SEM. **(F)** Pronounced expression of *CH25H*, *CSPG4* and *FN1* in myeloid cells, OPCs and endothelial cells respectively was confirmed in human GBM tumors. Expression levels in single cells of respective GBM subpopulations are displayed as mean ± SEM (Darmanis et al., 2017).

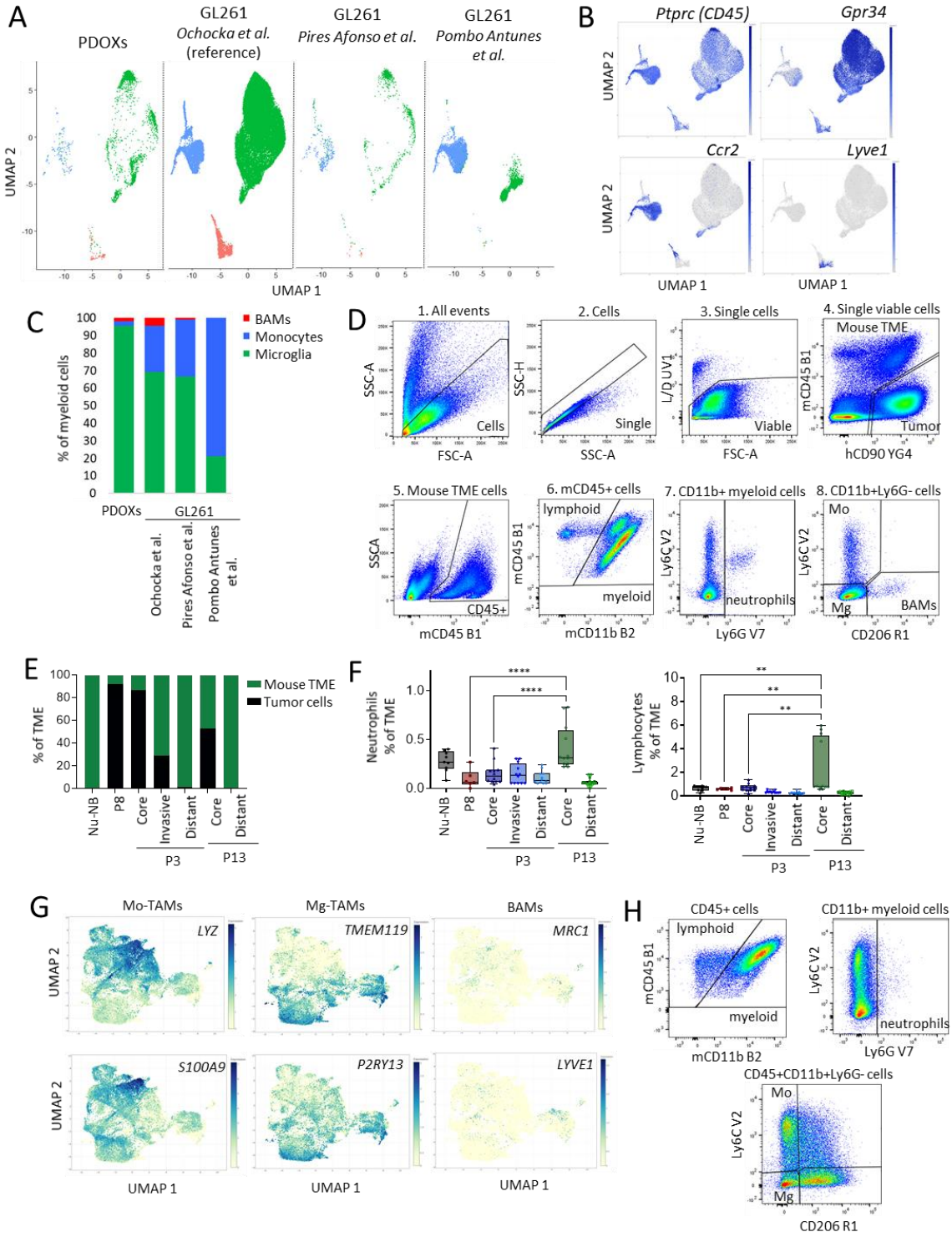

Figure S3. Myeloid cell heterogeneity in human and mouse-derived GBM TME. (A) Split UMAP projection of myeloid cells from different datasets. Myeloid cell types are color coded. **(B)** UMAPS showing expression of marker genes: pan-immune *Ptprc* (CD45), Mg *Gpr34*, monocytes *Ccr2*, BAMs *Lyve*. The color gradient represents expression levels. **(C)** Proportions of myeloid cell types in PDOXs and GL261 for three independent datasets (Ochocka et al., 2021; Pires-Afonso et al., 2021; Pombo Antunes et al., 2021). Percentage of Mo-TAMs depends on the tumor collection time and dissection strategy. **(D)** Gating strategy for flow cytometry. Example is shown for P13 PDOX tumor: (1) Cells were distinguished from debris based on the Forward Scatter (FSC) and Side Scatter (SSC). (2) Cell aggregates were gated out based on their properties displayed on the SSC area (SSC-A) versus height (SSC-H) dot plot. (3) Dead cells were recognized by their strong positivity for the dead cell marker (L/D) (4) Human tumor cells were recognized as CD90 positive with human-specific antibody. (5) Immune cells were recognized as CD45 positive. (6) Lymphocytes were recognized as

CD11b negative population. Negative gating includes also CD11b^{low} NK cells. CD11b positive cells correspond to myeloid cells. (7) CD11b^{+}Ly6C^{low}Ly6G^{+} cells represent neutrophils. (8) Ly6C and CD206 allows distinguishing Ly6C^{+}CD206- Mo-TAMs, Ly6C^{-}CD206^{-} Mg-TAMs and Ly6C^{-}CD206^{+} BAMs. **(E)** Ratio of human tumor cells over mouse-derived TME across the different tumor phenotypes and zones. The ratio of tumor cells to TME was higher in the tumor core compared to invasive zone and distal brain regions, reflecting a similar tumor core mass in all PDOX phenotypes. **(F)** Box plots show flow cytometry quantification of CD45^{+}CD11b^{+}Ly6G^{+}Ly6C^{low}CD206^{-} neutrophils and CD45^{+}CD11b^{-} lymphocytes in Nu-NB and PDOX TME across different tumor phenotypes and brain regions (n=6-15 from at least three different mouse brains each, one-way ANOVA, ***p<0.001, **p<0.01, *p<0.05). **(G)** UMAP projection of myeloid cells in GBM patient tumors. The color gradient represents expression levels of marker genes for Mg-TAMs, Mo-TAMs and BAMs. In contrary to mouse model, BAMs do not appear as a distinct cellular cluster. **(H)** Flow cytometry phenotyping of myeloid cells in GL261 tumors. GL261 present high proportion of Ly6C^{+} Mo-TAMs that acquire CD206 expression. Similarly, CD206 expression appears to be activated in Mg-TAMs, which overlap with rare BAMs.

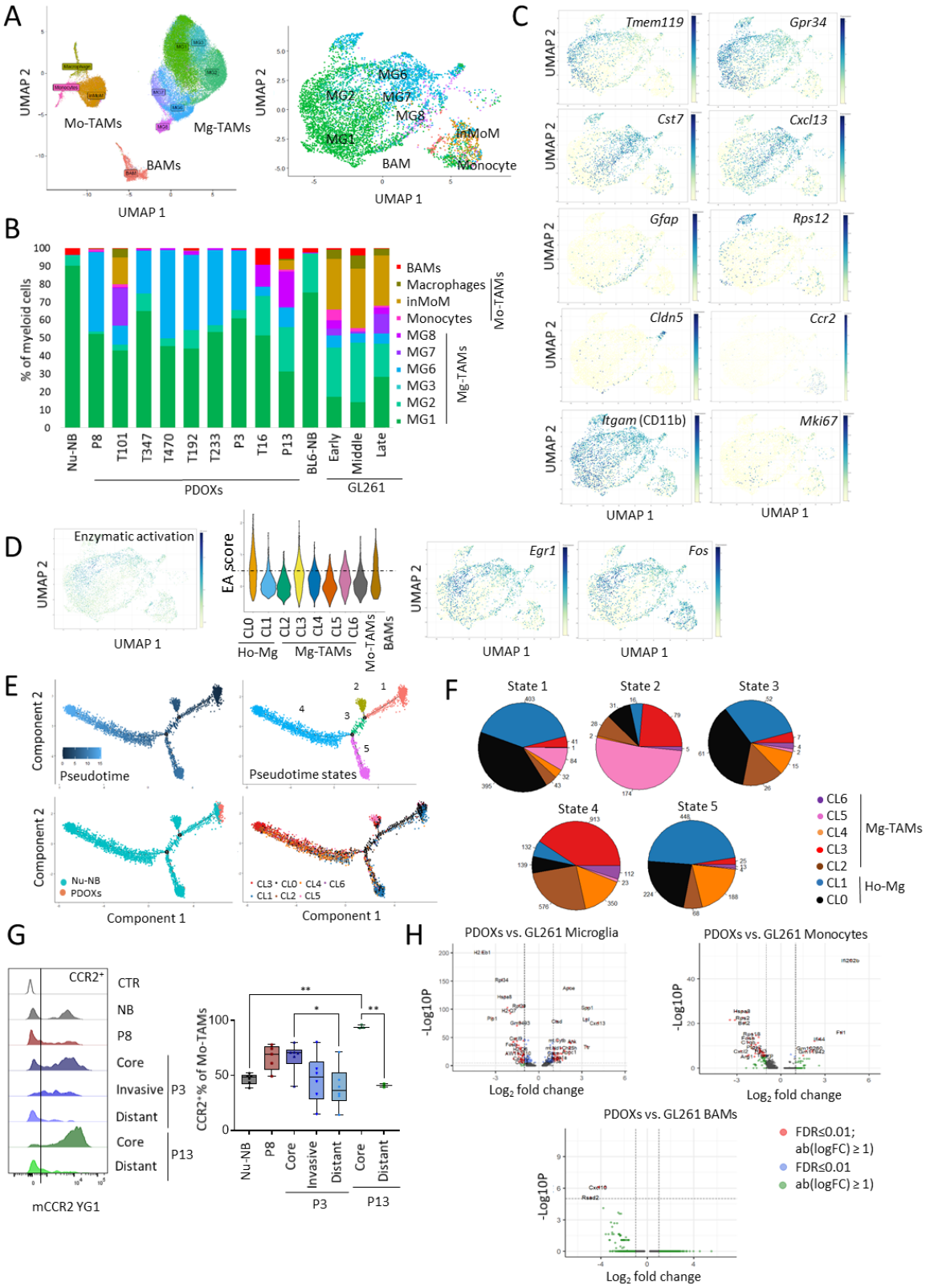

Figure S4. Analysis of heterogeneous Mg-TAMs in PDOXs. (A) UMAP projection of reference-based mapping (left) and unsupervised clustering (right) of myeloid cells. Myeloid cells were assigned to the Mg-TAM (MG1-8), Mo-TAM (Monocytes, intermediate Monocytes/Macrophages (inMoM), Macrophages) and BAM subpopulations described by Ochocka et al (Ochocka et al., 2021) **(B)** Graph displaying proportions of cells assigned to myeloid subpopulations described by Ochocka et al in nude mouse normal brain (Nu-NB), PDOXs (9 models), Black 6 mouse normal brain (BL6-NB), GL261 tumor (3 collection time points: early, middle late). Mg-TAMs in PDOXs were

predominantly composed of the previously defined MG1 (homeostatic Mg), MG2 (transcriptionally active Mg) and MG6 (associated with extracellular vesicles) phenotypic states. PDOXs with pronounced angiogenic features (T16, P13) showed higher myeloid heterogeneity, containing also MG8 proliferative Mg-TAMs, Mo-TAMs and BAMs. T101 PDOX (invasive phenotype) also showed presence of Mo-TAMs, BAMs and MG7 Mo-TAMs (MHC class I/II state). **(C)** UMAP projections displaying expression levels of representative genes characteristic for Mg-TAM clusters. In addition, pan-myeloid marker *Itgam* (CD11b) and proliferation parker *MiKi67* is depicted. The color gradient represents expression levels. **(D)** Left: UMAP projection displaying expression levels of gene signature associated with activation of Mg during enzymatic digestion (**Table S5**). Middle: Signature score is depicted per myeloid cluster, Right: Expression levels of two representative genes of the enzymatic activation signature (*Egr1, Fos*). (E) Trajectory analysis of Mg-TAM cells in Nu-NB and PDOXs cells. Mo-TAMs and BAMs were excluded from the analysis. For pseudotime states were revealed. **(F)** Graphs showing proportions of homeostatic Mg (Ho-Mg) and Mg-TAMs in each pseudotime state revealed during trajectory analysis. The analysis confirms transition from Ho-Mg (state1, CL0-1) to a gradient of heterogeneous Mg-TAMs. (**G**) Representative flow cytometry graphs of $CD45^{+}CD11b^{+}Ly6G^{-}Ly6C^{+}CD206^{-}$ Mo-TAMs showing increased levels of CCR2 in tumor core of three PDOX models. Right: quantification of $CCR2^{+}$ cells in Mo-TAMs across different tumor phenotypes and brain regions. (n=5-6 from at least three different mouse brains each, one-way ANOVA, ***p<0.001, **p<0.01, *p<0.05). **(H)** Volcano plots showing differentially expressed genes between PDOXs versus GL261 assessed for Mg, Mo and BAMs (the Wilcoxon rank sum test with Benjamini-Hochberg correction).

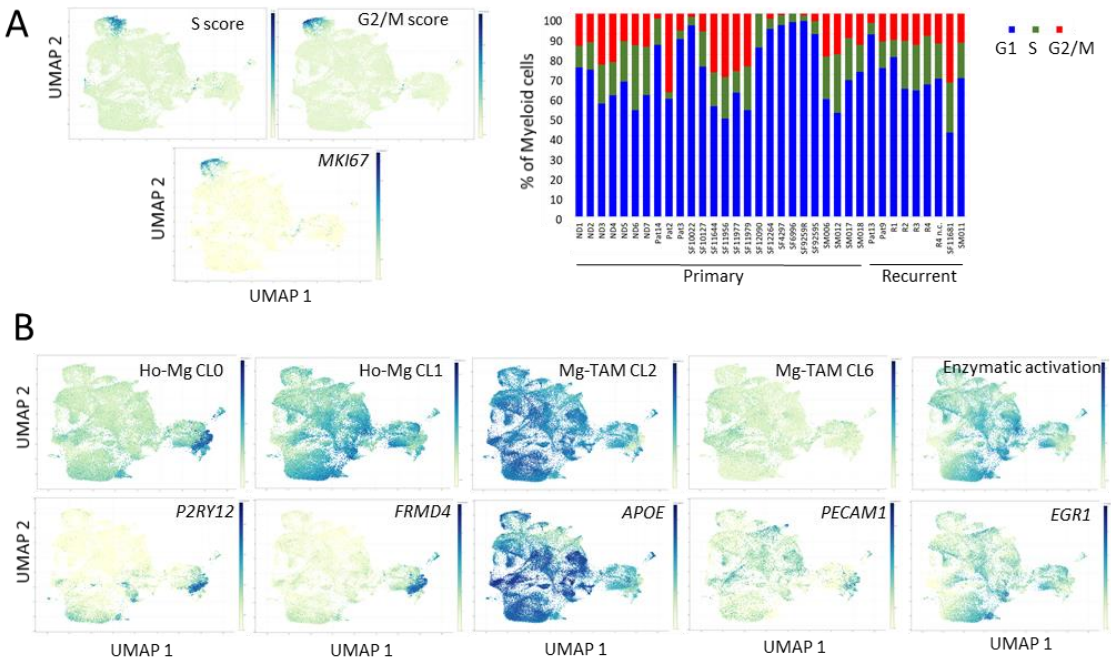

Figure S5. Analysis of heterogeneous Mg-TAMs in GBM patient tumors. (A) Left: UMAP projection of myeloid cells in GBM patient tumors. The color gradient represents expression levels of cell cycle signatures (S phase and G2/M phase signatures and *MKI67* gene expression levels). Right: Graph showing proportion of myeloid cells in different cell cycle phases in individual GBM patient tumors. Recurrent GBMs show similar proportions of Mo-TAMs than primary GBM tumors (two-tailed Student's t-test). **(B)** UMAP projection of human GBM myeloid cells displaying expression levels of signatures of Mg-TAM and Ho-Mg phenotypic states identified in PDOX TME. Signature associated with enzymatic activation of Mg cells is highlighted. Example of key marker gene is shown per signature. The color gradient represents expression levels.

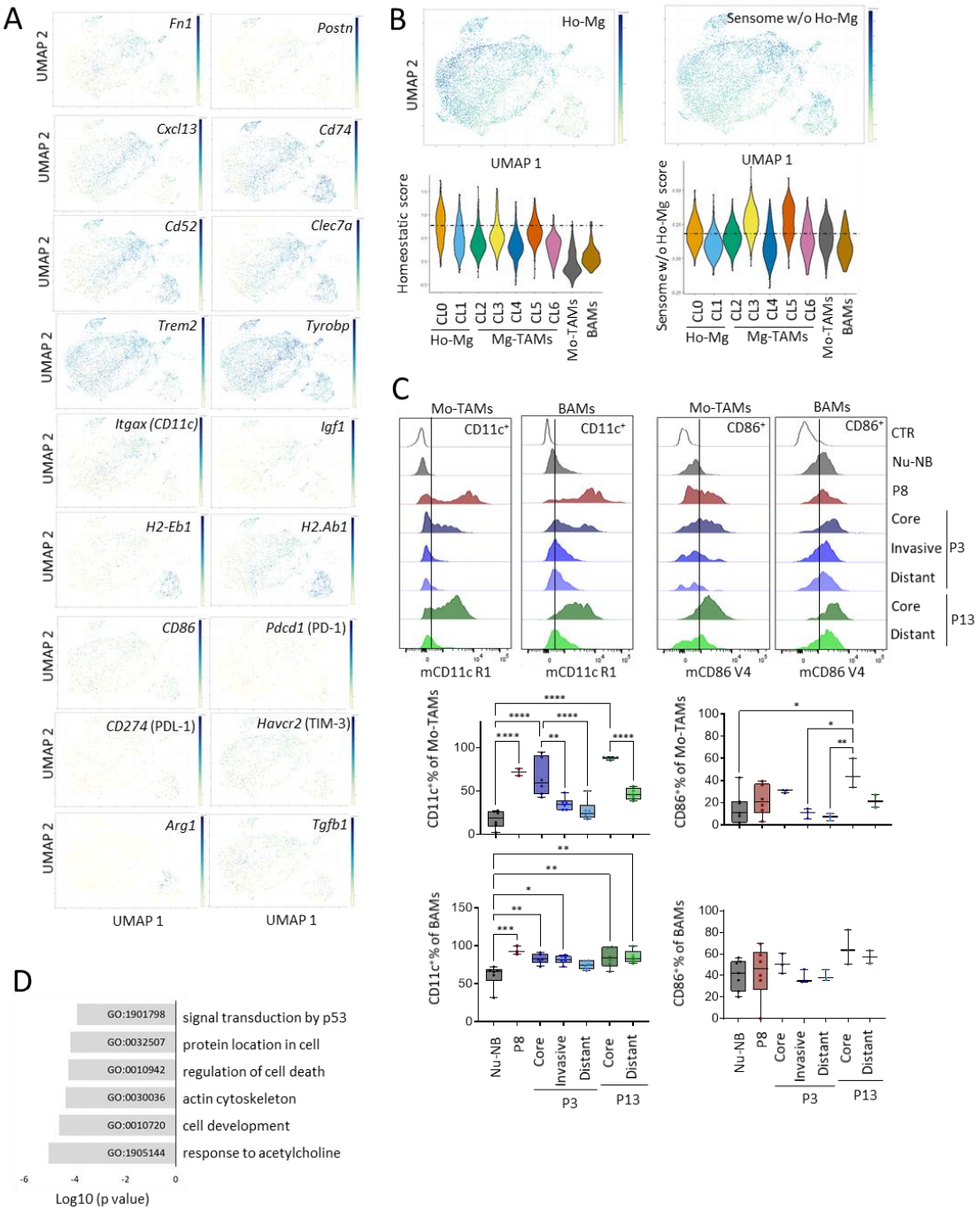

Figure S6. Analysis of functional markers in TAMs. (A) UMAP projections displaying expression levels of representative genes characteristic for migration, phagocytosis, antigen presentation and check point inhibition. The color gradient represents expression levels. **(B)** Top: UMAP projection displaying expression levels of gene signature associated with homeostatic Mg (Ho-Mg) and sensome-associated genes excluding Ho-Mg signature (**Table S5**). Bottom: Signature score is depicted per myeloid cluster. While homeostatic genes drive high levels of the sensome signature in Ho-Mg (**Fig 5**), other genes lead to increased sensome signature in Mg-TAMs. **(C)** Top: representative flow cytometry graphs of $CD45^+CD11b^+Ly6G^-Ly6C^+CD206^-$ Mo-TAMs and $CD45^+CD11b^+Ly6G^-Ly6C^-CD206^+$ BAMs showing levels of CD11c and CD86 in nude mouse normal brain (Nu-NB) and three PDOX models. Unstained control is shown for each population (CTR). Bottom: quantification of $CD11c^+$ and $CD86^+$ cells in Mo-TAMs and BAMs across different tumor phenotypes and brain regions (n=3-6 from at least three different mouse brains each, one-way ANOVA, ***p<0.001, **p<0.01, *p<0.05). **(D)** Summary of top six gene ontology terms characterizing DEGs in TMZ-treated versus CTR endothelial cells forming TME in P3 PDOX (FDR ≤0.01, |logFC| ≥ 0.5

Supplementary tables

Table S1. Characteristic of PDOX models applied in the study.

PDOX model	Patient	Patient treatment	Genetic aberrations	Glioma-specific gene mutations	DNA methylation profiles	MGMT promoter methylation	PDOX phenotypic characteristics
P3	BER0003	na	+[Chr7, 19p, 20q], -[1p36-1p34.1, 1q21.1-q44, -5p15.33-31, Chr9, Chr10, 11p15-14, 20p] --CDKN2A/B	TP53 (C176Y), PTEN (D236fs)	GBM, IDHwt, RTK I/II	methylated	intermediate
P8	BER0008	na	++EGFR, +[5p15.3-p12, 5q31.1-q35.3, Chr7, 8q24], -[6q21-q27, Chr10, 13q13.3-q34, 15q21.2-q23, 18q21.2-q22.4], --CDKN2A/B	EGFR (A289T), ATRX (S1348T), MET (A954S), PTEN (T319fs)	GBM, IDHwt, RTK II/I	methylated	invasive
P13	BER0013	na	+(Chr7, Chr19, Chr20), -(1p21.1-p31.2, 6q16.3-q21, Chr10, Chr13, 17q11-12), --CDKN2A/B	PTEN (D107V)	GBM, IDHwt, RTK II	methylated	angiogenic
T16	LIH0016	treated	++[EGFR, MDM4], +7q, - [6q, Chr10, 13q11-q31.1], --CDKN2A/B	EGFR ex25-27del	GBM, IDHwt, RTK II	unmethylated	intermediate
T101	LIH0101	treatment-naive	++[EGFR, MDM2] +[Chr1, Chr7, Chr9, Chr13, Chr16, Chr17, Chr19] -[3q, Chr4, Chr6, Chr10, Chr11, 14q11, Chr15], --CDKN2A/B,		GBM, IDHwt, RTK II	methylated	invasive
T192	LIH0192	treatment-naive	++[EGFR, 2q34], +[1q21.2-24.2, Chr7, Chr19, Chr20], - [9p24.3 -13.3, Chr10]	EGFR complex rearrangements (ex1-6), ex14-16	GBM, IDHwt, RTK II	unmethylated	invasive
T233	LIH0192	treated	++[EGFR, 2q34], +[1q21.2-24.2, Chr7, Chr19, Chr20], - [9p24.3 -13.3, Chr10]	EGFR vIII, complex rearrangements (ex1-6), ex14-17	GBM, IDHwt, RTK II	unmethylated	invasive
T347	LIH0347	treatment-naive	++EGFR, +[Chr7, 19p, Chr20], - [1p36.3-p34.3, 1q32.3-q44, Chr10, 13q12.11-31.1, 14q11.2-q21.3], --CDKN2A/B	EGFR ex2-15del, PTEN (C304fs)	GBM, IDHwt, RTK II	unmethylated	invasive
T470	LIH0347	treated	++EGFR, +[Chr7, 19p, Chr20], - [1p36.3-p34.3, 1q32.3-q44, 1p31.1-p11.21, Chr10, 13q12.11-31.1, 14q11.2-q21.3], --CDKN2A/B	EGFR ex2-15del, PTEN (C304fs)	GBM, IDHwt, RTK II	unmethylated	invasive

Table S2. List of antibodies used in the study .

*Flow cytometry test 106 cells/100µl

Antibody	Supplier	Catalog number	Concentration used
hCD90 PE-Cy7	BD	561558	5 µl/test*
hCD90 BV605	BD	562685	5 µl/test*
CD16/32	eBioscience	14-0161-85	1 µl/test*
mCD45 FITC	eBioscience	11-0454-82	1 µl/test*
mCD11b Percp-Cy5.5	BD	550993	5 µl/test*
mLy6C PB	Biolegend	128014	0.5 µl/test*
mLY6G BV785	Biolegend	127645	2.5 µl/test*
mCCR2 PE	R&D	FAB5538P	5 µl/test*
iso IgG PE	R&D	IC108P	5 µl/test*
mCD206 APC	Biolegend	141708	2.5 µl/test*
mCD11c APC-Cy7	Biolegend	117323	5 µl/test*
mCD86 BV605	Biolegend	105037	5 µl/test*
iso IgG2a BV606	Biolegend	400540	5 µl/test*
m I-A/I-E APC-Cy7	Biolegend	107628	1 µl/test*
Nestin	Abcam	AB6320	IHC:1/500
Vimentin	Thermo Fisher Scientific	Mab3400	IHC:1/200
CD31	Millipore	CBL1337	IHC:1/200
Iba1	Biocare Medical	CP 290A	IHC:1/1000
CD11c	Abcam	ab11029	IHC:1/100
MHC-II	Abcam	ab25333	IHC:1/100
Pdgfra	Biolegend	135905	IHC:1/100
Anti-Rat IgG Alexa Fluor 555	Invitrogen	A21434	IHC:1/1000
Anti-Rabbit IgG Alexa Fluor 555	Thermo Fisher Scientific	A-11039	IHC:1/500
Anti-Mouse IgG Alexa Fluor 647	Thermo Fisher Scientific	A-11037	IHC:1/500
Anti-Rat IgG Alexa Fluor 488	Thermo Fisher Scientific	A-21244	IHC:1/500

Table S3. Lists of differentially expressed genes between PDOXs and nude brain per each major cell type. Differentially expressed genes were defined at threshold: FDR <=0.01 and $|\log_2 FC|>=1$. Genes are listed from the highest to lowest $|\log_2 FC|$.

	Astrocytes		Endothelial cells		Ependymal cells		Myeloid cells		Oligodendrocytes		OPCs		Pericytes	
FC	up	down	up	down	up	down	up	down	up	down	up	down	up	down
No	186	129	304	105	21	22	287	136	7	124	286	199	2	71
	Gm42418	Sfrs18	Gm42418	Plp1	Tmsb4x	Gm26924	Spp1	Sfrs18	Olig1	Igfbp5	Pdgfra	Plp1	Gm42418	Wdr96
	Cryab	Ppap2b	Rpl14.ps1	Gm26924	Gm42418	Sez6	Gm42418	Snord49b	Pdgfra	Mal	Gm42418	Apod	Gm12346	Gm26924
	Vim	Gm26924	Adgrf5	Gpr116	Lyz2	Vps8	Cxcl13	Sepp1	Gria2	Plp1	Lhfpl3	Npy		1700009P17Rik
	Tmsb4x	Gm26339	Selenop	Sfrs18	Tyrobp	Rpl35	Clec7a	Gm26924	Cspg5	Phldb2	Pnisr	Sepp1		1700026D08Rik
	Pnisr	Snord42a	Gm6977	Ttyh1	Hexb	Vimp	Gm6977	4632428N05Rik	Cacng4	Cd200	Gap43	Igfbp5		Ptplad1
	Plpp3	Xist	Gm5905	Sepp1	C1qa	D3Bwg0562e	Gm5905	Epb4.1l2	mt.Cytb	4922501C03Rik	Cspg5	Slc4a4		Stxbp3a
	Rack1	Gm3764	Gm9794	Fabp7	C1qb	Gm6625	Gm14303	Gm26339	Actb	Slc4a4	3110035E14Rik	Clca1		A330021E22Rik
	Gm6977	2810055G20Rik	Rpl37rt	Igfbp5	B2m	Calml4	Gm9794	Entpd1		Ptn	Rpl14.ps1	Gja1		Wdr52
	Gm9625	Slc38a3	Gm11478	mt.Tc	Ctss	BC023829	Rpl14.ps1	Abca9		Sash1	Gm5905	Ptn		Ccdc135
	Rpl13.ps5	D4Wsu53e	Gm4617	Fut9	C1qc	1110001A16Rik	Ccl4	D4Wsu53e		Clca1	S100a1	Nr2f2		Ccdc19
	Rps3a3	Sepp1	Gm15427	D4Wsu53e	Ctsd	0610011F06Rik	Rpl37rt	P2ry12		Mxi1	Pllp	Ccdc80		2610015P09Rik
	Gm14892	Snord49b	Gm9385	Ppap2b	Cd63.ps	Ppia	Lpl	Gpr34		Ccdc157	Slc25a5	Vtn		Ccdc104
	Gm7558	Ptplad1	Rps16.ps2	Slc4a4	Ctsb	Ccdc41	Ttr	Il7r		Tlr3	Gng3	Gm26924		Spag6
	Fth.ps2	Vegfa	Gm14303	Eltd1	Rpl14.ps1	1110059M19Rik	H2.Ab1	Ddx26b		Sepp1	Scg5	Frzb		Rps17
	Rpl14.ps1	Sc4mol	Gm5805	Dcn	Gm9794	Rpl29	Gm15427	P2ry13		Ttyh1	Ramp1	Ttyh1		Sfrs18

	Rps5	Slco1c1	Rpl32	Gm26339	Wdr89	4922501C03Rik	Fth1	Csmd3		Lifr	Rps5	Apoe		Ifltd1
	Gm12346	Adrbk2	Gm4149	Rps6	Rack1	Gm9493	Gm11478	Gm17087		Frzb	Gm9385	Hmgcs2		2510003E04Rik
	Gm12857	2610017I09Rik	Gm10080	Snord49b	Lamp1	Cox7b	Cd63.ps	Ccdc55		Wdr60	Olig2	Timp3		Gm872
	Gm13215	Slc1a2	Gm5963	Hnrnpa3	Sparc	Stk39	H2.Aa	Maf		Timp3	Rpl3.ps1	Ncam1		Ppap2b
	Gm6136	Vimp	Pnisr	Ptn	Cst3	Selt	Rack1	Gpr56		Trp53bp2	Gm12346	Inhba		2010015L04Rik
	Rps16.ps2	Zfml	Rpl3.ps1	Slc7a11	Actb	Enpp2	Cd74	Hnrnpa3		Mybpc1	Rpl37rt	Sash1		A030009H04Rik
	Gm13498	Tmem66	Adgrl4	Vimp		4930546H06Rik	Ccl3	Tmem66		Ralgps2	Gm9794	Iqub		Pax3
	Gm22567	Syne1	Rpl38.ps2	Pcdhga9			Gm16580	Ppap2b		Sfrs18	Gm11478	Col5a2		Vps28
	Gm12183	St6galnac5	Tpt1.ps3	Atp1a2			Gm11942	Zfhx3		Aspa	Tnr	Tspan15		D2Wsu81e
	Gm9385	CT030684.1	Gm9843	Abca9			Gm5963	Jund		Slc7a11	Gm11560	Stmn1		Gm6625
	Gm5805	Nim1	Rack1	Hes5			Gm4149	CT030684.1		Gja1	Olig1	Lpar1		Ccdc41
	Rn7s6	Fut9	Rps24.ps3	Slc1a3			Rps24.ps3	Zfml		Plekha4	Clu	Igf1		Selk
	Id1	Cwc22	Gm14586	Cyp2j9			Selenop	Nrip1		Rgag4	Rack1	Wls		Lsmd1
	Fth1	Gnao1	Gm6204	Timp3			Cst7	Slco2b1		Gas7	Gm15427	Sparc		6720401G13Rik
	Gm12222	Pcdhga9	Gm11966	Fam213a			Rps16.ps2	Tmem119		Ahctf1	Rsrp1	Col23a1		B630005N14Rik
	Gm5370	2610203C20Rik	Rflnb	mt.Tp			Gm9385	Vimp		Inhba	Bcas1	Slc7a11		AK129341
	Gm11560	Trim9	Gm11560	Nell2			Gm5805	Hpgds		Fmo1	Rps16.ps2	Fam213a		Gm26339
	Gm12165	S1pr1	Rps13.ps2	Scd2			Rpl3.ps1	Lrrc58		Gtpbp2	Gm4617	Sfrs18		Sept15
	Gm13340	Macf1	Rpl36a.ps2	Sash1			Rps13.ps2	Cx3cr1		Fbln2	Tmem100	Gm26339		Ankrd32
	Rpl10l	5830428H23Rik	Gm11942	Ptgds			Pnisr	Il6ra		Gm872	Stmn3	Hey2		Dpcd
	Gm11942	Ttyh1	Fn1	Vegfa			Apoe	Cep110		Cldn5	Gm12338	Phldb2		CT030684.1
	Rpl17.ps4	Ank2	Gm16580	Gm17087			Fn1	Gm13476		Mdk	Calm1	Cd59a		Gm12942

	Gm4332	4930546H06Rik	Wdr89	Mllt4			Ccl6	Mertk		Cyp4v3	Nap1l5	Gdpd4		Gm5918
	Gm11810	Ctage5	Gm10073	2810055G20Rik			Gm6204	Wapal		Pla2g16	Bex3	Fmo1		Pet112
	Rps15.ps2	Dclk1	Gm4332	Slc1a2			Gm8995	Naalad2		Scd1	Id2	Pla2g16		Sc4mol
	Gm14450	Malat1	Rsrp1	Colec12			Rpl36a.ps2	RP24.312B12.1		Wls	Pcdh15	Mfap3l		2410018M08Rik
	Gm12696	Clmn	Rps26	Wapal			Cd52	Rps23		Pbxip1	Rpsa.ps10	Atp1a2		l7Rn6
	Gm6368	Acss1	Rplp0	Mdk			H2.K1	Snord42a		Fam213a	Ranbp1	Mybpc1		BC023829
	Wdr89	Itih3	Slc38a5	Gm14964			Kctd12	Rpl5		Igf1	C1ql1	Mal		Ccdc37
	Gm2225	Vwa1	Gm9800	Mboat2			Epb41l2	Ppp1r9a		Dab2	Cd81	Col27a1		Epb4.1l4a
	Gm5963	Pitpnc1	Rplp1	Rpl15			Rpl10a.ps1	Smap2		Col5a2	Ostf1	Dnajc1		9330101J02Rik
	Ttr	Fam21	Gm6863	Suv420h1			Rps5	Jhdm1d		Slc43a2	Gria3	Pex11a		Epb4.1l2
	Gm11472	Cep110	Rpl31.ps8	Fbln2			Ch25h	Rps29		Lysmd3	Igfbp2	Abca8a		4922501C03Rik
	Rps12.ps19	4930402H24Rik	Gm12338	Rpl13a			Gm4617	Rpl21		Fstl1	Cox8a	Dock7		2700089E24Rik
	Gm17909	Appl2	Rpsa.ps10	Atp13a5			Gm14586	2810055G20Rik		Frg1	Dynll1	Fbln2		1700094D03Rik
	Rac1	Tril	Rps10.ps1	Rpl5			Gm4332	Tanc2		Hey2	Nxph1	Rnd3		Bai3
	Gm12152	Epb4.1l2	Gm10288	Sept15			Rsrp1	Son		Ncam1	Selenok	Filip1l		Sepn1
	Cd63.ps	Mycbp2	Gm6265	4933426M11Rik			Rpsa.ps10	Slc16a6		Atp8a1	Alcam	Golgb1		Lphn3
	Gm5835	Atp1a2	Scgb3a1	Gja1			Ctsd	D15Ertd621e		Acss1	Gm4149	Thrsp		2310044G17Rik
	Gm9843	Zfp949	Fth1	Gpm6b			Lilrb4a	RP24.288C12.6		Cd82	Actb	2610203C20Rik		Rpl24
	Cald1	Acsl6	Ctla2a	Kcnj16			Ifi27l2a	Arid4a		Glul	Rps26	Gas7		Nim1
	Id3	Gja1	Rps5	Kmt2a			Rps26	A430104N18Rik		Mfsd6	Gm14586	Glul		2410066E13Rik
	Hspd1.ps3	Timp3	Gm10275	Tmem66			Rps25.ps1	Chd9		Selk	Gm6863	Sdc4		Gm10311
	Gm2178	Son	Apold1	Spag9			Tpt1.ps3	Numb		Lgi1	Tpt1.ps3	Cry2		Gm13225

	Gm9794	Ccdc104	Gm12183	Ptms			Mt1	Srgap2		Gramd1b	Emid1	Scd1		5430417L22Rik
	Map1b	Btbd17	Gm7809	Gprasp1			Gm6030	Elmo1		Npy	Ndufa4	Hsd17b11		Gm17388
	Gm44010	Ddhd1	Afdn	Morf4l1			Calr.ps	Pwwp2a		Sco1	Igfbp3	Vimp		Gpr125
	Rps19.ps6	Suv420h1	Gm15500	Rpl10			Lyz2	Ctage5		Slc25a13	Car8	Mllt4		Grlf1
	Gm5778	Ppia	Gm5835	Zbtb20			Gm10288	Col27a1		Adam23	B2m	Gucy1b3		Leprel2
	Gm4204	Slc1a3	Rps25.ps1	Hspa8			Wdr89	Ogfrl1		Tgfbr1	Rps13.ps2	Fam3c		Trp53rk
	Selenop	Ttc14	Gm9892	Htra1			Gm10073	Mycbp2		Fgd4	Gm14303	Gpr56		Zbed6
	Gm15159	Slc7a10	Calr.ps	S1pr3			H2.D1	Scamp2		Tmem66	Gm6977	Abca5		Fam101a
	RP23.390K13.4	Nrcam	Rpl18.ps1	Rpl23a			Gm15500	Lpar6		Nr2f2	Pcsk1n	Edil3		Fam115a
	Gm11478	Pdcd4	Rpl10a.ps1	Kcnj10			Rpl31.ps8	Marcks		BC016423	2900011O08Rik	Huwe1		9830147E19Rik
	Cxxc5	Pla2g7	Gm8894	Ccdc80			Rpl18.ps1	Erbb2ip		Zmat1	Gm5805	Ift57		Rom1
	Bex3	Fam115a	Gm8292	Rps23			Apoc1	Rbm5		Gm26339	Ndufb6	Aldh2		Zfp191
	Gm16580	Gyk	Rps6.ps4	Ncam2			Gm5835	Tmem100		Aim1	Cd63.ps	Ahcyl2		
	Gm15896	Csgalnact1	Selenom	Gnb2l1			AU020206	Rps6		Dock7	Ndufa8	Efnb2		
	Gm27046	Nrxn1	Ly6c1	Inhba			Gm9843	Macf1		Tiam1	Rpl22l1	Grik3		
	Gm29228	Hlf	Eif1.ps1	Cwc22			Gm8276	Ythdc1		4931406C07Rik	Banf1	Mgst1		
	Cnot2	Rorb	Gm12254	Prrc2c			Rplp1	Ssh2		Vtn	Ddah1	Hmgn2		
	Gm9294	D14Abb1e	Cd34	Ncam1			Tyrobp	Qk		Osbpl11	Ttr	Gm12688		
	Gm11517	Flrt1	Rps15a.ps5	Zfml			Il1b	Hmgb1		Phf17	Gpm6a	Sparcl1		
	Rpl34.ps2	Frmd4a	Rps11	Gpx4			Ccrl2	Med12l		Hspa8	Scrg1	Fut9		
	Gm9521	Fjx1	Ttr	S100b			Kcnq1ot1	Arl4c		Cpt1a	Wdr89	Mest		
	Gm8513	Acin1	Tmsb4x	Rps17			AC149090.1	Cwc22		5830418K08Rik	Gm12222	Map4k4		
	Gm4321	Arhgap5	Gm3531	Xist			Rpl32	Dusp6		Tpr	S100a16	Ptgds		
	Gm15427	Hnrnpa3	B2m	4932438A13Rik			Rps10.ps1	Sall1		Apoe	Gm12696	Plcb4		
	Gm18014	Mfge8	Ly6e	Ahcyl2			Axl	Dip2b		Tmem245	Tuba1a	Slc27a1		

	Gm12482	C030037D09Rik	Rps9	RP24.288C12.6			Id2	Rps27a		Hadha	Cdo1	Mex3a		
	RP23.408J7.2	Tnik	Rps26.ps1	Ddit3			Vim	Frmd4a		Atp1a2	Tceal3	Grin3a		
	Gm17511	Selk	Selenok	Ppia			Ctsb	Rps28		Nnat	Gm9892	Cyp2d22		
	Gm6543	Ubn2	Gm12346	Rps27			Itgax	P4ha1		Snx24	Gm6204	Rgag4		
	Matr3.ps2	Slc4a4	Cdkn1a	Mga			Vsir	Morf4l1		Dnajc1	Gm5778	Fabp7		
	Gm7308	Tmed5	Rpl8	Ccdc104			Rps20	Olfml3		Plk1s1	Nrxn1	Cd200		
	Gm5514	Cadm2	Selenof	Rps12			Cd300c2	Hspa8		Clca2	Plpp3	Wapal		
	Gm4366	Nwd1	Gm12350	Kdm5b			Gm6863	Prrc2c		Ccdc39	Tmem176b	Syne2		
	Rsrp1	Dio2	Gm15772	Igfbp2			Ccl12	Fau		Stmn1	Gm5835	Ccnd2		
	Id2	P4ha1	Igfbp7	Diap2			Gm11560	Map4k4		Cd55	Calr.ps	D3Bwg0562e		
	Rps3	Acsl3	Pomp	Rpl21			Gm14681	Safb		2700089E24Rik	Cox6b1	Nid1		
	S100a6	Tex9	Gm6472	Apod			Ints6l	Arhgap5		Mfap3l	Mmp15	Suv420h1		
	Gm3531	Myo6	Sparc	Nupr1			mt.Cytb	Acin1		P2ry12	Dynlt1.ps1	Hadha		
	Gm7618	Sparcl1	Slc25a5	Wdr60			mt.Nd1	Ifngr1		Fabp7	Cfap20	Tlr3		
	Gm5905	Mfn1	Gm7027	Tmx4			Cd83	Bin2		Fut9	Ccnd1	Clca2		
	Gm12912	Gm973	Gm6368	Son			Gm10275	Srrm2		Fam3c	Gm5963	Dtx4		
	Gm13815	Slc6a11	Gm14681	Ednrb			Gm9892	Tsc22d4		Trim41	Cfap36	Abcb1a		
	Rps11	Kcnj16	Ppfibp1	Stmn1			Rps15a.ps5	Selplg		Mecp2	Tagln2	Gm6483		
	Gm11488	Ythdc1	Rab1a	Casc4			Gnas	Zfp292		Rbms3	Gm6265	Gpd1		
	Pabpc1	Mdn1	Rpl22.ps1	Asph			Rpl38.ps2	Mtdh		Scd2	H2.D1	Slc1a3		
	Dclk2	Ntrk2	Gm4366	Nr2f2			Flt1	Ccr5		P2rx4	Rpl36a.ps2	Slc13a3		
	Gm12020	Sycp2	Rpl9.ps7				Gm7027	Adap2		E130311K13Rik	Hspd1.ps3	Gpd2		
	Gm15773	Trpm3	Gm8995				Selenos	Abcb4		Lrig1	Grm5	Zbtb20		
	Calm2	Wapal	Gm15421				Ank	Vwa1		Rnd3	Pcp4	Itsn2		
	App	AI464131	Hsp25.ps1				Gm12338	Ivns1abp		Paqr6	Cacng4	Chd9		
	Gm6204	Mmp14	Gm14539				Rps6.ps4	Plcl2		Ltn1	Meg3	Sat1		

	Calr.ps	Pfkp	Plpp3				B2m	Pde3b		Lama4	Dnm3	4922501C03Rik		
	Vcan	Neat1	Gm6563				Srgn	Sox4		Nek9	Rab31	Hnrnpa3		
	Spp1	Nebl	Anp32.ps				Gm12346	Fchsd2		Son	Slc38a3	Ptms		
	Marcks	Chrdl1	Tpm3.rs7				Atf3	Rps27		Slc16a1	Pdcd5.ps	Tspan18		
	Fos	Dtna	Gm12696				Cd63	Malat1		B4galt6	Ubb	Arhgap5		
	Hacd3	Aifm3	Saraf				Atox1	Rock2		Zbtb20	Gm10288	Magt1		
	Gm6863	Utp14b	Ctsd				Ifi202b	Ttc14		Ccdc171	Ppib	Son		
	Gm21399	Peg3	Gm5436				Cstb	Tgfbr1		Nexn	Dpp6	Gbp7		
	Atp5e	9330159F19Rik	Gm5865				Nfkbia	Ubn2		Colgalt2	Oxct1	Nupr1		
	Ctsd	Sfxn5	S100a11				Rps26.ps1	March1		Sparcl1	Serpine2	Nfat5		
	Gm12892	Slc7a11	Cyb5a				Ctsz	Pnn		Calr	Arl2bp	9330159F19Rik		
	Golim4	Prpf4b	RP23.123D6.12				Ms4a6c	Rbm25		4930480K23Rik	Gm3531	Cyp39a1		
	B2m	Slitrk2	Cd63.ps				Gm12254	Rpl35		Kdm2a	Gm11966	Igfbp4		
	Jun	Gprasp1	Rpl39				Rps10.ps2	Ppia			Rtn1	Ccdc104		
	Selenos	Ankrd11	Ybx1.ps2				Npc2	Pmepa1			Gng11	Gm6625		
	Gfap	Cxcl14	Shfm1				Atp5e	Serinc3			Rpl10a.ps1	Snx29		
	Gm11966	Gapdh	AU021092				Ifi44	Rpl10			Arpc2	Tec		
	Sept7	Kcnk1	Gm8276				Csf1	Nav3			Rps26.ps1	Cmtm5		
	F3	Ccdc50	Gm13835				Gm15772	Gnb2l1			Agpat5	Mboat2		
	Hacd2		Gm5644				Tnf	Rpl18a			Ndufs4	Kdm5b		
	Gnas		Gm8730				Mia2	Rpl17			Gm5865	Abca1		
	Cct2		Smim10l1				Gm15421	Ptgs1			Phlda1	RP24.288C12.6		
	Rps20		Gm5778				Rpl9.ps6	Ywhah			Rps24.ps3	M6pr		
	Rpl32		Gimap4				Plpp3	Hmha1			Cox4i1	Nfe2l2		
	Gatm		Gm6733				Rgs1	Basp1			Tmem179	Zfhx3		
	Rpl8		Vim				Calm1	Srrm1			Ahi1	Sort1		

	Sbds		Pdcd5.ps				Rpl39				Fis1	Wnt6		
	Skp1a		Cfap36				Rpl22.ps1				Selenof	Tmem132b		
	Msmo1		Rps3				Gm11966				Eif3i	Frmd4a		
	Snx3		Tspan13				Gm7266				Ly6h	Phf17		
	Ybx1		Rpl18.ps2				Gm12183				Rplp1	Entpd1		
	H3f3b		Nsrp1				Cox4i1				Ndufa7	Agt		
	Eif3k		Rps19.ps6				Ctsl				Gm16580	Cldn5		
	Sox4		Wfdc1				Gm9800				Gm15500	Crip2		
	Hint1		Ifitm3				Cox6a1				Gm4204	Plcd4		
	Calm1		Selenow				Rps15				Omg	Lix1		
	Psma7		mt.Cytb				Dbi				Ednrb	Ctbp2		
	Fez1		Tcea1.ps1				Rps11.ps1				Gria2	Cyp2j6		
	Rheb		Higd2a				Cxcl2				Rpl36al	Baz2b		
	Nucks1		Ier2				Saraf				Tspan13	Socs2		
	Eef2		H2.K1				Rps19.ps6				Gm6368	Atp8a1		
	Cbr1		Gm7266				Cox6b1				Cox7b	Cyp4v3		
	H2.D1		Selenos				Hacd2				Il1rap	Snord49b		
	Tcf12		Gm12481				Wfdc17				Commd6	Stx5a		
	Eef1a1		Gm15920				mt.Nd4				Gm14681	Cep85l		
	Matr3		Cox7a2				Capg				Mpc2	Nell2		
	Rps9		Gpx1				Prdx1				Atp5g3	Fxyd1		
	Anapc11		Rps10.ps2				Pld3				Ndufa1	Parp4		
	Rps14		mt.Nd1				Lgals3bp				Cct7	Zfp191		
	Gtf2i		Cox4i1				Postn				Nsg1	2310022B05Rik		
	Bcan		Actb				Gm6136				Psmb1	Bmp7		
	Rps4x		Igf1r				Gm4366				Cfl1	Hspa8		
	Ubb		Ostf1				Gm8730				Prdx2	Foxo1		
	Hnrnpd		Mia2				Grn				Dbi	Eps15		

	Dync1li2		Fkbp1a				Slc25a5				Sulf2	Cdh8		
	Rps21		Eif3j2				Rplp0				Dtd1	Paqr6		
	Rps15		Rps15.ps2				Gm4604				Cspg4	Slc43a3		
	Tpm3.rs7		Ube2d3				Fcer1g				Pcyt1b	Chd2		
	Rpl4		Arpc2				Cd9				Dscam	Fnbp1l		
	Rplp1		Gm4604				Zfp638				Mlf2	Notch2		
	Dstn		Tonsl				Cox8a				Gm1673	Sipa1l1		
	Sec11c		Ramp2				Rps3				Nop10	Tmtc2		
	Cnn3		Pabpc1				Pabpc1				Uqcrq	Lipg		
	Nasp		Gm14253				Eif1.ps1				Atxn10	Prrg3		
	Ppp1cb		Hint1				Gusb				Ckb	Scd2		
	Vapa		Id3				Cntrl				A730017C20Rik	Megf10		
	Ilf3		Gm9840				Gm6265				Serpina3n	Hivep3		
	Pcbp2		Slc16a4				Ier3				Aplp1	Slc25a13		
	Cct6a		Rps15				Lgals1				Higd2a	Ncoa7		
	Ywhab		Rpl9.ps6				Tmsb10				Cxcl14	Synm		
	Pcbp1		Pglyrp1				Gpx1				Rps9	Leprel2		
	Ctss		Gstp.ps				Csf2ra				Dner	RP23.32A8.1		
	Zhx1		BC002163				Gm43712				Pcbp2	Prss56		
	Ywhae		Tpm4				Hpf1				Olfm1	Fam107a		
	Arpc2		Epb41l2				Gm6368				Cryab	Tiam1		
	Rpl23		Naa38				Rps15.ps2				Kcnd2	Gm4076		
			Gm12020				Rps9				Znhit6	CT030684.1		
			Ndufa11				Anxa5				Gtf2h5	Tmem47		
			Calm1				E230029C05Rik				Ndufc2	Cpne8		
			S100a16				Gm5644				Opcml	Ccdc173		
			Gm6542				Uqcrq				1810037I17Rik	Erbb3		

			AC149090.1				Rpl18.ps2				Uchl3	Vwa1		
			Ssr2				Gm6472				Cdh13	Cgnl1		
			Rpl37				Wapl				Sfr1	Tnfrsf19		
			Gm13436				Rps19				Gm2a	Itga6		
			Gm10039				Nsrp1				Cp	Zfp609		
			Grrp1				Mir703				Tubb2a	mt.Rnr1		
			S100a13				Sh3bgrl3				3632451O06Rik	Alx4		
			Tpm3				Rpl9.ps7				Gjc3	Prrc2c		
			Gm7407				Gm10080				Atp6v1g1			
			Fam204a				Rps11				Lnx1			
			Myl12a				Cotl1				Adam9			
			Gm10031				Gm8606				Pea15a			
			Txn.ps1				Lyzl4				Sfxn1			
			Atp5j				H2.DMa				Pfn1			
			Psma5				Plau				Uqcrc1			
			Ccdc186				Akr1a1				Srp14			
			Gm6136				Gm12020				Cdk4			
			Ifi27l2a				Cybb				Itgb8			
			Rplp2				Psme2b				Deb1			
			Dynlt1.ps1				Ssr4				Megf11			
			Sf3b6				Cd72				Cox6c			
			Zfp638				Selenof				Myo5a			
			Rps11.ps1				Gm15148				Pou3f1			
			Wapl				Zfas1				Tacc2			
			Icam2				Ndufa2				Atp5j			
			Rac1				Gm9294				Gnb4			
			Gm14513				Shfm1				Cadm2			
			Bag1				Il4i1				Atp6v1a			

			Gm43712				Gm13436				Gria4			
			Gm21399				Gm12481				Sept7			
			Tmem252				Erbin				Brinp1			
			Rps15a				Ppp1r15a				Eif5a			
			P4hb				Selenok				S100a13			
			Lgals1				Rpl22l1				Ndufb8			
			Tmsb10				Eif3f				Pgp			
			Pcbp1				Ifitm3				Psmb3			
			Uqcrh.ps2				Rps21				Bcan			
			Gm11964				Zeb2os				Gm10250			
			H2.D1				Gm1966				Ptprn			
			RP23.269H21.1				Gm14513				Krtcap2			
			Ilk				Ctsh				Atp5b			
			Cox6b1				Mt2				Sri			
			Lmo2				Glmp				Cask			
			Rasip1				Gm10076				Tceb2			
			Psme2b				Pdcd5.ps				Mt3			
			Erbin				Pfdn5				Ppp1r14c			
			Zmat2				Cxcl16				Park7			
			Gm9294				Crip1				C4b			
			Gata2				Gm6394				Sox6			
			Oaz1.ps				Cspg4				Pcdh9			
			Anp32b.ps1				Ier2				Uqcrb			
			Atox1				Myeov2				Rgs20			
			Rras				Cd68				Hint1			
			Rhoj				Gm8692				Ugp2			
			Ly6a				RP24.389J11.1				Mdh2			

			Mydgf				Gm4204				6330403K07Rik			
			Rps19				Gm3531				Ndufab1			
			Uqcr11				Gm14539				Mt1			
			Esam				Lgals3				Atp6v0e			
			Rps20				Nfkbiz				Rpl32			
			Gm8129				Gm8292				Pomp			
			Gm8566				Gm11361				Rps3			
			Psmb2				Snhg8				Rpl39			
			Cldn5				Ifi207				Psma7			
			Bvht				Rps14				Isoc1			
			Snhg8				Gm12696				Zcchc24			
			Gm12231				Ybx1.ps2				Bzw1			
			Junb				2010107E04Rik				Cdc42			
			Hpf1				Diaph2				Cox6a1			
			Chchd2				Mydgf				Lrrtm3			
			Ndufa8				Bcl2a1b				Pafah1b1			
			Pea15a				Mpeg1				Phyhipl			
			Alas1				Cox7a2				Ptpre			
			Anxa2				Rpl8				Ran			
			Hspd1.ps3				Spcs2.ps				Gm10260			
			Csnk2b				Cox6c				Cox7a2			
			Suclg1				Gadd45b				Wbp5			
			Gm16399				Hspd1.ps3				Acat1			
			Id1				Atp6v1f				Cd9			
			Ost4				Rab1a				Rps14			
			Eea1				Ccl9				Atpif1			
			Gabarapl1				RP23.123D6.12				Atp5a1			

			Dpm3				Arpc1b				Tmem176a			
			Spcs2.ps				Tspo				mt.Cytb			
			Gng5				Txn1				Phactr3			
			Txndc17				Rpl39.ps				Atp5e			
			Sec61b				Ndufa1				Sdhb			
			Gm6394				Psmb8				Ndufa2			
			Atp5o				Eef2				Rps20			
			Rbx1				Gm15920				Ywhab			
			Snx3				Ifi211				mt.Nd1			
			Tcaf1				Cd14				Gnas			
			Cstb				Hcar2				Tpm1			
			BC028528				H2.T23				Atp5c1			
			Gm2000				Bcl2a1a				Fermt2			
			Gm9392				Mif							
			Mrps5											
			Uri1											
			Gm8692											
			Rpl7.ps7											
			Dynll1											
			Snrpb											
			Gm8606											
			Srgn											
			Lrp8											
			Gm5881											
			Col4a2											
			Anapc11											
			Gm11361											
			RP24.389J11.1											

			Cox8a										
			Myh10										
			Gm12966										

Table S4. Lists of differentially expressed genes between clusters identified within myeloid cells (Drop-seq data only). Marker genes for each cluster were defined at threshold: FDR <=0.01 and log_2FC>=0.05. Genes are listed from the highest to lowest log_2FC

Cluster number	CL_0	CL_1	CL_2	CL_3	CL_4	CL_5	CL_6	CL_7	CL_8
Ontogeny	Ho-Mg	Ho-Mg	Mg-TAMs transitory	Mg-TAMs anti-inflamatory	Mg-TAMs astrocytic-like	Mg-TAMs transcriptionally active	Mg-TAMs EC-like	Mo-TAMs	BAMs
Correclation to Ochocka et al states	part of MG1	part of MG1+MG2	part of MG1	MG6 & MG7	part of MG8 & MG1	MG6	MG1 & MG6	monocytes & inMoM & Macrophage	BAMs
Marker genes	Jun	Sfrs18	Cxcl13	Cxcl13	Sparcl1	Rps12	Ly6c1	Ly6c2	Mrc1
	Egr1	Frmd4a	Cst7	Ccl4	Clu	Rps27a	Cldn5	Plac8	F13a1
	P2ry12	Malat1	Spp1	Cst7	Slc1a2	Rps29	Itm2a	H2.Eb1	Dab2
	Tmem119	Pnn	Cd63.ps	Cd63.ps	Ptn	Rps27	Gkn3	AA467197	Pf4
	Fos	Prpf4b	Ccl6	Spp1	Ttr	Rpl17	Abcb1a	Lyz2	Ms4a7
	Hspa1a	Akap9	Cd63	Ccl3	Ttyh1	Rpl23a	Igfbp7	Il1b	Cd163
	Ier5	Jmjd1c	Lpl	Gm11942	Mt2	Gnb2l1	Flt1	Thbs1	Wfdc17
	Gpr34	Dock10	Tyrobp	Ccl12	Atp1a2	Rps28	Ptprb	Tgfbi	Cp
	Rhob	Atrx	Apoe	Tyrobp	Plp1	Rps23	Spock2	Arg1	Ccl8
	Zfp36	Ssh2	Creg1	Ctsd	Aldoc	Rpl21	Bsg	Ifitm3	Wwp1
	Btg2	Smap2	Rpl32	Gm14303	Cpe	Rpl11	Adgrf5	Ms4a4c	Clec10a
	Jund	Ythdc1	Cd52	Cd63	Plpp3	Fau	Slco1a4	Ly6a	Cbr2
	Selplg	Blnk	Cd9	Cd52	Scg3	Rpl13a	Slco1c1	Lgals3	Ccl7
	Cx3cr1	Cx3cr1	Rps5	Ctsz	Gfap	Rpl18a	Cxcl12	H2.Ab1	Maf
	Siglech	Rdx	mt.Nd1	Rps25.ps1	Ptprz1	Rpl12	Pltp	Ccr2	Stab1
	Junb	Fnbp4	Ctsb	Apoc1	Gja1	Rps6	Ctla2a	Ly6i	Lyve1

	Ptgs1	Myo9a	Ctsd	Ctsl	Fabp7	Rps17	Ly6a	AW112010	Gas6
	Vsir	Golgb1	Npc2	Rpl37rt	Apod	Epb4.1l2	Sptbn1	Crip1	Ccl24
	Cst3	Il6ra	Ctsl	Gm4149	Fxyd1	Sepp1	Slc2a1	S100a11	Ccl2
	Abca9	Smarca2	Gnas	Ch25h	Mt1	Rpl10	Pcp4l1	Cxcl9	Selenop
	P2ry13	Nav3	Tmsb4x	Cd9	Dbi	Rpl9	Gng11	Srgn	Mgl2
	Olfml3	Ncor1	mt.Cytb	Ctsb	Slc4a4	Rps13	Ablim1	Cxcl2	Itsn1
	Txnip	Ivns1abp	Gm6977	Clec7a	Slc1a3	Rpl19	Adgrl4	Fxyd5	Cmah
	Nav3	Ogfrl1	Trem2	Grn	Gpm6b	D4Wsu53e	Egfl7	Cdkn1a	Fcgr2b
	Ltc4s	Tcf4		Syngr1	Cspg5	RP24.288C12.6	Esam	Mndal	Cd209a
	Tgfbr1	Rsrc2		Gm15421	Aqp4	Rpl5	Sdpr	Ifi204	Pltp
	Srgap2	Pip4k2a		Gm10269	Ednrb	Rpl31	Tm4sf1	Isg15	Folr2
	Ivns1abp	Nipbl		Rps16.ps2	Mt3	Ptplb	Kitl	Plbd1	Igfbp4
	Ubc	Phf14		Gm9794	Cald1	Rpl3	Id3	Gbp2	Stard8
	Golm1	Wnk1		Gm10076	Prnp	AF251705	Tsc22d1	Slfn4	Igf1
	Il6ra	Dnajc7		B2m	Enpp2	Rpl36a	Slc39a10	Pim1	Ifi203
	Ccr5	Bptf		C1qc	Acsl3	4632428N05Rik	Ramp2	H2.Aa	Gpx3
	Hpgds	Gtf2h2		Gm10288	Ndrg2	Cep110	Car4	Rsad2	Ehd4
	Elmo1	Acin1		Glmp	Atp1b2	Rpl27	Ccdc141	Cfp	Vcam1
	Pde3b	Ubash3b		Gm6977	Syt11	Lilrb4	Mal	Tnfaip2	Iqgap2
	Nrip1	Git2		Gm15427	Gria2	Rps7	9430020K01Rik	Ccl5	Pla2g2d
	Slco2b1	Bod1l		Gm6030	Gpr37l1	Sfrs18	Palmd	S100a6	Pla2g7
	Crybb1	Rps6ka1		Rpl36a.ps2	Scd2	Ddx26b	Pecam1	Clec4n	Clec4a3
	Hpgd	Arglu1		Cd300c2	Luzp2	Rpl35	Slc16a1	Ifi209	Blvrb
	Zfhx3	Tardbp		Rps26	Bcan	Rpl7a	Golim4	Ifi203	Cd36
	Lpcat2	Ddx17		Ccl2	Ntrk2	Apoc1	Slc38a5	Msrb1	Cd209b
	Csmd3	Pnisr		Fcer1g	Htra1	Ctage5	Ppfibp1	Slfn2	Sdc4
	Tanc2	Gcnt1		Lgals3bp	Dclk1	Tmem66	Fam13c	Vegfa	Myo5a
	Mertk			Gm14586	Asrgl1	Ppia	Sgms1	Vim	Nrp1
	Rnase4			Rpl32	Gstm1	Rps25	Cd93	Il1rn	Cfp

	Serinc3			Pld3	Nnat	Erbb2ip	Edn1	Ifi211	Snx6
	Csf1r			Tmsb4x	S100b	Gm26924	Sema3c	Cebpb	Hpgd
	Arhgap5			Rps24.ps3	Nrxn1	Postn	Ets1	Ms4a7	Lgals1
	Maf			Cd68	Id3	Rpl13	Utrn	Cd14	Fcna
	Mef2a			Gm9843	Lsamp	2700029M09Rik	C130074G19Rik	Ptgs2	Ifi207
	Lgmn			C1qa	Rgs5	Ccdc55	Ptn	Iqgap1	Snx2
	Mef2c			Rpl3.ps1	Tuba1a	Tpt1	Cd59a	Mxd1	Clec4n
	Srrm2			Gm10073	Timp3	Rps18	Epas1	S100a4	Fosb
	Itgam			Rpl39	Mgp	Spp1	Col4a1	Prdx5	Ms4a6b
	Son			Ier3	Gpm6a	Rpl30	Podxl	Clec4e	Ctsc
	Marcks			Gm11478	Igfbp5	Rps8	Sox17	Samhd1	Dse
	Malat1			Gm5805	Gabrb1	Rps16	Fermt2	Txn1	Apod
	Apbb1ip			Rpl10a.ps1	Sox9	Rps2	Slc6a6	S100a10	Ifitm3
	Hexb			Gm15772	Car2	BC016423	Crip2	Ifi205	Mndal
				Rps13.ps2	Cadm2	Diap2	Erg	Ifi27l2a	Fcrls
				Gm4332	Prdx6	Cd74	Itih5	Ms4a6c	Ifitm2
				Calr.ps	Ncam1	Lrrc58	Pglyrp1	Fosl2	Lyz2
				Rps19	Igfbp2	Rpl7	Arhgap29	Slfn5	Fos
				Ccl6	Pdgfra	Zfml	Nes	Cytip	Lilra5
				Rack1	Tmem47	Rpl37a	Cp	Tmsb10	Fcgrt
				Ssr4	Olig1	A430104N18Rik	Ptprg	Ms4a6b	
				H2.D1	S1pr1	0610031J06Rik	App	Cxcl10	
				Itgb2	Ntsr2	Rpl27a	Foxq1	Ahnak	
				Cox6a2	Itih3	1500012F01Rik	Id1	Calm1	
				C1qb	Ckb	Vimp	Kdr	Cd74	
				Gm7266	Nedd4	4933426M11Rik	Vwa1	Msr1	
				Rpl31.ps8	Atp1b1	Cwc22	Rflnb	Nr4a2	
				Ndufa1	Fam213a	D17Wsu104e	Fn1	Psmb8	
				Rpl22l1	Vim	Rpl15	Ltbp4	Il2rg	

				Gm5963	Fermt2	Rpl10a	Tek	Cybb	
				Hexa	Kcnj10	Fam105b	Selenom	Ifitm2	
				Rpl22.ps1	S100a1	Wapal	Arl4a	Ifi202b	
				Npc2	Acsl6	Rab1	Abcg2	Cstb	
				Lpl	Cryab	Snord49b	Maoa	Lilrb4a	
				Rps26.ps1	Tspan7	Gm13476	Grrp1	Ifit2	
				Gm9385	Id4	Sept15	Ece1	Irf7	
				Rpl41	Sox2	Selk	Timp3	Clec7a	
				Rpl14.ps1	Tpm1	Erdr1	Stmn2	Lgals1	
				Gnas	Scrg1	Ccl6	Ptprr	Fgl2	
				Ifi27l2a	Tril	Asph	Slc22a8	Emb	
				Gm11361	S100a6	Lpl	Apod	Fth1	
				Gm10260	Agt	B630005N14Rik	Col4a2	Cd44	
				Gm6204	Zbtb20	RP24.312B12.1	Ptrf	Ifi207	
				Rpl39.ps	Cnn3	A630007B06Rik	Lef1	Iigp1	
				Ank	Meg3	Rpl38	Slc16a2	Ccr1	
				Ctsh	S100a16	Hnrnpa3	Uaca	Gm6977	
				Rnaset2a	Fam107a	Rps4x	AU021092	Samd9l	
				Cd83	Pou3f3	Rpsa	Rgs5	Nr4a3	
				Rps15a	Cldn10	Ptms	Nostrin	Slamf7	
				Rps15a.ps5	Pla2g7	Ccdc41	Akap12	Bst2	
				Lyzl4	Slco1c1	Gm26339	Slc9a3r2	H2.Q7	
				Rpl38.ps2	Map2	Snord42a	Dynll1	Bcl2a1b	
				Rps20	Igfbp7	Clcn4.2	Aplp2	Txn.ps1	
				Gm5905	Ntm	Rplp2	Slc7a1	Sp140	
				Gm6472	Cacng4	Jhdm1d	Ushbp1	Nampt	
				Selenof	Gm42418	Rpl37	Ifitm3	F10	
				Gusb	Hepacam	Siglec5	Paqr5	Ifrd1	
				Gm2000	Ncan	Rpl18	Apold1	Gbp3	

				Gm8730	Gm12222	Smap2	Edn3	Tagln2	
					Mlc1	Tnfsf8	Tspan13	Fcgr2b	
					Serpina3n	2700089E24Rik	Hspb1	Amica1	
					Chchd10	D14Abb1e	Tpm1	Tpt1.ps3	
					Mfge8	Suv420h1	Ifitm2	Emp3	
					Mmd2	Abcd2	Vcam1	Tiparp	
					F3	Ing4	Cgnl1	Pla2g7	
					Ddah1	1110001A16Rik	Adcy4	Clec12a	
					Syne1	Leprot	Eng	Gda	
					Limch1	Ccdc104	Anxa2	Ifi30	
					Ldhb	Slc11a1	Mpzl1	Cyp4f18	
					Slc6a1	Rps24	Ebf1	Rpl34	
					Tpm2	Myo1e	Ctnnb1	Slfn1	
					Lhfpl3	D15Ertd621e	Crip1	Gm7676	
					Nrcam	Apoe	Wfdc1	Zbp1	
					Fut9	Tec	Heg1	C3	
					Nrxn2	Niacr1	Tfrc	Emilin2	
					Kif1b	Colec12	Col4a3bp	Phf11d	
					Dmd	Plgrkt	Clec14a	Lst1	
					Aplp1	Rpl36	Tceb2	Cxcl16	
					Sdc4	2610305D13Rik	Cd200	Crem	
					Myo6	D19Bwg1357e	Ndrg1	Rps2	
					Rgcc	Cox7c	Nedd4	Shfm1	
					Tspan3	Rin2	Sema7a	Tgm2	
					Gm5514	2510009E07Rik	Scgb3a1	Stat1	
					Prex2	Phyhd1	Net1	Phf11b	
					Fez1	Gtl3	Actn4	Lsp1	
					Slc38a3	Arl6ip5	Luzp1	Klra2	
					Dtna	Sc4mol	Cyyr1	Myof	

					Fjx1	Apobec1	Fnbp1l	H2.K1	
					Chpt1	Sfi1	Prnp	Dab2	
					Sash1	Creg1	Tshz2	Acp5	
					Map1b	Il4i1	Tmsb10	Anxa1	
					Hmgcs1	Uba52	Car2	Psme2b	
					Nap1l5	Hmgb1	Bmx	Sp100	
					Dner	Cd84	Plcb1	AI662270	
					Cbx5	Tial1	Igfbp4	Gpnmb	
					Slc6a11	Mnda	BC002163	Wfdc17	
					2900052N01Rik	Cfh	Prex2	Mmp14	
					Sept7	Ftl1	Sparcl1	Ccrl2	
					mt.Rnr1	Calr	S100a13	Itga4	
					Gpld1	4632419I22Rik	Igf1r	Nfil3	
					Vcan	Rpl23	Afap1l1	Sh3bgrl	
					Epn2	Dnajb14	Afdn	Pde4b	
					Tnik	Ccdc66	Kank3	H2.DMa	
					RP23.4P23.1	Gm10263	Foxc1	Hspa8	
					Gnao1	Rpl6	Gm3531	Osm	
					Gng11	Gapdh	Fzd6	Runx3	
					Klf9	Mpeg1	Snx3	Epsti1	
					Sptbn1	Cd63	Hip1	Gm12854	
					Itgb8	5830428H23Rik	Gm5436	Anxa2	
					Glud1	Myl6	Wwtr1	H2.T23	
					Psip1	2810055G20Rik	Uqcc2	Anxa5	
					Hbegf	D19Ertd737e	Hes1	Stk17b	
					Agpat5	Cyth4	Lsr	Taldo1	
					Rarres2	Cnpy2	Nos3	Gbp4	
					Slc25a4	Ptplad2	Ap2m1	Clec4d	
					Kif21a	RP23.32A8.1	Ctnna1	Sh3bgrl3	

					Tubb2b	St8sia6	Prom1	Mgst1	
					Ezr	Slc15a3	Plcb4	Psmb9	
					Col16a1	Tmem179b	Rpl38.ps2	Gbp5	
					C4b	4922501C03Rik	Rgs12	Tspo	
					Pcsk1n	Gm11206	Tmem252	Bcl2a1d	
					Acsbg1	Galnt7	Wbp5	AB124611	
					Gstm5	Ccdc50	Atox1	Ass1	
					Sdc2	Akap8l	Gm7809	Rpl35a	
					Gap43	Ctss	Serpinb6a	Btg1	
					Gjb6	mt.Tm	Arhgef12	Ms4a6d	
					Pcdh10	Abcg1	Dab2ip	Bhlhe40	
					Cyp2j9	Ptplad1	Calm1	Txnrd1	
					Skp1a	Agpat6	Mfsd2a	Pygl	
					Fgfr3	Hiat1	Myl12b	Oasl1	
					Arhgef12	Aim2	Fgd5	Ifit3	
					Nfia	Smad4	Mt2	Rnf149	
					Bex3	Apbb1ip	Vat1	Mcl1	
					Ccnd2	Hspa4	Itga1	Lyz1	
					Msi2	Rp2h	Ttyh2	Tpm4	
					Add3	Fmn1	Lama4	H2.DMb1	
					Gm9625	Rpl24	Serpinb6b	Parp14	
					Fam184a	Cacna1a	Alas1	Gm6377	
					Myo10	Ank	Icam2	Fabp5	
					Pcdh17	Pros1	Myl12a	Alox5ap	
					Tcf12	Naalad2	Dynlt3	Ifih1	
					Fam171b	Brwd1	Osbpl1a	Mcemp1	
					Rcn2	AI607873	Fkbp1a	Oasl2	
					Pcdh9	Ptprc	Thra	Trim30a	
					Tmod2	Usp12	Iqgap1	Rps27l	

					Msmo1	Cldn25	Cript	Ldha	
					Pcdh7	Rpl14	Tmem256	Lrrfip1	
					Mapt	Morf4l1	Ahnak	Pirb	
					Plcd4	Actg1	Tonsl	Dusp5	
					Cdh2	Rpl28	Dkk2	Malt1	
					Phyhipl	Myo5a	Eci1	Gpr35	
					Gm12346	Atp2b1	Gm4617	Rps18	
					Gm3764	Selt	Sema3g	Ctsc	
					Mdk	Cd9	Limch1	Cd274	
					2900011O08Rik	Csf2ra	Pir	Prdx6	
					Dlgap1	Zbed6	Lrp8	Tpi1	
					Ccdc88a	Osbpl8	Sorbs2	Gadd45b	
					Phactr3	Prdm2	Tes	Pfn1	
					Chl1	Naa35	St6galnac2	Mif	
					Gm12892	Gm17087	Cald1	Nfkbie	
					4930402H24Rik	Col27a1	Slc30a1	Csrnp1	
					Dkk3	Fgd3	Mecom	B2m	
					Nkain4	Tgfbr1	Gm8894	Sod2	
					Serpine2	Fam134b	Arpc1a	Actr3	
					Cyp2j6	Nptn	Dnajc10	Myl12a	
					Kcnj16	Ramp1	Esyt2	Psma7	
					Rev3l	Acer3	Nfib	Gbp7	
					Hmgn5	C230081A13Rik	Clec2d	Bcl2a1a	
					Cfap36	Pdia3	Bcl2l1	RP23.354J5.3	
					Phlda1	Tm9sf3	Ddit4	Pkm	
					Pantr1	Plxdc2	Ccser2	Fcgr4	
					Npas3	Zfp949	Tinagl1	Neurl3	
					Cnp	Timm21	S100a16	Igsf6	
					Cxcl14	Golga4	Aes	Plaur	

					Atp5g3	Gm21092	Fam63a	Psme2	
					Syne2	5430435G22Rik	Ctdnep1	Sdcbp	
					Ctnnd2	Cxcl14	Syne1	Rps24.ps3	
					Pmm1	Arrdc4	Gm8186	Ets2	
					Pea15a	Tmem57	Grb14	Arhgap15	
					Cmtm5	Ptpra	Hsp25.ps1	Prdx1	
						Pgrmc2	Ifnar1	Gm15427	
						1200014J11Rik	Zic3	Gm9794	
						Tmed3	Gm11223	Rps13.ps2	
						Cux1	Sec61b	Abracl	
						Zmiz1	Arhgap31	Wdr89	
						Nr2c2	Igf1	Cd52	
						Eml4	Clic5	Psma2	
						Nsa2	Robo4	Cfb	
						ZEB2-AS1-2	Polk	Slc16a3	
						Nufip2	Usp46	Gbp8	
							Rabac1	H2.T22	
							Use1	Ptprc	
							Plscr2	Chmp4b	
							Kdelr1	Plin2	
							Capns1	Coro2a	
							Sntb2	C130026I21Rik	
							Rnpepl1	Cyba	
							Bola3	Oas1a	
							Rell1	Spty2d1	
							Map1b	Rpl22	
							Cfdp1	Rps15a	
							Atp5j	H3f3b	
							Myo1b	Rel	

							Myh10	Rbms1	
							Pinx1	Klf4	
							Ndufa3	Rps3	
							Agfg1	Gm15753	
							Vim	Nr4a1	
							Gm11942	H2.D1	
								Clic4	
								Diaph1	
								Atp11b	
								Rps10.ps2	
								Cd47	
								Rnf213	
								Gm4332	
								Cd300lf	
								Cdk2ap2	
								Ccnd2	
								Rtp4	
								Metrnl	
								Snx10	
								Arpc5	
								Cox17	
								Gm9843	
								Ly6e	
								Il18bp	
								Nfkb2	
								Gm1966	
								Fosb	
								Capg	
								Rps9	

								Gm5905	
								Gm6472	
								Vasp	
								Rps16.ps2	
								Tuba1c	
								Lcp1	
								Rplp0	
								Psmb10	
								Ezr	
								Irf1	
								Rpl29	
								Ell2	
								Psap	
								Rbpsuh.rs3	
								Rpl39	
								Gm9385	
								Sec61b	
								Gm12254	
								Trim25	
								H2.Q6	
								Stat2	
								Nfe2l2	
								Nfkbia	
								Rps15a.ps5	
								Slk	
								Gm8995	
								Gm9835	
								Myl12b	
								Ccl2	

								Cast	
								Gpr65	
								Gpx1	
								Clec4a3	
								Gm6030	
								Gm10169	
								Aldoa	
								Rps15a.ps7	
								Cnn2	
								Neat1	
								Rpl36al	
								Gm5963	
								Gm15500	
								Rpl18.ps1	
								H2.Q4	
								Rps24.ps2	
								Sub1	
								Gm8822	
								Tmem123	
								Esyt1	
								Tpt1	
								Arpc2	
								Rps20	
								1810037I17Rik	
								Glrx	
								Prelid1	
								Sp110	
								Syngr2	
								Rps14	

								Xaf1	
								Gm4204	
								Zfas1	
								Arpc3	
								F13a1	
								Psme1	
								Pid1	
								Rpl9.ps7	
								Hif1a	
								Mdfic	
								Lmnb1	
								Selenow	
								Trps1	
								Ncf4	
								Card19	
								Gm5835	
								Shisa5	
								Tap1	
								Irgm1	
								Spop	
								Tpm3.rs7	
								Pmaip1	
								Arl5c	
								Cyth1	
								Daxx	
								Ccl9	
								Atox1	
								Baz1a	
								Tes	

								Gm5805	
								Ninj1	
								Mrpl33	
								Gm6204	
								Rps26	
								Herc6	
								Gsn	
								Arpc1b	
								Gm4617	
								Gm10250	
								Fth.ps3	
								Gm14586	
								Snx20	
								AI504432	
								Litaf	
								Rps5	
								Gm13092	
								Rps3a1	
								Got1	
								Pttg1	
								Gm11478	
								Rpl14.ps1	
								Atp5h	
								Rps19	
								Sri	
								Tax1bp1	
								Lsm4	
								Gm7809	
								Gm10443	

								Dnaja2	
								Nlrp3	
								Cmpk1	
								Rps10.ps1	
								Gm9493	
								Gm14539	
								Apobec1	
								Trafd1	
								Nmi	
								Cox5a	
								Etf1	
								Rpl37rt	
								Sap18b	
								Ddx58	
								Slc7a2	
								Rpl38.ps2	
								Sdc4	
								Tgif1	
								Npc2	
								Trim30d	
								Gmfg	
								H3f3a	
								Gm4149	
								Rack1	
								Rpsa.ps10	
								Anxa4	
								Gm10275	
								Pilra	
								Eif4ebp1	

								Kdm7a	
								Fos	
								Sf3b6	
								Rps11	
								Scand1	
								Pitpna	
								2010107E04Rik	
								Gabarap	
								Arhgdib	
								Rpl8	
								Nufip1	

Table S5. List of gene signatures applied for scRNA-seq analysis.

Signature	Human Mg	Human Mo	Enzymatic activation	Homeostatic Mg	Sensome	Sensome w/o homeostatic Mg	Migration	APC	Phagocytosis
Genes	12	13	25	35	140	127	464	106	219
	HEXB	CCR2	Rgs1	Bhlhe41	4632428N05Rik	Abcc3	Abl1	Abcb9	4932438A13Rik
	P2RY12	PLAC8	Hist2h2aa1	Crybb1	Abcc3	Adora3	Acvrl1	Ap3b1	4933434E20Rik
	P2RY13	CLEC12A	Hist1h4i	Csf1r	Adora3	Adrb2	Adam17	Ap3d1	Abca1
	TMEM119	FCN1	Nfkbiz	Ctsd	Adrb2	Bin2	Adam8	Arl8b	Abca7
	GPR34	VCAN	Klf2	Ctsf	AF251705	C3ar1	Adam9	Atg5	Abl1
	CXCR1	LYZ	Junb	Cttnbp2	Bin2	C5ar1	Adamts9	B2m	Abl2
	TGFBR1	LGALS3	Dusp1	Cttnbp2nl	C3ar1	Ccr5	Adgra2	Bag6	Abr
	CST3	CRIP1	Ccl3	Cx3cr1	C5ar1	Ccrl2	Adgrb1	Calr	Adgrb1
	OLFML3	S100A4	Hspa1a	Fcrls	C5ar2	Cd14	Adgrg1	Ccr7	Aif1
	SALL1	S100A6	Hsp90aa1	Golm1	Ccr5	Cd180	Adipor1	Cd1d1	Ano6
	SELPLG	S100A8	Fos	Gpr34	Ccrl2	Cd22	Adora2b	Cd68	Anxa1
	TREM2	S100A9	Hspa1b	Gpr84	Cd101	Cd300a	Agt	Cd74	Anxa3

		CD44	Jun	Hexb	Cd14	Cd33	Aif1	Clec4a1	Appl1
			Jund	Hpgds	Cd180	Cd37	Akirin1	Clec4a2	Appl2
			Nfkbid	Hspa1a	Cd22	Cd48	Akt1	Clec4a3	Arhgap12
			Gem	Lgmn	Cd300a	Cd52	Akt3	Ctsl	Arhgap25
			Ccl4	Lrrc3	Cd33	Cd53	Amot	Ctss	Arl8b
			Ier5	Ltc4s	Cd37	Cd68	Amotl1	Erap1	Atg3
			Txnip	Mafb	Cd48	Cd74	Angpt1	Ext1	Atg5
			Hist1h2bc	Nuak1	Cd52	Cd83	Angpt2	Fcer1g	Atg7
			Zfp36	Olfml3	Cd53	Cd84	Anln	Fcgr1	Axl
			Hist1h1c	P2ry12	Cd68	Cd86	Ano6	Fcgr2b	Bcr
			Egr1	P2ry13	Cd74	Clec4a2	Anxa1	Fcgr3	Becn1
			Atf3	Plxdc2	Cd79b	Clec4a3	Anxa3	Fcgr4	Bin2
			Rhob	Rab3il1	Cd83	Clec5a	Apoe	Fgl2	C2
				Sall1	Cd84	Clec7a	App	Gba	C3
				Scoc	Cd86	Cmklr1	Aqp1	Gm8909	C4b
				Serpine2	Clec4a2	Cmtm6	Arf6	H2.Aa	Calr
				Siglech	Clec4a3	Cmtm7	Arl13b	H2.Ab1	Camk1d
				Slc2a5	Clec4b1	Csf2rb2	Arsb	H2.D1	Ccl2
				Tgfbr1	Clec5a	Csf3r	Atoh8	H2.DMa	Ccr2
				Tmem119	Clec7a	Cxcl16	Atp2b4	H2.DMb1	Ccr7
				Atp8a2	Cmklr1	Cysltr1	Atp5a1	H2.DMb2	Cd300a
				Lag3	Cmtm6	Daglb	Atp5b	H2.Eb1	Cd300lf
				Slco4a1	Cmtm7	Ecscr	Axl	H2.K1	Cd302
					Csf1r	Entpd1	Bcar1	H2.M3	Cd36
					Csf2rb2	Fcer1g	Bcas3	H2.Oa	Cd47
					Csf3r	Fcgr1	Bmpr2	H2.Q10	Cdc42
					Cx3cr1	Fcgr2b	Bsg	H2.Q4	Cdc42se1
					Cxcl16	Fcgr3	Bst1	H2.Q6	Cdc42se2
					Cysltr1	Fcgr4	C1qbp	H2.Q7	Cfp

					Daglb	Gpr160	C3ar1	H2.T22	Clcn3
					Ecscr	Gpr183	C5ar1	H2.T23	Clec7a
					Emr1	Gsdmd	Calr	H2.T24	Cln3
					Entpd1	H2.Oa	Camk1d	H2.T3	Cnn2
					Fcer1g	H2.Ob	Capn7	Hfe	Colec12
					Fcgr1	H2.T23	Card10	Icam1	Coro1a
					Fcgr2b	Havcr2	Ccdc141	Ide	Coro1c
					Fcgr3	Hfe	Ccl12	Ifi30	Csk
					Fcgr4	I830077J02Rik	Ccl17	Ighm	Cyba
					Fcrl1	Icam1	Ccl2	Mfsd6	Dnm2
					Fcrls	Icosl	Ccl24	Mr1	Dock1
					Gpr160	Ifitm6	Ccl25	Nod1	Dock2
					Gpr183	Ifngr1	Ccl3	Nod2	Eif2ak1
					Gpr34	Igsf6	Ccl4	Pdia3	Elmo1
					Gpr56	Il10ra	Ccl5	Pikfyve	Elmo2
					Gpr84	Il21r	Ccl6	Psap	Elmo3
					Gsdmd	Il4ra	Ccl7	Psmb8	Fcer1g
					H2-Oa	Il6ra	Ccl8	Psmb9	Fcgr1
					H2-Ob	Itgam	Ccl9	Psme1	Fcgr2b
					H2-T23	Itgb2	Ccr1	Psme2	Fcgr3
					Havcr2	Itgb5	Ccr2	Ptpn22	Fgr
					Hfe	Kctd12	Ccr7	Pycard	Gas6
					I830077J02Rik	Lair1	Cd200	Rab10	Gata2
					Icam1	Laptm5	Cd200r1	Rab27a	Gsn
					Icam4	Lat2	Cd40	Rab32	Gulp1
					Icosl	Lgals9	Cd63	Rab33a	Hck
					Ifitm6	Lilra5	Cd74	Rab34	Hmgb1
					Ifngr1	Ly86	Cd81	Rab35	Hspa8
					Igsf6	Nckap1l	Cd9	Rab3b	Ighm

					Il10ra	Nfam1	Cdh13	Rab3c	Il15
					Il21r	Ninj1	Cdh5	Rab4a	Il15ra
					Il4ra	Numb	Cdk5	Rab5b	Il1b
					Il6ra	P2ry6	Cdk5r1	Rab6a	Il2rg
					Itgam	Pilra	Ceacam1	Rab8b	Irf8
					Itgb2	Plekho1	Cib1	Relb	Itga2
					Itgb5	Pmepa1	Cklf	Rftn1	Itgal
					Kctd12	Pmp22	Clasp1	Slc11a1	Itgam
					Lag3	Ptafr	Clasp2	Tap1	Itgav
					Lair1	Ptprc	Clec14a	Tap2	Itgb1
					Laptm5	Selplg	Cmklr1	Tapbp	Itgb2
					Lat2	Sirpa	Cntn2	Tapbpl	Itgb3
					Lgals9	Slamf9	Col3a1	Thbs1	Jmjd6
					Lilra5	Slc11a1	Coro1b	Traf6	Lbp
					Liph	Slc16a3	Coro1c	Trem2	Ldlr
					Lpar5	Slc44a2	Creb3	Unc93b1	Lepr
					Ltf	Slc46a1	Csf1	Was	Letmd1
					Ly86	Slc7a7	Csf3r	Wdfy4	Lman2
					Nckap1l	Slc7a8	Csnk2b	Ythdf1	Lrp1
					Nfam1	Slco2b1	Ctnnb1	H2.M5	Lyar
					Ninj1	Stab1	Ctsh	Kdm5d	Lyst
					Numb	Tcirg1	Cul5	Flt3	Masp2
					P2ry12	Tgfbr2	Cx3cl1	Gm11127	Megf10
					P2ry13	Tlr13	Cxadr	H2.Ob	Mertk
					P2ry6	Tlr2	Cxcl1	H2.Eb2	Met
					Pilra	Tlr4	Cxcl10	H2.M2	Mex3b
					Plekho1	Tlr6	Cxcl12	H2.Q1	Mfge8
					Plxdc2	Tlr7	Cxcl13	H2.Q2	Msr1
					Pmepa1	Tmem173	Cxcl2	Treml4	Myd88

					Pmp22	Tmem206	Cxcl9	Ifng	Myh9
					Ptafr	Tmem37	Cxcr4	Clec4b1	Myo18a
					Ptprc	Tnfrsf13b	Cyp1b1	Ctse	Myo1g
					Selplg	Tnfrsf1a	Daam2	H2.M9	Myo7a
					Siglec5	Tnfrsf1b	Dab1	Azgp1	Ncf2
					Siglece	Trem2	Dab2ip	Gm7030	Ncf4
					Siglech	Trpv2	Dcn	Ccl21a	Nckap1l
					Sirpa	Tyrobp	Dicer1		Nod2
					Slamf9	Icam4	Disc1		Nr1h3
					Slc11a1	Cd79b	Dixdc1		P2rx7
					Slc16a3	Siglece	Dnaja4		P2ry6
					Slc2a5	Tlr1	Dnm1l		Pear1
					Slc44a2	C5ar2	Dock1		Pecam1
					Slc46a1	Cd101	Dock5		Pik3ca
					Slc7a7	Liph	Dpp4		Pikfyve
					Slc7a8	Tlr12	Dusp1		Pip5k1c
					Slco2b1	Tnfrsf17	Dusp10		Pla2g5
					Stab1	Upk1b	Edn1		Plcg2
					Tcirg1	Fcrl1	Edn3		Pld4
					Tgfbr1	Tmem8c	Ednra		Pot1b
					Tgfbr2	Clec4b1	Ednrb		Prkcg
					Tlr1	Lpar5	Efhc1		Pros1
					Tlr12	4632428N05Rik	Efna1		Pten
					Tlr13	AF251705	Efnb2		Ptk2
					Tlr2	Emr1	Egf		Ptprc
					Tlr4	Gpr56	Egfr		Ptprj
					Tlr6	Siglec5	Emc10		Ptx3
					Tlr7	Ltf	Emilin1		Pycard
					Tmem119		Emp2		Rab11fip2

					Tmem173		Emx2		Rab14
					Tmem206		Enpp1		Rab20
					Tmem37		Enpp2		Rab27a
					Tmem8c		Epb41l4b		Rab31
					Tnfrsf13b		Epb41l5		Rab34
					Tnfrsf17		Epha2		Rab5a
					Tnfrsf1a		Ephb4		Rab7
					Tnfrsf1b		Ets1		Rab7b
					Trem2		Evl		Rac1
					Trpv2		Fap		Rac2
					Tyrobp		Fbxo45		Rack1
					Upk1b		Fbxw7		Rap1a
							Fcer1g		Rap1gap
							Fcgr3		Rapgef1
							Fgf1		Rara
							Fgf2		Rhobtb1
							Fgf7		Rhobtb2
							Fgfr1		Rhog
							Flt1		Rhoh
							Flt4		Scarb1
							Foxc2		Sh3bp1
							Foxg1		Sirpa
							Foxp1		Slc11a1
							Fstl1		Snx3
							Fut10		Sod1
							Gab2		Spg11
							Gadd45a		Sphk1
							Gata2		Stap1
							Gbf1		Syk

							Gipc1		Syt11
							Gli3		Syt7
							Glipr2		Tgfb1
							Glul		Tgm2
							Gpi1		Thbs1
							Gpld1		Tlr2
							Gpr35		Tlr4
							Gpx1		Tm9sf4
							Grn		Tmem175
							Has2		Tnf
							Hbegf		Trbc2
							Hc		Trem2
							Hdac5		Tub
							Hdac6		Tusc2
							Hdac7		Tyro3
							Hdac9		Tyrobp
							Hif1a		Unc13d
							Hmgb1		Vamp7
							Hmox1		Vav1
							Hspb1		Xkr5
							Hyal1		Xkr6
							Igf1		Xkr8
							Igf2		Fer1l5
							Il1b		Icam5
							Il34		Trbc1
							Iqsec1		Apoa2
							Itga1		Il2rb
							Itga2		Mbl2
							Itga3		Cfb

							Itga9		Siglece
							Itgam		Sirpb1b
							Itgav		Sirpb1c
							Itgb1		Ticam2
							Itgb1bp1		Xkr4
							Itgb2		Gm9733
							Itgb3		Dysf
							Jam3		Gm5150
							Jun		Ighd
							Jup		Igkc
							Kank1		Iglc3
							Kank2		Rab39
							Kdr		Sirpb1a
							Kit		Slamf1
							Klf4		Treml4
							Krit1		F2rl1
							Lamb1		Ifng
							Lbp		Marco
							Lemd3		Prtn3
							Lgals3		Ager
							Lgals8		Apoa1
							Loxl2		Cd209b
							Lpxn		Iglc1
							Lrp6		Iglc2
							Lrp8		Masp1
							Lrrk2		Spon2
							Lyn		Srpx
							Macf1		Tulp1
							Map2k3		Alox15

							Map2k5		Havcr1
							Map3k3		Timd4
							Map4k4		Trdc
							Mapk1		Colec11
							Mapk3		
							Mapre2		
							Mboat7		
							Mcc		
							Mcu		
							Mdk		
							Mecp2		
							Mef2c		
							Met		
							Mia3		
							Mif		
							Mmp14		
							Mmp28		
							Mmrn2		
							Mospd2		
							Mpp1		
							Mtor		
							Mtus1		
							Myh9		
							Myo9b		
							Nanos1		
							Nbl1		
							Nckap1l		
							Ndel1		
							Nf1		

							Nfe2l2		
							Ninj1		
							Nod2		
							Nos3		
							Notch1		
							Nr2e1		
							Nr2f2		
							Nr4a1		
							Nrp1		
							Nup85		
							Nus1		
							P2rx4		
							Pafah1b1		
							Patz1		
							Paxip1		
							Pdcd10		
							Pdcd6		
							Pde4b		
							Pde4d		
							Pdgfb		
							Pdpk1		
							Pecam1		
							Pex13		
							Pex5		
							Pf4		
							Pfn1		
							Pfn2		
							Pik3c2a		
							Pik3cb		

							Pik3cd		
							Pik3cg		
							Pik3r2		
							Pikfyve		
							Pkn1		
							Pkn2		
							Pkn3		
							Pla2g7		
							Plcg1		
							Plcg2		
							Plekhg5		
							Plk2		
							Plpp3		
							Plxnd1		
							Pou3f2		
							Pou3f3		
							Ppard		
							Ppia		
							Ppib		
							Ppm1f		
							Prcp		
							Prex1		
							Prkca		
							Prkce		
							Prkd1		
							Prkd2		
							Prox1		
							Psen1		
							Pten		

							Ptgs2		
							Ptk2		
							Ptk2b		
							Ptp4a3		
							Ptpn11		
							Ptpn23		
							Ptprg		
							Ptprj		
							Ptprm		
							Ptpro		
							Pxn		
							Rab11a		
							Rab13		
							Rac1		
							Rac2		
							Rarres2		
							Reln		
							Rgcc		
							Rhoa		
							Rhob		
							Rhoj		
							Rin2		
							Rnf7		
							Robo1		
							Rock1		
							Rock2		
							Rpl13a		
							Rps19		
							Rras		

							Rreb1		
							Rtn4		
							Sash1		
							Scarb1		
							Sell		
							Sema3a		
							Sema4a		
							Sema5a		
							Serpine1		
							Serpinf1		
							Sh3bp1		
							Sirt1		
							Slc37a4		
							Slit2		
							Smoc2		
							Snai2		
							Socs7		
							Sox9		
							Sp1		
							Sp100		
							Sparc		
							Spp1		
							Spred1		
							Src		
							Srf		
							Srgap2		
							Srpx2		
							Stap1		
							Stard13		

							Stat5a		
							Sun1		
							Sun2		
							Svbp		
							Syk		
							Syne2		
							Synj2bp		
							Tbxa2r		
							Tek		
							Tesk1		
							Tgfb1		
							Tgfb2		
							Tgfbr2		
							Tgfbr3		
							Thbs1		
							Tirap		
							Tnf		
							Tnfaip6		
							Tnr		
							Trem1		
							Trem2		
							Trpv4		
							Tyro3		
							Vash1		
							Vav1		
							Vav3		
							Vegfa		
							Vhl		
							Vil1		

							Wdpcp		
							Wnt5a		
							Zc3h12a		
							Zeb2		
							Zfp580		
							Zmiz1		
							Il23a		
							Mst1		
							Ccl22		
							Xcl1		
							Apoh		
							Cxcl3		
							Gata3		
							Gdf2		
							S100a14		
							Arx		
							Bmper		
							Ccl11		
							Dcx		
							Dll4		
							Fezf2		
							Fgf13		
							Lcn2		
							Ptprr		
							Stc1		
							Thbs4		
							Wnt7a		
							Cdk5r2		
							Bmp4		

							C5ar2		
							Ccr6		
							Dysf		
							Nrg1		
							S100a8		
							Slamf1		
							Slamf8		
							Trem3		
							Vegfc		
							Vstm4		
							Mcoln2		
							Dapk2		
							Ccl1		
							Ifng		
							Tac1		
							Tnfsf11		
							Ager		
							Alox12		
							Apoa1		
							Cxcl5		
							Defb25		
							Fgf18		
							Fgfbp1		
							Foxb1		
							Lgals12		
							Mdga1		
							Slit1		
							Adtrp		
							Ccbe1		

							Drd1		
							Fgf10		
							Lhx6		
							Lrg1		
							Meox2		
							Mmp9		
							Msmp		
							Mstn		
							Ror2		
							S100a9		
							Tacr1		
							Cxcr2		
							Egr3		
							Trim55		
							Nrg3		
							Fermt1		
							Ccl21a		

Table S6. Lists of differentially expressed genes between TMZ treated and control P3 PDOXs per each major cell type analysed. Differentially expressed genes were defined at threshold: FDR <=0.01 and $|\log_2 FC| >= 0.5$. Genes are listed from the highest to lowest $|\log_2 FC|$.

Cell origin	mouse TME						human GBM	
Cell type	**Astrocytes**		**Endothelial cells**		**Myeloid cells**		**Tumor cells**	
Fold change	upregulated	downregulated	upregulated	downregulated	upregulated	downregulated	upregulated	downregulated
Number of genes	2	1	41	47	127	28	90	78
	Scg2	Gm12222	RP23.269H21.1	Ttr	Rnaset2b	Rpl26	GDF15	BCAN
	Aldoc		Rnaset2b	Rpl26	Gm14513	Rpl35a	CDKN1A	ID3

			mt.Tc	Rpl35a	Cxcl13	Igfbp7	SCG2	C1orf61
			Gm7638	Hexb	Gm7638	Ttr	CHI3L1	HES5
			Abcb1a	Apln	Pde3b	Ptn	NEAT1	CSPG5
			Cxcl12	Rpl39.ps	Ptgs1	Gng5	GADD45A	FABP7
			Pcp4l1	Ctsd	Jund	Rps15a.ps5	RPS27L	HMGCS1
			Paqr5	Cwc22	Slco2b1	Gm10076	FTL	CST3
			Timp3	Lrp8	Spp1	Rpl22.ps1	MDM2	HSPA1A
			Slc6a6	Myh10	Zfhx3	Enpp2	DDB2	HSPA1B
			H2.D1	Ctss	Rpsa	Gm12338	GAP43	NCAN
			Hsp25.ps1	Tyrobp	Apoe	Rps15a.ps7	OCIAD2	MSMO1
			Degs2	Ndufs5	P2ry12	Gm5644	NRP2	TTYH1
			Fam32a	Rpl36a.ps2	Tmem119	Gas5	S100A6	ACAT2
			Ly6a	Dok4	Cfl1	Gm10269	BTG1	HEY1
			Ppil4	Hopx	Cnpy2	Cd52	PHLDA1	FDPS
			Ucp2	Hspa5	Cx3cr1	Rpl36a.ps2	SPP1	DBI
			Hspb1	Slc7a1	Rpl9.ps6	Ndufa4	SQSTM1	IDH1
			Ly6c1	Lyz2	Cited2	Rpl37rt	TIMP1	METRN
			Serinc3	Gm7266	Tubgcp5	Gm4332	SLC3A2	LMO4
			Sparcl1	Wwtr1	Mpc1	Rplp2	ZMAT3	PEA15
			Lrg1	Ccny	Fscn1	Rpl23	C6orf141	MT3
			Maoa	Rpl38.ps2	Ltc4s	Gm4149	TUBA1C	EDNRB
			Aldh2	Rps15a.ps5	Gm10263	Rps16.ps2	IGFBP3	SCRG1
			mt.Rnr1	Slc38a2	Mylip	Rps21	PHPT1	NDRG2
			Tspo	Rps11.ps3	Ftl1	Ndufs5	PHLDA3	CYP51A1
			U2af1	Gas5	Aimp1	Rpl32	IDS	CNN3
			Pltp	Gm10076	Dtnbp1	Rps15	GAS5	HIST1H4C
			mt.Rnr2	Gm15148	C1qa		VGF	RPS10
			Cd59a	RP23.288C18.3	Ucp2		DDIT3	YWHAE
			Gm694	Cst3	Pwwp2a		ARL4C	FDFT1
			Mal	Pmepa1	Rhob		MALAT1	FAM181B

			Gm14513	Gm10269	Coro1a		FDXR	ARC
			Ly6e	Rflnb	Pik3cg		RPS19	ATP1A2
			Bsg	Rpl37rt	Zfp90		BAX	IDI1
			Malat1	Nostrin	Rpl13		LMNA	MARCKS
			Ifitm2	Trf	Gpr34		GABPB1-AS1	ASCL1
			Utrn	Calr	Frmd4a		CAMK2D	FOS
			Ubb	Rps11.ps2	Ifngr1		RCAN1	GNAI2
			Gm11560	Gm4149	Scamp2		PMEPA1	SAMD1
			Cldn5	Sparc	Rpl18.ps1		IGFBP5	HES4
				Tmsb4x	Lrp1		LONRF2	SDC3
				Hsp90b1	Sox4		MDK	STMN1
				Gm9794	Selplg		ENC1	IGFBP2
				Tmsb10	Qpct		AEN	LRRC17
				Rpl32	Sltm		PGM2L1	TUBB2B
				Rplp1	Rpl10.ps3		TNFRSF12A	TMSB4X
					Gpsm3		CEBPB	TUBA1B
					Lamtor1		ZFAS1	ITM2C
					Ier3		SRPX	NRARP
					Tmem100		NUPR1	MGST3
					Sdhd		HBEGF	SQLE
					Commd2		YBX3	SLC1A3
					Eif4g2		ANXA2	CHMP4B
					Arl4c		PMAIP1	ID1
					Mknk1		VMP1	GFAP
					Dnm2		ASCC3	TMSB15A
					Kctd12		RBP1	PLPP3
					Scd2		PLK3	CAMTA1
					Fam76b		TRIAP1	GATM
					Ankle2		TMSB10	MDFI
					Scarb2		APLP1	HSPA8

					Ly6e		PLXNB2	HNRNPA2B1
					Gm15536		SLC25A37	QKI
					Rab10		AC010198.2	SLC6A11
					Gm10443		TMEM158	ARL6IP6
					Hpgds		KCNF1	TUBB2A
					Mxi1		SESN2	OLIG1
					Zfand6		AL353138.1	MT1M
					Prdx5		CMBL	APCDD1
					H2.T.ps		CCND1	TSPAN3
					Naa50		CIRBP	FGFBP3
					Tmem86a		FBXO22	AC004540.2
					Slc29a3		S100A16	MT2A
					Abca1		SMIM3	ID2
					Atp6v0a1		JAG1	MARCKSL1
					Ninj1		LGALS3	PAFAH1B3
					Limd2		ARHGEF2	SAPCD2
					Olfml3		PDLIM4	
					Elf1		XPC	
					Prune2		TIGAR	
					Arpc4		BLOC1S2	
					Zfp36l1		TXNIP	
					Timp2		CEBPG	
					Msr1		METTL7B	
					Bin1		PRKCQ-AS1	
					Parvg		QDPR	
					Marcks		SCG5	
					Gm8979		SH3BGRL3	
					Ywhae		PDGFC	
					Phyh			
					Rgs19			

					Sp3			
					Arl6ip4			
					Tuba1b			
					Ndufs7			
					Cd37			
					Comt			
					Brk1			
					Rpl10a			
					Sun2			
					Scoc			
					Rtn4rl1			
					Colgalt1			
					Crebrf			
					Pla2g7			
					H2.D1			
					Abcg1			
					Srgap2			
					Gla			
					Gm8399			
					Ube2d3			
					Lgmn			
					mt.Co1			
					Bmyc			
					Csf1r			
					Gm8606			
					Id2			
					Cndp2			
					Zfp62			
					Lyl1			
					Iah1			

					Dock10			
					Fam49b			
					Kdm7a			
					Psmc4			
					Selenop			

Chapter 7

Discussion, Conclusions and Outlook

7.1 Discussion

Intratumoral heterogeneity and phenotypic plasticity are important hallmarks of GBM. They contribute to treatment failure and the development of resistance in GBM. To develop effective therapeutic strategies against GBM, understanding and targeting the heterogeneous GBM cells and TME is essential. In this thesis, I aimed to understand intratumoral heterogeneity and phenotypic adaptation of GBM cells and how GBM cells interact and co-evolve with TME components. To do this, I took advantage of the cohort of glioma PDOX models established in the NORLUX Neuro-Oncology laboratory and extensively characterized them using different histopathological and molecular techniques. I generated and interrogated scRNA-seq data of GBM cells and TME cell types using computational strategies to evaluate the heterogeneity between GBM cells, and the crosstalks between GBM cells and TME components. I found that the transcriptomic features of PDOX models closely resemble patient tumors and differ with cell lines and cell line-derived xenografts. Transcriptomic differences between patient tumors and PDOX were found to be due to the replacement of human TME with mouse TME. Single-cell profiling of tumor cells of PDOXs showed extensive inter and intratumoral heterogeneity. Subsequent characterization of the TME of PDOX models revealed extensive changes in the gene expression profiles indicating instruction of the TME by GBM cells. Myeloid cells, astrocytes, endothelial cells, and OPCs were found to change their gene expression profiles the most, as a result of the crosstalk with GBM cells. Importantly, heterogeneous subpopulations of microglia within the myeloid compartment of PDOX models were identified. These subpopulations show a transition from homeostatic microglia to activated microglia phenotype. To understand the short and long-term adaptations of tumor cells and TME to treatment pressure I generated scRNA-seq data from treated and longitudinal PDOX models. Treatment-induced tumor and TME adaptations were found in the treated PDOX model. Transcriptomic heterogeneity was observed in longitudinal PDOX models.

7.1.1 Using scRNA-seq to interrogate intratumoral heterogeneity

Methods relying on the generation and analysis of data from bulk tissue samples have proved to be ineffective in dissecting the complexity of organ systems made up of different cellular components. Single-cell techniques emerged as a suitable option for the mapping of cell types in a tissue or organ of an organism (Aldridge and Teichmann, 2020; Han et al., 2018; Van Hove et al., 2019; The Tabula Muris Consortium, 2018). scRNA-seq allows the transcriptional profiling of individual cells rather than a group of cells, hence giving more information on the gene expression in each cell of interest and has thus proved to be beneficial in delineating the cellular composition and heterogeneity of tumor samples (Liang

and Fu, 2017; Valihrach et al., 2018). scRNA-seq techniques avoid the loss of information resulting from the aggregation of signals emanating from different cell types and cellular compartments as presented by the other transcriptomic techniques such as the bulk RNA-seq and microarray technology (Nath and Bild, 2021; Stegle et al., 2015). Furthermore, studies of cancer cells at the single-cell level are required to decipher the evolutionary dynamics of cancer cells and how this process contributes to intratumoral heterogeneity. Sensitive scRNA-seq techniques allowed the dissection of the transcriptomic profiles of gliomas (Patel et al., 2014; Tirosh and Suvà, 2018; Tirosh et al., 2016; Venteicher et al., 2017).

Different single-cell techniques such as Drop-seq, Smart-seq, CEL-seq2, MARS-seq, and SCRB-seq are used with varying degrees of precision in single-cell capture and transcriptional profiling (Zhang et al., 2019; Ziegenhain et al., 2017). Recently 10x Genomics, a droplet-based technique was developed with increased throughput, speed, and of comparable or greater sensitivity to other single-cell techniques (Zheng et al., 2016). Among other available scRNA-seq protocols, Drop-seq (Macosko et al., 2015) was among the earliest scRNA-seq protocols and the precursor for 10x Genomics (Zheng et al., 2016). Both protocols apply UMIs (unique molecular identifiers) to quantify unique mRNA molecules, which confer to it the advantage of having a reduced noise due to PCR-based amplification errors. In addition to its comparable performance to other scRNA-seq techniques, Drop-seq is considered to have the added advantage of being the most cost-effective when more cells are to be processed. Other protocols like Smart-seq, SCRB-seq, and other plate-based protocols are more preferred if a fewer number of cells and/or purified FACS sorted cells are to be analyzed. In addition, they offer the advantage of sequencing the whole transcript (Zhang et al., 2019; Ziegenhain et al., 2017).

Thus, I used Drop-seq and 10x Genomics protocols to profile tumor and TME cells in PDOX models to unravel the transcriptomic features of the heterogeneous GBM ecosystem recreated in these preclinical models. scRNA-seq allowed us to characterize the heterogeneity of the TME and to understand the reciprocal crosstalk between GBM cells and tumor-associated myeloid subpopulations. It further allowed detailed analysis revealing how ITH is affected by treatment response and resistance.

7.1.1.1 Establishing a scRNA-seq protocol for single-cell purification and preservation

Majority of scRNA-seq protocols are based on sample collection and processing protocols that rely on the use of fresh tissue. This has made scRNA-seq very tedious and more expensive to implement. Designing robust and broadly applicable experiments that may

require tissue material from the same patient at different time points or from different mice models with variable endpoints is challenging. In addition, the use of archived patient material is limited. The optimization toward single-nucleus RNA sequencing (sNuc-seq) allows the extraction of nuclei from frozen and formalin-fixed tissue samples enhancing the use of the technologies in historical collections (Foley et al., 2019; Habib et al., 2017). However, these protocols still suffer from limited capture of the nuclear fraction of the mRNA, which requires specific analytical protocols for unmatured RNA molecules. Recently, single-cell purification and preservation protocols allowing the purification of tumor cells and the use of purified cryopreserved single-cell suspension have also emerged. Here, we have optimized a protocol allowing for efficient separation of human tumor cells and mouse-derived TME isolated from PDOXs. Our protocol involved mechanical and enzymatic dissociation of the developed tumor tissue followed by magnetic cell sorting, which allowed to deplete myelin fibers and separate mouse and human cell fractions (Oudin et al., 2021). This has yielded a sufficient amount of purified single tumor cells for the generation of organoids, scRNA-seq, or drug screening. Cell number and cell types recovered using our tumor dissociation protocol are comparable to other published protocols for fresh tumor biopsies and in xenograft models (Agorku et al., 2016; Johnson et al., 2021; Neftel et al., 2019; Patel et al., 2014). Interestingly, purification of the mouse-derived TME cells was sufficient to assess transcriptomic profiles of distinct cell types. The comparison to a normal mouse brain allowed for the efficient assessment of transcriptomic changes in the GBM-educated TME, which is more challenging in human GBM. In human tumors, only a fragment of the tumor core is available, while in the PDOXs, the entire tumor, including the invasive niche, can be excised. The initial scRNA-seq protocols applied to glioma patient tumors did not allow for the assessment of TME cells, due to enrichment of tumor cells via CD45 cell depletion (Filbin et al., 2018; Patel et al., 2014; Tirosh et al., 2016). The unbiased scRNA-seq protocols of GBM patient tumors in general yield sufficient amounts of myeloid, OPC, and astrocytic cells (Friedrich et al., 2021; Johnson et al., 2021; Neftel et al., 2019; Wang et al., 2019), whereas analysis of less pronounced TME components, such as T cells and endothelial cells requires additional purification step (Darmanis et al., 2017; Mathewson et al., 2021). Additionally, differences in tissue handling, preservation, and storage may all contribute to variation in cell type recovery as recently reported (Denisenko et al., 2020). Since tumor cells separation in PDOXs is not 100% accurate, I further developed a computational strategy to separate contaminating mouse cells from human tumor cells and vice versa. For experiments requiring accurate separation between human and mouse cells, the magnetic sorting of cells should be replaced with fluorescent-activated cell sorting (Oudin et al., 2021).

Our cryopreservation protocol is similar to Wohnhaas et al. (Wohnhaas et al., 2019) and is based on DMSO-based preservation in 90% of serum. Indeed, the cell recovery protocol that does not contain any culture medium was shown to lead to a higher number of good quality cells following scRNA-seq when compared to the cell recovery protocol recommended by 10x Genomics that contains cell culture medium (Denisenko et al., 2020). More reports are indicating the utility and accuracy of scRNA-seq data obtained using an optimized cryopreservation protocol (Guillaumet-Adkins et al., 2017; Massoni-Badosa et al., 2020; Wu et al., 2021). Interestingly, in line with our observations, cryopreserved tissue and single-cell suspension using a similar freezing medium (10% DMSO and 90% FBS) were shown to yield high-quality data that preserve cancer cells heterogeneity and TME with no alteration in the cellular proportion and gene expression profiles (Chen et al., 2021b; Wohnhaas et al., 2019; Wu et al., 2021). Data obtained from our optimized protocol and using other protocols presented in recent publications provide us and others with the experimental support to use these protocols for scRNA-seq experiments in the absence of logistical support needed to allow the use of fresh tumor samples. This optimized protocol will facilitate the use of scRNA-seq in PDOX models as well as longitudinal tumor samples.

7.1.1.2 scRNA-seq data analyses pipeline

Despite the progress made in single-cell transcriptomics, there are still challenges that are yet to be overcome, mostly relating to the analyses of the massive data generated by the different scRNA-seq platforms (Fan et al., 2020; Lähnemann et al., 2020). So far, efforts within the community to address these challenges have led to the development of more than 1000 computational tools (Zappia and Theis, 2021). I took advantage of existing computational tools (Butler et al., 2018; Trapnell et al., 2014) that have been extensively used within the community, to analyze our scRNA-seq generated from both Drop-seq and 10x Genomics technologies (Macosko et al., 2015; Zheng et al., 2017). Due to the peculiarity of our datasets generated from PDOX models that may contain some proportion of cells contaminating either the mouse TME or the human tumor cells initially separated we developed a computational strategy to further analytically deplete contaminating human GBM cells in the TME dataset and vice versa. Although *in silico* methods have been developed to separate human from mouse transcripts, these methods were designed for situations when human and mouse cells are not separated before sequencing (Chivukula et al., 2015; Conway et al., 2012; Kluin et al., 2018). More also, these existing tools were specifically developed for bulk transcriptomics and do not consider the peculiarity of the single-cell datasets. Our in silico strategy is simple to implement and allows us to separate human tumor cells and mouse cells by mapping the scRNA-seq reads to both human and mouse reference genomes. The distributions of UMI counts and genes expressed in each

cell for each of the reference genomes are quantified. Only cells with the highest number of genes mapping to the mouse or human genome are classified as a mouse or human cell respectively (as applied in **Chapter 6** of this thesis). This approach uses a similar principle of mapping transcripts to both genomes as also implemented in the bulk transcriptomic tools, however, it is implemented on a cell by cell bases and can be linked with cell clustering to interrogate single-cell clusters. Our *in silico* approach can easily be implemented in the pipeline for the analysis of scRNA-seq data from PDOX/PDXs and other cross-species animal models.

Due to the different sets of scRNA-seq data we generated over the years from different mouse models and using different platforms, we optimized the data integration protocol that allows the efficient integration of data from different scRNA-seq technologies mainly the microfluidic-based Drop-seq (Macosko et al., 2015) and the automated 10x Genomics (Zheng et al., 2017) technologies. Although, both technologies are droplet-based with similar principles and similar designs containing primers with PCR handles, cell barcodes, UMI, and poly-T for mRNA capture attached to beads (Zhang et al., 2019). However, these technologies differ in the chemistry of the material used in making their beads and during the process of reverse transcription. While reverse transcription takes place outside the droplets in Drop-seq, in 10x Genomics it takes place inside the droplets. These differences may influence the mRNA capture rates and may introduce technical differences between the technologies. While scRNA-seq data generated using 10x Genomics was found to have fewer dropouts and better coverage in terms of the number of cells and genes captured compared to Drop-seq data, it is significantly more expensive (Zhang et al., 2019). Thus, batch correction and data integration of datasets with technical variations posed a challenge in scRNA-seq data analyses. Although other approaches including machine learning for single-cell data integration have recently emerged (Liu et al., 2021b; Lotfollahi et al., 2021; Peng et al., 2021), we found that using Harmony for batch correction (Korsunsky et al., 2019) and Seurat based reference mapping (Hao et al., 2021) for data integration preserves the biological similarities of cell types in our datasets better. This finding based on our experience may be because most machine learning approaches are trained using datasets of normal cell types, while in our case, we have tumor-instructed cell types that have an altered transcriptomic profile compared to the normal brain cells. However, a robust, well-structured comparative study will be needed to confirm this observation.

7.1.2 PDOX models recapitulate human GBMs

The physiological relevance of preclinical cancer models is an important determinant of the efficacy of novel therapeutics in human patients (Unger et al., 2014). An interesting question within the cancer research community remains, how closely do different preclinical cancer models resemble human cancers? This is even more important in GBM mainly because it occurs in a highly complex organ, with many unique features and anatomical barriers to the rest of the body. To address this problem, several approaches have been used over the last decades to closely recapitulate human GBMs. Although many of the models developed using these approaches contributed to our current understanding of GBM, they failed to recapitulate the intrinsic, microenvironmental, and physiological features in which GBM cells exist in the brain. As a result, many potential anti-GBM agents found to be effective in preclinical models failed to show superior efficacy in GBM patients over existing treatment modalities in the clinical trials. This has contributed to the higher attrition rate of potential anticancer drugs compared to drugs developed for other diseases (Ocana et al., 2011). Thus, the absence of robust preclinical GBM models that fully recapitulate patient tumors is an impediment to curing GBMs and other brain tumors (Aldape et al., 2019).

To address these identified problems, we generated and extensively characterized a cohort of 40 PDOXs from gliomas of different grades including 15 PDOXs generated from the same patient before and after treatment, and compared their molecular profiles with the parental tumors and cell lines generated from some of the tumors. To avoid pitfalls identified with other approaches for generating PDOXs, such as the long term *in vitro* culture and preselected GSCs that often lead to the loss of clonal heterogeneity and the cellular and extracellular composition of tumor tissue, our PDOXs were established by generating organoids from mechanically minced tumor fragments that are only briefly cultured *ex vivo*. Our approach produces stable PDOXs that are reproducible. We have also published the full derivation protocol to promote our model in the research community and to enhance reproducibility (Oudin et al., 2021).

7.1.2.1 Histopathologic features of PDOXs

Unlike other GBM models that fail to recapitulate the classical GBM histopathology, PDOXs show a gradient of histological features from highly invasive to highly angiogenic phenotypes likely reflecting inter-tumoral differences present in human GBM as demonstrated in pediatric high-grade glioma (Bougnaud et al., 2016; Wei et al., 2021). Immunofluorescence staining of brain sections of the PDOX model in our cohort against mouse-specific CD31 revealed a spectrum of blood vessel size and area present in different tumor niches. The highly angiogenic PDOXs show enlarged and highly aberrant blood

vessels in the tumor core, while the highly invasive PDOXs show blood vessel area and size similar to the normal brain (Golebiewska et al., 2020). These results indicate that indeed the blood vessel in mouse brains recapitulates the morphology and molecular features of endothelial cells seen in human GBM following instructions from human GBM cells implanted in mouse brain. These results are in line with reports by others indicating a gradient of phenotypic features in GBM PDOX models, other glioma mouse models, and other tumors such as head and neck cancers (Folaron et al., 2019; Inoue et al., 2012; Vaubel et al., 2020; Wakimoto et al., 2012). However, PDOXs generated in mice were generally observed to show less pronounced angiogenic features and pseudopalisading necrosis in comparison to rat models. This may be attributed to the smaller anatomic size of the mouse brain and/or the differences arising from cross-species molecular interactions and the varying speed of biochemical processes between human tumors and the mouse endothelial cells (Bakken et al., 2021; Golebieswka et al., 2021; Matsuda et al., 2020; Rangarajan and Weinberg, 2003). In contrast to PDOXs, subcutaneous tumors in PDXs are highly vascularized (Wakimoto et al., 2012). This suggests that the anatomic location of the tumors in subcutaneous PDXs that allow the growth of larger and more vascularized tumors than in the brain may likely explain the presence of enhanced angiogenic features in PDXs.

7.1.2.2 PDOX models recapitulate GBM inter and intra-tumoral heterogeneity

In order to interrogate the molecular fidelity of our PDOX models, we conducted extensive molecular characterization of the genetic, epigenetic, and transcriptomic features of PDOXs, their parental tumors, and patient-derived cell lines. In line with previous reports indicating that PDOX models retain patient tumor ploidy (Stieber et al., 2014), we investigated whether individual genetic events in patient tumors are also retained in PDOXs. Here we provide further evidence that in addition to chromosomal aberrations, PDOXs also retain patient-specific genetic amplification of key genes such as *PDGFRα*, *EGFR*, *CDK4/6, MET,* and *MDM2/4* (Golebiewska et al., 2020). Interestingly, PDOXs did not only preserve CNAs and individual genetic events in parental primary tumors but also in recurrent tumors obtained from the same patient after treatment and only minor differences were observed between some PDOXs and the parental tumors. These minor differences were similar to differences observed in biopsies taken from different regions of the same tumor as reported in PDOXs and PDX models from different tumor types (Vaubel et al., 2020; Woo et al., 2021). In contrast to PDOXs, GBM cells propagated *in vitro* were shown to rapidly acquire new CNAs and genetic events over time when compared to the parental tumors (Golebiewska et al., 2020). At the intra-tumor level, PDOXs also retained genetic events present in parental tumors. These results indicate that PDOXs recapitulate both inter- and intra-tumor heterogeneity at the genetic level.

At the transcriptomic level, PDOXs showed a remarkable similarity with patient tumors, and a pronounced transcriptional difference was observed between patient tumors and both the classical adherent cell lines and stem-like cultures. Marginal difference observed in PDOXs was due to the replacement of human TME with mouse counterparts in PDOXs which is known to impact gene expression profiles of tumor samples at the bulk level (Wang et al., 2017). Interestingly, PDOXs show a marked similarity with patient tumors in terms of the enrichment of their transcriptomic profiles with tumor intrinsic signatures of different GBM molecular subtypes (Wang et al., 2017), indicating the retention of inter-patient transcriptomic heterogeneity. Furthermore, PDOXs showed a striking resemblance to patient tumor intratumoral features. Specifically, tumor cells in PDOXs display variable expression of cell cycle and hypoxia signature as well the presence of different cellular states described in GBM (Neftel et al., 2019; Patel et al., 2014). These results strongly indicate the recapitulation of both inter- and intratumoral transcriptomic heterogeneity in PDOXs.

7.1.2.3 TME diversity and crosstalk with GBM cells in PDOX models

Understanding the TME in GBM represents one of the biggest challenges in curing brain tumors (Aldape et al., 2019). Although the cellular and molecular features can be nowadays assessed directly in patient tumors, functional studies will require adequate preclinical models. PDOX models provide the unique advantage of modeling GBM cells in their natural environment and conserving the physiological and anatomical features and barriers within which the tumor cells grow. This offers the advantage of studying the interactions between GBM cells and other cells within their natural environment. The TME is vital in maintaining the growth and proliferation of tumor cells (Pine et al., 2020). In addition, it also aids tumor cells to escape from therapeutic and immune attacks. Thus, it is important to better understand the TME and how each TME component interacts with the tumor cells and other cells within the TME. Our PDOX models recapitulate the majority of TME cells types present in human GBMs. Using an unbiased scRNA-seq approach, we revealed the transcriptomic profiles of TME compartments in the PDOX models and GL261 glioma models. Our analysis uncovered the presence of distinct cell types in the TME of PDOXs similar to previously identified cell types in tumor biopsies. Notably, I identified the presence of diverse myeloid cells subpopulations that are the major resident immune cells in the brain and account for the highest proportion of TME cell types in GBM as previously reported (Klemm et al., 2020; Ochocka et al., 2021; Pombo Antunes et al., 2021). Other cell types identified with distinct transcriptomic profiles include astrocytes, endothelial cells, oligodendrocytes, OPCs, ependymal cells, pericytes, and lymphocytes (Bhaduri et al., 2020; Johnson et al., 2021;

Neftel et al., 2019; Wang et al., 2019). These cell types showed enhanced tumor-specific transcriptomic profiles in the PDOXs and GL261 model compared to the non-tumor-bearing brains used as controls. The upregulation of key markers of reactive astrocytes in the TME of PDOXs compared to the normal brain indicates efficient crosstalk between human GBM cells and mouse astrocytes as earlier reported in patient tumors (Bhaduri et al., 2020; Darmanis et al., 2017; Wang et al., 2019). Endothelial cells also express key genes expressed by GBM-associated endothelial cells as previously reported in our PDOX models and patient tumors (Bougnaud et al., 2016). I further identified the upregulation of tumor-related genes in OPCs and oligodendrocytes, which were reported to consist of different subpopulations in human GBMs, indicating heterogeneity and tumor-specific activation of these cell types (Bhaduri et al., 2020). Our data suggest that the human GBM cells in PDOXs can instruct the mouse TME towards GBM specific phenotypic states. In this work, I concentrated on the transcriptomic heterogeneity of the myeloid cell compartment. Further work should investigate transcriptomic heterogeneity in other TME cell types. In particular, my preliminary analysis revealed heterogeneous transcriptomic states within astrocytic cells, which warrants a more detailed analysis in the future.

Importantly, the TME in our PDOXs is limited by the absence of T lymphocytes. Although it was reported that $CD3^+$ lymphocytes have been identified in tumors from intracranial xenografts (Candolfi et al., 2007), these cells were not identified in our PDOXs. Interestingly, we identified other cells of lymphocytic lineage, mainly the B lymphocytes and the NK cells in the PDOX models derived in nude mice. The relevance of B and NK cells in GBM is still under intense investigation. Initial findings suggest that B cells possess antigen presentation capacity, presenting tumor antigens to T cells and thus aiding in the expansion of tumor-specific T cells which results in tumor regression in mouse models (Candolfi et al., 2011). Recently, contradictory functions have been linked to the presence of B cells in GBM and other tumors (Lee-Chang et al., 2019; Yuen et al., 2016). Different B cells subpopulations differ in their function based on their location within the tumor (Lee-Chang et al., 2019). This suggests variable functionalities based on what other cell types they interact with. Accumulating evidence emerging from studies with larger datasets in other tumors including gliomas associates response to treatment with increased B cell infiltration in tumors (Cabrita et al., 2020; Helmink et al., 2020; Petitprez et al., 2020; Wheeler et al., 2021). It remains to be seen if B cells can establish crosstalks with other cell types as was reported for T cells and the impact of this interaction in remodeling the TME if established. Our results and that of others suggest that B cells are an integral part of GBM TME, although very limited in number, they may be exploited as a potential target for immunotherapy in GBM. This data provides important insight into the alterations in the TME following GBM

instruction as well as a resource for the testing of certain immunotherapeutic targets against the TME components that are present and activated in the PDOX models. It remains to be seen whether reintegration of human T cells into the TME of PDOXs will be successful. Various protocols emerge, allowing for implantation of human tumor cells into the so called ‘humanized mice’’, that partially reconstitute human T cell compartment (Klein et al., 2020).

7.1.2.4 Phenotypic and functional heterogeneity and plasticity of microglia in GBM

Among the myeloid cells, macrophages-derived TAMs have been extensively studied in the context of GBM. Recent studies taking advantage of improved imaging and sequencing techniques are increasingly uncovering the role and function of microglia-derived TAMs (Mg-TAMs). In this work, I demonstrate using scRNA-seq that Mg-TAMs display heterogeneous transcriptional programs with functional significance. I showed that Mg-TAMs exist in distinct transcriptional states ranging from homeostatic to activated states with an intermediary transitory state that may be the key driver of Mg activation. Each Mg-TAMs state is controlled by key master transcriptional regulators. Targeting these master transcriptional factors (TFs) may interfere with the Mg-TAMs activation process which provides an anti-inflammatory environment needed for GBM proliferation and invasion. Recent studies using scRNA-seq profiling have also identified heterogeneous Mg-TAMs clusters, marking the departure from the traditional M1/M2 binary classification (Abdelfattah et al., 2022; Ochocka et al., 2021). Notably, our analyses revealed Mg subpopulations with astrocytic and endothelial cell-like transcriptomic features while expressing classical Mg markers. Activated myeloid cells in the brain and gliomas were reported to express angiogenic markers such as VEGF that are linked to the pro-angiogenic function of TAMs (Glass and Synowitz, 2014). The expression of these markers instructs endothelial cells to grow within the tumors thereby supporting the growth and proliferation of surrounding tumor cells (Nishie et al., 1999). These subpopulations however displayed lower phagocytosis and antigen presentation capacity suggesting other functions. Additional studies are needed to reveal their localization and role in the context of GBM.

Mg has since been linked to phagocytic functions in gliomas (Penfield, 1925). However, recent studies mainly focused on the phagocytic roles of Mo-TAMs in tumor immunity (Gordon et al., 2017; Poh and Ernst, 2018; Zhang et al., 2016a). I show that MG subpopulations in PDOXs possess variable phagocytic and antigen presentation capacity as well as sensome features as previously reported (Goddery et al., 2021; Hickman et al., 2013; Saavedra-López et al., 2020). In addition, I identified an increase in migratory capacity of Mg-TAMs from homeostatic towards activated subpopulations, in line with the typical features of activated Mg (Hammond et al., 2019). This suggests that activated Mg-

TAMs are more capable of sensing changes within their environment and can detect foreign pathogens as well as cellular debris to phagocytize and present their antigens. It also suggests enhanced migratory ability effects these functions in activated subpopulations. This is also in line with accumulating evidence supporting microglial plasticity that enables Mg cells to have anti-inflammatory and pro-inflammatory roles during CNS injury (Gomes-Leal, 2012; Ye et al., 2021). The phagocytic function of Mg was shown to be spatiotemporally dependent in GBM as well as in the injured brain (Hammond et al., 2019; Saavedra-López et al., 2020). The spatial location of Mg-TAMs in GBM was found to also dictate their role in either tumor progression or tumor regression (Saavedra-López et al., 2020). Mg-TAMs migrate to populate the pseudopalisades with an enhanced phagocytic ability in this region. Their function was shown to mainly target cellular debris in the necrotic tumor niche, thereby aiding in GBM cells invasion. On the other hand, Mg-TAMs in the pro-inflammatory region were shown to phagocytose tumor cells (Saavedra-López et al., 2020). This further suggests the plasticity of Mg-TAMs enabling them to play dual roles depending on their spatial location. Interestingly, hypoxia was shown to alter the phenotypes of Mg-TAMs and enhance their migratory ability towards the necrotic areas of the tumor (Saavedra-López et al., 2020), indicating the importance of TME niches in the functions of Mg-TAMs.

Tumor cells are known to overexpress CD47, the “don’t eat me” signal, to evade phagocytic cells, and therefore represent a therapeutic target against tumors. Anti-CD47, as well as anti-PD-1 and PD-L1 treatments, were shown to increase tumor cells phagocytosis by TAMs mainly carried out by Mo-TAMs (Gordon et al., 2017; Li et al., 2018; Willingham et al., 2012; Zhang et al., 2016a). Interestingly, Mg was recently shown to also impact tumor cell phagocytosis on their own following anti-CD74 treatment (Hutter et al., 2019). Mg displayed a reduced inflammatory response compared to Mo-TAMs following anti-CD47 treatment, further indicating the benefit of targeting Mg-TAMs for immunotherapy.

Although previous reports indicate increased phagocytic capacity of Mo-TAMs compared to Mg-TAMs (Müller et al., 2017; Pombo Antunes et al., 2021), this was not observed in activated Mg-TAMs subpopulations and Mo-TAMs in this study. This may be due to the comparison between all Mg-TAMs and Mo-TAMs in the other studies, which did not assess individual subpopulations as performed in the present study. Homeostatic Mg-TAMs with low phagocytic signals may have diluted the signals coming from activated Mg-TAMs leading to an overall lower signal for Mg-TAMs. These results highlight the different subpopulations in Mg-TAMs and their functional characteristics that, if functionally validated, will provide important information for the development of potential immune therapies that

will exploit the anti-tumor functions of TAMs and/or redirect pro-tumor TAMs towards anti-tumor functions.

In addition to their phagocytic ability, activated Mg has been shown to have an enhanced migratory and invasion capacity over other Mg phenotypes (Lively and Schlichter, 2013). Mg is also reported to act as APCs to promote CD8 T cells infiltration in the brain during viral infections (Goddery et al., 2021). However, unlike the classical APCs such as DCs that are shown to present tumor antigens to T cells (Huang et al., 1994), it is not fully clear how Mg presents processed antigens to T cells and/or other cell types in the brain (Schetters et al., 2018). Antigen presentation by conventional APCs to T cells classically occurs in the lymph nodes where naïve T cells are primed (Lecoultre et al., 2020). Recently, the dural sinuses and the meninges in the brain have also been shown to be antigen presentation hubs in the brain (Hu et al., 2020b; Louveau et al., 2015; Rustenhoven et al., 2021). However, TAMs are unable to travel to the lymph nodes to present the antigens of phagocytosed cells, thus they have been shown to present antigens to T cells within the TME (Engelhardt et al., 2012). This suggests T reactivation rather than priming of naïve T cells. This could however still be beneficial for immunotherapy in the context of adoptive T cell transfer (Muraoka et al., 2019). Specifically, in PDOXs, where T cells are absent, it remains unclear to which cell types antigens processed by APCs including Mg are presented. The role of Mg-TAMs as effector cells triggering cytotoxic T cell infiltration in GBM is still under investigation. Since PDOXs models are T cell-deficient, the use of other preclinical models with T cells and Mg in situ, such as the patient-derived organoids, GL261, or humanized mouse models will help in revealing the crosstalk between activated Mg-TAMs and T cells.

7.1.3 Interrogating treatment-induced transcriptomic changes in GBM

Although there are available therapeutic options for GBM patients, most GBMs resist the treatment and inevitably recur shortly after with most patients eventually dying from the recurrence (Aldape et al., 2018). Thus there is a need to elucidate the molecular mechanisms of treatment resistance in GBM. So far genetic analysis of treated GBMs did not reveal common and or consistent changes in recurrent GBMs and tumor evolution following therapy mostly occurs in a stochastic manner (Barthel et al., 2019). More also epigenetic profiling of longitudinal GBMs revealed a largely unchanged epigenome at recurrence, with only a minute difference between primary and recurrent tumors that are restricted to a subset of patients (Klughammer et al., 2018; Malta et al., 2021), prompting the need to look at individual cell populations within each tumor at different time points.

Patient data on the transcriptomic profiles of matched primary and recurrent tumors at the single-cell level is currently not available.

7.1.3.1 Deciphering longitudinal changes in GBM

I took advantage of our longitudinal PDOX models to investigate the transcriptomic changes between matched primary and recurrent GBMs using scRNA-seq. Analysis of the scRNA-seq data obtained revealed transcriptomic differences between primary and recurrent samples coming from the same patient. Differences between patients at the transcriptional level were dictated by their genetic backgrounds. Interestingly, using copy number inference analysis, I identified that differences between longitudinal samples were not influenced by genomic alterations. Primary and recurrent tumors had similar copy number variations in line with the preservation of the copy number variations earlier identified on a cohort of 15 longitudinal gliomas including these samples. Furthermore, targeted sequencing using a diagnostic panel specific to gliomas also confirmed the conservation of genetic variants at recurrence (Golebiewska et al., 2020). These data is in accordance with previous reports that profiled a larger cohort of GBMs and found only limited instances of treatment-induced genetic changes at recurrence that are largely patient-specific (Barthel et al., 2019). I also revealed the presence of different cellular states and molecular subtypes in both primary and recurrent GBMs as reported in several studies that profiled GBMs using bulk and single-cell transcriptomics and including primary, recurrent as well as matched longitudinal samples (Dekker et al., 2020; Johnson et al., 2021; Kim et al., 2020a; Neftel et al., 2019). This suggests that both inter-and intra-tumoral heterogeneity are intrinsic properties of both primary and recurrent GBMs. We did not observe a consistent variation or a switch in cellular state and or molecular subtypes in our matched longitudinal GBMs as previously reported (Phillips et al., 2006). Recent bulk transcriptomic profiling of matched primary and recurrent GBM did not also find any evidence of molecular subtype switch at recurrence and reports preservation of transcriptomic features of primary tumors at recurrence (Dekker et al., 2020; Kim et al., 2020a). Our differential expression analysis between primary and recurrent samples revealed mostly mutually exclusive lists of differentially expressed genes with only a few common genes between the two patients. The variable differentially expressed genes may have reflected the genetic differences between the patients or the influence of the different treatment regimens each patient received. The absence of pronounced differences may reflect long-term adaptation to treatment facilitated by the discontinuation of treatment in cancer patients, often referred to as “drug holiday”. Trajectory inference analyses revealed varying subpopulations with distinct transcriptional states and regulatory networks representing heterogeneous subpopulations from both primary and recurrent tumors. This result is similar to previous observations indicating

subpopulation differences in longitudinal samples (Bastola et al., 2020). This suggests that changes at recurrence mirror different cellular phenotypes with different mechanisms of resistance, including cells with pre-existing resistance that are also present in primary tumors. The lack of a definite transcriptomic and genetic difference between primary and recurrent tumors suggests that investigating individual molecular features may not explain the difference but rather a multi-omic approach may be beneficial. More also, focusing on and targeting subpopulation changes upon treatment may be more beneficial than targeting the whole tumors (Keshava et al., 2019).

7.1.3.2 Understanding short-term treatment changes

Unlike in longitudinal samples, TMZ treated PDOX revealed marked transcriptomic changes upon treatment. I observed differences in transcriptomic features in tumor cells between treated and untreated PDOX models. Copy number inference analyses revealed largely similar genomic alterations between TMZ treated and untreated tumors. Intriguingly, we observed a marked shift in the GBM cellular state's distribution, with an increase in the proportion of mesenchymal-like GBM cells in TMZ treated. This is in line with a recent report indicating an expansion of mesenchymal cluster following short-term exposure of GBM cells to environmental stress specifically hypoxic condition (Johnson et al., 2021) or targeted therapy (Eyler et al., 2020; Liau et al., 2017). More also mesenchymal transition was observed following single-cell profiling of circulating tumor cells in lung cancer after treatment (Stewart et al., 2020). Therapy-induced cellular state changes in residual disease were also reported following treatment (Maynard et al., 2020). These results taken together, suggest treatment-induced phenotypic changes in GBMs and other tumors that are observed shortly after treatment.

Furthermore, transcriptomic characterization of the TME cells of TMZ treated PDOX revealed variations in the proportions of TME cell types. Importantly, I observed an upward shift in the proportion of myeloid cells with a decrease in the proportion of endothelial cells in TMZ treated compared to untreated PDOX. The correlation between an increase in the MES-like cells and the proportion of myeloid cells in the treated PDOX corroborates recent findings linking myeloid cells infiltration with a switch towards a mesenchymal phenotype in GBM (Hara et al., 2021). Single-cell profiling revealed an increased proportion of myeloid cells following treatment. This observation was confirmed by immunostaining showing a significant increase in Mg-TAMs in the tumor core of treated PDOXs when compared with untreated PDOXs. Interestingly, Mg-TAMs adapted their transcriptomic profiles towards inflammatory responses such as migration, chemotaxis, and gliogenesis as well as regulation of translation, endocytosis, cholesterol homeostasis, and actin cytoskeleton. This

was concomitant with decreased levels of TAM markers involved in promoting tumor growth and an increase in the homeostatic and transitory Mg-TAMs subpopulations. These changes upon treatment further indicate the plasticity of myeloid cells during therapy and corroborate earlier findings showing an increase in the number of myeloid cells during TMZ and anti-CD47 treatment in GBM (von Roemeling et al., 2020). This finding is also in agreement with several recent reports revealing TME related changes in recurrent tumors (Pombo Antunes et al., 2021; Sa et al., 2020; Varn et al., 2021).

7.2 Conclusions

In this doctoral thesis, I presented original research work that aimed at answering important questions regarding the suitability of PDOXs as relevant pre-clinical models for GBM research. I used scRNA-seq and different computational techniques to interrogate the transcriptomic features of GBM cells and to understand the crosstalk between GBM cells and TME in PDOX models. Additionally, as proof of concept, I used a special cohort of longitudinal PDOXs and a treated PDOX model to decipher the mechanisms of treatment resistance in GBM. The findings from this work further highlight the relevance of GBM PDOX models as a powerful platform for high-quality preclinical research that enables the identification and characterization of longitudinal tumors from the same patient. It also confirmed the clinical relevance of GBM PDOXs for the testing of novel therapeutics including immunotherapeutics designed to target myeloid cell types. Results from our scRNA-seq analysis demonstrate the value of single-cell transcriptomics for interrogating intratumoral heterogeneity and the identification of novel subpopulations that have been masked in bulk transcriptomic techniques.

In Chapter 3, I presented an overview of the concept of cellular heterogeneity and plasticity and their role in enhancing treatment resistance in GBM. Based on the recent research findings presented, the heterogeneous GBM ecosystem appears to be heavily dependent on the tumor's intrinsic features such as genetics, transcriptomics, epigenetics as well as the TME niches. The intrinsic developmental plasticity in GBM is at variance with the proposed hierarchical model described in CSCs that mirrors normal neural development. In GBM, cellular plasticity allows for the maintenance of dynamic tumor cell populations that can easily transit into the different cellular states following TME cues. Importantly, this allows GBM to easily maintain intratumoral heterogeneity and adapt to treatment pressure giving rise to drug-tolerant persister cells. More also, cells with a pre-existing genetic and phenotypic advantage also give rise to different resistant clones within the GBM following therapy. It is therefore important to target the different dynamic subpopulations within GBM to effectively eliminate all tumor cells and completely cure the disease. To achieve this, extensive research should be embarked on to fully understand the molecular features and regulators enabling plasticity in GBM.

In Chapter 4, I presented our protocol for the derivation of PDOX models. This protocol provided detailed guidelines on the generation of PDOXs used in this thesis. Additionally, we described in detail our optimized tumor tissue processing technique for the purification of single cells that can be used for *ex vivo* functional assays, generation of tumor organoids, and scRNA-seq. Using our protocol, debris-free TME cells can be obtained for further

analysis such as co-culture of organoids and TME in a controlled ratio. Following single-cell dissociation, purification, and freezing of single-cell suspensions, I optimized the use of thawed single cells for scRNA-seq. While scRNA-seq is currently being adapted to be applied on frozen and or fixed tissue samples, so far current protocols are largely optimized to capture single cells from fresh samples. Our protocol for single-cell purification and preservation is a viable option that will aid the rapid transition toward the utilization of archival tissue samples and especially for the longitudinal profiling of tumors in PDOX models. However, this protocol should be used with caution in dissociating TME cells in the brain, especially when targeting microglia. As this protocol involves an enzymatic dissociation step, recent studies indicate the possibility of enzymatically activating microglia cells (Van Den Brink et al., 2017; Marsh et al., 2022). Importantly, our analysis showed that this procedure impacts more homeostatic microglia in the normal brain, rather than in GBM-educated TAMs.

In Chapter 5, I presented our work on the extensive molecular profiling of PDOX models. Our PDOXs models show a remarkable recapitulation of tumor intrinsic genetic, transcriptomic, and epigenetic features. PDOXs also retain both inter- and intratumoral heterogeneity observed in patient tumors. I also demonstrated the presence of GBM specific TME suggesting evidence of tumor-TME crosstalk in the PDOX models. An important relevance of our PDOXs is the ability to study longitudinal patient biopsies implanted in the PDOX models. Hence, PDOXs and other preclinical models are an invaluable option to study and monitor treatment responses in GBM patients. Based on its recapitulation of major molecular features of the parental tumor and an intact TME that allows tumor-TME crosstalks in a physiologically relevant environment, the PDOX model is invaluable for preclinical GBM studies including testing of novel therapeutics (Hidalgo et al., 2014; Jacob et al., 2020; Sun et al., 2021).

In Annex 1, I presented data on the use of the PDOX model to understand longitudinal changes in GBM. Obtaining matched primary and recurrent patient tumor biopsies has remained a challenge, mainly because most recurrent GBMs are inoperable due to the deteriorating conditions of the patients and other concerns such as insufficient tumor tissue that are prioritized for diagnosis as well as other clinical and ethical concerns relating to patient welfare (Aldape et al., 2019; Turajlic et al., 2019). Thus, our PDOX models are an important tool to investigate longitudinal changes in GBM. With the advent of new protocols optimized for the single-cell transcriptomic profiling of frozen and formalin-fixed tissues, a large cohort of longitudinal GBMs will be available for in-depth analyses to reveal molecular changes following treatment. I initially planned to profile the longitudinal tumors from six

patients obtained before and after treatment. As a result of the massive restrictions imposed by the COVID-19 pandemic, only data from two patients were available for analysis. Therefore, this study was constrained by the limited data available which represents only a pilot study that is difficult to infer any solid conclusions from the preliminary observations. Hence, there is the need to further profile sufficiently large cohorts of PDOXs generated from longitudinal GBMs to be able to fully decipher the transcriptomic changes upon treatment at the single-cell level. We also performed TMZ treatment in a PDOX model to understand the adaptation of GBM tumor and TME subpopulations directly upon treatment. However, data from the treated PDOX model is also limited by sample size and the lack of other components of the standard-of-care treatment, namely surgical resection and radiotherapy.

In Chapter 6, I presented the single-cell transcriptomic phenotyping of TME in PDOXs and GL261 glioma models. TME in PDOXs models showed an outstanding similarity with the patient GBM TME. TME subpopulations reflected a GBM-specific transcriptomic profile indicating instruction by GBM tumor cells. The tumor-associated myeloid compartment was shown to be predominantly of microglial origin in both PDOX models and human GBMs. We demonstrated that Mg-derived TAMs are heterogeneous with distinct subpopulations controlled by specific transcriptional regulators. We further revealed using computational analyses that microglia-TAMs displayed functional features such as chemotaxis, phagocytic, sensome, and antigen presentations capacity toward GBM cells. We further showed that TMZ treatment leads to a rapid transcriptional adaptation of both tumor cells and TME in PDOX models demonstrating the utility of the TME in PDOX models for the assessment of treatment response. Our findings highlight the similarity of the TME of PDOX models with that of human GBM, especially the TAMs subpopulations, further indicating the relevance of these models for preclinical research, especially for the testing of immunotherapies targeting TAMs and other TME subpopulations like B cell and NK cells but not T cells.

Overall, the finding presented in this thesis demonstrated an optimized protocol and analytical pipelines for single-cell purification and transcriptomics characterization of GBM cells and TME in PDOX models. This work also revealed the transcriptomic fidelity of GBM cells and TME in PDOXs to human GBM cell and TME, that further establish the relevance of PDOX models as clinically relevant models. Using longitudinal PDOXs and a treated PDOX model, I presented evidence on the relevance of PDOX in understanding treatment-induced changes in GBM. Finally, I presented evidence on the importance of focussing on the microglia subpopulations as potential antitumor agents within the TME, indicating that

the successful elimination of this dynamic entity, GBM, would require taking the fight directly to the tumor microenvironment.

7.3 Outlook

Reprogramming TME to exploit GBM vulnerabilities

Characterization of PDOX models has mainly focused on the interrogation of the degree of the fidelity of tumor cells propagated in PDOX in comparison to human tumor cells. In addition to the characterization of tumor cells, I present here, to my knowledge, the first report of extensive characterization of the TME in PDOX models. More research efforts are needed to fully characterize all the different TME components in PDOXs and other preclinical models. Among the different TME subpopulations, myeloid cells especially the macrophages have been extensively studied for their role in maintaining an immunosuppressive TME in GBM. There is the need to extensively study other cells types especially the astrocytes, endothelial cells, OPCs, and oligodendrocytes for their potential role in promoting a pro- or anti-tumorigenic environment in GBM. Recent findings that may be studied in the context of GBM to exploit the potential phagocytic and antigen-presenting capacities of reactive astrocytes and “immunological” OPCs in the brain (Absinta et al., 2021; Kirby et al., 2019; Liddelow and Barres, 2017; Rostami et al., 2020) and neutralizing the pro-tumoral functions of reactive astrocytes as they have been reported to aid therapy resistance in GBM (Niklasson et al., 2019). While T cells have also been deeply characterized with available knowledge points to the regulatory T cells as the prime suspects for immunosuppression and failure of immunotherapies in GBM, other lymphocytic cells such as the B cells are less studied but have been shown to possess an immune regulatory ability (Lee-Chang et al., 2019). In-depth characterization of these less interrogated cell types can provide vital information that could be exploited to design efficient immunotherapies against GBM. It is also important to interrogate the mechanisms of the interactions between tumor cells and TME at the molecular level. Although, the species differences between human tumor cells and mouse TME as well as the sample size variation in terms of the cell abundance between the bulky tumor cells and TME are currently a barrier to directly studying the tumor cell interactions in PDOXs, targeting a higher cell number, and developing computational techniques that will be able to handle and compare transcriptomes from different species may be a viable option.

Less attention has been given to Mg even though they form the highest proportion of TME cell types in GBM (Woolf et al., 2021). Functional validation of the phagocytic functions of the subset of Mg we identified should be functionally validated. If validated, the population of Mg-TAMs subpopulations with phagocytic capacity can be increased with the ultimate goal of enhancing tumor innate immunity and facilitating T cell adaptive response in GBM. Additionally, perturbation experiments to remodel anti-inflammatory Mo-TAMs and Mg-

TAMs to pro-inflammatory Mg-TAMs by overexpressing the identified transcription factors maintaining pro-inflammatory Mg-TAMs cell state may be a viable approach to reprogramming the TME against GBM cells.

Multiomic profiling of longitudinal GBMs in a larger cohort

So far no specific consistent changes have been reported in tumor cells at GBM recurrence. Changes reported in recurrent tumors are mostly restricted to the TME specifically the myeloid compartment where higher monocyte infiltration was reported in recurrent tumors (Pombo Antunes et al., 2021; Sa et al., 2020). Upregulation of T cell activation pathways in GBM patients that received standard-of-care treatment (Kim et al., 2020a) as well as immunotherapy (Zhao et al., 2019) was also reported. An extensive analysis of immune signatures in different tumors following immune therapy further confirmed T cell infiltration following treatment (Chen et al., 2016; Wang et al., 2020a). In addition, massive B cell infiltration following therapy is a feature of TME remodeling following treatment (Helmink et al., 2020). To understand the treatment-induced changes enabling GBM cells adaptability and treatment escape, future studies should be designed to comprehensively characterize longitudinal tumors in a larger cohort using tumor multisampling, spatial-omics, and emerging multi-omics technologies permitting the simultaneous assessment of genetic, epigenetic, and transcriptomic information to understand the dynamic states in the spatio-temporal context within distinct TME niches. This may require the development of new or the optimization of existing computational tools with high sensitivity of detecting and compounding salient changes coming from each layer of the molecular data.

Understanding drug-tolerant persister cells in a larger cohort of treated PDOXs receiving the full standard-of-care regimen

An emerging model of treatment resistance in tumors is the plasticity of tumor cells upon treatment giving rise to varying subpopulations such as the drug persister cell that survive treatment and become the origin of recurrent tumors (Sharma et al., 2018). Their immediate response and adaptation to treatment pressure should be studied to better design effective treatment strategies. Studying the impact of treatment on GBM cells directly in patients is limited by technical difficulties and concerns about patient consent and welfare. The use of non-invasive approaches such as liquid biopsies and enhanced imaging techniques to monitor tumors following treatment is currently under intense investigation and provides a platform for monitoring tumor cells response to treatment (Aldape et al., 2019; Fontanilles et al., 2020; Piccioni et al., 2019; Sharma et al., 2021b; Turajlic et al., 2019). When using PDOX models as a viable experimental model, in addition to increasing sample size, surgical resection and radiotherapy that are an integral part of the standard treatment

strategies in GBM should be incorporated into the treatment modalities to fully recapitulate the treatment administered to human patients.

Annexes

Annex 1

Deciphering treatment-induced changes in tumor cells and TME in GBM PDOXs using scRNA-seq

Yabo YA, Oudin A, Grzyb K, Nazarov PV, Skupin A, Niclou SP, Golebiewska A.

Result report

The rationale of the study

In this work, we aimed to understand longitudinal transcriptomic changes in GBM using scRNA-seq. We took advantage of the longitudinal PDOX models generated from patient tumor biopsies obtained before and after treatment. We systematically compared gene expression between primary and recurrent samples from the same patient. We used frozen single cells from the dissociated tumors developed in the PDOXs to circumvent the logistical difficulties associated with collecting and processing longitudinal patient samples and PDOXs reaching the endpoint at the same time. In this work, we generated an important and unique set of data that profiles the transcriptome of primary and recurrent GBM from 4 patients at the single-cell level. This work represents to our knowledge the first available datasets with the potential to reveal important insights into the transcriptomic landscape of treated GBMs at the single-cell level.

Personal contributions

I have collected and cryopreserved single cells from longitudinal PDOXs for 12 PDOXs representing 6 patients. Up to date, 8 PDOXs have been processed by the 10x Genomics platform and sequenced. This work was severely delayed by the lockdown imposed due to the COVID-19 pandemic and the fallouts of the lockdown resulted in a protracted delay in receiving laboratory supplies and consumables that affected the normal operations of the laboratories and the sequencing platform. Due to these challenges faced, here I present data from only 4 PDOXs representing 2 patients. In **Figures 1A and B**, I illustrated the patients' treatment regimens. In **Figure 1C,** I show the histopathological features of the selected PDOXs. I summarized the clinical information of patients' tumors used to generate the PDOX models in **Table 1** and the scRNA-seq data generated in **Table 2**. I illustrated the scRNA-seq workflow in **Figure 2A.** Using the generated scRNA-seq data, I performed dimensionality reduction using UMAP shown in **Figure 2B** where primary and recurrent samples clustered based on the patient of origin indicating close similarity in their genetic background. I showed that all GBM cell states and molecular subtypes are present in both primary and recurrent GBM in **Figure 2C**. I reconstructed the copy number profiles from the gene expression data in **Figure 2D** showing the absence of pronounced genetic changes following treatment. I identified common differentially expressed genes and enriched pathways between primary and recurrent tumors in **Figures 3A, B, C, and D**. I reconstructed the trajectory and identified transcriptional regulators of different subpopulations in primary and recurrent GBM as shown in **Figures 4A, B, and C**. I contributed to project design, data generation, and analysis and also prepared this preliminary report.

Result

Deciphering longitudinal changes in glioblastoma patient-derived orthotopic xenograft models using scRNA-seq

Yahaya A. Yabo[1,2], Anaïs Oudin[1], Kamil Grzyb[3], Petr V. Nazarov[4], Alexander Skupin[3], Simone P. Niclou[1], Anna Golebiewska[1,#,]

[1]NORLUX Neuro-Oncology Laboratory, Luxembourg Institute of Health, Luxembourg, Luxembourg
[2]Faculty of Science, Technology and Medicine, University of Luxembourg, L-4367 Belvaux, Luxembourg; [3]Luxembourg Centre for Systems Biomedicine, University of Luxembourg, Esch-sur-Alzette, Luxembourg; [4]Multiomics Data Science, Department of Oncology, Luxembourg Institute of Health, L-1445 Strassen, Luxembourg;
corresponding author: anna.golebiewska@lih.lu,

Running title: Treatment resistance in GBM

Corresponding author:
Anna Golebiewska, PhD
Luxembourg Institute of Health (LIH)
Department of Oncology
NORLUX Neuro-Oncology Laboratory
84, Val Fleuri, L- 1526 Luxembourg
Tel + 352-26970-244
Fax + 352-26970-390
E-mail: anna.golebiewska@lih.lu

Funding

We acknowledge the financial support by the Luxembourg Institute of Health, the GLIOTRAIN ITN funded by the European Union's Horizon 2020 research and innovation programme under the Marie Skłodowska-Curie grant agreement No 766069 and the Fondation du Pélican de Mie et Pierre Hippert-Faber Under the Aegis of Fondation de Luxembourg.

Conflict of Interest

The authors declare no competing interests.

Authorship

Conceptualization: YAY, SPN, AG; Methodology: YAY, AO, KG, AS, SPN, AG; Investigation: YAY, AO, KG, AG; Formal analysis: YAY, AlM, AG; Resources: SPN, AG; Supervision: AS, SPN, AG; Writing - Original Draft: YAY, AG

ABSTRACT

Intra-tumoral heterogeneity and phenotypic plasticity are major barriers in the treatment of many tumor types. In glioblastoma (GBM) – the most aggressive brain tumor - survival of patients following standard therapy has stagnated to an average of 14 months, largely due to the inherent heterogeneity and phenotypic plasticity. Patient-derived orthotopic xenografts (PDOX) are important tools for preclinical cancer studies. We have shown that they recapitulate histological and molecular features of patient tumors, thus producing more clinically relevant study outcomes when compared to other preclinical models. To understand the longitudinal evolution of phenotypic intratumoral heterogeneity, we applied single-cell RNA-seq in GBM PDOX models generated from naive and treatment-exposed patient tumors. Advanced computational algorithms, were applied to identify treatment resistance signatures and master regulators of the identified treatment-resistant subpopulations. We show that both treated and untreated PDOX models recapitulate inter and intra-tumoral transcriptional programs reported in GBM patient samples. Differential expression analyses identified treatment-induced signatures and GO terms linked to GBM recurrence. Trajectory and transcription factor inference analyses revealed variable cell state changes and transcriptional regulators at recurrence. Our GBM PDOX models provide a platform for high-quality preclinical research and an improved clinical relevance in the development and testing of novel therapeutics.

Keywords

Glioblastoma, Preclinical models, Recurrence, Patient-derived orthotopic xenografts, Treatment resistance, Single-cell RNA-sequencing.

INTRODUCTION

Glioblastomas (GBMs) are among the most heterogeneous tumors, which hampers patient stratification and the development of effective therapies (Aldape et al., 2018; Wen & Kesari, 2008). The standard-of-care in GBM involves surgical resection followed by radiotherapy and chemotherapy with temozolomide (TMZ) (Stupp et al., 2005). However, following the aggressive standard treatment, most GBMs resist treatment and invariably recur into a more aggressive tumor. The nature and mechanism of treatment resistance in GBM is not fully understood. TMZ is an alkylating agent that is shown to benefit GBM patients with a methylated *MGMT* (O^6-methylguanine–DNA methyltransferase) gene promoter (Hegi et al., 2005). Both TMZ and radiation are cytotoxic agents that exert DNA damage to proliferating cells (Chalmers, Ruff, Martindale, Lovegrove, & Short, 2009). The expression of *MGMT* is regulated by the methylation of its promoter. Thus, in the absence of this promoter methylation, the active MGMT enzyme renders TMZ treatment ineffective, therefore GBM cells with a methylated *MGMT* promoter lack MGMT-mediated DNA repair ability and are more sensitive to TMZ treatment (Haar et al., 2012). Intra-tumoral heterogeneity and phenotypic plasticity are intrinsic features of GBMs and are thus considered to be important factors contributing to the resistance mechanisms in GBM (Qazi et al., 2017; Yabo, Niclou, & Golebiewska, 2021). GBM cells manifest remarkable plasticity and respond flexibly to selective pressures including therapeutic pressure by transiting towards states favorable to the new tumor microenvironment (Dirkse et al., 2019; Johnson et al., 2021; Neftel et al., 2019). How intra-tumoral heterogeneity and phenotypic plasticity contributes to treatment resistance is currently less clear. The exact nature of treatment-resistant, tolerant and sensitive GBM cells remains unresolved. Treatment resistance is currently viewed to be multifaceted in GBM and treatment-resistant cells display varying degrees of sensitivity to treatment (Yabo et al., 2021). The development of treatment-resistant genetic clones or phenotypic states may be driven by pre-existing resistant cells with genetic or phenotypic advantages favored by Darwinian selection (Shen, Vagner, & Robert, 2020; J. Wang et al., 2016). Other tumor cells develop resistance through adaptation towards a drug-tolerant persister state with a plastic ability (Oren et al., 2021). Transcriptomic profiling of cells within each tumor niche at the single-cell level allows the revealing of transient and long-term signatures of the resistant states (Rabé et al., 2020). In the past years, bulk sequencing technologies have revolutionized investigations of inter-patient heterogeneity of cancer tissues for precision medicine. However, bulk sequencing alone is not sufficient to deeply characterize the intra-tumoral heterogeneity of each individual tumor. Thus, molecular analyses at the single-cell level will be crucial to the understanding of resistance mechanisms in cancer. Recent development of sensitive scRNA-seq opened promising

opportunities for dissecting transcriptomic profiles of heterogeneous tumors (Neftel et al., 2019; Patel et al., 2014; Tirosh et al., 2016; Q. Wang et al., 2017). Unlike the bulk RNA-seq, scRNA-seq can identify different sub-population of cells within a tumor and the changes arising from the impact of therapy on different tumor cells sub-populations. scRNA-seq was shown to be instrumental in unveiling plasticity and gene regulatory, which can be further exploited to limit therapy resistance networks (Aibar et al., 2017; Neftel et al., 2019; Rambow et al., 2018). scRNA-seq profiles further allow for elucidating cell-cell cross-talks in heterogeneous tissues (Kumar et al., 2018; Raredon et al., 2019; Yuan, Tao, Chen, & Shi, 2019). Key molecular regulators of tumor cell plasticity towards treatment resistance states represent novel targets for future combinatory treatments. Understanding treatment-induced changes in GBM will help in revealing key molecular regulators enhancing tumor cell plasticity and resistance that could be targeted in combinatory treatments. In this study, we profiled the histologic and transcriptomic features of longitudinal GBMs implanted in PDOX models derived from patients prior to and after treatment. We identified transcriptomic adaptations of GBM cells to therapeutic pressure.

MATERIALS AND METHODS

Patient samples and derivation of PDOX

Fresh glioblastoma tumor tissues biopsies were collected from patients following surgeries on primary tumors and at recurrence at the Centre Hospitalier of Luxembourg (CHL; Neurosurgical Department) All patients gave their consent and the study was approved by the local research ethics committee (National Committee for Ethics in Research (CNER) Luxembourg). 3D organoids from patient samples were prepared as previously described (Oudin et al., 2021). The handling of animals and the surgical procedures were performed in accordance with the regulations of the European Directive on animal experimentation (2010/63/EU). The experimental protocols were approved by the Animal Welfare Structure of the Luxembourg Institute of Health (protocols LRNO-2014-01, LUPA2019/93 and LRNO-2016-01) and by the Luxembourg Ministries of Agriculture and of Health.

Immunohistochemistry and histopathological analysis

Paraffin-embedded brains were sectioned and stained and stained with hematoxylin (Dako) and 1% eosin (H&E) (Sigma). For immunostaining, brain sections were pre-treated with Proteinase K (Dako) for 5min followed by incubation at 95°C for 30 min in retrieval solution (Dako). The Dako Envision+System-HRP was used according to the manufacturer's

instructions. Primary and secondary antibodies were incubated for 1h. Signal was developed with 3,3′-diaminobenzidine chromogen in 5–20 min. Additional immunohistochemistry (IHC) preparations were performed using a Discovery XT automated staining module (Ventana) and standard protocols as reported (Golebiewska et al., 2020). The existence of necrosis and the degree of invasion was assessed on the basis of H&E and human-specific Nestin staining. IHC of mouse endothelial cells (CD31) was performed on isopentane flash-frozen tissues sectioned with cryostat (10µm) were fixed with acetone and chloroform. Nonspecific binding was blocked with 2% FBS in TBS and antibodies were incubated for 1h at RT. Pictures were acquired with a Leica DMI 6000B microscope. Vessel quantification was done using ImageJ software. Average vessel area (µm2) was used as a proxy for vessel abnormality.

Single-cell isolation and sequencing using 10x Genomics

PDOXs were deeply anesthetized and transcardially perfused with PBS before dissecting the tumor-bearing brain. To purify human tumor cells and mouse TME cells, tumor-bearing brains from PDOXs were mechanically and enzymatically dissociated followed by MACS-based purification with Myelin Removal Beads II and then Mouse Cell Depletion Kit (Miltenyi Biotec) in accordance with manufacturer's recommendations and as described (Oudin et al., 2021). Purified single tumor cells were placed in a medium containing 10% DMSO and 90% FBS and frozen using Mr Frosty, first in -80^{o} freezer overnight and then transferred to the liquid nitrogen tank. Vials containing frozen cells were suspended in a 4^{o}C water bath until they thaw. 10ml of RNAse free DPBS + 0.05 % FBS were slowly added to thawed cells to wash out the DMSO. The cells were then centrifuged at 300g for 5min at 4^{o}C. This was repeated 3 times until all the DMSO is washed out. Cells were then diluted to 10^{6} cells/ ml with RNAse free DPBS + 0.05 % FBS. Diluted cells were filtered using a 50µm filter. The viability of cells was verified using Bechman coulter automatic cell counter and C-Chip – Disposable Haemocytometer (NanoEntek) viability analyzer. Cell concentration was adjusted to target the encapsulation of 3000 cells according to 10x Genomics cell preparation guidelines. Chromium Next GEM Chip with single-cell suspension was loaded to the Chromium Controller (10x Genomics) for generation of encapsulated cells and GEMs. scRNA-seq libraries were prepared using the Chromium Next GEM Single Cell 3' GEM, Library & Gel Bead Kit v3.1 and a Chromium i7 Multiplex kit according to the manufacturer's protocol. Libraries were purified using SPRIselect magnetic beads and analyzed using Agilent 2100 Bioanalyzer. Sequencing was performed using NextSeq 500/550 High Output Kit v2.5 (75 Cycles).

scRNA-seq data analysis

FASTQ files were assembled from the raw BCL files using Illumina's bcl2fastq converter and ran through the FASTQC codes [Babraham bioinformatics; https://www.bioinformatics.babraham.ac.uk/projects/fastqc/] to check library qualities by the assessment parameters a) quality per base sequence, b) per base N content, c) per base sequence content and d) over-represented sequences. Libraries with significant deviation were re-sequenced. FASTQ files were subsequently merged and converted to binaries using PICARD's fastqtosam algorithm. Barcode processing and UMI filtering were performed using the Cell Ranger 4.0.0. To generate DGE matrices mouse library (mm10) and human library (GRCh38) was used. The mean reads average per cell across the gene expression libraries was 7207, and the average saturation of the sequencing was 30-40%, as calculated by Cell Ranger. The generated digital gene expression matrix (DGE) was filtered using the Seurat (version 3) in R (version 3.6.0) based on ribosomal and mitochondrial genes as well as on low and high transcript content. The following threshold filters were used: only cells that expressed at least 200 genes, and only genes that were expressed in at least 5 cells were selected for further analysis. To normalize for transcript capturing between the beads, Seurat 'LogNormalize' function was used. Dimensionality reduction and the identification of marker genes and visualization were done using UMAP implemented in the Seurat package version 3 (Stuart et al., 2019). Differentially expressed genes between primary and recurrent samples were calculated using the Wilcoxon rank-sum test via the Seurat 'FindMarkers' function. *P-value* adjustment was performed using the Bonferroni correction method. Differentially expressed genes (DEGs) were generated using 'FindAllMarkers' function in Seurat.

Single-cell signature scores for cellular phenotypic states and meta-modules (MES, AC, NPC, and OPC-like) were implemented as described in Neftel et al., 2019 (Neftel et al., 2019). TCGA subtypes of single cells were assessed based on signatures described in Wang et al., 2017 (Q. Wang et al., 2017). The signature scores for TCGA subtypes were determined using a similar approach as in Neftel et al., 2019 (Neftel et al., 2019). Briefly, scores (averages expression levels) of signature genes of the cell state or subtypes were calculated in every single cell and then subtracted the total scores of the control gene sets. Analyzed genes were binned based on the averaged expression, and the control genes were automatically and randomly selected from each bin. METASCAPE gene functional classification tool (https://metascape.org/) was used for gene ontology analysis. Single-cell trajectory inference analysis was done with Monocle v2 (Qiu et al., 2017). Gene regulatory network inference, identification of regulons, motif enrichment TFs prediction as well as the

quantification of the activity of identified regulons in each cell were done according the standard SCENIC workflow (Aibar et al., 2017).

RESULTS

PDOX models retain histopathologic features of primary and recurrent human GBMs

We selected from the cohort of our PDOXs models earlier characterized two longitudinal models (LIH192 and LIH347) (Golebiewska et al., 2020). Four PDOXs from two patients were generated from primary and recurrent tumors of each patient. We selected patients with IDH wildtype and *MGMT* unmethylated GBMs to represent GBM patients that are known to have the natural ability to resist TMZ treatment (clinical data of patients shown in **Table 1**). All patients received standard-of-care treatment in GBM as illustrated in **Figure 1A-B** patients LIH192 and LIH347 respectively. Interestingly, additional PDOX is available for patient LIH192 from the third surgery, however, the patient did not receive additional treatment between the second and third surgery. Thus this PDOX has received lower priority and will be processed later in the project. The PDOXs were histopathologically characterized for the presence of human tumor cells using human-specific Nestin or Vimentin antibody and GBM pathological lesions such as blood vessel aberrations using mouse-specific CD31 antibodies (**Figure 1C**). All models show invasive tumor phenotypes and no particular differences were observed between PDOXs derived from treatment naïve and treated tumors. Thus, histopathologic features of primary tumors especially the invasive phenotype are retained at recurrence.

Table 1. A summary of clinical information of patients tumors used to generate the corresponding PDOX model. NA= not available, TMZ = temoxolomide, PDOX = patient-derived orthotopic xenografts, MGMT = *O^6-methylguanine-DNA methyltransferase*, RTK = receptor tyrosine kinase.

Patient	PDOX	Sex	Age	Tumor type	MGMT mythylation	Treatment received	Methylation class
LIH192	T192	F	42	Primary	Unmethylated	Untreated	Mesenchymal-like
LIH192	T233	F	42	Recurrence	Unmethylated	Radiotherapy +TMZ	Mesenchymal-like
LIH347	T347	M	41	Primary	Unmethylated	Untreated	Classic-like
LIH347	T470	M	42	Recurrence	Unmethylated	Radiotherapy +TMZ	Classic-like

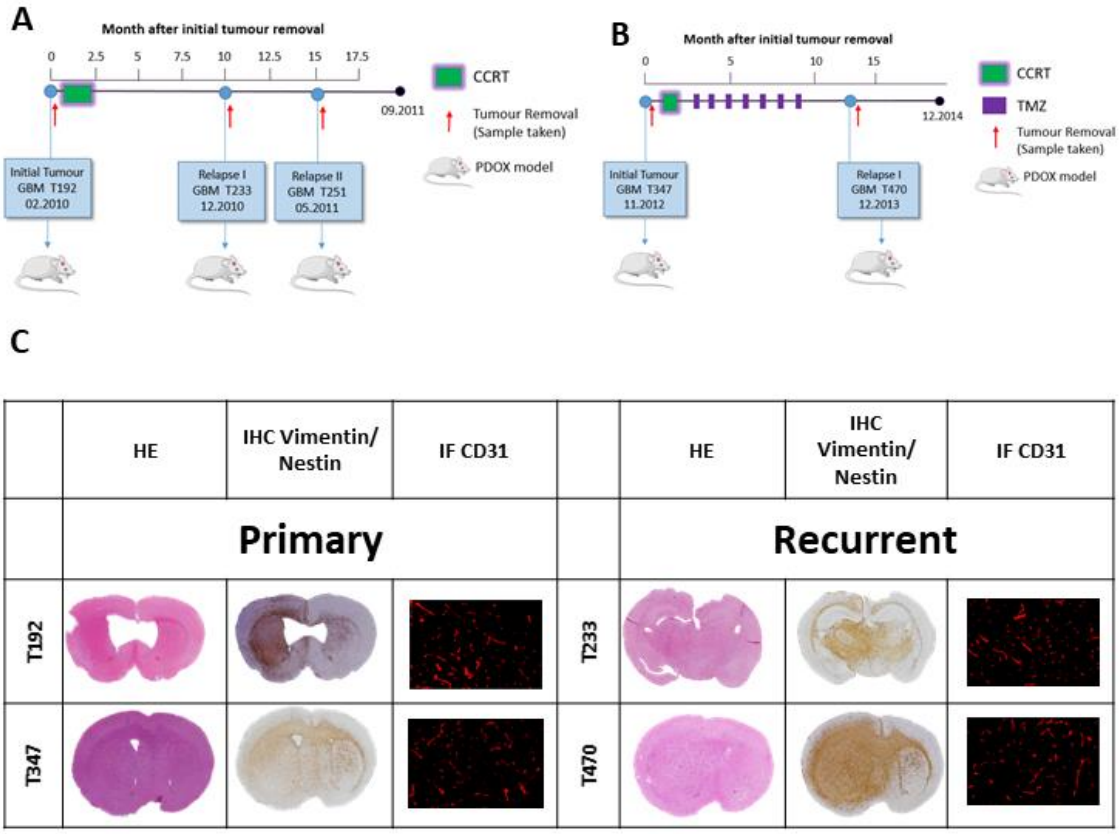

Figure 1. Generation of longitudinal GBM PDOX models

A-B. Schematic illustration of the derivation of longitudinal PDOXs from the tumors obtained at different stages of the disease of the patient LIH192 (**A**) and LIH347 (**B**). The treatment received by each patient is depicted; CCRT = concurrent chemoradiotherapy with temozolomide **C**. Histopathological characterization of the PDOX models used for the experiments. Hematoxylin/Eosin, human-specific Nestin/Vimentin, and mouse-specific CD31 stainings were performed to assess histopathological characteristics of PDOXs. H&E and human-specific stainings indicate tumor center and varying levels of tumor cells invasion of the contralateral hemisphere. CD31 staining shows varying levels of aberrant vessels across the samples.

Single-cell RNA-seq analysis of longitudinal PDOXs reveals transcriptomic differences between treatment naïve and treated tumor cells

To investigate the transcriptional adaptation of GBM cells upon treatment at the single-cell level we performed scRNA-seq using 10x Genomics Chromium technology on the selected longitudinal PDOX models. Tumor mass was excised from the perfused mice brain was mechanically and enzymatically dissociated. Tumor cells were purified via magnetic cell separation, including myelin removal and the depletion of mouse TME as previously described (Oudin et al., 2021) and illustrated in **Figure 2A**. Single-cell suspension for each

PDOX was frozen to process all samples at the same time. A summary of the scRNA-seq data generated per each sample is presented in **Table 2**. We projected the normalized gene expression matrix on 2D dimensionality space using UMAP (Uniform Manifold Approximation and Projection for Dimension Reduction) algorithm to understand the transcriptomic diversity of the different samples (**Figure 2B**). Primary and recurrent tumors from each patient (LIH192 and LIH347) clustered close to each other, demonstrating the similarity of tumors originating from the same patient as dictated by similar genetic backgrounds, while cells from different patients clustered away from each other indicating patient-specific differences. Although longitudinal tumors from each patient clustered close to each other, marked differences in the transcriptomic profiles were observed between primary and recurrent tumors. We then scored each cell with the signatures for GBM cells states (Neftel et al., 2019) and TCGA subtype (Q. Wang et al., 2017) signatures and plotted the distribution of the cell states and subtypes for each sample (**Figure 2C**). We observed the presence of all GBM cell states and subtypes previously described in primary GBM in both primary and recurrent tumor samples. There was no consistent difference in the proportions of primary and recurrent tumor samples. To verify if the transcriptomic difference observed was as a result of genomic changes we inferred the copy number variations from the scRNA-seq data (**Figure 2D**). Copy number variation inference analysis revealed similar genomic alterations between naive and treated PDOX models, suggesting that the transcriptional changes did not arise from the acquisition of novel genetic changes upon treatment.

Table 2. Summary of scRNA-seq data per sample and cells

Patient number ID per cell	PDOX	Number of cells	Average number of genes per cell	Average % mitochondrial genes per cell	Average of counts
LIH192	T192	374	2932.703	11.50	9073.05
LIH192	T233	617	2164.543	15.36	6068.382
LIH347	T347	2495	1969.007	22.20	5903.588
LIH347	T470	1142	2398.626	22.36	7787.963

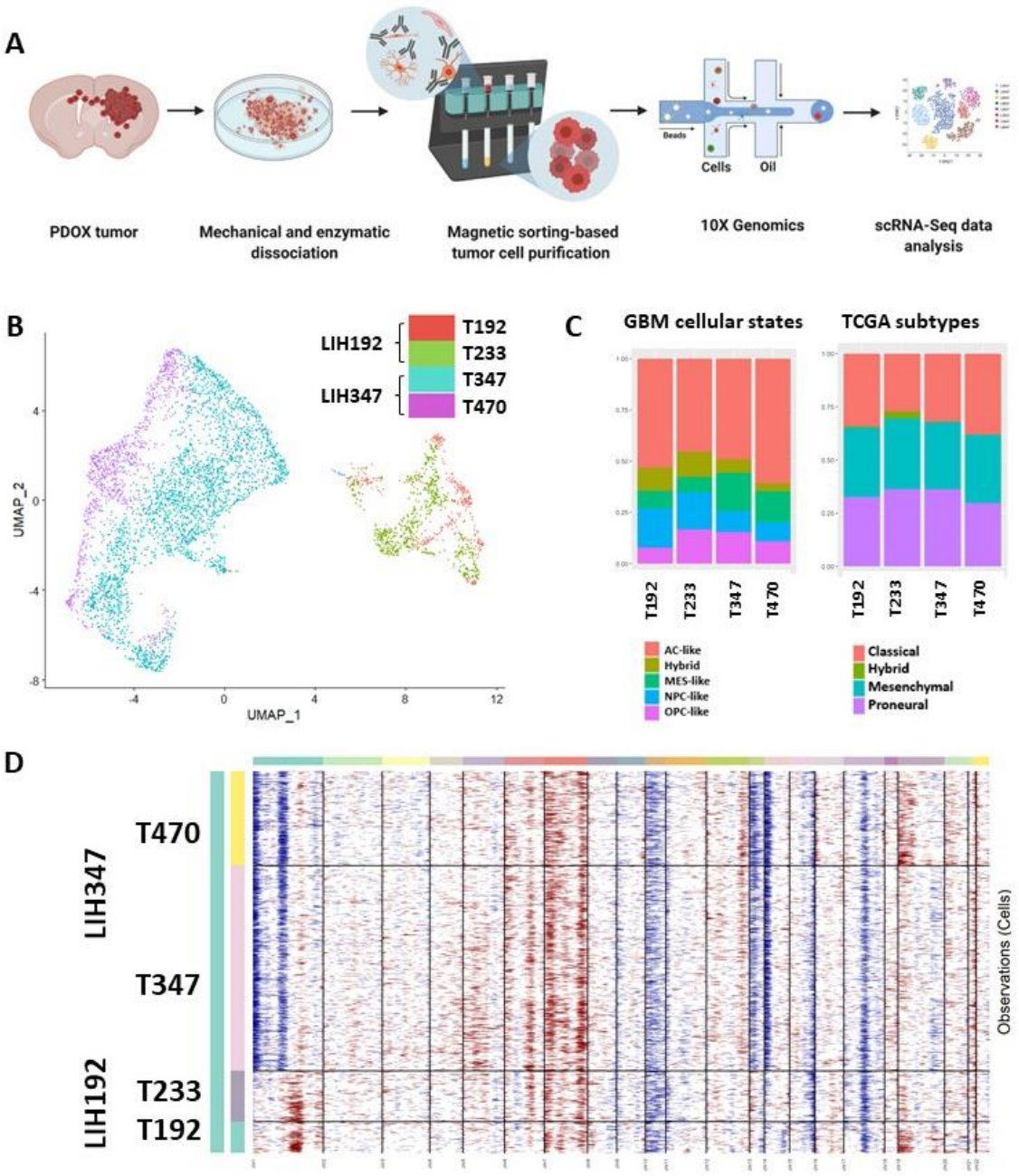

Figure 2. scRNA-seq analysis of longitudinal PDOX models.

A. Workflow of scRNA-seq showing mechanical and enzymatic dissociation of PDOX-derived tumor tissue followed by single cells separation into tumor cells and TME cells using MACS purification, single cells isolation using 10x Genomics technology, sequencing, and bioinformatics data analysis. **B.** Dimensionality reduction of scRNA-seq data showing tumor cells of longitudinal PDOXs derived from LIH192 (T192, T233) and LIH347 (T347, T470). **C.** GBM cell states and TCGA subtypes classification of single cells in each PDOX model. **D**. Copy number variation inference analysis based on scRNA-seq data comparing genomic alterations between longitudinal PDOX models generated from the 2 patients.

Identification of longitudinal transcriptomic changes

Next, we generated the list of differentially expressed genes (DEGs) by comparing primary (treatment-naïve) and recurrent (treated) tumor samples from each of the 2 patients and compared up and down-regulated genes. Comparison of DEGs from the two patients identified only 3 genes (*SEC61G*, *FOS*, *KHDBS3*) commonly upregulated (**Figure 3A**) and 6 genes (*CH13L1*, *IGFBP3*, *MT2A*, *TIMP1*, *IGFBP5*, *PMP2*) commonly downregulated between the patients (**Figure 3B**). Gene ontology analysis for both up and down-regulated DEGs revealed biological processes related to tumor intrinsic properties such as developmental process, biological adhesion, signaling, and cell proliferation (**Figure 3C and D**). Interestingly, metabolic processes were highly enriched in both primary and recurrent tumors. Overall, the GO terms identified appear to be similar in the longitudinal pairs, but were not necessarily commonly up or downregulated. Further analysis is needed to identify transcriptomic differences at the subpopulation level after removing inter-patient differences.

A **Common Upregulated**

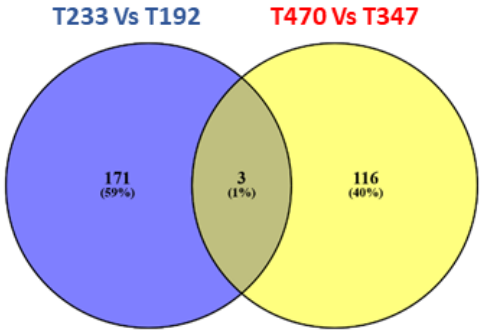

B **Common downregulated**

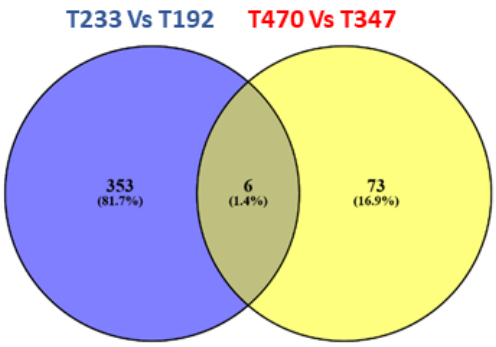

C **T233 vs T192 Upregulated**

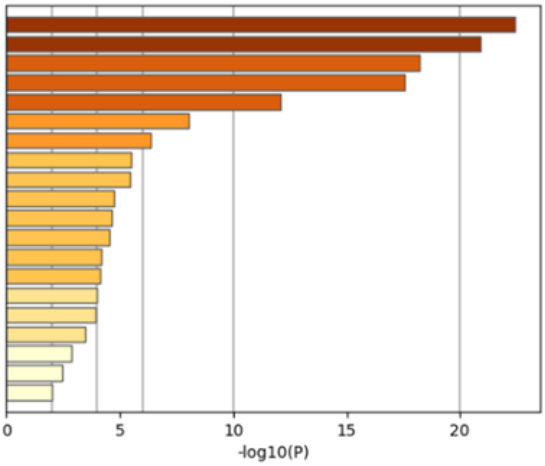

GO:0051179: localization
GO:0048519: negative regulation of biological process
GO:0008152: metabolic process
GO:0051704: multi-organism process
GO:0032502: developmental process
GO:0050896: response to stimulus
GO:0071840: cellular component organization or biogenesis
GO:0022610: biological adhesion
GO:0023052: signaling
GO:0050789: regulation of biological process
GO:0040011: locomotion
GO:0007610: behavior
GO:0048518: positive regulation of biological process
GO:0040007: growth
GO:0065007: biological regulation
GO:0032501: multicellular organismal process
GO:0008283: cell proliferation
GO:0009987: cellular process
GO:0022414: reproductive process
GO:0048511: rhythmic process

T233 vs T192 Downregulated

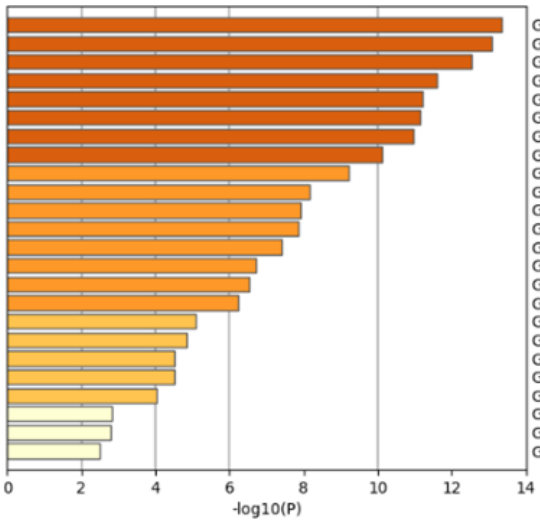

GO:0050789: regulation of biological process
GO:0048519: negative regulation of biological process
GO:0008152: metabolic process
GO:0009987: cellular process
GO:0065007: biological regulation
GO:0050896: response to stimulus
GO:0002376: immune system process
GO:0040007: growth
GO:0023052: signaling
GO:0071840: cellular component organization or biogenesis
GO:0032502: developmental process
GO:0048518: positive regulation of biological process
GO:0051179: localization
GO:0040011: locomotion
GO:0051704: multi-organism process
GO:0008283: cell proliferation
GO:0032501: multicellular organismal process
GO:0022610: biological adhesion
GO:0007610: behavior
GO:0098754: detoxification
GO:0022414: reproductive process
GO:0048511: rhythmic process
GO:0043473: pigmentation
GO:0001906: cell killing

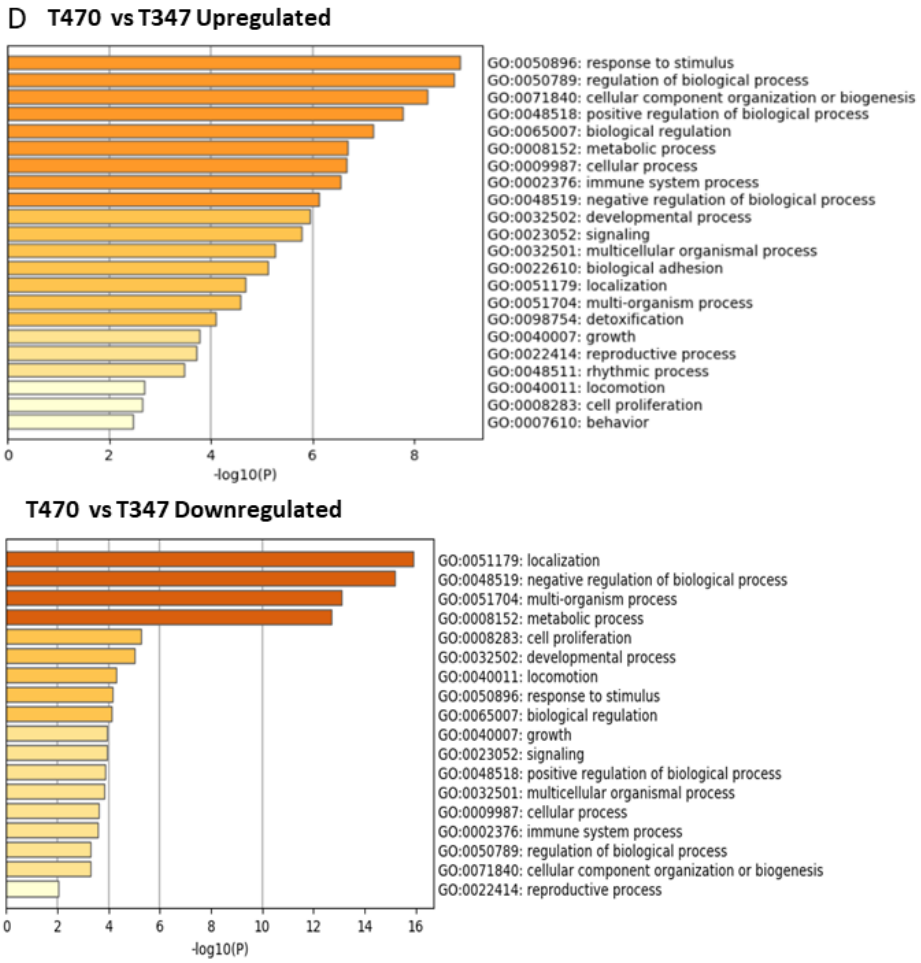

Figure 3. Differential expression analysis of longitudinal PDOX models.

A. Venn diagram of common up-regulated genes between recurrent and primary tumors in each patient. **B.** Venn diagram of common down-regulated genes between recurrent and primary tumors in each patient. (Adjusted P-value ≤0.01, $\log_2$FC ≥1 and ≤-1, the Wilcoxon rank-sum test with Bonferroni correction); **C.** Gene ontology terms characterizing up and down-regulated genes in patient LIH192 (T233 vs T192). **D.** Gene ontology terms characterizing up and down-regulated genes in patient LIH347 (T470 vs T347).

Trajectory and transcriptional regulators inference analysis

To further understand the differences between primary and recurrent tumors, we applied Monocle (Qiu et al., 2017) to order all single cells from both primary and recurrent tumors for each patient along a trajectory base on their transcriptional profiles (**Figure 4A**). This analysis showed that cells from both primary and recurrent tumors are present in all the cellular states along a trajectory. This indicates that although different cellular states exist in both primary and recurrent tumors, there is no specific cellular state dominated in longitudinal tumors. We applied SCENIC (Aibar et al., 2017) to identify complex cellular states and gene regulatory networks (GRN) regulating potential treatment-resistant

subpopulations in recurrent tumors (**Figures 4B and C**). This analysis revealed different subpopulations consisting of cells from both primary and recurrent tumors, further highlighting the higher importance of intra-tumoral transcriptomic heterogeneity present in each PDOX over the longitudinal transcriptomic changes. We identified key master regulators controlling the different cell states identified that are resented by both primary and recurrent tumors. We did not identify transcriptional regulators exclusive to either primary or recurrent tumors.

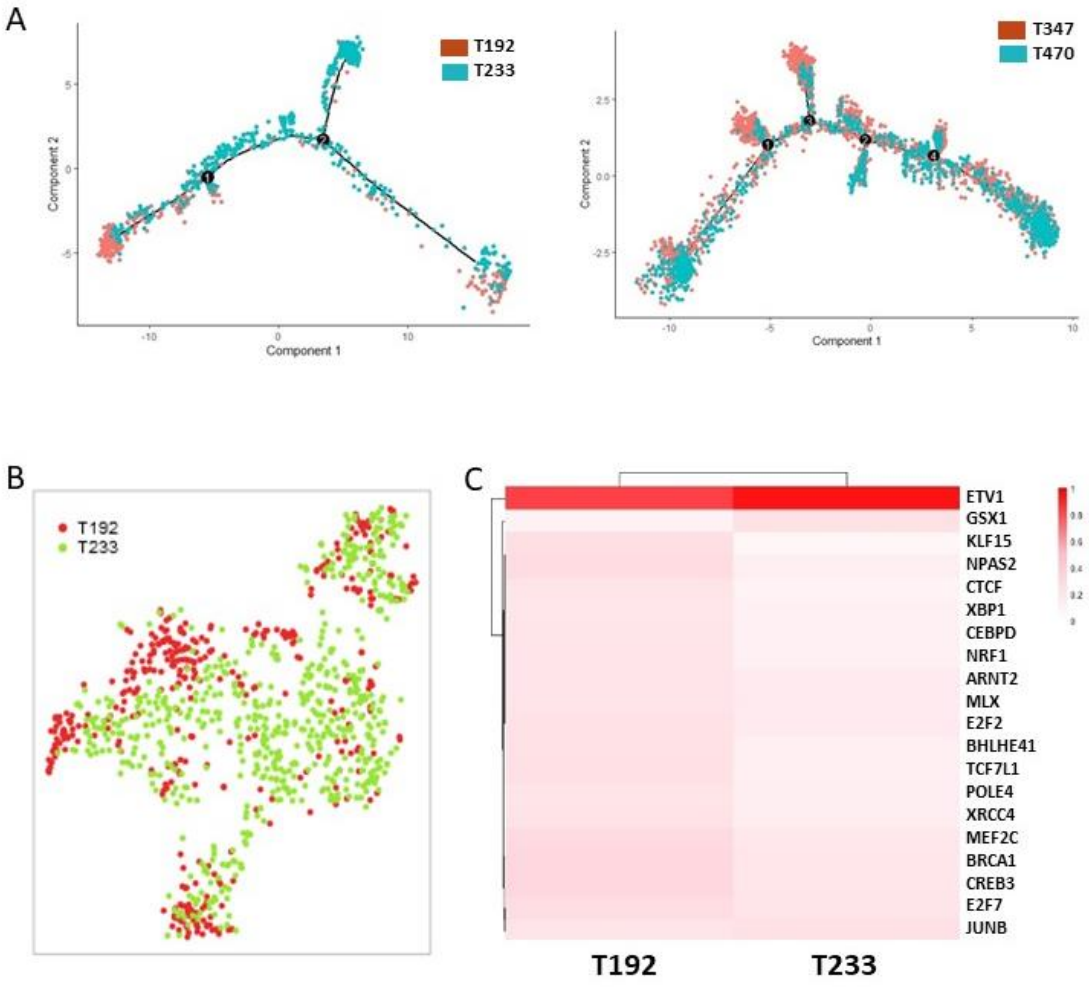

Figure 4. Trajectory and regulatory networks inference analysis revealed relevant cell states and GRNs in longitudinal PDOXs. A. Trajectory inference analysis showing the distribution of tumor cells along a trajectory. Tumor cells isolated from PDOXs of each longitudinal patients were analyzed separately **B.** tSNE of single cells based on the activity of transcriptional regulons in patient LIH192 **C.** Heatmap of the relative transcription factor activity between naïve and treated tumor cells from PDOXs of patient LIH192.

Discussion

Although the standard-of-care has been shown to confer survival benefits to a subset of GBM patients, it only offers about 14 months of survival advantage. Most GBMs resist the treatment and inevitably recur shortly after with a more aggressive tumor that eventually leads to the death of most patients even before a second surgery (Aldape et al., 2018; Hegi et al., 2005; Stupp et al., 2005). Thus there is a need to fully understand the molecular mechanisms of treatment resistance in GBM. So far genetic analysis of treated GBMs did not reveal common targetable changes in recurrent GBMs and tumor evolution following therapy mostly occurs in a stochastic manner (Barthel et al., 2019). More also epigenetic profiling of longitudinal GBMs revealed a largely unchanged epigenome at recurrence, with only a minute difference between primary and recurrent tumors that are restricted to a subset of patients (Klughammer et al., 2018; Malta et al., 2021), prompting the need to look at individual cell populations within each tumor at different time points. Patient data of the transcriptomic profiles of matched primary and recurrent tumors at the single-cell level is currently not available. We took advantage of our longitudinal PDOX models to investigate the transcriptomic changes between matched primary and recurrent GBMs using scRNA-seq. Analysis of the scRNA-seq data obtained revealed transcriptomic differences between primary and recurrent samples coming from the same patient. Differences between patients at the transcriptional level were dictated by their genetic backgrounds. Interestingly, using copy number inference analysis, we identified that differences between longitudinal samples were not influenced by genomic alterations. Primary and recurrent tumors had similar copy number variations in line with the preservation of the copy number variations earlier identified in a cohort of 15 longitudinal gliomas including these samples (Golebiewska et al., 2020). Furthermore, targeted sequencing using a diagnostic panel specific to gliomas also confirmed the conservation of genetic variants at recurrence (Golebiewska et al., 2020). This data is in accordance with previous reports that profiled a larger cohort of GBMs and found only limited instances of treatment-induced genetic changes at recurrence and are patient-specific (Barthel et al., 2019). We show that PDOX models recapitulate all the major cellular states and transcriptional programs reported in GBM patient samples (Dekker et al., 2020; Johnson et al., 2021; Kim et al., 2020; Neftel et al., 2019). This suggests that both inter-and intra-tumoral heterogeneity are intrinsic properties of both primary and recurrent GBMs. We did not observe a consistent variation or a switch in cellular state and or molecular subtypes in our matched longitudinal GBMs as previously reported (Phillips et al., 2006). Recent bulk transcriptomic profiling of matched primary and recurrent GBM did not also find any evidence of molecular subtype switch at recurrence and reports preservation of transcriptomic features of primary tumors at

recurrence (Dekker et al., 2020; Kim et al., 2020). Our differential expression analysis between primary and recurrent samples revealed mostly mutually exclusive lists of differentially expressed genes with only a few common genes between the two patients. The variable differentially expressed genes may have reflected the genetic differences between the patients or the influence of the different treatment regimens each patient received. The absence of pronounced differences may reflect limited long-term adaptation to treatment facilitated by the discontinuation of treatment in cancer patients, often referred to as “drug holiday”. Trajectory inference analyses revealed varying subpopulations with distinct transcriptional states and regulatory networks representing heterogeneous subpopulations from both primary and recurrent tumors. This result is similar to previous observations indicating subpopulation differences in longitudinal samples (Bastola et al., 2020). This suggests that changes at recurrence mirror different cellular phenotypes with different mechanisms of resistance, including cells with pre-existing resistance that are also present in primary tumors. The lack of a definite transcriptomic and genetic difference between primary and recurrent tumors suggests that investigating individual molecular features may not explain the difference but rather a multi-omic approach may be beneficial. More also, focusing on and targeting subpopulation changes upon treatment may be more beneficial than targeting the whole tumors (Keshava et al., 2019). Future studies should be designed to comprehensively characterize longitudinal tumors in a larger cohort using tumor multisampling, spatial-omics, and emerging multi-omics technologies permitting the simultaneous assessment of genetic, epigenetic, and transcriptomic information to understand the dynamic states in the spatio-temporal context. This may require the development of new or the optimization of existing computational tools with high sensitivity to detecting and compounding salient changes coming from each layer of the molecular data. In conclusion, we show that our longitudinal PDOX models are clinically relevant models for investigating the longitudinal adaptation of tumor cells during treatment progression.

References

Aibar, S., González-Blas, C. B., Moerman, T., Huynh-Thu, V. A., Imrichova, H., Hulselmans, G., … Aerts, S. (2017). SCENIC: Single-cell regulatory network inference and clustering. *Nature Methods*, *14*(11), 1083–1086. https://doi.org/10.1038/nmeth.4463

Aldape, K., Amin, S. B., Ashley, D. M., Barnholtz-Sloan, J. S., Bates, A. J., Beroukhim, R., … Stead, L. (2018). Glioma through the looking GLASS: Molecular evolution of diffuse gliomas and the Glioma Longitudinal Analysis Consortium. *Neuro-Oncology*, *20*(7), 873–884. https://doi.org/10.1093/neuonc/noy020

Barthel, F. P., Johnson, K. C., Varn, F. S., Moskalik, A. D., Tanner, G., Kocakavuk, E., … Verhaak, R. G. W. (2019). Longitudinal molecular trajectories of diffuse glioma in adults. *Nature*, *576*(7785), 112–120. https://doi.org/10.1038/s41586-019-1775-1

Bastola, S., Pavlyukov, M. S., Yamashita, D., Ghosh, S., Cho, H., Kagaya, N., … Nakano, I. (2020). Glioma-initiating cells at tumor edge gain signals from tumor core cells to promote their malignancy. *Nature Communications*, *11*(1), 1–17. https://doi.org/10.1038/s41467-020-18189-y

Chalmers, A. J., Ruff, E. M., Martindale, C., Lovegrove, N., & Short, S. C. (2009). Cytotoxic effects of temozolomide and radiation are additive- and schedule-dependent. *International Journal of Radiation Oncology, Biology, Physics*, *75*(5), 1511–1519. https://doi.org/10.1016/j.ijrobp.2009.07.1703

Dekker, L. J. M., Kannegieter, N. M., Haerkens, F., Toth, E., Kros, J. M., Steenhoff Hov, D. A., … Luider, T. M. (2020). Multiomics profiling of paired primary and recurrent glioblastoma patient tissues. *Neuro-Oncology Advances*, *2*(1), 1–12. https://doi.org/10.1093/noajnl/vdaa083

Dirkse, A., Golebiewska, A., Buder, T., Nazarov, P. V., Muller, A., Poovathingal, S., … Niclou, S. P. (2019). Stem cell-associated heterogeneity in Glioblastoma results from intrinsic tumor plasticity shaped by the microenvironment. *Nature Communications*, *10*(1), 1–16. https://doi.org/10.1038/s41467-019-09853-z

Golebiewska, A., Hau, A.-C., Oudin, A., Stieber, D., Yabo, Y. A., Baus, V., … Niclou, S. P. (2020). Patient-derived organoids and orthotopic xenografts of primary and recurrent gliomas represent relevant patient avatars for precision oncology. *Acta Neuropathologica*, *140*(6), 919–949. https://doi.org/10.1007/s00401-020-02226-7

Haar, C. P., Hebbar, P., Wallace, G. C., Das, A., Vandergrift, W. A., Smith, J. A., … Banik, N. L. (2012). Drug resistance in glioblastoma: A mini review. *Neurochemical Research*, *37*(6), 1192–1200. https://doi.org/10.1007/s11064-011-0701-1

Hegi, M. E., Diserens, A.-C., Gorlia, T., Hamou, M.-F., de Tribolet, N., Weller, M., … Stupp, R. (2005). *MGMT* Gene Silencing and Benefit from Temozolomide in Glioblastoma. *New England Journal of Medicine*, *352*(10), 997–1003. https://doi.org/10.1056/NEJMoa043331

Johnson, K. C., Anderson, K. J., Courtois, E. T., Gujar, A. D., Barthel, F. P., Varn, F. S., … Verhaak, R. G. W. G. W. G. (2021). Single-cell multimodal glioma analyses identify epigenetic regulators of cellular plasticity and environmental stress response. *Nature Genetics*, *53*(10), 2020.07.22.215335. https://doi.org/10.1038/s41588-021-00926-8

Keshava, N., Toh, T. S., Yuan, H., Yang, B., Menden, M. P., & Wang, D. (2019). Defining subpopulations of differential drug response to reveal novel target populations. *Npj Systems Biology and Applications*, *5*(1). https://doi.org/10.1038/s41540-019-0113-4

Kim, E. L., Sorokin, M., Kantelhardt, S. R., Kalasauskas, D., Sprang, B., Fauss, J., … Buzdin, A. (2020). Intratumoral heterogeneity and longitudinal changes in gene expression predict differential drug sensitivity in newly diagnosed and recurrent glioblastoma. *Cancers*, *12*(2). https://doi.org/10.3390/cancers12020520

Klughammer, J., Kiesel, B., Roetzer, T., Fortelny, N., Nemc, A., Nenning, K. H., … Bock, C. (2018). The DNA methylation landscape of glioblastoma disease progression shows extensive heterogeneity in time and space. *Nature Medicine*, *24*(10), 1611–1624.

https://doi.org/10.1038/s41591-018-0156-x

Kumar, M. P., Du, J., Lagoudas, G., Jiao, Y., Sawyer, A., Drummond, D. C., … Raue, A. (2018). Analysis of Single-Cell RNA-Seq Identifies Cell-Cell Communication Associated with Tumor Characteristics. *Cell Reports*, *25*(6), 1458-1468.e4. https://doi.org/10.1016/j.celrep.2018.10.047

Malta, T. M., Sabedot, T. S., Datta, I., Garofano, L., Vallentgoed, W., Varn, F. S., … Noushmehr, H. (2021). The epigenetic evolution of gliomas is determined by their IDH1 mutation status and treatment regimen. *BioRxiv*, 2021.08.09.455687. https://doi.org/10.1101/2021.08.09.455687

Nazarov, P. V., Muller, A., Kaoma, T., Nicot, N., Maximo, C., Birembaut, P., … Vallar, L. (2017). RNA sequencing and transcriptome arrays analyses show opposing results for alternative splicing in patient derived samples. *BMC Genomics*, *18*(1), 1–18. https://doi.org/10.1186/s12864-017-3819-y

Nazarov, P. V., Wienecke-Baldacchino, A. K., Zinovyev, A., Czerwińska, U., Muller, A., Nashan, D., … Kreis, S. (2019). Deconvolution of transcriptomes and miRNomes by independent component analysis provides insights into biological processes and clinical outcomes of melanoma patients. *BMC Medical Genomics*, *12*(1), 1–17. https://doi.org/10.1186/s12920-019-0578-4

Neftel, C., Laffy, J., Filbin, M. G., Hara, T., Shore, M. E., Rahme, G. J., … Suvà, M. L. (2019). An Integrative Model of Cellular States, Plasticity, and Genetics for Glioblastoma. *Cell*, *178*(4), 835-849.e21. https://doi.org/10.1016/j.cell.2019.06.024

Oren, Y., Tsabar, M., Cuoco, M. S., Amir-Zilberstein, L., Cabanos, H. F., Hütter, J.-C., … Regev, A. (2021). Cycling cancer persister cells arise from lineages with distinct programs. *Nature*, *596*(June 2020), 576–582. https://doi.org/10.1038/s41586-021-03796-6

Oudin, A., Baus, V., Barthelemy, V., Fabian, C., Klein, E., Dieterle, M., … Golebiewska, A. (2021). Protocol for derivation of organoids and patient-derived orthotopic xenografts from glioma patient tumors. *STAR Protocols*, *2*(2). https://doi.org/10.1016/j.xpro.2021.100534

Patel, A. P., Tirosh, I., Trombetta, J. J., Shalek, A. K., Gillespie, S. M., Wakimoto, H., … Bernstein, B. E. (2014). Single-cell RNA-seq highlights intratumoral heterogeneity in primary glioblastoma. *Science*, *344*(6190), 1396–1401. https://doi.org/10.1126/science.1254257

Phillips, H. S., Kharbanda, S., Chen, R., Forrest, W. F., Soriano, R. H., Wu, T. D., … Aldape, K. (2006). Molecular subclasses of high-grade glioma predict prognosis, delineate a pattern of disease progression, and resemble stages in neurogenesis. *Cancer Cell*, *9*(3), 157–173. https://doi.org/10.1016/j.ccr.2006.02.019

Qazi, M. A., Vora, P., Venugopal, C., Sidhu, S. S., Moffat, J., Swanton, C., & Singh, S. K. (2017). Intratumoral heterogeneity: pathways to treatment resistance and relapse in human glioblastoma. *Annals of Oncology : Official Journal of the European Society for Medical Oncology*, *28*(7), 1448–1456. https://doi.org/10.1093/annonc/mdx169

Qiu, X., Mao, Q., Tang, Y., Wang, L., Chawla, R., Pliner, H. A., & Trapnell, C. (2017). Reversed graph embedding resolves complex single-cell trajectories. *Nature Methods*, *14*(10), 979–982. https://doi.org/10.1038/nmeth.4402

Rabé, M., Dumont, S., Álvarez-Arenas, A., Janati, H., Belmonte-Beitia, J., Calvo, G. F., … Vallette, F. M. (2020). Identification of a transient state during the acquisition of temozolomide resistance in glioblastoma. *Cell Death and Disease*, *11*(1). https://doi.org/10.1038/s41419-019-2200-2

Rambow, F., Rogiers, A., Marin-Bejar, O., Aibar, S., Femel, J., Dewaele, M., … Marine, J. C. (2018). Toward Minimal Residual Disease-Directed Therapy in Melanoma. *Cell*, *174*(4), 843-855.e19. https://doi.org/10.1016/j.cell.2018.06.025

Raredon, M. S. B., Adams, T. S., Suhail, Y., Schupp, J. C., Poli, S., Neumark, N., … Niklason, L. E. (2019). Single-cell connectomic analysis of adult mammalian lungs. *Science Advances*, *5*(12), 1–16. https://doi.org/10.1126/sciadv.aaw3851

Shen, S., Vagner, S., & Robert, C. (2020). Persistent Cancer Cells: The Deadly Survivors. *Cell*, *183*(4), 860–874. https://doi.org/10.1016/j.cell.2020.10.027

Sompairac, N., Nazarov, P. V., Czerwinska, U., Cantini, L., Biton, A., Molkenov, A., … Zinovyev, A. (2019). Independent component analysis for unraveling the complexity of cancer omics

datasets. *International Journal of Molecular Sciences*, *20*(18). https://doi.org/10.3390/ijms20184414

Stuart, T., Butler, A., Hoffman, P., Hafemeister, C., Papalexi, E., Mauck, W. M., … Satija, R. (2019). Comprehensive Integration of Single-Cell Data. *Cell*, *177*(7), 1888-1902.e21. https://doi.org/10.1016/j.cell.2019.05.031

Stupp, R., Mason, W., Bent, M. van den, Weller, M., Fisher, B., Taphoorn, M., & Jo. (2005). Radiotherapy plus concomitant and adjuvant temozolomide for globlastoma. *N Engl J Med*, *352*, 987–996. https://doi.org/10.1016/j.canrad.2005.05.001

Tirosh, I., Venteicher, A. S., Hebert, C., Escalante, L. E., Patel, A. A. P., Yizhak, K., … Suvà, M. L. (2016). Single-cell RNA-seq supports a developmental hierarchy in human oligodendroglioma. *Nature*, *539*(7628), 309–313. https://doi.org/10.1038/nature20123

Wang, J., Cazzato, E., Ladewig, E., Frattini, V., Rosenbloom, D. I. S. S., Zairis, S., … Rabadan, R. (2016). Clonal evolution of glioblastoma under therapy. *Nature Genetics*, *48*(7), 768–776. https://doi.org/10.1038/ng.3590

Wang, Q., Hu, B., Hu, X., Kim, H., Squatrito, M., Scarpace, L., … R.G.W., V. (2017). Tumor Evolution of Glioma-Intrinsic Gene Expression Subtypes Associates with Immunological Changes in the Microenvironment. *Cancer Cell*, *32*(1), 42-56.e6. https://doi.org/10.1016/j.ccell.2017.06.003

Wen, P. Y., & Kesari, S. (2008). Malignant Gliomas in Adults. *New England Journal of Medicine*, *359*(5), 492–507. https://doi.org/10.1056/NEJMra0708126

Yabo, Y. A., Niclou, S. P., & Golebiewska, A. (2021). Cancer cell heterogeneity and plasticity: A paradigm shift in glioblastoma. *Neuro-Oncology*. https://doi.org/10.1093/neuonc/noab269

Yuan, D., Tao, Y., Chen, G., & Shi, T. (2019). Systematic expression analysis of ligand-receptor pairs reveals important cell-to-cell interactions inside glioma. *Cell Communication and Signaling*, *17*(1), 1–10. https://doi.org/10.1186/s12964-019-0363-1

Annex 2

Elucidating tumour-associated microglia/macrophage diversity along glioblastoma progression and under ACOD1 deficiency

Pires-Afonso Y, Muller A, Grzyb K, Oudin A, **Yabo YA**, Sousa C, Scafidi A, Poli A, Cosma A, Halder R, Coowar D, Golebiewska A, Skupin A, Niclou SP, Michelucci A.

Under review in Molecular Oncology

The rationale of the study

In this paper, the heterogeneity and adaptation of TAMs at different stages of tumor growth were studied to decipher the different TAMs subpopulations, their evolution, and phenotypic changes using scRNA-seq, flow cytometry, and immunohistochemistry in the GL261 glioma mouse model. Heterogeneity of TAMs during tumor progression was also investigated in the absence of *Acod1/Irg1* in tumor TME subpopulations to understand how macrophages are metabolically programmed in GBM. *Acod1/Irg1* is crucial in reprogramming macrophages towards an anti-inflammatory function during inflammation. Different TAMs subpopulations were uncovered in the GL261 mouse model and verified in PDOX models and human GBMs. An enhanced antigen presentation capacity was uncovered in *Acod1/Irg1* deficient mice in comparison to the reduction observed in *Acod1/Irg1* wild-type mice. The work in this paper provided insight on TAMs heterogeneity and part of the data that was used in the paper presented in **Chapter 6**.

Personal contributions

I performed trajectory inference analysis using the scRNA-seq data of myeloid cells subpopulations of both *Acod1/Irg1* deficient and wildtype mice. This analysis revealed a diverse trajectory with four distinct cellular states in TAM II subsets of *Acod1/Irg1* deficient myeloid cells in comparison to wild-type myeloid cells. This result was shown in **Figures 5G, S10A-B** in the paper. This analysis further identified genes sets that are exclusively expressed by TAM II subsets in *Acod1/Irg1* deficient mice, supporting enhanced immunogenicity under *Acod1/Irg1* deficiency, these results are shown in **Figure S10C**. I compared the transcriptomic profiles of the TME in the angiogenic PDOX model (P13) with a naïve nude brain. This analysis revealed tumor-specific activation of myeloid and endothelial cells as observed in the GL261 model. These results were shown in **Figures S4B, C, and D**. Finally, in addition to the figures outlined, I also contributed to the writing, proofreading, and revision of the manuscript.

Result

Elucidating tumour-associated microglia/macrophage diversity along Glioblastoma progression and under ACOD1 deficiency

Yolanda Pires-Afonso[1,2], Arnaud Muller[3], Kamil Grzyb[4], Anaïs Oudin[5], Yahaya A Yabo[2,5], Carole Sousa[1,5], Andrea Scafidi[1,2], Aurélie Poli[1], Antonio Cosma[4], Rashi Halder[6], Djalil Coowar[6], Anna Golebiewska[5], Alexander Skupin[6,7], Simone P Niclou[5,8], Alessandro Michelucci[1*]

[1]Neuro-Immunology Group, Department of Oncology, Luxembourg Institute of Health, Luxembourg, Luxembourg

[2]Doctoral School of Science and Technology, University of Luxembourg, Esch-sur-Alzette, Luxembourg

[3]Quantitative Biology Unit, Bioinformatics Platform, Luxembourg Institute of Health, Luxembourg, Luxembourg

[4]Quantitative Biology Unit, National Cytometry Platform, Luxembourg Institute of Health, Luxembourg, Luxembourg

[5]NORLUX Neuro-Oncology Laboratory, Department of Oncology, Luxembourg Institute of Health, Luxembourg, Luxembourg

[6]Luxembourg Centre for Systems Biomedicine, University of Luxembourg, Esch-Belval, Luxembourg

[7]National Centre for Microscopy and Imaging Research, University of California San Diego, La Jolla, USA

[8]KG Jebsen Brain Tumour Research Center, Department of Biomedicine, University of Bergen, Bergen, Norway

* Corresponding author

Alessandro Michelucci, PhD

Luxembourg Institute of Health

Department of Oncology

Neuro-Immunology Group

84, rue Val Fleuri, L-1526 Luxembourg

Tel. + 352-26970-263

alessandro.michelucci@lih.lu

RUNNING TITLE

TAM diversity in GBM

ABSTRACT

In Glioblastoma (GBM), tumour-associated microglia/macrophages (TAMs) represent the major cell type of the stromal compartment and contribute to tumour immune escape mechanisms. Thus, targeting TAMs is emerging as a promising strategy for immunotherapy. However, TAM heterogeneity and metabolic adaptation along GBM progression represent critical features for the design of effective TAM-targeted therapies. Here, we comprehensively study the cellular and molecular changes of TAMs in the GL261 GBM mouse model combining single-cell RNA-sequencing with flow cytometry and immunohistological analyses along GBM progression and in the absence of *Acod1/Irg1*, a key gene involved in the metabolic reprogramming of macrophages towards an anti-inflammatory phenotype. We identify distinct TAM profiles, mainly based on their ontogeny and recapitulated in patients, which reiterate microglia- versus macrophage-like features showing key transcriptional differences and dynamically adapting along GBM stages. Notably, we uncover a decreased antigen-presenting cell signature in TAMs along tumour progression that is instead maintained in *Acod1/Irg1*-deficient mice. Overall, our results provide insight into TAM heterogeneity and highlight a novel role for *Acod1/Irg1* in TAM adaptation during GBM progression.

KEYWORDS

Tumour-associated microglia/macrophages, Glioblastoma, Heterogeneity, ACOD1/IRG1, Metabolic reprogramming, Single-cell RNA-sequencing

1. INTRODUCTION

Complex interactions between neoplastic cells and their microenvironment sustain cancer heterogeneity and evolution [1, 2]. In the brain, tumours develop within a network of resident central nervous system (CNS) cells, including neurons, astrocytes, oligodendrocytes, endothelial cells and microglia, together with peripheral infiltrating immune components. These cells, together with the extracellular matrix, constitute the tumour microenvironment (TME), which drives disease progression by affecting tumour growth, patient survival and response to therapy. In Glioblastoma (GBM), the most aggressive brain tumour in adults, the TME is mainly composed of tumour-associated microglia/macrophages (TAMs), which can represent up to 40% of the tumour mass, creating a supportive milieu that facilitates tumour proliferation, survival and migration [3]. TAMs are either resident parenchymal microglia, whose progenitors migrated to the CNS during early development [4, 5] or peripheral monocyte-derived cells that have crossed the blood-brain barrier [6]. Once in the CNS, the latter differentiate into tumour-associated macrophages becoming nearly indistinguishable from activated resident microglia [7]. Thus, how ontogeny contributes to TAM education has only been started to be described in GBM transgenic mouse models [8] or in patients [9, 10] as a result of recently discovered specific markers.

GBM recruits TAMs, which in turn release growth factors and cytokines that affect the tumour. TAMs display specific immune properties that are different from classical pro-inflammatory activated (immune-permissive) M1 or alternatively activated (immune-suppressive) M2 reactive profiles [11, 12] or even exhibit non-polarized M0 features [13]. The complex interplay between pro- and anti-tumour processes depending on the molecular signals within the TME, both within and across cell types, contributes to the difficulty in interpreting tissue-resolution bulk signatures of GBM. In this context, single-cell RNA-sequencing (scRNA-seq) provides a remarkable method to depict heterogeneous cell populations and measure cell-to-cell expression variability of thousands of genes [14-17]. Specifically, in GBM patients scRNA-seq has emerged as a critical tool to discriminate TAM heterogeneity and their contribution to distinct glioma subtypes [10, 18]. Notably, scRNA-seq analyses enabled to discover that TAMs frequently co-express canonical M1 and M2 genes in individual cells [9].

Here, we combine scRNA-seq analyses with flow cytometry and immunofluorescence studies to elucidate the cellular and molecular properties of the TME, with a specific focus on TAMs. Following the discrimination of microglia from monocyte-derived macrophages and the characterization of their transcriptional programmes along tumour progression, we assess the role of aconitate decarboxylase 1/immunoresponsive gene 1 (*Acod1/Irg1*) in TAM polarization. The ACOD1/IRG1 enzyme catalyses the production of the anti-microbial immunometabolite itaconate from *cis*-aconitate in the tricarboxylic acid (TCA) cycle [19]. In macrophages, the induction of itaconate under inflammatory conditions reprograms them into a more pronounced anti-inflammatory phenotype, participating to the resolution of inflammation [20, 21]. Notably, the induction of the ACOD1/IRG1-itaconate axis in monocytes contributes to the immune paralysis in sepsis [22], while its inhibition in macrophages reduces the tumour burden in peritoneal tumours [23]. Here, we identify discrete TAM profiles, which reiterate microglia- versus macrophage-like features showing key transcriptional differences and dynamically adapting along GBM stages. Notably, we demonstrate that TAMs display a decreased antigen-presenting cell signature along tumour progression, which is instead maintained in *Acod1/Irg1*-deficient mice.

The understanding of TAM diversity, and more systematically of TME heterogeneity, which significantly contributes to GBM growth, is of utmost relevance for the discovery of novel immunotherapeutic opportunities [24]. Hence, our results point to important aspects to take into consideration when targeting TAMs and highlight a novel role for *Acod1/Irg1* in TAM adaptation during GBM progression.

2. Materials and Methods

2.1. Animals

Acod1 KO mice were generated by Dr. Haruhiko Koseki at the RIKEN Institute using embryonic stem cells purchased from the Knockout Mouse Project Repository (KOMP, University of California, DAVIS) under strain ID $Irg1^{tm1a(KOMP)Wtsi}$ containing an insertion cassette between exons 3 and 5. Briefly, *Acod1 KO* C57BL/6N ESCs were injected into recipient female C57BL/6N mouse blastocysts and selected females were subsequently bred with wild-type C57BL/6N mice [25]. For the experiments, heterozygote animals were crossed to generate homozygote *Acod1 KO* mice and *WT* C57BL/6N littermate controls. We confirmed their genotype by PCR and we used a mix of male and female littermates for experiments. Mice were housed in 12 h light/dark cycle and had free access to sterile food and water. All animal procedures were approved by the national authorities and the animal welfare structure of LIH under the reference LUPA 2017/20. The animal work of the present study has been conducted and reported in accordance to the ARRIVE (Animal Research: Reporting of In Vivo Experiments) guidelines to improve the design, analysis and reporting of research using animals, maximizing information published and minimizing unnecessary studies.

2.2. Glioma cell line

Mouse glioma 261 (GL261) cells were kindly provided by Dr. Poli (Neuro-Immunology Group, Luxembourg Institute of Health) and were maintained at 37°C with 5% CO_2 in culture medium (Dulbecco's Modified Eagle's Medium (DMEM (Gibco/Life Technologies)) supplemented with 10% Fetal Bovine Serum (FBS; Gibco/Life Technologies) and pen-strep (100 U/ml/; Gibco/Life Technologies). Cells at 80% confluence were dissociated with 0.05% Trypsin-EDTA (Gibco/Life Technologies) and tested for mycoplasma (MycoAlert PLUS Mycoplasma Detection Kit, Westburg,

The Netherlands) before mice implantation. For mice orthotopic implantation, GL261 cells were re-suspended in serum-free medium.

2.3. Differentiation of murine bone marrow-derived macrophages and co-culture experiments with GL261 cells

Bone-marrow cells were obtained by flushing the tibia and femurs of WT and *Acod1* KO adult mice. Briefly, mice were euthanized and their legs were removed. Bone marrow precursors were flushed out and cell suspension was further incubated with red blood cells hypotonic lysis buffer. After washing, cells were plated in DMEM media containing 10% FBS supplemented with 20% of L929 supernatant for seven days for full differentiation of bone marrow-derived macrophages (BMDMs).
GL261 and BMDMs were co-cultured in 1:1 mix in DMEM medium containing 10% FBS. GL261 cells were plated on top of 1 μm pore size Boyden chambers (Thincert, Greiner), whereas BMDMs were plated on the bottom of the 6-well plates. The mRNA was isolated from BMDMs at 0, 24 and 48 hours using the RNeasy mini kit according to the manufacturer' instructions (QIAGEN, Germantown, USA).

2.4. GL261 orthotopic implantation and tumour volume measurement

Before the implantation, mice were intraperitoneally anesthetized with a mixture of ketamine (100 mg/kg) and xylazine (10 mg/kg) and placed in a stereotactic frame. A local anaesthetic was administered subcutaneously (Marcain 0.25% with Adrenalin) and 1 μl containing 500 GL261 cells were implanted into the frontal cortex of the brain using a Hamilton syringe (Hamilton, Reno, NV, USA). Mice were monitored weekly for the first 2 weeks and daily from day 15 post-implantation. Magnetic resonance imaging (MRI) was performed weekly upon 15 post-implantation to assess tumour volume, using a 3T preclinical horizontal bore scanner (MR Solutions, Guilford, UK), equipped with a quadrature volume coil designed for mouse head imaging. Animals were placed prone in the cradle and maintained asleep during the duration of the scans, using 2-3% isoflurane mixed with oxygen. The body temperature was kept constant at 37°C and breathing was monitored throughout the scan sessions. Anatomical series

were used to screen the animals and calculate tumour volumes. The Fast Spin Echo T2-weighted MRI sequence was acquired, with the following acquisition parameters: TE: 68 ms, TR: 3000 ms, echo train: 8, averages: 4, plane resolution: 256 µm, slice thickness: 1 mm, slices: 15, orientation: coronal. Tumour volume was measured on ImageJ software (NIH, Bethesda, MD, USA) as the sum of area obtained by delineating the tumour in each slice and multiplying by slice thickness. Tumour volume quantification was normalized to the initial tumour take.

2.5. GBM patient-derived orthotopic xenograft (PDOX) mouse model

Human glioma biopsy from Patient 13 diagnosed as grade 4 GBM IDH wild type was obtained from Haukeland University Hospital (Bergen, Norway) upon approval of the local ethics committee. 3D organoids were prepared as previously described [26, 27]. Fresh human biopsy was mechanically minced and seeded on agar coated flasks (0,85%) allowing the formation of spheroids until up to 2 weeks at 37°C under 5% CO2 and atmospheric oxygen in DMEM medium, 10% FBS, 2 mM L-Glutamine, 0.4 mM NEAA, and 100 U/ml Pen–Strep (all from Lonza). Re-suspended in serum-free medium, viable organoids of approximately 300 - 1000 µm size were collected and used for in vivo implantation (6 organoids per mouse) in the right frontal cortex of immunodeficient Nu/Nu Nude mice (Charles River Laboratories, France). Animals were maintained under SPF conditions and sacrificed at the appearance of neurological or behavioural abnormalities and weight loss. MRI was performed weekly upon tumour implantation, as described above.

2.6. Brain tissue processing and dissociation

Animals were intraperitoneally anesthetized with a mixture of ketamine (100 mg/kg) with medetomidine (0.5 mg/Kg) and buprenorphine (0.05 mg/kg) before intracardiac perfusion with ice-cold phosphate-buffered saline (PBS). Brain samples were isolated and processed according to the different applications. For immunofluorescence staining, brains were fixed in 4% PFA for 48 h at room temperature, immersed in 30% sucrose (dissolved in PBS) for 48 h at 4°C, embedded in optimal cutting

191 temperature (OCT, Tissue-Tek) solution, sectioned (12 µm), slide mounted and stored at -20C. For *ex*
192 *vivo* studies, naïve brains and tumour-bearing brains (demarcated taking the tumour core region based
193 on MRI scan) were dissociated using the Neural Dissociation Kit P (MACS Miltenyi Biotec)
194 accordingly to the manufacturer's instructions. Briefly, the cell pellet was re-suspended in pre-warmed
195 EM1 solution (50 µl of Enzyme P, 1900 µl of Buffer X and 2,5 µl of 2-mercaptoethanol) and incubated
196 for 15 minutes at 37°C by reverting tube every 5 minutes. Next, freshly prepared EM2 solution (20 µl
197 of Buffer Y and 10 µl of Enzyme A) was added to the cell pellet and tissue was mechanically dissociated
198 using glass pipettes and incubated for 10 minutes at 37°C to yield a single-cell suspension. The resultant
199 single-cell suspension was filtered through a 50 µm and centrifuged at 300g, 4°C for 10 min. Next, we
200 removed the myelin from the single cell suspension using the myelin removal beads kit (Myelin
201 Removal Beads II, MACS Miltenyi Biotec) accordingly to the manufacturer's instruction for 500 mg
202 of tissue. Briefly, brain tissue was suspended in 1800 µL of MACS buffer and incubated with 200 µl of
203 myelin Microbeads (MACS Miltenyi Biotec) at 4°C for 15 min. Cells were washed, centrifuged for 10
204 min at 300g and re-suspended in MACS buffer (3 x 1000 µl/mouse brain).
205 For the GBM PDOX model, tissue dissociation was performed using the Neural Dissociation Kit P
206 (MACS Miltenyi Biotec) followed by myelin removal beads kit (Myelin Removal Beads II, MACS
207 Miltenyi Biotec), as described above. An additional step was performed using the mouse cell depletion
208 kit (MACS Miltenyi Biotec) following the manufacturer's protocol. Specifically, this step allowed to
209 enrich murine stromal cells over human patient tumour cells. Briefly, the cell pellet was re-suspended
210 in 80 µl of cold HBSS with 0,5% BSA (Sigma-Aldrich) and incubated with 20 µl of cell depletion
211 cocktail for $1x10^7$ total cells at 4°C for 15 min.
212
213 **2.7. Single-cell RNA-sequencing using Drop-sequencing**
214
215 Single-cell suspensions derived from both naïve and GL261-tumour bearing mice (**Table 1**) were
216 obtained using an adapted protocol from MACS Miltenyi.
217

Table 1. *Tumour volume measurement by MRI for biopsy collection at early, intermediate and late stage in GL261 tumour-bearing WT and Acod1 KO mice used for scRNA-seq analyses (1 mouse per condition).*

		Tumour volume (mm^3)	
Time-point (stage)	**Weeks post implantation**	**WT (gender)**	***Acod1* KO (gender)**
Early	2	6,11 (female)	9,61 (male)
Intermediate	3/4	22,63 (male)	20,48 (female)
Late	4/5	33,14 (male)	33,83 (male)

Specifically, tissue enzymatic dissociation was performed using the Neural Dissociation Kit P (MACS Miltenyi Biotec) (as described above) and the cell suspension was subsequently added into "C tubes" for the gentleMACS Dissociator (gentleMACS™ Octo Dissociator with Heaters, Miltenyi Biotec). The 37C_ABDK_01 program was used to dissociate the brain tissue (>100 mg). We centrifuged the cellular suspension and we removed the myelin using the myelin removal beads kit (Myelin Removal Beads II, MACS Miltenyi Biotec) accordingly to the manufacturer's instruction for 500 mg of tissue. The eluted fraction was collected in 2% BSA RNAse free solution. Cell viability and counting was assessed prior injection into Drop-seq. A total of 5'659 single cells were successfully sequenced and analysed. Cells handling, microfluidics fabrication, single cell droplet encapsulation and next-generation sequencing preparation for Drop-seq libraries were done as previously described [28].

2.8. Single-cell RNA-sequencing bioinformatics processing, data and statistical analyses

The FASTQ files were assembled from the raw BCL files using Illumina's bcl2fastq converter and ran through the FASTQC codes [Babraham bioinformatics; https://www.bioinformatics.babraham.ac.uk/projects/fastqc/] to check for the consistency in the library qualities. The monitored quality assessment parameters were: a) quality per base sequence (especially for the read 2 of the gene); b) per base N content; c) per base sequence content and d) over-represented sequences. The libraries, which showed significant deviation, were re-sequenced. Then, the FASTQ

files were merged and converted to binaries using PICARD's fastqtosam algorithm. We have applied the Drop-seq bioinformatics pipeline [14]. The sequencing reads were converted to digital gene expression (DGE) matrix. To normalize for the transcript loading between the beads, the averaged normalized expression levels (log2(TPM+1)) were calculated. To distinguish between cell-containing and empty beads, a cumulative function of the total number of transcripts per barcode was plotted. Then, a threshold was applied empirically on the resulting "knee plot" to estimate the beads exposed to the cell content. For each experimental batch, we retained top 1'000 cell barcodes based on the cumulative distribution, leading to 8'000 cells. We removed low-abundance genes and only genes that were expressed in at least 30 cells were considered for further analysis. We additionally removed cells expressing less than 1'000 genes. Lastly, we concatenated each batch in a single matrix of the following dimensions: 5'659 cells x 18'338 genes. These pre-analytical filtering steps were processed using R environment with the tidyverse package. The tSNE projection was processed with the Rtsne package with a perplexity = 50, followed by a topological clustering with the library HDBSCAN (Hierarchical DBSCAN with a minimum of 19 points - cells - for a cluster to be considered). We conducted statistical analysis for significant expression between groups using pairwise Wilcoxon test, while p-values were adjusted with Benjamini Hochberg (BH) method.

Data visualization and downstream investigations were performed with Tableau Desktop software (Seattle, USA) and R environment (R Core Team, Vienna, Austria).

2.9. Kaplan-Meier survival curves

TCGA low and high grade glioma raw data together with the respective sample annotation were extracted from the GlioVis platform. Data was further normalized based on the library size (DESeq2) followed by a log2 transformation. Tumour-associated microglia- and macrophage-like transcriptional signatures were used to assign a score for each patient (ssGSEA). Signatures were obtained from identified TAM I and TAM II profiles in the GL261 mouse model, converting the corresponding mouse genes into human genes accessing Biomart from Ensembl using the R package biomaRt (version 2.44.1) and identifying shared genes between the GBM syngeneic murine model and patients from Muller et al

dataset [9] . In total, 702 TCGA patients (e.g. LGG: 351 and GBM: 351) have been stratified based on their ssGSEA score 50% of the highest and lowest ssGSEA score was selected to calculate the Kaplan-Meier survival curves using the R software packages *survival* and *ggplot2* for data visualization. The corresponding p-value was computed based on a log rank test.

For survival analyses conducted in the GL261 mouse model, they were performed according to humane endpoints guidelines, including loss of locomotor activity, weight loss (up to 20%) and central nervous system symptoms. The survival time was measured from the day of tumour cell implantation until the day of euthanasia and median mouse survival time was calculated in GraphPad for each group (WT mice = 8; *Acod1* KO mice = 8 mice) using the Mantel-Cox signed-rank statistical test.

2.10. Single cell trajectory inference analysis

Single cell trajectory inference analysis was done with Monocle 2 in R (version 3.6.3) using default parameters [29, 30]. The branching method orders cells along a trajectory based on gene expression similarities. Monocle 2 uses reversed graph embedding to describe multiple fate decisions in a fully unsupervised manner. Branches in the trajectory represent cell fate decisions through a developmental process.

2.11. Gene Ontology analyses

The DAVID (The Database for Annotation, Visualization and Integrated Discovery) gene functional classification tool (http://david.abcc.ncifcrf.gov) was used to investigate and interpret the respective functional biological terms from the large gene lists of differentially expressed genes. Representation of GO terms enrichment was done on Cytoscape Software (National Institute of General Medical Sciences, https://cytoscape.org/). Each node represents a GO term and the size of each node is proportional to the number of nodes from the correspondent query set with that term. Only nodes with p-value < 0.001 were chosen for network representation.

298 **2.12. Mouse brain CD11b+ cell isolation**

299

300 Murine brain CD11b+ isolated cells were enriched by magnetic separation using CD11b beads (MACS
301 Miltenyi Biotec) for RNA extraction or for flow cytometry phenotyping experiments. Briefly, 1×10^7
302 cells were resuspended in 90 µl of PBS supplemented with 0.5% BSA (Sigma-Aldrich) and 2 mM
303 EDTA (MACS buffer) and incubated with 10 µl of CD11b beads (MACS Miltenyi Biotec) at 4°C for
304 20 min. Cells were washed with MACS buffer, centrifuged for 10 min at 300g and resuspended in 500
305 µl of MACS buffer at a density of 1×10^8 cells. The cell suspension was applied into the LS columns
306 (MACS Miltenyi Biotec) and the CD11b+ fraction was eluted. Flow cytometry experiments to evaluate
307 the lymphocytic population were performed without prior CD11b+ beads isolation. Flow cytometry
308 acquisition was performed using a FACSAria IIu SORP cytometer (Becton Dickinson) and data was
309 further analysed using FlowJo version 10.6.1 (Becton Dickinson).

310

311 **2.13. Flow cytometry analyses**

312

313 Single-cell suspension was obtained as previously described. The cells were resuspended in ice-cold
314 HBSS with 2% FBS and 10 mM HEPES (FACS buffer) and filtered through a 70 µm nylon mesh
315 (CellTrics). For multicolour phenotyping, cells were blocked with Fc receptor binding inhibitor (anti-
316 mouse CD16/CD32 monoclonal antibody; 1:100; eBioscience) for 15 min at 4°C to reduce binding of
317 non-specific Fc-gamma receptors, and then stained with fluorochrome-conjugated antibodies for 30 min
318 at 4°C in the dark. The following antibodies were used in the present study: rat anti-mouse CD45
319 monoclonal antibody (clone 30-F11), FITC; rat anti-mouse CD74 monoclonal antibody (clone In-1),
320 FITC; rat anti-mouse CD11b monoclonal antibody (clone M1/70), Percp-Cy5.5; rat anti-mouse
321 P2RY12 monoclonal antibody (clone S16007D) PE and mouse anti-mouse MHC-II (clone AF6-120,1)
322 APC. Unstained (control) and stained cells were washed and re-suspended in 100 µL of FACS buffer
323 prior acquisition. Before acquisition, the performance of the instrument was assessed using CS&T beads
324 according to the manufacturer's instructions. Single-stain controls were prepared with UltraComp
325 eBeads (eBioscience) following the manufacturer's instructions and thus used to calculate the

compensation matrix. Hoechst (0.1 µg/ml, Bisbenzimide, 33342; Sigma) or Zombie NIR (1:1000 dilution in PBS, Biolegend) was added for dead cell discrimination. Samples were run on FACSAria IIu SORP cytometer (Becton Dickinson) and flow cytometry data was analysed using FlowJo software (v. 10.6.1, Becton Dickinson).

2.14. RNA extraction and qPCR analyses

Total RNA was extracted from BMDMs and freshly isolated CD11b+ cells from tumour-bearing mice at late stage using the RNeasy Mini Kit (Qiagen, Germantown, MD), according to the manufacturer's instructions. RNA concentration was quantified by NanoDrop (NanoDrop Technologies) and RNA quality was assessed by the quotient of the 28S to 18S ribosomal RNA electropherogram peak using a bioanalyser (Agilent 2100; Agilent Technologies). For cDNA synthesis, RNA was reverse-transcribed using SuperScript™ III reverse transcriptase (10,000 U; Invitrogen/Life Technologies) with 1 µl (50 µM)/reaction oligo(dT)20 (25 µM; Invitrogen/Life Technologies) as primer according to the manufacturer's instructions. Reverse transcription was performed at 50°C for 60 min. Gene expression reaction mixtures contained 2 µl of diluted cDNA, 10 µl of Fast SYBR Green Master Mix (Applied Biosystems/Thermo Fisher Scientific) and 0.5 µl of each 10 µM forward and reverse primers. PCRs were carried out in 384-well plates on a ViiA™ 7 real-time PCR system (Applied Biosystems/Thermo Fisher Scientific) using the following programme: 95°C for 20 s, 40 cycles at 95°C for 1 s and 60°C for 20 s. Samples were run in triplicates, and the mean Ct (threshold cycle) values were used to calculate the relative amount of product by the $\Delta\Delta C$ t method using 60S ribosomal protein L27 (Rpl27) as housekeeping gene. The specific primer sequences were as follows: Acod1 forward: 5' GCA ACA TGA TGC TCA AGT CTG 3'; Acod1 reverse: 5' TGC TCC TCC GAA TGA TAC CA 3'; Cd74 forward: 5' GAC CCA GGA CCA TGT GAT GC 3'; Cd74 reverse: 5' TTC CTG GCA CTT GGT CAG TAC TTT A 3'; H2-Ab1 forward: 5' TCA CTG TGG AGT GGA GGG CA 3'; H2-Ab1 reverse: 5' GGC AGT CAG GAA TTC GGA GC 3'; H2-Aa forward: 5' TCT GTG GAG GTG AAG ACG AC 3'; H2-Aa reverse: 5' AGG AGC CTC ATT GGT AGC TGG 3'; Irf1 forward: 5' ACT CGA ATG CGG ATG

353 AGA CC 3'; Irf1 reverse: 5' GCT TTG TAT CGG CCT GTG TG 3'; RpL27 forward: 5' TGG AAT
354 TGA CCG CTA TCC CC 3'; Rpl27 reverse: 5' CCT GTC TTG TAT CGC TCC TCA A 3'.
355
356 **2.15. Immunofluorescence staining and microscopy imaging acquisition**
357
358 Coronal sections of 12 μm tickness were prepared adopting the standard protocol with minor
359 modifications [31]. Briefly, sections were washed (PBS with 0.1% Triton X-100), permeabilised (PBS
360 with 1.5% Triton X-100), blocked (PBS with 5% BSA) and incubated with the following primary
361 antibodies: rabbit anti-Iba1 (1:1000; Biocare Medical), rat anti-MHC-II (1:100; Abcam), rat anti-CD74
362 FITC (1:50; eBiocience) and mouse anti-IRF1 (1:100; Santa Cruz Biotechnology). Secondary
363 antibodies against the appropriate species were incubated for 2 h at room temperature. Cell nuclei were
364 counterstained with Hoechst (1 mg/ml; Sigma). Sections were mounted on glass slides cover slipped
365 using FluoromountTM Aqueous Mounting Medium (Sigma). For each brain section, at least 5 random
366 40X and 63X confocal images along the tumour margin and the tumour core were acquired with a Zeiss
367 LSM880 microscope (Jena, Germany). High-resolution XYZ stack images (1.024 x 1.024 pixels per Z
368 step) were taken with a step size of 0.50 μm. Cell quantifications were peformed using NIH ImageJ
369 software (NIH, Bethesda, MD, USA) and values for single mouse are represented with distict shape.
370 Hoechst staining was used as reference for tumour localization.
371
372 **2.16 SDS/PAGE and western blotting analyses**
373
374 Cells were collected in 600 μl RIPA lysis buffer and stored at -80°C before protein extraction. Samples
375 were centrifuged at 10'000g for 10 minutes at 4°C and supernatants were harvested. Protein
376 concentrations were measured with Bio-Rad Protein Assay Dye Reagent Concentrate (500-0006, Bio-
377 Rad). Proteins were diluted in RIPA lysis and loading buffers. Heat-denatured protein samples were
378 separated on 4-12% BisTris-polyacrylamide gel electrophoresis (NP0322BOX, Invitrogen) followed
379 by transfer to PVDF membranes 0.2 μm (LC2005, Invitrogen). After blocking with 5% (wt/vol) dry

milk in TBS containing 0.1% triton (TBST), the membrane was incubated overnight at 4°C with primary anti-IRG1 antibody (Ab222411, Abcam) diluted 1:250 in 1% (wt/vol) BSA in TBST with constant shaking. After three washing steps with TBST, the membrane was incubated with anti-rabbit antibody coupled to horseradish peroxidase and revealed by chemoluminescence using Pierce™ ECL detection reagents (Thermo Fisher Scientific). For the second hybridization, the membrane was incubated with anti-actin antibody (MAB 1501, Millipore) for 90 min at RT in 1% (wt/vol) BSA in TBST with constant shaking. After three washing steps with TBST, the membrane was incubated with anti-mouse antibody coupled to horseradish peroxidase and revealed by chemoluminescence.

2.17. Raw data files

All relevant datasets are whithin the paper and its supporting information files (Fig. S1-S10) and Tables S1-S6). We deposited the raw scRNA-seq data in Gene Expression Omnibus (GEO) database under the accession number GSE158016.

2.18. Statistical analyses

Data were analyzed using the GraphPad Prism 8 software (GraphPad software, La Jolla, CA, USA) and R environment (R Core Team, Vienna, Austria). Unless otherwise indicated, all data are presented as mean ± standard error of the mean (SEM) of at least three independent biological experiments. Statistical analysis was performed using Unpaired t test or Two-way ANOVA. All differences were considered significantly different at p-value <0.05 and were annotated as follows: *< 0.05, **< 0.01, ***< 0.001, ns> 0.05.

403 ## 3. RESULTS AND DISCUSSION

404

405 ### 3.1. Single-cell transcriptomics reveals cellular diversity and cell type-specific differential
406 gene expression in naïve and GL261 tumour-bearing wild type and ACOD1/IRG1 knock-out
407 mice

408

409 To investigate the heterogeneity of the TME in GBM, both at baseline and under ACOD1/IRG1
410 deficiency, we dissected brain tissue from naïve and GL261 tumour-bearing mice at early (5-10 mm^3),
411 intermediate (20-25 mm^3) and late (30-35 mm^3) stage of tumour progression, both from wild type (WT)
412 and age-matched ACOD1/IRG1 knock-out (KO) C57BL/6N mice. Briefly, we took advantage of the
413 GL261 (mouse glioma 261) syngeneic murine model as a widely used paradigm for immunotherapy
414 studies in GBM [32]. This model allows the engraftment of immortalized tumour cells from the same
415 strain with low immune rejection, thus enabling the investigation of an immunocompetent TME *in vivo*,
416 including functional T and B cells [33-35]. Recent studies aimed at comparing datasets obtained in
417 GBM patients with distinct GBM syngeneic mouse models identified high correlation levels with both
418 the 005 and GL261 models, thus serving as reliable preclinical models recapitulating several GBM
419 patient features [36]. For our aims, the tissue was digested to a single-cell suspension and analysed
420 using scRNA-seq to profile hundreds of cells isolated from the corresponding naïve and orthotopic
421 syngeneic GL261-implanted mice (**Fig. 1A**). Following pre-analytical filtering of the scRNA-seq
422 experiments, we obtained a matrix composed of 5'659 single cells (n = 18'338 genes). In order to reduce
423 the dimensionality of the matrix, we applied t-Distributed Stochastic Neighbourhood Embedding
424 followed by unsupervised topological clustering with DBSCAN on the 2D projection of the tSNE. We
425 identified 12 cell clusters with distinct gene expression signatures, irrespective of the tumour burden
426 and genotype (**Fig. 1B**). We annotated 11 of them (n > 30 cells) based on cell type-specific gene markers
427 [37, 38] and gene set enrichment analysis (GO) of up-regulated genes in the correspondent clusters.
428 Specifically, in addition to tumour cells (*Cd44*$^+$, n = 3'332 cells), we identified 10 stromal clusters that
429 we classified as pericytes (*Dbi*$^+$, n = 61 cells), lymphocytes (*Trac*$^+$, n = 178 cells), ependymal cells (*Ttr*$^+$,
430 n = 73 cells), endothelial cells (*Pecam1*$^+$, n = 328 cells), astrocytes (*Slc1a2*$^+$, n = 289 cells),

oligodendrocytes (*Plp1*$^{+}$, n = 365 cells), oligodendrocyte precursor cells (OPCs, *Pdgfra*$^{+}$, n = 60 cells), neural stem cells (NSCs, *Meg3*$^{+}$, n = 36 cells) and myeloid cells 1 and 2 (*Itgam*$^{+}$, n = 836 cells) (**Fig. 1C, Fig. S1A**). Cells in the additional small subset (n = 20 cells) expressed myeloid markers (e.g. *Itgam, Aif1*), but clustered independently from the annotated main myeloid clusters (**Fig. 1B**). The analysis of additional specific markers provided robust molecular definitions of the major cell types present in the brain of naïve and tumour-bearing mice (**Fig. S1**). Notably, identities, markers, and proportions of cell types in naïve mice matched previous single-cell droplet-based sequencing data from mouse brain tissue [39], indicating that our results were robust to the inclusion of tumour-affected brains. In addition, the proportion of the cell types identified here were similar to the ones described in recent single-cell studies conducted in GBM patients [18, 40, 41]. Lastly, GBM is an archetypal heterogeneous tumour characterized by a significant extent of common genetic alterations affecting tumour progression [42]. In line with previous studies [43], *Myc* and *Trp53* were the main highly overexpressed genes in tumour cells compared to non-malignant cells (**Fig. S2**).

Focusing on the TME, we first observed that lymphocytes, OPCs and a subset of myeloid cells were solely present in tumour-bearing mice (**Fig. 1D**). Next, a direct comparison of tumour-associated cells versus the corresponding cells in naïve mice enabled to identify differentially expressed genes (p -value < 0.01; log FC > ± 0.5) (**Fig. 1E, Table S1**) according to the defined cell types. We observed a prominent transcriptional adaptation in tumour-associated endothelial cells, oligodendrocytes as well as in the myeloid subset (**Fig. 1D**), which has been described also in patients [18, 41]. We detected cell-type specific up-regulated genes across the four CNS resident cells (**Fig. 1E, Fig. S3A**). Notably, all four cell types displayed a shared antigen processing and presentation gene signature (e.g. *H2-D1*, *H2-K1* and *B2m*) (**Table S1**). Specifically, approximately 15% of the genes, representing more than 90 genes (e.g. *Junb*, *Spp1*, *Cd74, B2m, H2-K1 and H2-Q7*), were up-regulated in both tumour-associated endothelial and myeloid cells 1 compared to the corresponding naïve cells (**Fig. S4A**), indicating that endothelial cells are also active immune modulators in the TME of GBM. Indeed, the tumour vasculature is a key element of the TME, which largely contributes to the immunosuppressive features of GBM [44]. We corroborated these observations in a patient-derived orthotopic xenograft (PDOX) preclinical mouse model characterized by its angiogenic nature, as previously described [26]. By

459 conducting scRNA-seq analyses of the tumour biopsy and the whole brain, respectively from the PDOX
460 model and naïve nude mouse, we discriminated naïve from tumour-associated cells (**Fig. S4B**) and, in
461 line with the results obtained in the GL261 model, we identified the corresponding myeloid cell subsets
462 (naïve, myeloid cells 1 and 2) as well as the endothelial cluster (**Fig. S4C**). In the PDOX model, we
463 detected 27% shared up-regulated genes (n = 335) between tumour-educated myeloid cells 1 and
464 endothelial cells (**Fig. S4D**). Taken together, we detected 8% shared up-regulated genes (n = 32 genes)
465 between myeloid cells 1 and tumour endothelial cells across syngeneic GL261 and PDOX GBM murine
466 models (**Fig. S4E**). Specifically, we identified genes involved in antigen presentation via MHC class I
467 (e.g. *B2m* and *H2-K1*) (**Fig. S4C**), thus indicating that endothelial cells display immunological
468 signatures maintained across various GBM murine models.
469 Overall, these results show that, in analogy to GBM patients, the growing tumour in the analysed
470 syngeneic mouse model induces the emergence of lymphocytes, OPCs and a subset of myeloid cells in
471 the TME that are normally absent in the homeostatic CNS. Further, it specifically affects the
472 transcriptional signature of the major resident CNS cell types, with the myeloid compartment displaying
473 high heterogeneity, major tumour-associated education and specific gene expression signatures shared
474 with endothelial cells.
475
476 **3.2. Tumour-associated myeloid cells in Glioblastoma are heterogeneous and display distinct**
477 **transcriptional programmes**
478
479 Similar to GBM patients, the myeloid compartment constituted the biggest cluster in the TME of the
480 GL261 GBM mouse model (39.3% of the TME) (**Fig. S3B**) and displayed prominent transcriptional
481 adaptation and heterogeneity, thus representing a relevant paradigm to deepen and address its molecular
482 profile. Resident parenchymal microglia are difficult to segregate from peripheral monocyte-derived
483 cells, which prevalently constitute the myeloid compartment in GBM. Thus, we took advantage of our
484 scRNA-seq dataset obtained in WT mice to analyse the expression of known microglia and monocyte-
485 derived macrophage markers across naïve and the two TAM subsets identified by 2D-tSNE, irrespective
486 of the tumour stage (**Fig. 2A**). Naïve and TAM I clusters showed high expression levels of the microglia

homeostatic genes (e.g. *Gpr34, Hexb, P2ry12, Siglech, Sparc*), while these genes were almost undetectable (except *Hexb*) in the TAM II cluster. Accordingly, the TAM II cluster exhibited high levels of peripheral monocytic-derived macrophage markers (e.g. *Arg1, Ccr2, Ly6c2, Mrc1, Tgfbi*) **(Fig. 2B)**. These observations were supported by flow cytometry analyses of the macro-dissected tumour region to discriminate CD11b+ P2ry12+ from CD11b+ P2ry12-/low cells **(Fig. S5A)**. Compared to naïve mice, where more than 95% of CD11b+ cells were P2ry12+ resident microglial cells, the amount of CD11b+ P2ry12+ cells in tumour-bearing mice was significantly reduced (mean 58.16 ± 5.6 %) **(Fig. 2C)**. These analyses allowed to discriminate microglia-like (TAM I) from macrophage-like (TAM II) cells in the GL261 syngeneic model. Notably, our results are in line with recent single-cell profiling studies of myeloid cells uncovering similar cellular distributions in the corresponding GBM mouse model and patients [45, 46].

Two-way hierarchical heat-map clustering analyses of the most differentially expressed genes (p-value < 0.01) between naïve, microglia- and macrophage-like cells **(Table S2)** revealed, in agreement with their different ontogeny, a less pronounced difference between naïve and tumour-associated microglia compared to the monocyte/macrophage cluster **(Fig. 2D)**. In line with the decrease of homeostatic genes in microglia under inflammatory conditions [28], tumour-associated microglia displayed a decreased expression of these genes (e.g. *P2ry12, Sparc*, *Csf1r, Cx3Cr1, Fcrls, Gpr34, Siglech, Mef2c, Olfml3, Tmem119*) when compared to the naïve group **(Fig. 2D)**. Moreover, as expected these genes were not detected in the TAM II population **(Fig. 2D)**. On the other hand, TAM II subset showed up-regulated genes associated with positive regulation of angiogenesis (e.g. *Vegfa*, *Lgals3, Il1β, Cybb, Thbs1, Plek, Vim, Stat1*) and metabolic redox metabolism (e.g. *Cybb, Msrb1*) **(Fig. 2D)**. Both TAM I and TAM II exhibited increased expression levels of genes associated with antigen presentation (e.g., *Cd74, H2-Ab1, H2-Aa, H2-Eb1, H2-D1 and H2-K1*) compared to the naïve group **(Fig.2D)**. Overall, these results point towards the heterogeneous composition of TAMs and their distinct adaptation profiles in the TME of GBM.

Gene set enrichment analysis of tumour-associated microglia or tumour-associated-monocyte/macrophage transcriptional programmes revealed immunological terms shared by both cell types (e.g. inflammatory response and innate immune response). We also identified terms specifically

associated with TAM I (e.g. positive regulation of phagocytosis and T cell mediated cytotoxicity) or TAM II (e.g. positive regulation of cell migration and oxidation-reduction process), suggesting distinct ontogeny-based functional adaptations to the tumour (**Fig. 2E**). The comparison of the TAM I signature with distinct microglia-like clusters identified by *Ochocka and colleagues* [45] uncovered similarities with the defined microglial group 7 (MG7), independently from the gender, and with the female-associated MG2 cluster (**Fig. S5B**). The MG7 cluster exhibits overexpression of genes encoding components of MHC class I (e.g. *H2-D1, H2-K1, B2m),* while the MG2 cluster is characterized by high expression levels of early activation genes (e.g. *Nfkbia*, *Ccl3*, *Ccl12).* By conducting a similar comparison for the TAM II signature, we found great similarity with the defined intermediate state of monocyte and macrophage (intMoMΦ) cluster, characterized by specific genetic markers (e.g. *Lyz2*, *Tgfbi*, *Fth1*), in both male and female mice (**Fig. S5C**). As the intMoMΦ cluster represents the main cluster of infiltrative cells to the tumour described by *Ochocka and colleagues* [45], it corroborates the relevance of our identified TAM II signature.

Next, to strengthen our findings obtained in the GL261 syngeneic mouse model, we compared microglia-like (TAM I) and monocyte/macrophage-like (TAM II) transcriptional signatures with putative corresponding cell types recently described in GBM patients at single-cell resolution [9]. Overall, 8.6% of up-regulated genes in TAM I ($p < 0.01$; Log FC > 0.5) were shared with tumour-associated microglia-like cells in GBM patients. In addition, 7% of differentially expressed genes characterizing TAM II ($p < 0.01$; Log FC > 0.5) were mutually up-regulated in blood monocyte-derived macrophage-like cells in GBM patients (**Fig. S6A**). We used the identified transcriptional signatures discriminating tumour-associated microglia (n = 21 genes; e.g. *CCL4, CCL3, P2RY12, CX3CR1, BIN1, SELPLG, CD83, SALL1*) and macrophages (n = 84 genes; e.g. *TGFBI, THBS1, VIM, IL1B, IL1RN, F13A1, CYBB*) both in the GBM syngeneic murine model and in patients (**Fig. S6A, Table S3**), to verify their prognostic value in low and high grade glioma patients. For this, we took advantage of The Cancer Genome Atlas (TCGA) datasets allowing to link patient survival with corresponding bulk transcriptional data from two publicly available TCGA-databases (TCGA-LGG: low grade glioma and TCGA-GBM: high grade glioma). Notably, a macrophage-like enriched signature correlated with a

worse patient survival compared to a microglia-like enhanced program in LGG patients. Nevertheless, our signatures did not allow to stratify GBM patients, which are overall characterized by higher levels of peripheral monocytic infiltration associated with a worse survival compared to LGG patients (**Fig. 2F**). Of note, we verified these signatures in our PDOX model and identified corresponding up-regulated genes in TAM I and TAM II compared to naïve microglia ($p < 0.01$; Log FC > 0.5). Similarly to the GL261 model, we found microglia- and macrophage-like signatures shared between the PDOX model and GBM patients (TAM I, n = 15 genes; e.g. *CCL4, CCL3, P2RY12, CX3CR1, BIN1*; TAM II, n = 9 genes; e.g. *TGFBI, PLAC8, IFITM3, TMSB10*) (**Fig. S6B**).

Taken together, our scRNA-seq analyses enabled a clear separation of microglia from peripheral monocytic-derived macrophages displaying key transcriptional and functional differences along their adaptation to the tumour, both in the GBM syngeneic mouse model and patients. Our results are in agreement with recent prognostic studies conducted in GBM patients showing that immunosuppressive immune cell infiltrates increase from grade II to grade IV [47] and a reduced immune suppressive phenotype correlates with extended survival, as observed in LGG patients [48]. Collectively, we demonstrate the relevance of discriminating between microglia and monocyte-derived macrophages for prognostic purposes in glioma patients. We take advantage of this critical distinction to separately characterizing tumour-associated microglia and macrophage subsets along GBM progression.

3.3. TAMs rapidly infiltrate the tumour and adapt along GBM progression

By studying TAM heterogeneity along GBM progression in WT mice at single-cell resolution, we detected microglia-like and macrophage-like cell subsets in all analysed tumour stages (i.e. early, intermediate and late time points), indicating that, in agreement with prior observations [8], in this model the infiltration of monocyte-derived macrophages occurs early during tumour growth (**Fig. 3A**). Notably, we observed a gradual decrease in the number of up-regulated genes (early n = 372, intermediate n = 291 and late n = 143) and a relatively constant number of down-regulated genes (early n = 138; intermediate n = 110 and late n = 167) between macrophage-like and microglia-like cells along

tumour stages. These results indicate that the transcriptional programmes of microglia and peripheral infiltrated macrophages converge over time (**Fig. 3B**). Overall, the ratios of microglia-like and macrophage-like cells in the GBM TME did not change across early (TAM I: 29,35%; TAM II: 70,65%) and late (TAM I: 24,43%; TAM II: 75,57%) stages (**Fig. 3C**). Next, we sought to investigate microglia-like and peripheral macrophage-like cell transcriptional programmes along tumour progression separately, with a special focus at early and late stages.

Two-way hierarchical heat-map clustering analyses of the most differentially expressed genes (p-value < 0.01) in TAM I across the tumour stages revealed three clusters mainly represented by naïve microglia, tumour-associated microglia at early stages and an intermediate/late-enriched group (**Fig. S7A**). We analysed up-regulated genes characterizing microglia-like cells at early and late tumour stages versus naïve microglia (**Fig. 3D**). We found great overlap (34.1%) of genes expressed by microglia-like cells between the two stages (e.g. *H2-D1, H2-K1, Cd83, Il1b, Ccl12, Ccl4, Lyz2, Fth1, Ctsb, Atf3, Cst7, B2m, Cd52, Nfkbia*), indicating a core transcriptional programme maintained along GBM progression (**Table S4**). When comparing the levels of specific differentially expressed genes between early (n = 112) and late (n = 329) tumour stages, markers associated with antigen processing and presentation (e.g. *Cd74*, *H2-Ab1*, *H2-Aa*) or T-cell activation and cytotoxicity (e.g. *H2-T23*, *H2-Q7*) and inflammatory response (e.g. *Axl*, *Cybb*) were largely decreased at later tumour stages (**Fig. 3E, Fig. S7B**). In parallel, genes associated with chromatin remodelling (e.g. *Cbx5*, *Ezh2, Nasp)* and actin nucleation/polymerization (e.g. *Arpc1a, Arpc1b*) were enhanced at later stages (**Fig. 3E**). In particular, we found a subset of microglia-like cells up-regulating *Ezh2* expression at late stage. Although studies have demonstrated that *Ezh2* is frequently overexpressed in a wide variety of cancers, mechanistic links of *Ezh2* expression in TAMs to cancer progression remains to be elucidated. In ovarian cancer, *Ezh2* has direct roles on T cell response and inhibition of *Ezh2* in tumour-specific T cells increases the tumour burden *in vivo* [49].

We conducted similar analyses for the macrophage-like subset. Two-way hierarchical heat-map clustering analyses of the most differentially expressed genes (p-value < 0.01) in TAM II along the tumour stages revealed two main clusters represented by tumour-associated macrophages at early stage and an intermediate/late-enriched group (**Fig. S7C**, **Table S4**). We found prominent overlap (54.3%)

of genes up-regulated both at early and late tumour stages expressed by macrophage-like cells compared to naïve microglia (e.g. *Lyz2, Apoe, Fth1, Il1β, H2-K1, H2-D1, Vim, Cd14, Cybb, Tgfbi*) indicating, similarly to microglia-like cells, a main transcriptional programme preserved along GBM progression (**Fig. 3F**).

The comparison of the levels of specific differentially expressed genes between early and late tumour stages revealed the decrease of macrophage activation markers (e.g. *Ccl5, Ass1, Tlr2, Itgb2, Klf4*) as well as, similarly to microglia-like cells, the down-regulation of genes associated with antigen processing and presentation (e.g. *Cd74, H2-Ab1, H2-Aa*) and regulation of T-helper cells (e.g. *H2-Q7, H2-T23*). In addition, type I interferon genes (e.g. *Irf1, Stat1*) were drastically reduced at late stage (**Fig. 3G, Fig. S7D**). Taken together, the reduced antigen cross-presentation ability of both microglia- and macrophage-like cells at later time points may add to the recognised poor recruitment of T cells to the tumour site in GBM [50], thus dampening potential T-cell-mediated tumour eradication along its progression.

To corroborate these results at the protein level, we compared the expression levels of CD74 and MHC-II (encoded by *H2-Ab1*) at early and late stages in corresponding tissue sections. To discriminate brain-resident microglia and blood derived-monocytes/macrophages in immunohistological analyses, we took advantage of the Ivy Glioblastoma Atlas Project to infer TAM spatial localization in laser-micro-dissected regions of GBM patients [51]. Here, we observed an enrichment of microglia-like cells (expressing *BIN1, CX3CR1, P2RY12*) at the leading edge of the tumour, while macrophage-like cells (expressing *IL1RN, TGFBI, THBS1*) were mostly detected in the microvascular compartment (**Fig. 3H**). Similar findings were described by spatial scRNA-seq of the myeloid compartment in GBM patients where *TGFBI*, *VEGFA* and *IL1RN* were mainly expressed by macrophages in the tumour core, while microglial cells enriched in the tumour periphery displayed a reduced expression of these genes [18]. Supporting these observations, 2-photon microscopy in murine GBM sections recently revealed two distinct cell types with different morphological properties composing TAMs. Specifically, cells with reduced branching and increased surface area compared to naïve resident parenchymal cells mainly accumulated at the tumour margins and represented tumour-associated microglia, while monocyte-derived macrophages displaying shrank surface area and increased migratory properties were mainly

located in the tumour core [52]. In agreement with this, we observed a significant reduction of the surface area of macrophage-like infiltrative cells in the tumour core compared to larger and branched microglia-like enriched cells in the tumour margin independent of tumour stage (**Fig. 3I-J** and **Fig. S7E**). In line with our scRNA-seq data, we observed a significant decrease of the antigen presenting cell markers MHC-II (**Fig. 3K**) and CD74 (**Fig. 3L**) at late GBM stage in both the tumour margin and core. Notably, we observed a higher percentage of Iba1+ MHC-II+ cells in the tumour margin compared to tumour core both at early and late stages (**Fig. 3K**), highlighting spatial heterogeneity of TAMs at the protein level. These differences were independent from the mouse gender.

Collectively, these analyses show that TAMs display distinct transcriptional programmes along GBM progression, with both microglia and monocytic-derived macrophages exhibiting decreased antigen presenting cell features at later tumour stages compared to earlier phases.

3.4. TAMs display higher immunological reactivity under aconitate decarboxylase 1 deficiency affecting T cell recruitment

In mammals, immune-responsive gene 1 protein (IRG1), encoded by aconitate decarboxylase 1/immunoresponsive gene 1 (*Acod1/Irg1*), catalyses the production of itaconate from the decarboxylation of cis-aconitate, an intermediate metabolite of the TCA cycle [19, 53]. Itaconate is one of the most up-regulated metabolites in activated macrophages [54] exhibiting anti-inflammatory properties, thus contributing to the resolution of inflammation [20, 21]. Interestingly, it has been recently shown that low doses of itaconate inhibits inflammation, while it promotes inflammation at high doses [55]. Due to the emerging role of various immune metabolites in macrophage reprogramming towards specific phenotypes, we sought to analyse the role of *Acod1/Irg1* in TAM adaptation along GBM progression and characterize TAM subsets under ACOD1 deficiency at single cell resolution. *Acod1* deficiency did not affect the distinct cell types identified by scRNA-seq (**Fig. S8A**). In the GL261 model, we exclusively detected *Acod1/Irg1* induction across the myeloid compartment and, at a larger extent, within the macrophage-like subset (**Fig. 4A**). We observed similar

652 results in the Brain Tumour Immune Micro Environment dataset acquired in GBM patients by RNA-
653 seq [56]. Indeed, *ACOD1/IRG1* expression was up-regulated in both CD49D^{low} microglial cells and
654 CD49D^{high} macrophages, with higher expression levels in IDH-wildtype compared to IDH-mutant
655 gliomas (**Fig. S8B**). Microarray analysis of RNA extracted from CD11b+ MACS-isolated cells from
656 naïve and GL261-implanted mouse brains showed also a significant increase of *Acod1/Irg1* expression
657 in tumour-bearing (n = 3) compared to naïve mice (n = 3) (**Fig. S8C**) [11]. Bone marrow-derived
658 macrophages (BMDMs) co-cultured with GL261 tumour cells *in vitro* showed increased expression of
659 *Acod1* compared to mono-cultured BMDMs, while its expression was undetectable in BMDMs
660 obtained from *Acod1* KO mice (**Fig. 4B**). However, in these co-culture conditions, contrarily to
661 BMDMs treated with LPS (100 ng/ml) for 6 hours, IRG1/ACOD1 protein was not detectable (**Fig.**
662 **S8D**). These results are in agreement with its weak induction at the mRNA level in these co-culture
663 conditions.
664 The analysis of TAM subsets by scRNA-seq across all the stages suggested an over-representation of
665 the macrophage-like population in *Acod1* KO mice (81.15%, 298 cells sequenced) compared to age-
666 matched WT mice (63.11%, 159 cells sequenced) (**Fig. 4C**). Moreover, a higher proportion of TAM II
667 cells versus tumour cells was observed in *Acod1* KO compared to WT mice, while we found no
668 differences for TAM I cells (**Fig. 4D**). Albeit we did not detect differences in the total number of bone-
669 marrow precursors between naïve WT and *Acod1* KO mice (**Fig. S8E**), we observed an increase in the
670 number of CD11b+ cells in the brain of *Acod1* KO compared to WT tumour-bearing mice (**Fig. 4E**).
671 Indeed, immunofluorescence analyses revealed a significant increase in the number of Iba1+ cells at
672 early stages at both the tumour margin and core, thus confirming enhanced infiltration of myeloid cells
673 in *Acod1* KO mice (**Fig. 4F**). Investigation of the exclusively up-regulated genes in microglia-like and
674 macrophage-like cells at early stages in *Acod1* KO mice versus their corresponding counterparts in WT
675 mice identified a major transcriptional effect on macrophage-like (n = 41 genes) compared to microglia-
676 like (n = 3 genes) cells (**Fig. 4G**). Genes associated with TAM recruitment, such as *Ccr2, Mif, Ldha*
677 *and Tspo*, were uniquely overexpressed in macrophage-like cells from *Acod1* KO mice (**Fig. 4G**).
678 Specifically, the CCL2/CCR2 axis is essential for monocyte migration into the inflamed CNS [57, 58].
679 Further, macrophage migration inhibitory factor (MIF) plays an important role in regulating

680 inflammatory responses in innate immune cells [59] and can directly interact with CXCR2 and CXCR4
681 promoting inflammatory activity and leukocyte chemotaxis in cancer [60].
682 Similarly to early stages, the number of exclusively up-regulated genes was higher in macrophage-like
683 (n = 68 genes) compared to microglia-like (n = 9 genes) cells when comparing *Acod1* KO with WT
684 tumour-bearing mice at late stage (**Fig. 5A**, **Table S5**), confirming that the lack of *Acod1/Irg1* mainly
685 affected the transcriptional programme of peripheral infiltrating macrophages compared to microglia.
686 Gene set enrichment analysis of macrophage-like cell exclusively up-regulated genes at late GBM stage
687 in *Acod1 KO* compared to WT mice uncovered enrichment of terms associated with inflammation (e.g.
688 *Irf1*), antigen processing and presentation via MHC class I (e.g. *H2-K1*) and T cell mediated cytotoxicity
689 (e.g. *H2-T23*) (**Fig. 5A**, **Fig. S9A**). The common 15 microglia-like and macrophage-like cell up-
690 regulated genes in *Acod1* KO compared to WT mice were associated with antigen presenting cell (e.g.
691 *Cd74, H2-Ab1*) and inflammatory (*Stat1*) markers (**Fig. 5A**), reflecting an enhanced immune activation
692 at late stage in *Acod1* KO mice. In agreement with these results at single-cell resolution, we detected a
693 higher induction of antigen presentation (e.g. *Cd74*, *H2-Ab1*, *H2-Aa*) and inflammatory (e.g. *Irf1*)
694 transcripts in *ex vivo* CD11b+ isolated TAMs from *Acod1* KO compared to WT tumour-bearing mice
695 at late stages (**Fig. 5B**). IRF family members play essential roles in regulating immune responses [61,
696 62] and seminal work has shown that *Irf1* KO mice exhibit impaired NK cell maturation and defective
697 Th1 responses [63, 64]. Additionally, IRF1 operates as a tumour suppressor and its inactivation has
698 been shown to significantly increase risk of malignancy [65]. To investigate the expression of IRF1 at
699 the protein level, we conducted immunofluorescence analysis and detected higher numbers of
700 IBA1+IRF1+ positive cells in the tumour core in *Acod1* KO compared to WT mice (**Fig. 5C**). Amongst
701 the downstream targets of IRF1, we detected by flow cytometry an increased expression of MHC-II in
702 TAMs isolated at late stage from *Acod1* KO compared to WT mice (**Fig. 5D, Fig. S9B**). Additionally,
703 in brain sections from *Acod1* KO tumour-bearing mice, we detected a significant increase of CD74
704 expressed by macrophage-like cells, which were enriched in the tumour core, compared to WT mice
705 (**Fig. 5E**). As gliomas are characterized as "immunologically silent" in IDH-mutant or "lymphocyte-
706 depleted" in IDH-wildtype subtypes [66], we sought to investigate whether the ablation of *Acod1*, which
707 induces an enhanced TAM immunogenic phenotype, could influence the recruitment of T cells to the

tumour site. Indeed, we observed an increase of the lymphocytic population in *Acod1 KO* compared to WT mice, both in our scRNA-seq dataset (**Fig. S9C**) and by flow cytometry (**Fig. 5F, Fig. S9B**), thus suggesting an effective crosstalk between TAMs and the adaptive immune cell compartment. We further identified up-regulated genes comparing lymphocytes isolated from *Acod1* KO and WT mice at early stages ($p < 0.01$; Log FC > 0.5; n = 17 genes; e.g. *Dbi, Ifitm3, Lgals1, Mt1, Pfn1*) (**Fig. S9D, Table S6**), while we did not conduct the corresponding analysis at late stage due to the low number of gathered lymphocytes in WT mice (**Fig. S9C**).

Lastly, in order to elucidate if specific TAM subsets under ACOD1 deficiency display enhanced immunogenic phenotypes, we conducted single cell trajectory inference analyses. We showed higher macrophage-like cell heterogeneity in *Acod1 KO* compared to WT mice, thus suggesting that ACOD1 deficiency also supports TAM diversity (**Fig. 5G**). Specifically, pseudo-time analyses uncovered four distinct cellular states across the TAM II subset under *Acod1* deficiency (**Fig. S10A-B**). Further analysis of exclusive genes driving the most prominent cellular state (cellular state four) revealed a TAM II subset exclusively present in *Acod1* deficient tumour-bearing mice, which might support leukocyte migration and T cell activation (e.g. *Ccl17, Ccl22, Ccr7, IL12b, Cd1d1*) to the tumour site (**Fig. S10C**). This subset was also characterized by higher expression levels of genes encoding serine proteinase inhibitors (e.g. *Serpinb6b* and *Serpinb9*) (**Fig. S10C**), which have been described to play a critical role in T lymphocyte mediated immunity [67]. Although *Acod1/Irg1* silencing in macrophages has been shown to significantly reduce the peritoneal tumour burden [23], the analysis of tumour growth in GL261 tumour-bearing mice did not show significant differences between WT and *Acod1* KO (data not shown), neither we detected differences in the mouse survival (**Fig. S10D**), most probably due to the very high aggressiveness of the tumour in the analysed model.

730 **4. CONCLUSION**

731

732 In summary, we here elucidated the diversity of the myeloid compartment along GBM progression and
733 under ACOD1 deficiency. Specifically, we demonstrate that the myeloid compartment is the most
734 affected and heterogeneous stromal cell component in GBM, with microglia and macrophages acquiring
735 key transcriptional differences and rapidly adapting along GBM progression. Specifically, we show that
736 TAMs display a decreased antigen-presenting cell signature along GBM progression, which is retained
737 under ACOD1 deficiency. Collectively, these results are in line with the anti-inflammatory role of
738 ACOD1/itaconate [68], since their absence skewed TAMs in GBM towards a more reactive and
739 immunogenic phenotype. Mechanistically, itaconate modifies a range of proteins in macrophages,
740 including KEAP1, which leads to NRF2 activation and induction of NRF2-dependent genes encoding
741 anti-inflammatory and antioxidant factors. Similarly, itaconate might also modify GILT (IFI30), a
742 protein that regulates antigen presentation [68]. However, how itaconate and GILT might potentially
743 contribute to the decrease of antigen presentation marks warrants further investigation. From a
744 therapeutic point of view, although immune checkpoint blockade therapy has markedly improved
745 survival in several immunogenic cancers, such as melanoma, its efficacy has not been extended to GBM
746 patients, as observed in a randomized phase III clinical trial for recurrent GBM (CheckMate 143;
747 Identifier NCT 02017717) [69]. As it is becoming increasingly evident that a mono-therapeutic
748 approach is unlikely to provide anti-tumour efficacy, the combination of ACOD1 suppression in TAMs,
749 which enables to harness both the innate and adaptive immune systems, together with the inhibition of
750 immune checkpoints may advance therapeutic successes against GBM and other solid tumours.

751 **ACKNOWLEDGMENTS**

752

753 We thank Amandine Bernard for mouse genotyping and western blotting, Virginie Baus for helping
754 with the MRI as well as Thomas Cerutti for the support with flow cytometry experiments. We are
755 grateful to Dr Oihane Uriarte and Dr Tony Heurtaux for aiding with gentleMACS™ Dissociator. Y.P.A.
756 and C.S. were supported by the Luxembourg National Research Fund (PRIDE15/10675146/CANBIO
757 and AFR6916713, respectively) and the Fondation du Pélican de Mie et Pierre Hippert-Faber under the
758 aegis of Fondation de Luxembourg. Y.A.Y. was supported by GLIOTRAIN ITN funded by the
759 European Union's Horizon 2020 research and innovation programme under the Marie Skłodowska-
760 Curie grant agreement No 766069 (The material presented and views expressed here are the
761 responsibility of the author(s) only. The EU Commission takes no responsibility for any use made of
762 the information set out). A.S. was supported by the C14/BM/7975668/CaSCAD project as well as by
763 the National Biomedical Computation Resource (NBCR) through the NIH P41 GM103426 grant from
764 the National Institutes of Health. A.M. was supported by Action Lions "Vaincre le Cancer"
765 Luxembourg. We acknowledge financial support by the Luxembourg Institute of Health (MIGLISYS)
766 and the Luxembourg Centre for Systems Biomedicine.

767

768 **AUTHOR CONTRIBUTIONS**

769

770 YPA, SPN and AlM designed the project; YPA, KG, AO, CS, AS and RH performed experiments;
771 YPA, ArM, KG, AC, YAY, AG and AlM analysed experiments; AP supported in silico analyses; DC
772 provided animals; AS set up and supervised scRNA-seq analyses; YPA and AlM wrote the manuscript;
773 all the authors edited and approved the manuscript.

774

775 **CONFLICT OF INTEREST**

776 The authors declare no competing interests.

777 **FIGURE TITLES AND LEGENDS**

778

779 **Fig. 1. Cell type diversity in naïve and GL261 tumour-bearing mice at different tumour stages,**
780 **both from wild type and ACOD1/IRG1 knock-out mice.** (**A**) Flowchart depicting the overall design
781 of the scRNA-seq analyses. Naïve- and macro-dissected brain tumour regions from both wild type and
782 ACOD1/IRG1 knock-out (KO) mice were processed by scRNA-seq analyses. Samples were collected
783 at different time points (early: 5-10 mm3; intermediate: 20-25 mm3; late: 30-35 mm3) according to
784 tumour volume measured by magnetic resonance imaging (MRI). One biological replicate per
785 experimental condition (WT/naïve; WT/early; WT/intermediate; WT/late; ACOD1/IRG1 KO/naïve;
786 ACOD1/IRG1 KO/early; ACOD1/IRG1 KO/intermediate; ACOD1/IRG1 KO/late) has been taken into
787 account for subsequent analyses. (**B**) 2D-tSNE representation of all single cells included in the study (n
788 = 5'659 cells) grouped within 12 cell clusters. (**C**) Cell type-specific markers allowing the identification
789 of stromal cell types: pericytes (*Dbi*$^+$), lymphocytes (*Trac*$^+$), ependymal cells (*Ttr*$^+$), endothelial cells
790 (*Pecam1*$^+$), astrocytes (*Slc1a2*$^+$), oligodendrocytes (*Plp1*$^+$), oligodendrocyte precursor cells (OPCs,
791 *Pdgfra*$^+$), neural stem cells (NSCs, *Meg3*$^+$), myeloid cells 1 (*Itgam*$^+$) and myeloid cells 2 (*Itgam*$^+$). See
792 **Fig. S1** for additional cell type-specific markers used for clusters annotation. (**D**) 2D-tSNE
793 representation showing naïve (in black) and tumour-associated (in red) cells. (**E**) Examples of the most
794 up-regulated genes (p-value < 0.01, logFC > 0.5) per cell type in tumour-bearing mice.

795

796 **Fig. 2. Microglia- (TAM I) and macrophage-like (TAM II) subsets display discrete functional**
797 **adaptation in the GBM syngeneic GL261 murine model.** (**A**) Colour-coded 2D-tSNE representation
798 showing three distinct myeloid cell subsets in WT mice: naïve, TAM I and TAM II clusters, irrespective
799 of the tumour stage. Results show one biological replicate per experimental condition (WT/naïve;
800 WT/early; WT/intermediate; WT/late). (**B**) 2D-tSNE representation showing the expression of
801 microglia homeostatic genes (*Gpr34*, *Hexb*, *P2ry12*, *Siglech* and *Sparc*) and macrophage-like markers
802 (*Arg1, Ccr2, Ly6c2, Mrc1 and Tgfbi*). (**C**) Percentage of CD11b+ P2ry12+ cells in naïve and tumour-
803 bearing mice quantified by flow cytometry at late stage of the disease. (**D**) Two-way hierarchical heat-

map clustering analyses of the most differentially expressed genes (p-value < 0.01) for each myeloid cluster: naïve, TAM I and TAM II, irrespective of the tumour stage, **Table S2**). Scale bar represents color-coded z-scores. (**E**) Gene ontology functional network of TAM I (left graph) and TAM II (right graph) versus naïve microglia. Node size correlates to gene set numbers and annotated nodes were defined as containing ≥ 15 genes. (**F**) Kaplan-Meier survival analysis in low and high grade glioma patients (TCGA-LGG and TCGA-GBM databases) with high and low TAM II enriched signature. Statistical analysis for (**C**) Unpaired Student *t* test (WT = 4, *Acod1* KO n = 3), mean ± SEM, ** p < 0.01.

Fig. 3. TAM subsets spatial and temporal characterisation along Glioblastoma development. (**A**) Myeloid tSNE plot colour coded representation for tumour progression (green: early; blue: intermediate; purple: late stage). Results show one biological replicate per experimental condition (WT/naïve; WT/early; WT/intermediate; WT/late). (**B**) Number of up- and down-regulated genes (p-value < 0.01, FC > ± 0.5) between TAM II and TAM I along GBM progression. (**C**) Relative proportions of TAM I and TAM II subsets at early and late GBM stages obtained by scRNA-seq analysis. (**D**) Venn diagram representation showing TAM I shared (n = 228) and exclusively up-regulated genes at early (n = 112) and late (n = 329) stages versus naïve microglia. (**E**) Single-cell bar plots showing selected top differentially expressed genes in TAM I between early and late GBM stages. (**F**) Venn diagram representation showing TAM II shared (n = 403) and exclusively up-regulated genes at early (n = 262) and late (n = 77) stages versus naïve microglia. (**G**) Single-cell bar plots showing selected top differentially expressed genes in TAM II between early and late GBM stages. (**H**) RNA-seq profiles of laser-microdissected regions of GBM patients for microglia (*BIN1, CX3CR1, P2RY12*) and peripheral monocyte-derived cell (*IL1RN, TGFBI, THBS1*) marker genes. Data extracted from the Ivy Glioblastoma Atlas Project (PCAN: pseudopalisading cells around necrosis; MvP: microvascular proliferation). (**I**) Representative immunofluorescence pictures of Iba1 positive cells in the tumour margin and core in murine brain sections. (**J**) Quantification of Iba1 surface area in the tumour margin and tumour core at early and late stages. (**K-L**) Representative immunofluorescence pictures and

quantification for (**K**) MHC-II and (**L**) CD74 staining in the tumour margin and core at early and late stages.

Statistical analysis for (**J**) Two-way ANOVA with Sidak's multiple comparison corrections (early n = 3 (2 females and 1 male) and late n = 3 (females)), (**K-L**) Two-way ANOVA with Sidak's multiple comparison corrections (early n = 3 (2 females and 1 male) and late n = 4 (2 females and 2 males), mean ± SEM, * $p < 0.05$; ** $p < 0.01$; *** $p < 0.001$; ns = not significant. Scale bars in I, K and L = 50µm. TAM I, tumour-associated microglia, TAM II, tumour-associated macrophage; PCAN, Pseudopalisading cells around necrosis; MvP, Microvascular proliferation; T. margin, tumour margin; T. core, tumour core; Iba1, Allograft inflammatory factor 1; MHC-II, Major histocompatibility complex class II molecules; CD74, HLA class II histocompatibility antigen gamma chain.

Fig. 4. *Acod1* expression is induced in TAMs and its deficiency affects their recruitment. (**A**) *Irg1/Acod1* expression levels across the main 10 stromal cell-types identified by scRNA-seq. Results show one biological replicate per experimental condition (WT/naïve; WT/early; WT/intermediate; WT/late; ACOD1/IRG1 KO/naïve; ACOD1/IRG1 KO/early; ACOD1/IRG1 KO/intermediate; ACOD1/IRG1 KO/late). (**B**) Expression levels of *Acod1* in BMDMs from WT and *Acod1* KO mice upon co-culture with GL261 tumour cells at 24 and 48h (WT n = 2, *Acod1* KO n = 2). (**C**) Myeloid tSNE plot colour coded (brown: WT; orange: *Acod1* KO) and respective number of myeloid cells sequenced by scRNA-seq according to the genotype (WT, naïve: 86 cells; TAM I: 87 cells; TAM II 159 cells. *Acod1* KO, naïve: 112 cells; TAM I: 91 cells; TAM II: 298 cells) taking into account all the tumour stages. (**D**) Graphical representation depicting the proportions of TAMs and tumour cells in WT (upper) and *Acod1* KO (bottom) mice taking into account all the tumour stages. (**E**) Number of CD11b+ cells isolated from WT and *Acod1* KO from tumour-bearing mouse brains at late stage. Bars represent the ratio of the number of CD11b+ cells over the number of total cells applied to the columns. (**F**) Immunofluorescence pictures depicting Iba1 positive cells in the tumour margin (left) and core (right). Number of Iba1 positive cells were quantified in WT and *Acod1* KO mice at early GBM stage. Different geometrical forms (triangles, squares and circles) represent individual mice and technical replicates within each mouse are displayed with the same form. (**G**) Venn diagram representation showing shared

and exclusive up-regulated genes in *Acod1* KO TAM I (n = 3) and TAM II (n = 41) at early stage versus their respective counterparts in age-matched WT cells. Notch plot representation of selected genes exclusively up-regulated by TAM II in *Acod1* KO mice compared with WT mice at early stage. Statistical analysis for (**A**) pairwise Wilcoxon test with p-value adjusted with Benjamini Hochberg method; (**E**) Unpaired Student *t* test (WT = 6, *Acod1* KO n= 4); (**F**) Unpaired Student *t* test (WT early n = 4*; Acod1* KO early n = 3), mean ± SEM. * $p < 0.05$, *** $p < 0.001$. Scale bars in F = 50µm. WT, wild-type; KO, knock-out; *Acod1*, aconitate decarboxylase 1; TAM I, tumour-associated microglia; TAM II, tumour-associated macrophage; BMDMs, bone marrow-derived macrophages; Iba1, Allograft inflammatory factor 1; *Ccr2*, C-C chemokine receptor type 2; *Mif*, Macrophage migration inhibitory factor; *Ldha*, Lactate dehydrogenase A; *Tspo*, Translocator protein.

Fig. 5. TAMs under *Acod1* deficiency display higher antigen presenting cell programmes associated with increased lymphocytic recruitment at late GBM stage. (**A**) Venn diagram representation showing shared (n = 15) and exclusive up-regulated genes in *Acod1* KO TAM I (n = 9) and TAM II (n = 68) at late stage versus their respective counterparts in age-matched WT cells (**Table S5**). Corresponding notch plot representations of selected shared or unique genes up-regulated in TAM I and TAM II cells in *Acod1* KO mice compared to age-matched WT mice at late stage. Results show one biological replicate per experimental condition (WT/naïve; WT/early; WT/late; ACOD1/IRG1 KO/naïve; ACOD1/IRG1 KO/early; ACOD1/IRG1 KO/late). (**B**) Expression levels of *Cd74, H2-Ab1, H2-Aa* and *Irf1* genes in CD11b+ cells isolated from WT and *Acod1* KO mice at late stages. (**C**) Immunofluorescence pictures (left) and quantification (right) of IRF1 expression in Iba1+ cells in the tumour core region at late stage in *Acod1* KO and WT mouse brain sections. (**D**) Representative overlay histogram (left) and quantification (right) of MHC-II expression in TAMs analysed in WT and *Acod1* KO mice at late stage by flow cytometry. (**E**) Immunofluorescence pictures (left) and quantification (right) of CD74 expression in Iba1+ cells in the tumour core region at late stage in *Acod1* KO and WT mouse brain sections. Different geometrical forms (triangles, squares and circles) represent individual mice and technical replicates within each mouse are displayed with the same form (**F**). Percentage of CD11b- CD45+ lymphocytes at late stage quantified by flow cytometry. (**G**) Single cell trajectory

887 inference analysis of 335 myeloid cells from WT naïve and tumour-bearing mice (left graph) and 501
888 myeloid cells from *Acod1* KO naïve and tumour-bearing mice (right graph). Statistical analysis for (**B**)
889 Unpaired Student t test (WT n = 4 (3 females and 1 male), *Acod1* KO n = 2 (females)); (**C**) Unpaired
890 Student t test (WT n = 3 (females), *Acod1* KO n = 3 (2 females and 1 male); (**D**) Unpaired Student t test
891 (WT n = 7 (2 females and 5 males), *Acod1* KO n = 3 (males)), (**E**) Unpaired Student t test (WT n = 3
892 (females), *Acod1* KO n = 3 (2 females and 1 male)), (**F**) Unpaired Student t test (WT n = 5 (2 females
893 and 3 males), *Acod1* KO n = 3 (males)), mean ± SEM, * $p < 0.05$; ** $p < 0.01$. Scale bars = 20μm in
894 (**C**) and 50μm in (**E**). and. *Cxcl9*, C-X-C Motif Chemokine Ligand 9; *Cd36*, CD36 Molecule; *Clec7a*,
895 C-Type Lectin Domain Containing 7A; *Cd74*, CD74 Molecule; *H2-Ab1*, Major Histocompatibility
896 Complex, Class II; *Stat1*, Signal Transducer And Activator Of Transcription 1; *Irf1*, Interferon
897 Regulatory Factor 1; *H2-K1*, Major Histocompatibility Complex, Class I, A; *H2-T23*, Major
898 Histocompatibility Complex, Class I, E; *H2-Aa*, Major Histocompatibility Complex, Class II; WT,
899 wild-type; KO, knock-out; TAM I, tumour-associated microglia; TAM II, tumour-associated
900 macrophage.

901 **REFERENCES**
902
903 1. Lathia, J.D., et al., *Deadly teamwork: neural cancer stem cells and the tumor*
904 *microenvironment*. Cell Stem Cell, 2011. **8**(5): p. 482-5.
905 2. Venkatesan, S. and C. Swanton, *Tumor Evolutionary Principles: How Intratumor Heterogeneity*
906 *Influences Cancer Treatment and Outcome*. Am Soc Clin Oncol Educ Book, 2016. **35**: p. e141-
907 9.
908 3. Quail, D.F. and J.A. Joyce, *The Microenvironmental Landscape of Brain Tumors*. Cancer Cell,
909 2017. **31**(3): p. 326-341.
910 4. Ginhoux, F., et al., *Fate mapping analysis reveals that adult microglia derive from primitive*
911 *macrophages*. Science, 2010. **330**(6005): p. 841-5.
912 5. Schulz, C., et al., *A lineage of myeloid cells independent of Myb and hematopoietic stem cells*.
913 Science, 2012. **336**(6077): p. 86-90.
914 6. Glass, R. and M. Synowitz, *CNS macrophages and peripheral myeloid cells in brain tumours*.
915 Acta Neuropathol, 2014. **128**(3): p. 347-62.
916 7. Hambardzumyan, D., D.H. Gutmann, and H. Kettenmann, *The role of microglia and*
917 *macrophages in glioma maintenance and progression*. Nat Neurosci, 2016. **19**(1): p. 20-7.
918 8. Bowman, R.L., et al., *Macrophage Ontogeny Underlies Differences in Tumor-Specific Education*
919 *in Brain Malignancies*. Cell Rep, 2016. **17**(9): p. 2445-2459.
920 9. Muller, S., et al., *Single-cell profiling of human gliomas reveals macrophage ontogeny as a*
921 *basis for regional differences in macrophage activation in the tumor microenvironment*.
922 Genome Biol, 2017. **18**(1): p. 234.
923 10. Friebel, E., et al., *Single-Cell Mapping of Human Brain Cancer Reveals Tumor-Specific*
924 *Instruction of Tissue-Invading Leukocytes*. Cell, 2020. **181**(7): p. 1626-1642 e20.
925 11. Szulzewsky, F., et al., *Glioma-associated microglia/macrophages display an expression profile*
926 *different from M1 and M2 polarization and highly express Gpnmb and Spp1*. PLoS One, 2015.
927 **10**(2): p. e0116644.
928 12. Zeiner, P.S., et al., *Distribution and prognostic impact of microglia/macrophage*
929 *subpopulations in gliomas*. Brain Pathol, 2018.
930 13. Gabrusiewicz, K., et al., *Glioblastoma-infiltrated innate immune cells resemble M0*
931 *macrophage phenotype*. JCI Insight, 2016. **1**(2).
932 14. Macosko, E.Z., et al., *Highly Parallel Genome-wide Expression Profiling of Individual Cells Using*
933 *Nanoliter Droplets*. Cell, 2015. **161**(5): p. 1202-1214.
934 15. Shalek, A.K., et al., *Single-cell transcriptomics reveals bimodality in expression and splicing in*
935 *immune cells*. Nature, 2013. **498**(7453): p. 236-40.
936 16. Tang, F., et al., *mRNA-Seq whole-transcriptome analysis of a single cell*. Nat Methods, 2009.
937 **6**(5): p. 377-82.
938 17. Jordao, M.J.C., et al., *Single-cell profiling identifies myeloid cell subsets with distinct fates*
939 *during neuroinflammation*. Science, 2019. **363**(6425).
940 18. Darmanis, S., et al., *Single-Cell RNA-Seq Analysis of Infiltrating Neoplastic Cells at the*
941 *Migrating Front of Human Glioblastoma*. Cell Rep, 2017. **21**(5): p. 1399-1410.
942 19. Michelucci, A., et al., *Immune-responsive gene 1 protein links metabolism to immunity by*
943 *catalyzing itaconic acid production*. Proc Natl Acad Sci U S A, 2013. **110**(19): p. 7820-5.
944 20. Mills, E.L., et al., *Itaconate is an anti-inflammatory metabolite that activates Nrf2 via*
945 *alkylation of KEAP1*. Nature, 2018. **556**(7699): p. 113-117.
946 21. Hooftman, A. and L.A.J. O'Neill, *The Immunomodulatory Potential of the Metabolite Itaconate*.
947 Trends Immunol, 2019. **40**(8): p. 687-698.
948 22. Dominguez-Andres, J., et al., *The Itaconate Pathway Is a Central Regulatory Node Linking*
949 *Innate Immune Tolerance and Trained Immunity*. Cell Metab, 2019. **29**(1): p. 211-220 e5.
950 23. Weiss, J.M., et al., *Itaconic acid mediates crosstalk between macrophage metabolism and*
951 *peritoneal tumors*. J Clin Invest, 2018. **128**(9): p. 3794-3805.

952 24. Pires-Afonso, Y., S.P. Niclou, and A. Michelucci, *Revealing and Harnessing Tumour-Associated Microglia/Macrophage Heterogeneity in Glioblastoma.* Int J Mol Sci, 2020. **21**(3).
954 25. Cordes, T., et al., *Immunoresponsive Gene 1 and Itaconate Inhibit Succinate Dehydrogenase to Modulate Intracellular Succinate Levels.* J Biol Chem, 2016. **291**(27): p. 14274-14284.
956 26. Bougnaud, S., et al., *Molecular crosstalk between tumour and brain parenchyma instructs histopathological features in glioblastoma.* Oncotarget, 2016. **7**(22): p. 31955-71.
958 27. Golebiewska, A., et al., *Patient-derived organoids and orthotopic xenografts of primary and recurrent gliomas represent relevant patient avatars for precision oncology*. Acta Neuropathol, 2020. **140**(6): p. 919-949.
961 28. Sousa, C., et al., *Single-cell transcriptomics reveals distinct inflammation-induced microglia signatures*. EMBO Rep, 2018. **19**(11).
963 29. Trapnell, C., et al., *The dynamics and regulators of cell fate decisions are revealed by pseudotemporal ordering of single cells.* Nat Biotechnol, 2014. **32**(4): p. 381-386.
965 30. Qiu, X., et al., *Reversed graph embedding resolves complex single-cell trajectories.* Nat Methods, 2017. **14**(10): p. 979-982.
967 31. Buttini, M., et al., *Expression of human apolipoprotein E3 or E4 in the brains of Apoe-/- mice: isoform-specific effects on neurodegeneration*. J Neurosci, 1999. **19**(12): p. 4867-80.
969 32. Oh, T., et al., *Immunocompetent murine models for the study of glioblastoma immunotherapy*. J Transl Med, 2014. **12**: p. 107.
971 33. Aslan, K., et al., *Heterogeneity of response to immune checkpoint blockade in hypermutated experimental gliomas.* Nat Commun, 2020. **11**(1): p. 931.
973 34. Fecci, P.E., et al., *Systemic CTLA-4 blockade ameliorates glioma-induced changes to the CD4+ T cell compartment without affecting regulatory T-cell function.* Clin Cancer Res, 2007. **13**(7): p. 2158-67.
976 35. Qian, J., et al., *TLR2 Promotes Glioma Immune Evasion by Downregulating MHC Class II Molecules in Microglia*. Cancer Immunol Res, 2018. **6**(10): p. 1220-1233.
978 36. Khalsa, J.K., et al., *Immune phenotyping of diverse syngeneic murine brain tumors identifies immunologically distinct types.* Nat Commun, 2020. **11**(1): p. 3912.
980 37. Tasic, B., et al., *Adult mouse cortical cell taxonomy revealed by single cell transcriptomics.* Nat Neurosci, 2016. **19**(2): p. 335-46.
982 38. Cahoy, J.D., et al., *A transcriptome database for astrocytes, neurons, and oligodendrocytes: a new resource for understanding brain development and function.* J Neurosci, 2008. **28**(1): p. 264-78.
985 39. Tabula Muris, C., et al., *Single-cell transcriptomics of 20 mouse organs creates a Tabula Muris.* Nature, 2018. **562**(7727): p. 367-372.
987 40. Sankowski, R., et al., *Mapping microglia states in the human brain through the integration of high-dimensional techniques.* Nat Neurosci, 2019. **22**(12): p. 2098-2110.
989 41. Venteicher, A.S., et al., *Decoupling genetics, lineages, and microenvironment in IDH-mutant gliomas by single-cell RNA-seq.* Science, 2017. **355**(6332).
991 42. Patel, A.P., et al., *Single-cell RNA-seq highlights intratumoral heterogeneity in primary glioblastoma.* Science, 2014. **344**(6190): p. 1396-401.
993 43. Szatmari, T., et al., *Detailed characterization of the mouse glioma 261 tumor model for experimental glioblastoma therapy*. Cancer Sci, 2006. **97**(6): p. 546-53.
995 44. Schaaf, M.B., A.D. Garg, and P. Agostinis, *Defining the role of the tumor vasculature in antitumor immunity and immunotherapy*. Cell Death Dis, 2018. **9**(2): p. 115.
997 45. Ochocka, N., et al., *Single-cell RNA sequencing reveals functional heterogeneity of glioma-associated brain macrophages.* Nat Commun, 2021. **12**(1): p. 1151.
999 46. Pombo Antunes, A.R., et al., *Single-cell profiling of myeloid cells in glioblastoma across species and disease stage reveals macrophage competition and specialization.* Nat Neurosci, 2021. **24**(4): p. 595-610.

47. Pinton, L., et al., *The immune suppressive microenvironment of human gliomas depends on the accumulation of bone marrow-derived macrophages in the center of the lesion.* J Immunother Cancer, 2019. **7**(1): p. 58.
48. Alban, T.J., et al., *Global immune fingerprinting in glioblastoma patient peripheral blood reveals immune-suppression signatures associated with prognosis.* JCI Insight, 2018. **3**(21).
49. Zhao, E., et al., *Cancer mediates effector T cell dysfunction by targeting microRNAs and EZH2 via glycolysis restriction.* Nat Immunol, 2016. **17**(1): p. 95-103.
50. Woroniecka, K.I., et al., *T-cell Dysfunction in Glioblastoma: Applying a New Framework.* Clin Cancer Res, 2018. **24**(16): p. 3792-3802.
51. Puchalski, R.B., et al., *An anatomic transcriptional atlas of human glioblastoma.* Science, 2018. **360**(6389): p. 660-663.
52. Chen, Z., J.L. Ross, and D. Hambardzumyan, *Intravital 2-photon imaging reveals distinct morphology and infiltrative properties of glioblastoma-associated macrophages.* Proc Natl Acad Sci U S A, 2019. **116**(28): p. 14254-14259.
53. Cordes, T., A. Michelucci, and K. Hiller, *Itaconic Acid: The Surprising Role of an Industrial Compound as a Mammalian Antimicrobial Metabolite.* Annu Rev Nutr, 2015. **35**: p. 451-73.
54. Lampropoulou, V., et al., *Itaconate Links Inhibition of Succinate Dehydrogenase with Macrophage Metabolic Remodeling and Regulation of Inflammation.* Cell Metab, 2016. **24**(1): p. 158-66.
55. Muri, J., et al., *Electrophilic Nrf2 activators and itaconate inhibit inflammation at low dose and promote IL-1beta production and inflammatory apoptosis at high dose.* Redox Biol, 2020. **36**: p. 101647.
56. Klemm, F., et al., *Interrogation of the Microenvironmental Landscape in Brain Tumors Reveals Disease-Specific Alterations of Immune Cells.* Cell, 2020. **181**(7): p. 1643-1660 e17.
57. Chen, Z., et al., *Cellular and Molecular Identity of Tumor-Associated Macrophages in Glioblastoma.* Cancer Res, 2017. **77**(9): p. 2266-2278.
58. Zhang, J., et al., *A dialog between glioma and microglia that promotes tumor invasiveness through the CCL2/CCR2/interleukin-6 axis.* Carcinogenesis, 2012. **33**(2): p. 312-9.
59. Calandra, T. and T. Roger, *Macrophage migration inhibitory factor: a regulator of innate immunity.* Nat Rev Immunol, 2003. **3**(10): p. 791-800.
60. Guda, M.R., et al., *Pleiotropic role of macrophage migration inhibitory factor in cancer.* Am J Cancer Res, 2019. **9**(12): p. 2760-2773.
61. Taniguchi, T., et al., *IRF family of transcription factors as regulators of host defense.* Annu Rev Immunol, 2001. **19**: p. 623-55.
62. Borden, E.C., et al., *Interferons at age 50: past, current and future impact on biomedicine.* Nat Rev Drug Discov, 2007. **6**(12): p. 975-90.
63. Ogasawara, K., et al., *Requirement for IRF-1 in the microenvironment supporting development of natural killer cells.* Nature, 1998. **391**(6668): p. 700-3.
64. Lohoff, M., et al., *Interferon regulatory factor-1 is required for a T helper 1 immune response in vivo.* Immunity, 1997. **6**(6): p. 681-9.
65. Alsamman, K. and O.S. El-Masry, *Interferon regulatory factor 1 inactivation in human cancer.* Biosci Rep, 2018. **38**(3).
66. Thorsson, V., et al., *The Immune Landscape of Cancer.* Immunity, 2018. **48**(4): p. 812-830 e14.
67. Ashton-Rickardt, P.G., *An emerging role for Serine Protease Inhibitors in T lymphocyte immunity and beyond.* Immunol Lett, 2013. **152**(1): p. 65-76.
68. O'Neill, L.A.J. and M.N. Artyomov, *Itaconate: the poster child of metabolic reprogramming in macrophage function.* Nat Rev Immunol, 2019. **19**(5): p. 273-281.
69. Reardon, D.A., et al., *Effect of Nivolumab vs Bevacizumab in Patients With Recurrent Glioblastoma: The CheckMate 143 Phase 3 Randomized Clinical Trial.* JAMA Oncol, 2020. **6**(7): p. 1003-1010.

SUPPLEMENTARY INFORMATION

Supplementary Figure 1. Gene expression of distinct cell-types identified by scRNA-seq in the GL261 syngeneic murine model and naïve mice, related to figure 1.

Supplementary Figure 2. Expression of *Myc* and *Trp53* genes in the GL261 GBM murine model, related to figure 1.

Supplementary Figure 3. Gene expression of distinct cell-types present in naïve and tumour-bearing mice, related to figure 1.

Supplementary Figure 4. Comparisons of gene expression profiles between myeloid cells 1 and tumour endothelial cells in the GBM syngeneic GL261 and patient-derived orthotopic xenograft (PDOX) mouse models, related to figure 1.

Supplementary Figure 5. Characterization of TAM I and TAM II subsets by FACS and by comparing their gene expression signatures with datasets gathered from the literature, related to figure 2.

Supplementary Figure 6. Microglia- versus macrophage-like features in GBM, related to figure 2.

Supplementary Figure 7. Differential microglia and monocytic-derived macrophage transcriptional adaptation along GBM progression, related to figure 3.

Supplementary Figure 8. *Acod1* expression levels in TAMs, related to figure 4.

Supplementary Figure 9. TAM and lymphocytic signatures under *Acod1* deficiency, related to figure 5.

Supplementary Figure 10. TAM II cellular state diversity under *Acod1* deficiency, related to figure 5.

Supplementary Table 1. Up-regulated differentially expressed genes in tumour-associated clusters (astrocytes, endothelial, oligodendrocytes, myeloid) versus correspondent naïve cells (p-value < 0.01 and logFC > 0.5), related to figure 1.

Supplementary Table 2. List of the most differentially expressed genes across the myeloid clusters (Naïve, TAM I and TAM II), irrespective of the tumour stage (p-value < 0.01), related to figure 2.

Supplementary Table 3. Common transcriptional signatures between tumour-associated microglia and macrophages in the GBM syngeneic murine model and in patients used to assign a score for each TCGA patient, related to figure 2.

Supplementary Table 4. Up-regulated differentially expressed genes at early and late stages for TAM I and TAM II versus naïve cells (p-value < 0.001 and logFC > 0.5), related to figure 3.

Supplementary Table 5. Up-regulated differentially expressed genes at late stage for TAM I KO and TAM II KO versus correspondent WT cells (p-value < 0,001 and logFC > 0,5), related to figure 5.

1105 **Supplementary Table 6. Up-regulated differentially expressed genes at early stage comparing**
1106 **lymphocytes from KO and WT mice (p-value < 0.01 and LogFC > 0.5), related to Supplementary**
1107 **figure 9.**

Figure 1

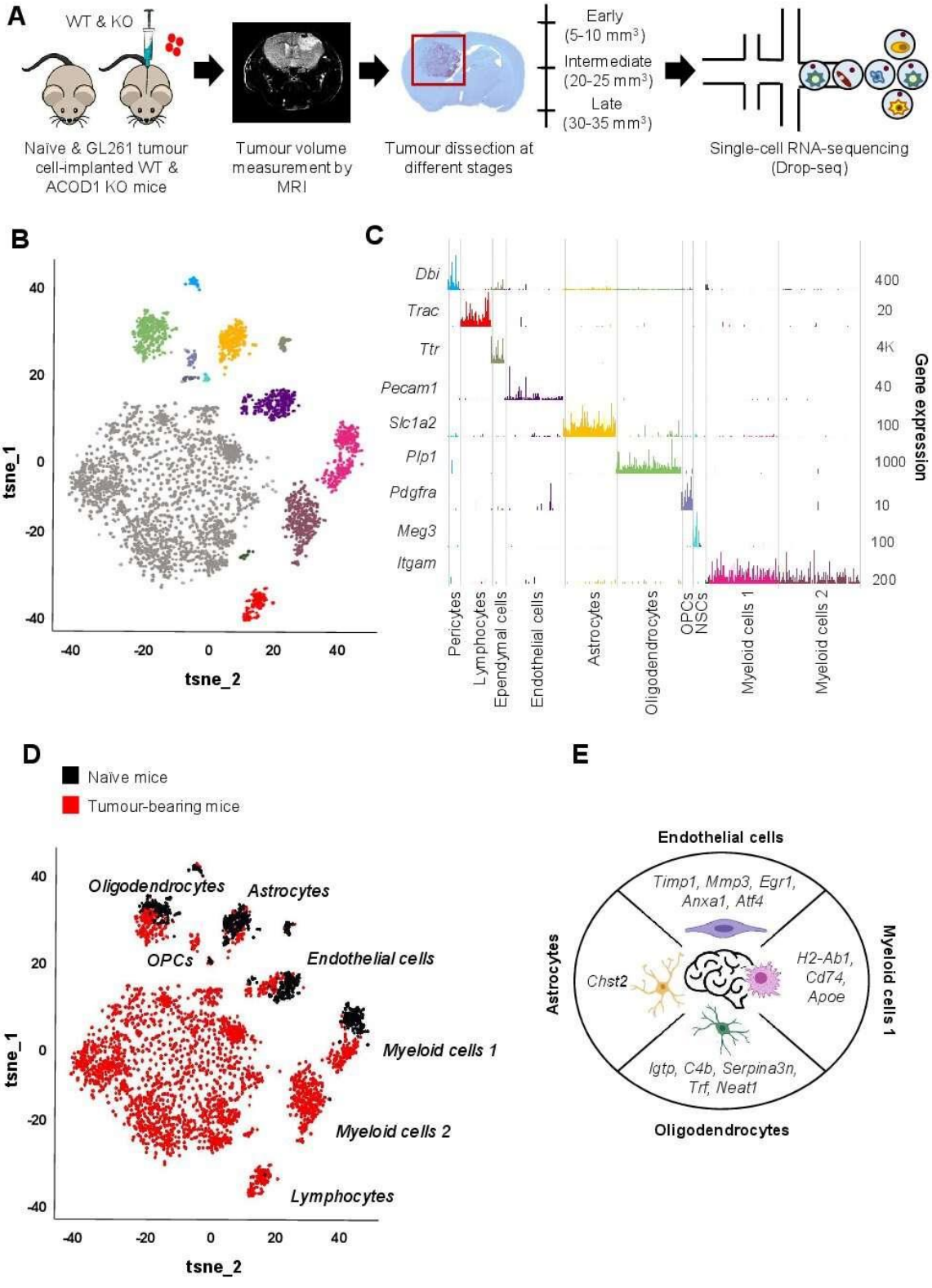
A
WT & KO
Naïve & GL261 tumour cell-implanted WT & ACOD1 KO mice
Tumour volume measurement by MRI
Tumour dissection at different stages
Early (5-10 mm³)
Intermediate (20-25 mm³)
Late (30-35 mm³)
Single-cell RNA-sequencing (Drop-seq)
B
tsne_1
tsne_2
C
Dbi
Trac
Ttr
Pecam1
Slc1a2
Plp1
Pdgfra
Meg3
Itgam
Gene expression
Pericytes
Lymphocytes
Ependymal cells
Endothelial cells
Astrocytes
Oligodendrocytes
OPCs NSCs
Myeloid cells 1
Myeloid cells 2
D
Naïve mice
Tumour-bearing mice
Oligodendrocytes
Astrocytes
OPCs
Endothelial cells
Myeloid cells 1
Myeloid cells 2
Lymphocytes
E
Endothelial cells
Timp1, Mmp3, Egr1, Anxa1, Atf4
Astrocytes
Chst2
Myeloid cells 1
H2-Ab1, Cd74, Apoe
Igtp, C4b, Serpina3n, Trf, Neat1
Oligodendrocytes

Figure 2

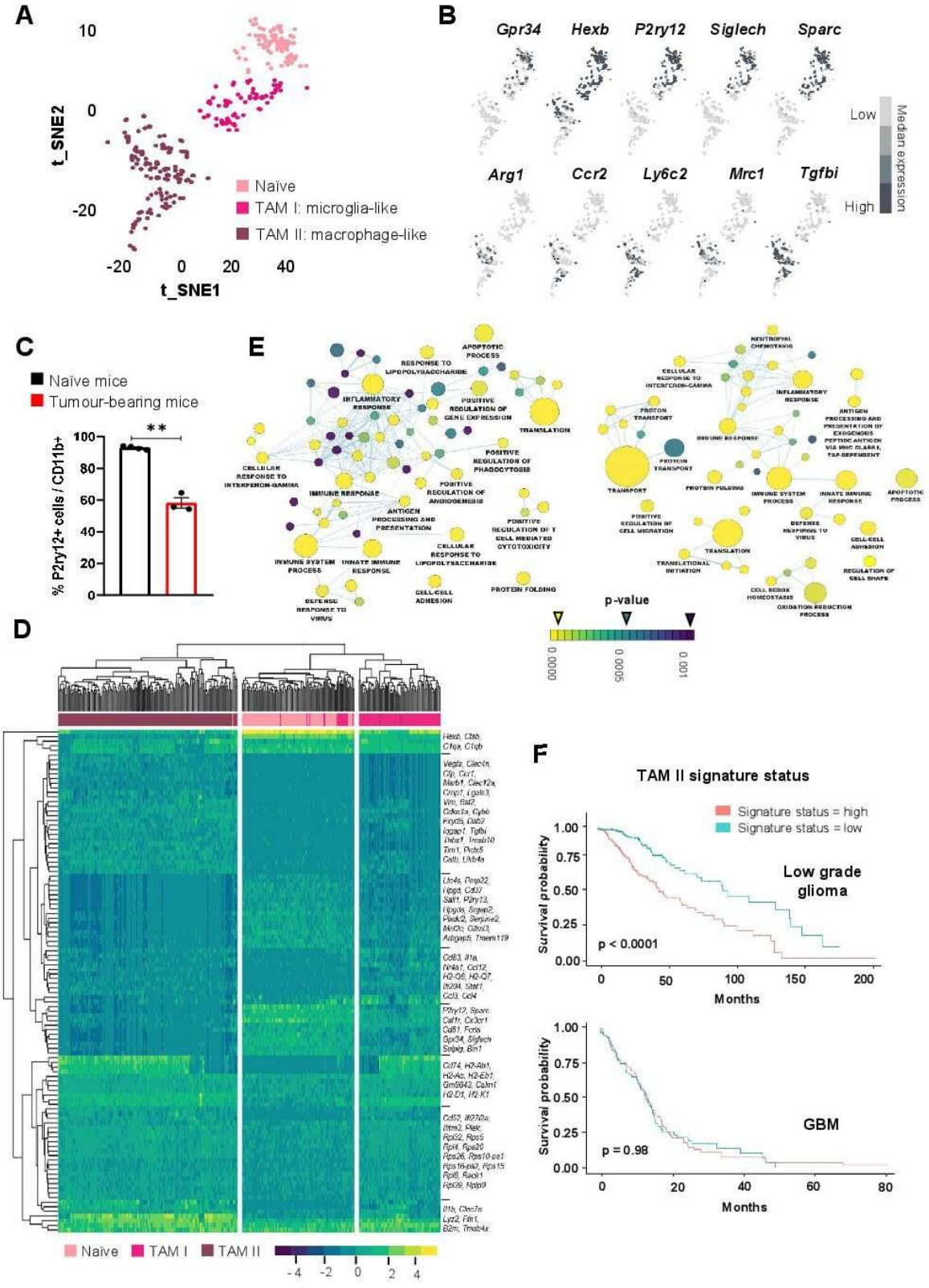
A
t_SNE2
t_SNE1
Naïve
TAM I: microglia-like
TAM II: macrophage-like
B
Gpr34
Hexb
P2ry12
Siglech
Sparc
Arg1
Ccr2
Ly6c2
Mrc1
Tgfbi
Low
High
Median expression
C
Naïve mice
Tumour-bearing mice
% P2ry12+ cells / CD11b+
E
p-value
D
Naive
TAM I
TAM II
F
TAM II signature status
Signature status = high
Signature status = low
Low grade glioma
p < 0.0001
GBM
p = 0.98
Survival probability
Months

Figure 3

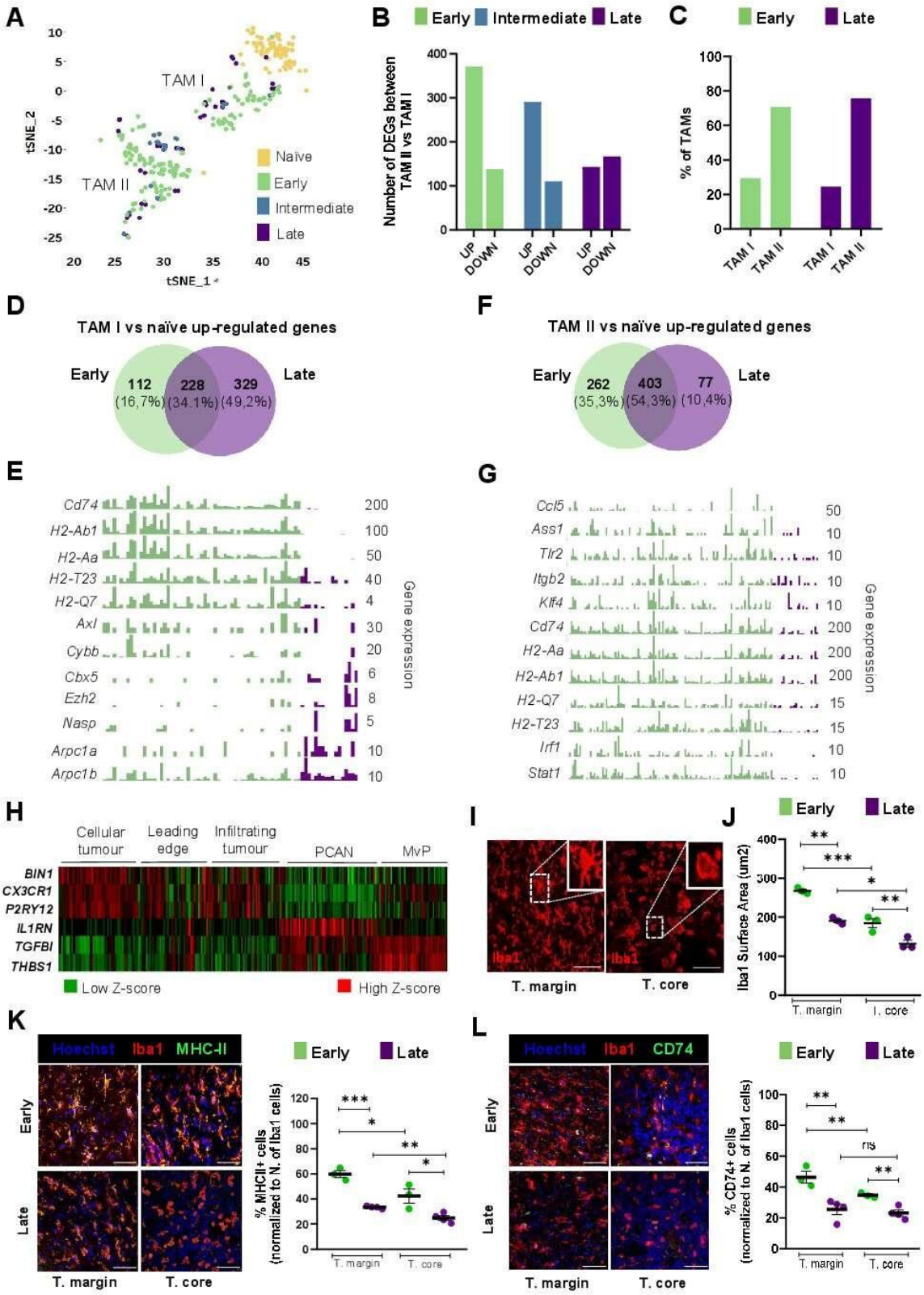
A
TAM I
TAM II
Naïve
Early
Intermediate
Late
tSNE_1
tSNE_2
B
Early Intermediate Late
Number of DEGs between TAM II vs TAM I
UP DOWN UP DOWN UP DOWN
C
Early Late
% of TAMs
TAM I TAM II TAM I TAM II
D
TAM I vs naïve up-regulated genes
Early 112 (16,7%) 228 (34.1%) 329 (49,2%) Late
F
TAM II vs naïve up-regulated genes
Early 262 (35,3%) 403 (54,3%) 77 (10,4%) Late
E
Cd74 H2-Ab1 H2-Aa H2-T23 H2-Q7 Axl Cybb Cbx5 Ezh2 Nasp Arpc1a Arpc1b
Gene expression
G
Ccl5 Ass1 Tlr2 Itgb2 Klf4 Cd74 H2-Aa H2-Ab1 H2-Q7 H2-T23 Irf1 Stat1
Gene expression
H
Cellular tumour
Leading edge
Infiltrating tumour
PCAN
MvP
BIN1 CX3CR1 P2RY12 IL1RN TGFBI THBS1
Low Z-score
High Z-score
I
Iba1
T. margin
T. core
J
Early Late
Iba1 Surface Area (um2)
T. margin
T. core
K
Hoechst Iba1 MHCII
Early
Late
T. margin
T. core
% MHCII+ cells (normalized to N. of Iba1 cells)
L
Hoechst Iba1 CD74
Early
Late
T. margin
T. core
% CD74+ cells (normalized to N. of Iba1 cells)
ns

Figure 4

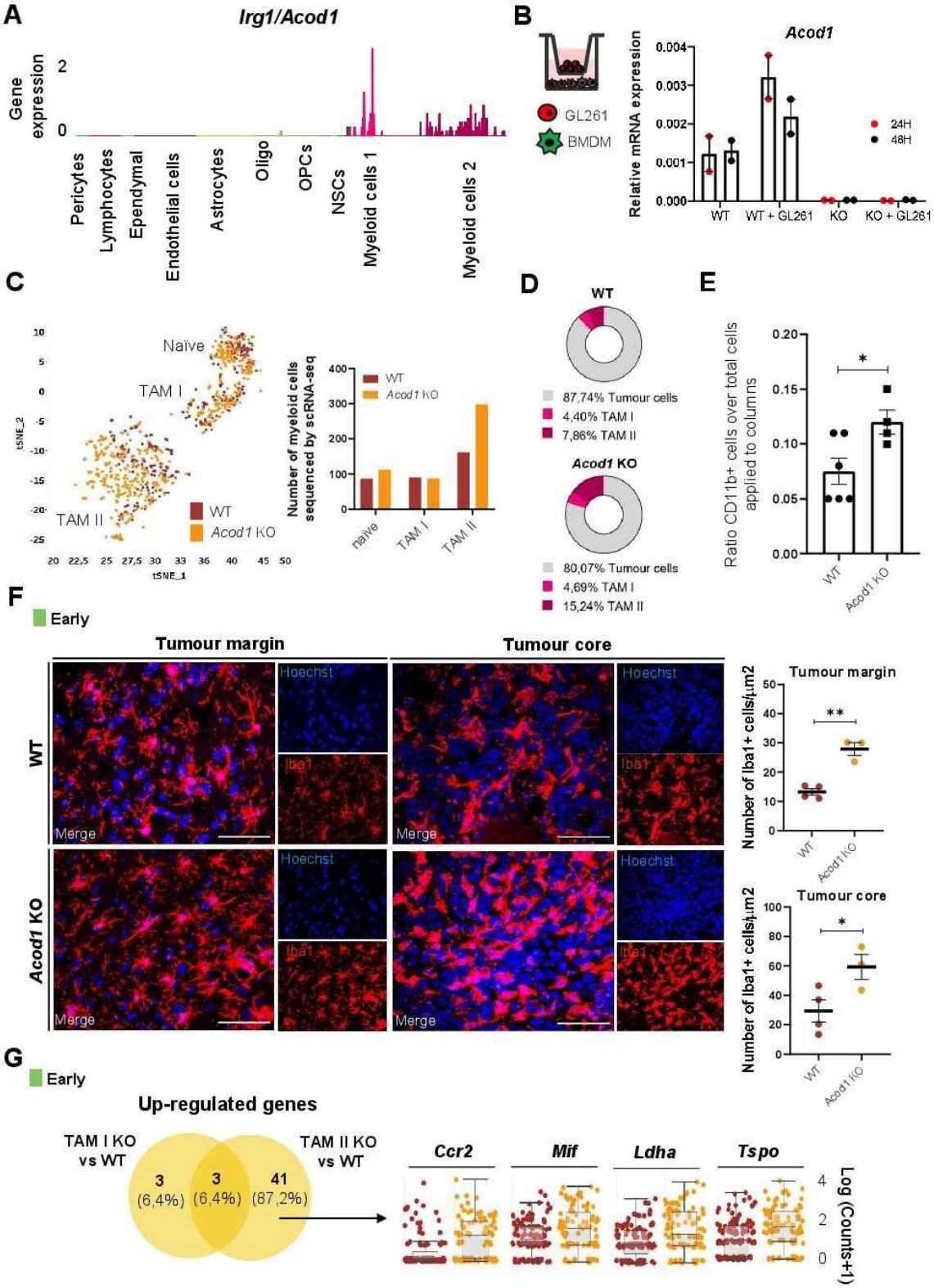
A
Irg1/Acod1
Gene expression
Pericytes
Lymphocytes
Ependymal
Endothelial cells
Astrocytes
Oligo
OPCs
NSCs
Myeloid cells 1
Myeloid cells 2
B
GL261
BMDM
Acod1
Relative mRNA expression
24H
48H
WT
WT + GL261
KO
KO + GL261
C
Naïve
TAM I
TAM II
WT
Acod1 KO
tSNE_1
tSNE_2
Number of myeloid cells sequenced by scRNA-seq
naive
TAM I
TAM II
D
WT
87,74% Tumour cells
4,40% TAM I
7,86% TAM II
Acod1 KO
80,07% Tumour cells
4,69% TAM I
15,24% TAM II
E
Ratio CD11b+ cells over total cells applied to columns
F
Early
Tumour margin
Tumour core
WT
Acod1 KO
Hoechst
Iba1
Merge
Number of Iba1+ cells/µm2
G
Early
Up-regulated genes
TAM I KO vs WT
TAM II KO vs WT
3 (6,4%)
3 (6,4%)
41 (87,2%)
Ccr2
Mif
Ldha
Tspo
Log (Counts+1)

Figure 5

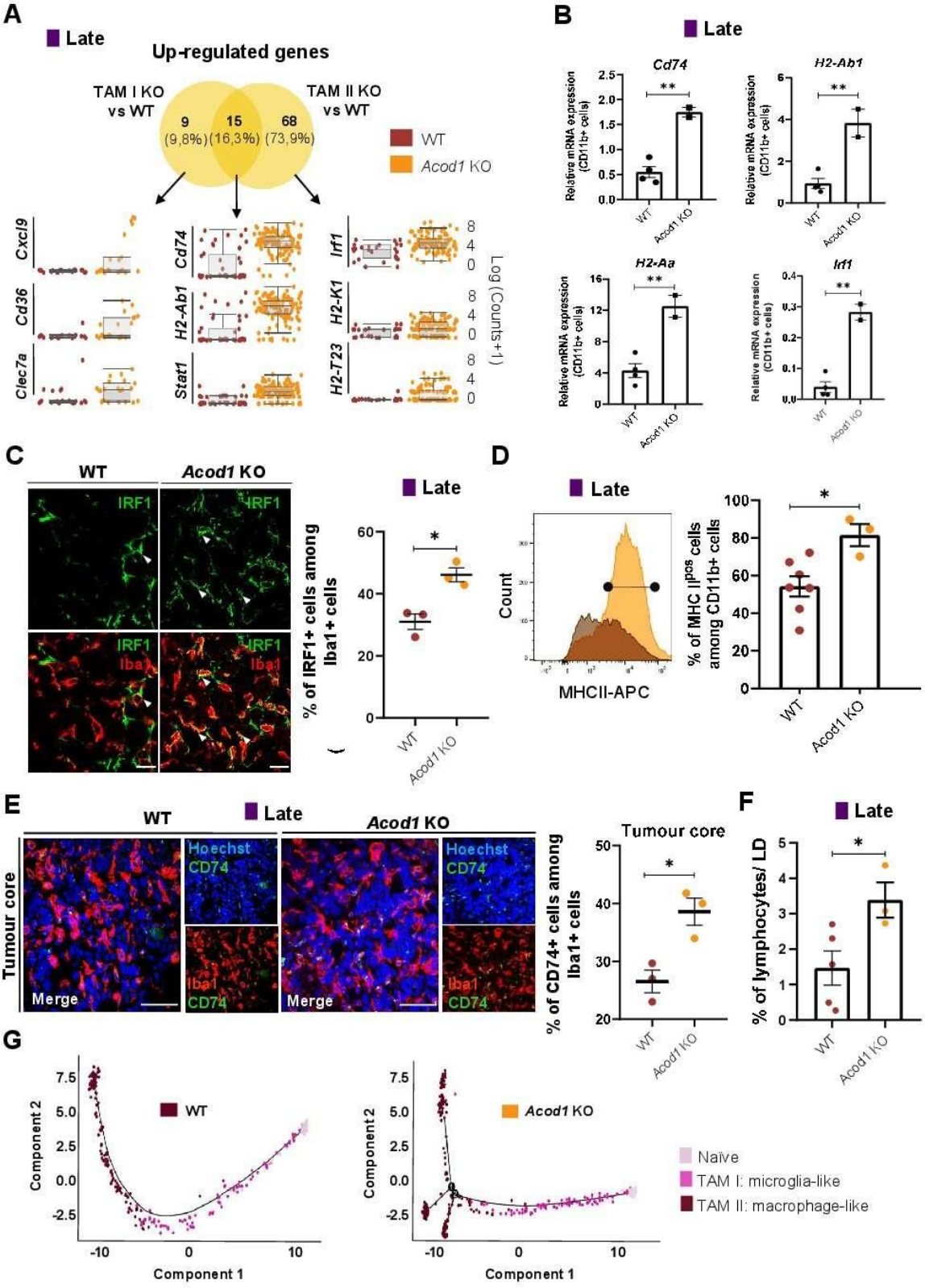
A
Late
Up-regulated genes
TAM I KO vs WT
TAM II KO vs WT
9 (9,8%)
15 (16,3%)
68 (73,9%)
WT
Acod1 KO
Cxcl9
Cd36
Clec7a
Cd74
H2-Ab1
Stat1
Irf1
H2-K1
H2-T23
Log (Counts+1)
B
Late
Cd74
H2-Ab1
H2-Aa
Irf1
Relative mRNA expression (CD11b+ cells)
WT
Acod1 KO
C
WT
Acod1 KO
IRF1
Iba1
Late
% of IRF1+ cells among Iba1+ cells
D
Late
Count
MHCII-APC
% of MHC II pos cells among CD11b+ cells
E
WT
Acod1 KO
Late
Tumour core
Hoechst
CD74
Iba1
Merge
% of CD74+ cells among Iba1+ cells
F
Late
% of lymphocytes/ LD
G
WT
Acod1 KO
Component 1
Component 2
Naïve
TAM I: microglia-like
TAM II: macrophage-like

Supplementary Figure 1

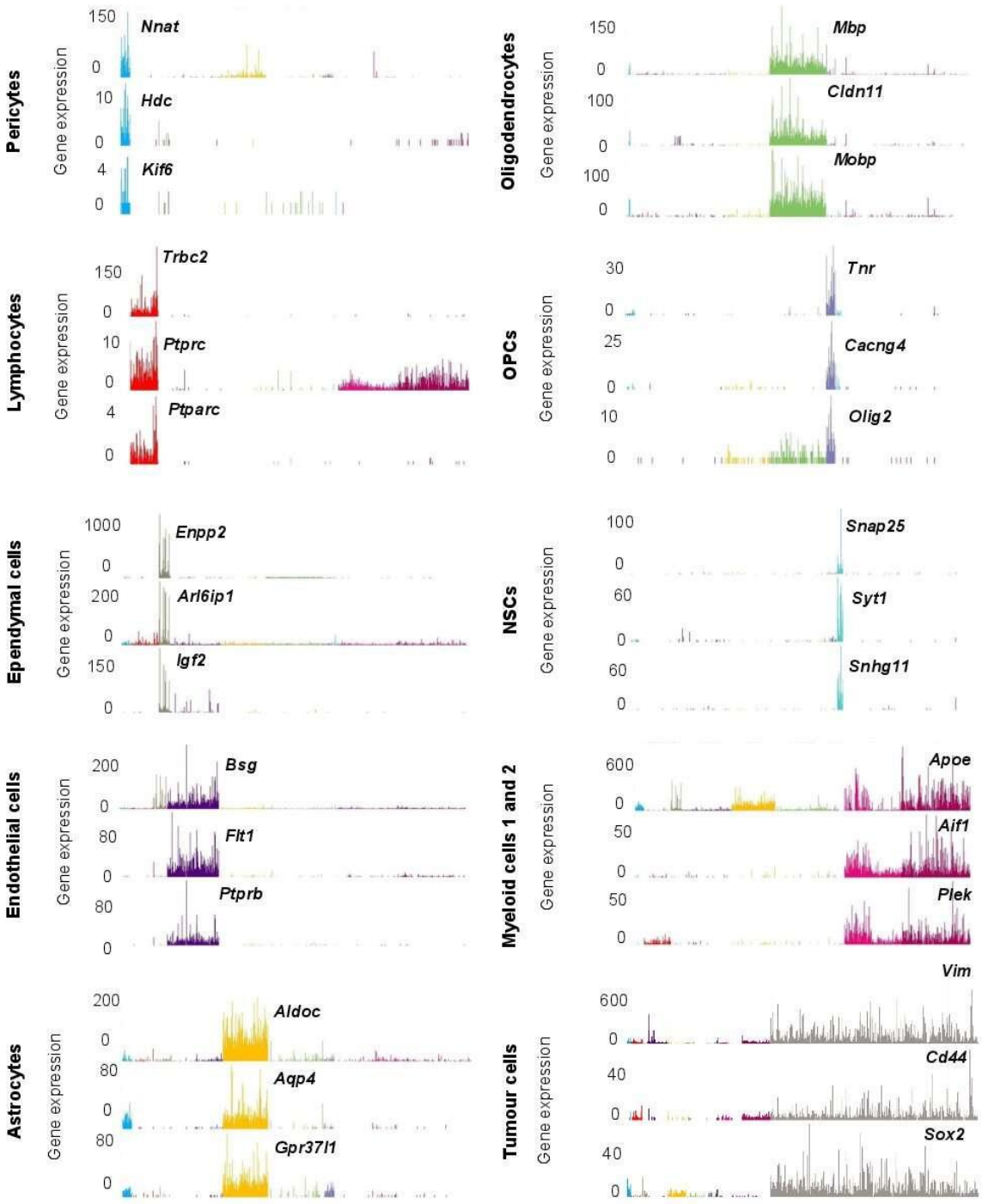

Supplementary Figure 1. Gene expression of distinct cell-types identified by scRNA-seq in the GL261 syngeneic murine model and naïve mice, related to figure 1.

Bar plots of additional cell type-specific markers. Pericytes (*Nnat*, *Hdc*, *Kif6*), lymphocytes (*Trbc2*, *Ptprcap*, *Ptprc*), ependymal cells (*Enpp2*, *Arl6ip1*, *Igf2*), endothelial cells (*Bsg*, *Flt1*, *Ptprb*), astrocytes (*Aldoc*, *Aqp4*, *Gpr37l1*), oligodendrocytes (*Mbp*, *Cldn11*, *Mobp*), OPCs (*Tnr*, *Cacng4*, *Olig2*), NSCs (*Snap25*, *Syt1*, *Snhg11*), myeloid cells 1 and 2 (*Apoe*, *Aif1*, *Plek*), tumour cells (*Vim*, *Cd44*, *Sox2*). Abbreviations: OPCs, oligodendrocyte precursor cells; NSCs, neural stem cells.

Supplementary Figure 2

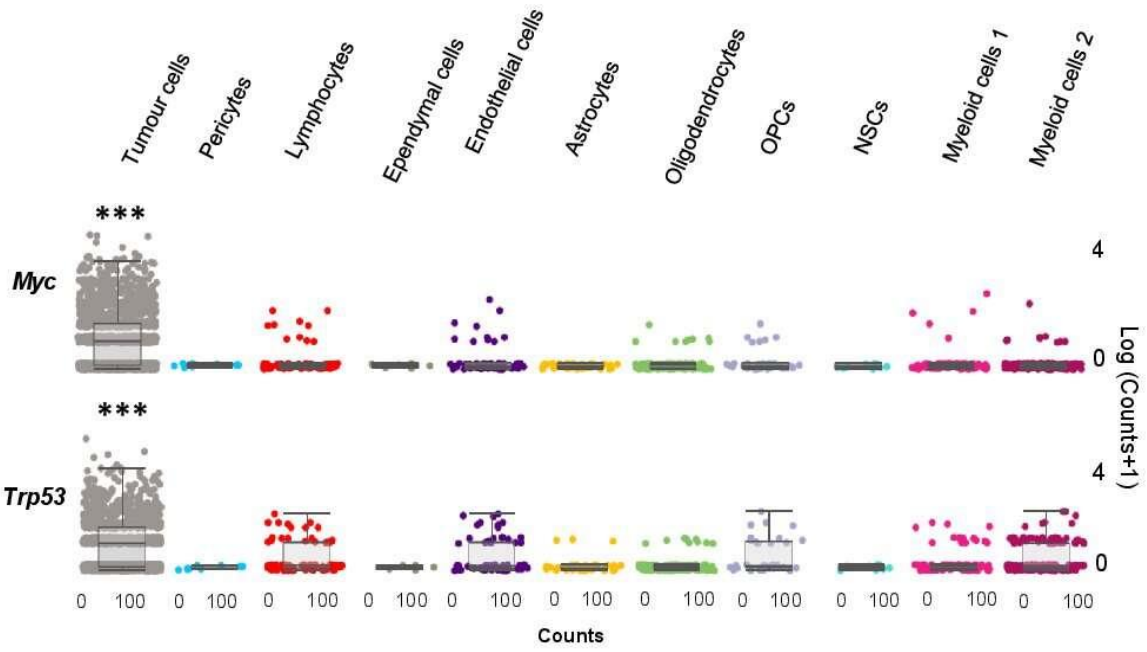

Supplementary Figure 2. Expression of *Myc* and *Trp53* genes in the GL261 GBM murine model, related to figure 1.

Myc and *Trp53* gene expression levels across tumour cells and 10 main stromal cell-types identified by scRNA-seq analyses. Data are represented as mean ± SEM, *** $p < 0.001$.

Supplementary Figure 3

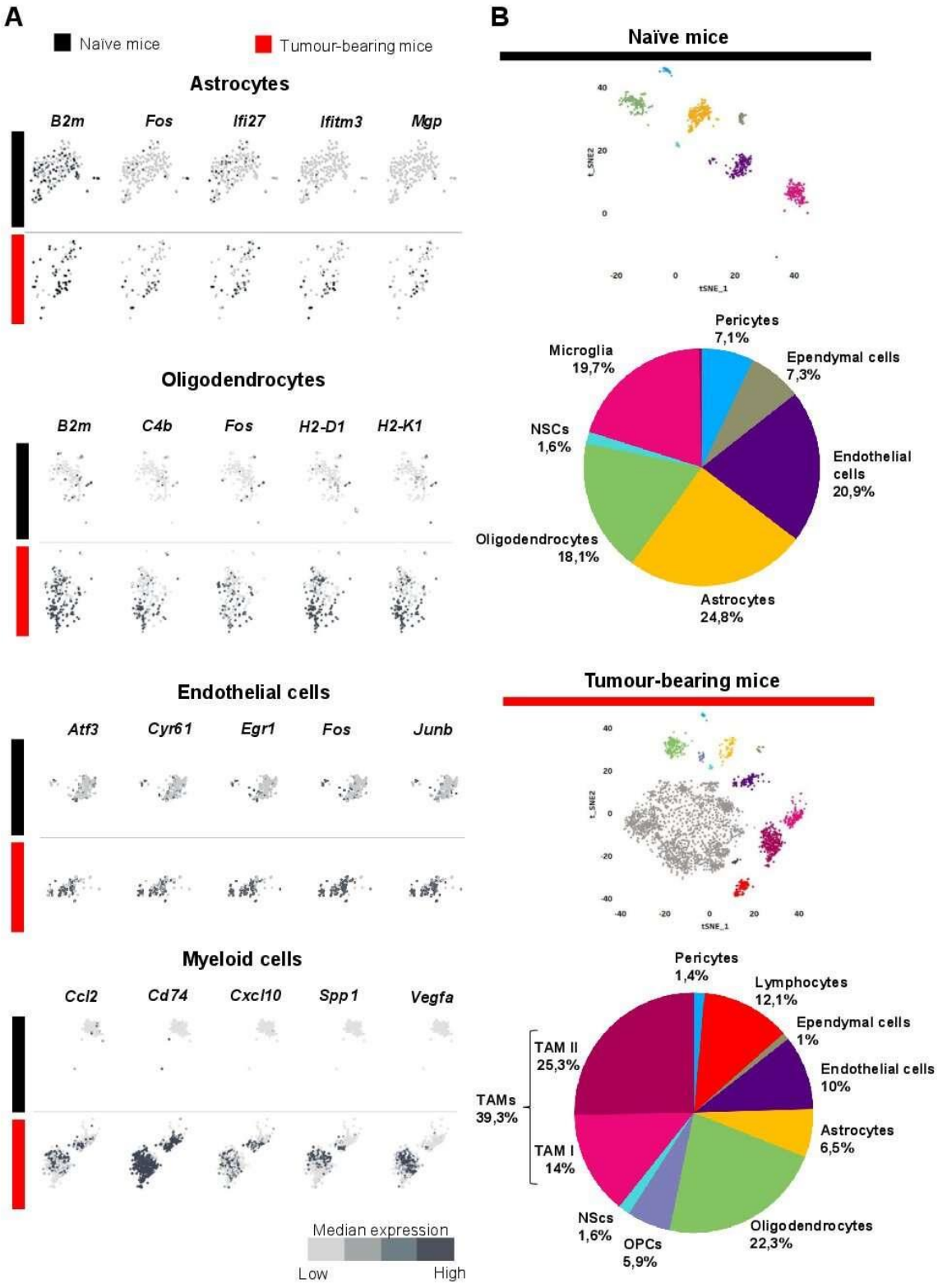

Supplementary Figure 3. Gene expression of distinct cell-types present in naïve and tumour-bearing mice, related to figure 1.

(A) 2D-tSNE representation of the top up-regulated genes in tumour-associated clusters (astrocytes, oligodendrocytes, endothelial cells, myeloid cells) compared to their naïve counterparts. **(B)** 2D-tSNE plot and respective cell-type proportion shown in pie chart of 2'282 isolated cells from naïve samples (upper panels) and 3'377 isolated cells from tumour-bearing samples (lower panels).

Supplementary Figure 4

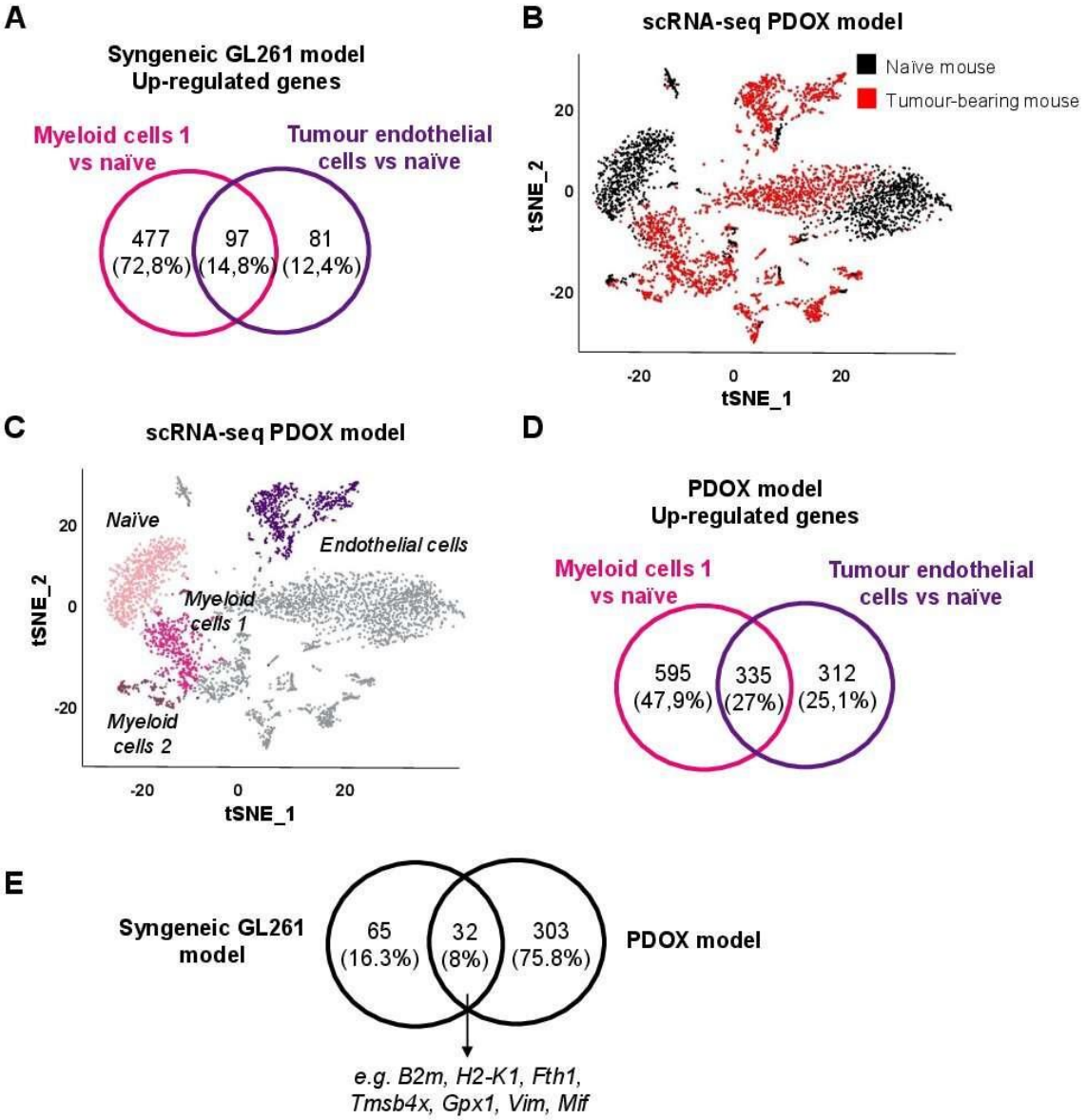

Supplementary Figure 4. Comparisons of gene expression profiles between myeloid cells 1 and tumour endothelial cells in GBM syngeneic GL261 and patient-derived orthotopic xenograft (PDOX) mouse models, related to figure 1.

(A) Venn diagram representation showing shared and exclusive up-regulated genes in myeloid cells 1 and tumour endothelial cells in syngeneic GL261 model. **(B)** 2D-tSNE representation showing naïve (in black) and tumour-associated (in red) cells in the PDOX preclinical model. **(C)** Colour-coded 2D-tSNE representation showing three distinct myeloid cell subsets (naïve, myeloid cells 1 and 2) and endothelial cells in naïve and PDOX model. **(D)** Venn diagram representation showing shared and exclusive up-regulated genes in myeloid cells 1 and tumour endothelial cells in PDOX model. **(E)** Venn diagram representation of common up-regulated genes in myeloid cells 1 and tumour endothelial cells across the syngeneic GL261 and PDOX GBM murine models.

Supplementary Figure 5

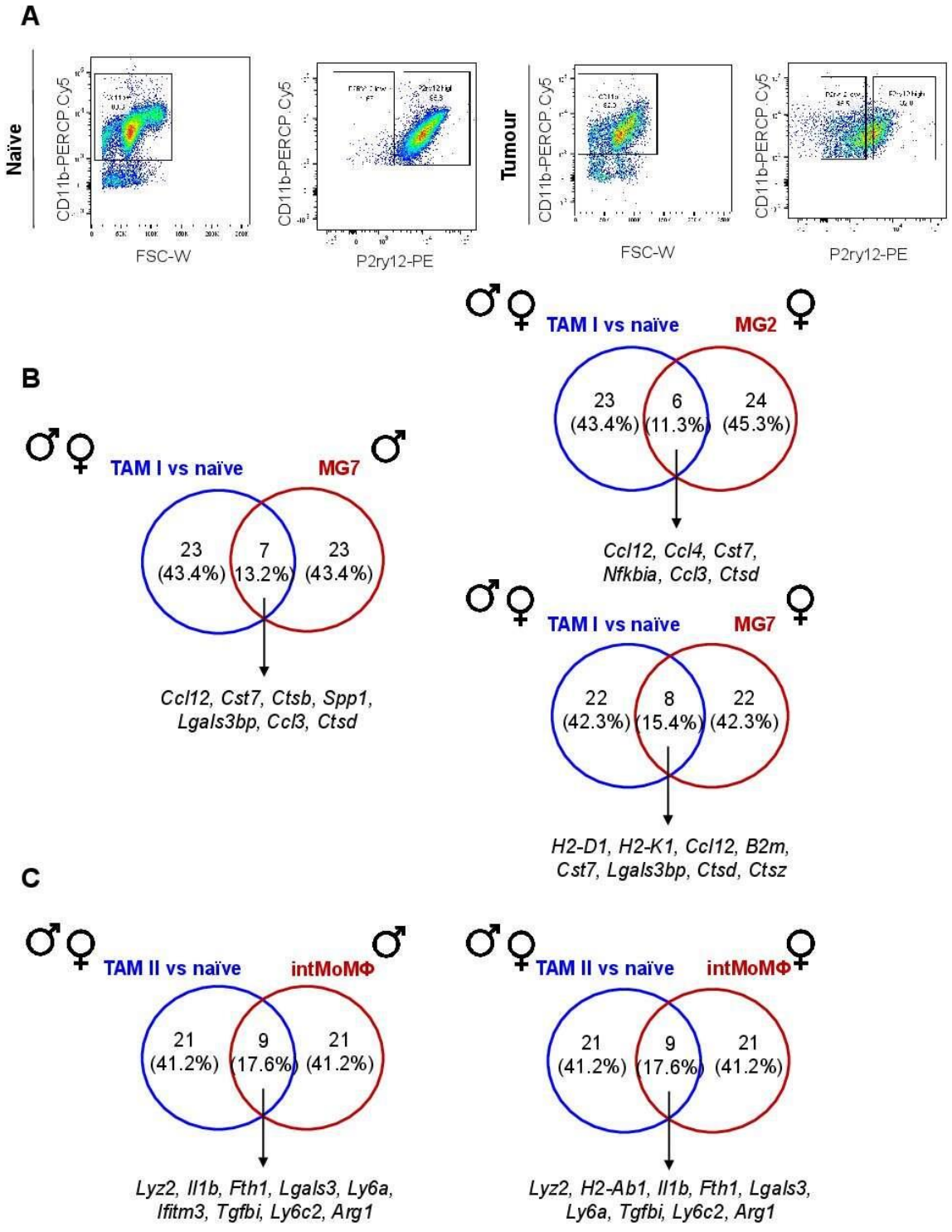

Supplementary Figure 5. Characterization of TAM I and TAM II subsets by FACS and by comparing their gene expression signatures with datasets gathered from the literature, related to figure 2.

(A) Gating strategy used to discriminate CD11b+ P2ry12+ and CD11b+ P2ry12-/low cells in naïve and syngeneic GL261 tumour-bearing mice by flow cytometry. **(B-C)** Venn diagram representations showing shared and exclusive genes with the study by Ochocka and colleagues [44] comparing **(B)** microglia-like cells and **(C)** macrophage-like cells. Comparisons are based on top 30 up-regulated genes defining TAM I, TAM II and the various myeloid clusters described in the syngeneic GL261 GBM model by Ochocka and colleagues [44] . Comparisons resulting in more than 10% overlap are represented.

Supplementary Figure 6

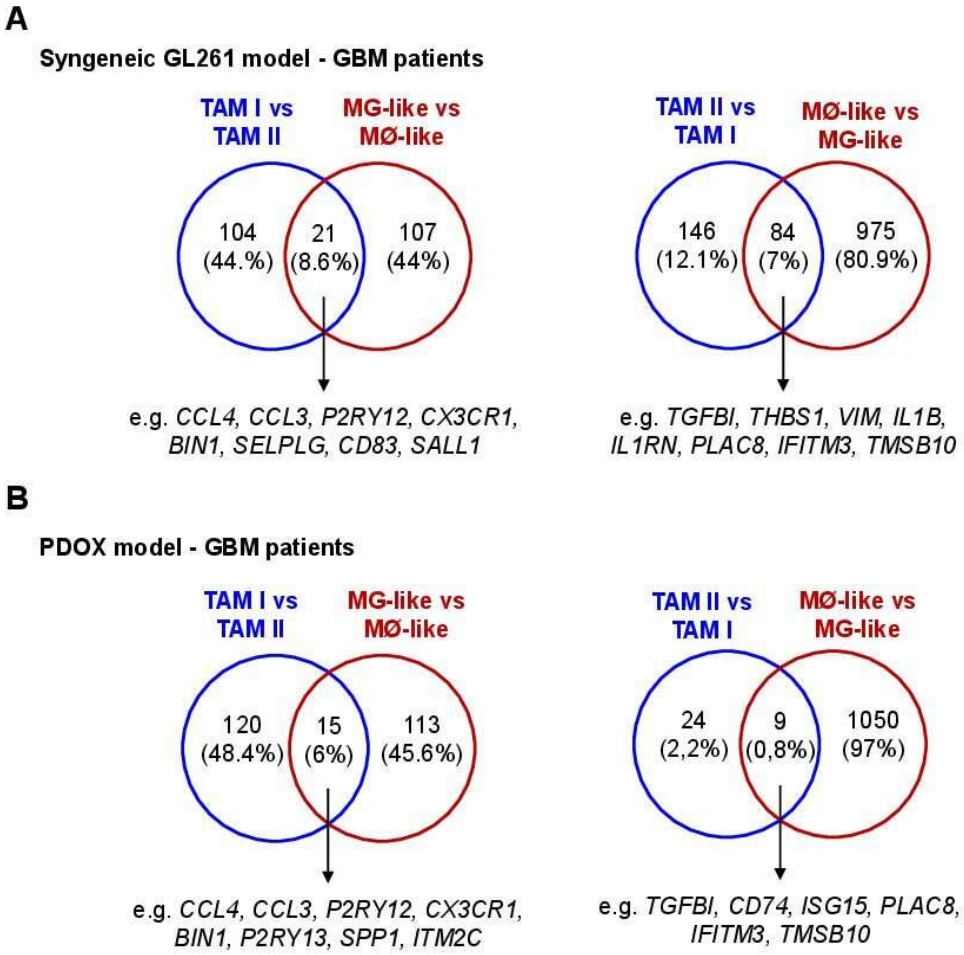

Supplementary Figure 6. Microglia- versus macrophage-like features in GBM, related to figure 2.

(A-B) Venn diagram representations showing shared and exclusive genes in microglia-like (TAM I) and macrophage-like (TAM II) cells in **(A)** syngeneic GL261 and **(B)** PDOX models (blue circles) with putative corresponding cell types described in GBM patients (red circles) from Muller and colleagues [9]. A selection of shared genes is annotated. MG: microglia; MØ: macrophage.

Supplementary Figure 7

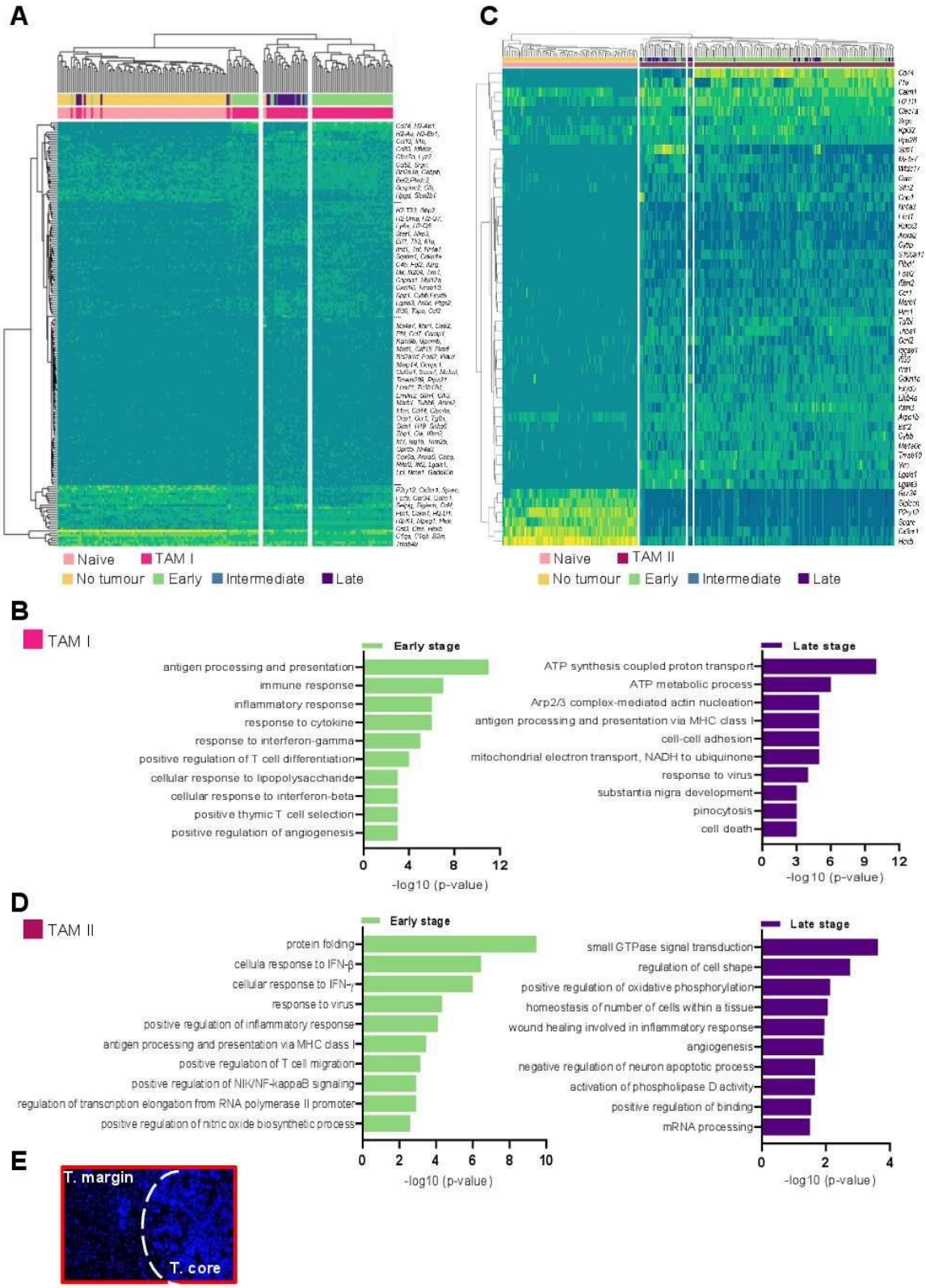

Supplementary Figure 7. Differential microglia and monocytic-derived macrophage transcriptional adaptation along GBM progression, related to figure 3.

(A) Two-way hierarchical heat-map clustering analyses of the most differentially expressed genes (p value < 0.01) in TAM I along tumour progression. Scale bar represents the colour-coded z-scores. (**B)** Gene ontology terms of TAM I exclusive up-regulated genes at early (left) and late (right) GBM stages. **(C)** Two-way hierarchical heat-map clustering analyses of the most differentially expressed genes (p value < 0.01) in TAM II along tumour progression. Scale bar represents the colour-coded z-scores. **(D)** Gene ontology terms of TAM II exclusive up-regulated genes at early (left) and late (right) GBM stages. **(E)** Picture representing Hoechst-stained nuclei used to discriminate tumour margin and core in mouse brain sections. Colour coding in (**B** and **D**) is consistent with **Fig 3A**.

Supplementary Figure 8

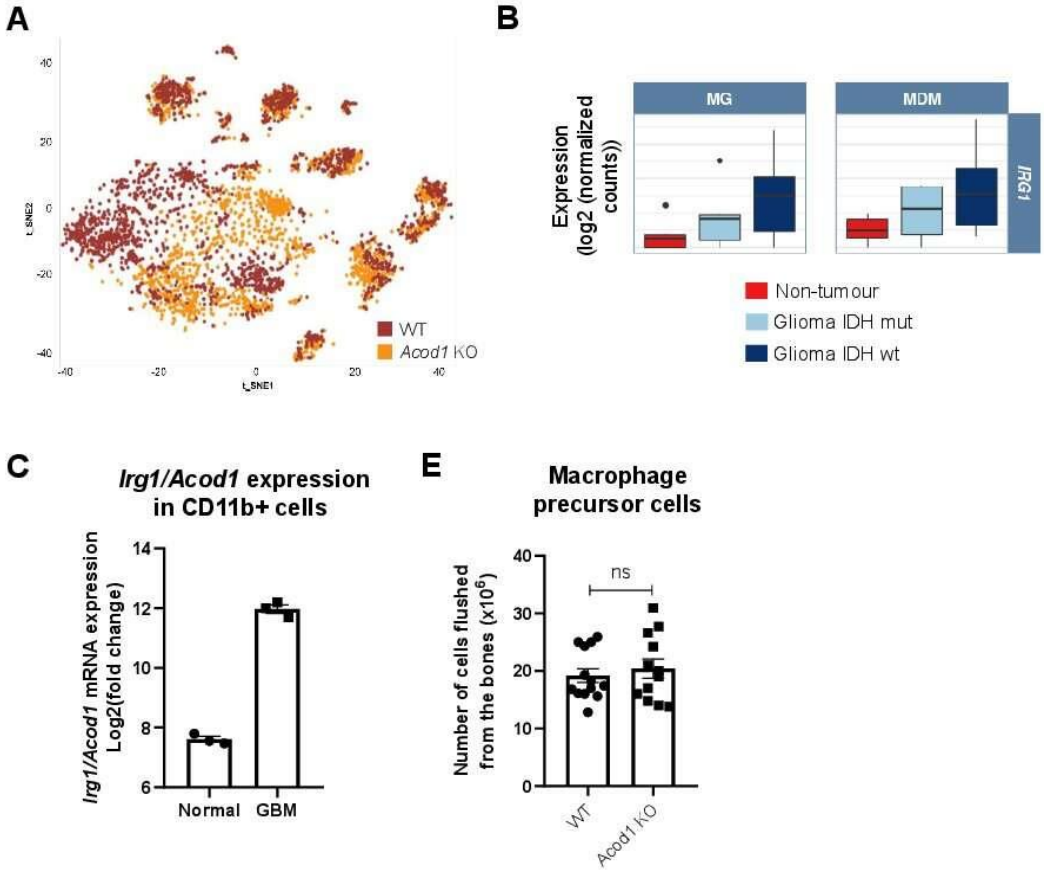

Supplementary Figure 8. IRG1/ACOD1 expression levels in TAMs, related to figure 4.

(A) 2D-tSNE representation of all single cells included in the study (n = 5'659 cells) grouped within 12 cell clusters (brown: WT; orange: *Acod1* KO). **(B)** *IRG1/ACOD1* expression in both microglia (MG) and macrophages (MDM) in GBM patients from Brain Tumor Immune Micro Environment dataset [56]. **(C)** *Irg1/Acod1* expression in CD11b+ cells isolated from naïve (n=3) and GL261-implanted mice (n=3) (E-MTAB-2660 dataset) [11]. **(D)** Western blot analysis showing IRG1/ACOD1 expression in BMDMs at baseline and in co-culture with GL261 cells for 24 and 48h. BMDMs treated with LPS (100 ng/ml) for 6h were used as positive control. **(E)** Total number of bone marrow precursor cells flushed from the legs of WT and *Acod1* KO mice. Data are not normalized and are represented as mean ± SEM (n.s. - not significant).

Supplementary Figure 9

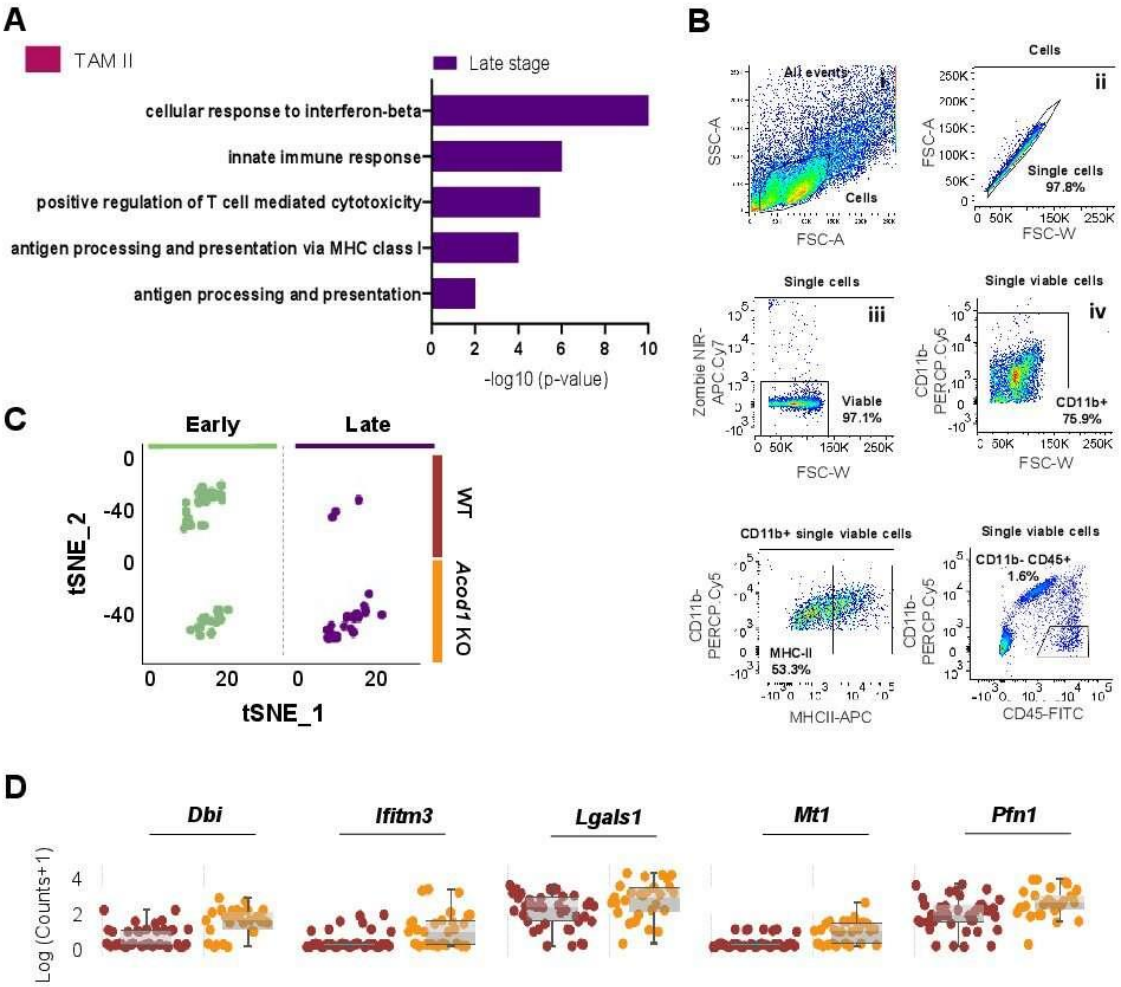

Supplementary Figure 9. TAM and lymphocytic signatures under *Acod1* deficiency, related to figure 5.

(A) Gene set enrichment analysis of TAM II uniquely up-regulated genes in Acod1 KO mice versus WT mice at late stages. **(B)** Flow cytometry gating strategy. (i) Cells of interest were gated based on forward (FSC) and side scatter (SSC). (ii) Doublets were excluded based on the forward scatter height (FSC-H) versus forward scatter area (FSC-A). (iii) Zombie NIR-APC.cy7 was used to discriminate living cells. (iv) CD11b-PERCP.cy5 was used to gate the myeloid compartment. Lastly, we gated MHC-II-expressing cells and lymphocytes (CD11b- CD45+). **(C)** 2D-tSNE representation showing the lymphocytic population detected at early and late stages of tumour development by scRNA-seq. **(D)** Notch plot representation of selected genes up-regulated by lymphocytes in *Acod1* KO mice compared with WT mice at early stage.

Supplementary Figure 10

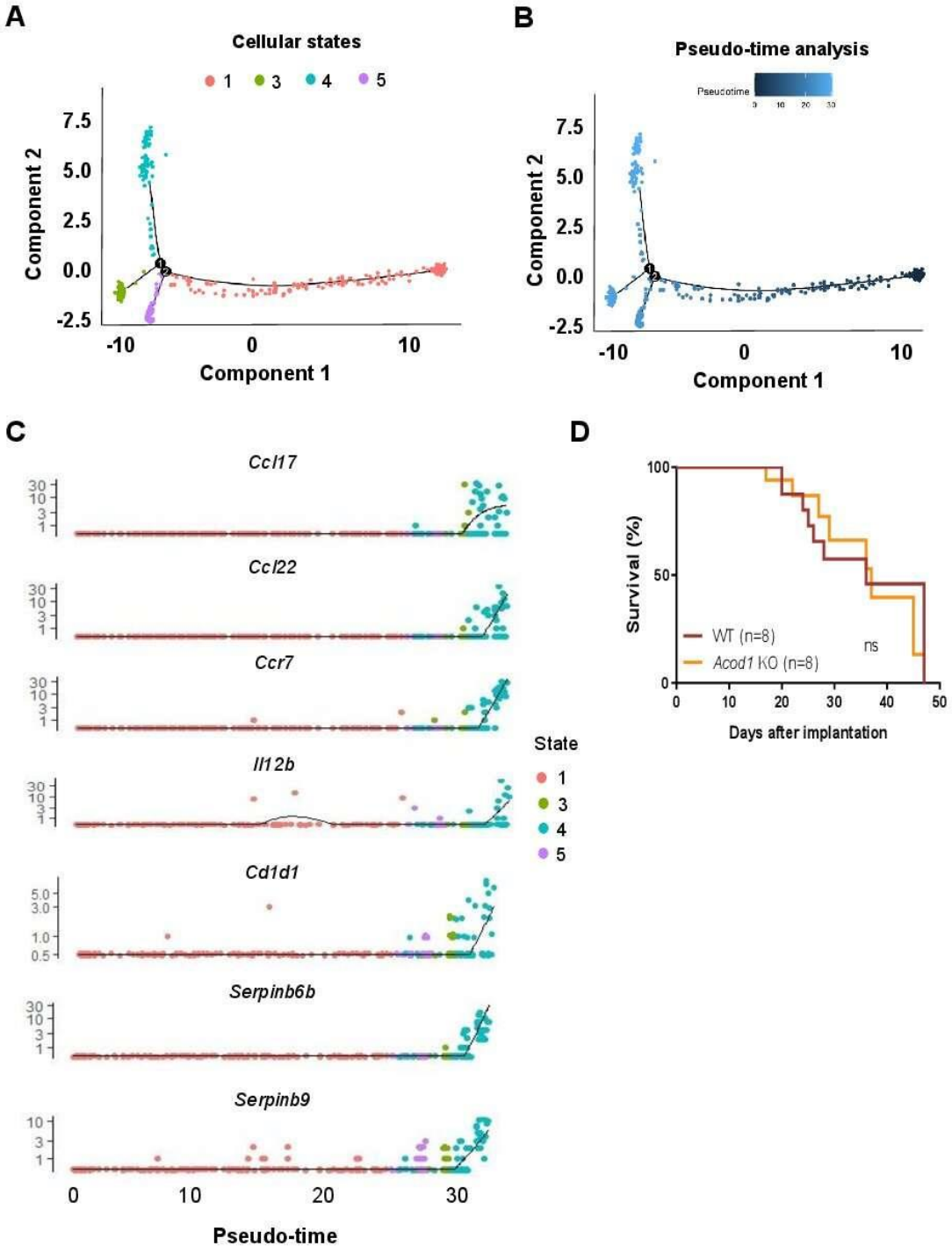

Supplementary Figure 10. TAM II cellular state diversity under *Acod1* deficiency, related to figure 5.

(A) Pseudo-time analysis of TAM II from *Acod1* KO showing four distinct cellular states in a two-dimensional state space (see Materials and Methods). **(B)** Pseudo-time analysis showing each cell along the inferred cell trajectory state. **(C)** Relative expression of exclusive genes driving the correspondent cellular state in TAM II subset under *Acod1* deficiency. (**D**) Kaplan-Meier curves showing survival rates in WT (n = 8) and *Acod1 KO* (n = 8) mice.

References

Abdel Hadi, L., Anelli, V., Guarnaccia, L., Navone, S., Beretta, M., Moccia, F., Tringali, C., Urechie, V., Campanella, R., Marfia, G., et al. (2018). A bidirectional crosstalk between glioblastoma and brain endothelial cells potentiates the angiogenic and proliferative signaling of sphingosine-1-phosphate in the glioblastoma microenvironment. Biochim. Biophys. Acta - Mol. Cell Biol. Lipids *1863*, 1179–1192.

Abdelfattah, N., Kumar, P., Wang, C., Leu, J.-S., Flynn, W.F., Gao, R., Baskin, D.S., Pichumani, K., Ijare, O.B., Wood, S.L., et al. (2022). Single-cell analysis of human glioma and immune cells identifies S100A4 as an immunotherapy target. Nat. Commun. *13*, 767.

Abdul Rahim, S.A.S.A.S.A., Dirkse, A., Oudin, A., Schuster, A., Bohler, J., Barthelemy, V., Muller, A., Vallar, L., Janji, B., Golebiewska, A., et al. (2017). Regulation of hypoxia-induced autophagy in glioblastoma involves ATG9A. Br. J. Cancer *117*, 813–825.

Absinta, M., Maric, D., Gharagozloo, M., Garton, T., Smith, M.D., Jin, J., Fitzgerald, K.C., Song, A., Liu, P., Lin, J.-P., et al. (2021). A lymphocyte–microglia–astrocyte axis in chronic active multiple sclerosis. Nature.

Agnihotri, S., and Zadeh, G. (2016). Metabolic reprogramming in glioblastoma: The influence of cancer metabolism on epigenetics and unanswered questions. Neuro. Oncol. *18*, 160–172.

Agorku, D.J., Tomiuk, S., Klingner, K., Wild, S., Rüberg, S., Zatrieb, L., Bosio, A., Schueler, J., and Hardt, O. (2016). Depletion of Mouse Cells from Human Tumor Xenografts Significantly Improves Downstream Analysis of Target Cells. J. Vis. Exp. e54259.

Akkari, L., Bowman, R.L., Tessier, J., Klemm, F., Handgraaf, S.M., de Groot, M., Quail, D.F., Tillard, L., Gadiot, J., Huse, J.T., et al. (2020). Dynamic changes in glioma macrophage populations after radiotherapy reveal CSF-1R inhibition as a strategy to overcome resistance. Sci. Transl. Med. *12*.

Akter, F., Simon, B., de Boer, N.L., Redjal, N., Wakimoto, H., and Shah, K. (2021). Pre-clinical tumor models of primary brain tumors: Challenges and opportunities. Biochim. Biophys. Acta - Rev. Cancer *1875*, 188458.

Alcantara Llaguno, S.R., and Parada, L.F. (2016). Cell of origin of glioma: biological and clinical implications. Br. J. Cancer *115*, 1445–1450.

Aldape, K., Amin, S.B., Ashley, D.M., Barnholtz-Sloan, J.S., Bates, A.J., Beroukhim, R., Bock, C., Brat, D.J., Claus, E.B., Costello, J.F., et al. (2018). Glioma through the looking GLASS: Molecular evolution of diffuse gliomas and the Glioma Longitudinal Analysis Consortium. Neuro. Oncol. *20*, 873–884.

Aldape, K., Brindle, K.M., Chesler, L., Chopra, R., Gajjar, A., Gilbert, M.R., Gottardo, N., Gutmann, D.H., Hargrave, D., Holland, E.C., et al. (2019). Challenges to curing primary brain tumours. Nat. Rev. Clin. Oncol. *16*, 509–520.

Aldridge, S., and Teichmann, S.A. (2020). Single cell transcriptomics comes of age. Nat. Commun. *11*, 9–12.

Allen, M., Bjerke, M., Edlund, H., Nelander, S., and Westermark, B. (2016). Origin of the U87MG glioma cell line: Good news and bad news. Sci. Transl. Med. *8*.

Alston-Roberts, C., Barallon, R., Bauer, S.R., Butler, J., Capes-Davis, A., Dirks, W.G., Elmore, E., Furtado, M., Kerrigan, L., Kline, M.C., et al. (2010). Cell line misidentification: The beginning of the end. Nat. Rev. Cancer *10*, 441–448.

Amberger-Murphy, V. (2009). Hypoxia helps glioma to fight therapy. Curr. Cancer Drug Targets *9*, 381–390.

Andersen, B.M., Faust Akl, C., Wheeler, M.A., Chiocca, E.A., Reardon, D.A., and Quintana, F.J. (2021). Glial and myeloid heterogeneity in the brain tumour microenvironment. Nat. Rev. Cancer *0123456789*, 1–17.

Anido, J., Sáez-Borderías, A., Gonzàlez-Juncà, A., Rodón, L., Folch, G., Carmona, M.A., Prieto-Sánchez, R.M., Barba, I., Martínez-Sáez, E., Prudkin, L., et al. (2010). TGF-β Receptor Inhibitors Target the CD44high/Id1high Glioma-Initiating Cell Population in Human Glioblastoma. Cancer Cell *18*, 655–668.

Arita, H., Yamasaki, K., Matsushita, Y., Nakamura, T., Shimokawa, A., Takami, H., Tanaka, S., Mukasa, A., Shirahata, M., Shimizu, S., et al. (2016). A combination of TERT promoter mutation and MGMT methylation status predicts clinically relevant subgroups of newly diagnosed glioblastomas. Acta Neuropathol. Commun. *4*, 79.

Ausman, J.I., Shapiro, W.R., and Rall, D.P. (1970). Studies on the chemotherapy of experimental brain tumors: development of an experimental model. Cancer Res. *30*, 2394–2400.

Bakken, T.E., Jorstad, N.L., Hu, Q., Lake, B.B., Tian, W., Kalmbach, B.E., Crow, M., Hodge, R.D., Krienen, F.M., Sorensen, S.A., et al. (2021). Comparative cellular analysis of motor cortex in human, marmoset and mouse. Nature *598*, 111–119.

Balvers, R.K., Kleijn, A., Kloezeman, J.J., French, P.J., Kremer, A., van den Bent, M.J., Dirven, C.M.F., Leenstra, S., and Lamfers, M.L.M. (2013). Serum-free culture success of glial tumors is related to specific molecular profiles and expression of extracellular matrix–associated gene modules. Neuro. Oncol. *15*, 1684–1695.

Barth, R.F., and Kaur, B. (2009). Rat brain tumor models in experimental neuro-oncology: the C6, 9L, T9, RG2, F98, BT4C, RT-2 and CNS-1 gliomas. J. Neurooncol. *94*, 299–312.

Barthel, F.P., Johnson, K.C., Varn, F.S., Moskalik, A.D., Tanner, G., Kocakavuk, E., Anderson, K.J., Abiola, O., Aldape, K., Alfaro, K.D., et al. (2019). Longitudinal molecular trajectories of diffuse glioma in adults. Nature *576*, 112–120.

Baskaran, S., Mayrhofer, M., Kultima, H.G., Bergström, T., Elfineh, L., Cavelier, L., Isaksson, A., and Nelander, S. (2018). Primary glioblastoma cells for precision medicine: a quantitative portrait of genomic (in)stability during the first 30 passages. Neuro. Oncol. *20*, 1080–1091.

Bastola, S., Pavlyukov, M.S., Yamashita, D., Ghosh, S., Cho, H., Kagaya, N., Zhang, Z., Minata, M., Lee, Y., Sadahiro, H., et al. (2020). Glioma-initiating cells at tumor edge gain signals from tumor core cells to promote their malignancy. Nat. Commun. *11*, 1–17.

Batiuk, M.Y., Martirosyan, A., Wahis, J., de Vin, F., Marneffe, C., Kusserow, C., Koeppen, J., Viana, J.F., Oliveira, J.F., Voet, T., et al. (2020). Identification of region-specific astrocyte subtypes at single cell resolution. Nat. Commun. *11*, 1220.

Bayraktar, O.A., Bartels, T., Holmqvist, S., Kleshchevnikov, V., Martirosyan, A., Polioudakis, D., Ben Haim, L., Young, A.M.H., Batiuk, M.Y., Prakash, K., et al. (2020). Astrocyte layers in the mammalian cerebral cortex revealed by a single-cell in situ transcriptomic map. Nat. Neurosci. *23*, 500–509.

Behnan, J., Finocchiaro, G., and Hanna, G. (2019). The landscape of the mesenchymal

signature in brain tumours. Brain *142*, 847–866.

Ben-David, U., Ha, G., Tseng, Y.-Y., Greenwald, N.F., Oh, C., Shih, J., McFarland, J.M., Wong, B., Boehm, J.S., Beroukhim, R., et al. (2017). Patient-derived xenografts undergo mouse-specific tumor evolution. Nat. Genet. *49*, 1567–1575.

Ben-David, U., Siranosian, B., Ha, G., Tang, H., Oren, Y., Hinohara, K., Strathdee, C.A., Dempster, J., Lyons, N.J., Burns, R., et al. (2018). Genetic and transcriptional evolution alters cancer cell line drug response. Nature *560*, 325–330.

Ben-David, U., Beroukhim, R., and Golub, T.R. (2019). Genomic evolution of cancer models: perils and opportunities. Nat. Rev. Cancer *19*, 97–109.

Bergles, D.E., and Richardson, W.D. (2015). Oligodendrocyte Development and Plasticity. Cold Spring Harb. Perspect. Biol. *8*, a020453.

Bhaduri, A., Di Lullo, E., Jung, D., Müller, S., Crouch, E.E., Espinosa, C.S., Ozawa, T., Alvarado, B., Spatazza, J., Cadwell, C.R., et al. (2020). Outer Radial Glia-like Cancer Stem Cells Contribute to Heterogeneity of Glioblastoma. Cell Stem Cell *26*, 48-63.e6.

Bjerkvig, R., Tønnesen, A., Laerum, O.D., and Backlund, E.O. (1990). Multicellular tumor spheroids from human gliomas maintained in organ culture. J. Neurosurg. *72*, 463–475.

Bommarito, P.A., and Fry, R.C. (2018). The role of DNA methylation in gene regulation (Elsevier Inc.).

Bougnaud, S., Golebiewska, A., Oudin, A., Keunen, O., Harter, P.N., Mäder, L., Azuaje, F., Fritah, S., Stieber, D., Kaoma, T., et al. (2016). Molecular crosstalk between tumour and brain parenchyma instructs histopathological features in glioblastoma. Oncotarget *7*, 31955–31971.

Bowman, R.L., Klemm, F., Akkari, L., Pyonteck, S.M., Sevenich, L., Quail, D.F., Dhara, S., Simpson, K., Gardner, E.E., Iacobuzio-Donahue, C.A., et al. (2016). Macrophage Ontogeny Underlies Differences in Tumor-Specific Education in Brain Malignancies. Cell Rep. *17*, 2445–2459.

Brandao, M., Simon, T., Critchley, G., and Giamas, G. (2019). Astrocytes, the rising stars of the glioblastoma microenvironment. Glia *67*, 779–790.

Brennan, C.W., Verhaak, R.G.W., McKenna, A., Campos, B., Noushmehr, H., Salama, S.R., Zheng, S., Chakravarty, D., Sanborn, J.Z., Berman, S.H., et al. (2013). The somatic genomic landscape of glioblastoma. Cell *155*, 462–477.

Van Den Brink, S.C., Sage, F., Vértesy, Á., Spanjaard, B., Peterson-Maduro, J., Baron, C.S., Robin, C., and Van Oudenaarden, A. (2017). Single-cell sequencing reveals dissociation-induced gene expression in tissue subpopulations. Nat. Methods *14*, 935–936.

Buonfiglioli, A., and Hambardzumyan, D. (2021). Macrophages and microglia: the cerberus of glioblastoma. Acta Neuropathol. Commun. *9*, 1–21.

Butler, A., Hoffman, P., Smibert, P., Papalexi, E., and Satija, R. (2018). Integrating single-cell transcriptomic data across different conditions, technologies, and species. Nat. Biotechnol. *36*, 411–420.

Byrne, A.T., Alférez, D.G., Amant, F., Annibali, D., Arribas, J., Biankin, A. V., Bruna, A., Budinská, E., Caldas, C., Chang, D.K., et al. (2017). Interrogating open issues in cancer

precision medicine with patient-derived xenografts. Nat. Rev. Cancer *17*, 254–268.

Cabrita, R., Lauss, M., Sanna, A., Donia, M., Skaarup Larsen, M., Mitra, S., Johansson, I., Phung, B., Harbst, K., Vallon-Christersson, J., et al. (2020). Tertiary lymphoid structures improve immunotherapy and survival in melanoma. Nature *577*, 561–565.

Candolfi, M., Curtin, J.F., Nichols, W.S., Muhammad, A.G., King, G.D., Pluhar, G.E., McNiel, E.A., Ohlfest, J.R., Freese, A.B., Moore, P.F., et al. (2007). Intracranial glioblastoma models in preclinical neuro-oncology: neuropathological characterization and tumor progression. J. Neurooncol. *85*, 133–148.

Candolfi, M., Curtin, J.F., Yagiz, K., Assi, H., Wibowo, M.K., Alzadeh, G.E., Foulad, D., Muhammad, A.G., Salehi, S., Keech, N., et al. (2011). B cells are critical to T-cell-mediated antitumor immunity induced by a combined immune-stimulatory/conditionally cytotoxic therapy for glioblastoma. Neoplasia *13*, 947–960.

Capes-Davis, A., Theodosopoulos, G., Atkin, I., Drexler, H.G., Kohara, A., MacLeod, R.A.F., Masters, J.R., Nakamura, Y., Reid, Y.A., Reddel, R.R., et al. (2010). Check your cultures! A list of cross-contaminated or misidentified cell lines. Int. J. Cancer *127*, 1–8.

Capper, D., Jones, D.T.W., Sill, M., Hovestadt, V., Schrimpf, D., Sturm, D., Koelsche, C., Sahm, F., Chavez, L., Reuss, D.E., et al. (2018). DNA methylation-based classification of central nervous system tumours. Nature *555*, 469–474.

Caruso, F.P., Garofano, L., D'Angelo, F., Yu, K., Tang, F., Yuan, J., Zhang, J., Cerulo, L., Pagnotta, S.M., Bedognetti, D., et al. (2020). A map of tumor-host interactions in glioma at single-cell resolution. Gigascience *9*, 1–14.

Ceccarelli, M., Barthel, F.P., Malta, T.M., Sabedot, T.S., Salama, S.R., Murray, B.A., Morozova, O., Newton, Y., Radenbaugh, A., Pagnotta, S.M., et al. (2016). Molecular Profiling Reveals Biologically Discrete Subsets and Pathways of Progression in Diffuse Glioma. Cell *164*, 550–563.

Chaligne, R., Gaiti, F., Silverbush, D., Schiffman, J.S., Weisman, H.R., Kluegel, L., Gritsch, S., Deochand, S.D., Gonzalez Castro, L.N., Richman, A.R., et al. (2021). Epigenetic encoding, heritability and plasticity of glioma transcriptional cell states. Nat. Genet. *53*, 1469–1479.

Chalmers, A.J., Ruff, E.M., Martindale, C., Lovegrove, N., and Short, S.C. (2009). Cytotoxic effects of temozolomide and radiation are additive- and schedule-dependent. Int. J. Radiat. Oncol. Biol. Phys. *75*, 1511–1519.

Chandra, A., Jahangiri, A., Chen, W., Nguyen, A.T., Yagnik, G., Pereira, M.P., Jain, S., Garcia, J.H., Shah, S.S., Wadhwa, H., et al. (2020). Clonal ZEB1-driven mesenchymal transition promotes targetable oncologic antiangiogenic therapy resistance. Cancer Res. *80*, 1498–1511.

Chatterjee, R. (2007). Cases of Mistaken Identity. Science (80-.). *315*, 928–931.

Chen, A.X., Gartrell, R.D., Zhao, J., Upadhyayula, P.S., Zhao, W., Yuan, J., Minns, H.E., Dovas, A., Bruce, J.N., Lasorella, A., et al. (2021a). Single-cell characterization of macrophages in glioblastoma reveals MARCO as a mesenchymal pro-tumor marker. Genome Med. *13*, 88.

Chen, D., Abu Zaid, M.I., Reiter, J.L., Czader, M., Wang, L., McGuire, P., Xuei, X., Gao, H., Huang, K., Abonour, R., et al. (2021b). Cryopreservation Preserves Cell-Type Composition

and Gene Expression Profiles in Bone Marrow Aspirates From Multiple Myeloma Patients. Front. Genet. *12*, 1–10.

Chen, J., Li, Y., Yu, T.-S.S., McKay, R.M., Burns, D.K., Kernie, S.G., and Parada, L.F. (2012). A restricted cell population propagates glioblastoma growth after chemotherapy. Nature *488*, 522–526.

Chen, J., Mao, S., Li, H., Zheng, M., Yi, L., Lin, J.-M., and Lin, Z. (2017a). The pathological structure of the perivascular niche in different microvascular patterns of glioblastoma. PLoS One *12*, e0182183.

Chen, P.-L., Roh, W., Reuben, A., Cooper, Z.A., Spencer, C.N., Prieto, P.A., Miller, J.P., Bassett, R.L., Gopalakrishnan, V., Wani, K., et al. (2016). Analysis of Immune Signatures in Longitudinal Tumor Samples Yields Insight into Biomarkers of Response and Mechanisms of Resistance to Immune Checkpoint Blockade. Cancer Discov. *6*, 827–837.

Chen, Z., Feng, X., Herting, C.J., Garcia, V.A., Nie, K., Pong, W.W., Rasmussen, R., Dwivedi, B., Seby, S., Wolf, S.A., et al. (2017b). Cellular and molecular identity of tumor-associated macrophages in glioblastoma. Cancer Res. *77*, 2266–2278.

Chivukula, I. V., Ramsköld, D., Storvall, H., Anderberg, C., Jin, S., Mamaeva, V., Sahlgren, C., Pietras, K., Sandberg, R., and Lendahl, U. (2015). Decoding breast cancer tissue–stroma interactions using species-specific sequencing. Breast Cancer Res. *17*, 109.

Chongsathidkiet, P., Jackson, C., Koyama, S., Loebel, F., Cui, X., Farber, S.H., Woroniecka, K., Elsamadicy, A.A., Dechant, C.A., Kemeny, H.R., et al. (2018). Sequestration of T cells in bone marrow in the setting of glioblastoma and other intracranial tumors. Nat. Med. *24*, 1459–1468.

Chow, R.D., Guzman, C.D., Wang, G., Schmidt, F., Youngblood, M.W., Ye, L., Errami, Y., Dong, M.B., Martinez, M.A., Zhang, S., et al. (2017). AAV-mediated direct in vivo CRISPR screen identifies functional suppressors in glioblastoma. Nat. Neurosci. *20*, 1329–1341.

Clark, M.J., Homer, N., O'Connor, B.D., Chen, Z., Eskin, A., Lee, H., Merriman, B., and Nelson, S.F. (2010). U87MG Decoded: The Genomic Sequence of a Cytogenetically Aberrant Human Cancer Cell Line. PLoS Genet. *6*, e1000832.

Clevers, H. (2016). Modeling Development and Disease with Organoids. Cell *165*, 1586–1597.

Cohen, M.H., Johnson, J.R., and Pazdur, R. (2005). Food and Drug Administration Drug Approval Summary: Temozolomide Plus Radiation Therapy for the Treatment of Newly Diagnosed Glioblastoma Multiforme. Clin. Cancer Res. *11*, 6767–6771.

Conway, T., Wazny, J., Bromage, A., Tymms, M., Sooraj, D., Williams, E.D., and Beresford-Smith, B. (2012). Xenome--a tool for classifying reads from xenograft samples. Bioinformatics *28*, i172–i178.

Cooper, L.A.D., Gutman, D.A., Chisolm, C., Appin, C., Kong, J., Rong, Y., Kurc, T., Van Meir, E.G., Saltz, J.H., Moreno, C.S., et al. (2012). The tumor microenvironment strongly impacts master transcriptional regulators and gene expression class of glioblastoma. Am. J. Pathol. *180*, 2108–2119.

Cudalbu, C., Bady, P., Lai, M., Xin, L., Gusyatiner, O., Hamou, M.-F., Lepore, M., Brouland, J.-P., Daniel, R.T., Hottinger, A.F., et al. (2021). Metabolic and transcriptomic profiles of glioblastoma invasion revealed by comparisons between patients and corresponding

orthotopic xenografts in mice. Acta Neuropathol. Commun. *9*, 1–16.

Cugurra, A., Mamuladze, T., Rustenhoven, J., Dykstra, T., Beroshvili, G., Greenberg, Z.J., Baker, W., Papadopoulos, Z., Drieu, A., Blackburn, S., et al. (2021). Skull and vertebral bone marrow are myeloid cell reservoirs for the meninges and CNS parenchyma. Science (80-.). *373*.

Dang, L., White, D.W., Gross, S., Bennett, B.D., Bittinger, M.A., Driggers, E.M., Fantin, V.R., Jang, H.G., Jin, S., Keenan, M.C., et al. (2009). Cancer-associated IDH1 mutations produce 2-hydroxyglutarate. Nature *462*, 739–744.

Darmanis, S., Sloan, S.A., Croote, D., Mignardi, M., Chernikova, S., Samghababi, P., Zhang, Y., Neff, N., Kowarsky, M., Caneda, C., et al. (2017). Single-Cell RNA-Seq Analysis of Infiltrating Neoplastic Cells at the Migrating Front of Human Glioblastoma. Cell Rep. *21*, 1399–1410.

Davis, M.E. (2016). Glioblastoma: Overview of Disease and Treatment. Clin. J. Oncol. Nurs. *20*, S2-8.

Decarvalho, A.C., Kim, H., Poisson, L.M., Winn, M.E., Mueller, C., Cherba, D., Koeman, J., Seth, S., Protopopov, A., Felicella, M., et al. (2018). Discordant inheritance of chromosomal and extrachromosomal DNA elements contributes to dynamic disease evolution in glioblastoma. Nat. Genet. *50*, 708–717.

Dekker, L.J.M., Kannegieter, N.M., Haerkens, F., Toth, E., Kros, J.M., Steenhoff Hov, D.A., Fillebeen, J., Verschuren, L., Leenstra, S., Ressa, A., et al. (2020). Multiomics profiling of paired primary and recurrent glioblastoma patient tissues. Neuro-Oncology Adv. *2*, 1–12.

Denisenko, E., Guo, B.B., Jones, M., Hou, R., de Kock, L., Lassmann, T., Poppe, D., Clément, O., Simmons, R.K., Lister, R., et al. (2020). Systematic assessment of tissue dissociation and storage biases in single-cell and single-nucleus RNA-seq workflows. Genome Biol. *21*, 130.

Desjardins, A., Gromeier, M., Herndon, J.E., Beaubier, N., Bolognesi, D.P., Friedman, A.H., Friedman, H.S., McSherry, F., Muscat, A.M., Nair, S., et al. (2018). Recurrent Glioblastoma Treated with Recombinant Poliovirus. N. Engl. J. Med. *379*, 150–161.

Dietmann, S., Agathou, S., Spitzer, S.O., Kronenberg-Versteeg, D., Káradóttir, R.T., de Faria, O., Evans, K.A., Sitnikov, S., and Kamen, Y. (2019). Oligodendrocyte Progenitor Cells Become Regionally Diverse and Heterogeneous with Age. Neuron 1–13.

Díez Valle, R., Tejada Solis, S., Idoate Gastearena, M.A., García De Eulate, R., Domínguez Echávarri, P., and Aristu Mendiroz, J. (2011). Surgery guided by 5-aminolevulinic fluorescence in glioblastoma: Volumetric analysis of extent of resection in single-center experience. J. Neurooncol. *102*, 105–113.

Dirkse, A., Golebiewska, A., Buder, T., Nazarov, P. V., Muller, A., Poovathingal, S., Brons, N.H.C.C., Leite, S., Sauvageot, N., Sarkisjan, D., et al. (2019). Stem cell-associated heterogeneity in Glioblastoma results from intrinsic tumor plasticity shaped by the microenvironment. Nat. Commun. *10*, 1–16.

Draaisma, K., Chatzipli, A., Taphoorn, M., Kerkhof, M., Weyerbrock, A., Sanson, M., Hoeben, A., Lukacova, S., Lombardi, G., Leenstra, S., et al. (2020). Molecular evolution of IDH wild-type glioblastomas treated with standard of care affects survival and design of precision medicine trials: A report from the EORTC 1542 study. J. Clin. Oncol. *38*, 81–99.

Drost, J., and Clevers, H. (2018). Organoids in cancer research. Nat. Rev. Cancer *18*, 407–418.

Eatz, T.A., Eichberg, D.G., Lu, V.M., Di, L., Komotar, R.J., and Ivan, M.E. (2022). Intraoperative 5-ALA fluorescence-guided resection of high-grade glioma leads to greater extent of resection with better outcomes: a systematic review. J. Neurooncol. 1–24.

Eiraku, M., and Sasai, Y. (2012). Self-formation of layered neural structures in three-dimensional culture of ES cells. Curr. Opin. Neurobiol. *22*, 768–777.

Engelhardt, J.J., Boldajipour, B., Beemiller, P., Pandurangi, P., Sorensen, C., Werb, Z., Egeblad, M., and Krummel, M.F. (2012). Marginating Dendritic Cells of the Tumor Microenvironment Cross-Present Tumor Antigens and Stably Engage Tumor-Specific T Cells. Cancer Cell *21*, 402–417.

Erasimus, H., Gobin, M., Niclou, S., and Van Dyck, E. (2016). DNA repair mechanisms and their clinical impact in glioblastoma. Mutat. Res. - Rev. Mutat. Res. *769*, 19–35.

Escartin, C., Galea, E., Lakatos, A., O'Callaghan, J.P., Petzold, G.C., Serrano-Pozo, A., Steinhäuser, C., Volterra, A., Carmignoto, G., Agarwal, A., et al. (2021). Reactive astrocyte nomenclature, definitions, and future directions. Nat. Neurosci. *24*, 312–325.

Eyler, C.E., Matsunaga, H., Hovestadt, V., Vantine, S.J., van Galen, P., and Bernstein, B.E. (2020). Single-cell lineage analysis reveals genetic and epigenetic interplay in glioblastoma drug resistance. Genome Biol. *21*, 1–21.

Fabian, C., Han, M., Bjerkvig, R., and Niclou, S.P. (2021). Novel facets of glioma invasion (Elsevier Inc.).

Fabian, D., Guillermo Prieto Eibl, M., Alnahhas, I., Sebastian, N., Giglio, P., Puduvalli, V., Gonzalez, J., and Palmer, J. (2019). Treatment of Glioblastoma (GBM) with the Addition of Tumor-Treating Fields (TTF): A Review. Cancers (Basel). *11*, 174.

Fack, F., Espedal, H., Keunen, O., Golebiewska, A., Obad, N., Harter, P.N., Mittelbronn, M., Bähr, O., Weyerbrock, A., Stuhr, L., et al. (2015). Bevacizumab treatment induces metabolic adaptation toward anaerobic metabolism in glioblastomas. Acta Neuropathol. *129*, 115–131.

Fan, J., Slowikowski, K., and Zhang, F. (2020). Single-cell transcriptomics in cancer: computational challenges and opportunities. Exp. Mol. Med. *52*, 1452–1465.

Fares, J., Ahmed, A.U., Ulasov, I. V., Sonabend, A.M., Miska, J., Lee-Chang, C., Balyasnikova, I. V., Chandler, J.P., Portnow, J., Tate, M.C., et al. (2021). Neural stem cell delivery of an oncolytic adenovirus in newly diagnosed malignant glioma: a first-in-human, phase 1, dose-escalation trial. Lancet Oncol. *22*, 1103–1114.

Fernández-Castañeda, A., Chappell, M.S., Rosen, D.A., Seki, S.M., Beiter, R.M., Johanson, D.M., Liskey, D., Farber, E., Onengut-Gumuscu, S., Overall, C.C., et al. (2020). The active contribution of OPCs to neuroinflammation is mediated by LRP1. Acta Neuropathol. *139*, 365–382.

Filbin, M.G., Tirosh, I., Hovestadt, V., Shaw, M.L., Escalante, L.E., Mathewson, N.D., Neftel, C., Frank, N., Pelton, K., Hebert, C.M., et al. (2018). Developmental and oncogenic programs in H3K27M gliomas dissected by single-cell RNA-seq. Science (80-.). *360*, 331–335.

Flavahan, W.A., Wu, Q., Hitomi, M., Rahim, N., Kim, Y., Sloan, A.E., Weil, R.J., Nakano, I., Sarkaria, J.N., Stringer, B.W., et al. (2013). Brain tumor initiating cells adapt to restricted nutrition through preferential glucose uptake. Nat. Neurosci. *16*, 1373–1382.

Folaron, M., Merzianu, M., Duvvuri, U., Ferris, R.L., and Seshadri, M. (2019). Profiling the Stromal and Vascular Heterogeneity in Patient-derived Xenograft Models of Head and Neck Cancer: Impact on Therapeutic Response. Cancers (Basel). *11*, 951.

Foley, J.W., Zhu, C., Jolivet, P., Zhu, S.X., Lu, P., Meaney, M.J., and West, R.B. (2019). Gene expression profiling of single cells from archival tissue with laser-capture microdissection and Smart-3SEQ. Genome Res. *29*, 1816–1825.

Fontanilles, M., Marguet, F., Beaussire, L., Magne, N., Pépin, L.-F., Alexandru, C., Tennevet, I., Hanzen, C., Langlois, O., Jardin, F., et al. (2020). Cell-free DNA and circulating TERT promoter mutation for disease monitoring in newly-diagnosed glioblastoma. Acta Neuropathol. Commun. *8*, 179.

Fortunato, A., Boddy, A., Mallo, D., Aktipis, A., Maley, C.C., and Pepper, J.W. (2017). Natural selection in cancer biology: From molecular snowflakes to trait hallmarks. Cold Spring Harb. Perspect. Med. *7*.

Fossati, G., Ricevuti, G., Edwards, S.W., Walker, C., Dalton, A., and Rossi, M.L. (1999). Neutrophil infiltration into human gliomas. Acta Neuropathol. *98*, 349–354.

Francis, J.M., Zhang, C.Z., Maire, C.L., Jung, J., Manzo, V.E., Adalsteinsson, V.A., Homer, H., Haidar, S., Blumenstiel, B., Pedamallu, C.S., et al. (2014). EGFR variant heterogeneity in glioblastoma resolved through single-nucleus sequencing. Cancer Discov *4*, 956–971.

Frederico, S.C., Hancock, J.C., Brettschneider, E.E.S., Ratnam, N.M., Gilbert, M.R., and Terabe, M. (2021). Making a Cold Tumor Hot: The Role of Vaccines in the Treatment of Glioblastoma. Front. Oncol. *11*, 1591.

Friebel, E., Kapolou, K., Unger, S., Núñez, N.G., Utz, S., Rushing, E.J., Regli, L., Weller, M., Greter, M., Tugues, S., et al. (2020). Single-Cell Mapping of Human Brain Cancer Reveals Tumor-Specific Instruction of Tissue-Invading Leukocytes. Cell 1–17.

Friedrich, M., Sankowski, R., Bunse, L., Kilian, M., Green, E., Ramallo Guevara, C., Pusch, S., Poschet, G., Sanghvi, K., Hahn, M., et al. (2021). Tryptophan metabolism drives dynamic immunosuppressive myeloid states in IDH-mutant gliomas. Nat. Cancer.

Fu, W., Wang, W., Li, H., Jiao, Y., Huo, R., Yan, Z., Wang, J., Wang, S., Wang, J., Chen, D., et al. (2020). Single-Cell Atlas Reveals Complexity of the Immunosuppressive Microenvironment of Initial and Recurrent Glioblastoma. Front. Immunol. *11*, 1–12.

Galdieri, L., Jash, A., Malkova, O., Mao, D.D., DeSouza, P., Chu, Y.E., Salter, A., Campian, J.L., Naegle, K.M., Brennan, C.W., et al. (2021). Defining phenotypic and functional heterogeneity of glioblastoma stem cells by mass cytometry. JCI Insight *6*.

Galli, R., Binda, E., Orfanelli, U., Cipelletti, B., Gritti, A., De Vitis, S., Fiocco, R., Foroni, C., Dimeco, F., and Vescovi, A. (2004). Isolation and characterization of tumorigenic, stem-like neural precursors from human glioblastoma. Cancer Res. *64*, 7011–7021.

Gandhi, S., Meybodi, A.T., Belykh, E., Cavallo, C., Zhao, X., Pasha Syed, M., Borba Moreira, L., Lawton, M.T., Nakaji, P., and Preul, M.C. (2019). Survival outcomes among patients with high-grade glioma treated with 5-aminolevulinic acid–guided surgery: A systematic review and meta-analysis. Front. Oncol. *9*, 1–13.

García-Romero, N., González-Tejedo, C., Carrión-Navarro, J., Esteban-Rubio, S., Rackov, G., Rodríguez-Fanjul, V., Cruz, J.O.-D. La, Prat-Acín, R., Peris-Celda, M., Blesa, D., et al. (2016). Cancer stem cells from human glioblastoma resemble but do not mimic original tumors after *in vitro* passaging in serum-free media. Oncotarget *7*, 65888–65901.

Garofano, L., Migliozzi, S., Oh, Y.T., D'Angelo, F., Najac, R.D., Ko, A., Frangaj, B., Caruso, F.P., Yu, K., Yuan, J., et al. (2021). Pathway-based classification of glioblastoma uncovers a mitochondrial subtype with therapeutic vulnerabilities. Nat. Cancer *2*, 141–156.

Gates, E.D.H., Yang, J., Fukumura, K., Lin, J.S., Weinberg, J.S., Prabhu, S.S., Long, L., Fuentes, D., Sulman, E.P., Huse, J.T., et al. (2019). Spatial Distance Correlates With Genetic Distance in Diffuse Glioma. Front. Oncol. *9*, 676.

Gatto, N.M., Ogata, P., and Lytle, B. (2021). Farming , Pesticides , and Brain Cancer : A 20-Year Updated Systematic Literature Review and Meta-Analysis.

Gholamin, S., Mitra, S.S., Feroze, A.H., Liu, J., Kahn, S.A., Zhang, M., Esparza, R., Richard, C., Ramaswamy, V., Remke, M., et al. (2017). Disrupting the CD47-SIRPα anti-phagocytic axis by a humanized anti-CD47 antibody is an efficacious treatment for malignant pediatric brain tumors. Sci. Transl. Med. *9*.

Gilbert, M.R., Dignam, J.J., Armstrong, T.S., Wefel, J.S., Blumenthal, D.T., Vogelbaum, M.A., Colman, H., Chakravarti, A., Pugh, S., Won, M., et al. (2014). A Randomized Trial of Bevacizumab for Newly Diagnosed Glioblastoma. N. Engl. J. Med. *370*, 699–708.

Ginhoux, F., Greter, M., Leboeuf, M., Nandi, S., See, P., Gokhan, S., Mehler, M.F., Conway, S.J., Ng, L.G., Stanley, E.R., et al. (2010). Fate Mapping Analysis Reveals That Adult Microglia Derive from Primitive Macrophages. Science (80-.). *330*, 841–845.

Glass, R., and Synowitz, M. (2014). CNS macrophages and peripheral myeloid cells in brain tumours. Acta Neuropathol. *128*, 347–362.

Goddery, E.N., Fain, C.E., Lipovsky, C.G., Ayasoufi, K., Yokanovich, L.T., Malo, C.S., Khadka, R.H., Tritz, Z.P., Jin, F., Hansen, M.J., et al. (2021). Microglia and Perivascular Macrophages Act as Antigen Presenting Cells to Promote CD8 T Cell Infiltration of the Brain. Front. Immunol. *12*, 1–19.

Golebiewska, A., Bougnaud, S., Stieber, D., Brons, N.H.C., Vallar, L., Hertel, F., Klink, B., Schröck, E., Bjerkvig, R., and Niclou, S.P. (2013). Side population in human glioblastoma is non-tumorigenic and characterizes brain endothelial cells. Brain *136*, 1462–1475.

Golebiewska, A., Hau, A.-C., Oudin, A., Stieber, D., Yabo, Y.A., Baus, V., Barthelemy, V., Klein, E., Bougnaud, S., Keunen, O., et al. (2020). Patient-derived organoids and orthotopic xenografts of primary and recurrent gliomas represent relevant patient avatars for precision oncology. Acta Neuropathol. *140*, 919–949.

Gomes-Leal, W. (2012). Microglial physiopathology: how to explain the dual role of microglia after acute neural disorders? Brain Behav. *2*, 345–356.

Gómez-Oliva, R., Domínguez-García, S., Carrascal, L., Abalos-Martínez, J., Pardillo-Díaz, R., Verástegui, C., Castro, C., Nunez-Abades, P., and Geribaldi-Doldán, N. (2021). Evolution of Experimental Models in the Study of Glioblastoma: Toward Finding Efficient Treatments. Front. Oncol. *10*, 1–16.

Gomez-Roman, N., Stevenson, K., Gilmour, L., Hamilton, G., and Chalmers, A.J. (2016). A novel 3D human glioblastoma cell culture system for modeling drug and radiation

responses. Neuro. Oncol. *19*, now164.

Gomez Perdiguero, E., Klapproth, K., Schulz, C., Busch, K., Azzoni, E., Crozet, L., Garner, H., Trouillet, C., De Bruijn, M.F., Geissmann, F., et al. (2015). Tissue-resident macrophages originate from yolk-sac-derived erythro-myeloid progenitors. Nature *518*, 547–551.

Gordon, S.R., Maute, R.L., Dulken, B.W., Hutter, G., George, B.M., McCracken, M.N., Gupta, R., Tsai, J.M., Sinha, R., Corey, D., et al. (2017). PD-1 expression by tumour-associated macrophages inhibits phagocytosis and tumour immunity. Nature *545*, 495–499.

Grabowski, M.M., Sankey, E.W., Ryan, K.J., Chongsathidkiet, P., Lorrey, S.J., Wilkinson, D.S., and Fecci, P.E. (2021). Immune suppression in gliomas. J. Neurooncol. *151*, 3–12.

Greaves, M. (2015). Evolutionary determinants of cancer. Cancer Discov. *5*, 806–821.

Guilhamon, P., Chesnelong, C., Kushida, M.M., Nikolic, A., Singhal, D., Macleod, G., Tonekaboni, S.A.M., Cavalli, F.M.G., Arlidge, C., Rajakulendran, N., et al. (2021). Single-cell chromatin accessibility profiling of glioblastoma identifies an invasive cancer stem cell population associated with lower survival. Elife *10*, 1–20.

Guillaumet-Adkins, A., Rodríguez-Esteban, G., Mereu, E., Mendez-Lago, M., Jaitin, D.A., Villanueva, A., Vidal, A., Martinez-Marti, A., Felip, E., Vivancos, A., et al. (2017). Single-cell transcriptome conservation in cryopreserved cells and tissues. Genome Biol. *18*, 45.

Guo, X., Pan, Y., Xiong, M., Sanapala, S., Anastasaki, C., Cobb, O., Dahiya, S., and Gutmann, D.H. (2020). Midkine activation of CD8+ T cells establishes a neuron–immune–cancer axis responsible for low-grade glioma growth. Nat. Commun. *11*, 1–15.

Gupta, P.B., Pastushenko, I., Skibinski, A., Blanpain, C., and Kuperwasser, C. (2019). Phenotypic Plasticity: Driver of Cancer Initiation, Progression, and Therapy Resistance. Cell Stem Cell *24*, 65–78.

Haar, C.P., Hebbar, P., Wallace, G.C., Das, A., Vandergrift, W.A., Smith, J.A., Giglio, P., Patel, S.J., Ray, S.K., and Banik, N.L. (2012). Drug resistance in glioblastoma: A mini review. Neurochem. Res. *37*, 1192–1200.

Habib, N., Avraham-Davidi, I., Basu, A., Burks, T., Shekhar, K., Hofree, M., Choudhury, S.R., Aguet, F., Gelfand, E., Ardlie, K., et al. (2017). Massively parallel single-nucleus RNA-seq with DroNc-seq. Nat. Methods *14*, 955–958.

Haddad, A.F., Young, J.S., Amara, D., Berger, M.S., Raleigh, D.R., Aghi, M.K., and Butowski, N.A. (2021). Mouse models of glioblastoma for the evaluation of novel therapeutic strategies. Neuro-Oncology Adv. *3*, 1–16.

Halliday, J., Helmy, K., Pattwell, S.S., Pitter, K.L., LaPlant, Q., Ozawa, T., and Holland, E.C. (2014). In vivo radiation response of proneural glioma characterized by protective p53 transcriptional program and proneural-mesenchymal shift. Proc. Natl. Acad. Sci. U. S. A. *111*, 5248–5253.

Hambardzumyan, D., and Bergers, G. (2015). Glioblastoma: Defining Tumor Niches. Trends in Cancer *1*, 252–265.

Hambardzumyan, D., Amankulor, N.M., Helmy, K.Y., Becher, O.J., and Holland, E.C. (2009). Modeling Adult Gliomas Using RCAS/t-va Technology. Transl. Oncol. *2*, 89-IN6.

Hambardzumyan, D., Parada, L.F., Holland, E.C., and Charest, A. (2011). Genetic modeling

of gliomas in mice: New tools to tackle old problems. Glia *59*, 1155–1168.

Hambardzumyan, D., Gutmann, D.H., and Kettenmann, H. (2015). The role of microglia and macrophages in glioma maintenance and progression. Nat. Neurosci. *19*, 20–27.

Hammond, T.R., Dufort, C., Dissing-Olesen, L., Giera, S., Young, A., Wysoker, A., Walker, A.J., Gergits, F., Segel, M., Nemesh, J., et al. (2019). Single-Cell RNA Sequencing of Microglia throughout the Mouse Lifespan and in the Injured Brain Reveals Complex Cell-State Changes. Immunity *50*, 253-271.e6.

Han, S., Liu, Y., Cai, S.J., Qian, M., Ding, J., Larion, M., Gilbert, M.R., and Yang, C. (2020). IDH mutation in glioma: molecular mechanisms and potential therapeutic targets. Br. J. Cancer *122*, 1580–1589.

Han, X., Wang, R., Zhou, Y., Fei, L., Sun, H., Lai, S., Saadatpour, A., Zhou, Z., Chen, H., Ye, F., et al. (2018). Mapping the Mouse Cell Atlas by Microwell-Seq. Cell *172*, 1091-1107.e17.

Hanahan, D., and Weinberg, R.A. (2011). Hallmarks of cancer: The next generation. Cell *144*, 646–674.

Hao, Y., Hao, S., Andersen-Nissen, E., Mauck, W.M., Zheng, S., Butler, A., Lee, M.J., Wilk, A.J., Darby, C., Zager, M., et al. (2021). Integrated analysis of multimodal single-cell data. Cell *184*, 3573-3587.e29.

Hara, T., Chanoch-Myers, R., Mathewson, N.D., Myskiw, C., Atta, L., Bussema, L., Eichhorn, S.W., Greenwald, A.C., Kinker, G.S., Rodman, C., et al. (2021). Interactions between cancer cells and immune cells drive transitions to mesenchymal-like states in glioblastoma. Cancer Cell *39*, 779-792.e11.

Hatoum, A., Mohammed, R., and Zakieh, O. (2019). The unique invasiveness of glioblastoma and possible drug targets on extracellular matrix. Cancer Manag. Res. *Volume 11*, 1843–1855.

He, C., Sheng, L., Pan, D., Jiang, S., Ding, L., Ma, X., Liu, Y., and Jia, D. (2021). Single-Cell Transcriptomic Analysis Revealed a Critical Role of SPP1/CD44-Mediated Crosstalk Between Macrophages and Cancer Cells in Glioma. Front. Cell Dev. Biol. *9*, 3184.

Hede, S.-M., Hansson, I., Afink, G.B., Eriksson, A., Nazarenko, I., Andrae, J., Genove, G., Westermark, B., and Nistér, M. (2009). GFAP promoter driven transgenic expression of PDGFB in the mouse brain leads to glioblastoma in a *Trp53 null* background. Glia *57*, 1143–1153.

Hegi, M.E., Diserens, A.-C., Gorlia, T., Hamou, M.-F., de Tribolet, N., Weller, M., Kros, J.M., Hainfellner, J.A., Mason, W., Mariani, L., et al. (2005). *MGMT* Gene Silencing and Benefit from Temozolomide in Glioblastoma. N. Engl. J. Med. *352*, 997–1003.

Helmink, B.A., Reddy, S.M., Gao, J., Zhang, S., Basar, R., Thakur, R., Yizhak, K., Sade-Feldman, M., Blando, J., Han, G., et al. (2020). B cells and tertiary lymphoid structures promote immunotherapy response. Nature *577*, 549–555.

Henrik Heiland, D., Ravi, V.M., Behringer, S.P., Frenking, J.H., Wurm, J., Joseph, K., Garrelfs, N.W.C., Strähle, J., Heynckes, S., Grauvogel, J., et al. (2019). Tumor-associated reactive astrocytes aid the evolution of immunosuppressive environment in glioblastoma. Nat. Commun. *10*, 2541.

Herranz, C., Fernández, F., Martín-Ibáñez, R., Blasco, E., Crespo, E., De la Fuente, C., Añor, S., Rabanal, R.M., Canals, J.M., and Pumarola, M. (2016). Spontaneously Arising Canine Glioma as a Potential Model for Human Glioma. J. Comp. Pathol. *154*, 169–179.

Hickman, S.E., Kingery, N.D., Ohsumi, T.K., Borowsky, M.L., Wang, L., Means, T.K., and El Khoury, J. (2013). The microglial sensome revealed by direct RNA sequencing. Nat. Neurosci. *16*, 1896–1905.

Hicks, J., Platt, S., Kent, M., and Haley, A. (2017). Canine brain tumours: a model for the human disease? Vet. Comp. Oncol. *15*, 252–272.

Hicks, W.H., Bird, C.E., Traylor, J.I., Shi, D.D., El Ahmadieh, T.Y., Richardson, T.E., McBrayer, S.K., and Abdullah, K.G. (2021). Contemporary mouse models in glioma research. Cells *10*, 1–18.

Hidalgo, M., Amant, F., Biankin, A. V, Budinská, E., Byrne, A.T., Caldas, C., Clarke, R.B., de Jong, S., Jonkers, J., Mælandsmo, G.M., et al. (2014). Patient-derived xenograft models: an emerging platform for translational cancer research. Cancer Discov. *4*, 998–1013.

Hjelmeland, A.B., Wu, Q., Heddleston, J.M., Choudhary, G.S., MacSwords, J., Lathia, J.D., McLendon, R., Lindner, D., Sloan, A., and Rich, J.N. (2011). Acidic stress promotes a glioma stem cell phenotype. Cell Death Differ *18*, 829–840.

Van Hove, H., Martens, L., Scheyltjens, I., De Vlaminck, K., Pombo Antunes, A.R., De Prijck, S., Vandamme, N., De Schepper, S., Van Isterdael, G., Scott, C.L., et al. (2019). A single-cell atlas of mouse brain macrophages reveals unique transcriptional identities shaped by ontogeny and tissue environment. Nat. Neurosci. *22*, 1021–1035.

Hu, J., Xiao, Q., Dong, M., Guo, D., Wu, X., and Wang, B. (2020a). Glioblastoma Immunotherapy Targeting the Innate Immune Checkpoint CD47-SIRPα Axis. Front. Immunol. *11*, 3113.

Hu, X., Deng, Q., Ma, L., Li, Q., Chen, Y., Liao, Y., Zhou, F., Zhang, C., Shao, L., Feng, J., et al. (2020b). Meningeal lymphatic vessels regulate brain tumor drainage and immunity. Cell Res. *30*, 229–243.

Huang, A.Y.C., Golumbek, P., Ahmadzadeh, M., Jaffee, E., Pardoll, D., and Levitsky, H. (1994). Role of Bone Marrow-Derived Cells in Presenting MHC Class I-Restricted Tumor Antigens. Science (80-.). *264*, 961–965.

Hubert, C.G., Rivera, M., Spangler, L.C., Wu, Q., Mack, S.C., Prager, B.C., Couce, M., McLendon, R.E., Sloan, A.E., and Rich, J.N. (2016). A three-dimensional organoid culture system derived from human glioblastomas recapitulates the hypoxic gradients and cancer stem cell heterogeneity of tumors found in vivo. Cancer Res. *76*, 2465–2477.

Hughes, E.G., Kang, S.H., Fukaya, M., and Bergles, D.E. (2013). Oligodendrocyte progenitors balance growth with self-repulsion to achieve homeostasis in the adult brain. Nat. Neurosci. *16*, 668–676.

Huse, J.T., and Holland, E.C. (2009). Genetically Engineered Mouse Models of Brain Cancer and the Promise of Preclinical Testing. Brain Pathol. *19*, 132–143.

Huszthy, P.C., Daphu, I., Niclou, S.P., Stieber, D., Nigro, J.M., Sakariassen, P.Ø., Miletic, H., Thorsen, F., and Bjerkvig, R. (2012). In vivo models of primary brain tumors: Pitfalls and Perspectives. Neuro. Oncol. *14*, 979–993.

Huszthy, P.C., Sakariassen, P., Espedal, H., Brokstad, K.A., Bjerkvig, R., and Miletic, H. (2015). Engraftment of human glioblastoma cells in immunocompetent rats through acquired immunosuppression. PLoS One *10*, 1–17.

Hutter, G., Theruvath, J., Graef, C.M., Zhang, M., Schoen, M.K., Manz, E.M., Bennett, M.L., Olson, A., Azad, T.D., Sinha, R., et al. (2019). Microglia are effector cells of CD47-SIRPα antiphagocytic axis disruption against glioblastoma. Proc. Natl. Acad. Sci. *116*, 997–1006.

Iacobuzio-Donahue, C.A., Litchfield, K., and Swanton, C. (2020). Intratumor heterogeneity reflects clinical disease course. Nat. Cancer *1*, 3–6.

Inoue, S., Ichikawa, T., Kurozumi, K., Maruo, T., Onishi, M., Yoshida, K., Fujii, K., Kambara, H., Chiocca, E.A., and Date, I. (2012). Novel Animal Glioma Models that Separately Exhibit Two Different Invasive and Angiogenic Phenotypes of Human Glioblastomas. World Neurosurg. *78*, 670–682.

Irtenkauf, S.M., Sobiechowski, S., Hasselbach, L.A., Nelson, K.K., Transou, A.D., Carlton, E.T., Mikkelsen, T., and deCarvalho, A.C. (2017). Optimization of Glioblastoma Mouse Orthotopic Xenograft Models for Translational Research. Comp. Med. *67*, 300–314.

Jackson, C.M., Choi, J., and Lim, M. (2019). Mechanisms of immunotherapy resistance: lessons from glioblastoma. Nat. Immunol. *20*, 1100–1109.

Jacob, F., Salinas, R.D., Zhang, D.Y., Nguyen, P.T.T., Schnoll, J.G., Wong, S.Z.H., Thokala, R., Sheikh, S., Saxena, D., Prokop, S., et al. (2020). A Patient-Derived Glioblastoma Organoid Model and Biobank Recapitulates Inter- and Intra-tumoral Heterogeneity. Cell *180*, 188-204.e22.

Jin, X., Kim, L.J.Y., Wu, Q., Wallace, L.C., Prager, B.C., Sanvoranart, T., Gimple, R.C., Wang, X., Mack, S.C., Miller, T.E., et al. (2017). Targeting glioma stem cells through combined BMI1 and EZH2 inhibition. Nat. Med. *23*, 1352.

Johanns, T.M., Ward, J.P., Miller, C.A., Wilson, C., Kobayashi, D.K., Bender, D., Fu, Y., Alexandrov, A., Mardis, E.R., Artyomov, M.N., et al. (2016). Endogenous Neoantigen-Specific CD8 T Cells Identified in Two Glioblastoma Models Using a Cancer Immunogenomics Approach. Cancer Immunol. Res. *4*, 1007–1015.

John Lin, C.-C.C., Yu, K., Hatcher, A., Huang, T.-W.W., Lee, H.K., Carlson, J., Weston, M.C., Chen, F., Zhang, Y., Zhu, W., et al. (2017). Identification of diverse astrocyte populations and their malignant analogs. Nat. Neurosci. *20*, 396–405.

Johnson, K.C., Anderson, K.J., Courtois, E.T., Gujar, A.D., Barthel, F.P., Varn, F.S., Luo, D., Seignon, M., Yi, E., Kim, H., et al. (2021). Single-cell multimodal glioma analyses identify epigenetic regulators of cellular plasticity and environmental stress response. Nat. Genet. *53*, 2020.07.22.215335.

Jones, P.A., and Baylin, S.B. (2007). The Epigenomics of Cancer. Cell *128*, 683–692.

Joo, K.M., Kim, J., Jin, J., Kim, M., Seol, H.J., Muradov, J., Yang, H., Choi, Y.-L., Park, W.-Y., Kong, D.-S., et al. (2013). Patient-Specific Orthotopic Glioblastoma Xenograft Models Recapitulate the Histopathology and Biology of Human Glioblastomas In Situ. Cell Rep. *3*, 260–273.

Joshi-Tope, G., Gillespie, M., Vastrik, I., D'Eustachio, P., Schmidt, E., de Bono, B., Jassal, B., Gopinath, G.R., Wu, G.R., Matthews, L., et al. (2005). Reactome: A knowledgebase of biological pathways. Nucleic Acids Res. *33*, 428–432.

Jun, H.J., Appleman, V.A., Wu, H.-J., Rose, C.M., Pineda, J.J., Yeo, A.T., Delcuze, B., Lee, C., Gyuris, A., Zhu, H., et al. (2018). A PDGFRα-driven mouse model of glioblastoma reveals a stathmin1-mediated mechanism of sensitivity to vinblastine. Nat. Commun. *9*, 3116.

Jung, E., Osswald, M., Blaes, J., Wiestler, B., Sahm, F., Schmenger, T., Solecki, G., Deumelandt, K., Kurz, F.T., Xie, R., et al. (2017). Tweety-homolog 1 drives brain colonization of gliomas. J. Neurosci. *37*, 6837–6850.

Jung, E., Osswald, M., Ratliff, M., Dogan, H., Xie, R., Weil, S., Hoffmann, D.C., Kurz, F.T., Kessler, T., Heiland, S., et al. (2021). Tumor cell plasticity, heterogeneity, and resistance in crucial microenvironmental niches in glioma. Nat. Commun. *12*, 1014.

Keime-Guibert, F., Chinot, O., Taillandier, L., Cartalat-Carel, S., Frenay, M., Kantor, G., Guillamo, J.-S., Jadaud, E., Colin, P., Bondiau, P.-Y., et al. (2007). Radiotherapy for Glioblastoma in the Elderly. N. Engl. J. Med. *356*, 1527–1535.

Kersten, K., Visser, K.E., Miltenburg, M.H., and Jonkers, J. (2017). Genetically engineered mouse models in oncology research and cancer medicine. EMBO Mol. Med. *9*, 137–153.

Kesari, S., Ram, Z., and Investigators, on behalf of E.-14 T. (2017). Tumor-treating fields plus chemotherapy versus chemotherapy alone for glioblastoma at first recurrence: a *post hoc* analysis of the EF-14 trial. CNS Oncol. *6*, 185–193.

Keshava, N., Toh, T.S., Yuan, H., Yang, B., Menden, M.P., and Wang, D. (2019). Defining subpopulations of differential drug response to reveal novel target populations. Npj Syst. Biol. Appl. *5*.

Keunen, O., Johansson, M., Oudin, A., Sanzey, M., Rahim, S.A.A., Fack, F., Thorsen, F., Taxt, T., Bartos, M., Jirik, R., et al. (2011). Anti-VEGF treatment reduces blood supply and increases tumor cell invasion in glioblastoma. Proc. Natl. Acad. Sci. U. S. A. *108*, 3749–3754.

Khalsa, J.K., Cheng, N., Keegan, J., Chaudry, A., Driver, J., Bi, W.L., Lederer, J., and Shah, K. (2020). Immune phenotyping of diverse syngeneic murine brain tumors identifies immunologically distinct types. Nat. Commun. *11*.

Kim, E.L., Sorokin, M., Kantelhardt, S.R., Kalasauskas, D., Sprang, B., Fauss, J., Ringel, F., Garazha, A., Albert, E., Gaifullin, N., et al. (2020a). Intratumoral heterogeneity and longitudinal changes in gene expression predict differential drug sensitivity in newly diagnosed and recurrent glioblastoma. Cancers (Basel). *12*.

Kim, H., Nguyen, N.-P., Turner, K., Wu, S., Gujar, A.D., Luebeck, J., Liu, J., Deshpande, V., Rajkumar, U., Namburi, S., et al. (2020b). Extrachromosomal DNA is associated with oncogene amplification and poor outcome across multiple cancers. Nat. Genet. *52*, 891–897.

Kim, J., Lee, I.H., Cho, H.J., Park, C.K., Jung, Y.S., Kim, Y., Nam, S.H., Kim, B.S., Johnson, M.D., Kong, D.S., et al. (2015). Spatiotemporal Evolution of the Primary Glioblastoma Genome. Cancer Cell *28*, 318–328.

Kim, K.M., Shim, J.K., Chang, J.H., Lee, J.H., Kim, S.H., Choi, J., Park, J., Kim, E.H., Kim, S.H., Huh, Y.M., et al. (2016). Failure of a patient-derived xenograft for brain tumor model prepared by implantation of tissue fragments. Cancer Cell Int. *16*, 1–6.

Kim, S., Kon, M., and DeLisi, C. (2012). Pathway-based classification of cancer subtypes.

Biol. Direct *7*, 1–22.

Kim, Y., Varn, F.S., Park, S.-H.H., Yoon, B.W., Park, H.R., Lee, C., Verhaak, R.G.W.W., and Paek, S.H. (2021). Perspective of mesenchymal transformation in glioblastoma. Acta Neuropathol. Commun. *9*, 1–20.

Kirby, L., Jin, J., Cardona, J.G., Smith, M.D., Martin, K.A., Wang, J., Strasburger, H., Herbst, L., Alexis, M., Karnell, J., et al. (2019). Oligodendrocyte precursor cells present antigen and are cytotoxic targets in inflammatory demyelination. Nat. Commun. *10*, 3887.

Klein, E., Hau, A.-C.C., Oudin, A., Golebiewska, A., and Niclou, S.P. (2020). Glioblastoma Organoids: Pre-Clinical Applications and Challenges in the Context of Immunotherapy. Front. Oncol. *10*, 1–18.

Klemm, F., Maas, R.R., Bowman, R.L., Kornete, M., Soukup, K., Nassiri, S., Brouland, J.-P.P., Iacobuzio-Donahue, C.A., Brennan, C., Tabar, V., et al. (2020). Interrogation of the Microenvironmental Landscape in Brain Tumors Reveals Disease-Specific Alterations of Immune Cells. Cell *181*, 1–18.

Klughammer, J., Kiesel, B., Roetzer, T., Fortelny, N., Nemc, A., Nenning, K.H., Furtner, J., Sheffield, N.C., Datlinger, P., Peter, N., et al. (2018). The DNA methylation landscape of glioblastoma disease progression shows extensive heterogeneity in time and space. Nat. Med. *24*, 1611–1624.

Kluin, R.J.C., Kemper, K., Kuilman, T., de Ruiter, J.R., Iyer, V., Forment, J. V., Cornelissen-Steijger, P., de Rink, I., ter Brugge, P., Song, J.-Y., et al. (2018). XenofilteR: computational deconvolution of mouse and human reads in tumor xenograft sequence data. BMC Bioinformatics *19*, 366.

Körber, V., Yang, J., Barah, P., Wu, Y., Stichel, D., Gu, Z., Fletcher, M.N.C., Jones, D., Hentschel, B., Lamszus, K., et al. (2019). Evolutionary Trajectories of IDHWT Glioblastomas Reveal a Common Path of Early Tumorigenesis Instigated Years ahead of Initial Diagnosis. Cancer Cell *35*, 1–13.

Korsunsky, I., Millard, N., Fan, J., Slowikowski, K., Zhang, F., Wei, K., Baglaenko, Y., Brenner, M., Loh, P. ru, and Raychaudhuri, S. (2019). Fast, sensitive and accurate integration of single-cell data with Harmony. Nat. Methods *16*, 1289–1296.

Kreisl, T.N., Kim, L., Moore, K., Duic, P., Royce, C., Stroud, I., Garren, N., Mackey, M., Butman, J.A., Camphausen, K., et al. (2009). Phase II trial of single-agent bevacizumab followed by bevacizumab plus irinotecan at tumor progression in recurrent glioblastoma. J. Clin. Oncol. *27*, 740–745.

Kreso, A., and Dick, J.E. (2014). Evolution of the cancer stem cell model. Cell Stem Cell *14*, 275–291.

Lähnemann, D., Köster, J., Szczurek, E., McCarthy, D.J., Hicks, S.C., Robinson, M.D., Vallejos, C.A., Campbell, K.R., Beerenwinkel, N., Mahfouz, A., et al. (2020). Eleven grand challenges in single-cell data science (Genome Biology).

Lan, X., Jörg, D.J., Cavalli, F.M.G., Richards, L.M., Nguyen, L. V., Vanner, R.J., Guilhamon, P., Lee, L., Kushida, M.M., Pellacani, D., et al. (2017). Fate mapping of human glioblastoma reveals an invariant stem cell hierarchy. Nature *549*, 227–232.

Lancaster, M.A., Renner, M., Martin, C.-A., Wenzel, D., Bicknell, L.S., Hurles, M.E., Homfray, T., Penninger, J.M., Jackson, A.P., and Knoblich, J.A. (2013). Cerebral organoids

model human brain development and microcephaly. Nature *501*, 373–379.

Lapointe, S., Perry, A., and Butowski, N.A. (2018). Primary brain tumours in adults. Lancet *392*, 432–446.

Lathia, J.D., Mack, S.C., Mulkearns-Hubert, E.E., Valentim, C.L.L., and Rich, J.N. (2015). Cancer stem cells in glioblastoma. Genes Dev. *29*, 1203–1217.

Laug, D., Glasgow, S.M., and Deneen, B. (2018). A glial blueprint for gliomagenesis. Nat. Rev. Neurosci. *19*, 393–403.

Lecoultre, M., Dutoit, V., and Walker, P.R. (2020). Phagocytic function of tumor-associated macrophages as a key determinant of tumor progression control: a review. J. Immunother. Cancer *8*, e001408.

Ledur, P.F., Onzi, G.R., Zong, H., Lenz, G., Ledur, P.F., Onzi, G.R., Zong, H., and Lenz, G. (2017). Culture conditions defining glioblastoma cells behavior: what is the impact for novel discoveries? Oncotarget *8*, 69185–69197.

Lee-Chang, C., Rashidi, A., Miska, J., Zhang, P., Pituch, K.C., Hou, D., Xiao, T., Fischietti, M., Kang, S.J., Appin, C.L., et al. (2019). Myeloid-Derived Suppressive Cells Promote B cell–Mediated Immunosuppression via Transfer of PD-L1 in Glioblastoma. Cancer Immunol. Res. *7*, 1928–1943.

Lee, S.Y. (2016). Temozolomide resistance in glioblastoma multiforme. Genes Dis. *3*, 198–210.

Lee, J., Kotliarova, S., Kotliarov, Y., Li, A., Su, Q., Donin, N.M., Pastorino, S., Purow, B.W., Christopher, N., Zhang, W., et al. (2006). Tumor stem cells derived from glioblastomas cultured in bFGF and EGF more closely mirror the phenotype and genotype of primary tumors than do serum-cultured cell lines. Cancer Cell *9*, 391–403.

Lee, J.H., Lee, J.E., Kahng, J.Y., Kim, S.H., Park, J.S., Yoon, S.J., Um, J.-Y., Kim, W.K., Lee, J.-K., Park, J., et al. (2018). Human glioblastoma arises from subventricular zone cells with low-level driver mutations. Nature *560*, 243–247.

Lenting, K., Verhaak, R., ter Laan, M., Wesseling, P., and Leenders, W. (2017). Glioma: experimental models and reality. Acta Neuropathol. *133*, 263–282.

De Leo, A., Ugolini, A., and Veglia, F. (2021). Myeloid cells in glioblastoma microenvironment. Cells *10*, 1–20.

Li, A., Walling, J., Kotliarov, Y., Center, A., Steed, M.E., Ahn, S.J., Rosenblum, M., Mikkelsen, T., Zenklusen, J.C., and Fine, H.A. (2008). Genomic Changes and Gene Expression Profiles Reveal That Established Glioma Cell Lines Are Poorly Representative of Primary Human Gliomas. Mol. Cancer Res. *6*, 21–30.

Li, F., Lv, B., Liu, Y., Hua, T., Han, J., Sun, C., Xu, L., Zhang, Z., Feng, Z., Cai, Y., et al. (2018). Blocking the CD47-SIRPα axis by delivery of anti-CD47 antibody induces antitumor effects in glioma and glioma stem cells. Oncoimmunology *7*, e1391973.

Liang, S.B., and Fu, L.W. (2017). Application of single-cell technology in cancer research. Biotechnol. Adv. *35*, 443–449.

Liau, B.B., Sievers, C., Donohue, L.K., Gillespie, S.M., Flavahan, W.A., Miller, T.E., Venteicher, A.S., Hebert, C.H., Carey, C.D., Rodig, S.J., et al. (2017). Adaptive Chromatin

Remodeling Drives Glioblastoma Stem Cell Plasticity and Drug Tolerance. Cell Stem Cell *20*, 233-246.e7.

Liddelow, S., and Barres, B. (2015). SnapShot: Astrocytes in Health and Disease. Cell *162*, 1170-1170.e1.

Liddelow, S.A., and Barres, B.A. (2017). Reactive Astrocytes: Production, Function, and Therapeutic Potential. Immunity *46*, 957–967.

Liffers, K., Lamszus, K., and Schulte, A. (2015). *EGFR* Amplification and Glioblastoma Stem-Like Cells. Stem Cells Int. *2015*, 1–11.

Liu, C., Sage, J.C., Miller, M.R., Verhaak, R.G.W., Hippenmeyer, S., Vogel, H., Foreman, O., Bronson, R.T., Nishiyama, A., Luo, L., et al. (2011). Mosaic Analysis with Double Markers Reveals Tumor Cell of Origin in Glioma. Cell *146*, 209–221.

Liu, S., Shi, W., Zhao, Q., Zheng, Z., Liu, Z., Meng, L., Dong, L., and Jiang, X. (2021a). Progress and prospect in tumor treating fields treatment of glioblastoma. Biomed. Pharmacother. *141*, 111810.

Liu, Y., Wang, T., Zhou, B., and Zheng, D. (2021b). Robust integration of multiple single-cell RNA sequencing datasets using a single reference space. Nat. Biotechnol. *39*, 877–884.

Lively, S., and Schlichter, L.C. (2013). The microglial activation state regulates migration and roles of matrix-dissolving enzymes for invasion. J. Neuroinflammation *10*, 843.

Lotfollahi, M., Naghipourfar, M., Luecken, M.D., Khajavi, M., Büttner, M., Wagenstetter, M., Avsec, Ž., Gayoso, A., Yosef, N., Interlandi, M., et al. (2021). Mapping single-cell data to reference atlases by transfer learning. Nat. Biotechnol.

Louis, D.N., Perry, A., Reifenberger, G., von Deimling, A., Figarella-Branger, D., Cavenee, W.K., Ohgaki, H., Wiestler, O.D., Kleihues, P., and Ellison, D.W. (2016). The 2016 World Health Organization Classification of Tumors of the Central Nervous System: a summary. Acta Neuropathol. *131*, 803–820.

Louis, D.N., Perry, A., Wesseling, P., Brat, D.J., Cree, I.A., Figarella-Branger, D., Hawkins, C., Ng, H.K., Pfister, S.M., Reifenberger, G., et al. (2021). The 2021 WHO Classification of Tumors of the Central Nervous System: a summary. Neuro. Oncol. *23*, 1231–1251.

Louveau, A., Smirnov, I., Keyes, T.J., Eccles, J.D., Rouhani, S.J., Peske, J.D., Derecki, N.C., Castle, D., Mandell, J.W., Lee, K.S., et al. (2015). Structural and functional features of central nervous system lymphatic vessels. Nature *523*, 337–341.

Lynes, J., Sanchez, V., Dominah, G., Nwankwo, A., and Nduom, E. (2018). Current options and future directions in immune therapy for glioblastoma. Front. Oncol. *8*, 1–22.

Macleod, K.F., and Jacks, T. (1999). Insights into cancer from transgenic mouse models. J. Pathol. *187*, 43–60.

Macosko, E.Z., Basu, A., Satija, R., Nemesh, J., Shekhar, K., Goldman, M., Tirosh, I., Bialas, A.R., Kamitaki, N., Martersteck, E.M., et al. (2015). Highly parallel genome-wide expression profiling of individual cells using nanoliter droplets. Cell *161*, 1202–1214.

Maes, W., and Van Gool, S.W. (2011). Experimental immunotherapy for malignant glioma: lessons from two decades of research in the GL261 model. Cancer Immunol. Immunother.

60, 153–160.

Malta, T.M., Sabedot, T.S., Datta, I., Garofano, L., Vallentgoed, W., Varn, F.S., Aldape, K., D'Angelo, F., Bakas, S., Barnholtz-Sloan, J.S., et al. (2021). The epigenetic evolution of gliomas is determined by their IDH1 mutation status and treatment regimen. BioRxiv 2021.08.09.455687.

Mansour, A.A., Gonçalves, J.T., Bloyd, C.W., Li, H., Fernandes, S., Quang, D., Johnston, S., Parylak, S.L., Jin, X., and Gage, F.H. (2018). An in vivo model of functional and vascularized human brain organoids. Nat. Biotechnol. *36*, 432–441.

Mao, X.-Y., Dai, J.-X., Zhou, H.-H., Liu, Z.-Q., Jin, W.-L., Mao, X.-Y., Dai, J.-X., Zhou, H.-H., Liu, Z.-Q., and Jin, W.-L. (2016). Brain tumor modeling using the CRISPR/Cas9 system: state of the art and view to the future. Oncotarget *7*, 33461–33471.

Marsh, S.E., Walker, A.J., Kamath, T., Dissing-Olesen, L., Hammond, T.R., de Soysa, T.Y., Young, A.M.H., Murphy, S., Abdulraouf, A., Nadaf, N., et al. (2022). Dissection of artifactual and confounding glial signatures by single-cell sequencing of mouse and human brain. Nat. Neurosci. *25*, 306–316.

Massoni-Badosa, R., Iacono, G., Moutinho, C., Kulis, M., Palau, N., Marchese, D., Rodríguez-Ubreva, J., Ballestar, E., Rodriguez-Esteban, G., Marsal, S., et al. (2020). Sampling time-dependent artifacts in single-cell genomics studies. Genome Biol. *21*, 1–16.

Masuda, T., Sankowski, R., Staszewski, O., Böttcher, C., Amann, L., Sagar, Scheiwe, C., Nessler, S., Kunz, P., van Loo, G., et al. (2019). Spatial and temporal heterogeneity of mouse and human microglia at single-cell resolution. Nature *566*, 388–392.

Masuda, T., Sankowski, R., Staszewski, O., and Prinz, M. (2020). Microglia Heterogeneity in the Single-Cell Era. Cell Rep. *30*, 1271–1281.

Mathewson, N.D., Ashenberg, O., Tirosh, I., Gritsch, S., Perez, E.M., Marx, S., Jerby-Arnon, L., Chanoch-Myers, R., Hara, T., Richman, A.R., et al. (2021). Inhibitory CD161 receptor identified in glioma-infiltrating T cells by single-cell analysis. Cell *184*, 1281-1298.e26.

Matsuda, M., Hayashi, H., Garcia-Ojalvo, J., Yoshioka-Kobayashi, K., Kageyama, R., Yamanaka, Y., Ikeya, M., Toguchida, J., Alev, C., and Ebisuya, M. (2020). Species-specific segmentation clock periods are due to differential biochemical reaction speeds. Science (80-.). *369*, 1450–1455.

Maynard, A., McCoach, C.E., Rotow, J.K., Harris, L., Haderk, F., Kerr, D.L., Yu, E.A., Schenk, E.L., Tan, W., Zee, A., et al. (2020). Therapy-Induced Evolution of Human Lung Cancer Revealed by Single-Cell RNA Sequencing. Cell *182*, 1232-1251.e22.

McLendon, R., Friedman, A., Bigner, D., Van Meir, E.G., Brat, D.J., Mastrogianakis, G.M., Olson, J.J., Mikkelsen, T., Lehman, N., Aldape, K., et al. (2008). Comprehensive genomic characterization defines human glioblastoma genes and core pathways. Nature *455*, 1061–1068.

Mega, A., Hartmark Nilsen, M., Leiss, L.W., Tobin, N.P., Miletic, H., Sleire, L., Strell, C., Nelander, S., Krona, C., Hägerstrand, D., et al. (2020). Astrocytes enhance glioblastoma growth. Glia *68*, 316–327.

Meyer, M., Reimand, J., Lan, X., Head, R., Zhu, X., Kushida, M., Bayani, J., Pressey, J.C., Lionel, A.C., Clarke, I.D., et al. (2015). Single cell-derived clonal analysis of human glioblastoma links functional and genomic heterogeneity.

Miller, K.D., Ostrom, Q.T., Kruchko, C., Patil, N., Tihan, T., Cioffi, G., Fuchs, H.E., Waite, K.A., Jemal, A., Siegel, R.L., et al. (2021). Brain and other central nervous system tumor statistics, 2021. CA. Cancer J. Clin. *71*, 381–406.

Miyai, M., Tomita, H., Soeda, A., Yano, H., Iwama, T., and Hara, A. (2017). Current trends in mouse models of glioblastoma. J. Neurooncol. *135*, 423–432.

Molinaro, A.M., Taylor, J.W., Wiencke, J.K., and Wrensch, M.R. (2019). Genetic and molecular epidemiology of adult diffuse glioma. Nat. Rev. Neurol. *15*, 405–417.

Molinaro, A.M., Hervey-Jumper, S., Morshed, R.A., Young, J., Han, S.J., Chunduru, P., Zhang, Y., Phillips, J.J., Shai, A., Lafontaine, M., et al. (2020). Association of Maximal Extent of Resection of Contrast-Enhanced and Non-Contrast-Enhanced Tumor with Survival Within Molecular Subgroups of Patients with Newly Diagnosed Glioblastoma. JAMA Oncol. *6*, 495–503.

Monje, M. (2020). Synaptic communication in brain cancer. Cancer Res. canres.0646.2020.

Moore, L.D., Le, T., and Fan, G. (2013). DNA Methylation and Its Basic Function. Neuropsychopharmacology *38*, 23–38.

Müller, S., Kohanbash, G., Liu, S.J., Alvarado, B., Carrera, D., Bhaduri, A., Watchmaker, P.B., Yagnik, G., Di Lullo, E., Malatesta, M., et al. (2017). Single-cell profiling of human gliomas reveals macrophage ontogeny as a basis for regional differences in macrophage activation in the tumor microenvironment. Genome Biol. *18*, 1–14.

Muraoka, D., Seo, N., Hayashi, T., Tahara, Y., Fujii, K., Tawara, I., Miyahara, Y., Okamori, K., Yagita, H., Imoto, S., et al. (2019). Antigen delivery targeted to tumor-associated macrophages overcomes tumor immune resistance. J. Clin. Invest. *129*, 1278–1294.

Nabilsi, N.H., Deleyrolle, L.P., Darst, R.P., Riva, A., Reynolds, B.A., and Kladde, M.P. (2014). Multiplex mapping of chromatin accessibility and DNA methylation within targeted single molecules identifies epigenetic heterogeneity in neural stem cells and glioblastoma. Genome Res. *24*, 329–339.

Nath, A., and Bild, A.H. (2021). Leveraging Single-Cell Approaches in Cancer Precision Medicine. Trends in Cancer *7*, 359–372.

Nayak, L., Lee, E.Q., and Wen, P.Y. (2012). Epidemiology of Brain Metastases. Curr. Oncol. Rep. *14*, 48–54.

Neftel, C., Laffy, J., Filbin, M.G., Hara, T., Shore, M.E., Rahme, G.J., Richman, A.R., Silverbush, D., Shaw, M.L., Hebert, C.M., et al. (2019). An Integrative Model of Cellular States, Plasticity, and Genetics for Glioblastoma. Cell *178*, 835-849.e21.

Niclou, S.P. (2018). Revival of the VEGF ligand family? Neuro. Oncol. 1–2.

Niklasson, M., Bergström, T., Jarvius, M., Sundström, A., Nyberg, F., Haglund, C., Larsson, R., Westermark, B., Segerman, B., and Segerman, A. (2019). Mesenchymal transition and increased therapy resistance of glioblastoma cells is related to astrocyte reactivity. J. Pathol. *249*, 295–307.

Nishie, A., Ono, M., Shono, T., Fukushi, J., Otsubo, M., Onoue, H., Ito, Y., Inamura, T., Ikezaki, K., Fukui, M., et al. (1999). Macrophage infiltration and heme oxygenase-1 expression correlate with angiogenesis in human gliomas. Clin. Cancer Res. *5*, 1107–1113.

Noushmehr, H., Weisenberger, D.J., Diefes, K., Phillips, H.S., Pujara, K., Berman, B.P., Pan, F., Pelloski, C.E., Sulman, E.P., Bhat, K.P., et al. (2010). Identification of a CpG Island Methylator Phenotype that Defines a Distinct Subgroup of Glioma. Cancer Cell *17*, 510–522.

Nugoli, M., Chuchana, P., Vendrell, J., Orsetti, B., Ursule, L., Nguyen, C., Birnbaum, D., Douzery, E.J., Cohen, P., and Theillet, C. (2003). Genetic variability in MCF-7 sublines: evidence of rapid genomic and RNA expression profile modifications. BMC Cancer *3*, 13.

Ocana, A., Pandiella, A., Siu, L.L., and Tannock, I.F. (2011). Preclinical development of molecular-targeted agents for cancer. Nat. Rev. Clin. Oncol. *8*, 200–209.

Ochocka, N., Segit, P., Walentynowicz, K.A., Wojnicki, K., Cyranowski, S., Swatler, J., Mieczkowski, J., and Kaminska, B. (2021). Single-cell RNA sequencing reveals functional heterogeneity of glioma-associated brain macrophages. Nat. Commun. *12*, 1–14.

Ogden, A.T., Waziri, A.E., Lochhead, R.A., Fusco, D., Lopez, K., Ellis, J.A., Kang, J., Assanah, M., McKhann, G.M., Sisti, M.B., et al. (2008). Identification of A2B5+CD133-tumor-initiating cells in adult human gliomas. Neurosurgery *62*, 505.

Oh, T., Fakurnejad, S., Sayegh, E.T., Clark, A.J., Ivan, M.E., Sun, M.Z., Safaee, M., Bloch, O., James, C.D., and Parsa, A.T. (2014). Immunocompetent murine models for the study of glioblastoma immunotherapy. J. Transl. Med. *12*, 1–10.

Ohgaki, H., and Kleihues, P. (2013). The definition of primary and secondary glioblastoma. Clin. Cancer Res. *19*, 764–772.

Okolie, O., Bago, J.R., Schmid, R.S., Irvin, D.M., Bash, R.E., Miller, C.R., and Hingtgen, S.D. (2016). Reactive astrocytes potentiate tumor aggressiveness in a murine glioma resection and recurrence model. Neuro. Oncol. *18*, 1622–1633.

Oronsky, B., Reid, T.R., Oronsky, A., Sandhu, N., and Knox, S.J. (2021). A Review of Newly Diagnosed Glioblastoma. Front. Oncol. *10*, 2292.

Osswald, M., Jung, E., Sahm, F., Solecki, G., Venkataramani, V., Blaes, J., Weil, S., Horstmann, H., Wiestler, B., Syed, M., et al. (2015). Brain tumour cells interconnect to a functional and resistant network. Nature *528*, 93–98.

Ostrom, Q.T., Patil, N., Cioffi, G., Waite, K., Kruchko, C., and Barnholtz-Sloan, J.S. (2020). CBTRUS statistical report: Primary brain and other central nervous system tumors diagnosed in the United States in 2013-2017. Neuro. Oncol. *22*, IV1–IV96.

Oudin, A., Baus, V., Barthelemy, V., Fabian, C., Klein, E., Dieterle, M., Wantz, M., Hau, A.C., Dording, C., Bernard, A., et al. (2021). Protocol for derivation of organoids and patient-derived orthotopic xenografts from glioma patient tumors. STAR Protoc. *2*.

Pan, Y., Xiong, M., Chen, R., Ma, Y., Corman, C., Maricos, M., Kindler, U., Semtner, M., Chen, Y.H., Dahiya, S., et al. (2018). Athymic mice reveal a requirement for T-cell-microglia interactions in establishing a microenvironment supportive of Nf1 low-grade glioma growth. Genes Dev. *32*, 491–496.

Parsons, D.W., Jones, S., Zhang, X., Lin, J.C.-H., Leary, R.J., Angenendt, P., Mankoo, P., Carter, H., Siu, I.-M., Gallia, G.L., et al. (2008). An Integrated Genomic Analysis of Human Glioblastoma Multiforme. Science (80-.). *321*, 1807–1812.

Pascual-García, M., Bonfill-Teixidor, E., Planas-Rigol, E., Rubio-Perez, C., Iurlaro, R.,

Arias, A., Cuartas, I., Sala-Hojman, A., Escudero, L., Martínez-Ricarte, F., et al. (2019). LIF regulates CXCL9 in tumor-associated macrophages and prevents CD8+ T cell tumor-infiltration impairing anti-PD1 therapy. Nat. Commun. *10*, 1–11.

Patel, A.P., Tirosh, I., Trombetta, J.J., Shalek, A.K., Gillespie, S.M., Wakimoto, H., Cahill, D.P., Nahed, B. V., Curry, W.T., Martuza, R.L., et al. (2014). Single-cell RNA-seq highlights intratumoral heterogeneity in primary glioblastoma. Science (80-.). *344*, 1396–1401.

Patel, A.P., Fisher, J.L., Nichols, E., Abd-Allah, F., Abdela, J., Abdelalim, A., Abraha, H.N., Agius, D., Alahdab, F., Alam, T., et al. (2019). Global, regional, and national burden of brain and other CNS cancer, 1990–2016: a systematic analysis for the Global Burden of Disease Study 2016. Lancet Neurol. *18*, 376–393.

Patrizii, M., Bartucci, M., Pine, S.R., and Sabaawy, H.E. (2018). Utility of Glioblastoma Patient-Derived Orthotopic Xenografts in Drug Discovery and Personalized Therapy. Front. Oncol. *8*, 23.

Penfield, W. (1925). Microglia and the Process of Phagocytosis in Gliomas. Am. J. Pathol. *1*, 77-90.15.

Peng, M., Li, Y., Wamsley, B., Wei, Y., and Roeder, K. (2021). Integration and transfer learning of single-cell transcriptomes via cFIT. Proc. Natl. Acad. Sci. U. S. A. *118*.

Petitprez, F., de Reyniès, A., Keung, E.Z., Chen, T.W.-W., Sun, C.-M., Calderaro, J., Jeng, Y.-M., Hsiao, L.-P., Lacroix, L., Bougoüin, A., et al. (2020). B cells are associated with survival and immunotherapy response in sarcoma. Nature *577*, 556–560.

Phillips, H.S., Kharbanda, S., Chen, R., Forrest, W.F., Soriano, R.H., Wu, T.D., Misra, A., Nigro, J.M., Colman, H., Soroceanu, L., et al. (2006). Molecular subclasses of high-grade glioma predict prognosis, delineate a pattern of disease progression, and resemble stages in neurogenesis. Cancer Cell *9*, 157–173.

Piao, Y., Liang, J., Holmes, L., Henry, V., Sulman, E., and De Groot, J.F. (2013). Acquired resistance to anti-VEGF therapy in glioblastoma is associated with a mesenchymal transition. Clin. Cancer Res. *19*, 4392–4403.

Piccioni, D.E., Achrol, A.S., Kiedrowski, L.A., Banks, K.C., Boucher, N., Barkhoudarian, G., Kelly, D.F., Juarez, T., Lanman, R.B., Raymond, V.M., et al. (2019). Analysis of cell-free circulating tumor DNA in 419 patients with glioblastoma and other primary brain tumors. CNS Oncol. *8*, CNS34.

Pine, A.R., Cirigliano, S.M., Nicholson, J.G., Hu, Y., Linkous, A., Miyaguchi, K., Edwards, L., Singhania, R., Schwartz, T.H., Ramakrishna, R., et al. (2020). Tumor microenvironment is critical for the maintenance of cellular states found in primary glioblastomas. Cancer Discov. *10*, 964–979.

Pires-Afonso, Y., Niclou, S.P., and Michelucci, A. (2020). Revealing and Harnessing Tumour-Associated Microglia/Macrophage Heterogeneity in Glioblastoma. Int J Mol Sci *21*.

Poh, A.R., and Ernst, M. (2018). Targeting Macrophages in Cancer: From Bench to Bedside. Front. Oncol. *8*, 49.

Pollard, S.M., Yoshikawa, K., Clarke, I.D., Danovi, D., Stricker, S., Russell, R., Bayani, J., Head, R., Lee, M., Bernstein, M., et al. (2009). Glioma Stem Cell Lines Expanded in Adherent Culture Have Tumor-Specific Phenotypes and Are Suitable for Chemical and Genetic Screens. Cell Stem Cell *4*, 568–580.

Pombo Antunes, A.R., Scheyltjens, I., Lodi, F., Messiaen, J., Antoranz, A., Duerinck, J., Kancheva, D., Martens, L., De Vlaminck, K., Van Hove, H., et al. (2021). Single-cell profiling of myeloid cells in glioblastoma across species and disease stage reveals macrophage competition and specialization. Nat. Neurosci. *In Press*, 595–610.

PONTÉN, J., and MACINTYRE, E.H. (2009). LONG TERM CULTURE OF NORMAL AND NEOPLASTIC HUMAN GLIA. Acta Pathol. Microbiol. Scand. *74*, 465–486.

Prager, B.C., Xie, Q., Bao, S., and Rich, J.N. (2019). Cancer Stem Cells: The Architects of the Tumor Ecosystem. Cell Stem Cell *24*, 41–53.

Puchalski, R.B., Shah, N., Miller, J., Dalley, R., Nomura, S.R., Yoon, J.-G.G., Smith, K.A., Lankerovich, M., Bertagnolli, D., Bickley, K., et al. (2018). An anatomic transcriptional atlas of human glioblastoma. Science (80-.). *360*, 660–663.

Quail, D.F., and Joyce, J.A. (2017). The Microenvironmental Landscape of Brain Tumors. Cancer Cell *31*, 326–341.

Rangarajan, A., and Weinberg, R.A. (2003). Comparative biology of mouse versus human cells: modelling human cancer in mice. Nat. Rev. Cancer *3*, 952–959.

von Roemeling, C.A., Wang, Y., Qie, Y., Yuan, H., Zhao, H., Liu, X., Yang, Z., Yang, M., Deng, W., Bruno, K.A., et al. (2020). Therapeutic modulation of phagocytosis in glioblastoma can activate both innate and adaptive antitumour immunity. Nat. Commun. *11*, 1–12.

Rominiyi, O., Vanderlinden, A., Clenton, S.J., Bridgewater, C., Al-Tamimi, Y., and Collis, S.J. (2021). Tumour treating fields therapy for glioblastoma: current advances and future directions. Br. J. Cancer *124*, 697–709.

Rong, Y., Durden, D.L., Van Meir, E.G., and Brat, D.J. (2006). “Pseudopalisading” necrosis in glioblastoma: A familiar morphologic feature that links vascular pathology, hypoxia, and angiogenesis. J. Neuropathol. Exp. Neurol. *65*, 529–539.

Rostami, J., Fotaki, G., Sirois, J., Mzezewa, R., Bergström, J., Essand, M., Healy, L., and Erlandsson, A. (2020). Astrocytes have the capacity to act as antigen-presenting cells in the Parkinson’s disease brain. J. Neuroinflammation *17*, 119.

Rusch, T., Bayry, J., Werner, J., Shevchenko, I., and Bazhin, A. V. (2018). Immunotherapy as an Option for Cancer Treatment. Arch. Immunol. Ther. Exp. (Warsz). *66*, 89–96.

Rustenhoven, J., Drieu, A., Mamuladze, T., de Lima, K.A., Dykstra, T., Wall, M., Papadopoulos, Z., Kanamori, M., Salvador, A.F., Baker, W., et al. (2021). Functional characterization of the dural sinuses as a neuroimmune interface. Cell *184*, 1000-1016.e27.

Sa, J.K., Chang, N., Lee, H.W., Cho, H.J., Ceccarelli, M., Cerulo, L., Yin, J., Kim, S.S., Caruso, F.P., Lee, M., et al. (2020). Transcriptional regulatory networks of tumor-associated macrophages that drive malignancy in mesenchymal glioblastoma. Genome Biol. *21*, 1–17.

Saavedra-López, E., Roig-Martínez, M., Cribaro, G.P., Casanova, P. V, Gallego, J.M., Pérez-Vallés, A., and Barcia, C. (2020). Phagocytic glioblastoma-associated microglia and macrophages populate invading pseudopalisades. Brain Commun. *2*.

Sakariassen, P.Ø., Prestegarden, L., Wang, J., Skaftnesmo, K.-O., Mahesparan, R., Molthoff, C., Sminia, P., Sundlisaeter, E., Misra, A., Tysnes, B.B., et al. (2006). Angiogenesis-independent tumor growth mediated by stem-like cancer cells. Proc. Natl.

Acad. Sci. U. S. A. *103*, 16466–16471.

Sampson, J.H., Gunn, M.D., Fecci, P.E., and Ashley, D.M. (2020). Brain immunology and immunotherapy in brain tumours. Nat. Rev. Cancer *20*, 12–25.

Sankowski, R., Böttcher, C., Masuda, T., Geirsdottir, L., Sagar, Sindram, E., Seredenina, T., Muhs, A., Scheiwe, C., Shah, M.J., et al. (2019). Mapping microglia states in the human brain through the integration of high-dimensional techniques. Nat. Neurosci. *22*, 2098–2110.

Schetters, S.T.T., Gomez-Nicola, D., Garcia-Vallejo, J.J., and Van Kooyk, Y. (2018). Neuroinflammation: Microglia and T Cells Get Ready to Tango. Front. Immunol. *8*, 1905.

Schiffer, D., Annovazzi, L., Casalone, C., Corona, C., and Mellai, M. (2019). Glioblastoma: Microenvironment and niche concept. Cancers (Basel). *11*, 1–17.

Segerman, A., Niklasson, M., Haglund, C., Bergström, T., Jarvius, M., Xie, Y., Westermark, A., Sönmez, D., Hermansson, A., Kastemar, M., et al. (2016). Clonal Variation in Drug and Radiation Response among Glioma-Initiating Cells Is Linked to Proneural-Mesenchymal Transition. Cell Rep. *17*, 2994–3009.

Seligman, A.M., Shear, M.J., and Alexander, L. (1939). Studies in Carcinogenesis: VIII. Experimental Production of Brain Tumors in Mice with Methylcholanthrene. Am. J. Cancer *37*, 364–395.

Shahzad, U., Taccone, M.S., Kumar, S.A., Okura, H., Krumholtz, S., Ishida, J., Mine, C., Gouveia, K., Edgar, J., Smith, C., et al. (2021). Modeling human brain tumors in flies, worms, and zebrafish: From proof of principle to novel therapeutic targets. Neuro. Oncol. *23*, 718–731.

Sharma, A., Cao, E.Y., Kumar, V., Zhang, X., Leong, H.S., Wong, A.M.L., Ramakrishnan, N., Hakimullah, M., Teo, H.M.V., Chong, F.T., et al. (2018). Longitudinal single-cell RNA sequencing of patient-derived primary cells reveals drug-induced infidelity in stem cell hierarchy. Nat. Commun. *9*.

Sharma, A.B., Erasimus, H., Pinto, L., Caron, M.-C., Gopaul, D., Peterlini, T., Neumann, K., Nazarov, P.V., Fritah, S., Klink, B., et al. (2021a). XAB2 promotes Ku eviction from single-ended DNA double-strand breaks independently of the ATM kinase. Nucleic Acids Res. *49*, 9906–9925.

Sharma, P., Siddiqui, B.A., Anandhan, S., Yadav, S.S., Subudhi, S.K., Gao, J., Goswami, S., and Allison, J.P. (2021b). The Next Decade of Immune Checkpoint Therapy. Cancer Discov. *11*, 838–857.

Shen, Y., Grisdale, C.J., Islam, S.A., Bose, P., Lever, J., Zhao, E.Y., Grinshtein, N., Ma, Y., Mungall, A.J., Moore, R.A., et al. (2019). Comprehensive genomic profiling of glioblastoma tumors, BTICs, and xenografts reveals stability and adaptation to growth environments. Proc. Natl. Acad. Sci. U. S. A. *116*, 19098–19108.

Singh, R., Stoltzfus, K.C., Chen, H., Louie, A. V, Lehrer, E.J., Horn, S.R., Palmer, J.D., Trifiletti, D.M., Brown, P.D., and Zaorsky, N.G. (2020). Epidemiology of synchronous brain metastases. Neuro-Oncology Adv. *2*.

Singh, S.K., Hawkins, C., Clarke, I.D., Squire, J.A., Bayani, J., Hide, T., Henkelman, R.M., Cusimano, M.D., and Dirks, P.B. (2004). Identification of human brain tumour initiating cells. Nature *432*, 396–401.

Skaga, E., Kulesskiy, E., Fayzullin, A., Sandberg, C.J., Potdar, S., Kyttälä, A., Langmoen, I.A., Laakso, A., Gaál-Paavola, E., Perola, M., et al. (2019). Intertumoral heterogeneity in patient-specific drug sensitivities in treatment-naïve glioblastoma. BMC Cancer *19*, 628.

Snuderl, M., Fazlollahi, L., Le, L.P., Nitta, M., Zhelyazkova, B.H., Davidson, C.J., Akhavanfard, S., Cahill, D.P., Aldape, K.D., Betensky, R.A., et al. (2011). Mosaic amplification of multiple receptor tyrosine kinase genes in glioblastoma. Cancer Cell *20*, 810–817.

Son, M.J., Woolard, K., Nam, D.H., Lee, J., and Fine, H.A. (2009). SSEA-1 Is an Enrichment Marker for Tumor-Initiating Cells in Human Glioblastoma. Cell Stem Cell *4*, 440–452.

Sottoriva, A., Spiteri, I., Piccirillo, S.G.M., Touloumis, A., Collins, V.P., Marioni, J.C., Curtis, C., Watts, C., and Tavaré, S. (2013). Intratumor heterogeneity in human glioblastoma reflects cancer evolutionary dynamics. Proc. Natl. Acad. Sci. U. S. A. *110*, 4009–4014.

Sousa, C., Golebiewska, A., Poovathingal, S.K., Kaoma, T., Pires-Afonso, Y., Martina, S., Coowar, D., Azuaje, F., Skupin, A., Balling, R., et al. (2018). Single-cell transcriptomics reveals distinct inflammation-induced microglia signatures. EMBO Rep. *19*, 1–17.

de Souza, C.F., Sabedot, T.S., Malta, T.M., Stetson, L., Morozova, O., Sokolov, A., Laird, P.W., Wiznerowicz, M., Iavarone, A., Snyder, J., et al. (2018). A Distinct DNA Methylation Shift in a Subset of Glioma CpG Island Methylator Phenotypes during Tumor Recurrence. Cell Rep. *23*, 637–651.

Spiteri, I., Caravagna, G., Cresswell, G.D., Vatsiou, A., Nichol, D., Acar, A., Ermini, L., Chkhaidze, K., Werner, B., Mair, R., et al. (2019). Evolutionary dynamics of residual disease in human glioblastoma. Ann. Oncol. *30*, 456–463.

Srinivasan, E.S., Deshpande, K., Neman, J., Winkler, F., and Khasraw, M. (2021). The microenvironment of brain metastases from solid tumors. Neuro-Oncology Adv. *3*, v121–v132.

Stegle, O., Teichmann, S.A., and Marioni, J.C. (2015). Computational and analytical challenges in single-cell transcriptomics. Nat. Rev. Genet. *16*, 133–145.

Stewart, C.A., Gay, C.M., Xi, Y., Sivajothi, S., Sivakamasundari, V., Fujimoto, J., Bolisetty, M., Hartsfield, P.M., Balasubramaniyan, V., Chalishazar, M.D., et al. (2020). Single-cell analyses reveal increased intratumoral heterogeneity after the onset of therapy resistance in small-cell lung cancer. Nat. Cancer *1*, 423–436.

Stieber, D., Golebiewska, A., Evers, L., Lenkiewicz, E., Brons, N.H.C., Nicot, N., Oudin, A., Bougnaud, S., Hertel, F., Bjerkvig, R., et al. (2014). Glioblastomas are composed of genetically divergent clones with distinct tumourigenic potential and variable stem cell-associated phenotypes. Acta Neuropathol. *127*, 203–219.

Stummer, W., Pichlmeier, U., Meinel, T., Wiestler, O.D., Zanella, F., and Reulen, H.J. (2006). Fluorescence-guided surgery with 5-aminolevulinic acid for resection of malignant glioma: a randomised controlled multicentre phase III trial. Lancet Oncol. *7*, 392–401.

Stupp, R., Mason, W., Bent, M. van den, Weller, M., Fisher, B., Taphoorn, M., and Jo (2005). Radiotherapy plus concomitant and adjuvant temozolomide for globlastoma. N Engl J Med *352*, 987–996.

Stupp, R., Hegi, M.E., Mason, W.P., van den Bent, M.J., Taphoorn, M.J., Janzer, R.C.,

Ludwin, S.K., Allgeier, A., Fisher, B., Belanger, K., et al. (2009). Effects of radiotherapy with concomitant and adjuvant temozolomide versus radiotherapy alone on survival in glioblastoma in a randomised phase III study: 5-year analysis of the EORTC-NCIC trial. Lancet Oncol. *10*, 459–466.

Stupp, R., Wong, E.T., Kanner, A.A., Steinberg, D., Engelhard, H., Heidecke, V., Kirson, E.D., Taillibert, S., Liebermann, F., Dbalý, V., et al. (2012). NovoTTF-100A versus physician's choice chemotherapy in recurrent glioblastoma: A randomised phase III trial of a novel treatment modality. Eur. J. Cancer *48*, 2192–2202.

Stupp, R., Taillibert, S., Kanner, A.A., Kesari, S., Steinberg, D.M., Toms, S.A., Taylor, L.P., Lieberman, F., Silvani, A., Fink, K.L., et al. (2015). Maintenance Therapy With Tumor-Treating Fields Plus Temozolomide vs Temozolomide Alone for Glioblastoma. JAMA *314*, 2535.

Stupp, R., Taillibert, S., Kanner, A., Read, W., Steinberg, D.M., Lhermitte, B., Toms, S., Idbaih, A., Ahluwalia, M.S., Fink, K., et al. (2017). Effect of Tumor-Treating Fields Plus Maintenance Temozolomide vs Maintenance Temozolomide Alone on Survival in Patients With Glioblastoma. JAMA *318*, 2306.

Sun, H., Cao, S., Mashl, R.J., Mo, C., Zaccaria, S., Wendl, M.C., Davies, S.R., Bailey, M.H., Primeau, T.M., Hoog, J., et al. (2021). Comprehensive characterization of 536 patient-derived xenograft models prioritizes candidates for targeted treatment.

Sung, H., Ferlay, J., Siegel, R.L., Laversanne, M., Soerjomataram, I., Jemal, A., and Bray, F. (2021). Global Cancer Statistics 2020: GLOBOCAN Estimates of Incidence and Mortality Worldwide for 36 Cancers in 185 Countries. CA. Cancer J. Clin. *71*, 209–249.

Szatmári, T., Lumniczky, K., Désaknai, S., Trajcevski, S., Hídvégi, E.J., Hamada, H., and Sáfrány, G. (2006). Detailed characterization of the mouse glioma 261 tumor model for experimental glioblastoma therapy. Cancer Sci. *97*, 546–553.

Szerlip, N.J., Pedraza, A., Chakravarty, D., Azim, M., McGuire, J., Fang, Y., Ozawa, T., Holland, E.C., Huse, J.T., Jhanwar, S., et al. (2012). Intratumoral heterogeneity of receptor tyrosine kinases EGFR and PDGFRA amplification in glioblastoma defines subpopulations with distinct growth factor response. Proc Natl Acad Sci U S A *109*, 3041–3046.

Tan, A.C., Ashley, D.M., López, G.Y., Malinzak, M., Friedman, H.S., and Khasraw, M. (2020). Management of glioblastoma: State of the art and future directions. CA. Cancer J. Clin. *70*, 299–312.

Tchoghandjian, A., Baeza, N., Colin, C., Cayre, M., Metellus, P., Beclin, C., Ouafik, L., and Figarella-Branger, D. (2010). A2B5 Cells from Human Glioblastoma have Cancer Stem Cell Properties. Brain Pathol. *20*, 211–221.

Tchougounova, E., Kastemar, M., Bråsäter, D., Holland, E.C., Westermark, B., and Uhrbom, L. (2007). Loss of Arf causes tumor progression of PDGFB-induced oligodendroglioma. Oncogene *26*, 6289–6296.

Terry, S., Engelsen, A.S.T., Buart, S., Elsayed, W.S., Venkatesh, G.H., and Chouaib, S. (2020). Hypoxia-driven intratumor heterogeneity and immune evasion. Cancer Lett. *492*, 1–10.

The Tabula Muris Consortium (2018). Single-cell transcriptomics of 20 mouse organs creates a Tabula Muris. Nature *562*, 367–372.

Thommen, D.S., and Schumacher, T.N. (2018). T Cell Dysfunction in Cancer. Cancer Cell *33*, 547–562.

Tirosh, I., and Suvà, M.L. (2018). Dissecting human gliomas by single-cell RNA sequencing. Neuro. Oncol. *20*, 37–43.

Tirosh, I., Venteicher, A.S., Hebert, C., Escalante, L.E., Patel, A.A.P., Yizhak, K., Fisher, J.M., Rodman, C., Mount, C., Filbin, M.G., et al. (2016). Single-cell RNA-seq supports a developmental hierarchy in human oligodendroglioma. Nature *539*, 309–313.

Torsvik, A., Stieber, D., Enger, P.O., Golebiewska, A., Molven, A., Svendsen, A., Westermark, B., Niclou, S.P., Olsen, T.K., Chekenya Enger, M., et al. (2014). U-251 revisited: Genetic drift and phenotypic consequences of long-term cultures of glioblastoma cells. Cancer Med. *3*, 812–824.

Touat, M., Li, Y.Y., Boynton, A.N., Spurr, L.F., Lorgulescu, B., Bohrson, C.L., Cortes-Ciriano, I., Iorgulescu, J.B., Bohrson, C.L., Cortes-Ciriano, I., et al. (2020). Mechanisms and therapeutic implications of hypermutation in gliomas. Nature *580*.

Trapnell, C., Cacchiarelli, D., Grimsby, J., Pokharel, P., Li, S., Morse, M., Lennon, N.J., Livak, K.J., Mikkelsen, T.S., and Rinn, J.L. (2014). The dynamics and regulators of cell fate decisions are revealed by pseudotemporal ordering of single cells. Nat. Biotechnol. *32*, 381–386.

Turajlic, S., Sottoriva, A., Graham, T., and Swanton, C. (2019). Resolving genetic heterogeneity in cancer. Nat. Rev. Genet. *20*, 404–416.

Turner, K.M., Deshpande, V., Beyter, D., Koga, T., Rusert, J., Lee, C., Li, B., Arden, K., Ren, B., Nathanson, D.A., et al. (2017). Extrachromosomal oncogene amplification drives tumour evolution and genetic heterogeneity. Nature *543*, 122–125.

Unger, C., Kramer, N., Walzl, A., Scherzer, M., Hengstschläger, M., and Dolznig, H. (2014). Modeling human carcinomas: Physiologically relevant 3D models to improve anti-cancer drug development. Adv. Drug Deliv. Rev. *79–80*, 50–67.

Valihrach, L., Androvic, P., and Kubista, M. (2018). Platforms for single-cell collection and analysis. Int. J. Mol. Sci. *19*, 22–24.

Varn, F.S., Johnson, K.C., Wade, T.E., Malta, T.M., Sabedot, T.S., Barthel, F.P., Kim, H., Ahmed, N., Datta, I., Barnholtz-Sloan, J.S., et al. (2021). Longitudinal analysis of diffuse glioma reveals cell state dynamics at recurrence associated with changes in genetics and the microenvironment. BioRxiv 2021.05.03.442486.

Vasan, N., Baselga, J., and Hyman, D.M. (2019). A view on drug resistance in cancer. Nature *575*, 299–309.

Vaubel, R.A., Tian, S., Remonde, D., Schroeder, M.A., Mladek, A.C., Kitange, G.J., Caron, A., Kollmeyer, T.M., Grove, R., Peng, S., et al. (2020). Genomic and phenotypic characterization of a broad panel of patient-derived xenografts reflects the diversity of glioblastoma. Clin. Cancer Res. *26*, 1094–1104.

Velásquez, C., Mansouri, S., Mora, C., Nassiri, F., Suppiah, S., Martino, J., Zadeh, G., and Fernández-Luna, J.L. (2019). Molecular and Clinical Insights into the Invasive Capacity of Glioblastoma Cells. J. Oncol. *2019*, 1–16.

Vella, G., and Bergers, G. (2018). Where Have All the T Cells Gone? Immunity *49*, 592–

594.

Venkataramani, V., Tanev, D.I., Strahle, C., Studier-Fischer, A., Fankhauser, L., Kessler, T., Körber, C., Kardorff, M., Ratliff, M., Xie, R., et al. (2019). Glutamatergic synaptic input to glioma cells drives brain tumour progression. Nature *573*, 532–538.

Venkatesh, H.S., Johung, T.B., Caretti, V., Noll, A., Tang, Y., Nagaraja, S., Gibson, E.M., Mount, C.W., Polepalli, J., Mitra, S.S., et al. (2015). Neuronal activity promotes glioma growth through neuroligin-3 secretion. Cell *161*, 803–816.

Venkatesh, H.S., Morishita, W., Geraghty, A.C., Silverbush, D., Gillespie, S.M., Arzt, M., Tam, L.T., Espenel, C., Ponnuswami, A., Ni, L., et al. (2019). Electrical and synaptic integration of glioma into neural circuits. Nature *573*, 539–545.

Venteicher, A.S., Tirosh, I., Hebert, C., Yizhak, K., Neftel, C., Filbin, M.G., Hovestadt, V., Escalante, L.E., Shaw, M.L., Rodman, C., et al. (2017). Decoupling genetics, lineages, and microenvironment in IDH-mutant gliomas by single-cell RNA-seq. Science (80-.). *355*.

Verhaak, R.G.W., Hoadley, K.A., Purdom, E., Wang, V., Qi, Y., Wilkerson, M.D., Miller, C.R., Ding, L., Golub, T., Mesirov, J.P., et al. (2010). Integrated Genomic Analysis Identifies Clinically Relevant Subtypes of Glioblastoma Characterized by Abnormalities in PDGFRA, IDH1, EGFR, and NF1. Cancer Cell *17*, 98–110.

Verhaak, R.G.W., Bafna, V., and Mischel, P.S. (2019). Extrachromosomal oncogene amplification in tumour pathogenesis and evolution. Nat Rev Cancer *19*, 283–288.

Vescovi, A.L., Galli, R., and Reynolds, B.A. (2006). Brain tumour stem cells. Nat. Rev. Cancer *6*, 425–436.

Vollmann-Zwerenz, A., Leidgens, V., Feliciello, G., Klein, C.A., and Hau, P. (2020). Tumor cell invasion in glioblastoma. Int. J. Mol. Sci. *21*, 1–21.

Wakimoto, H., Mohapatra, G., Kanai, R., Curry, W.T., Yip, S., Nitta, M., Patel, A.P., Barnard, Z.R., Stemmer-Rachamimov, A.O., Louis, D.N., et al. (2012). Maintenance of primary tumor phenotype and genotype in glioblastoma stem cells. Neuro. Oncol. *14*, 132–144.

Wang, S., and Wu, W. (2018). DNA Methylation Alterations in Human Cancers (Elsevier Inc.).

Wang, B., Liu, M., Ran, Z., Li, X., Li, J., and Ou, Y. (2020a). Analysis of Gene Signatures of Tumor Microenvironment Yields Insight Into Mechanisms of Resistance to Immunotherapy. Front. Bioeng. Biotechnol. *8*, 1–12.

Wang, G.-M., Cioffi, G., Patil, N., Waite, K.A., Lanese, R., Ostrom, Q.T., Kruchko, C., Berens, M.E., Connor, J.R., Lathia, J.D., et al. (2021). Importance of the intersection of age and sex to understand variation in incidence and survival for primary malignant gliomas. Neuro. Oncol. 1–9.

Wang, J., Miletic, H., Sakariassen, P.Ø.T., Huszthy, P.C., Jacobsen, H., Brekkå, N., Li, X., Zhao, P., Mørk, S., Chekenya, M., et al. (2009). A reproducible brain tumour model established from human glioblastoma biopsies. BMC Cancer *9*, 1–13.

Wang, L., Babikir, H., Müller, S., Yagnik, G., Shamardani, K., Catalan, F., Kohanbash, G., Alvarado, B., Di Lullo, E., Kriegstein, A., et al. (2019). The phenotypes of proliferating glioblastoma cells reside on a single axis of variation. Cancer Discov. *9*, 1708–1719.

Wang, Q., Hu, B., Hu, X., Kim, H., Squatrito, M., Scarpace, L., deCarvalho, A.C., Lyu, S., Li, P., Li, Y., et al. (2017). Tumor Evolution of Glioma-Intrinsic Gene Expression Subtypes Associates with Immunological Changes in the Microenvironment. Cancer Cell *32*, 42-56.e6.

Wang, Z., Sun, D., Chen, Y.-J.J., Xie, X., Shi, Y., Tabar, V., Brennan, C.W., Bale, T.A., Jayewickreme, C.D., Laks, D.R., et al. (2020b). Cell Lineage-Based Stratification for Glioblastoma. Cancer Cell *38*, 1–14.

Ward, J.M., and Rice, J.M. (1982). Naturally occurring and chemically induced brain tumors of rats and mice in carcinogenesis bioassays. Ann. N. Y. Acad. Sci. *381*, 304–319.

Wauters, E., Van Mol, P., Garg, A.D., Jansen, S., Van Herck, Y., Vanderbeke, L., Bassez, A., Boeckx, B., Malengier-Devlies, B., Timmerman, A., et al. (2021). Discriminating mild from critical COVID-19 by innate and adaptive immune single-cell profiling of bronchoalveolar lavages. Cell Res. *31*, 272–290.

Wculek, S.K., Cueto, F.J., Mujal, A.M., Melero, I., Krummel, M.F., and Sancho, D. (2020). Dendritic cells in cancer immunology and immunotherapy. Nat. Rev. Immunol. *20*, 7–24.

Wei, X., Meel, M.H., Breur, M., Bugiani, M., Hulleman, E., and Phoenix, T.N. (2021). Defining tumor-associated vascular heterogeneity in pediatric high-grade and diffuse midline gliomas. Acta Neuropathol. Commun. *9*, 142.

Weil, S., Osswald, M., Solecki, G., Grosch, J., Jung, E., Lemke, D., Ratliff, M., Hänggi, D., Wick, W., and Winkler, F. (2017). Tumor microtubes convey resistance to surgical lesions and chemotherapy in gliomas. Neuro. Oncol. *19*, 1316–1326.

Weinstein, J.N., Collisson, E.A., Mills, G.B., Shaw, K.R.M., Ozenberger, B.A., Ellrott, K., Sander, C., Stuart, J.M., Chang, K., Creighton, C.J., et al. (2013). The cancer genome atlas pan-cancer analysis project. Nat. Genet. *45*, 1113–1120.

Weller, M., Wick, W., Aldape, K., Brada, M., Berger, M., Pfister, S.M., Nishikawa, R., Rosenthal, M., Wen, P.Y., Stupp, R., et al. (2015). Glioma. Nat. Rev. Dis. Prim. *1*, 15017.

Weller, M., van den Bent, M., Preusser, M., Le Rhun, E., Tonn, J.C., Minniti, G., Bendszus, M., Balana, C., Chinot, O., Dirven, L., et al. (2021). EANO guidelines on the diagnosis and treatment of diffuse gliomas of adulthood. Nat. Rev. Clin. Oncol. *18*, 170–186.

Wen, P.Y., Weller, M., Lee, E.Q., Alexander, B.M., Barnholtz-Sloan, J.S., Barthel, F.P., Batchelor, T.T., Bindra, R.S., Chang, S.M., Antonio Chiocca, E., et al. (2020). Glioblastoma in adults: A Society for Neuro-Oncology (SNO) and European Society of Neuro-Oncology (EANO) consensus review on current management and future directions. Neuro. Oncol. *22*, 1073–1113.

Wenger, A., Vega, S.F., Kling, T., Bontell, T.O., Jakola, A.S., and Carén, H. (2019). Intratumor DNA methylation heterogeneity in glioblastoma: Implications for DNA methylation-based classification. Neuro. Oncol. *21*, 616–627.

Wheeler, D.A., Takebe, N., Hinoue, T., Hoadley, K.A., Cardenas, M.F., Hamilton, A.M., Laird, P.W., Wang, L., Johnson, A., Dewal, N., et al. (2021). Molecular Features of Cancers Exhibiting Exceptional Responses to Treatment. Cancer Cell *39*, 38-53.e7.

Wick, W., Gorlia, T., Bendszus, M., Taphoorn, M., Sahm, F., Harting, I., Brandes, A.A., Taal, W., Domont, J., Idbaih, A., et al. (2017). Lomustine and Bevacizumab in Progressive Glioblastoma. N. Engl. J. Med. *377*, 1954–1963.

William, D., Mullins, C.S., Schneider, B., Orthmann, A., Lamp, N., Krohn, M., Hoffmann, A., Classen, C.F., and Linnebacher, M. (2017). Optimized creation of glioblastoma patient derived xenografts for use in preclinical studies. J. Transl. Med. 1–11.

Willingham, S.B., Volkmer, J.-P., Gentles, A.J., Sahoo, D., Dalerba, P., Mitra, S.S., Wang, J., Contreras-Trujillo, H., Martin, R., Cohen, J.D., et al. (2012). The CD47-signal regulatory protein alpha (SIRPa) interaction is a therapeutic target for human solid tumors. Proc. Natl. Acad. Sci. *109*, 6662–6667.

Winkler, F., and Wick, W. (2018). Harmful networks in the brain and beyond. Science (80-.). *359*, 1100–1101.

Wohnhaas, C.T., Leparc, G.G., Fernandez-Albert, F., Kind, D., Gantner, F., Viollet, C., Hildebrandt, T., and Baum, P. (2019). DMSO cryopreservation is the method of choice to preserve cells for droplet-based single-cell RNA sequencing. Sci. Rep. *9*, 1–14.

Woo, X.Y., Giordano, J., Srivastava, A., Zhao, Z.-M.M., Lloyd, M.W., de Bruijn, R., Suh, Y.-S.S., Patidar, R., Chen, L., Scherer, S., et al. (2021). Conservation of copy number profiles during engraftment and passaging of patient-derived cancer xenografts. Nat. Genet. *53*, 86–99.

Woolf, Z., Swanson, M.E. V, Smyth, L.C., Mee, E.W., Schweder, P., Heppner, P., Kim, B.J.H., Turner, C., Oldfield, R.L., Curtis, M.A., et al. (2021). Single-cell image analysis reveals a protective role for microglia in glioblastoma. Neuro-Oncology Adv. *3*.

Wu, S.Z., Roden, D.L., Al-Eryani, G., Bartonicek, N., Harvey, K., Cazet, A.S., Chan, C.L., Junankar, S., Hui, M.N., Millar, E.A., et al. (2021). Cryopreservation of human cancers conserves tumour heterogeneity for single-cell multi-omics analysis. Genome Med. *13*, 1–17.

Wurm, J., Behringer, S.P., Ravi, V.M., Joseph, K., Neidert, N., Maier, J.P., Doria-Medina, R., Follo, M., Delev, D., Pfeifer, D., et al. (2019). Astrogliosis Releases Pro-Oncogenic Chitinase 3-Like 1 Causing MAPK Signaling in Glioblastoma. Cancers (Basel). *11*, 1437.

Xie, R., Kessler, T., Grosch, J., Hai, L., Venkataramani, V., Huang, L., Hoffmann, D.C., Solecki, G., Ratliff, M., Schlesner, M., et al. (2021). Tumor cell network integration in glioma represents a stemness feature. Neuro. Oncol. *23*, 757–769.

Yan, H., Parsons, D.W., Jin, G., McLendon, R., Rasheed, B.A., Yuan, W., Kos, I., Batinic-Haberle, I., Jones, S., Riggins, G.J., et al. (2009). *IDH1* and *IDH2* Mutations in Gliomas. N. Engl. J. Med. *360*, 765–773.

Ye, Z., Ai, X., Zhao, L., Fei, F., Wang, P., and Zhou, S. (2021). Phenotypic plasticity of myeloid cells in glioblastoma development, progression, and therapeutics. Oncogene *40*, 6059–6070.

Yee, P.P., Wei, Y., Kim, S.-Y., Lu, T., Chih, S.Y., Lawson, C., Tang, M., Liu, Z., Anderson, B., Thamburaj, K., et al. (2020). Neutrophil-induced ferroptosis promotes tumor necrosis in glioblastoma progression. Nat. Commun. *11*, 5424.

Yu, K., Hu, Y., Wu, F., Guo, Q., Qian, Z., Hu, W., Chen, J., Wang, K., Fan, X., Wu, X., et al. (2020). Surveying brain tumor heterogeneity by single-cell RNA-sequencing of multi-sector biopsies. Natl. Sci. Rev. *7*, 1306–1318.

Yuan, J., Levitin, H.M., Frattini, V., Bush, E.C., Boyett, D.M., Samanamud, J., Ceccarelli, M., Dovas, A., Zanazzi, G., Canoll, P., et al. (2018). Single-cell transcriptome analysis of

lineage diversity in high-grade glioma. Genome Med. *10*, 1–31.

Yuen, G.J., Demissie, E., and Pillai, S. (2016). B Lymphocytes and Cancer: A Love–Hate Relationship. Trends in Cancer *2*, 747–757.

Zappia, L., and Theis, F.J. (2021). Over 1000 tools reveal trends in the single-cell RNA-seq analysis landscape. Genome Biol. *22*, 301.

Zeiner, P.S., Preusse, C., Golebiewska, A., Zinke, J., Iriondo, A., Muller, A., Kaoma, T., Filipski, K., Müller-Eschner, M., Bernatz, S., et al. (2019). Distribution and prognostic impact of microglia/macrophage subpopulations in gliomas. Brain Pathol. *29*, 513–529.

Zeng, W., Tang, Z., Li, Y., Yin, G., Liu, Z., Gao, J., Chen, Y., and Chen, F. (2020). Patient-derived xenografts of different grade gliomas retain the heterogeneous histological and genetic features of human gliomas. Cancer Cell Int. *20*, 1–12.

Zhang, M., Hutter, G., Kahn, S.A., Azad, T.D., Gholamin, S., Xu, C.Y., Liu, J., Achrol, A.S., Richard, C., Sommerkamp, P., et al. (2016a). Anti-CD47 Treatment Stimulates Phagocytosis of Glioblastoma by M1 and M2 Polarized Macrophages and Promotes M1 Polarized Macrophages In Vivo. PLoS One *11*, e0153550.

Zhang, X., Li, T., Liu, F., Chen, Y., Yao, J., Li, Z., Huang, Y., and Wang, J. (2019). Comparative Analysis of Droplet-Based Ultra-High-Throughput Single-Cell RNA-Seq Systems. Mol. Cell *73*, 130-142.e5.

Zhang, Y., Sloan, S.A., Clarke, L.E., Caneda, C., Plaza, C.A., Blumenthal, P.D., Vogel, H., Steinberg, G.K., Edwards, M.S.B., Li, G., et al. (2016b). Purification and Characterization of Progenitor and Mature Human Astrocytes Reveals Transcriptional and Functional Differences with Mouse. Neuron *89*, 37–53.

Zhao, J., Chen, A.X., Gartrell, R.D., Silverman, A.M., Aparicio, L., Chu, T., Bordbar, D., Shan, D., Samanamud, J., Mahajan, A., et al. (2019). Immune and genomic correlates of response to anti-PD-1 immunotherapy in glioblastoma. Nat. Med. *25*, 462–469.

Zheng, G.X.Y., Lau, B.T., Schnall-Levin, M., Jarosz, M., Bell, J.M., Hindson, C.M., Kyriazopoulou-Panagiotopoulou, S., Masquelier, D.A., Merrill, L., Terry, J.M., et al. (2016). Haplotyping germline and cancer genomes with high-throughput linked-read sequencing. Nat. Biotechnol. *34*, 303–311.

Zheng, G.X.Y., Terry, J.M., Belgrader, P., Ryvkin, P., Bent, Z.W., Wilson, R., Ziraldo, S.B., Wheeler, T.D., McDermott, G.P., Zhu, J., et al. (2017). Massively parallel digital transcriptional profiling of single cells. Nat. Commun. *8*, 14049.

Zhu, H., Acquaviva, J., Ramachandran, P., Boskovitz, A., Woolfenden, S., Pfannl, R., Bronson, R.T., Chen, J.W., Weissleder, R., Housman, D.E., et al. (2009). Oncogenic EGFR signaling cooperates with loss of tumor suppressor gene functions in gliomagenesis. Proc. Natl. Acad. Sci. U. S. A. *106*, 2712–2716.

Zhu, Y., Guignard, F., Zhao, D., Liu, L., Burns, D.K., Mason, R.P., Messing, A., and Parada, L.F. (2005). Early inactivation of p53 tumor suppressor gene cooperating with NF1 loss induces malignant astrocytoma. Cancer Cell *8*, 119–130.

Ziegenhain, C., Vieth, B., Parekh, S., Reinius, B., Guillaumet-Adkins, A., Smets, M., Leonhardt, H., Heyn, H., Hellmann, I., and Enard, W. (2017). Comparative Analysis of Single-Cell RNA Sequencing Methods. Mol. Cell *65*, 631-643.e4.

Zuckermann, M., Hovestadt, V., Knobbe-Thomsen, C.B., Zapatka, M., Northcott, P.A., Schramm, K., Belic, J., Jones, D.T.W.W., Tschida, B., Moriarity, B., et al. (2015). Somatic CRISPR/Cas9-mediated tumour suppressor disruption enables versatile brain tumour modelling. Nat. Commun. *6*, 1–9.

Zülch KJ (ed) (1979) Histological typing of tumours of the central nervous system. World Health Organization, Geneva.